

WL-TR-91-2079

**AD-A260 941**



**FLOW CONTROL OF LOW HEAT LOAD TURBINE AIRFOILS**

Alan H. Epstein, G.R. Guenette, T.D. Stone, W.J. Steptoe  
Massachusetts Institute of Technology  
31-266  
77 Massachusetts Ave.  
Cambridge, MA 02139

February 28, 1992

**FINAL** Report for Period July 1987 - February 1991

Approved for public release; distribution unlimited.



93 1 22 054

**93-01166**



31205

AERO PROPULSION & POWER DIRECTORATE  
WRIGHT LABORATORY  
AIR FORCE SYSTEMS COMMAND  
WRIGHT-PATTERSON AIR FORCE BASE, OHIO 45433-6563

## NOTICE

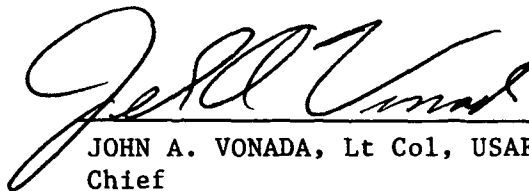
When Government drawings, specifications, or other data are used for any purpose other than in connection with a definitely Government-related procurement, the United States Government incurs no responsibility or any obligation whatsoever. The fact that the government may have formulated or in any way supplied the said drawings, specifications, or other data, is not to be regarded by implication, or otherwise in any manner construed, as licensing the holder, or any other person or corporation; or as conveying any rights or permission to manufacture, use, or sell any patented invention that may in any way be related thereto.

This report is releasable to the National Technical Information Service (NTIS). At NTIS, it will be available to the general public, including foreign nations.

This technical report has been reviewed and is approved for publication.



CHARLES D. MACARTHUR, Ph.D.  
Project Engineer  
Components Branch  
Turbine Engine Division  
Aero Propulsion and Power Directorate



JOHN A. VONADA, Lt Col, USAF  
Chief  
Components Branch  
Turbine Engine Division  
Aero Propulsion and Power Directorate



RICHARD J. HILL  
Acting Deputy for Technology  
Turbine Engine Division  
Aero Propulsion & Power Directorate

If your address has changed, if you wish to be removed from our mailing list, or if the addressee is no longer employed by your organization please notify WL/POTC, WPAFB, OH 45433-6563 to help us maintain a current mailing list.

Copies of this report should not be returned unless return is required by security considerations, contractual obligations, or notice on a specific document.

## REPORT DOCUMENTATION PAGE

1a. REPORT SECURITY CLASSIFICATION Unclassified			1b. RESTRICTIVE MARKINGS	
2a. SECURITY CLASSIFICATION AUTHORITY			3. DISTRIBUTION / AVAILABILITY OF REPORT Approved for Public Release Distribution Unlimited	
2b. DECLASSIFICATION / DOWNGRADING SCHEDULE				
4. PERFORMING ORGANIZATION REPORT NUMBER(S)			5. MONITORING ORGANIZATION REPORT NUMBER(S) WL-TR-91-2079	
6a. NAME OF PERFORMING ORGANIZATION Gas Turbine Laboratory Mass. Institute of Technology	6b. OFFICE SYMBOL (If applicable) 31-265	7a. NAME OF MONITORING ORGANIZATION Aero Propulsion & Power Directorate Wright Laboratory (WL/POTC)		
6c. ADDRESS (City, State, and ZIP Code) 77 Massachusetts Ave. Cambridge, MA 02139		7b. ADDRESS (City, State, and ZIP Code) Wright-Patterson AFB, OH 45433-6563		
8a. NAME OF FUNDING / SPONSORING ORGANIZATION	8b. OFFICE SYMBOL (If applicable)	9. PROCUREMENT INSTRUMENT IDENTIFICATION NUMBER F33615-87-C-2729		
8c. ADDRESS (City, State, and ZIP Code)		10. SOURCE OF FUNDING NUMBERS		
		PROGRAM ELEMENT NO. 61101F	PROJECT NO. ILIR	TASK NO. P7
		WORK UNIT ACCESSION NO. 01		
11. TITLE (Include Security Classification) FLOW CONTROL OF LOW HEAT LOAD TURBINE AIRFOILS				
12. PERSONAL AUTHOR(S) A.H. Epstein, G.R. Guenette, T.D. Stone, W.J. Stentoe				
13a. TYPE OF REPORT Final	13b. TIME COVERED FROM 7/87 TO 2/91	14. DATE OF REPORT (Year, Month, Day) 2/28/92	15. PAGE COUNT 310	
16. SUPPLEMENTARY NOTATION This research was partially funded by the In-House Independent Research Fund.				
17. COSATI CODES			18. SUBJECT TERMS (Continue on reverse if necessary and identify by block number)	
FIELD	GROUP	SUB-GROUP		
			Boundary Layers, Flow Control, Turbine Cooling, Heat Transfer, Riblets	
19. ABSTRACT (Continue on reverse if necessary and identify by block number) The goal of this work was to examine how the heat load to turbines may be reduced by aerodynamic design. The effort consisted of three separate investigations: (1) determination of the effect of small grooves in the flow direction (riblets) on heat transfer, (2) an investigation of the role of inviscid flow aerodynamics on heat load, and (3) examination of the measurement technology required to assess heat transfer and aerodynamic performance in a short duration turbine test facility. For the first effort, a low turbulence, constant wall temperature wind tunnel was constructed with one wall containing riblets. Measurements indicated a maximum of 5% reduction in heat transfer and 7% in skin friction drag. In the second effort, an integral technique was developed to predict laminar flow heat transfer and drag losses for a two-dimensional airfoil. The integral method was incorporated into the ISES inverse design code and comparisons were made to existing calculational methods and experimental data. For the third effort, errors associated with heat transfer and (SEE REVERSE)				
20. DISTRIBUTION / AVAILABILITY OF ABSTRACT <input checked="" type="checkbox"/> UNCLASSIFIED/UNLIMITED <input type="checkbox"/> SAME AS RPT <input type="checkbox"/> DTIC USERS			21. ABSTRACT SECURITY CLASSIFICATION Unclassified	
22a. NAME OF RESPONSIBLE INDIVIDUAL Charles D. MacArthur			22b. TELEPHONE (Include Area Code) 513/255-4830	22c. OFFICE SYMBOL WL/POTC

Block 19 Abstract Con't:

aerodynamic performance measurements in short duration (isothermal) test facilities were found to be small but not negligible. It is shown that these errors can be estimated to sufficient accuracy so that data from short duration facilities will have equal or better accuracy than that from conventional turbine rigs.

Accession For	
NTIS CRA&I	<input checked="" type="checkbox"/>
DTIC TAB	<input type="checkbox"/>
Unannounced	<input type="checkbox"/>
Justification .....	
By .....	
Distribution /	
Availability Codes	
Dist	Avail and/or Special
A-1	

DTIC QUALITY INSPECTED 5



## **EXECUTIVE SUMMARY**

Turbine design has been driven by the need to increase turbine inlet temperature and aerodynamic efficiency while achieving adequate life through cooling. Turbines could be further improved if the aerodynamic design could reduce the heat transfer to the wall. This would benefit the turbine either in the form of higher gas temperature at fixed wall temperature and cooling flow, reduced cooling flow, reduced wall temperature, or some combination of the three. At the current state of the art, this type of integration of the turbine aerodynamics and cooling is still primitive – commonly limited to attempting to preserve laminar flow over as much of the suction surface of the airfoils as possible.

The overall goal of this work was to examine, in a preliminary fashion, how the heat load to turbines might be reduced by aerodynamic design. The effort consisted of three distinct investigations: (1) a look at boundary layer modification to reduce heat transfer, (2) an examination of the role of inviscid flow aerodynamics on heat load, and (3) an estimation of measurement technology required to assess the heat transfer and aerodynamic performance in a modern turbine test facility. This report is thus organized into three independent sections, the important results of which are summarized in the following paragraphs.

An examination of the literature indicated that riblets – shallow wall grooves oriented in the streamwise direction – offered the most promising method of influencing the boundary layer to reduce turbine heat transfer. Riblets have been extensively tested and shown to reduce drag on the order of 5 to 10 percent. Their influence on heat transfer had not been well documented. Since riblets are not well understood theoretically, heat transfer effects could not be established analytically or numerically; an experiment was required.

As a starting point, the influence of riblets on heat transfer in an incompressible, zero-pressure gradient, flat plate boundary layer was parametrically investigated. A two-dimensional, low turbulence, constant pressure, constant wall temperature wind tunnel was constructed with one wall flat and the other with riblets. Measurements were conducted simultaneously on both walls. The walls were heated electrically and the heat flux to the fluid was inferred from a measurement

of the electrical dissipation after accounting for other heat losses. Overall heat transfer coefficient accuracy was estimated at better than 0.5%. The boundary layer profile was measured with traversing probes. The observed drag reduction followed that reported by other investigators reaching a maximum of 7% at 15 wall units. The heat transfer reduction followed that of the drag, reaching a maximum value of 5%, also at 15 wall units.

Overall, the results of these tests were encouraging. Future work in this area might include extending the wind tunnel testing to boundary layers with curvature and pressure gradient and eventually rig testing a turbine with riblets. Should these flat plate results translate directly to similar performance on an engine turbine, a 5 percent reduction in cooling air and a 0.2 to 0.7 percent improvement in aerodynamic efficiency would result. For a large gas turbine, the riblet dimensions would be on the order of 20 microns. Thus, they might be considered a patterning on the surface or thermal barrier coating.

Section 2 of this report deals with the development of a two-dimensional turbine airfoil design tool to facilitate design optimization for minimum heat transfer. In particular, an integral method was developed for predicting heat transfer and boundary layer losses in a two-dimensional airfoil. The objective was to develop a fast computer code capable of predicting loss and heat transfer trends that was compatible with the ISES inverse design code that is widely used by industry for the two-dimensional design of airfoils. By adding the heat transfer to the coupled inviscid-boundary layer formulation of ISES, the optimization of airfoil shape for minimum heat transfer would be facilitated.

Losses and heat transfer in the code were characterized by the boundary layer momentum and enthalpy thicknesses respectively. These integral parameters are calculated by the forward integration of three simultaneous differential equations using closure relations developed from the Falkner-Skan wedge flows. Local heat transfer was estimated from a new empirical integral formula developed from finite difference solutions. The resulting code gave good comparison with a much slower finite difference code. Comparison with experimental data was as good as that with the finite difference code.

Further work in this area would be to fully integrate the new boundary layer solver with the inviscid flow solver and its design optimization tools. Design of optimized nonadiabatic turbine blading could then be attempted.

The third section of this report deals with estimation of the errors associated with measuring heat transfer and aerodynamic performance in a modern, short test duration, turbine test facility as might be best suited to the testing of many of the concepts evolving from the previous two sections.

The analysis centered on estimating the nonadiabatic influences on aerodynamic efficiency measurements arising from the transient nature of short duration testing. These effects are quantitatively small but nonnegligible. It is shown that they can be estimated to sufficient precision so that the aerodynamic measurements in short duration facilities can yield the same or better accuracy data than the more expensive continuous operating ones. The development of new types of instrumentation is not required.

## **TABLE OF CONTENTS**

	<b><u>Page</u></b>
Executive Summary	iii
Table of Contents	vi
 <b>Section One – The Effect of Riblets on Heat Transfer in the Incompressible, Turbulent Boundary Layer Over A Flat Plate</b>	 1
List of Symbols	1
List of Figures	4
List of Tables	6
1. Introduction	7
2. Theoretical and Experimental Background	9
2.1 The Turbulent Boundary Layer Over a Flat Plate	9
2.2 Riblets	22
3. Experimental Design	32
3.1 Design Basis	32
3.2 Experimental Design	34
4. Experimental Apparatus	44
4.1 Wind Tunnel	44
4.2 Instrumentation and Data Acquisition	49
5. Test Procedures	54
5.1 Heat Transfer Measurement	54
5.2 Drag Measurement	54
6. Summary of Data Analysis and Results	56
6.1 Skin Friction Analysis	56
6.2 Heat Transfer Analysis	61
6.3 Estimating Riblet Effect on Turbine Efficiency	65
6.4 Test Results	65
7. Conclusions and Recommendations	69
7.1 Conclusions	69
7.2 Recommendations	70
Appendix A – Statistical and Uncertainty Analysis Terminology and Methodology	71
Appendix B – RTD Calibration Analysis and Error Analysis Methodology and Results	77
Appendix C – Momentum Transfer Analysis, Error Analysis, Programs, and Results	90
Appendix D – Heat Transfer Analysis, Error Analysis, Programs, and Results	119
Bibliography	130
Figures	141
Tables	196
 <b>Section Two – Integral Boundary Layer Heat Transfer Prediction on Turbine Blades</b>	 202
1. Nomenclature	202
1.1 Subscripts	202
1.2 Definitions	202
2. Introduction	206
3. Modes of Heat Transfer	211
3.1 Radiation	211

3.2 Conduction	214
3.3 Convection	214
4. Heat Transfer vs. Aerodynamic Efficiency	216
5. Analysis Code	221
5.1 Integral Boundary Layer Equations	221
5.2 Dimensions & Non-Dimensionalization	222
5.3 Unified Heat Transfer and Loss Prediction Code (UNI)	223
6. Test Cases	229
6.1 Development	229
6.2 Comparison With Experiment	247
7. Discussion and Conclusions	254
7.1 Discussion	254
7.2 Conclusions	257
Bibliography	259
Appendix A – Gaseous Radiant Heat Transfer	262
Appendix B – Derivation of Fundamental Equations	264
 <b>Section Three – Turbine Aerodynamic Performance Measurements                     in Short Duration Facilities</b>	 268
Abstract	268
1. Introduction	268
2. Current State of the Art in Aerodynamic Performance Measurements	270
3. Short Duration Facility Operation	272
4. Short Duration vs. Conventional Turbine Rigs	274
5. Nonadiabatic Turbine Analysis	276
6. Measuring Efficiency	279
7. Measuring Mass Flow	281
8. Instrumentation for Short Duration Facilities	282
8.1 Pressure Measurement	283
8.2 Temperature Measurement	284
8.3 Heat Transfer Measurement	285
8.4 Torque Measurement	285
9. Discussion and Conclusions	286
10. Acknowledgement	288
Bibliography	288
Figures	290

**SECTION 1**  
**THE EFFECT OF RIBLETS ON HEAT TRANSFER IN THE INCOMPRESSIBLE,**  
**TURBULENT BOUNDARY LAYER OVER A FLAT PLATE**

**LIST OF SYMBOLS**

**English Symbols**

a	pipe radius, equation 2.37; RTD calibration coefficient, equation 8.3
A	area; wall law constant, equation 2.22; temperature law intercept, equation 2.61
b	RTD calibration coefficient, equation 8.9; experimental error
B	wall-law intercept, equation 2.21
c	plate temperature variable, equation 3.15
$C_D$	coefficient of drag, $\equiv (D/A) / \frac{1}{2} \rho U_\infty^2$
$C_f$	skin friction coefficient, $\equiv \tau_w / \frac{1}{2} \rho U_\infty^2$
$C_h$	integral Stanton number, $\equiv (Q_w/A) / \rho U_\infty^2 C_p (T_w - T_e)$
$C_p$	specific heat at constant pressure
$C_v$	specific heat at constant volume
D	drag
e	2.718282...
f	function
G	shear velocity integral, equation 2.48
h	enthalpy, equation 2.35; riblet height
H	shape factor, equation 2.31
I	current
k	thermal conductivity
K	shear parameter
l	heated section length
L	length
M	molecular weight
p	pressure
Pr	Prandtl number
q	heat flux per unit area
Q	heat flux
R	resistance; gas constant
$R^2$	coefficient of determination
$\mathcal{R}$	universal gas constant

Re	Reynolds number
St	Stanton Number $q_w / \rho U_\infty^2 C_p (T_e - T_w)$
s	riblet spacing; plate temperature variable, equation 6.1; deviation statistic
T	temperature
u	uncertainty
U	freestream velocity
u, v, w	Cartesian velocity components
V	voltage
w	riblet width; heated section width
W	Coles wake function, equation 2.26
x, y, z	Cartesian components
Z	boundary layer variable, equation 2.54

### **Greek Symbols**

$\alpha$	coefficient of thermal expansivity; RTD calibration coefficient, equation 8.1
$\beta$	Clauser pressure gradient parameter, equation 2.24; RTD calibration coefficient, equation 8.1
$\chi^2$	chi-square statistic
$\delta$	boundary layer thickness; RTD calibration coefficient, equation 8.1; displacement thickness, equation 2.32
$\epsilon$	emissivity, equation 3.8
$\eta$	enthalpy thickness, equation 2.33
$\kappa$	Kàrmàn constant, $\approx 0.4$
$\lambda$	boundary layer variable, equation 2.49; plate temperature variable, equation 3.20
$\mu$	viscosity
$\nu$	kinematic viscosity
$\pi$	3.14159...
$\Pi$	Coles wake parameter, equation 2.27
$\theta$	momentum thickness, equation 2.30
$\rho$	density
$\sigma$	Stefan-Boltzmann constant, equation 3.8; standard deviation
$\tau$	shear
$\Omega$	ohms

### **Subscripts**

b	back
---	------

c	calculated
CVD	Callendar-VanDusen
e	boundary layer edge
ec	effective center
h	heater; heat transfer
i	inner; i-th
l	laminar
m	measured
n	n-th
o	outer; stagnation; constant temperature; at 0°C
p	constant pressure
r	radiative
s	side
SB	Stefan-Boltzmann
t	turbulent
T	thermal
v	constant volume
w	wall
x, y, z	at x, y, x
$\tau$	shear
$\infty$	freestream

### **Superscripts**

'	turbulent fluctuation
*	plate temperature variable; boundary layer displacement thickness
+	law of the wall variable

### **Operators**

$\Delta ( )$	difference
$d( )/d( )$	derivative
$\partial( )/\partial( )$	partial derivative
$\overline{ ( ) }$	time average
$\nabla ( )$	gradient
$\nabla^2 ( )$	Laplacian
$O ( )$	order of magnitude



## **LIST OF FIGURES**

- 2.1. The Distribution of Stress in the Wall Region of a Turbulent Boundary Layer
- 2.2. The Bursting Process
- 2.3. Riblet Placement and Terminology
- 2.4. Drag Reduction of Thin Element Riblets
- 3.1. Stanton Number Measurement Error
- 3.2. Actual and Simplified Tunnel Wall Boundary Conditions
- 3.3. Tunnel Height Setting and Predicted Boundary Layer Thickness @ 10 m/s
- 3.4. Heaters and RTDs in the Pretest Segment
- 3.5. Heaters and RTDs in the Test and Spacer Segments
- 3.6. Pretest Segment Heater Control Circuitry
- 3.7. Test Segment Heater Control Circuitry
- 3.8. Spacer Segment and Guard Heater Control Circuitry
- 3.9. RTD Placement in the Pretest Segment
- 3.10. RTD Placement in the Test Segment
- 3.11. RTD Placement in the Spacer Segment
- 4.1. Wind Tunnel Apparatus
- 4.2. Tunnel Quarter Cross Section
- 4.3. Photograph of the Ribleted Test Plate
- 4.4. Photograph of the Leading Edge of the Ribleted Test Plate
- 4.5. Photograph of a Riblet Cross Section
- 4.6. Thin Film RTD
- 4.7. RTD in Epoxy Plug
- 4.8. Boundary Layer Probe
- 4.9. Calibration Curve for RTD #1
- 4.10. Distribution of RTD Error
- 4.11. Distribution of RTD Chi-squared
- 6.1. Effect of Riblets on Coefficient of Skin Friction
- 6.2. Drag Reduction of Thin Element Riblets
- 6.3. Average Test Section Stanton Number versus Turbulent  
Reynolds Number for the Flat and Ribleted Plates
- 6.4. Effect of Riblets on Integral Stanton Number
- 6.5. Reynolds Analogy Factor Variation with Reynolds Number
- 6.6. Reynolds Analogy Factor Variation with  $s^+$
- C.1. Boundary Layer Thickness versus Reynolds Number for Flat and Ribleted Plates

- C.2. Displacement Thickness versus Reynolds Number for Flat and Ribletted Plates
- C.3. Momentum Thickness versus Reynolds Number for Flat and Ribletted Plates
- C.4. Test of Velocity Profile Repeatability
- C.5. Validation of Velocity Profile Analysis Program
- C.6. Mean Velocity Profiles Fore and Aft of the Flat Test Section at 8.41 m/s
- C.7. Mean Velocity Profiles Fore and Aft of the Ribletted Test Section at 8.41 m/s
- C.8. Mean Velocity Profiles Fore and Aft of the Flat Test Section at 10.08 m/s
- C.9. Mean Velocity Profiles Fore and Aft of the Ribletted Test Section at 10.08 m/s
- C.10. Mean Velocity Profiles Fore and Aft of the Flat Test Section at 10.88 m/s
- C.11. Mean Velocity Profiles Fore and Aft of the Ribletted Test Section at 10.88 m/s
- C.12. Mean Velocity Profiles Fore and Aft of the Flat Test Section at 15.02 m/s
- C.13. Mean Velocity Profiles Fore and Aft of the Ribletted Test Section at 15.02 m/s
- C.14. Mean Velocity Profiles Fore and Aft of the Flat Test Section at 41.65 m/s
- C.15. Mean Velocity Profiles Fore and Aft of the Ribletted Test Section at 41.65 m/s
- D.1. Wall Temperature at 8.48 m/s
- D.2. Wall Temperature at 9.95 m/s
- D.3. Wall Temperature at 10.03 m/s
- D.4. Wall Temperature at 12.47 m/s
- D.5. Wall Temperature at 14.88 m/s
- D.6. Wall Temperature at 20.06 m/s
- D.7. Local Stanton Number over the Flat Plate
- D.8. Local Stanton Number over the Ribletted Plate

## **LIST OF TABLES**

- 4.1. Size and Room Temperature Resistances of the Pretest Segment Heaters
- 4.2. Size and Room Temperature Resistances of the Test and Spacers Segment Heaters
- 4.3. Shunt Resistor Room Temperature Resistances
- B.1 RTD Calibration Results

## 1. INTRODUCTION

A great number and variety of technological applications of interest to the aerospace engineer involve turbulent, convective heat transfer. A few prominent examples are supersonic flight vehicles, heat exchangers, and gas turbine engines. Accurate prediction and control of turbulent heat transfer are of particular importance in the design of the turbine section of aircraft engine gas turbines, where the freestream temperature of the fluid flowing past the turbine blades is above the melting temperature of the blade material. Indeed, the savings from a decrease in the design heat transfer to a turbine blade of a single percent could easily be on the order of hundreds of thousands of dollars. The proven, turbulent drag reduction device riblets shows some potential to effect just such a decrease.

Recent research has validated riblets as a method of reducing turbulent skin friction. Researchers have found that the turbulent drag of a fairly flat surface can be reduced as much as 8 percent by riblets with heights and spacings near 10 wall units, where one wall unit or viscous length is:

$$L_{\tau} \equiv \frac{\nu}{u_{\tau}} = \nu / U_{\infty} \sqrt{\frac{C_f}{2}}.$$

Indeed, Caram and Ahmed (1989) have measured up to 13 percent total drag reduction on a ribletted NACA 0012 airfoil with a freestream Reynolds number of  $2.5 \times 10^5$ .

If the Reynolds analogy, that heat transfer and momentum transfer behave similarly, is valid in this case, this reduction in drag should be accompanied by a corresponding decrease in total heat transfer, which could be used to increase turbine efficiency. If the Reynolds analogy is applicable to riblets, a total reduction in blade heat transfer and hence percent cooling needed of about 5 percent might be expected. The loss in turbine efficiency per percent of cooling air has been estimated to be between 1 and 3 percent. A typical turbine might have 3 to 5 percent cooling air. Thus, the successful application of riblets on a turbine blade might result in a rise in turbine efficiency of between 0.15 and 0.75 percent per cooled blade row, not an insignificant amount. Typical values over the turbulent region of a turbine blade are:  $T \approx 1800$  K,  $U \approx 850$  m/s,  $\nu \approx 6 \times 10^{-5}$  m<sup>2</sup>/s, and  $Re_x \approx 2 \times 10^5$  to  $1 \times 10^6$ , so that  $C_f \approx 4 \times 10^{-3}$ . To obtain riblet height and spacing of around 10 in wall units, the riblet dimensions would therefore have to be on the order of 10 microns, which appears to be feasible. However, previous research in this area has been inconclusive, so that it has not been possible to predict the effect of riblets on heat transfer with any certainty.

The motivation for this project is the desire to determine whether riblets may be used to reduce heat transfer on a turbine blade. Based on this, the specific goals of the project are:

- measure with high accuracy the effects of riblets on flat plate heat transfer,

- determine the relation between this effect and the effect of riblets on skin friction,
- ascertain the dominant parameter or parameters which affect this relation.

Towards these ends, theoretical and experimental backgrounds on both the turbulent boundary layer and riblets are presented. The design criteria and process of a low speed, turbulent boundary layer, heat transfer wind tunnel and test section are detailed. The experimental apparatus, procedure, analysis, and results are described. In depth treatments of the calibration, calibration accuracy, test, and test accuracy analyses are appended.

## **2. THEORETICAL AND EXPERIMENTAL BACKGROUND**

### **2.1. The Turbulent Boundary Layer Over a Flat Plate**

**A. Introduction.** Most flows of interest to the aerodynamicist contain bounded shear layers which exhibit rapid, nonlinear, unsteady motion: turbulent boundary layers. The fluid motion in these regions is so complex that full, analytical solutions are intractable. Indeed, the analysis of turbulent flow is limited to the statistical theory of turbulent correlation functions and the semiempirical analysis of turbulent mean quantities.

The former method is outside the focus of this project and will not be discussed. Similarly, many numerical methods of solving both the integral and differential forms of the time averaged momentum and energy equations using digital computers exist, one survey of which may be found in White (1974), but are outside the scope of this project and so have not been examined.

The mean flow equations used in the experimental design are briefly derived below. The time averaged thin shear layer equations of motion are given. The velocity profile similarity laws are derived via dimensional analysis. The integral form of the equations of motion and the empirical formulae derived from them are described. The White formula for skin friction and its derivation using inner law variables are treated. A brief description of the Reynolds analogy and its use in predicting Stanton number are given.

The coherent structures of the turbulent boundary layer and their ramifications are briefly examined. A comparison is made of the momentum and heat transfer structures in an attempt to gauge the robustness of the Reynolds analogy. Research to date supports the soundness of the basic assumption and its rooting in physical mechanisms, but the accuracy of the results are low enough that no refinement of the analogy with them can be made.

The effect of wall roughness on the turbulent boundary layer is very briefly described. Essentially, each type of roughness has its own particular set of dynamics and mean flow effects and so must be treated individually.

**B. Mean Flow Analysis.** Following the original approach of Reynolds (1895), the properties of the flow are treated as the superposition of a steady element and unsteady fluctuations and analyzed via the time-averaged equations of motion. Incompressible turbulent flow with constant transport properties but with possible significant fluctuations in velocity, pressure, and temperature are considered. Taking coordinates  $x$  parallel to the freestream and  $y$  normal to the wall, a thin shear layer is assumed so that:

$$\frac{\delta}{x} \ll 1,$$

where:

$$\delta \equiv y \quad (\bar{u} = 0.99 U_e),$$

from which follows the standard approximations:

$$\bar{u} \gg \bar{v}$$

and:

$$\frac{\partial}{\partial y}(\ ) \gg \frac{\partial}{\partial x}(\ ).$$

The mean flow structure is assumed to be two-dimensional so that:

$$\bar{w} = 0$$

and:

$$\frac{\partial}{\partial z}(\ ) \approx 0.$$

These assumptions yield for the time-averaged continuity equation:

$$\frac{\partial \bar{u}}{\partial x} + \frac{\partial \bar{v}}{\partial y} = 0, \quad (2.1)$$

x-momentum:

$$\bar{u} \frac{\partial \bar{u}}{\partial x} + \bar{v} \frac{\partial \bar{u}}{\partial y} = -\frac{1}{\rho} \frac{\partial \bar{p}}{\partial x} + \nu \frac{\partial^2 \bar{u}}{\partial y^2} - \frac{\partial \overline{u'v'}}{\partial y} - \frac{\partial \overline{u'^2}}{\partial x}, \quad (2.2)$$

y-momentum:

$$\frac{\partial \bar{p}}{\partial y} = -\rho \frac{\partial \overline{v'^2}}{\partial y}, \quad (2.3)$$

and energy:

$$\rho C_v (\bar{u} \frac{\partial \bar{T}}{\partial x} + \bar{v} \frac{\partial \bar{T}}{\partial y}) = \frac{\partial}{\partial y} (k \frac{\partial \bar{T}}{\partial y} - \rho C_v \overline{v'T'}) + \frac{\partial \bar{u}}{\partial y} (\mu \frac{\partial \bar{u}}{\partial y} - \rho \overline{u'v'}). \quad (2.4)$$

Bernoulli's incompressible relation at the edge of the boundary layer:

$$dp_e = -\rho U_e dU_e, \quad (2.5)$$

can be integrated to obtain:

$$\bar{p} = p_e(x) - \rho \overline{v'^2}. \quad (2.6)$$

Substituting this relation into equations 2.1 through 2.4, with the assumption:

$$\frac{\partial}{\partial x}(\overline{v'^2} - \overline{u'^2}) \approx 0$$

and the notation:

$$\tau \equiv \mu \frac{\partial \bar{u}}{\partial y} - \rho \overline{u'v'}, \quad (2.7)$$

and:

$$q \equiv k \frac{\partial \bar{T}}{\partial y} - \rho C_v \overline{v'T'}, \quad (2.8)$$

yields for x-momentum:

$$\bar{u} \frac{\partial \bar{u}}{\partial x} + \bar{v} \frac{\partial \bar{u}}{\partial y} = U_e \frac{dU_e}{dx} + \frac{1}{\rho} \frac{\partial \tau}{\partial y}, \quad (2.9)$$

and energy:

$$\bar{u} \frac{\partial \bar{T}}{\partial x} + \bar{v} \frac{\partial \bar{T}}{\partial y} = \frac{\partial q}{\partial y} + \tau \frac{\partial \bar{u}}{\partial y}. \quad (2.10)$$

**C. Dimensional Analysis.** Several useful dimensional analyses of the momentum properties of the flow in the boundary layer are based on observation of data of the distribution across the layer of the viscous stress:

$$\mu \frac{\partial \bar{u}}{\partial y}$$

and the turbulent , or Reynolds, stress:

$$- \rho \overline{u'v'}.$$

To allow simple comparison, both terms are nondimensionalized by dividing by  $\rho u_\tau^2$ , where:

$$u_\tau \equiv \sqrt{\frac{\tau_w}{\rho}} = U_e \sqrt{\frac{C_f}{2}}. \quad (2.11)$$

As in figure 2.1, The Distribution of Stress in the Wall Region of a Turbulent Boundary Layer, three regions are apparent: first, the outer layer or inertial sublayer ( $y^+ > 30$ ) where:



$$-\frac{\overline{u'v'}}{u_\tau^2} \gg \frac{du^+}{dy^+},$$

second, the overlap layer or buffer region ( $5-10 < y^+ < 30$ ) where:

$$-\frac{\overline{u'v'}}{u_\tau^2} \approx \frac{du^+}{dy^+},$$

and, third, the inner layer, laminar sublayer, wall region, or viscous layer ( $y^+ < 5-10$ ) where:

$$-\frac{\overline{u'v'}}{u_\tau^2} \ll \frac{du^+}{dy^+}.$$

Dimensional analysis has proved fruitful in describing these different regions.

For the inner region, Prandtl (1933) deduced that:

$$\bar{u} = f(\tau_w, \rho, \mu, y), \quad (2.12)$$

the proper nondimensional form of which is:

$$u^+ = f(y^+), \quad (2.13)$$

where:

$$u^+ \equiv \frac{\bar{u}}{u_\tau}, \quad (2.14)$$

and:

$$y^+ \equiv \frac{y u_\tau}{\nu}. \quad (2.15)$$

Very near the wall, the viscous shear dominates and the velocity profile should be linear to the first order so that equation 2.7 gives:

$$\tau_w \approx \mu \frac{\bar{u}}{y} \quad (2.16)$$

or, after nondimensionalizing:

$$u^+ = y^+. \quad (2.17)$$

Kármán (1930) deduced that in the outer region:

$$U_c - \bar{u} = f(\tau_w, \rho, y, \delta) \quad (2.18)$$

or:

$$\frac{U_e - \bar{u}}{u_\tau} = f\left(\frac{y}{\delta}\right). \quad (2.19)$$

As first noted by Millikan (1938), the two functions must merge smoothly:

$$\bar{u}_i = \bar{u}_o, \quad (2.20)$$

which can only be true if, in the outer layer:

$$u^+ = \frac{1}{\kappa} \ln y^+ + B \quad (2.21)$$

or:

$$\frac{U_e - \bar{u}}{u_\tau} = -\frac{1}{\kappa} \ln\left(\frac{y}{\delta}\right) + A, \quad (2.22)$$

where values of (k,B) of (0.4,5.5) by Nikuradse (1930) and (0.41,5.0) by Coles (1955) and of A of 2.35 by Schultz-Grunow (1940) have been suggested. The useful formula for all three regions:

$$y^+ = u^+ + e^{-\kappa B} \left[ e^{\kappa u^+} - 1 - \kappa u^+ - \frac{(\kappa u^+)^2}{2} - \frac{(\kappa u^+)^3}{6} \right] \quad (2.23)$$

was deduced separately by Spalding (1961) and Kleinstein (1967) by matching the formulas for eddy-viscosity in the inner and log regions. However, experimentally measured velocity profiles, depending very strongly on pressure gradient, diverge from these formulae for  $y^+ > 300$ , often called the wake region. Clauser (1954, 1956) modified the outer law to account for this effect by introducing an equilibrium parameter  $\beta$ :

$$\frac{U_e - \bar{u}}{u_\tau} = f\left(\frac{y}{\delta}, \beta\right), \quad (2.24)$$

where:

$$\beta \equiv \frac{\delta^*}{\tau_w} \frac{dp_e}{dx}. \quad (2.24)$$

With this in mind, Coles (1956) proposed an approximate wake function which could be used to correct equation 2.21:

$$u^+ = \frac{1}{\kappa} \ln y^+ + B + \frac{\Pi}{\kappa} W\left(\frac{y}{\delta}\right), \quad (2.25)$$

where:

$$W\left(\frac{y}{\delta}\right) \approx 2 \sin^2 \left( \frac{\Pi}{2} \frac{y}{\delta} \right) \quad (2.26)$$

and:

$$\Pi \approx 0.8 (\beta + 0.5)^{0.75}. \quad (2.27)$$

**D. Integral Analysis.** Further information about the various boundary layer attributes may be obtained from the momentum and energy equations in their integral form. As in the case of the laminar equations, both 2.9 and 2.10 can be integrated across the boundary layer as suggested by Kármán (1921) with the no-slip/no-jump conditions:

$$\bar{u}(x, 0) = \bar{v}(x, 0) = 0$$

and:

$$\bar{T}(x, 0) = T_w(x)$$

and the freestream matching conditions:

$$\bar{u}(x, \delta) = U_e(x)$$

and:

$$\bar{T}(x, \delta) = T_e(x)$$

to obtain:

$$\frac{d\theta}{dx} + (2 + H) \frac{\theta}{U_e} \frac{dU_e}{dx} = \frac{\tau_w}{\rho U_e^2} = \frac{C_f}{2} \quad (2.28)$$

and:

$$\frac{d\eta}{dx} = \frac{q_w}{\rho U_e C_p (T_e - T_w)} = St, \quad (2.29)$$

where:

$$\theta \equiv \int_0^\infty \frac{\bar{u}}{U_e} \left(1 - \frac{\bar{u}}{U_e}\right) dy \approx \delta \int_0^1 \frac{\bar{u}}{U_e} \left(1 - \frac{\bar{u}}{U_e}\right) d\left(\frac{y}{\delta}\right), \quad (2.30)$$

$$H \equiv \frac{\delta^*}{\theta}, \quad (2.31)$$

$$\delta^* \equiv \int_0^\infty \left(1 - \frac{\bar{u}}{U_e}\right) dy \approx \delta \int_0^1 \left(1 - \frac{\bar{u}}{U_e}\right) d\left(\frac{y}{\delta}\right), \quad (2.32)$$

$$\eta \equiv \int_0^{\infty} \frac{\bar{u}}{U_e} \frac{\bar{h}_{o_e}}{C_p(T_e - T_w)} \left( \frac{\bar{h}_o}{\bar{h}_{o_e}} - 1 \right) dy \approx \delta_T \int_0^1 \frac{\bar{u}}{U_e} \frac{\bar{h}_{o_e}}{C_p(T_e - T_w)} \left( \frac{\bar{h}_o}{\bar{h}_{o_e}} - 1 \right) d\left(\frac{y}{\delta_T}\right), \quad (2.33)$$

$$\delta_T \equiv y \left( \bar{T} = 0.99 T_e \right), \quad (2.34)$$

and:

$$\bar{h}_o \equiv C_p \bar{T} + \frac{\bar{u}^2}{2}. \quad (2.35)$$

A simple solution of the Kármán integral momentum equation for a flat plate, where:

$$C_f \approx 2 \frac{d\theta}{dx}, \quad (2.36)$$

was found by Prandtl (1927) by assuming that the pipe-friction relation:

$$C_f \propto a^{-1/4}, \quad (2.37)$$

holds for a flat plate with  $\delta$  replacing pipe radius  $a$  and by deducing from velocity-profile data that:

$$\theta \approx \frac{\delta}{10}. \quad (2.38)$$

Substituting into the momentum equation and integrating yields:

$$\delta \propto x^{4/5}, \quad (2.39)$$

which can then be used to obtain the following formulae with empirically determined constants:

$$C_f \approx 0.0592 \text{Re}_x^{-1/5}, \quad (2.40)$$

$$\frac{\delta}{x} \approx 0.37 \text{Re}_x^{-1/5}, \quad (2.41)$$

$$\frac{\theta}{x} \approx 0.036 \text{Re}_x^{-1/5}, \quad (2.42)$$

and:

$$\frac{\delta^*}{x} \approx 0.046 \text{Re}_x^{-1/5}, \quad (2.43)$$

where:

$$\text{Re}_x \equiv \frac{U_e x}{\nu}, \quad (2.44)$$

and  $x$  is the the streamwise distance from the apparent turbulent origin.

Another useful empirical relation was formulated along similar lines by Kármán (1931) and Schoenherr (1932):

$$C_f \approx \frac{0.0586}{\log_{10}^2 (2 \text{Re}_\theta) + 0.8686 \log_{10} (2 \text{Re}_\theta)} \quad (2.45)$$

**E. Inner Law Analysis.** A second useful approach to the governing equations, taken by Kestin and Persen (1962), concentrates on using inner-law variables. With the Spalding-Kleinstein formula, the continuity equation can be integrated for  $v$ , from which the convective acceleration can be calculated. Substituting into the  $x$ -momentum equation yields:

$$u \frac{du}{dx} = \frac{\tau}{\mu} \frac{d\tau}{dy^+}, \quad (2.46)$$

which can be integrated to obtain:

$$\tau(x, y) - \tau_w(x, 0) = \mu \frac{du}{dx} G(u^+), \quad (2.47)$$

where:

$$G \equiv \int_0^{y^+} u^{+2} dy^+. \quad (2.48)$$

Evaluating this equation at the outer edge of the boundary layer, where:

$$y = \delta,$$

$$\tau \approx 0,$$

and:

$$u^+ \approx \lambda(x),$$

with:

$$\lambda(x) \equiv \frac{U_e}{u_\tau(x)}, \quad (2.49)$$

yields, after some rearrangement:

$$\frac{U_e}{v} = G(\lambda) \frac{d\lambda}{dx}. \quad (2.50)$$

This can then be integrated to give:

$$\text{Re}_x = \int_0^{\lambda} G(\lambda) d\lambda, \quad (2.51)$$

which in turn can be integrated using the Spalding-Kleinstein formula, equation 2.23, to obtain the most accurate formulae for turbulent skin-friction known presently:

$$G(\lambda) = \frac{1}{3} \lambda^3 + \frac{e^{-\kappa B}}{\kappa^2} \left[ e^Z (Z^2 - 2Z + 2) - 2 - \frac{Z^3}{3} - \frac{Z^4}{4} \right] \quad (2.52)$$

and:

$$\text{Re}_x = \frac{1}{12} \lambda^4 + \frac{e^{-\kappa B}}{\kappa^3} \left[ e^Z (Z^2 - 4Z + 6) - 6 - 2Z - \frac{Z^4}{12} - \frac{Z^5}{20} \right], \quad (2.53)$$

where:

$$Z \equiv \kappa \lambda. \quad (2.54)$$

The form of these equations is, however, rather unwieldy so that the more commonly used form is that of a least-squares approximation made by White (1969):

$$G(\lambda) \approx 8.0 e^{0.48 \lambda}, \quad (2.55)$$

which yields the simpler formula, accurate to 2 percent:

$$C_f \approx \frac{0.455}{\ln^2 (0.06 \text{Re}_x)}. \quad (2.56)$$

**F. The Reynolds Analogy.** The basis of most analyses of heat flux and temperature distribution in the turbulent boundary layer is still the analogy of Reynolds (1874). In this analogy, a dimensionless ratio is formed of the Boussinesq eddy-viscosity and eddy-conductivity called the turbulent Prandtl number:

$$\text{Pr}_t \equiv \frac{C_p \mu_t}{k_t}, \quad (2.57)$$

where:

$$\mu_t \equiv - \frac{\overline{\rho u'v'}}{\partial \bar{u} / \partial y} \quad (2.58)$$

and:

$$k_t \equiv - \frac{\rho C_p \overline{v'T'}}{\partial \bar{T} / \partial y}. \quad (2.59)$$

Reynolds postulated that since momentum and heat flux are equivalent phenomena:

$$Pr_t = f(Pr) \approx O(1).$$

From this, a law of the wall is expected for the temperature profile similar to that of velocity.

Kármán (1939) provided a method of calculating this profile by noting that the ratio of heat flux and shear was approximately constant across the boundary layer:

$$\frac{q}{\tau} = \frac{k + k_t}{\mu + \mu_t} \frac{d\bar{T}}{d\bar{u}} \approx \frac{q_w}{\tau_w}.$$

By introducing the turbulent Prandtl number, this may be separated and rewritten in the non-dimensional form:

$$T^+ \equiv \frac{(\bar{T} - T_w) \rho C_p u_\tau}{q_w} = \int_0^{\bar{u}} \frac{1 + \mu_t/\mu}{1/Pr + \mu_t/\mu Pr_t} d\bar{u}. \quad (2.60)$$

For Prandtl number near unity, this can be integrated using the Spalding-Kleinstein relation.

However, the algebra is quite complicated so that it is more convenient to use a curve fit for the log layer provided again by White (1974):

$$T^+ \approx \frac{1}{\kappa} \ln y^+ + A(Pr), \quad (2.61)$$

where:

$$A(Pr) \approx 12.8 Pr^{0.68} - 7.3. \quad (2.62)$$

This law of the wall and the velocity log law can be evaluated at  $\delta$  and the former subtracted from the latter to give:

$$q_w \left[ \frac{U_e}{u_\tau} + (A - B) \right] \approx (T_w - T_e) C_p \tau_w, \quad (2.63)$$

which can be used to form the Reynolds analogy. Kármán's approximation to this formula, including a temperature correction for variable viscosity:

$$St = \frac{C_f}{2 Pr^{0.4} (T_w/T_e)^{0.4}} \quad (2.64)$$

was found by Reynolds et al. (1958) to be accurate to within 4.5 percent. Although this analogy has received much attention, such as in Kestin and Richardson (1963) and Taylor et al. (1990), no

simple improvement has yet been found.

**G. Coherent Structures.** One way of testing the assumptions of the Reynolds analogy is to examine the correspondence, if any, between the physical structures of the two modes of transport in the boundary layer. The investigation of ordered structures in the turbulent boundary layer began with Fage and Townsend (1932). The existence of coherent vortical structures in the wall layer and their key role in the production of turbulence were first hypothesized by Theodore von Kármán (1952). The measurements of Laufer (1954) and Klebanoff (1954) showed that both the production and dissipation of turbulent energy peak near the outer edge of the wall layer ( $y^+ \approx 11.5$ ). In the past two decades, much interest has arisen over the coherent eddy structures observed in turbulent boundary layers in the near wall region. Most researchers agree that these reacting parcels of vortical fluid control the dynamics of the boundary layer and are responsible for the majority of transport of momentum, heat, and mass.

One particular sequence of quasi-deterministic, randomly located coherent structures collectively called the bursting process was identified by Kline et al. (1967) and Kim et al. (1971) as playing a key role in the production of new turbulence and the transport of turbulence within the boundary layer on smooth walls. A sketch of this is shown in Figure 2.2, The Bursting Process. This process is actually a conceptual grouping of many elements:

- streamwise vortices,
- low speed streaks,
- inflectional velocity profiles,
- lifting and oscillation of the streaks,
- ejection from the wall of a portion of low-momentum fluid, or a burst,
- a large-scale sweep of the wall by high-momentum outer fluid.

Blakewell and Lumley (1967) were the first to show that previous hot-wire anemometry velocity data in turbulent pipe-flow were consistent with a pair of counter-rotating streamwise vortices in the near wall region ( $y^+ < 50$ ) by using a set of space-time correlations with an orthogonal decomposition theorem. Later analysis by Blackwelder and Eckelman (1978) suggested that these structures have a lateral wavelength of  $\approx 100$  wall units, a streamwise length of  $\approx 1000$  wall units, and random occurrence in space and time. Kim and Moin (1979) found that these vortical structures tend to angle upwards at  $\approx 45$  degrees. Jang et al. (1986) have proposed a mechanism for their production by using weakly nonlinear perturbation methods to show that direct resonance theories exhibit a mean secondary flow consistent with their existence. Aubry et al. (1988) have carried out an extremely complicated modelling of the wall region with dynamical systems and bifurcation theory and claim that the resulting equations model the behavior of streamwise rolls which exhibit the characteristics of the counter-rotating vortices described above.



However, a "vortex" is not a mathematically well-defined entity and streamwise vorticity is difficult both to calculate and to measure. Indeed, if their existence were not strongly supported by the visualization studies of Head and Bandyopadhyay (1981) and Smith and Schwartz (1983), few would not be skeptical of their existence.

The pair of vortices is thought to produce between them low speed streaks, which are easily observed and therefore well-accepted. These structures have random length scales with a width of  $\approx 20$  wall units and a length of  $\approx 1000$ . Oldaker and Tiederman (1977) and later Smith and Metzler (1983) found a lognormal distribution of their spacing with an average of  $\approx 100$  wall units and a most probable value of  $\approx 80$ . The latter found an average persistence of  $\approx 480$  wall time units, with some streaks lasting up to 2500.

In the later stages of their evolution, the streaks lift up perpendicularly from the near wall region. Offen and Kline (1974) showed that this lift-up is typically 100 to 400 wall units long. At a height above the wall between 10 and 20 wall units, oscillation begins. Kline et al. (1967) and Emmerling (1973) estimate oscillation wavelengths of  $\approx 200$  wall units, but little data exist because the oscillation period is very brief. Suggestions have been made that this oscillation and the resulting breakup are due to the spanwise and streamwise inflectional profiles, but current inflection instability theory is valid only for steady, two-dimensional situations and so this cannot be corroborated.

Downstream of the lift-up, parcels of low speed fluid are ejected to between 20 and 50 wall units, often in groups of two or more. As the parcels reach closer to 50 wall units, they develop a chaotic motion and breakup, dispersing and mixing with the outer layer. As indicated by Nakagawa and Nezu (1981), this is responsible for the majority of turbulence production at this height. A sweep of high speed fluid from the outer layer follows the mixing and disperses the small scale mixing motion. Falco (1979) estimated the sweeps to be  $\approx 100$  wall units square.

Further details of the bursting process and coherent structures in general exist in abundance in surveys such as A.K.M.F. Hussain (1983), R.F. Blackwelder (1988), and Kline and Robinson (1988) to name three, but they are not germane.

As with mean flow analysis, most research and analysis effort in the study of coherent structures in the turbulent boundary layer until fairly recently have concentrated upon momentum properties, with the result that the relationship between the near wall structures and heat flux is much less clear than with shear. Zaric (1972a, 1972b, 1973, 1974, 1975) appears to have been the first to study the statistical relationship between the momentum and the heat transfer in the near wall region on a smooth surface. These and other studies summarized in Khabakhpasheva (1986) reported close correspondence between the two modes of transfer. More recently, Khabakhpasheva (1988), Nagano and Hishida (1988), Perepelitsa (1988), Kasagi (1988), Slanciauskas (1988), and Kays and Moffat (1988) have shown conclusive evidence that for the

canonical smooth, flat plate, turbulent boundary layer, instantaneous turbulent heat transfer is strongly associated with and dominated by the coherent turbulent momentum structures. All have noted a similarity between the more obvious coherent momentum structures such as streaks and bursts and equivalent coherent heat flux structures. Perry and Hoffman (1976) found that the momentum bursts and sweeps were accompanied by similar occurrences in heat flux  $\approx 75$  percent of the time. Iritani et al. (1983) used temperature-sensitive liquid crystal display tunnel walls and hydrogen bubbles to verify the existence of high-temperature streaks, their association with  $\approx 70$  percent of the low-speed streaks, and a spacing within 10 percent of the spacing of the low speed streaks. They further observed low temperature streaks with  $\approx 72$  percent of the sweep events.

As in the research that has concentrated on direct examination through measurement of  $C_f$  and  $St$ , the research on the physical structures of heat and momentum transfer seems to indicate that the basis of the Reynolds analogy is sound to within the accuracy of the current experimental methods and instrumentation for the canonical, smooth, flat-plate case. Unfortunately, this accuracy is low enough to prevent using the results to refine the analogy and, even if this were not the case, no results are available for noncanonical cases. Indeed, while this conceptual model of the primary method of turbulence production in the wall boundary layer has provided a useful framework within which to organize and direct boundary layer research, it has yet to provide quantitative prediction schemes of use to the engineer.

**H. The Effects of Wall Roughness.** Surface roughness has only a minor effect on laminar flow because the laminar boundary layer is entirely dominated by viscous effects. Indeed, Gatski and Grosch (1984) have shown that for low speeds the pressure drag associated with laminar flow over roughness elements is almost exactly equal to the skin friction drag on the equivalent flat surfaces.

Even small roughness elements on the solid surface of a turbulent boundary layer will break up the viscous layer and cause a dramatic increase in vertical momentum exchange, however, resulting in higher bursting frequency and intensity as well as skin friction. A large body of research, one survey of which may be found in Clauser (1956), on many types of rough walls has shown that roughness has the effect of shifting the mean velocity profile downward a constant amount that only weakly depends upon the type of roughness. Studies such as Grass (1971) and Lewkowicz and Das (1978) have shown that the flow dynamics very near the roughness elements are altered in magnitude but not in general nature. Therefore, the assumption that the lowest possible skin friction attainable in a turbulent boundary layer is that over a smooth wall has usually been made.

In the last decade, however, researchers have discovered that each type or class of roughness has its own set of dynamics and mean flow effects. In particular, a surface with small

ribs aligned in the streamwise direction, or riblets, has lower total skin friction than a smooth surface under certain flow conditions.

## **2.2. Riblets**

**A. Introduction.** Riblets are very small ribs placed into the turbulent boundary layer in alignment with the freestream for the purpose of reducing skin friction. A simple picture of their placement and the terminology, height  $h$ , width  $w$ , and spacing  $s$ , used in their description is presented in Figure 2.3, Riblet Placement and Terminology.

Experiments have shown that the data for the variation of riblet drag reduction with riblet height and spacing approximately collapse onto one curve of similar shape when plotted as the ratio of the drag of the ribleted test plate to the drag of the flat test plate minus one versus spacing in law of the wall units. This curve is shown for riblets of various ratios of height to spacing in Figure 2.4, Drag Reduction of Thin Element Riblets. Each curve has two distinct regions: a "drag bucket" or region of drag reduction for  $h^+$  between  $\approx 5$  and  $\approx 25$  wall units, with maximum drag reduction of  $\approx 7$  percent at  $h^+ \approx 10$  wall units, and a drag increase region for  $h^+$  above  $\approx 25$  wall units, with the rate of drag increase with  $h^+$  proportional to aspect ratio ( $h/s$ ). The core of riblet research and validation was done primarily by Walsh in the late 70's and early 80's at NASA Langley.

The Langley work aroused great interest in both research and industry circles. In the area of research, many papers have been published in the last 5 years on riblets in an attempt to understand better the mechanism behind them. In industry, most large companies in fields where drag is important, such as aerospace, maritime, pipe transmission, etc., have looked at the possible application of riblets in their areas. The 3M corporation manufactures vinyl laminates with riblet surfaces, which have already been used successfully on yachts and planes. British Maritime Technologies has developed a versatile method of molding riblets into a thermoplastic coating which may be economically sprayed onto many surfaces.

Many mechanisms of riblet drag reduction have been proposed but, as yet, no consensus has been formed on which theory, if any, is valid. The most likely mechanism seems to be the damping of turbulent fluctuations near the base of the riblets. Many researchers, however, feel that more than one mechanism is at work.

No conclusive research has been conducted on the effect of riblets on heat transfer.

**B. Previous Research into Riblet Effects on Skin Friction and Turbulent Boundary Layer Structure.** The first person to examine the possibility of reducing the turbulent drag of a surface with riblets seems to have been Liu in 1966 at Stanford University. As part of a process of

studying the bursting process and its effect on turbulent shear, Liu (1966) and Liu et al. (1966) hoped to use the riblets to suppress the finer scale near wall turbulence and confine the turbulent bursts to their initial propagation region. Although they measured reduction in bursting rates of 20 to 25 percent and two instances of possible drag reduction of up to 3 percent in their range of  $h^+=45-110$  and  $s^+=190-370$ , they did not feel that their data indicated sufficient turbulence suppression to result in tangible overall drag reduction. In addition, they encountered the problem that has plagued all riblet and most turbulent boundary layer research: the accuracy of the experiment is the same order of magnitude as the effect under scrutiny.

Bath (1968) was led to consider the possibility of reducing pressure drop in pipelines with riblets by reports of turbulent skin friction reduction near a corner. He performed a semi-empirical analysis of riblets based on the data from these reports from which he predicted the possibility of significant drag reduction at  $h^+=10-20$ . Kennedy et al. (1973) attempted to test this prediction. However, numerical discrepancies are present in their paper. They claimed to have tested at  $h^+=20$  but print figures which, if correct, indicate that they instead tested at much higher values. At their test point, whatever it was, they found skin friction per surface area reduction but no total drag reduction.

In the late 70's and throughout the 80's, the ideas of Liu and Bath were validated at NASA Langley as part of the drag reduction programs of D.M. Bushnell outlined in:

- Hefner and Bushnell (1977),
- Bushnell (1983),
- Hefner et al. (1983),
- Wilkinson et al. (1987),
- Bushnell and McGinley (1989).

Apparently, initial interest at NASA was generated in the early 70's by observations of reduced drag on aerospace vehicles with very small, streamwise-aligned cooling fins. Over the course of their research in the 70's and 80's, the effect of riblets on skin friction, including repeatable total drag reduction of up to 7 percent, was measured with a variety of riblet shapes and sizes over the entire range of  $h^+$ ,  $s^+$  and  $h/s$ , and their use in reducing total aircraft drag was validated. This was primarily due to the careful and systematic work of M.J. Walsh:

- Walsh and Weinstein (1978, 1979),
- Walsh (1980, 1982, 1983, 1985, 1990a, 1990b),
- Walsh and Lindemann (1984),
- Walsh et al. (1988, 1989),
- Walsh and Anders (1989).

Other research at Langley on riblets includes Lindemann (1985), Lazos and Wilkinson (1987a, 1987b), Wilkinson (1988), and Lazos (1989). Walsh and Weinstein (1978, 1979) tested

rectangular, triangular grooved, razor blade, semicircular grooved, and alternating transverse curvature riblets. They obtained up to 4 percent drag reduction with two of the triangular grooved models. Walsh (1980) further tested the drag characteristics of triangular or V-groove and transverse curvature riblets, with in depth boundary layer tests over the V-groove model, and found up to 7 percent drag reduction for  $h^+$  below 30. This analysis was continued in Walsh (1982, 1983) and Walsh and Lindemann (1984), confirming the aspects of the "drag bucket" at various Reynolds numbers and attempting to optimize the riblet geometry. Walsh (1985) examined the preliminary results of the application of riblets on a Learjet, estimating a possible overall drag reduction of 4 percent, with side benefits such as increased corrosion resistance, reduced cabin leakage, and reduced paint need. Walsh et al. (1988, 1989) obtained up to 6 percent drag reduction on the riblet test sections applied on the fuselage of the Learjet at flight conditions. Walsh (1990a) ascertained that small deviations in the peak geometry of riblet films suitable for application on commercial transport can result in up to 40 percent degradation in drag reduction performance. Lazos and Wilkinson (1987a, 1987b) obtained up to 8 percent drag reduction with "thin-element" rectangular riblets and Lazos ascertained that riblet performance is unaffected by average aircraft skin contamination. Wilkinson (1988) determined that suction and blowing do not increase the drag reduction ability of riblets measurably. Walsh and Anders (1989) and Walsh (1990b) have provided in depth summaries of the riblet research performed to date.

During the same period, riblet research was being conducted in Germany based on observations of the squamation, or ribbed scales, of certain sharks (although the author has heard a story, probably apocryphal, from someone who worked under Dennis Bushnell that his interest in riblets was initially spurred by examination of the skin of a shark he caught in the Chesapeake Bay). Although biologists have known of the very fine ribs on the scales of certain sharks for almost a century, the first to speculate on the fluid dynamic purpose of these structures were the Russian scientists Burdak (1969) and Chernyshov and Zayets (1970) in the late 60's. Later work by Reif (1982), Reif and Dinkelacker (1982), Rashi and Musick (1984), and Reif (1985) confirmed the existence of riblet-like structures on shark scales aligned with the skin surface flow and of the same order of magnitude in size in wall units as riblets. Spurred on by these observations, Nitschke (1983) and Dinkelacker et al. (1988) measured up to 3 percent drag reduction due to riblets in pipe flow; Bechert et al. (1985, 1987) confirmed the findings of Walsh; Bechert (1987) experimented with three-dimensional riblets but found no addition to the drag increase over that of regular riblets, and Bartenwerfer and Bechert (1987) and Bechert and Bartenwerfer (1989) attempted a theoretical analysis of riblets, the demerits of which are discussed below.

Other basic corroborations of Walsh's results include:

- Hooshmand et al. (1983),

- Bacher and Smith (1985a, 1985b),
- Chen (1986),
- Khalid (1986),
- Wallace and Balint (1987),
- Enyutin et al. (1987),
- Sawyer and Winter (1987),
- Savill (1987),
- Reidy (1987),
- Pulles (1988).

Coustols et al. (1987), Reidy and Anderson (1988), Choi et al. (1989), and Rohr et al. (1989) have studied riblets in tandem with some other drag reduction device. The characteristics of riblets at high subsonic and transonic speeds were examined by Squire and Savill (1987, 1989), Gaudet (1989), and Coustols (1989). Gaudet (1989) has estimated the penalties of off-design operation. A list of studies of the use of riblets in some application and the application under research would include:

- Johansson and Alfredsson (1985)- ship drag reduction,
- Eilers et al. (1985)- sailboat drag reduction,
- Choi et al. (1987)- yacht drag reduction,
- McLean et al. (1987)- Learjet drag reduction,
- Anon. (1987a)- the same,
- Beauchamp and Phillips (1988)- drag reduction on an axisymmetric body,
- Valkenberg (1988)- bobsled drag reduction,
- Caram and Ahmed (1989)- airfoil drag reduction,
- Truong and Pulvin (1989)- diffuser efficiency rise, and
- Lin et al. (1990)- control of turbulent flow separation over a ramp.

The effect of riblets on the structure of the turbulent boundary layer has been studied by:

- Gallagher and Thomas (1984),
- Nieuwstadt et al. (1986),
- Djenidi et al. (1987a, 1987b),
- Choi (1985, 1986, 1988),
- Choi and Johnson (1989),
- Pulles et al. (1989).

Choi (1988, 1989), Vukoslavcevic et al. (1987), Djenidi et al. (1988), and Pearson (1989) have suggested various drag reduction mechanisms. The effect of riblets on skin friction in the laminar boundary layer has been examined in Khan (1986), de Saint Victor (1987), Djenidi et al. (1987a, 1988, 1989), and Launder and Li (1989) as well as in several unpublished papers

summarized in Coustols and Savill (1989). In addition to those coming from NASA Langley, recent surveys of riblet research include Choi (1984), Guezennec and Nagib (1985), Savill et al. (1988), and Coustols and Savill (1989).

Despite this large body of research, some disagreement exists on the basic effects of riblets on the turbulent boundary layer structure. For example, a rich variety of conflicting data has been reported on the effect of riblets on the bursting process. Hooshmand et al. (1983), Hooshmand (1985), and Pulles (1988) found an increase in burst frequency over riblets. Bacher and Smith (1985a, 1985b), and Pulles et al. (1989) found no change. Walsh (1982) found no change in frequency but a drop in intensity. Liu (1966), Liu et al. (1966), Gallagher and Thomas (1984), and Savill (1987) found a reduction in frequency. Choi (1989) found a substantial increase in frequency but a drop in burst duration of almost 50 percent.

Researchers do show agreement, however, that low speed fluid is entrained between the riblets, damping and displacing upwards the turbulent fluctuations. That riblets damp rms turbulent fluctuations by up to 10 percent in the lower half of the boundary layer for  $s^+ < 50$  wall units has been shown by:

- Walsh (1980),
- Hooshmand et al. (1983),
- Nitschke (1983),
- Hooshmand (1985),
- Vukoslavcevic (1987),
- Lazos and Wilkinson (1987b),
- Choi (1989),
- Pulles et al. (1989).

In addition, Kozlov et al. (1989) have shown evidence of an increase in transition Reynolds number of 20 to 50 percent over riblets under low freestream turbulence level conditions. Furthermore, Bacher and Smith (1985a, 1985b), Gallagher and Thomas (1984), Lazos and Wilkinson (1987b), and Choi (1989) found an increase in streak spacing over riblets of  $\approx 30$  percent.

Lazos and Wilkinson (1987b) found evidence of discontinuous doubling of vertical distance of the point of peak turbulence intensity above thin-element riblet "valley floors" at  $s^+ \approx 50$  wall units. This result would seem to point to the existence of a minimum value of riblet spacing below which a significant percentage of the turbulent fluctuations is excluded from the groove. That this value of spacing is approximately one-half the average spanwise streak spacing has been taken as evidence of interaction between riblets and the coherent structures of the turbulent boundary layer. However, questions remain as to why the value of riblet spacing at which the discontinuity occurs should be one-half the streak spacing and not some other multiple. Further,

this discontinuity is not accompanied by any corresponding discontinuity in drag, so that one may conclude either that this characteristic is a second-order effect with minor influence on mean values or that it was produced by some probe-model interference.

Research on riblets in tandem with some other drag reduction scheme, such as polymers or LEBUs, has shown that the drag reduction effect is essentially additive. Research on yaw has shown that riblet drag reduction decreases linearly with yaw rise to zero at about 30 degrees. Similarly, researchers have found that riblet drag reduction decreases linearly with pressure gradient rise to zero at  $\beta \approx 0.5$ . No degradation in riblet performance due to high subsonic and transonic freestream flow has been observed. Despite the results of Bechert (1987), very recent research on three-dimensional riblets summarized in Coustols and Savill (1989) suggests that they might be used to increase maximum total drag reduction to as much as 11 percent.

Interest has arisen recently on riblet use in laminar flow. Computational treatments such as Khan (1986), de Saint Victor (1987), Djenidi et al. (1987a, 1988, 1989) as well as several unpublished papers summarized in Coustols and Savill (1989) indicated the possibility of up to 4 percent drag reduction due to riblets in the laminar boundary layer. This has not been encountered experimentally and more recent computational work such as Launder and Li (1989) has cast some doubt on the past calculations. Further discussion of these views is presented below in section 2.2.D.

**C. Previous Research into Riblet Effects on Heat Transfer.** Only three studies have been done on the effect of riblets on heat transfer to date that the author is aware of, all inconclusive: Walsh and Weinstein (1978, 1979) and Lindemann (1985). All found that the Reynolds analogy factor, the ratio of the Stanton number to half the coefficient of friction, was changed by anywhere from -10 percent to +30 percent, depending on the particular riblet model. The variation of the ratio of riblet heat transfer to flat plate heat transfer in these studies seems very generally to follow the same characteristics as the drag reduction but, since the scatter of the data is so large, in both cases this is difficult to tell. However, minimal heat transfer data were taken in the region of drag reduction in Walsh and Weinstein (1978, 1979) and, furthermore, the heat transfer effects are not presented versus riblet height or spacing in wall units. Again, in Lindemann (1985), the Reynolds analogy factors measured are shown, but not any specific drag or heat transfer effects versus height or spacing in wall units.

**D. Suggested Riblet Drag Reduction Mechanisms.** Almost as many suggestions for riblet drag reduction mechanisms have been made as papers on riblets published, none with any wide success. A list of the more plausible suggestions would include reduction in some burst parameter, thickening of the viscous sublayer, streamwise vorticity diffusion, and reduction in



turbulent intensities.

Various studies have suggested that riblets affect burst frequency, duration, and intensity. However, the bursting process is not rigorously defined. Further, some questions, which time constraints prevented the author from examining in any detail, have arisen as to the validity of the VITA burst detection method currently used by researchers. As well, Gallagher and Thomas (1984) have detected significant spanwise variation of the burst parameters over riblets. Until these three problems have been resolved, it would be premature to draw any conclusions about the effect of riblets on bursting as a mechanism. In addition, the technique most often used to detect thickening of the viscous sublayer is the measurement of the decrease in bursting rates, so that the same conclusions must be drawn about this mechanism as well as its association with bursting.

Some agreement appears to exist that the longitudinal pair of vortices associated with bursting are indeed more widely spaced over riblets. Bacher and Smith (1985a) have proposed that the riblets act to dampen these vortices by allowing the production of secondary opposing vortices at their peaks. As yet, this secondary vorticity has not been detected, but it might well be beyond the resolution of today's instruments.

Pearson (1989), hypothesizing that vorticity data in the turbulent boundary layer are as well explained by one vortex as by two, has used the technique he developed in Pearson and Abernathy (1984) coupled with conformal mapping to show that riblets act to diffuse a single time-evolving vortex, which should then reduce skin friction. Two critical weaknesses are immediately apparent in this theory: the assumption of a single vortex and the use of conformal mapping.

The first assumption is based on the fact that the time averaged vorticity data can be as well explained by a pair of counter rotating vortices as by one vortex rotating one direction half the time and the other way the other half. However, many of the flow visualization studies appear to show pairs of vortices. Computations of  $w$  from the continuity equation using conditionally sampled data of  $u$  and  $v$  as done in Choi (1989) seem to bear this out.

The use of conformal mapping, the second weak link in the analysis, is predicated on the argument that the mean convective terms and the Reynolds stress term in the Navier-Stokes equations are very tiny near the riblets. However, while this is true in the riblet valleys, it does not seem to be true near the peaks, and it is certainly not true at the height at which the presence of the vortices has been measured. Furthermore, while the absolute value of the turbulent fluctuations does indeed asymptote to zero at the wall, so does the mean velocity, with the consequence that the relative local turbulence level reaches a maximum and constant value, determined in studies such as Klebanoff (1954), Spalart (1986), Kim et al. (1987), and Alfredsson et al. (1988) to be approximately 0.4, throughout the viscous region. Indeed, if one ignores these terms, then one is in actuality analyzing the laminar boundary layer, the aspects of which in relation to such an approach are discussed below.

In addition, and perhaps more critically, even if such assumptions were valid, the method of conformal mapping would be incapable of producing any quantitative predictions about the effect of riblets on skin friction because inviscid theory does not give realistic results near a solid boundary. The only way to satisfy the no-slip condition at a solid boundary in inviscid theory is to specify arbitrarily some type of flow with zero velocity at the boundary, such as Couette flow over a stationary wall, in which trivial case the predicted skin friction is merely the viscosity times the specified value of the slope of the Couette flow at the wall. The theory of Bechert and Bartenwerfer (1989) of a correspondence between an apparent riblet height and drag reduction is also based on inviscid theory and conformal mapping and so is limited in usefulness to the generation of orthogonal computational grids.

Some researchers have argued that if the mechanism of riblet drag reduction were purely viscous, riblets should work in the laminar boundary layer as well as the turbulent. Many computational treatments of riblets in the laminar boundary layer have been performed, primarily due to the relative simplicity of the calculations involved. The use of conformal mapping in these treatments to calculate skin friction effects, and hence the treatments themselves, are invalid for the same reason as in the treatments of the turbulent boundary layer described above. Other researchers have used finite element techniques to perform similar calculations predicting up to 4 percent drag reduction. Some questions have arisen, however, as to the numerical accuracy of the computational grids used in these studies. As pointed out in Launder and Li (1989), Djenidi et al. (1988) used only four calculational nodes in the upper quarter of the riblet peak, the region where 90 percent of the drag of their computational model occurred. Since insufficient grid refinement in viscous flow finite element analyses may lead to drag underestimation, their drag reduction results could be due to numerical error. Neither experimental research nor calculations by Launder and Li (1989) using a very fine mesh have detected any such laminar riblet drag reduction.

The evidence seems to indicate that it would be incorrect to assume that the drag reduction can be explained without accounting for turbulent effects. In particular, the finding of Kozlov (1988), that riblets delay transition by 20 to 50 percent, can be explained only by the damping of turbulent fluctuations. In this vein, many researchers have noted that the riblets have the effect of creating a higher apparent spanwise viscosity in the wall region similar to that found in a turbulent boundary layer near a corner in studies such as Bragg (1969).

Indeed, one of the first suggestions of the possibility of using riblets to reduce turbulent drag, the empirical analysis of Bath (1968), was based on the data contained in Nikuradse (1926, 1930) and Leutheusser (1963) of decrease in skin friction near a corner. Bath assumed that between the riblets and halfway up their side the skin friction may be calculated by a non-dimensionalized fit of these sets of data and that on the top half of the riblets the skin friction is equal to some constant,  $M$ , times the flat wall skin friction. He then integrated to obtain the drag

for a variety of values of riblet height, spacing, and  $M$ . His results indicated that if  $M$  is  $\approx 5$  or less than for riblet heights less than 20 wall units, drag reduction will occur for  $s^+$  between 5 and 100 wall units, with a minimum between 10 and 20 wall units. That such a simple, empirical approach predicted correctly the ranges of drag reduction seems to indicate strongly that riblet drag reduction can be explained by viscous damping of the turbulent fluctuations alone.

The author notes that the effect of riblets on the turbulent fluctuations is highly similar to the damping of shear turbulence by a transverse magnetic field. In particular, the percent damping of the Reynolds stress as shown in Walsh (1980) and Pulles et al. (1989) is almost the same as that present in a magneto-hydrodynamic flow with values of the ratio of Hartmann number to Reynolds number of  $\approx 100$ , as shown in Lykoudis (1980). Unsurprisingly, the reduction in turbulent skin friction and hence drag for this value of Hartmann to Reynolds number are approximately 10 percent, very close to that of riblets.

**E. Predicting Riblet Effects On Heat Transfer.** The standard method of calculating heat transfer effects, the Reynolds analogy, is of dubious value in predicting the effects of riblets on heat transfer for two reasons. The first reason is that its accuracy is the same order of magnitude as the probable effect of the riblets. Second, its validity depends upon local conditions such as surface roughness. Specifically, Walsh and Weinstein (1978) note in their survey of the field that the rise in heat transfer due to wall roughness has always been found to be less than the rise in drag. More recent studies of "spire" geometry roughness, however, have shown net heat transfer reduction in the presence of drag rise.

The previous research on heat transfer over riblets is problematical for many reasons. The three studies at NASA Langley measured heat transfer effects varying from 10 percent reduction to 40 percent increase. The first difficulty in applying their results is that their data are not presented versus riblet height or spacing in wall units. The second is the extremely large scatter, the same order of magnitude as the effect measured, of the data as it is presented. Third, the research was performed before the optimization of riblet drag reduction and so may not represent the heat transfer effects at the point of maximum drag reduction. Fourth, the author notes that while the repeatability claimed in Walsh and Weinstein (1978, 1979) and Lindemann (1985) was quite small (2 percent), the experimental error of the measurements, although not mentioned, must certainly be higher than that. The author bases this on the fact that their driving temperature differential was only 5 degrees Fahrenheit (compared with 25 at the Stanford heat transfer facilities described in Moffat and Kays (1984), the acme of the field) and the fact that they used thermocouples, a temperature measuring device the accuracy of which is estimated in Eckert and Goldstein (1976) and Anon. (1988) to be 0.2 degrees Fahrenheit or above. Thus, the error of their temperature differential measurement would be at least 5 percent!

Riblets could have four possible effects on heat transfer: a rise, none at all, a decrease, or variable effect depending upon some flow or riblet property which does not affect the momentum transfer. Although the latter case seems the most unlikely, no convincing indications exist as to which of the other three is the most probable.

### **3. EXPERIMENTAL DESIGN**

#### **3.1. Design Basis**

**A. Project Goals.** This project was motivated by the desire to increase turbine efficiency via decreasing turbine blade heat transfer. Therefore, the overall project objective is to gage the potential for using riblets to reduce turbulent convective heat transfer on a turbine blade. Towards this end, the specific primary goal is to measure with high accuracy the effects of riblets on turbulent convective heat transfer. In addition, secondary goals are to examine the relation between this effect and the effect of riblets on turbulent skin friction, and to determine the dominant parameter or parameters, if any, which affect this relation.

**B. Design Criteria.** Based on these goals, the primary criteria of the design were taken to be:

- heat transfer measurement accuracy,
- the ability to test at appropriate riblet spacing in wall units,  
and the following secondary criteria were chosen:
- skin friction measurement accuracy,
- the ability to test at streamwise distance Reynolds numbers similar to those of the turbulent section of a typical turbine blade.

The primary criterion of heat transfer measurement accuracy was based on the primary goal of the project. A major difficulty in research into the effect of riblets on the turbulent boundary layer is the limits of the accuracy of current measurement techniques. The difficulty is that this accuracy is often the same magnitude as the effects under scrutiny. Since the primary goal of this project was to measure the effect of riblets on heat transfer, the accuracy of the heat transfer measurement was taken as a primary design criteria to obviate this difficulty. The effect of riblets on drag is on the order of a single percent. The Reynolds analogy indicates that the effect on heat transfer should be the same order of magnitude. Therefore, to resolve the effect on heat transfer, the heat transfer measurement accuracy should be less than 1 percent. Based on this, the level of accuracy of plus or minus half a percent was taken as the major design objective.

The primary criterion of ability to test at appropriate riblet height was based on the project objective. According to the Reynolds analogy, reduction in heat transfer is most likely to occur during reduction in skin friction. The project objective focuses on the reduction of heat transfer. To maximize the chance of measuring heat transfer reduction, the ability to test at riblet heights and spacings, where skin friction reduction is likely to occur, was taken as a design criterion.

The secondary criterion of skin friction measurement accuracy was motivated indirectly by

the primary goal, since the skin friction must be known accurately to determine the wall unit scaling length, and directly by the secondary goal of ascertaining the relation between riblet effect on heat transfer and on skin friction.

The secondary criterion of test Reynolds number was based on the project objective. Although the effect of riblets does not seem to be a strong function of Reynolds number, many boundary layer characteristics are. Thus, to be certain that the measured results could be applied to a turbine blade, the ability to test at Reynolds numbers equal to those that might be expected on the turbulent region of a turbine blade was chosen as a secondary criterion. As mentioned in the introduction, this Reynolds number range is  $2 \times 10^5$  to  $1 \times 10^6$ .

**C. Design Constraints.** Two design constraints, other than the ubiquitous ones of finite time, money, and experience, were the tunnel dimensions and flow regime and the limits of riblet machining available.

**D. Design Parameters.** The design parameters were:

- riblet type, height (h), and spacing (s);
- test section streamwise distance (x);
- freestream velocity ( $U_\infty$ );
- wall temperature ( $T_w$ );
- test plate width (w) and thickness (t);
- heater number ( $N_H$ ), size ( $x_{Hi}$ ), and resistance ( $R_i$ );
- temperature sensor type, number, and location.

**E. Design Process.** Because of the difficult nature of accurately measuring skin friction and heat transfer in the turbulent boundary layer, careful error analysis was incorporated into the design process from the very first stages and is described in some detail, both in Section 3.2 and in Appendix D.

The base of the design process of choosing values for the design parameters consisted of deciding upon the general configuration of the experiment. This decision for both the skin friction and heat transfer aspects of the experiment was based upon the standards of previous research. Given the general configuration, the riblet physical type and size were determined from the limits of machining available for the project and the limitations due to the heat transfer aspects of the research. The range of test riblet spacing in wall units was determined from a survey of the NASA Langley research results. These parameters, coupled with the velocity range of the wind tunnel, then determined the streamwise distance of the test section necessary for various test section Reynolds numbers. Based on these determinations, the test section was sized. The

physical details of the design of the test walls themselves were established from considerations of the limitations imposed by having to machine the riblets directly onto one of the test walls and of the measurement accuracy of different heat transfer configurations. Tunnel wall test temperature was chosen to minimize heat transfer measurement error. Given the desired wall temperature, heater sizes were determined so as to minimize the streamwise variations in this temperature, and hence the measurement error, due to the discreteness of their heat flux input. Their size and necessary heat flux input, coupled with the power supplies available, set the heater control circuitry needs. Based on these needs and the available electronics, the circuitry was designed. The type of temperature sensors used in the experiment was chosen for accuracy and affordability. Their size and placement were determined from the dimensions of the tunnel wall and heaters.

### **3.2. Experimental Design**

**A. Test Configuration.** The starting point for the test design was the search for a general configuration suited to the standards of previous research on riblet skin friction effects, coherent structures, and momentum transfer as well as that on heat transfer in the turbulent boundary layer.

In the first three areas, the standard experimental configuration centers around the canonical, flat plate, turbulent boundary layer case. The standard features of this case are:

- a flat, solid wall, smooth other than the presence of the transition trip and riblets in riblet experiments,
- a fully turbulent boundary layer,
- zero pressure gradient,
- two-dimensional mean flow,
- steady outer flow with low freestream turbulence,
- Newtonian, single phase, incompressible test fluid,
- no force fields.

This case is the simplest and easiest to test and analyze because it contains the least number of independent parameters possible without curtailing the validity and applicability of the results. Furthermore, it is a momentum transfer research community standard, allowing the widest comparison of test results. For these two reasons, the momentum transfer aspects of the experiment were designed around this canonical case.

In the realm of heat transfer research, two standards prevail: constant heat-flux and constant temperature test walls. In each of these cases, the streamwise length of the heated wall upstream of the test section, the heated starting length, may vary from the starting length of the momentum boundary layer to nothing. A configuration of constant temperature wall with heated starting length equal to the momentum boundary layer starting length was chosen so as to simplify

the design calculations, allow for direct comparison of  $C_f$  and  $St$ , minimize forward test section heat loss, decrease the sensitivity of the temperature boundary layer to variations in wall temperature in the test section, and to enhance similarity between momentum and heat transfer conditions. In addition, this configuration is what would be expected on a turbine blade, since the amount of cooling flow used in a turbine blade is determined from how much cooling is needed to keep the blade temperatures below a certain upper limit and not vice versa.

To avoid one of the primary sources of measurement error, the repeatability of a particular flow state in comparing test runs, the standard practice of simultaneous testing of flat and ribletted areas was incorporated into the design. The most common riblet test configuration, adjacent ribletted and flat test sections, ensures the most similar boundary layer conditions and so is the optimum for determining effect on skin friction. However, this setup does not allow for simple thermal isolation of the test sections from each other. For this reason, it was decided to have two separate, heated walls on opposite sides of the tunnel, one with a flat test section and one with a ribletted test section, termed A side and B side respectively. As in the majority of riblet tests, the riblets were designed to begin far enough before the test section to allow flow adjustment, generally several inches, as well as to cover the entire test section. To ensure equal buoyancy effects upon the heated air over the two test sections, these walls were oriented vertically.

**B. Riblet Type and Physical Size.** Choice of riblet type and size was based on machining and heat transfer limitations. Most riblet research uses the plastic V-groove type riblet laminates manufactured by 3M. However, the plastic from which the laminate is made is unsuitable for use in a heat transfer experiment. Thus, the choice of riblet type was limited to what could reasonably be machined in the lab machine shop into a test plate suitable for heating. The simplest such configuration is the thin-element-type riblet, rectangular grooves with extremely fine ribs, validated by Lazos and Wilkinson (1987).

The spacing was constrained to 0.020 in, the smallest width of jeweller's circular saws generally available. Riblet height was chosen to be 0.015 in by taking the height-to-spacing ratio of the optimum riblet configuration of Lazos and Wilkinson (1987). The material of the heated walls was taken to be Aluminum both for the relative ease of machining it and for its high conductivity, which it was hoped would tend to decrease the temperature variation in the test section due to heater misadjustment. Lengthy trial machining on Aluminum plate indicated that, with the available equipment, a riblet width of 0.005 in was the minimum attainable without riblet deformation.

**C. Test Range of Riblet Spacing in Wall Units.** According to the Reynolds analogy, the most likely situation for heat transfer reduction is during maximum drag reduction. The ability to



be able to test under conditions of maximum drag reduction is therefore necessary to fulfill the second primary design criteria. As can be seen in Figure 2.4, Drag Reduction of Thin Element Riblets, the optimum condition for height-to-spacing ratio of about 0.8 is  $s^+ \approx 10$ . The region of drag reduction is  $s^+ < 20$  and sufficient range to cover the variation of the riblet effect on transfer is obtained from  $s^+ = 10$  to 50. Based on these observations, the test range of  $s^+ = 10$  to 50 was taken with the focus of  $s^+ = 10$  to 15 as a possible point of maximum reduction.

**D. Test Section Sizing.** The test section streamwise distance was constrained by the wind tunnel velocity range, the riblet physical size and range of test spacing in wall units, and the test Reynolds numbers. The wind tunnel designated for use in the experiment had a flow regime of freestream velocity from 15 to 45 m/s. The values of test section Reynolds number predicated by the second of the secondary design criteria thus constrain the test section streamwise distance since, from equations 2.11, 2.15, 2.44, and 2.56:

$$h^+ = f(h, U_\infty, C_f, \text{test fluid}) = \frac{h}{L_\tau} = \frac{h u_\tau}{\nu} = \frac{h U_\infty \sqrt{\frac{C_f}{2}}}{\nu}, \quad (3.1)$$

$$C_f = f(Re_x) \approx \frac{0.455}{\ln^2(0.06 Re_x)}, \quad (3.2)$$

and:

$$Re_x = f(U_\infty, x, \text{test fluid}) = \frac{U_\infty x}{\nu}, \quad (3.3)$$

where  $x$ , the apparent turbulent streamwise distance, is approximately the streamwise distance. For  $Re_x \approx 2 \times 10^5$  to  $1 \times 10^6$ ,  $C_f \approx 4 \times 10^{-3}$ . At room temperature and pressure, the viscosity,  $\nu$ , of the tunnel working fluid, air, is approximately  $1.8 \times 10^{-5}$  N-s/m<sup>2</sup>. Therefore, in the region of optimum drag reduction, from equation 3.1:

$$U_\infty = \frac{h^+ \nu}{h \sqrt{\frac{C_f}{2}}} \approx 8 \text{ to } 10 \text{ m/s}, \quad (3.4)$$

lower than the original velocity regime of the wind tunnel, but close enough to be reached with minor modifications to the apparatus. The approximate streamwise location of the test section for the desired test regime is then, from equation 3.3:

$$x = \frac{\text{Re}_x v}{U_\infty} \approx 0.5 \text{ to } 2.25 \text{ m} \quad (3.5)$$

The general dimensions of the test section inlet area, 8.1 cm by 24.29 cm, were sized to fit the tunnel contraction built and attached to the wind tunnel during previous research activities. This section area constrained the streamwise distance for the desired velocity range to below 2 m to avoid pipe flow in the test section. Due to the space limitations of the test cell and for simplicity sake, this was decreased to 1.8288 m.

To allow for testing at a particular Reynolds number over the entire range of  $s^+$ , a modular tunnel section form was chosen. The modules were to consist of groups of heated strips which could be used to form the two test walls by attachment to the tunnel frame in different combinations, making it possible to position the test segment at different streamwise distances.

The particular modules chosen for the tunnel configuration were the pretest section, 0.9144 m in length, to ensure fully developed, similar heat and momentum transfer turbulent boundary layers; the test section, 0.3048 m in length; and two 0.3048 m length spacer sections. To allow flush abutment of the sections, the tunnel frame was designed with four rails along each corner of the tunnel onto which the wall segments could be bolted, allowing test section midpoint streamwise distances of 1.066 m, 1.371 m, and 1.676 m. A heat-resistant clear plastic was chosen as the material for the two side walls to allow visually dependent probe positioning and the possibility of flow visualization.

**E. Test Wall Design.** Given the riblet machining experience and general tunnel layout, the configuration of the heaters was chosen. The most common design of heated elements comprising the test wall of a heated boundary layer experiment as evident in, for example, Satterlee (1955), Reynolds (1958), Reynolds et al. (1958a, b), or Moffat and Kays (1985), is that of thin, thermally insulated, individually heated, metal strips with heat flux gages to measure side and back losses. Several elements of this type of design were rejected in an attempt to increase measurement accuracy as well as to compensate for the constraints imposed by the necessity of machining the riblets directly onto the B side test section.

Trial and error in the lab machine shop indicated that the only way to ensure riblet uniformity and alignment to within 5 percent of riblet height, or 25 microns, was to machine them into a single, precision plate. Therefore, all the individually heated strips to be ribletted were sized from a single precision plate, rebonded and thereby thermally insulated with syntactic foam epoxy, and then, in the resulting single plate, machined to specifications. To allow this latter plate to withstand the stresses of machining and attachment to the tunnel frame without having to include some type of strengthening member perforating, and so compromising by some unknown amount

the effectiveness of the epoxy insulation, the number of epoxy joints was minimized by insulating the individual test sections only from the surrounding guard heater sections and not from themselves. This, it should be pointed out, sacrificed the accuracy of the resolution of the heat transfer measurements within the test section relative to one another for the sake of the viability of the entire ribletted plate, but not the accuracy of the heat transfer measurements as a whole. Evaluation of this feature of the design in practice and its influence on the results are presented in Section 6 and Appendix D.

Research into the limits of the current heat flux gage technology led the author to conclude that the back and side heat losses could be more accurately measured with the use of adjustable guard heaters and direct insulation temperature measurements.

**F. Setting Wall Temperature.** Given the general physical dimensions of the test section, the operating wall temperature was constrained by the goal of high accuracy of  $St$  measurement. From an energy balance of the  $i$ -th heated section of tunnel wall, the convected heat flux at the wall surface at the streamwise midpoint of the section is:

$$q_{w_i} = \frac{Q_{h_i} - Q_{b_i} - Q_{s_i}}{A_i} - q_{r_i}, \quad (3.6)$$

where  $Q_{h_i}$  is the heat flux from the  $i$ -th heater,  $Q_{b_i}$  the back loss of the  $i$ -th section,  $Q_{s_i}$  the side losses from the  $i$ -th section, and  $q_{r_i}$  the radiated surface heat loss. The Stanton number is then, from equation 2.29:

$$St_i = \frac{q_{w_i}}{\rho U_e C_p (T_{w_i} - T_e)}. \quad (3.7)$$

The primary source in error in  $St_i$  is the error in  $T_{w_i}$ , contributed through the driving temperature differential,  $(T_{w_i} - T_e)$ , and the radiated heat loss,  $q_{r_i}$ . The latter is given by Stefan-Boltzmann Law of Radiation:

$$q_{r_i} = \epsilon \sigma (T_{w_i}^4 - T_e^4), \quad (3.8)$$

where  $\epsilon$  is the emissivity of the body surface and  $\sigma$  the Stefan-Boltzmann constant. Using a Taylor series approximation as described in Appendix C, the error in Stanton number is thus:

$$u_{St_i} \approx \sqrt{u_{T_{w_i}}^2 \left( \frac{St_i}{T_{w_i} - T_e} \right)^2 + u_{q_{r_i}}^2 \left( \frac{1}{\rho U_e C_p (T_{w_i} - T_e)} \right)^2}, \quad (3.9)$$

where:

$$u_{q_{ri}} \approx u_{T_{wi}} 4 \epsilon \sigma T_{wi}^3. \quad (3.10)$$

To minimize this error, the most accurate, affordable temperature measurement device was chosen for use: thin-film, platinum resistance temperature detectors (RTD's) with a four-wire resistance measurement configuration. The minimum error attainable with such a configuration and the calibration apparatus available were estimated to be  $\approx 0.1^\circ \text{C}$ . For this value and the general design parameter values above, the error in Stanton number, approximately a function of  $T_{wi}$  only, is shown versus  $(T_{wi} - T_e)$  in Figure 3.1, Stanton Number Measurement Error. As can be seen, the primary reduction in Stanton number error occurs below  $50^\circ \text{C}$ . Because the minor reduction in error above  $50^\circ \text{C}$  would be offset by other factors such as viscosity variation, this was taken as the design driving temperature differential.

**G. Heater Sizing.** The width of each of the heated strips was determined from a simplified thermal analysis of the tunnel walls. The governing equation for two-dimensional heat transfer with no heat generation in a medium with temperature invariant properties is Laplace's equation:

$$\nabla^2 T = 0. \quad (3.11)$$

The actual and simplified boundary conditions for the tunnel walls are shown in Figure 3.2, Actual and Simplified Tunnel Wall Boundary Conditions. The actual boundary conditions for the tunnel walls along the center span, ignoring back and side losses, as shown in the top of Figure 3.2, are so complicated that an analytical solution is not tractable. These boundary conditions consist of laminar and turbulent convective, as well as radiation, heat flux out of the flow side of the strips and the discrete heater heat flux into the individual strips on the other. The shaded rectangle represents one of the two heated tunnel walls. The more darkly shaded section within this rectangle is the  $i$ -th heated strip, of length  $l_i$ , located at a streamwise distance  $x_i$ , with  $Q_i$  heat flux input. The simplified boundary conditions shown below the actual ones are an approximation for the  $i$ -th heated strip. In the simplified case, radiation effects are assumed to be negligible. The simplified boundary conditions are thus: one, insulated ends:

$$\frac{\partial T}{\partial x^*} (x^* = 0) = \frac{\partial T}{\partial x^*} (x^* = l_i) = 0, \quad (3.12)$$

where:

$$x^* \equiv x - x_i + \frac{l_i}{2}, \quad (3.13)$$

two, linear approximation of the convective heat flux out of the top of the strip using the value of the flux and its slope calculated at the midpoint from some empirical formula:

$$\frac{\partial T}{\partial y} (x^*, y = w) = \frac{1}{k} \left( q_{w, x_i} + c \left( 1 - \frac{2x^*}{l_i} \right) \right), \quad (3.14)$$

where:

$$c \equiv \frac{\partial q_{w, x_i}}{\partial x} \frac{l_i}{2}, \quad (3.15)$$

and, three, constant heater heat flux into the bottom of the strip:

$$\frac{\partial T}{\partial y} (x^*, y = 0) = - \frac{q_{w, x_i}}{k}, \quad (3.16)$$

where heat flux is defined positive into the strip. All four of these boundary conditions are linear but only the first two are homogeneous, so that simple solution by separation of variables is not possible. However, this simplified case may be broken down further into the superposition of the trivial one-dimensional problem:

$$\frac{dT}{dy} = - \frac{q_{w, x_i}}{k}, \quad (3.16)$$

and the simpler two-dimensional problem with boundary conditions 3.12:

$$\frac{\partial T}{\partial y} (x^*, y = 0) = 0, \quad (3.17)$$

and:

$$\frac{\partial T}{\partial y} (x^*, y = w) = \frac{c}{k} \left( 1 - \frac{2x^*}{l_i} \right). \quad (3.18)$$

Three of these are homogeneous so that a solution may be found via separation of variables and the use of Fourier series representation and then superposed with the one dimensional solution to give:

$$T(x^*, y) = T_w - \frac{q_{w, x_i}}{k} (y - w) + \sum_{n=0}^{\infty} \frac{8c/k}{\lambda_n^3 l_i^2 \sinh(\lambda_n w)} \cosh(\lambda_n y) \cos(\lambda_n x^*), \quad (3.19)$$

where:

$$\lambda_n \equiv \frac{2n+1}{l_i} \pi. \quad (3.20)$$

With this formula, the streamwise temperature differential across strip  $i$  for various lengths  $l_i$  can be calculated from the predicted boundary layer values of Stanton number given the streamwise

transition distance.

A transition Reynolds number of  $1 \times 10^5$  was chosen to ensure both that no transition would occur spontaneously before the trip position and that at and past the transition point, the boundary layer would be unstable and hence remain turbulent. This Reynolds number then constrained the boundary layer trip position to be 11.43 cm.

Given the transition point, the flat plate solution for laminar boundary layer thickness, given in Blasius (1908) as:

$$\frac{\delta}{x} = \frac{4.950}{Re_x^{0.5}}, \quad (3.21)$$

was solved with equation 2.41, under the constraint that at transition:

$$\delta_1 = \delta_t,$$

for the apparent turbulent origin. The Blasius solution for laminar skin friction:

$$C_f = \frac{0.664}{Re_x^{0.5}}, \quad (3.22)$$

was then used with equations 2.41, 2.42, 2.43, 2.56, 2.64, and 3.21 to solve for the boundary layer values along the tunnel walls for various test speeds.

The actual flow area calculated from the displacement thickness was used to iterate for a tunnel wall angle setting for each segment that produced flow as close to zero pressure gradient as possible. Given flow of velocity  $u$  in the direction  $x$  through a rectangular duct of width  $l$  and height  $h$  with a boundary layer displacement thickness along each wall  $\delta^*$ , the actual flow area is:

$$A_{flow} = (l - 2\delta^*) (h - 2\delta^*). \quad (3.23)$$

If the height can be adjusted to any new value  $h'$ , then the new height which gives a zero pressure gradient is:

$$h' = 2\delta^* + \left( \frac{l}{l - 2\delta^*} \right) h. \quad (3.24)$$

The values given by this equation throughout the flow regime were used in choosing the height setting at each of the wall height adjusters that most closely approximated zero pressure gradient flow. Half this tunnel height setting is shown in Figure 3.3, Tunnel Height Setting and Predicted Boundary Layer Thickness @ 10 m/s, not to scale.

Given the actual tunnel area as a function of streamwise distance, the velocity and pressure gradients for various flow conditions can be calculated. From the design values of height setting, the effect on the velocity is given by continuity to be:

$$\frac{du}{dx} = - \frac{u}{A} \frac{dA}{dx}. \quad (3.25)$$

The boundary layer values along the tunnel walls at their actual can then be calculated from this freestream velocity and the streamwise distance. The boundary layer thickness and the displacement thickness determined via this method are plotted in Figure 3.3 in their actual positions relative to the tunnel wall. From the x-momentum equation, the pressure gradient resulting from the velocity gradient is:

$$\frac{dp}{dx} = - \rho u \frac{du}{dx}, \quad (3.26)$$

or, after nondimensionalizing and substituting in equation 3.25:

$$\beta \equiv \frac{\delta^*}{\tau_w} \frac{dp}{dx} = - \rho u \frac{\delta^*}{\tau_w} \frac{du}{dx} = 2 \frac{\delta^*}{C_f} \frac{1}{A} \frac{dA}{dx}. \quad (3.27)$$

Calculations indicated that this pressure gradient parameter for the tunnel wall height settings chosen was below 0.01 for the regime of tunnel freestream velocity below 15 m/s, practically zero pressure gradient and certainly low enough to have no measurable effect on riblet performance.

Equations 2.21, 2.23, and 2.25 through 2.27 were used to calculate velocity profiles immediately fore (denoted as position 1) and aft (denoted as position 2) of the test section. These profiles were then used to plan the boundary layer traversals.

From these results, equation 3.19 was used to find the streamwise strip lengths,  $l_i$ , in the three-foot pretest section such that the streamwise temperature differential across the strip was less than 0.1° C for test speeds less than 20 m/s and less than 0.05° C for test speeds less than 10 m/s, except at the leading edge of the heated section. These lengths are shown along with the general dimensions of the pretest section in Figure 3.4, Heaters and RTD's in the Pretest Segment.

In the test segment, a uniform strip length of 5.08 cm was chosen to give temperature differentials less than 0.02° C for test speeds less than 20 m/s and less than 0.01° C for those less than 10 m/s. The side guard heaters in the test segment were sized to be 15.24 cm by 4.445 cm to prevent the boundary layers of the clear side tunnel walls from interfering with the flow over the test section. The width of the border of epoxy insulating the test section from these guard heaters was sized to be 0.15875 cm from the constraint that the heat flux through the epoxy for a driving temperature differential of 0.1° C be less than 1 percent of the convective heat transfer. These lengths are shown along with general dimensions in Figure 3.5, Heaters and RTD's in the Test and Spacer Segments.

In the spacer segments, strip lengths of 15.24 cm were determined to be sufficient. Their configuration is also shown in Figure 3.5.

**H. Heater Circuitry Design.** Given the strip dimensions and the boundary layer values, the wall heat flux was integrated to determine the minimum heater flux needed for each strip heater at each test condition. Since only four power supplies were available for the experiment, the heaters were divided into four sets of parallel circuits. The heater resistances were chosen to give a maximum power density of  $1.55 \text{ W/cm}^2$  to allow the tunnel walls to be heated to operating temperature within 1 hour. From the heater resistances and power inputs, the necessary voltages were determined. The voltage of each circuit was taken to be the maximum of the heater voltages needed in that circuit. The ideal resistance values of the heater control circuitry necessary to allow the proper drop in voltage for the rest of the heaters in the circuit were then determined for each planned test point. The actual resistance values were determined by taking a safety factor of 1.5. The resulting heater control circuitry design is shown in Figures 3.6 through 3.8.

The heater type was chosen to be etched foil elements to avoid the deformation of the test plates necessary for the use of types such as wire inlays as well as the complexity of types such as fluid heat exchangers.

**I. Temperature Sensor Type and Placement.** For the purpose of sufficiently resolving the surface temperature of the tunnel walls, the general figure of three sensors per heated strip was taken. The order of magnitude of the number of temperature sensors was then determined from the number of heaters to be 150. The actual number was constrained to 140 by the data acquisition system purchased for the experiment. The geometry of the riblets prevented the emplacement of any sensor on or flush with the tunnel wall surface, so that the sensors were restricted to placement from the rear of the heated strips some finite distance beneath the surface. For simplicity, the sensors were designed to be cylindrical plugs that would fit into precisely reamed, flat bottom holes with the platinum sensing element parallel to the plane of the heated wall surface. To conserve money, miniature, rectangular, thin-film sensors were set into the bottom of cylindrical plugs of thixotropic epoxy in Teflon molds. The epoxy with thermal conductivity and coefficient of thermal expansion closest to those of Aluminum was chosen. The distance of the sensing element beneath the wall surface was chosen to be 0.254 cm so as to prevent, first, any chance of sensor deformation of the surface, especially on the ribleted side, and, second, detecting any local temperature distribution effects caused by the riblets, while still having the temperature of the sensor be within  $0.01^\circ \text{ C}$  of the temperature of the wall surface for test speeds below 10 m/s. The RTD labelling is shown in Figures 3.4 and 3.5 and their placement in Figures 3.9 through 3.11.

Further details of the test apparatus are given in Section 4, Experimental Apparatus.



## **4. EXPERIMENTAL APPARATUS**

### **4.1. Wind Tunnel**

**A. Introduction.** The low speed wind tunnel used in the experiment, shown in Figure 4.1, Wind Tunnel Apparatus, consisted of an inlet, a compressor, and the following segments: orientation, turbulence diffuser, contraction, pretest, test, and spacer. Directions parallel to the flow are referred to as streamwise and denoted by the symbol  $x$ ; directions perpendicular to the flow and parallel to the plane of the test walls, the vertical plane, are termed spanwise and denoted as  $z$ ; and, those perpendicular to both the flow direction and the test walls, the horizontal and  $y$ .

**B. Inlet.** The inlet, designed and constructed by A. Bodenhorn, was a tube of 5052 Aluminum sheet, 33.97 cm in diameter and 76.2 cm in length, with three outer wooden ribs and a large, tear-drop cross-section shaped, wooden lip, 58.42 cm in outside diameter.

Because the original exit velocity range of the apparatus, 15 to 45 m/s, was higher in the original configuration than the desired experimental range of 8 to 40 m/s, two layers of coarse wire mesh and three layers of fine wire mesh were positioned across the mouth of the blower inlet and sealed around the edges to produce the desired drop in total pressure.

**C. Compressor.** The compressor, a 5-Hp Westinghouse Silentvane, type BSY-4103, consisted of a single stage, radial fan, with 8.26-cm-wide blades and a tip radius of 15.56 cm, rotating at a nominal speed of 1725 rpm. Exit velocity was controlled by variable angle, noncambered, inlet guide vanes. The vane angle was set by depressing or raising a steel rod. The rod was attached, through a universal joint, to a lever which rotated the hub upon which the leading edges of the vanes were hinged. After positioning, the rod was secured with a clamping bracket bolted to the inlet wall. The exit area of the blower was a rectangle 24.45 cm by 32.7 cm, with the longer side oriented vertically.

Further description of the inlet and compressor may be found in Bodenhorn (1982).

**D. Orientation, Turbulence Diffusion, and Contraction Segments.** The orientation segment, 30.48 cm in length, was built from 1.9-cm plywood to turn this orientation 90 degrees.

The turbulence diffuser and contraction segments were built from 1.27-cm Plexiglass. The turbulence diffuser segment, 48.26 cm in length, contained three honeycomb layers. The honeycomb sheets, 5.08 cm thick, with honeycomb sides 1.59 mm wide, were positioned 2.54 cm apart. The contraction segment was 53.34 cm long and had a contraction ratio of 4 to 1. The final flow area exiting into the pretest segment was 24.29 cm by 8.098 cm.

The different segments were bolted together with a 1.59-mm layer of silicon rubber tape at the joins to prevent leakage. Internal rough spots on the tunnel walls were sanded smooth and any indentations were filled with clear epoxy and auto body filler in the Plexiglass sections and wood filler in the plywood section and then also sanded smooth. These segments were supported by a Unistrut, steel U-beam frame, modified to allow levelling of the tunnel.

**E. Tunnel Frame.** The tunnel frame consisted of two sets of two Unistrut U-beams, onto each of which were bolted the two clear, Lexan walls and the two sets of discrete sections of removeable, heated, wall which comprised the pretest, test, and spacer segments.

The base of the tunnel frame consisted of four 1.8336-m lengths of 3.49-cm by 4.13-cm Unistrut U-beams, formed from 2.38-mm-thick, extruded, stainless steel. These members were bolted in pairs with two, 1.27-cm by 3.175-cm by 12.38-cm Aluminum brackets at each end, which in turn were bolted onto 9.525-mm-thick Aluminum end plates to form the tunnel frame parallelopiped.

The end plates were rectangular, metal sheets, 42.069 cm by 23.336 cm in outside dimension, with a rectangular hole the size of the contraction exit flow area in the fore plate and the size of the maximum flow area required for zero pressure gradient flow at the lowest design speed in the aft plate machined from their centers. The fore plate was bolted permanently to the contraction segment while the rear plate was supported by a second Unistrut frame which allowed streamwise and spanwise tunnel levelling.

The clear side walls, Lexan polycarbonate sheets, 1.27 cm by 7.779 cm by 1.84309 cm in size, were bolted directly to the inside of the Unistrut tunnel frame using 0.635-cm 1/4-20 Helicoil inserts set into the Lexan at 15.24-cm intervals. Silicon sponge tape insulation, 1.59 mm thick, was applied to their surfaces of contact with the heated walls. Three types of probe ports were machined into the Lexan walls at various positions: pitot-static probe ports, boundary layer, and hot-wire.

The pitot-static and hot-wire ports were located at the horizontal or y midpoint of the Lexan walls at streamwise distances equal to the midpoints of the four tunnel segments, the former in the bottom Lexan wall and the latter in the top, so as to allow positioning of the probe tips in the geometric centers of each segment parallelopiped. The pitot-static ports were 3/8-27 threaded holes with 4.76-mm inset lips. The probes were passed through the ports and secured at the correct position and flow relative angle with 3/8-27 tightening pipe collars that were screwed flush with the inside of the tunnel walls. The same configuration was arranged for the hot-wire probe, except with 1/2-20 pipe collars.

The boundary layer probe ports were located in both of the Lexan walls to allow boundary layer traversals immediately fore and aft of the test section of both heated walls for all three of the

tunnel configurations. These ports were slots, 1.27 cm by 6.03 cm, with the longer dimension of the slot oriented horizontally, having a 6.35-mm external lip, 4.76 mm deep, on the upstream and downstream sides of the port. These lips allowed the bolting of port inserts to the 1/16-36 Helicoil inserts set into the Lexan around the port and prevented the port inserts from slipping through the port. Two types of port inserts were machined from Plexiglass. The first type was a solid block constructed to sit flush with the inside of the Lexan walls when bolted in position. They were placed in all the ports not in use to prevent flow disturbances. The second type was constructed from two, lipped strips of Plexiglass, 3.174 mm by 6.03 cm each, connected on the bottom with a slitted, rubber strip, 1.27 cm by 6.03 cm by 1.59 mm. This insert was bolted into position around the tube of the boundary layer probe, after it had been placed through the port, so as to minimize the disturbance of the flow at the inner lip of the port while still allowing horizontal movement of the probe.

**F. Tunnel Heated Walls.** The heated tunnel walls, from the flow side to the external side, were comprised of:

- a layer of metal plate, into which the RTD's were epoxied,
- a layer of heaters glued to the back of the plate,
- a layer of insulation glued to the heaters,
- guard heaters glued onto this layer of insulation, and finally,
- a second layer of insulation glued onto the guard heaters.

A tunnel cross section area perpendicular to the freestream is shown in Figure 4.2, Tunnel Quarter Cross Section, exhibiting these layers. Since the tunnel cross section is rectangular, it exhibits symmetry about y and z axes passing through its center. Therefore, only one quadrant is necessary to show the full details of the tunnel.

The metal layer in the pretest, test, and spacer segments was 1.27 cm thick, 1060 Aluminum plate with a spanwise width of 26.67 cm, machined to a tolerance of 0.13 mm. Measurements showed that the variation in any plate dimension was not more than 8.47 microns per cm. The two pretest plates were 0.9144 m in length. The test and spacer plates were 0.3048 m in length.

The test sections of the two test plates were sawed out of the original plates with 1.59-mm saws to allow for insulation of these sections with foam adhesive. Using a precision clamping frame, the test plates were epoxied back together with Eccobond SF40 syntactic foam adhesive as insulation, filling the saw cuts around the test sections as completely and as exactly as possible (see Figure 3.9). The material properties of the SF-40 epoxy, as given in Anon. (1979), were:  $k = 0.125 \text{ J/m-s-}^\circ\text{C}$  and  $\alpha = 37.8 \times 10^{-6} \text{ m/m/}^\circ\text{C}$ . For simplicity and for greater precision, these saw cuts extended fully across the plate in the spanwise direction, resulting in one spanwise strip of

insulating epoxy in each of the side guard heated plate sections (i.e., those sections heated by guard heaters H23 through H25). This may be seen in Figure 4.3, Photograph of the Ribleted Test Plate, where the epoxy joints show as white strips. This was assumed to have negligible effect on the heat transfer in the test sections. The tolerances on the joints were 5 percent, i.e., 76.2 microns, due to minor misalignment of the test section during bonding. Care was taken to ensure that no discontinuities existed at any of the epoxy joints as well as that the tolerances of the test plate dimensions were not increased by the joining process.

After insulating the test sections, one of the test plates, denoted as plate B, was ribleted by cutting the grooves with a saw on a milling machine. This plate is shown in Figure 4.3. As can be seen, the riblets were of uniformly good quality except for three rows located 3.8 cm from the vertical edge of the plate. These rows appear as white streaks close to the ruler in Figure 4.3. Fortunately, these rows were outside the test section and, therefore, of minimal importance. Measurements with a disc micrometer and a depth gage indicated that the riblet midpoint-to-midpoint spacing was  $0.67 \text{ mm} \pm 0.02 \text{ mm}$ , the height  $0.38 \text{ mm} \pm 0.012 \text{ mm}$ , and the width  $0.14 \text{ mm} \pm 0.01 \text{ mm}$ , where the error includes both streamwise and spanwise variations. A photograph of the leading edge of the ribleted plate is shown in Figure 4.4, Photograph of the Leading Edge of the Ribleted Plate, and a cross section of the riblets in 4.5, Photograph of a Riblet Cross Section.

Close inspection of the riblets in the regions of the spanwise and streamwise epoxy joints with a stereoscopic microscope indicated that there were no detectable discontinuities along the riblets at the joints. Indeed, the riblets in the epoxy joints were actually of higher quality (i.e., greater uniformity) than those in the test plate itself.

The RTD holes were machined into the back of the metal plates with precision, flat bottom reamers as per Figures 3.13 through 3.15. The RTD's were then epoxied into the plates as described below in Section 4.2.A.

The wall heaters were etched foil elements, from 12.7 microns to 25.4 microns in thickness, sandwiched between two layers of 50.8 micron Kapton Polyimide sheeting with a 25.4-micron-thickness of FEP Teflon adhesive. Their areas and room temperature resistances are given in Tables 4.1 and 4.2. Their leads consisted of 25 cm of 18 gage, Teflon insulated, silver-tinned, stranded copper wire soldered to the foil elements at 0.5-cm square, 0.25-mm thick tabs. These wires were in turn connected to 1 m of 14 gage, stranded, copper wire. For each test segment, these leads led to a wire-strain-relieved, 10-cm by 25-cm by 30-cm Aluminum box, in each of which were bolted seven strips of 10-screw-post terminal connectors. At these connectors, the shunt resistors, the various voltage measurement leads, and the heater control circuitry were interfaced. The heater control circuitry, which was connected to these two interface boxes with 3 m lengths of 14-gage wire, was contained in three standard, 48.26-cm wide, fan cooled, panel

racks.

The heaters were attached to the back of the Aluminum plate with 0.254 cm of RTV Silicon rubber adhesive. A 2.54-cm-thick layer of Calcium Silicate board insulation, sprayed with high gloss, high temperature paint to deter crumbling, was affixed on top of the heaters with a 1.27-cm-wide strip of RTV Silicone rubber adhesive 0.635 cm thick. The thermal conductivity of the insulation board at its test operating temperature, as described in Anon. (1988b), was  $k = 0.04625 \text{ J/m-s-}^\circ\text{C}$ . This combination of board and RTV adhesive provided a sealed, insulating pocket of air 0.635 cm thick between the back side of the heaters and the insulation. Etched foil guard heaters, similar in type to, but of a thicker and more rugged construction than the tunnel wall heaters, 30.48 cm in streamwise width and equal in spanwise width to the heated plate, were affixed to this insulation with another layer of RTV Silicon rubber adhesive and similarly insulated at the rear with a second 1.27-cm-layer of Calcium Silicate board.

The tunnel wall heaters were powered by four Hewlett-Packard SCR-10 series, model 6479C, option 003, 10kW, DC Power Supplies. The guard heaters were powered by a STACO, type 3PN2210, 3kW Variac.

The heated wall segments were attached to the tunnel frame between the two Unistrut members of one side so that they rested against the tops of the two clear Lexan walls. They were bolted to height adjusters on the tunnel frame via 1/4-20 Helicoil inserts set 1.27 cm into the plates 5.08 cm from either end. The height adjusters were 1.27-cm by 1.27-cm by 2.22-cm steel blocks attached to the Unistrut members with spring loaded bolts, which allowed them to be raised and lowered so as to vary the tunnel wall angle (see Figure 4.2).

Large shear on the epoxy joints during wall angle adjustment caused a hairline fracture in one joint which necessitated a design change and clamping of the joints. Due to warping of the Unistrut members, the bolts passing through the steel blocks into the Helicoil inserts in the plates were subjected to extremely high moments. In one test plate, this caused a hairline fracture in one of the epoxy joints during wall angle adjustment. For this reason, only the plates without epoxy joints were secured to the tunnel frame and adjusted in this manner. To clamp the fractured joint back together and strengthen the other joints, small U-brackets were precisely machined to slip onto the edges of the plate at the joints, thus effectively clamping the joint and preventing any shear force from acting on it. The brackets were sized so as not to extend into the flow. After the fractured joint had been clamped, the largest discontinuity at the fracture was less than 5 percent of the riblet height (i.e., less than 20 microns), almost undetectable, and so it is assumed the fracture effect on the flow was at least an order of magnitude smaller than the effect under scrutiny. To allow attachment of the two test plates to the tunnel frame at the correct angle, four spacers were machined from strips of PVC into wedges, shaped at an angle equal to the desired wall angle for a test speed of 10 m/s, for placement between the test plates and the Lexan walls. The two test plates

were then clamped tightly into place against these spacers with two large C clamps. Because of the great amount of time needed to make these adjustments, the tunnel walls were set at only one angle,  $0.0054 \text{ rad} \pm 1.5 \text{ percent}$ , with the use of an inside micrometer, and the design feature of variable streamwise test segment positioning was discarded.

The single tunnel configuration, shown in Figure 4.1 was thus pretest segment, followed by the test segment with a midpoint of 1.0676 m, in turn followed by the two spacer segments. Airtight, flush, butt seals at the segment joints were formed with tightly compressed Silicon rubber tape by carefully aligning the plates using a straight edge and visual sightings. The ribletted test plate was aligned with the tops of the riblets flush with the surface of the upstream pretest plate.

The misalignment of the tunnel from the true center line of the contraction was less than  $0.0035 \text{ rad}$ . The effect of this upon the flow field, as may be approximately calculated from the solutions for flow in divergent and convergent channels, was several orders of magnitude less than the effects being measured and so assumed to be zero.

## **4.2. Instrumentation and Data Acquisition**

**A. Temperature Sensor Apparatus.** Ambient temperature was measured with four liquid-in-glass, partial immersion, mercury thermometers, two of which were  $0.1^\circ\text{C}$  gradation,  $0^\circ\text{C}$  to  $100^\circ\text{C}$  range and two of which were  $0.2^\circ\text{C}$  gradation,  $0^\circ\text{C}$  to  $200^\circ\text{C}$  range. The thermometers were suspended via 1.27-cm wide, Styrofoam-insulated, thermometer clamps and shielded from radiation and convection heat loss with cylindrical shields, 20 cm in length and 7 cm in diameter, constructed of 1.5-mm Aluminum sheeting. Readings were taken using thermometer-attachable, magnifying eyepieces. The thermometers were readable to at least half their gradation spacing.

Test plate temperature was measured with 140 Omega, type F3105, thin-film, platinum, resistance temperature detectors (RTD's). Each sensor, a description of which may be found in Anon. (1988a), was comprised of a single-winding, platinum substrate, 0.1 mm by 1.75 mm by 2 mm in size, encased in a 2-mm by 2.3-mm by 1-mm ceramic block, shown in Figure 4.6, Thin Film RTD. The leads consisted of two 2 mm lengths of strain-relieved silver-palladium protruding from the ceramic block onto each of which which were soldered, with the use of a stereoscopic microscope, two 0.5 m lengths of color-coded, Teflon-coated, 36-gage, 7/44 stranded, silver-plated copper wires. Each of these four-wire sensors was potted in 9.91-mm-long, 3.23-mm-diameter cylinders of Eccobond 285 epoxy with the ceramic block positioned flat at the bottom, as shown in Figure 4.7, RTD in Epoxy Plug. The material properties of the epoxy used in the plugs, as given in Anon. (1985), were:  $k = 1.507 \text{ J/m-s-}^\circ\text{C}$ , and  $\alpha = 2.9 \times 10^{-5} \text{ m/m}^\circ\text{C}$ . After calibration, they were epoxied into the metal tunnel walls, with the same epoxy used to form

the cylinders, in holes 10.16 cm deep, with a diameter of 3.45 mm, machined with precision, flat bottom reamers.

Some difficulties occurred during the potting of the cylinders in the pretest section, probably due to some reamer wear, and several RTD's were destroyed. The rest of the RTD's read the same temperature to within their accuracy with the wind tunnel running but the heaters off, so that it seems reasonable to assume that the RTD's which were not destroyed were not adversely affected.

The four 36-gage leads running from the RTD's were twined tightly and then attached to the back of the metal plates with Teflon tape in a symmetric pattern so as to allow easy gluing of the heaters over them. These leads were in turn soldered to 6 m of 20-gage, 20-twisted-pair, flat-ribbon, wire cable at micro-solder terminal strips. The terminal strips were bonded inside an Aluminum box, 5 cm by 8 cm by 4 cm in size, with wire strain-relief. The 6-m lengths of flat-ribbon wire cable were joined through strain relief ribbon connectors to 30-cm lengths of similar cable, in turn linked to the screw-post terminal strips in the front end data acquisition four-wire input connector.

The RTD's were read through the Fluke Helios I system front end via serial port by a 16 MHz, NEC Powermate SX brand, AT-type, personal computer running Labtech Notebook under the DOS operating system. The front end system consisted of the main Helios I chassis and an extendor chassis both containing A/D boards. The main chassis contained five pairs of 20-channel RTD/Resistance Four-wire Connectors and High Performance Scanners. The extendor chassis contained two pairs of 20-channel RTD/Resistance four-wire Connectors and High Performance Scanners and one pair each of a 20-channel Voltage Input Connector and Scanner and a 20-channel Current Input Connector and Scanner. During calibration, the four wire scanners were used to read the resistance of the RTD's. Given the calibration curve constants, the data acquisition program calculated temperature directly from resistance, using a Newton-type algorithm to solve the Callendar-VanDusen equation. The temperatures were output directly to files which were ported to a DEC Vaxstation II for analysis using the FORTRAN 77 program HEATCALC2.

**B. Heater Power Sensor Apparatus.** The power output of the twenty heaters in the test segment was determined by directly measuring the voltage drop across each of the heaters ( $V_h$ ) and by indirectly measuring the current via the voltage measurement across shunt resistors ( $V_{sh}$ ) with known resistances as shown in Figure 3.11. The 20 channels of voltage input on the Helios I were used to read the voltage drop across the heaters directly by connecting a set of two 3-m leads from the front end in parallel with each heater. The 20 channels of current input were modified to allow the measurement of large currents. The shunt resistors originally wired into the current input connector were removed. Six-inch lengths of Inconel wire, used for its extremely low resistance

sensitivity to temperature, were connected in the test segment interface boxes in series with each heater and a set of two 3-m leads were then connected to the front end in parallel with each of these new shunt resistors. Four-wire resistance measurements of the new shunt resistors over the range of test currents showed no detectable change due to temperature effects. Their resistances are shown in Table 4.3.

**C. Velocity Sensor Apparatus.** Dynamic head of the freestream flow was measured directly using four United Sensor, type PAA-12-KL, pitot-static probes, constructed of 3.175-mm diameter stainless steel tubing, with a flow-angle variation insensitive, manifolded, triple static hole arrangement. The probe tips were positioned in the center of the tunnel cross section. These probes were connected via 3.175 mm inner diameter, 6.35 mm outer diameter, color coded, rubber, ribbon tubing to a set of pressure valves. The pressure valves were used to control the probe or probes of origin of the total and static pressures. From the valves, both a total pressure and a static pressure line of 6.35 mm diameter, plastic hose led 61 m to a MKS Barotron, type 310 CD-100, differential pressure transducer. The transducer was read on a Graphon, type GO-230 VDT, over a DEC Vaxstation II, running the VMS operating system, using the FORTRAN 77 subroutine BARATN written by Philip Lavrich and the FORTRAN 77 program READPRESS2, with a type 170M-6C MKS Barotron Signal Conditioner and type 170M-27C Digital Readout, accurate to  $\pm 0.08$  percent. Dynamic head was converted to velocity using values of atmospheric density calculated from ambient pressure read with a Setra model 370 digital pressure gage accurate to 20 Pa and ambient temperature read with the mercury thermometers described above.

Boundary layer velocity was determined from the total pressure measured with a custom built, total pressure, boundary layer probe, shown in Figure 4.8, Boundary Layer Probe, and the static pressure from the pitot-static probe in the center of the test segment with a similar method as for the freestream velocity. The boundary layer probe was positioned using a three degree of freedom vernier slide apparatus constructed from a single degree of freedom 25.4 cm vernier slide and a 2-degrees of freedom 5-cm and 3-cm vernier positioning apparatus. This apparatus could be bolted to the tunnel frame at various positions to allow appropriate positioning of the probe.

Freestream turbulence levels were measured with a TSI, model 1213-20, hot wire probe via a Dantec, type 56C17, CTA Bridge and type 56C01 Mainframe both graphically and numerically. Graphical readings were taken visually using a Tektronix, type 555, Dual Beam Oscilloscope while numerical readings were performed using the NEC PC described above running ILS, with a Data Translation, type DT2821, 20 channel, A/D board.

**D. Sensor Calibration Summary.** A relative accuracy was assumed for the mercury thermometers based on their tracking during temperature cycling. Three of the four mercury



thermometers had been used in previous Gas Turbine Lab research and found to track accurately to within the limits of their readability. The new mercury thermometer purchased for this research as well as the three old ones performed in the same manner in tests. Therefore, the relative accuracy, the closeness of the difference in readings between two of the thermometers to their actual difference in temperature, was assumed to be equal to their readability, though the absolute accuracy, the closeness of the reading of any one of the thermometers to the International Practical Temperature Scale of 1968 (IPTS-68) defined temperature at the thermodynamic state of that thermometer, is certainly much lower. Since the primary source of temperature error in the present research originates in temperature differential terms, for which absolute accuracy is not essential, this was deemed acceptable. That the thermometers would read approximately zero degrees when immersed in an ice bath was verified, but due to constraints on time and money no attempt at rigorous, triple-point calibration was made.

The RTD's were calibrated from measurements made during two temperature cycles using a nonlinear least squares fit of the data to the Callendar-VanDusen equation. The RTD temperature cycling measurements were performed by sampling sensor resistance during cycling from room temperature to 100°C in a heated, insulated, mixed, calibration bath of Fluorinert fluid, with the four mercury thermometers, evenly spaced throughout the bath to assure temperature uniformity, as the reference temperature. A nonlinear least squares subroutine was used to find the coefficients of the Callendar-VanDusen equation, the standard equation used to relate temperature and resistance for platinum RTD's, from the calibration data. A first calibration of the RTD's was performed and analyzed. The RTD's were then subjected to temperature cycling, ten sets of 3 hours at room temperature and 3 hours at 100°C, roughly estimated to be equivalent to that of the actual testing. A second calibration was then performed to ascertain the stability of the sensors. The error due to this instability was incorporated into the second calibration. A third calibration had been planned after testing was complete but was prevented from being performed by time constraints.

The calibration results showed a combined statistical and experimental RTD calibration error of slightly under 0.1°C and good statistical agreement of the data with the calibration equation. A typical RTD calibration curve is shown in Figure 4.9, Calibration Curve for RTD #1. Over the range, the data show no hysteresis, little scatter, strong repeatability, and good agreement with the calibration curve. The distribution of the total, maximum, combined statistical and experimental, RTD error is shown in Figure 4.10, Distribution of RTD Error. The average error was 0.09°C, within the desired range of 0.1°C. The distribution of the reduced chi-squared statistic, often referred to as the "goodness-of-fit" statistic, for the second, nonlinear, least squares fit is shown in Figure 4.11, Distribution of RTD Chi-squared. More than 96 percent of the RTD's had a reduced chi-squared under one, the value which is usually taken as the benchmark near or

below which a fit is considered statistically reasonable. Approximately 77 percent of the RTD's had both total error under  $0.1^{\circ}\text{C}$  and reduced chi-squared less than 0.616, the value for which there exists a 95 percent probability that a random sample will have as large or larger chi-squared. Full details of the calibration procedure and results are given in Appendix B.

Although no rigorous calibration of the other data acquisition equipment was performed, every factory calibration was thoroughly checked for accuracy. The four-wire resistance channels of the Helios I were checked against those of a Fluke 8520A Digital multimeter. The voltage and current channels of the Helios I and the Data Translation A/D board were checked with a high precision voltage calibrator. All electrical inputs were checked with an oscilloscope to ensure the absence of significant, electrical noise. The Setra atmospheric pressure gage was validated with Logan airport pressure data. The dynamic head measurement apparatus was checked for leaks by being overpressurized. The accuracy of the Barotron both with and without the 200 ft of pressure tubing was checked with an inclined manometer. All of these were found to be within specifications.

## **5. TEST PROCEDURES**

### **5.1. Heat Transfer Measurement**

Heat transfer was determined through direct measurement of heater power at approximately constant wall temperature, which was then adjusted to account for side, back, and radiative loss, as well as for the minor variations in upstream wall temperature.

At the beginning of each test run, the heaters were turned on at close to maximum voltage to bring the tunnel walls up to temperature. Usually, for this, half an hour was sufficient. When the tunnel walls were within 5°C of the nominal operating temperature, the wind tunnel was turned on and adjusted to test speed. Real-time temperature displays of several of the RTD's in each segment were displayed and used to make the gross adjustments to the voltage controls on the four main power supplies and the back heaters Variac. An iterative procedure of fine tuning the temperature in each of the segments on each tunnel wall was performed by slowly adjusting the rheostats in the heater control circuitry using real-time temperature displays from the particular segment. Usually five sets of iterations over a period of approximately 3 hours were sufficient to bring the temperature of each of the tunnel walls to  $\pm 0.5^\circ\text{C}$ . An iterative, fine adjustment procedure was then performed on each of the two pretest and two test segments individually. After some initial trial and error with the most efficient temperature displays and rheostat adjustment techniques, this procedure was sufficiently refined so as to make it possible to bring test plate temperatures on both sides to within the accuracy of the RTD's, approximately  $0.1^\circ\text{C}$ , over a time period of 1 to 3 hours, for tunnel speeds greater than 9 m/s and less than 20 m/s. During this lengthy period of heater voltage adjustment, ambient temperature in the test cell was held constant to within  $0.1^\circ\text{C}$  by constant manual adjustment of an air conditioner and two heaters. Temperature gradients within the test cell were minimized with use four high-power fans.

Once the temperatures of both walls were within the desired range, test data consisting of 30 samples, at a sampling rate of 0.05 Hz, of the temperature of each of the 140 RTD's, the voltage drop across each of the 20 test segment heaters, and the voltage drop across each of the 20 shunt resistors in series with the test heaters, were taken. Simultaneously, the ambient temperature and pressure were measured and 30 samples of freestream dynamic head in the test segment were taken at a sampling rate of 2 Hz. This body of data was reduced to heat transfer results using the Fortran 77 program HEATCALC2, listed in Appendix B.

### **5.2. Drag Measurement**

Drag measurements were based on velocity profiles taken immediately fore and aft of the

test sections of both sides. After the tunnel had been adjusted to the desired test speed, the boundary layer probe and probe positioning apparatus were attached to the tunnel at the appropriate spot. The dynamic head of positions in the boundary layer was measured using the boundary layer probe total pressure and the static pressure measurement from the pitot-static probe at the center of the test segment. The probe was visually zeroed against the tunnel wall and manually adjusted to each new measurement position. Each measurement consisted of 30 samples of dynamic head readings taken and converted to velocity with the Fortran 77 program READPRESS2. Ambient properties were measured and maintained in the same manner, as described above in Section 5.1, as for the heat transfer measurement.

## **6. SUMMARY OF DATA ANALYSIS AND RESULTS**

### **6.1 Skin Friction Analysis**

**A. Introduction.** The coefficient of skin friction fore and aft of both the ribletted and flat test plates was measured by performing a nonlinear, least squares fit of the log law to mean boundary layer velocity profiles measured at these points. Essentially, the technique is a numerical implementation of the Clauser plot graphical method. Coefficient of drag was calculated by integrating coefficient of skin friction across the test sections.

**B. Background.** A correlation method for calculating coefficient of skin friction from mean velocity profiles was chosen as the most appropriate for this experiment of the various ways available. The methods of measuring coefficient of friction, the non-dimensionalized wall shear stress, fall into two categories: direct and indirect. The direct methods involve some form of floating element sensor and so are not practical for simultaneous drag-heat transfer measurements on the same surface. The indirect methods are comprised of momentum balance and correlation methods. The momentum balance methods include the measurement of pressure drop over a constant area duct and the use of the von Kármán integral momentum theorem to relate momentum thickness to shear. In this case, the first method is inapplicable because it requires fully developed pipe flow. The second method was discarded because of its inaccuracy, based both on an error analysis of the integral momentum equation itself as well as on evidence cited in Haritonidis (1989) and in the riblet studies Hooshmand et al. (1983), Walsh and Lindemann (1984), and Gallagher and Thomas (1984). Correlation methods include the Preston and Stanton tubes, the Clauser plot, and Reynolds number type correlations. Both the Preston and Stanton tubes are infeasible for use over riblets and so were not considered. Reynolds number type correlations such as equations 2.45 and 2.56 are only valid over a flat plate and so only useful for corroboration. The Clauser plot method, so called for the graphical technique employed in it, is based on the log law. The standard method involves iterating for  $u_\tau$  until  $u^+$  falls on the line given by equation 2.21. On log paper, this is just a straight line. Of the various methods, this approach was chosen as the easiest and the most accurate, under the circumstances.

However, as mentioned in Coles and Hirst (1969), the Clauser plot method requires a rather subjective choice of what percent of the boundary layer is used to make the fit, since the region of accuracy of the log law is not known a priori. More of the profile data may be used, so avoiding this problem, if the wake law is incorporated into the fitting. Coles and Hirst determined that, if the wake law were used, the data in the section of the boundary layer for  $y/\delta$  between 0.1 and 0.9 resulted in values of skin friction that had good correlation with those predicted by theory.

For this reason, the wake law rather than the log law was used to correlate data from the center 80% of the boundary layer with a value of skin friction.

The wake law, equation 2.25, may be rewritten by making use of definition 2.14 as:

$$\frac{u}{u_e} = \sqrt{\frac{C_f}{2}} \left\{ \frac{1}{\kappa} \ln Re_y + \frac{1}{\kappa} \ln \sqrt{\frac{C_f}{2}} + B + \frac{2\Pi}{\kappa} \sin^2 \left\{ \frac{\pi}{2} \frac{y}{\delta} \right\} \right\}. \quad (6.1)$$

Three approaches may be taken in using this equation to determine  $C_f$  by correlation with the velocity profile data: solving it numerically at  $\delta$ ; performing a nonlinear, least squares fit of it to the selected data with  $C_f$  as the coefficient of the fit; and, performing a nonlinear, least squares fit with both  $\delta$  and  $C_f$  as coefficients.

**C. Skin Friction Calculation Methodology.** The three methods of using equation 6.1 to determine  $C_f$  were evaluated via a Monte Carlo type analysis, with the result that the third method was found to be the most accurate and robust. Monte Carlo-analysis, one discussion of which may be found in Press et al. (1986), is the analysis of simulated input data, usually with some amount of simulated error generated by a computer according to a predetermined distribution, so as to gage the ability of the analytical methodology to reproduce the parameters used to generate the input data.

First, equation 6.1 may be evaluated at  $\delta$  and solved with a simple Newton root finder by rewriting it in the form:

$$\frac{u(y=\delta)}{u_e} - \sqrt{\frac{C_f}{2}} \left\{ \frac{1}{\kappa} \ln Re_\delta + \frac{1}{\kappa} \ln \sqrt{\frac{C_f}{2}} + B + \frac{2\Pi}{\kappa} \right\} = 0. \quad (6.2)$$

This method is referred to by the author, somewhat incorrectly but for convenience sake, as Coles-Hirst method number one (C-H1). Unfortunately, this is subject to the inaccuracies of determining  $\delta$ , the standard technique of which is linear interpolation. Since the slope of the velocity profile in this region is very large, this inaccuracy is quite high.

An attempt was made to use an alternate method of determining  $\delta$  but was halted by problems with the nonlinear iteration needed to perform it. Researchers such as Reynolds et al. (1958) have made the observation that if a least squares fit of the power function:

$$\frac{u}{u_e} = \left( \frac{y}{\delta} \right)^n \quad (6.3)$$

is performed, then via equation 2.32:

$$\delta = \frac{(n+1)}{n} \delta^*. \quad (6.4)$$

This has a much sounder basis than interpolation because it uses information from the whole boundary layer instead of just two points. However, some peculiarities inherent in this technique were noted. The peculiarities were first observed when it became evident that the two techniques would sometimes give predictions for  $\delta$  differing by significant percentages. It was felt that this could be due to the inaccuracy of the initial value calculated by interpolation, so that to refine the results, iteration was introduced. With iteration, the problem is essentially the minimization of a nonlinear function in one dimension, the solution of which is path dependent. An attempt was made to apply the Levenberg-Marquardt nonlinear least squares solution methodology outlined in Marquardt (1963) as implemented in the Fortran code of Bevington (1969) and Press et al. (1986). Unfortunately, this was unsuccessful due to time constraints. Trial and error on the experimental profiles were used to find a simple technique and tolerance that produced reasonable answers. However, when profiles artificially generated from the wake law with varying percentages of random perturbations were analyzed with the program, linear interpolation was found to be a more reliable predictor in about 70 percent of the cases. Most likely, this was due to the author's particular methodology which time constraints prevented being improved. For this reason, the results of this method are not treated in any depth and not used in the estimation of  $C_f$ .

The accuracy in  $C_f$  calculated by C-H1 is thus limited to the accuracy of the interpolation for  $\delta$ . Its worth lies mostly as an indicator of the accuracy of the interpolated  $\delta$ , i.e., when  $C_f$  calculated in this manner is close to  $C_f$  calculated by the more reliable methods then the value of the interpolated  $\delta$  itself may be regarded as fairly reliable.

The second method is a nonlinear least squares fit of equation 6.1 with the single coefficient  $C_f$ , denoted as method C-H2. The third method adds the extra coefficient  $\Pi$  and is denoted as method C-H3. After some evaluations, the latter method was chosen as the most accurate for four reasons. The first is that even though the tunnel was designed for zero pressure gradient, in general some finite pressure gradients, albeit very tiny ones, did exist in the test segment due to the discarding of the variable wall angle design feature and the limitations of wall adjustment. The former method is unable to account for this. Second, variation in the extra coefficient allows adjustment of the wake law function to fit the aggregate of data in cases where the value of interpolated  $\delta$  is inaccurate. Third, it was found to be a more reliable predictor approximately 75 percent of the time when used to analyze wake law generated profiles with random perturbations in a Monte Carlo-type analysis. Fourth, it was found to be more accurate in 100 percent of the analyses of wake law generated profiles with no random perturbations, especially as the number of generated sample points decreased. Indeed, fairly extensive Monte Carlo testing of the VPFIT7 program with wake law generated profiles indicated that this latter method was accurate on average to within 3 percent for random perturbations in velocity as large as 15 percent and to within 0.25 percent for perturbations less than 2 percent. For no perturbations,

it was accurate to within 0.01 percent for numbers of generated sample points as low as 8.

**D. Calculating Drag from Skin Friction.** Two approaches were taken in determining the  $C_d$  from  $C_f$ . The first of these was simple integration using the trapezoidal approximation. The second was integration using some assumed function. While the trapezoidal method is less sensitive to error propagation, it tends to overestimate drag. Calculations with the the assumed function method indicated that this overestimation was negligible.

Considering two-dimensional flow, the drag per spanwise length  $s$  is:

$$D/s = \int_{x_1}^{x_2} \tau_w dx. \quad (6.5)$$

Nondimensionally this is:

$$C_D \equiv \frac{D/s}{\frac{1}{2} \rho U_e^2 (x_2 - x_1)} = \frac{1}{x_2 - x_1} \int_{x_1}^{x_2} \frac{\tau_w}{\frac{1}{2} \rho U_e^2} dx = \frac{1}{x_2 - x_1} \int_{x_1}^{x_2} C_f dx \quad (6.6)$$

Therefore, the ratio of coefficient of drag of the ribletted plate to that of the flat plate is:

$$\frac{D}{D_{FP}} = \frac{C_D}{C_{D_{FP}}} = \frac{\int_{x_1}^{x_2} C_f dx}{\int_{x_1}^{x_2} C_{f_{FP}} dx}, \quad (6.7)$$

where the subscript FP denotes the flat plate value, because  $x_1$  and  $x_2$  are the same for the ribletted plate as for the flat plate. The integral of skin friction must be calculated numerically from the the measurements fore and aft of each of the two test sections.

The first method used to calculate this integral was a simple trapezoidal approximation:

$$\int_{x_1}^{x_2} C_f dx = (x_2 - x_1) (C_{f, x_1} + C_{f, x_2}) / 2. \quad (6.8)$$

In essence, this method is really just the use of a straight line fitted between the two points to calculate the integral. Since it is known that the variation of  $C_f$  with streamwise distance is not linear, some inaccuracies are inherent in this method.

It is known that:

$$C_f \propto x^{-1/n}, \quad (6.9)$$

where  $n$  of 5, as in equation 2.40, is usually taken. If the function:



$$C_f = \frac{a}{x^b} \quad (6.10)$$

is assumed to describe the variation of  $C_f$  with streamwise distance, then the constants  $a$  and  $b$  can be determined from the two measured values of  $C_f$ . Evaluating equation 6.10 at  $x_1$  and  $x_2$  and solving for  $a$  and  $b$  gives:

$$b = \frac{\ln (C_{f, x_1} / C_{f, x_2})}{\ln (x_2 / x_1)} \quad (6.11)$$

and:

$$a = C_{f, x_1} x_1^b \quad (6.12)$$

With these constants, the integral of  $C_f$  is given by:

$$\int_{x_1}^{x_2} C_f dx = \frac{a}{1-b} \left\{ x_2^{1-b} - x_1^{1-b} \right\}. \quad (6.13)$$

However, although this method avoids the overestimation inherent in a linear approximation, the error propagation due to the methods of calculating the constants overshadows this. Its use is restricted to a double check on the trapezoidal approximation. The results indicated that the difference between the two methods was very minor, much smaller than the error propagation through either equation.

**E. Calculating Riblet Spacing in Wall Units.** Local  $s^+$  is easily calculated via equations 2.15 and 2.11 once  $C_f$  is known. Since  $C_f$  varies quite slowly with  $x$ ,  $s^+$  is approximately constant across the test sections. In addition, the values of  $s^+$  on the ribleted test section are quite close to those on the ribleted test section. Thus, if we are interested only in an approximate value of  $s^+$  to characterize the test results at a particular test condition, it is quite reasonable to take the average of the four  $s^+$ 's calculated with the four  $C_f$ 's.

To extend this to a function of  $s^+$  versus Reynolds number for the purpose of calculating  $s^+$  for the St measurements, a least squares fit of equation 6.10 can be made to the riblet skin friction data.

**F. Comparing Flat Plate and Ribleted Drag Results.** Both the standard format of presentation of riblet research data and a more exact but less frequently used format are useful in illuminating different aspects of the results. The ratio of the drag of the ribleted plate to the drag of

the flat plate, or one minus this amount which gives the percent reduction, as a function of riblet spacing in wall units, is the most commonly used format to present riblet test results. This format is the most common because it succinctly presents the bottom line: the amount of drag reduction and how this varies with  $s^+$ . However, since the amount of total drag reduction is a function of total streamwise length of the ribleted section, albeit very weakly, in addition to  $s^+$ , this method has the potential for inaccuracy. Furthermore,  $s^+$  is not constant but a function of streamwise distance, since  $C_f$  varies with streamwise distance. In addition, some researchers have suggested that the effect of riblets on skin friction at a position is also a function of the distance from the leading edge of the riblets to that position as well as the distance from the leading edge of the boundary layer. Although the inaccuracies seem to be an order of magnitude smaller than the effect of riblets, no conclusive measurements have been performed to support this. The majority of these inaccuracies may be avoided by comparing riblet and flat plate drag results as skin friction versus Reynolds number. Since both methods illuminate the results in useful ways, both are used to present them. The same holds true for the effects on heat transfer.

Nondimensional values of friction and drag are used in the momentum transfer analysis and its presentation instead of the dimensional quantities most often used in riblet studies so as to mirror the heat transfer calculations, for which the nondimensional forms of the transfer are necessary. In most riblet studies, the most common format of presentation shows the percent change in drag due to riblets. If the ribleted and flat plate test sections are tested in the same flow, so that the density and freestream velocities are exactly the same over each test section, then the calculated amount of percent change in drag or skin friction will be identical to the percent change in coefficient of drag or skin friction. However, since it is practically impossible to attain exactly the same wall temperature in the ribleted and flat plate test sections, the same will not be true of the convective wall heat flux and the Stanton number. To allow meaningful comparison of this heat fluxes of the two test sections, non-dimensionalization must be used. To mirror this process, the momentum transfer calculations are performed and presented in similarly nondimensional form.

## **6.2. Heat Transfer Analysis**

**A. Introduction.** Stanton number, nondimensionalized convective heat flux, was calculated from direct measurements of heater heat flux and adjusted to account for back, side, and radiation losses and wall temperature variation based on an energy balance of the test sections. Interpolation, extrapolation, and splines were used to calculate the temperature in the pretest plate at three spanwise positions at the streamwise midpoint of each heater and in the test plate at four spanwise positions. These temperatures were used to estimate the radiation heat loss via equation 3.8, the side losses via Fourier's law of heat conduction, and using the temperatures at the back

guard heaters, the back losses again using Fourier's law. These values were then used to calculate the convective turbulent heat flux at the wall with equation 3.6. Definition 2.29 was used to calculate Stanton number from this. The solution for the effect of a step rise in temperature on Stanton number was used to correct these values for the variation in upstream wall temperature.

The choice of the method of measurement was a design decision because of its effect on test plate configuration. For this reason, the background of and reasoning behind the choice are discussed in the design Sections 3.2.A., E., and F.

**B. Local and Integral Stanton Number.** The heat transfer equivalents of local skin friction and total test section drag can be calculated from the calculated values of convective heat fluxes from the test sections into the flow. The local Stanton number is the nondimensionalized form of the local, convective heat flux at the wall,  $q_w$ :

$$St \equiv \frac{q_w}{\rho U_{\infty}^2 C_p (T_w - T_e)} \quad (6.14)$$

This coefficient is analogous to the local skin friction coefficient. A similar coefficient analogous to the coefficient of drag may be calculated based on the convective heat flux over the entire test section,  $Q_w$ :

$$C_h \equiv \frac{Q_w/A}{\rho U_{\infty}^2 C_p (T_w - T_e)} \quad (6.15)$$

This coefficient may be thought of as an integral form of the Stanton number. In addition, for the flat plate case tested in this research, it is equivalent to the average Stanton number over the test sections. These local and total convective heat fluxes may be found from an energy balance of the test sections.

**C. Energy Balance of the Test Sections.** The convective heat transfer at the tunnel wall was calculated from an energy balance of the test sections. Both an overall heat flux, analogous to the entire test section drag, and the heat flux of each heated subsection of the test sections, analogous to the local skin friction, were calculated.

The total convective heat transfer out of the test sections was calculated by considering them as control volumes and performing an energy balance. The Aluminum plate test section and the test section heaters were taken as the control volume on which the energy balance was performed. The Aluminum plate test section of each of the test plates, both the flat and the ribleted, was the 8-in by 7.06-in rectangle, 0.5 in thick, in the center of the Aluminum test plates (see the upper left of Figure 3.5). The test section heaters consisted of four of the 2-in by 7-in

Kapton heaters and the adhesive holding them to the rear of the plate. The heat flux from these heaters was treated as uniform heat generation in an infinitesimally thin plane located on the surface of the heaters closer to the flow. The heat transfer out of this control volume consisted of:

- loss out of the sides, through the strip of foam epoxy insulation into the surrounding plate, via conduction, noted as  $Q_s$ ;
- loss out of the front, into the flow, via forced convection, termed  $q_w$  locally and  $Q_w$  in total;
- loss out of the front, into the flow, via radiation,  $q_r$ ; and,
- loss out of the rear into the insulation via conduction,  $Q_b$ .

The heater heat flux was calculated from heater voltage and current. The conduction losses were calculated via Fourier's law of heat conduction from the test section and surrounding plate and insulation temperatures and conductivities. The radiation loss was calculated from Stefan-Boltzmann's law of radiation. This balance may be rephrased in equation form as:

$$\sum_{i=1}^4 Q_{h_i} = \sum_{i=1}^4 Q_{s_i} + \sum_{i=1}^4 (q_{w_i} + q_{r_i}) A_i + Q_{b_i}, \quad (6.16)$$

where  $Q_{h_i}$  are the heater flux inputs,  $Q_{s_i}$  are the losses out of the sides of each subsection,  $q_{w_i}$  and  $q_{r_i}$  are the convective and radiative losses out of the front of each subsection,  $A_i$  are the subsection areas, and  $Q_{b_i}$  are the back losses out of the subsections.

This equation may be solved for the sum of  $q_{w_i}$  times  $A_i$ , which is equal to  $Q_w$ . The same energy balance may be done for each subsection of the two test sections to allow solution for each  $q_{w_i}$ , but with low accuracy, since the subsections in each test section are insulated only from the surrounding plate, not from each other. Further discussion of this issue may be found in Appendix D.

**D. Heater Heat Flux Calculation.** Heater heat fluxes were calculated from direct measurements of heater voltage drops,  $V_{h_i}$ , and indirect measurements of heater current,  $I_{h_i}$ . The heater currents were calculated from measurements of the voltage drops,  $V_{sh_i}$ , across the shunt resistors, of known resistance  $R_{sh_i}$ , in series with the heaters. The two voltage measurements for each heater are shown in Figure 3.7. The  $i$ -th heater heat flux is thus:

$$Q_{h_i} = V_{h_i} I_{h_i} = V_{h_i} I_{sh_i} = V_{h_i} \frac{V_{sh_i}}{R_{sh_i}}. \quad (6.17)$$

**E. Conduction Loss Estimation.** The heat losses through the back of the test sections were calculated via a one-dimensional solution of Fourier's law of heat conduction through three materials from test plate temperature and insulation temperature measurements. Fourier's law of

heat conduction, as treated for example in Arpaci (1966), relating heat flux per unit area and temperature:

$$\bar{q} = -k \nabla T, \quad (6.18)$$

where  $k$  is thermal conductivity, can be solved for the case of one-dimensional heat transfer through three materials a, b, and c, given their conductivities and the temperature before material a,  $T_1$ , and after material c,  $T_4$ , to give:

$$q_{b_i} = -k_a \frac{T_2 - T_1}{y_2 - y_1}, \quad (6.19)$$

where:

$$T_2 = \frac{\left(1 + \frac{k_c / (y_4 - y_3)}{k_b / (y_3 - y_2)}\right) T_1 + \frac{k_c / (y_4 - y_3)}{k_a / (y_2 - y_1)} T_4}{1 + \frac{k_c / (y_4 - y_3)}{k_a / (y_2 - y_1)} + \frac{k_c / (y_4 - y_3)}{k_b / (y_3 - y_2)}}, \quad (6.20)$$

$y$  is length, station 2 is between materials a and b, and station 3 is between materials b and c. The total conduction heat loss may be found by multiplying equation 6.17 by the area of the loss plane.

Applied to the heat loss out of the back of the test sections (see Figure 4.2),  $T_1$  is the temperature at the back of the metal plate and  $T_4$  the temperature at the back of the first insulation layer; material a is the pocket of insulating air, material b the insulation, and c the layer of Silicon adhesive (see Figure 4.2).  $T_1$  can be estimated from the heater heat flux and the test plate wall temperature and  $T_4$  is measured directly by the insulation RTD's. Values of conductivity provided in the product specifications sheets were used to perform these calculations.

Side loss may be estimated in the same manner as back loss from the test section and guard heater section temperature measurements. For equations 6.16 and 6.17, material a is the Aluminum in the test section between the RTD and the layer of insulating foam adhesive, material b is the adhesive itself, and material c is the Aluminum in the side guard heater section between the foam adhesive and the other RTD (see Figure 3.5).

For the case of front or rear heat loss from a test section unit to a heated plate guard section, the same formula as for side loss applies. For heat loss from one test section unit to another, the formula may be simplified to the one material case.

**F. Radiation Loss Estimation.** Radiation heat loss was estimated from Stefan-Boltzmann's law of radiation, equation 3.8. An emissivity of 0.05 was used based on the experimental results described in Singham (1962). The difference between the temperature of the RTD's near the test wall surface and the actual surface, in general less than  $0.05^\circ\text{C}$ , due to the 0.1-in depth

of the RTD sensing element beneath the surface, can be included in addition to the uncertainty in the emissivity in the estimation of the radiation heat flux error as shown in Appendix D.

**G. Adjusting for Wall Temperature Variation.** The solution for the effect of a step rise in temperature on Stanton number, as given in, among others, Kays and Crawford (1980), was used to correct the coefficient of heat transfer values for the variation in upstream wall temperature via a discrete approximation of the standard formula:

$$\frac{St_{\Delta T(x)}(s)}{St_{\Delta T_o}} = 1 + \int_0^s \left\{ 1 - \left( \frac{x}{s} \right)^{9/10} \right\}^{-1/9} \frac{\Delta T(x)}{\Delta T_o} d\left( \frac{x}{s} \right), \quad (6.21)$$

where  $s$  is the streamwise distance at which the effect of some upstream variation  $\Delta T(x)$  from  $\Delta T_o$  is being evaluated.

### **6.3. Estimating Riblet Effect on Turbine Efficiency**

An approximate estimate of the effect of riblets on turbine efficiency can be made from the test results. Research such as that by Choi et al. (1987), Lin et al. (1990), and Caram and Ahmed (1989), who have measured up to 13 percent total drag reduction on a NACA 0012 airfoil at a freestream Reynolds number of  $2.5 \times 10^5$  due to riblets, indicates that the momentum transfer properties of riblets on surfaces with curvature are comparable to those measured over flat surfaces. Therefore, riblets should produce roughly as much total heat transfer reduction on a comparable airfoil as on a flat plate. Assuming that this reduction in total airfoil heat transfer was fully attainable on a turbine blade row, the amount of cooling air needed to keep the blade at its design operating temperature could be decreased by at least the same amount. The increase in turbine efficiency due to this decrease in needed cooling air can then be estimated from the approximate amount of decrease in turbine efficiency per percent of cooling air. This loss in turbine efficiency per percent of cooling air has been estimated by Hawthorne (1956) and experimentally ascertained by Barnes and Fray (1965) and Nouse et al. (1975) to be between 1 and 3 percent. Using a typical amount of percent turbine cooling, 3 to 5 percent, the increase in turbine efficiency can then be calculated.

### **6.4. Test Results**

**A. Introduction.** The measurements of flat plate skin friction coefficient agreed with the values predicted by the empirical formula equation 2.56 to within the predicted experimental error. The measurements of the effect of riblets on skin friction and drag validated the particular riblet

configuration used in the experiment as producing drag reduction below riblet spacing of 30 in wall units in a similar manner to the thin-element riblets used by Lazos and Wilkinson (1987). The maximum reduction in drag was approximately 7 percent with an error of  $\pm 4$  percent at a riblet spacing in wall units near 15. The measured flat plate Stanton number values agreed with the values predicted by equations 2.56 and 2.64 to within estimated experimental error of  $\pm 1.2$  percent for Reynolds numbers above  $7 \times 10^5$ . Below this Reynolds number, measured values were lower than predicted values by as much as 4 percent. However, this is still within the error margin of the empirical formulae. Convective heat transfer was lower over the riblets for  $s^+$  below 20, with maximum reduction of 5 percent at  $s^+$  of 15. This maximum reduction might translate to a 9-percent decrease in total heat transfer reduction to an airfoil. If this whole decrease could be realized on a turbine blade row, it might result in a turbine efficiency rise of between 0.15 and 0.75 percent.

**B. Effect on Skin Friction.** The coefficient of skin friction measured over the flat and ribleted test sections is shown in Figure 6.1, Effect of Riblets on Coefficient of Skin Friction, versus Reynolds number. The measurements over the flat plate, plotted as black diamonds, show close agreement with the values predicted from equation 2.56, plotted as a solid line. Indeed, a least squares fit of equation 6.10 to this data, plotted as a dotted line, gives results within 1 percent of equation 2.56, certainly well within experimental error and the uncertainty in the equation. The measurements over the ribleted plate, plotted as clear diamonds, are less than the flat plate measurements for Reynolds numbers below about  $1.5 \times 10^6$  and greater than for Reynolds numbers above. These data show more scatter than the flat plate results, as indicated in the lower R value of the least squares fit of equation 6.10 to them, plotted as the dashed line. Some of the data at lower Reynolds numbers seem to indicate that a point of maximum skin friction is reached at a Reynolds number of about 750,000 and that the riblet skin friction approaches the flat plate values with decreasing Reynolds number. This trend is consistent with previous riblet research. Maximum reduction is approximately 7 percent at Reynolds number of around 650,000.

**C. Effect on Drag.** The effect of riblets on coefficient of drag is shown in Figure 6.2, Drag Reduction of Thin Element Riblets. This graph shows the percent reduction in test plate drag due to riblets as a function of the average riblet spacing in wall units in the test sections. Four curves from Lazos and Wilkinson (1987) for similar riblets are shown as in Figure 2.4 for comparison. The results show drag reduction below  $s^+$  of about 30 wall units, with maximum reduction of 7 percent at approximately 15 wall units. The data in the drag reduction region are quite close to the results of Lazos and Wilkinson (1987) for the riblet aspect ratio of 0.58 used in the experiment. The single data point in the drag increase region, at  $s^+$  of 55, does not seem to

agree as closely. However, since time constraints prevented more data points from being obtained in this region, this trend could not be verified.

**D. Effect on Stanton Number.** The local Stanton number measurements were subject to fairly large conduction loss experimental error and showed fairly wide scatter. This error was due to the fact that the test plate subsections on which an energy balance was used to calculate the local values were not insulated from one another, merely from the surrounding plate, as discussed in Section 11.4.B. Due to this error, to which the calculation of the integral or average Stanton number was not subject, and because they were too numerous to present with any clarity in one graph, they are not discussed in any detail in this section.

The measurements of average or integral Stanton number, the calculations of the effect of riblets on which had uncertainties of 1.1 percent on average and less than 1.3 percent in all cases, showed reduction in heat transfer due to riblets for Reynolds number below 650,000 and  $s^+$  below 20. The effect of riblets on Stanton number versus turbulent Reynolds number is presented via the integral or average test section Stanton number in Figure 6.3, Average Test Section Stanton Number versus Turbulent Reynolds Number for the Flat and Ribletted Plates. The measurements over the flat plate, plotted as black diamonds, are uniformly lower than the values predicted from equations 2.56 and 2.64, plotted as a solid line. However, they are certainly within the error range of the prediction formulae. The measurements over the ribletted plate, plotted as clear diamonds, are less than the flat plate measurements for Reynolds numbers below about 650,000 and greater for Reynolds numbers above. Maximum reduction is approximately 5 percent at a Reynolds number of around 450,000. The effect of riblets on the integral Stanton number versus riblet spacing in wall units calculated from the curve fits shown in Figure 6.1 is shown in Figure 6.4, Effect of Riblets on Integral Stanton Number. The results show heat transfer reduction for  $s^+$  below 20 with maximum reduction of 5 percent at  $s^+$  of 15. The general trends of this effect are approximately the same as for the effect on drag, a region of drag reduction and a region of increasing drag with increasing  $s^+$  above this region.

**E. Effect on Reynolds Analogy Factor.** The effect of riblets on the Reynolds analogy factor as a function of Reynolds number is shown in Figure 6.5, Reynolds Analogy Factor Variation with Reynolds Number. The factor variation for the flat and ribletted test sections were calculated from the least squares power fits of the coefficient data as a function of Reynolds number. The results for the flat plate, the dotted line, agree to within the error range with the constant value predicted by equation 2.64. The results for the riblet, plotted as a dashed line, increase from approximately the flat plate value at a Reynolds number of  $5 \times 10^5$  to 35 percent higher than the flat plate value at a Reynolds number of  $2.5 \times 10^6$ . These results are quite similar to



those reported by Lindemann (1985). The variation of the analogy factor with riblet spacing, shown in Figure 6.6, Reynolds Analogy Factor Variation with  $s^+$ , was calculated easily from the fits of coefficient of friction to Reynolds number. The results are the same as for Figure 6.6, with riblet factor equaling flat plate factor at  $s^+$  approximately equal to 20 and 35 percent greater at  $s^+$  of 80. No rigorous error analysis of this calculation was attempted.

**F. Estimated Effect on Turbine Efficiency.** Assuming that the entire 5 percent reduction in Stanton number could be achieved upon a turbine airfoil, a reduction in cooling air needed to keep the blade at operating temperature of 5 percent would be expected. For a typical turbine, this reduction may be 0.15 to 0.25 percent of the total air flow. Using the sensitivity given in section 6.3, a rise in turbine efficiency of between 0.15 and 0.75 percent would thus be expected due to the implacement of properly sized riblets on turbine blades. Based on an  $s^+$  of 15, such riblets would have to have a spacing of 17 microns. To preserve the aspect ratio of the riblets used in this experiment, a height of 8 microns and a width of 2 microns would be needed.

## **7. CONCLUSIONS AND RECOMMENDATIONS**

### **7.1. Conclusions**

The thin element riblets used in this experiment have been shown to produce drag reduction characteristics similar to the thin element riblets studied in Lazos and Wilkinson (1988). They showed a reduction in drag for riblet spacing below 30 in wall units, with a maximum reduction of 7 percent at a spacing of around 15 wall units.

These riblets have also been shown to reduce turbulent convective heat transfer by up to 5 percent. This range of reduction occurred for riblet spacing below 20 in wall units with maximum reduction at 15 wall units. The effect of riblets on heat transfer was similar to that on turbulent skin friction with the exception that, outside the region of heat transfer and drag reduction, the rise in heat transfer over a ribleted surface versus that of a flat surface with increasing spacing in wall units was greater than the corresponding increase in drag. One way of restating this trend is that the Reynolds analogy factor rises from being approximately equal to the flat plate value at  $s^+$  equal to 20 to about 35 percent higher than the flat plate value at  $s^+$  of 80. Thus, the rise in drag with increasing  $s^+$  is exacerbated for heat transfer by rising Reynolds analogy factor.

These results indicate that it should be possible to use riblets to reduce the heat transfer to a turbine blade by approximately 5 percent, thereby increasing turbine efficiency by up to 0.75 percent. Assuming that the reduction in heat transfer over a flat plate due to riblets could be realized on a turbine blade, a reduction in the amount of cooling air required to cool the blade to operating temperature of about 5 percent might be expected. Using the calculation method described in Section 6.3, this reduction might produce a rise in turbine efficiency of between 0.15 and 0.75 percent.

Riblets sized for a typical turbine blade to have the value of  $s^+$  found to have the maximum heat transfer reduction in this study might be produced in the blade thermal barrier coating. The riblet dimensions in wall units of the measured point of maximum heat transfer reduction in this study were spacing of 15, height of 7, and width of 2. To produce these dimensions, using the typical values for turbulent flow over turbine blades given in the introduction, the blade riblets would need to have a physical size of spacing of 17 microns, height of 8 microns, and width of 2 microns. On a typical turbine inlet guide vane, the thermal barrier coating deposited on the surface to reduce heat transfer is often around 130 microns thick. A riblet of the correct size for reducing heat transfer might thus be produced on a turbine blade directly in the thermal barrier coating, although this study has not addressed the feasibility of producing such a microstructure.

## **7.2. Recommendations**

The present work indicates that riblets show a distinct potential to increase turbine efficiency by reducing turbulent convective heat transfer. In general, further research is needed to corroborate this result and to determine the optimum riblet geometry for maximum reduction. In addition, for the purpose of validating that these results will indeed be attainable on a turbine blade, the effects of wall curvature and freestream turbulence on riblet heat transfer reduction need to be examined.

## **APPENDIX A- STATISTICAL AND UNCERTAINTY ANALYSIS**

### **TERMINOLOGY AND METHODOLOGY**

#### **A.1. Measurement Uncertainty and Error Propagation**

**A. Introduction.** In the engineering world, rigorous uncertainty analyses are often not performed. In many cases, this is simply because they are not necessary. For many engineering purposes, approximate answers are quite satisfactory. However, as engineering fields such as gas turbine design become more developed, higher accuracy, and so more rigorous uncertainty analysis, becomes necessary. Since this is certainly the case with this project, an uncertainty analysis as rigorous and complete as time would allow was performed. Unfortunately, neither the definition of uncertainty nor its analysis are trivial. Indeed, some latitude exists in both the classification and analysis methodology. For this reason, the terminology of this analysis is described along with the method used to calculate error propagation in some detail.

Uncertainty is taken to mean the maximum error which might reasonably be expected. It is an estimate of the accuracy of a measurement, the closeness of that measurement to the "true" value. This uncertainty is assumed to be composed of statistical uncertainty, the scatter of the data, and instrumental uncertainty, the estimate of the total uncertainty inherent in each measurement. The Student's "t" test is used to form a combined estimate of the total, maximum uncertainty for a certain confidence level. The statistical concept of data weighting may be used to perform regression which takes into account this uncertainty.

**B. Statistical Uncertainty.** The statistical uncertainty, often called the random error, is the variation of repeated measurements. The most widely used method of gaging its magnitude is with the square root of the variance, called the standard deviation,  $\sigma$ . The standard deviation is defined to be the root mean square deviance of the data from the mean:

$$\sigma \equiv \sqrt{\lim_{N \rightarrow \infty} \left[ \frac{1}{N} \sum_{i=1}^N (x_i - \mu)^2 \right]}, \quad (\text{A.1})$$

where  $N$  is the number of observations,  $x_i$  are the observations, and  $\mu$  is the mean. For a set of observations distributed symmetrically about the mean and with the mean as the most likely value, approximately 68 percent will be contained between  $\mu + \sigma$  and  $\mu - \sigma$ . If the scatter is distributed according to a Gaussian distribution, as is assumed in all cases here, the standard deviation of a finite number of observations can be estimated by the statistic  $s$ :

$$\sigma \approx s \equiv \sqrt{\frac{\sum_{i=1}^n (x_i - \bar{x})^2}{n-1}}, \quad (\text{A.2})$$

where  $n$  is the number of measurements,  $x_i$  are the individual measurements, and  $\bar{x}$ , the average measurement value, is the maximum likelihood estimate of the mean.

The Student's "t" test is often used to weight the statistic  $s$  to account for the sample size not being infinite. The weighting value is a function of the specified confidence of the result and the degrees of freedom,  $\nu$ , the number of observations in excess of the number of parameters determined from the sample (e.g., when a sample of size  $n$  is used to determine the mean,  $\bar{x}$ , the degrees of freedom,  $\nu$ , are  $n-1$ ). The most common confidence level used in physical sciences and engineering is 95 percent. The weighting value for this level, the 95th percentile point of the two-tailed Student's "t" distribution, is denoted as  $t_{95}$ . For  $\nu=30$ , a sample number often chosen as small enough to be feasible and large enough to allow accurate gaging of statistical value,  $t_{95} = 2.04$ . Once this statistical parameter is known, we may conclude with a 95 percent confidence level that, for a finite number of measurements with no experimental uncertainty, there exists a 68 percent chance that the true mean of the data,  $\mu$ , will fall within the interval  $\bar{x} \pm t_{95}s$ .

It should be noted that for observations with inherent experimental uncertainty, the statistical uncertainty is not independent of the distribution of the experimental uncertainty. However, since this inaccuracy is conservative, i.e., causes the statistical uncertainty to be over-estimated, and more importantly, is usually miniscule, it is considered acceptable in general.

**C. Experimental Uncertainty.** The experimental uncertainty, also termed systematic error, is the estimate of the uncertainty inherent in each measurement due to factors such as the total uncertainty of the calibration, the material variation in instrument manufacturing, and unknowns. It is denoted as  $b$ .

Experimental uncertainty may be accounted for in calculations of the statistical parameters describing a set of data with weighting. If each data point  $x_i$  has its own standard deviation  $\sigma_i$ , the maximum likelihood estimator of the mean is:

$$\bar{x} = \frac{\sum (x_i / \sigma_i^2)}{\sum (1 / \sigma_i^2)}. \quad (\text{A.3})$$

For the case where the standard deviations for a body of data taken at one condition are comprised solely of experimental uncertainty, this weighting may be neglected, since experimental uncertainty is approximately equal for most measurements made under similar conditions. This is not true in

general for a body of data taken at different conditions, especially when those data points are themselves averages of sets of data, and so cannot be neglected when performing regression analyses, as covered below. The effect of the standard deviation of each datum on the confidence interval of the mean must also be included in any rigorous calculation via error propagation analysis.

**D. Error Propagation.** In many cases, and certainly in this case, the parameter of interest is measured indirectly by calculating its value from other more basic properties. In these calculations, the measurement uncertainty is propagated through the calculating functions to the parameter. This may be approximated by the Taylor series methods. Given a dependent variable  $f$  such that:

$$f = f(x_1, x_2, \dots, x_n), \quad (\text{A.4})$$

with uncertainties in the independent variables  $u_{x1}, u_{x2}, \dots, u_{xn}$ , the resulting uncertainty in  $f$  is:

$$u_f \approx \sqrt{u_{x_1}^2 \left( \frac{\partial f}{\partial x_1} \right)^2 + u_{x_2}^2 \left( \frac{\partial f}{\partial x_2} \right)^2 + \dots + u_{x_n}^2 \left( \frac{\partial f}{\partial x_n} \right)^2}. \quad (\text{A.5})$$

In strict analyses, the statistical and experimental uncertainty are propagated separately, but in this study, the decrease in accuracy in uncertainty estimate due to combined propagation is an order of magnitude smaller than the uncertainties themselves and so is deemed acceptable in general.

**E. Total Uncertainty.** For simplicity, a single estimate of the total expected uncertainty is used. The most widely accepted method, recognized both by the National Bureau of Standards and industry, is the combination:

$$u = \pm (b + t_{95} s), \quad (\text{A.6})$$

The parameter  $u$  itself, it should be noted, is not a statistical confidence interval because the distribution of  $b$  is both unknown and unknowable by definition. However, as mentioned in Abernathy et al. (1980), most reasonable assumptions for distributions of  $b$  result in  $u$  covering a statistical confidence level of at least 95 percent. Thus, if the distributions of the statistical and experimental uncertainties are roughly Gaussian, we may conclude with a 95 percent confidence that the true mean value of a dependent variable  $f$  will fall within the interval  $f \pm (b + t_{95}s)$  68 percent of the time, where  $f$  is the average of  $f_i$ ,  $b$  is the uncertainty in  $f$  due to the propagation of the uncertainties of the independent variables  $x_{ij}$  through  $f_i$ , and  $s$  is the root mean square deviation of  $f_i$  from  $f$ .

More detailed treatment of this subject may be found in the references from which the above is derived: Kline and McClintock (1953), Bevington (1969), Abernathy et al. (1980), and

Moffat (1982).

## **A.2. Regression and the Goodness of Fit**

**A. Introduction.** The analyses in this study often involved the fitting of an equation to a set of data. The fits were performed via the maximum likelihood method: the coefficients of the fit were chosen so as to maximize the probability of the observation of the actual measurements, assuming a Gaussian distribution. This was performed, as is standardly done, by minimizing chi-squared, the least squares method. Chi-squared is defined to be the weighted sum of the squares of the deviations:

$$\chi^2 \equiv \sum \left[ \frac{1}{\sigma_i^2} (y_i - y(x_i)) \right]^2, \quad (\text{A.7})$$

where  $y_i$  are the measurements of the dependent variable,  $x_i$  those of the independent variable,  $\sigma_i$  the standard deviation of the independent variable, and  $y(x_i)$  the fitting function evaluated at  $x_i$ . The minimization of equation A.7 can be performed analytically for fitting functions which are linear in their coefficients. Single value decomposition was used to avoid the spurious coefficients often generated by simple solution of the normal equations. In several segments of this study, least squares fitting was performed for equations which were nonlinear in their coefficients. In these instances, the solution had to be found by iterative, numerical techniques. The Levenberg-Marquardt method, as outlined in Marquardt (1963) was used for its robustness and simplicity. Algorithms from both Bevington (1969) and Press et al. (1986) were used at various points in this research by incorporation into Fortran programs. In addition, the results obtained from these algorithms were verified with the IMSL mathematical library of Fortran subroutines. Listouts of the subroutines as incorporated into the programs may be found in the listouts in Appendices B, C, and D.

### **B. Significant Uncertainty in Both the Independent and Dependent Variables.**

Some difficulties arise as to the proper procedure to be taken when the ratio of the standard deviation of the dependent variable to the dependent variable itself is of the same order of magnitude as the ratio of the standard deviation of the independent variable to the independent variable. For this case, rigorous solution via the least squares method is complicated enough to be considered intractable for most analyses. To circumvent this problem, Bevington (1969) suggests taking the root mean square of the two deviations and treating that as if it were the standard deviation of the independent variable in the standard case with zero dependent variable standard deviation. However, if the units of the dependent and independent variable do not agree, then this

will be dimensionally incorrect. Two other options exist to obtain a combined uncertainty: use the root mean square of the percentages of the standard deviations or nondimensionalize the data so that dimensionality will not enter the problem. The author feels that the former method makes the most sense and so has used it with the exception of the case where nondimensionalization produces variable ranges of equal magnitude, which in any event, is equivalent in result to the former method for monotonically decreasing or increasing functions.

**C.  $\chi^2$  Minimization Methodology.** For the case where the fitting function is linear in its coefficients, minimization of equation A.6 is quite simple to perform with standard techniques, but can produce spurious and occasionally numerically incorrect results. A set of normal equations may be found by setting the derivatives of equation A.6 with respect to the coefficients equal to zero. However, these equations are often very close to singular, especially for fitting functions such as the polynomial used to calibrate RTD's, equation B.3, where the coefficients of the higher terms may be very small and of opposing sign, so as to cancel each other out delicately. In this situation, in addition to containing spurious coefficients, the results are subject to large, and to a great extent, unpredictable numerical error.

A more robust technique uses single value decomposition to force these coefficients to tend towards zero. Single value decomposition is merely a technique of decomposing a matrix into two orthogonal matrices and a diagonal matrix. It may be used to decompose the inverse of the weighted fitting function matrix,  $m_{ij}^{-1}$ , into an orthogonal matrix  $u_{ij}$ , the transpose of an orthogonal matrix,  $v_{ji}$ , and a diagonal matrix,  $w_k$ . Using this method as in Press et al. (1986), the solution for the coefficients,  $a_i$ , of a set of fitting functions  $X_i$  is:

$$a_i = \sum_{j=1}^n \left( \frac{u_{ji} b_j}{1/w_j} \right) v_{ij}, \quad (\text{A.8})$$

where:

$$m_{ij} = \frac{X_j(x_i)}{\sigma_i}, \quad (\text{A.9})$$

are the error weighted fitting functions, and the error weighted independent variables are:

$$b_i = \frac{y_i}{\sigma_i}. \quad (\text{A.10})$$

The uncertainties in the coefficients may be derived from these equations to be:



$$\sigma_{a_j} = \sqrt{\sum_{i=1}^n \left( \frac{v_{ji}}{1/w_i} \right)^2} . \quad (\text{A.11})$$

The total uncertainty of the fit may be calculated as a function of the coefficients and the dependent variables from equations A.11 using the Taylor series error propagation method.

When the fitting function is nonlinear in its coefficients, minimization of equation A.6 must be performed via an iterative, numerical method. The most widely used and robust of the techniques available is the Levenberg-Marquardt method. This method is a coupling of two non-linear iteration schemes, the steepest descent method and the inverse-Hessian method. Both of these methods use the Hessian matrix, the second derivative of equation A.6 with respect to the coefficients of the fit, to iterate a solution. The steepest descent method is used far from the minimum to close in quickly on the general region of minimum  $\chi^2$  where the inverse-Hessian is used to refine the coefficient estimates nearby. Marquardt (1963) put forth an elegant criterion for switching between the two methods based on a suggestion of Levenberg, thereby combining the strengths of each of these methods. Since the solution is numerical, the uncertainty in the coefficients must be estimated numerically from the  $\chi^2$  curvature matrix. Fortunately, as shown in Bevington (1969), this is quite simple.

**D. Goodness of Fit.** The most common and very simple test of the goodness of a fit is whether the reduced  $\chi^2$  of the fit is less than 1.5. The reduced  $\chi^2$  is defined as  $\chi^2$  divided by the number of degrees of freedom,  $\nu$ . The reasoning behind this statistical test is quite simple: if the observed and predicted deviation of the data are approximately equal, the reduced  $\chi^2$  is approximately one. A more rigorous statement of the test can be made by considering the integral probability of observing a particular magnitude of reduced  $\chi^2$  based on the Gaussian distribution. Using this technique, for a reduced  $\chi^2$  of 0.616 or below, with a number of degrees of freedom of 30 or more, at least a 95 percent chance exists that a random sample of data points would yield at least as high a reduced  $\chi^2$ . Similar percentages may be calculated for various conditions for comparison.

## **APPENDIX B- RTD CALIBRATION ANALYSIS AND ERROR ANALYSIS**

### **METHODOLOGY AND RESULTS**

#### **B.1. Calibration and Calibration Error Analysis Methodology**

**A. Background.** The use of platinum resistance thermometers as a standard temperature interpolation instrument in the range 0 to 500°C was first suggested by H.L. Callendar (1887). Improvements in the purity of platinum and other construction materials as well as in design and calibration techniques increased the stability, accuracy, and repeatability of these instruments to such a degree that they have been used as a common standard for temperature measurements near room temperature for many years. Indeed, the most recent definition of an international temperature scale, the International Practical Temperature Scale of 1968 (IPTS-68), uses a particular type called the Standard Platinum Resistance Thermometer (SPRT) as the interpolation instrument for realizing the scale from -259.34 to 630.74°C.

The SPRT consists of a fine helical coil of pure platinum wire wound around a miniature X-beam formed from two thin strips of mica, which in turn are suspended in an evacuated Pyrex or quartz sheath. Most commonly, the resistance of the platinum element is read via a four-wire measurement such as the current source/voltmeter method used in this experiment. The standard interpolating equation for SPRT's relating resistance and temperature until 1968 was the original Callendar equation, with an extra term added by VanDusen (1925):

$$R(T_{CVD}) = R_0 + R_0 \alpha \left[ T_{CVD} - \delta \left( \frac{T_{CVD}}{100} - 1 \right) \left( \frac{T_{CVD}}{100} \right) - \beta \left( \frac{T_{CVD}}{100} - 1 \right) \left( \frac{T_{CVD}}{100} \right)^3 \right], \quad (B.1)$$

where:

- $T_{CVD}$  is Callendar-VanDusen temperature,
- $R$  the resistance at  $T_{CVD}$ ,
- $R_0$  the resistance at  $T_{CVD}$  equal to zero, usually 100  $\Omega$ ,
- $\alpha$  the temperature coefficient at  $T_{CVD}$  equal to zero, required by IPTS-68 to be 0.003925  $\Omega/\Omega/^\circ\text{C}$  or above,
- $\delta$  Callendar's original characteristic constant, typically 1.5, and,
- $\beta$  a characteristic constant added by VanDusen, most often below  $1 \times 10^{-13}$ .

The four constants in this equation are taken to be invariant with temperature, and are determined by taking resistance measurements at four triple points, usually those of Tin, Zinc, Oxygen, and Ice. This equation, termed the Callendar-VanDusen equation, was replaced in the IPTS-68 with a 20-th order polynomial. Between the ice and tin triple points, the difference between the two equations is given by:

$$T_{68} - T_{CVD} = 0.045 \left( \frac{T_{CVD}}{100} \right) \left( \frac{T_{CVD}}{100} - 1 \right) \left( \frac{T_{CVD}}{419.58} - 1 \right) \left( \frac{T_{CVD}}{630.74} - 1 \right). \quad (B.2)$$

With the use of the 20-th order calibration equation, the SPRT error between 0 and 100°C may be as low as  $1 \times 10^{-3}$ °C. A more detailed treatment of SPRT's may be found in Riddle et al. (1973, 1976).

Inexpensive, miniature platinum resistance temperature detectors (RTD's) have been developed recently in an attempt to retain some of the SPRT's' accuracy and repeatability while decreasing their expense and bulk. These RTD's consist of a miniature sensing element, a coil or film of platinum, embedded in some type of epoxy or enamel block. The particular type used in the present research is described in Section 4.2.A. While the accuracy of RTD's, approximately 0.1°C, is as much as 100 times worse than that of SPRT's, their cost is 100 times less. RTD's may be calibrated in the same manner as SPRT's.

**B. Calculation Methodology.** The RTD's were calibrated by using an iterative, non-linear least squares method to fit the solution of a simplified form of equation A.1 for temperature as a function of resistance to a large sample of resistance measurements in the range of interest, 0 to 100°C.

Unfortunately, the author did not have access to triple point calibration equipment. For this reason, the RTD calibration was performed by using a least squares method to fit the Callendar-VanDusen equation to a large sample of data.

A simplified form of the Callendar-VanDusen equation may be solved explicitly for temperature. The Callendar-VanDusen equation, equation B.1, is actually a fourth order equation for resistance as a function of temperature. For convenience, it may be rewritten as:

$$R(T_{CVD}) = a_0 + a_1 T_{CVD} + a_2 T_{CVD}^2 + a_3 T_{CVD}^3 + a_4 T_{CVD}^4, \quad (B.3)$$

where:

$$a_0 \equiv R_0, \quad (B.4)$$

$$a_1 \equiv R_0 \alpha \left( \frac{\delta}{100} + 1 \right), \quad (B.5)$$

$$a_2 \equiv - \frac{R_0 \alpha \delta}{100^2}, \quad (B.6)$$

$$a_3 \equiv \frac{R_0 \alpha \beta}{100}, \quad (B.7)$$

and:

$$a_4 \equiv - \frac{R_0 \alpha \beta}{100^2}. \quad (\text{B.8})$$

While this equation is quite easy to fit to a set of data, it must be solved numerically for temperature for a given resistance using some root finder subroutine. In general, however,  $\beta$  is either zero or extremely small (less than  $1 \times 10^{-13}$ ) for temperature measurements above  $0^\circ\text{C}$ . Thus,  $a_3$  and  $a_4$  are also extremely small (less than  $1 \times 10^{-16}$ ), with the consequence that the contribution of the third degree and higher terms is 10 orders of magnitude smaller than  $a_0$ . When solving equation B.3 numerically for temperature, the error introduced by neglecting their contribution is  $1 \times 10^{-3}^\circ\text{C}$  or less. Since this is two orders of magnitude smaller than the expected accuracy, it may be ignored. The resulting second order equation is not only simple to fit but also explicitly solvable for temperature as a function of resistance:

$$T_{\text{CVD}} = b_1 - \sqrt{b_2 - b_3 R}, \quad (\text{B.9})$$

where:

$$b_1 \equiv - \frac{a_1}{2 a_2}, \quad (\text{B.10})$$

$$b_2 \equiv \frac{1}{4} \left( \frac{a_1}{a_2} \right)^2 - \frac{a_0}{a_2}, \quad (\text{B.11})$$

and:

$$b_3 \equiv - \frac{1}{a_2}. \quad (\text{B.12})$$

To achieve acceptable propagation of experimental error in the calculation of these coefficients, they must be determined from a nonlinear least squares fit of equation B.9. The coefficients  $b_i$  are proportional to the inverse of  $a_2$ . Because  $a_2$  is very small, the error in determining its inverse is quite large. For this reason, the error in  $T_{\text{CVD}}$  calculated from equation B.9 using the coefficients determined with equations B.10 through B.12 is on the order of 100 percent. Acceptable error in equations B.1, B.3, and B.9 may be achieved by fitting equation B.9 to the data directly. Since this equation is not linear in its coefficients, this must be done using an iterative nonlinear least squares fit method. The Levenberg-Marquardt method, as detailed in Appendix A, was used for this purpose. The program used to perform this is listed in section B.2.A.

**C. Calibration Equipment Setup and Operation.** The calibration equipment included a stirred, combined heated and cooled, insulated bath of Fluorinert liquid, into which all the RTD's were placed along with the four partial immersion, mercury thermometers. The calibration bath was a cube approximately 1 cubic foot in size. The bath liquid, trade named Fluorinert, was a chemically inert, electrically nonconducting fluid with high thermal conductivity. The bath apparatus included a heating element used to heat the bath, a mechanical stirrer to ensure uniform temperature, a tap water inlet cooling element, and a temperature control device. The temperature control device consisted of an integrated bath thermometer and a temperature setting device to electrically control the heater. The cooling element was controlled manually with an on/off tap in the rear of the bath. The walls of the bath, themselves insulated, were further insulated with a uniform layer of half-inch-thick Styrofoam. The top to the bath opening used during this calibration was a similar layer of Styrofoam constructed by the author to allow insertion of the four mercury thermometers, evenly spaced across the bath, in addition to the RTD's, with minimal heat loss.

At low temperatures, stable bath temperature settings were achieved using the built in bath heater and cooler, where at higher temperatures, temperature settings only marginally stable, but stable enough to allow the successful taking of calibration data, could be achieved. The internal bath thermometer neither agreed with nor tracked with the mercury thermometers and so was not used to measure temperature. With the stirrer operating, the four mercury thermometers distributed across the calibration bath read to the same temperature to within their readability and tracked exactly. For this reason, it was concluded that the temperature variations across the bath were minimal. At lower temperatures, the heater and cooler could be used in some combination to set the bath temperature to a desired level, with the bath remaining stable at that temperature for at least 30 seconds, more than long enough to take data from all RTD's. At higher temperatures, between 75°C and 100°C, the heat loss from the bath was large enough that no combination of heater or cooler settings resulted in temperatures that were stable for more than 20 seconds. Through trial and error, it was discovered that between approximately 5 and 25 seconds after the heating elements shut off, the temperature of the bath was stable to within 0.075°C. For approximately 5 seconds after the heating elements were turned off, the bath temperature would continue to rise slightly as the element cooled to the temperature of the bath. Only 20 seconds after the bath temperature had stopped rising, it would begin to drop as the bath cooled. Fortunately, the software running the calibration data taking operation needed only 5 seconds to load after being activated and 15 seconds after loading to fully take data. This allowed the calibration data to be taken in the 20-second period of temperature stability by keying the software to run just as the heater element turned off. Thus, even though bath temperature was only marginally stable at higher temperatures, it was possible to ensure that calibration data were taken at constant bath

temperature.

In the first calibration run, measurements began at room temperature and proceeded to close to 100°C. In the second calibration, this order was reversed, with no apparent effect on the results.

**D. Calibration Error Analysis.** The uncertainty in temperature reading due to the error of the calibration, both statistical and experimental, was determined via equation A.5 from the uncertainty in the calibration constants calculated numerically by the programs listed below. An estimate of the uncertainty in temperature reading due to the effect of the cycling of the tests was derived from a second calibration performed after simulated temperature cycling. The maximum difference between the temperatures calculated from the first and the second calibration constants was used to estimate this uncertainty. The sum of these two values was then taken as an estimate of combined total temperature uncertainty.

The error in Callendar-VanDusen temperature calculated from resistance and various calibration constants may be determined using equation A.5. The inverse of the curvature, or Hessian, matrix used to perform a nonlinear least squares fit of equation B.9 to the calibration data is the variance of the coefficients. Thus, the square root of this numerically evaluated matrix gives the errors in the coefficients. Applying equation A.5 to equation B.9, the error in temperature calculated from equation B.9 due to these errors and the error in resistance measurement is:

$$u_{T_{CVD}} \approx \sqrt{\frac{\partial T^2}{\partial R} u_R^2 + \frac{\partial T^2}{\partial b_1} u_{b_1}^2 + \frac{\partial T^2}{\partial b_2} u_{b_2}^2 + \frac{\partial T^2}{\partial b_3} u_{b_3}^2}, \quad (B.10)$$

where  $u_{b_i}$  are the uncertainties calculated from the fit,  $u_R$  is the uncertainty in resistance:

$$\frac{\partial T}{\partial b_1} = 1, \quad (B.11)$$

$$\frac{\partial T}{\partial b_2} = -0.5 (b_2 - b_3 R)^{-1/2}, \quad (B.12)$$

$$\frac{\partial T}{\partial b_3} = 0.5 R (b_2 - b_3 R)^{-1/2}, \quad (B.13)$$

and:

$$\frac{\partial T}{\partial R} = 0.5 b_3 (b_2 - b_3 R)^{-1/2}. \quad (B.14)$$

A similar method may be used to calculate the errors in the Callendar-VanDusen temperature calculated via Newton-Raphson numerical solution of the Callendar-VanDusen

equation. Equations B.10 through B.12 may be solved for  $a_i$  to give:

$$a_0 = \frac{b_2 - b_1^2}{b_3}, \quad (B.15)$$

$$a_1 = \frac{2 b_1}{b_3}, \quad (B.16)$$

$$a_2 = -\frac{1}{b_3}, \quad (B.17)$$

and:

$$a_3 = a_4 = 0. \quad (B.18)$$

The errors are:

$$u_{a_0} = \sqrt{u_{b_1}^2 \left( \frac{2 b_1}{b_3} \right)^2 + u_{b_2}^2 \left( \frac{1}{b_3} \right)^2 + u_{b_3}^2 \left( \frac{b_2 - b_1^2}{b_3^2} \right)^2}, \quad (B.19)$$

$$u_{a_1} = \sqrt{u_{b_1}^2 \left( \frac{2}{b_3} \right)^2 + u_{b_3}^2 \left( \frac{2 b_1}{b_3^2} \right)^2}, \quad (B.20)$$

$$u_{a_2} = \frac{u_{b_3}}{b_3^2}. \quad (B.21)$$

The error due to assumption of zero  $a_3$  and  $a_4$  is contained in these and does not have to be accounted for separately. The Callendar-VanDusen coefficients and their errors may be calculated from  $a_i$  and  $u_{a_i}$  or  $b_i$  directly via equations B.4 through B.8:

$$R_0 = a_0, \quad (B.22)$$

$$\alpha = \frac{a_1 - 100 a_2}{a_0}, \quad (B.23)$$

$$\delta = \frac{10,000 a_2}{100 a_2 - a_1}, \quad (B.24)$$

$$\beta = 0, \quad (B.25)$$

$$u_{R_0} = u_{a_0}, \quad (B.26)$$

$$u_{\alpha} = \sqrt{u_{a_0}^2 \left( \frac{a_1 - 100 a_2}{a_0^2} \right)^2 + u_{a_1}^2 \left( \frac{1}{a_0} \right)^2 + u_{a_2}^2 \left( \frac{100}{a_0} \right)^2}, \quad (\text{B.27})$$

and:

$$u_{\delta} = \sqrt{u_{a_0}^2 \left( \frac{10,000 a_2}{\alpha a_0^2} \right)^2 + u_{a_2}^2 \left( \frac{10,000}{\alpha a_0} \right)^2 + u_{\alpha}^2 \left( \frac{10,000 a_2}{\alpha^2 a_0} \right)^2}. \quad (\text{B.28})$$

The Newton-Raphson method may be used to solve the formula:

$$f(x) = 0 \quad (\text{B.29})$$

for x. Rewriting the Callendar-VanDusen equation in this format yields:

$$f(T_{\text{CVD}}) = R_0 + R_0 \alpha T_{\text{CVD}} + R_0 \alpha \delta \left( \frac{T_{\text{CVD}}}{100} \right) - R_0 \alpha \delta \left( \frac{T_{\text{CVD}}}{100} \right)^2 - R = 0. \quad (\text{B.30})$$

The error in  $T_{\text{CVD}}$  calculated in this manner may be determined from the chain rule to be:

$$u_{T_{\text{CVD}}} = \sqrt{u_{R_0}^2 \frac{\partial T_{\text{CVD}}^2}{\partial R_0} + u_{\alpha}^2 \frac{\partial T_{\text{CVD}}^2}{\partial \alpha} + u_{\delta}^2 \frac{\partial T_{\text{CVD}}^2}{\partial \delta} + u_R^2 \frac{\partial T_{\text{CVD}}^2}{\partial R}}, \quad (\text{B.31})$$

where:

$$\frac{\partial T_{\text{CVD}}}{\partial R_0} = \frac{\partial f}{\partial R_0} \left\{ \frac{\partial f}{\partial T_{\text{CVD}}} \right\}^{-1}, \quad (\text{B.32})$$

$$\frac{\partial T_{\text{CVD}}}{\partial \alpha} = \frac{\partial f}{\partial \alpha} \left\{ \frac{\partial f}{\partial T_{\text{CVD}}} \right\}^{-1}, \quad (\text{B.33})$$

$$\frac{\partial T_{\text{CVD}}}{\partial \delta} = \frac{\partial f}{\partial \delta} \left\{ \frac{\partial f}{\partial T_{\text{CVD}}} \right\}^{-1}, \quad (\text{B.34})$$

$$\frac{\partial T_{\text{CVD}}}{\partial R} = \frac{\partial f}{\partial R} \left\{ \frac{\partial f}{\partial T_{\text{CVD}}} \right\}^{-1}, \quad (\text{B.35})$$

$$\frac{\partial f}{\partial T_{\text{CVD}}} = R_0 \alpha - 2 R_0 \alpha \delta T_{\text{CVD}} / 100^2, \quad (\text{B.36})$$

$$\frac{\partial f}{\partial R_0} = 1 + \alpha T_{\text{CVD}} + \alpha \delta \left( \frac{T_{\text{CVD}}}{100} \right) - \alpha \delta \left( \frac{T_{\text{CVD}}}{100} \right)^2, \quad (\text{B.37})$$



$$\frac{\partial f}{\partial \alpha} = R_0 T_{CVD} + R_0 \delta \left( \frac{T_{CVD}}{100} \right) - R_0 \alpha \delta \left( \frac{T_{CVD}}{100} \right)^2, \quad (B.38)$$

$$\frac{\partial f}{\partial \delta} = R_0 \alpha \left\{ \frac{T_{CVD}}{100} - \left( \frac{T_{CVD}}{100} \right)^2 \right\}, \quad (B.39)$$

and:

$$\frac{\partial f}{\partial R} = -1. \quad (B.40)$$

Since the computer front end used the numerical solution to calculate temperature from stored Callendar-VanDusen coefficients, equation B.31 was used to calculate Callendar-VanDusen temperature error.

As can be determined from equation B.2, in the range 0°C to 100°C, IPTS-68 and Callendar-VanDusen temperature differ by so little that they may be taken to be the same, with the difference being taken account of by adding their maximum difference in this range, 0.01°C, to the total maximum error, if the total desired error may be larger than 0.01°C. Thus:

$$T \equiv T_{\text{IPTS-68}} \approx T_{\text{CVD}} \quad (B.41)$$

and:

$$u_T = u_{T_{\text{CVD}}} + 0.01. \quad (B.42)$$

To account for the effect of the temperature cycling during data runs, the effect of simulated cycling was added to the error estimate. After the first calibration had been performed, the RTD's were subjected to a temperature cycling estimated to be approximately equivalent to that which they might experience during testing. This cycling consisted of 10 sets of 3 hours at room temperature and 3 hours at 100°C. After the cycling, a second calibration was performed. The maximum difference between temperature calculated using coefficients from the first and second calibrations, that at the highest calibration temperature, was then added to the final, total, maximum, error, estimate. The program written to perform this set of calculations is listed in section B.2.B.

## **2.2. Calibration Programs**

**A. Nonlinear, Least Squares, Calibration Program.** The following printout of program CURFIT shows the FORTRAN program written to perform the nonlinear, least squares fit of equation B.9 to the two sets of calibration data taken for the 140 RTD's.

```

program curfit
c
parameter(nterms=3,npts=32)
integer i,j,k
real res(npts,140),temp(npts),sigmare(npts),sigmatemp(npts),
+   sigmatot(npts),x(npts),yfit(npts),b(nterms),chiqr1,
+   sigmab(nterms),chiqr,cvd(3),sigmacvd(3),ast(nterms),
+   sigmayfit(npts),a(3),sigmaa(3),deltayfit(npts),gamma
real keepdata(5,npts,140)
character*8 flag
character*1 tab

c
c      initials program
c
chiqr=0.
chiqr1=0.
do 5 i=1,3
  a(i)=0.
  sigmab(i)=0.
  cvd(i)=0.
  sigmacvd(i)=0.
5  continue
do 20 i=1,npts
  temp(i)=0.
  x(i)=0.
  yfit(i)=0.
  deltayfit(i)=0.
  sigmayfit(i)=0.
  sigmare(i)=0.
  sigmatemp(i)=0.
  sigmatot(i)=0.
do 10 j=1,140
  res(i,j)=0.
10  continue
20  continue
do 30 i=1,nterms
  sigmab(i)=0.
30  continue
do 35 i=1,5
  do 34 j=1,npts
    do 33 k=1,140
      keepdata(i,j,k)=0.
33    continue
34    continue
35    continue
b(1)=2000.0
b(2)=5000000.0
b(3)=10000.0
tab=chr(9)

c
c      read in calibration data
c
write(*,*) 'Reading data'
open(9,file='stone.cal.dat',temp2.dat,status='old')
open(10,file='stone.cal.dat',rawcal2.dat,status='old')
open(11,file='stone.cal.dat',rfical2.dat,status='new')
open(12,file='stone.cal.dat',hlcgrcal2.dat,status='new',
+   recl=1000)
write(11,40)
40  format(1x,'*****',/1x,
+   '      RTD Calibration      ',/1x,
+   '*****',/1x,
+   'fit: T = b1 - sqrt(b2 - b3*R) [the CVD eqn. solved for T]',
+   //)
c
do 41 i=1,npts
  read(9,'(f8.3)',end=41) temp(i)
41  continue
close(9)
do 55 i=1,npts
  read(10,'(1x,a8)',end=55) flag
  if (flag.eq. 'The data') then
    read(10,60) (res(i,j),j=1,140)
  else
    goto 50
  endif
55  continue
60  format(f8.3,139(1x,f8.3))
c
c      calculate fit to data and writes it to file
c
write(*,*) 'Beginning data analysis'
do 70 i=1,npts
  if (temp(i).gt.51.) then
    sigmatemp(i)=0.0707
  else
    sigmatemp(i)=0.0395
  endif
70  continue
do 200 i=1,140
c
do 80 j=1,npts
  sigmare(j)=0.000142*res(j,1)+0.0057
  sigmatot(j)=sqrt(sigmatemp(j)**2+sigmare(j)**2)
  x(j)=res(j,1)
  keepdata(1,j,1)=res(j,1)
  keepdata(2,j,1)=sigmare(j)
  continue
c
  chiqr1=0.0
  gamma=0.001
81  call fit(gamma,x,temp,sigmatot,b,sigmab,yfit,chiqr)
  if (abs(chiqr-chiqr1).gt.0.00000001) then
    chiqr1=chiqr
    goto 81
  endif
  write(*,*) chiqr
c
  do 85 j=1,npts
    sigmayfit(j)=sqrt(sigmab(1)**2 +
+   sigmab(2)**2*0.25/(b(2)-b(3)*x(j)) +
+   sigmab(3)**2*0.25*x(j)**2/(b(2)-b(3)*x(j)) +
+   sigmare(j)**2*0.25*b(3)**2/(b(2)-b(3)*x(j)))+
+   0.01
    deltayfit(j)=yfit(j)-temp(j)
    keepdata(3,j,1)=yfit(j)
    keepdata(4,j,1)=sigmayfit(j)
    keepdata(5,j,1)=deltayfit(j)
85    continue
c
    a(1)=(b(2)-b(1)**2)/b(3)
    a(2)=2.*b(1)/b(3)
    a(3)=1./b(3)
    sigmaa(1)=sqrt(sigmab(1)**2*b(2)**2 +
+   sigmab(2)**2*b(3)**2 + sigmab(3)**2*(b(1)/b(3))**2)
    sigmaa(2)=sqrt(sigmab(1)**2*(2./b(3))**2 +
+   sigmab(3)**2*(2.*b(1)/b(3)**2)**2)
    sigmaa(3)=sigmab(3)/b(3)**2
c
    cvd(1)=a(1)
    cvd(2)=(a(2)-100.*a(3))/a(1)
    cvd(3)=10000.*a(3)/(a(1)**2*cvd(2))
    sigmacvd(1)=sigmaa(1)
    sigmacvd(2)=sqrt(sigmaa(1)**2*(cvd(2)/a(1))**2 +
+   sigmaa(2)**2*(1./a(1))**2 + sigmaa(3)**2*(100/a(1))**2)
    sigmacvd(3)=sqrt(sigmaa(1)**2*(cvd(3)/a(1))**2 +
+   sigmaa(2)**2*(10000./a(1)**2*cvd(2))**2 +
+   sigmacvd(2)**2*(cvd(3)/cvd(2))**2)
c
    write(11,90) i
    format(//,1x,'Calibration of RTD #',i3//,1x,
+   'Temp (C) sigmaT ResMe(0) sigmaR Tcalc(c) ',
+   'sigTcalc deltaT',/1x,
+   '-----',
+   '-----')
    do 110 j=1,npts
      write(11,100) temp(j),sigmatemp(j),res(j,1),sigmare(j),
+   yfit(j),sigmayfit(j),deltayfit(j)
100    format(1x,f8.3,2x,f8.6,2x,f8.3,2x,f8.6,2x,f8.3,2x,f8.6,
+   2x,f8.5)
110    continue
c
    write(11,120)
    format(//,1x,'Coefficients of Fit:')
    format(1x,'b',i1,' = ',a14.6,' +/- ',a14.6)
    do 140 j=1,nterms
      write(11,130) j,b(j),sigmab(j)
140    continue
c
    write(11,141)
    format(//,1x,'Callender-VanDusen Coefficients:')
    do 142 j=1,3
      write(11,143) j, cvd(j), sigmacvd(j)
142    continue
143    format(1x,'cvd',i1,' = ',a14.6,' +/- ',a14.6)
c
    write(11,180) chiqr
    format(//,1x,'Chi-squared = ',f8.4)
c
    write(*,190) i
    format(1x,'Finished fit for rtd #',i3)
200    continue
c
    write(*,*) 'Writing to file'
    do 230 i=1,10
      j=(i-1)*14
      write(12,205) tab,((tab(j+1),k=1,5),j=1,14)
      format(1x,' Times ',a1,' sigTm ',14(a1,'R',nterms,i3,a1,
+   'sigmR',i3,a1,'Tcalc',i3,a1,'sigTc',i3,a1,'diffT',i3))
      do 220 k=1,npts
        write(12,210) temp(k),tab,sigmatemp(k),
+   ((tab,keepdata(1,k,(j+1)),tab,keepdata(2,k,(j+1))),tab,
+   keepdata(3,k,(j+1)),tab,keepdata(4,k,(j+1))),tab,

```



```

if (test.le.0.) then
  write(*,*) 'Sqrt of neg # in sub. the function'
  test=1.
endif

```

```

c
y=double(b(1))-dsqr(test)
return
end

```

**B. Calibration Error Program.** The following printout of program CALTEST shows the FORTRAN program written to calculate the final, total, maximum, RTD calibration uncertainty.

```

program caltest5
  integer i,j,k,l,m,cfit(4),ikexp(4,100)
  real d1,d2,d3,d4,d5,xt(2,140),xt2(140),
  * xsqr(2,140),b(2,140,3),dtemp(140),
  * cvd(2,140,3),scvd(140,3),etot(140)
  real dfdro,dfda,dfdd,dfdt,ddro,dda,ddd
  character*8 flag
  character*1 com
  *
  read in calibration data
  *
  write(*,*) 'Reading data'
  open(10,file='stone.cal.dat',nlist=1,stat='old')
  open(11,file='stone.cal.dat',nlist=2,stat='old')

  i=1
  read(10,'(1x,a8)',end=110) flag
  if (flag.eq.'Calib') then
    do 55 m=1,17
      read(10,'(a8)') flag
      continue
    read(10,60) d1,d2,d3,d4,d5,xt(1,i),dt(1,i)
    format(1x,f8.3,2x,f8.6,2x,f8.3,2x,f8.6,2x,f8.3,2x,f8.6,
    * 2x,f8.5)
    do 70 j=1,8
      read(10,'(a8)') flag
      continue
    format(6x,e14.6)
    do 90 j=1,3
      read(10,80) b(1,j)
      continue
    read(10,'(a8)') flag
    read(10,'(a8)') flag
    do 92 j=1,3
      read(10,93) cvd(1,i,j)
      continue
    format(8x,e14.6)
    read(10,'(a8)') flag
    read(10,100) xsqr(1,i)
    format(15x,f8.4)
    i=i+1
    endif
    goto 50
    continue

  i=1
  read(11,'(1x,a8)',end=180) flag
  if (flag.eq.'Calib') then
    do 125 m=1,17
      read(11,'(a8)') flag
      continue
    read(11,130) d1,d2,d3,d4,d5,xt(2,i),dt(2,i)
    format(1x,f8.3,2x,f8.6,2x,f8.3,2x,f8.6,2x,f8.3,2x,f8.6,
    * 2x,f8.5)
    do 140 j=1,19
      read(11,'(a8)') flag
      continue
    format(6x,e14.6)
    do 160 j=1,3
      read(11,150) b(2,i,j)
      continue
    read(11,'(a8)') flag
    read(11,'(a8)') flag
    do 167 j=1,3
      read(11,168) cvd(2,i,j),scvd(i,j)
      continue
    format(8x,e14.6,5x,e14.6)
    read(11,'(a8)') flag
    read(11,170) xsqr(2,i)
    format(15x,f8.4)
    i=i+1
    endif
    goto 120
    continue

  close(10)
  close(11)

  do 190 i=1,140
    xsqr(2,i)=xsqr(2,i)/28
    dfda=cvd(2,i,1)*cvd(2,i,2)*(1.-cvd(2,i,3)*(2.*70./10000.
    * -0.01))
    dfdro=1.-cvd(2,i,2)*(70.-cvd(2,i,3)*
    * ((70./100.)*2*(70./100.)))
    dfda=cvd(2,i,1)*(70.-cvd(2,i,3))*
    * ((70./100.)*2*(70./100.)))
    dfdd=cvd(2,i,1)*cvd(2,i,2)*(70./100.)-(70./100.)*2)
    ddro=dfdro/dfdt
    dda=dfda/dfdt
    ddd=dfdd/dfdt
    st2(i)=sqrt((scvd(i,1)*ddro)**2+(scvd(i,2)*dda)**2
    * +(scvd(i,3)*ddd)**2+(0.024/dfdt)**2)
    dtemp(i)=(b(2,i,1)-sqrt(b(2,i,2)-b(2,i,3)*140.)-
    * (b(1,i,1)-sqrt(b(1,i,2)-b(1,i,3)*140.)))/5.
    etot(i)=abs(dtemp(i))+st2(i)
    if (i.le.1) then
      write(*,*) 'cvd',cvd(2,i,1),cvd(2,i,2),cvd(2,i,3)
      write(*,*) 'scvd',scvd(i,1),scvd(i,2),scvd(i,3)
      write(*,*) 'dfda,dfdro,dfda,dfdd,dfda,dfda,dfda,dfda'
      write(*,*) 'ddro,dda,ddd,ddro,dda,ddd'
      write(*,*) 'etot',st2(i)
    endif
    continue

  open(11,file='stone.cal.dat',caltest5.dat',status='new',
  * recl=2000)
  write(11,200)
  write(11,205)
  format(1x,'# Xsqr sigTcal2 sigT2cvd deltaT2 ',
  * 'delcalT ',
  * 'Terror cvd1 cvd2 cvd3 ',
  * 'a1 a2 a3')
  format(1x,'-----',
  * '-----',
  * '-----',
  * '-----')
  do 210 i=1,140
    write(11,220) i,xsqr(2,i),st2(i),dt(2,i),dtemp(i),
    * etot(i),cvd(2,i,j)=1,3),b(2,i,j)=1,3)
    continue
  format(1x,i3,2x,f8.4,2x,f8.5,2x,f8.5,2x,f8.5,2x,f8.5,
  * 2x,f10.4,2x,e10.4,2x,f10.6,2x,e10.4,2x,e10.4,2x,e10.4)

  do 240 j=1,5
    cfit(j)=0
    continue

  do 260 i=1,140
    if ((etot(i).lt.0.1).and.(xsqr(2,i).lt.0.605)) then
      cfit(1)=cfi(1)+1
      ikexp(1,cfi(1))=i
    elseif ((etot(i).lt.0.15).and.(xsqr(2,i).lt.0.976)) then
      cfit(2)=cfi(2)+1
      ikexp(2,cfi(2))=i
    elseif ((etot(i).lt.0.25).and.(xsqr(2,i).lt.1.476)) then
      cfit(3)=cfi(3)+1
      ikexp(3,cfi(3))=i
    else
      cfit(4)=cfi(4)+1
      ikexp(4,cfi(4))=i
    endif
    continue

  write(11,300)
  format(/,1x,'Terror,P(Xsqr) 1:(<0.1,95%) 2:(<0.15,50%),
  * 3:(<0.25,5%) 4:(the rest)')
  write(11,310) (cfi(i),i=1,4)
  format(1x,20x,i3,14x,i3,14x,i3,14x,i3)

```

```

320      write(11,320)
      format(1x,'The indices of the RTD's in ',
      *      'each (Terrorat,Xsep) group: ',
      *      'com=')

      write(11,340) 1,iksep(1,1),(com,iksep(1,j),j=2,20)
      write(11,340) 1,iksep(1,21),(com,iksep(1,j),j=22,40)
      write(11,340) 1,iksep(1,41),(com,iksep(1,j),j=42,60)
      write(11,340) 1,iksep(1,61),(com,iksep(1,j),j=62,80)
      write(11,341) 1,iksep(1,81),(com,iksep(1,j),j=82,98)
      write(11,340) 2,iksep(2,1),(com,iksep(2,j),j=2,20)

      write(11,342) 2,iksep(2,21),(com,iksep(2,j),j=22,34)
      write(11,343) 3,iksep(3,1),com,iksep(3,2)
      write(11,344) 4,iksep(4,1),(com,iksep(4,j),j=2,6)
      format(1x,j1,' ',j3,19(a1,i3))
      format(1x,j1,' ',j3,17(a1,i3))
      format(1x,j1,' ',j3,13(a1,i3))
      format(1x,j1,' ',j3,a1,i3)
      format(1x,j1,' ',j3,5(a1,i3))

340
341
342
343
344
      end

```

### B.3. Calibration Results

**A. Summary.** The calibration results showed an average, combined statistical and experimental, RTD calibration error of slightly under  $0.1^{\circ}\text{C}$  and good statistical agreement of the data with the calibration equation. Over the range of resistances and temperatures, the data showed no hysteresis, little scatter, strong repeatability, and good agreement with the calibration curve. The average total, maximum, combined statistical and experimental, RTD error was  $0.09^{\circ}\text{C}$ , within the desired range of  $0.1^{\circ}\text{C}$ . More than 96 percent of the RTD's had a reduced chi-squared under one, the value which is usually taken as the benchmark near or below which a fit is considered statistically reasonable. Approximately 77 percent of the RTD's had both total error under  $0.1^{\circ}\text{C}$  and reduced chi-squared less than 0.616, the value for which there exists a 95 percent probability that a random sample will have as large or larger chi-squared.

**B. Full Results.** Shown in table B.1 are the full results of the calibration. For each RTD are listed:

- $\chi^2/\nu$ , the reduced chi-squared of the second calibration;
- $\sigma_{T_{\text{cal2}}}$ , the maximum uncertainty in temperature calculated from the second set of fit coefficients via equation B.9;
- $\sigma_{T_{\text{CVD2}}}$ , the maximum uncertainty in temperature calculated from the second set of fit coefficients via iteration of equation B.1
- $\Delta T_2$ , the difference between the maximum temperature measured with the liquid-in-glass thermometers and that calculated via the second calibration constants from the resistance measured at that point in the calibration process;
- $\Delta T_{\text{cal}}$ , the maximum difference between the temperatures calculated from the first and second sets of calibration constants;
- $u_{T_{\text{tot}}}$ , the total, maximum uncertainty given by the sum of  $\sigma_{T_{\text{cal2}}}$  and  $\Delta T_{\text{cal}}$ ;
- the second set of fit coefficients  $R_0$ ,  $\alpha$ , and  $\delta$ ; and,
- the second set of fit coefficients  $b_i$ .

### **B.3. Calibration Results**

**A. Summary.** The calibration results showed an average, combined statistical and experimental, RTD calibration error of slightly under  $0.1^{\circ}\text{C}$  and good statistical agreement of the data with the calibration equation. Over the range of resistances and temperatures, the data showed no hysteresis, little scatter, strong repeatability, and good agreement with the calibration curve. The average total, maximum, combined statistical and experimental, RTD error was  $0.09^{\circ}\text{C}$ , within the desired range of  $0.1^{\circ}\text{C}$ . More than 96 percent of the RTD's had a reduced chi-squared under one, the value which is usually taken as the benchmark near or below which a fit is considered statistically reasonable. Approximately 77 percent of the RTD's had both total error under  $0.1^{\circ}\text{C}$  and reduced chi-squared less than 0.616, the value for which there exists a 95 percent probability that a random sample will have as large or larger chi-squared.

**B. Full Results.** Shown in table B.1 are the full results of the calibration. For each RTD are listed:

- $\chi^2/\nu$ , the reduced chi-squared of the second calibration;
- $\sigma_{T_{\text{cal}2}}$ , the maximum uncertainty in temperature calculated from the second set of fit coefficients via equation B.9;
- $\sigma_{T_{\text{CVD}2}}$ , the maximum uncertainty in temperature calculated from the second set of fit coefficients via iteration of equation B.1
- $\Delta T_2$ , the difference between the maximum temperature measured with the liquid-in-glass thermometers and that calculated via the second calibration constants from the resistance measured at that point in the calibration process;
- $\Delta T_{\text{cal}}$ , the maximum difference between the temperatures calculated from the first and second sets of calibration constants;
- $u_{T_{\text{cal}}}$ , the total, maximum uncertainty given by the sum of  $\sigma_{T_{\text{cal}2}}$  and  $\Delta T_{\text{cal}}$ ;
- the second set of fit coefficients  $R_0$ ,  $\alpha$ , and  $\delta$ ; and,
- the second set of fit coefficients  $b_i$ .

## **APPENDIX C- MOMENTUM TRANSFER ANALYSIS. ERROR ANALYSIS.** **PROGRAMS. AND RESULTS**

### **C.1. Momentum Transfer Measurement Equipment, Setup, and Operation**

**A. Static Pressure.** A Setra model 370 digital pressure gage, accurate to 20 Pa, was used to read static pressure. The accuracy of the factory calibration was verified with Logan Airport pressure data. The gage was read visually via its LCD display and the results were entered into the READPRESS2 program before taking velocity measurements. During velocity measurements, if the reading changed by more than 10 Pa, the program was stopped and rerun with the new value. In the majority of velocity measurement runs, these changes occurred infrequently and so, it was assumed, did not compromise the accuracy of the measurements.

**B. Dynamic Pressure.** Dynamic head of the flow was measured directly with pitot-static probes and a boundary layer probe via an MKS Barotron, type 310 CD-100, differential pressure transducer. The transducer was read with a type 170M-6C MKS Barotron Signal Conditioner and type 170M-27C Digital Readout, accurate to  $\pm 0.08$  percent. The readings were performed through a Graphon, type GO-230 VDT, over a DEC Vaxstation II, running the VMS operating system, using the FORTRAN 77 subroutine BARATN written by Philip Lavrich and the FORTRAN 77 program READPRESS2.

The accuracy of the pressure tubing and transducer apparatus was fully verified. The accuracy of the transducer itself was verified with an inclined manometer. The absence of leaks in the tubing from the probes to the transducer was verified by overpressurizing the system and measuring the drop in pressure with time. The effect of the tubing on the pressure readings was validated as being less than the error range of the instrumentation by comparing readings with and without the tubing in place.

A pressure variation check algorithm was used to ensure that the transducer was accurately reading the probe pressure. Due to the length of the tubing between the probe and the transducer, pressure changes at the probe took several minutes to be fully measured at the transducer. To ensure that, when the pressure taps were used to switch from probe to probe or the boundary layer probe was moved across the boundary layer, the true steady-state was being measured, a variation-check algorithm was built into the program READPRESS2. In the velocity measurement subroutine AVEPRESS, two sets of the average of ten velocity measurements were taken and their percent difference written to screen. As the pressure taps were adjusted or the probes moved, the variation and then asymptoting of the probe pressure to a new steady state value could thus be noted. When the difference was less than 0.5 percent, it was assumed that steady state had been

reached, and the actual measurement was taken. This stabilizing process usually lasted anywhere from 2 to 5 minutes, depending on the magnitude of the change in probe pressure.

The approximation for time-averaged dynamic pressure used in the experiment was the average of 31 readings taken over a period of approximately 45 seconds. Actual time-averaging was not used because of the complexity and error inherent in realizing such a process on the particular equipment used.

**C. Turbulent Intensity.** Turbulence levels were measured with a TSI, model 1213-20, hot wire probe via a Dantec, type 56C17, CTA Bridge and type 56C01 Mainframe both graphically and numerically. Readings were taken visually using a Tektronix, type 555, Dual Beam Oscilloscope and numerically using the NEC PC described above, running ILS, via a Data Translation, type DT2821, 20 channel, A/D board.

## **C.2. Momentum Transfer Analysis and Error Analysis Methodology**

**A. Introduction.** Various momentum transfer boundary layer parameters were calculated from the velocity profiles measured with the boundary layer probe and the pitot-static freestream probes. Using Bernouilli's equation, velocity was calculated from the measured dynamic head and the density given via the state equation from ambient pressure and temperature. The measured height of the boundary layer probe above the test walls was adjusted for the effective center displacement due to the total pressure gradient in the boundary layer. The boundary layer thickness was calculated via interpolation. The momentum and displacement thicknesses were calculated by numerical integration of the boundary layer velocity profile. The coefficient of skin friction was calculated from a nonlinear, least squares fit of the log law to mean boundary layer velocity profiles fore and aft of the test sections. As mentioned in section 6.1.B, this technique is a numerical implementation of the Clauser plot graphical method. Coefficient of drag was calculated by integrating coefficient of skin friction across the test sections. The error analysis, performed using the methodology discussed in Appendix A, indicated that the results were good to plus or minus 4 percent, exactly equal to the benchmark value given in Harotinidis (1989) as what should be expected.

**B. Calculating Velocity from Dynamic Head.** The measured dynamic head and density calculated from ambient pressure and temperature using the equation of state were converted to velocity via Bernouilli's equation. Bernouilli's equation gives:

$$P_o - P = \frac{1}{2} \rho u^2. \quad (C.1)$$



The density,  $\rho$ , can be found from the equation of state:

$$\rho = \frac{P}{RT}, \quad (C.2)$$

where  $R$ , the gas constant for air, is given by:

$$R = \frac{\mathfrak{R}}{M}, \quad (C.3)$$

using  $\mathfrak{R}$ , the universal gas constant, and  $M$ , the molecular weight of air. Thus:

$$u = \sqrt{2 \left( \frac{(\mathfrak{R}/M) T}{P} \right) (P_o - P)}. \quad (C.4)$$

where  $(P_o - P)$  is the notation used to symbolize the average of 31 dynamic head measurements. The uncertainty in velocity due to experimental error, statistical uncertainty, and actual fluctuation of the velocity itself is given by:

$$u_u \approx \sqrt{u_p^2 \frac{\partial u^2}{\partial \rho} + u_{(P_o - P)}^2 \frac{\partial u^2}{\partial (P_o - P)}}, \quad (C.5)$$

where the absolute values of the partial derivatives are:

$$\frac{\partial u}{\partial \rho} = \sqrt{\frac{1}{2} \frac{(P_o - P)}{\rho^3}}, \quad (C.6)$$

and:

$$\frac{\partial u}{\partial (P_o - P)} = \left( 2 \rho (P_o - P) \right)^{-\frac{1}{2}}. \quad (C.7)$$

The errors in  $\rho$  and  $(P_o - P)$  are:

$$u_\rho \approx \sqrt{u_P^2 \frac{\partial \rho^2}{\partial P} + u_T^2 \frac{\partial \rho^2}{\partial T}}, \quad (C.8)$$

and:

$$u_{(P_o - P)} = b_{(P_o - P)} + 2.04 s_{(P_o - P)}, \quad (C.9)$$

where:

$$\frac{\partial \rho}{\partial P} = 1 / \left( \frac{\mathfrak{R}}{M} \right) T, \quad (C.10)$$

$$\frac{\partial \rho}{\partial T} = - \frac{P}{(\mathcal{R} / M) T^2}, \quad (C.11)$$

$$u_p = 20 \text{ Pa}, \quad (C.12)$$

$$u_T = 0.05 \text{ K}, \quad (C.13)$$

$$b_{(P_o - P)} = \frac{0.0008 (P_o - P)}{\sqrt{31}}, \quad (C.14)$$

$s_{(P_o - P)}$  is the standard deviation of the 31 dynamic head measurements, and the 2.04 factor is the  $t_{95}$  value for 30 degrees of freedom. The same formulae were used for both freestream and boundary layer velocity calculation.

**C. Calculating Boundary Layer Probe Placement.** If a pitot probe is subjected to a gradient in total pressure in any direction other than parallel to the probe, the effective center of the probe is displaced from its geometric center towards the region of higher total pressure. As mentioned in Benedict (1984), this displacement,  $\delta_{ec}$ , for a square-edged pitot tube can be described by the empirical formula given by Sami (1967):

$$\frac{\delta_{ec}}{D} = 1.025 K - 4.05 K^3, \quad (C.15)$$

for  $K < 0.3$ , and:

$$\frac{\delta_{ec}}{D} = 0.195, \quad (C.16)$$

for  $K > 0.3$ , where  $D$  is the outside probe diameter and  $K$  is a shear parameter defined to be:

$$K \equiv \frac{D (\Delta u / \Delta y)}{2 u}, \quad (C.17)$$

The velocity,  $u$ , and the velocity differential,  $\Delta u$ , for the experiment were approximately 10 m/s; the height above the test plates,  $\Delta y$ , was approximately 0.0254 cm; the outside diameter of the probe,  $D$ , was  $2.5 \times 10^{-2} \pm 5 \times 10^{-4}$  cm. Thus,  $K$  was approximately  $0.01 \pm 0.01$ , which gives  $(\delta_{ec}/D) \approx 0.01 \pm 0.01$  or  $\delta_{ec} \approx 2.5 \times 10^{-4}$  cm. Fortunately, this displacement is tiny for the flow conditions of the experiment, and so the large uncertainty in its magnitude does not significantly degrade the probe placement accuracy.

The position of the effective center of the boundary layer probe, the position of the pressure measurement, can be determined from the distance between the test wall and the lower lip of the probe, the outside diameter of the probe, and the effective center displacement. The probe

placement vernier reading,  $y_v$ , was calibrated with the distance between the lower probe lip and the test wall by zeroing the probe against the wall to determine the zero distance vernier reading,  $y_{v0}$ . The actual distance between the position of pressure measurement and the wall is, therefore:

$$y = (y_v - y_{v0}) + \frac{1}{2} D + \delta_{ec}. \quad (C.18)$$

The  $y_{v0}$  was determined before each boundary layer traversal, at which time it was entered into the program READPRESS2. Before each pressure reading,  $y_v$  was read and entered into the program, which then automatically calculated  $y$ . The uncertainty in this distance  $y$  is

$$u_y \approx \sqrt{u_{y_v}^2 + u_{y_{v0}}^2 + u_D^2/4 + u_{\delta_{ec}}^2}. \quad (C.19)$$

However:

$$u_{y_v} = u_{y_{v0}} = 0.005 \text{ cm}, \quad (C.20)$$

$$u_D = 0.0005 \text{ cm}, \quad (C.21)$$

and:

$$u_{\delta_{ec}} = 0.00025 \text{ cm}, \quad (C.22)$$

so that:

$$u_y = 0.0071 \text{ cm} \quad (C.23)$$

**D. Interpolating for  $\delta$ .** A searching algorithm was incorporated into VPFIT7 to find the  $y$  position with  $u$  closest to but greater than  $0.99 u_e$  and the  $y$  position with  $u$  closest to but less than  $0.99 u_e$ . The standard interpolation formula was then used to find the  $y$  for  $u$  equal to  $0.99 u_e$ . The error propagation formula was then applied to this equation. The simple but lengthy resulting equation may be found in the subroutine BLCALC in BLCALC.FOR.

An attempt was made to use an alternate method of determining  $\delta$  but was halted by problems with the nonlinear iteration needed to perform it. As mentioned in Section 6, researchers such as Reynolds et al. (1958) have made the observation that if a least squares fit of the power function equation 6.3 is performed, then, via equation 2.32, the boundary layer thickness is given directly by equation 6.4. This method has a much sounder basis than interpolation because it uses information from the whole boundary layer instead of just two points. However, some peculiarities inherent in this technique became evident which, although they could possibly have been worked out given the time, the author felt were reason enough to regard its results with some suspicion. First, path dependent iteration was necessary to obtain similar initial and final values for  $\delta$ . With iteration, the problem is essentially the minimization of a nonlinear function in one

dimension, the solution of which is path dependent. An attempt was made to apply the Levenberg-Marquardt nonlinear least squares solution methodology. Unfortunately, this was unsuccessful due to time constraints. Second, when profiles artificially generated from the wake law with varying percentages of random perturbations were analyzed with the program, linear interpolation was found to be a more reliable predictor in about 70 percent of the cases. It is quite likely that this was due to the author's particular methodology, which time constraints prevented being improved. For this reason, the results of this method are not treated in any detail and not used in the estimation of  $C_f$ .

**E. Integrating for  $\theta$  and  $\delta^*$ .** A simple trapezoidal approximation was used to integrate the velocity profile to determine momentum and displacement thicknesses. For  $n$  measurements, the trapezoidal approximation of equation 2.32 is:

$$\frac{\delta^*}{\delta} = \sum_{i=2}^n \frac{1}{2} h_i (f_i + f_{i-1}), \quad (C.24)$$

where:

$$h_i \equiv \frac{(y_i - y_{i-1})}{\delta}, \quad (C.25)$$

and:

$$f_i \equiv 1 - \frac{u_i}{u_e}. \quad (C.26)$$

The approximation for equation 2.30 is:

$$\frac{\theta}{\delta} = \sum_{i=2}^n \frac{1}{2} h_i (g_i + g_{i-1}), \quad (C.27)$$

where:

$$g_i \equiv \frac{u_i}{u_e} f_i. \quad (C.28)$$

The uncertainty in the first integral is

$$u_{\delta^*/\delta} = \sqrt{\sum_{i=2}^n u_{h_i}^2 \left\{ \frac{1}{2} (f_i + f_{i-1}) \right\}^2 + u_{f_1}^2 \left( \frac{h_2}{2} \right)^2 + \sum_{i=3}^{n-1} u_{f_i}^2 \left\{ \frac{1}{2} (h_i + h_{i+1}) \right\}^2 + u_{f_n}^2 \left( \frac{h_n}{2} \right)^2}. \quad (C.29)$$

The error in the second integral,  $u_{\theta/\delta}$ , is the same except that  $g$  replaces  $f$ . These dimensionless integrals were converted to dimensional form by multiplying by  $\delta$ , with the resulting dimensional error given by:

$$u_{\delta^*, \theta} = \sqrt{u_{\delta}^2 \left( \frac{\delta^*}{\delta}, \frac{\theta}{\delta} \right)^2 + u_{(\delta^*/\delta), (\theta/\delta)}^2 \delta^2}. \quad (C.30)$$

**F. Determining Skin Friction.** The three methods of using equation 6.1 to determine  $C_f$  were taken: solving it numerically at  $\delta$ ; performing a nonlinear, least squares fit of it to the data with  $C_f$  as the coefficient of the fit; and, performing a nonlinear, least squares fit with both  $\delta$  and  $C_f$  as coefficients.

First, equation 6.1 may be evaluated at  $\delta$  and solved with a simple Newton root finder by rewriting it as equation 6.2. This method is referred to by the author, somewhat incorrectly but for convenience sake, as Coles-Hirst method number one (C-H1). Unfortunately, the method is subject to the inaccuracies of determining  $\delta$ , the inaccuracy of which is detailed above. Since the slope of the velocity profile in this region is very large, this inaccuracy is quite high. The accuracy in  $C_f$  calculated by C-H1 is thus limited to the accuracy of the interpolation for  $\delta$  and so its worth lies mostly as an indicator of the accuracy of the interpolated  $\delta$ . The formulae for the error in this  $C_f$ , derived in the same manner as equations B.31 through B.40, may be found in subroutine blcalc.

The second method is a nonlinear least squares fit of equation 6.1 with the single coefficient  $C_f$ , denoted as method C-H2. The third method adds the extra coefficient  $\Pi$  and is denoted as method C-H3. As mentioned in Section 6, the latter method was chosen as the most accurate for four reasons based on the results of a Monte-Carlo analysis. The first is that though the tunnel was designed for zero pressure gradient, in general some finite pressure gradients, albeit very tiny ones, did exist in the test segment due to the discarding of the variable wall angle design feature and the limitations of wall adjustment. The second method is unable to account for this. Second, variation in the extra coefficient allows adjustment of the wake law function to fit the aggregate of data in cases where the value of interpolated  $\delta$  is inaccurate. Third, it was found to be a more reliable predictor approximately 75 percent of the time when used to analyze wake law generated profiles with random perturbations in a Monte Carlo type analysis. Fourth, it was found to be more accurate in 100 percent of the analyses of wake law generated profiles with no random perturbations, especially as the number of generated sample points decreased. Indeed, fairly extensive Monte Carlo testing of the VPFIT7 program with wake law generated profiles indicated that this latter method was accurate on average to within 3 percent for random perturbations in velocity as large as 15 percent and to within 0.25 percent for perturbations less than 2 percent. For no perturbations, it was accurate to within 0.01 percent for numbers of generated sample points as low as 8.

The Levenberg-Marquardt method outlined in Appendix A.2.C was used to perform the

nonlinear least squares fit. The calculation of the error in  $C_f$  determined in this manner was performed by the fitting subroutines directly using the inverted curvature matrix.

**G. Integrating for Drag.** Two approaches were taken in determining the  $C_d$  from  $C_f$ . The first of these was simple integration using the trapezoidal approximation. The second was integration using some assumed function. While the trapezoidal method is less sensitive to error propagation, it tends to overestimate drag. Calculations with the the assumed function method indicated that this overestimation was negligible.

The ratio of coefficient of drag of the ribletted plate to that of the flat plate is given by equation 6.7. The integrals of skin friction in this equation must be calculated numerically from the the measurements fore and aft of each of the two test sections. The first method used to calculate this integral was a simple trapezoidal approximation given in equation 6.8. Essentially, the method is just the use of a straight line fitted between the two points to calculate the integral. Since it is known that the variation of  $C_f$  with streamwise distance is not linear, some inaccuracies are inherent in this method. The calculation of the error propagation through equation 6.8, the equation for which may be found in subroutine DRAGCALC in the file CALCDRAG.FOR, is quite simple.

The variation of  $C_f$  with streamwise distance is actually closer to that of equation 2.40. If the function equation 6.10 is assumed to describe this variation, then the constants  $a$  and  $b$  can be determined from the two measured values of  $C_f$ . Evaluating equation 6.10 at  $x_1$  and  $x_2$  and solving for  $a$  and  $b$  gives equations 6.11 and 6.12. With these constants, the integral of  $C_f$  is given by equation 6.13. However, although this method avoids the overestimation inherent in a linear approximation, the error propagation due to the methods of calculating the constants overshadows this.

This error in  $C_d$  propagation through equation 6.13 can be determined fairly simply in steps. If the definitions:

$$r_1 \equiv \frac{C_{f, x_1}}{C_{f, x_2}}, \quad (C.31)$$

and:

$$r_2 \equiv \frac{x_2}{x_1}, \quad (C.32)$$

are made, equation 6.11 becomes:

$$b = \frac{\ln(r_1)}{\ln(r_2)}, \quad (C.33)$$

so that:

$$u_b \approx \sqrt{u_{r_1}^2 \left( \frac{b}{r_1 \ln(r_1)} \right)^2 + u_{r_2}^2 \left( \frac{b}{r_2 \ln(r_2)} \right)^2}, \quad (C.34)$$

where:

$$u_{r_1} \approx \sqrt{u_{C_f, x_1}^2 \left( \frac{r_1}{C_{f, x_1}} \right)^2 + u_{C_f, x_2}^2 \left( \frac{r_1}{C_{f, x_2}} \right)^2}, \quad (C.35)$$

and:

$$u_{r_2} \approx \sqrt{u_{x_1}^2 \left( \frac{r_2}{x_1} \right)^2 + u_{x_2}^2 \left( \frac{r_2}{x_2} \right)^2}. \quad (C.36)$$

Equation 6.12 may be used to derive:

$$u_a \approx \sqrt{u_{C_f, x_1}^2 (x_1^b)^2 + u_{x_1}^2 (b x_1^{b-1})^2 + u_b^2 (a \ln(x_1))^2}. \quad (C.37)$$

With these values, the error in  $C_d$  is thus given by:

$$u_{C_d} \approx \sqrt{u_a^2 \left( \frac{C_d}{a} \right)^2 + \sum_{i=1}^2 u_{x_i}^2 (a x_i^{-b})^2 + u_b^2 \left( \frac{C_d}{1-b} + \frac{a}{1-b} \{ x_1^{1-b} \ln(x_1) - x_2^{1-b} \ln(x_2) \} \right)^2}. \quad (C.38)$$

Since the magnitude of this error is fairly large, the use of  $C_d$  calculated in this manner is restricted to a double checking the trapezoidal approximation. The results indicated that the difference between the two methods was very minor, much smaller than the error propagation through either equation. The error in the ratio of the drag of the ribletted plate to that of the flat plate is found very easily from the errors in both drags.

**H. Calculating Riblet Spacing in Wall Units.** Local  $s^+$  is easily calculated via equation 2.15 and 2.11 once  $C_f$  is known. The calculation of the error propagation through these two formulae, the equations for which may be found in the program VPFIT7, is very straightforward. Since  $C_f$  varies quite slowly with  $x$ ,  $s^+$  is approximately constant across the test sections. In addition, the values of  $s^+$  on the ribletted test section are quite close to those on the ribletted test section. Thus, if we are interested only in an approximate value of  $s^+$  to characterize the test results at a particular test condition, it is quite reasonable to take the average of the four  $s^+$ 's calculated with the four  $C_f$ 's. To extend this to a function of  $s^+$  versus Reynolds number for the purpose of calculating  $s^+$  for the  $C_h$  measurements, a least squares fit of equation 6.10 can be made to the

riblet skin friction data. Since this method is based on an approximation which is only good to 5 or 10 percent (i.e., that  $s^+$  is constant in the two test sections), no rigorous error propagation calculations were performed on the curve fit coefficients.

**I. Measuring Freestream Turbulence.** Several linear calibrations with velocity measured via the pressure transducer were used to transform hot wire voltage into velocity. A generalized form of King's Law relating mass flow to the fourth power of the voltage is usually used to calibrate hot wires. However, the form of the equation is rather inconvenient for simple least squares regression. Since the item of interest is a small fluctuation, a linear approximation in a small velocity range is sufficient to resolve the fluctuation at the velocity at the middle of the range. Repeated linear fits in various velocity ranges can be made to measure the fluctuation over the whole range of freestream velocity. For linear calibration ranges of 0.7 to 1.0 m/s, the coefficient of determination  $R^2$  was approximately 0.9, close enough to one to consider the linear approximations reasonable. Furthermore, though the linear approximation will tend to underestimate the velocity above and below the midrange of the approximation, due to the higher order variation of the actual curve, the error in the magnitude of the fluctuations above and below the midrange velocity will tend to cancel each other out. The time-average value of 2 seconds of voltage data taken at 27 kHz at four different velocities was used for each calibration. The turbulent fluctuation was then taken to be the root-mean-square fluctuation of the velocity calculated from 2 seconds of voltage data taken at 27 kHz at the velocity at the middle of the calibration range.

### **C.3. Momentum Transfer Analysis Programs**

**A. Velocity Measurement Program.** Listed below are the various program units comprising the program READPRESS2. The program was used to measure freestream and boundary layer velocity. The various units include:

- REGDEF.INC and READPRESS2.INC, the two include files used to define the data structure of the program;
- DRIVEREAD.FOR, the set of subroutines for driving the program menus;
- READPRESS2.FOR, the main set of subroutines driving the dynamic head measurements and performing the velocity calculations;
- AVEPRESS.FOR, the subroutine performing the stability check algorithm and calling the pressure reading subroutine;
- BARATN.FOR, the subroutine to read the transducer readout; and,
- DRV11.MAR, the transducer interface handler used by BARATN.FOR.



## REGDEF.INC:

C REGDEF.INC: Definitions needed for accessing device registers  
C on the Qbus. This routine must be LINKed with the macro routines  
C in DRV11.MAR. Routine, MAPQB, must be called before  
C accessing device registers. MAPQB creates a map to the Qbus  
C I/O space and puts the virtual addresses for the device registers in  
C COMMON /REGS/.

```
C
      INTEGER*4 DR1CS,DR1OU,DR1IN,
! DRV11 register addresses
      1 DR2CS, DR2OU, DR2IN,
      2 DRVCS, DRVOU, DRVIN,
      3 HCSRA, HDBRA, HCSRB, HDBRB,
      4 HCSRC, HDBRC, HCSRd, HDBRD
      COMMON /REGS/ DR1CS, DR1OU, DR1IN
! DR1 registers for Scanvalve #1
      1 DR2CS, DR2OU, DR2IN,
! DR2 registers for Scanvalve #2
      2 DRVCS, DRVOU, DRVIN,
! DRV registers for Traverser
      3 HCSRA, HDBRA, HCSRB, HDBRB,
! DRJ registers for Baratron
      4 HCSRC, HDBRC, HCSRd, HDBRD
! (note: DRV11-J has 8 regs)
      INTEGER*2 GETREG
      EXTERNAL GETREG
! Function to read a device register
```

## READPRESS2.INC:

```
*****
* READPRESS.INC: common block file for READPRESS2
*****
      PARAMETER(R=287.0379)
      COMMON/FLAGS/ FLAG
      COMMON/ATM/ RHO, SIGMARHO, PO, SIGMAPO, TO, SIGMTO
      COMMON/SEGDESCR/ TS1$,TS2$,TS3$,TS4$
      COMMON/MISC/ DUMMY

      REAL RHO,SIGMARHO,PO,SIGMAPO,TO,SIGMTO
      REAL HEAD,SIGMAHEAD,VEL,SIGMAVEL,SIHEXP
      REAL SIGHSTAT
      INTEGER I,J,K
      CHARACTER*20 TS1$,TS2$,TS3$,TS4$
      CHARACTER*1 DUMMY
      LOGICAL FLAG
```

## DRIVEREAD.FOR:

```
*****
* DRIVEREAD.FOR -
* A PROGRAM TO TAKE VARIOUS PRESSURE READINGS
* WITH THE MKS BARATRON, STORE THE DATA, AND CONVERT
* PROBE PRESSURE MEASUREMENTS TO VELOCITY
*****
      REQUIRES:      BARATN.FOR
                   DRV11.MAR
                   READPRESS2.POR
*****
      WRITTEN BY TIM STONE 9/16/89; REVISED 12/13/89
*****

      PROGRAM DRIVEREAD
      *
      * INITIALIZE PROGRAM
      *
      * CALL INIT
      *
      * INITIALIZE TUNNEL CONFIGURATION DATA
      *
      * CALL CONFIG
      *
      * CALL UP THE MENU DRIVER
      *
      * CALL MRNDRV
      *
```

```
      END
      *
      *
      *****
      * SUBROUTINE TO INITIALIZE PROGRAM VARIABLES AND CONSTANTS
      *
      *****
      *
      * SUBROUTINE INIT
      *
      * INCLUDE 'READPRESS.INC'
      * CHARACTER*1 TEST
      *
      * CALL MAPQB()
      *
      * FLAG=.TRUE.
      * IF (FLAG) THEN
      *   OPEN(UNIT=9,FILE='PDATA.DAT',STATUS='NEW')
      *   WRITE(9,5)
      *
      * 5   FORMAT(1X,'***** READPRESS MKS BARATRON PRESSURE
      *   READINGS *****',
      *   & //)
      *   ENDIF
      *
      * 6   WRITE(*,*) 'ENTER ATMOSPHERIC PRESSURE IN PASCALS'
      *   READ(*,*) PO
      *   SIGMAPO=0.0002*PO
      *   WRITE(*,*) 'ENTER ATMOSPHERIC TEMPERATURE IN CELCIUS'
      *   READ(*,*) TO
      *   TO=TO+273.15
      *   SIGMTO=0.05
      *   RHO=PO/(R*TO)
      *   SIGMARHO=SQRT((SIGMAPO/(R*TO))**2+((SIGMTO*PO/(R*TO**2))**
      *
      * 2)
      *   WRITE(*,10) PO,SIGMAPO,TO,SIGMTO,RHO,SIGMARHO
      *   IF (FLAG) WRITE(9,10) PO,SIGMAPO,TO,SIGMTO,RHO,SIGMARHO
      *   FORMAT(1X,PO='E14.6,' +/- 'E14.6,' Pa/,
      *   & 1X,TO='F8.2,' +/- 'F4.2,' Degrees Kelvin/,
      *   & 1X,Rho='F8.6,' +/- 'F8.6,' Kg/m^3/,
      *
      *   WRITE(*,*) 'ENTER R TO REDO RETURN TO CONTINUE'
      *   READ(*,11) TEST
      *   FORMAT(A1)
      *   IF (TEST.EQ.'R') GOTO 6
      *   TYPE 15
      *
      * 15  FORMAT(1X,READPRESS: VELOCITY MEASUREMENTS WITH THE
      *   BARATRON/,
      *   & 1X,'MAKE SURE THE BARATRON IS SET TO READ KPA',1X
      *   + 'AND THAT THE RANGE HEAD MULTIPLIER IS SET TO 0.1')
      *   RETURN
      *   END
      *
      *
      *****
      * SUBROUTINE TO STORE THE TUNNEL CONFIGURATION DATA
      *
      *****
      *
      * SUBROUTINE CONFIG
      *
      * INCLUDE 'READPRESS.INC'
      *
      * TS1$='3 FOOT SEGMENT'
      * TS2$='TEST SEGMENT'
      * TS3$='1ST 1 FOOT SEGMENT'
      * TS4$='2ND 1 FOOT SEGMENT'
      * GOTO 100
      *
      * 1   WRITE(*,10) '1ST'
      *
      * 10  FORMAT(1X,'ENTER 20 CHARACTER STRING DESCRIBING THE 'A3/,
      *   & 'TUNNEL SEGMENT AFTER THE 3 FOOT SEGMENT: ')
      *
      * 15  FORMAT(A20)
      *   READ(*,15) TS2$
      *   WRITE(*,10) '2ND'
      *   READ(*,15) TS3$
      *   WRITE(*,10) '3RD'
      *   READ(*,15) TS4$
      *
      *
      *   WRITE(*,20) TS1$, TS2$, TS3$, TS4$
      *
      * 20  FORMAT(1X,'TUNNEL CONFIGURATION:',
      *   & 6X,FIRST: 'A20/,6X;SECOND: 'A20/,6X;THIRD: 'A20/,
      *   & 6X,FOURTH: 'A20/,
      *   TYPE 25
      *
      * 25  FORMAT(1X,'ENTER R TO REDO, RETURN TO CONTINUE')
      *   READ(*,30) DUMMY
      *   FORMAT(A1)
      *   IF (DUMMY.EQ.'R') GOTO 1
      *
      * 100 IF (FLAG) WRITE(9,20) TS1$, TS2$, TS3$, TS4$
      *
      *   RETURN
      *   END
      *
      *
```

```

*****
* SUBROUTINE TO DRIVE THE MAIN PROGRAM MENU
*****
*
SUBROUTINE MENDRV
*
INCLUDE 'READPRESS.INC'
INTEGER CHOICE
*
1 TYPE 10
10 FORMAT(1X,'READPRESS: MAIN MENU',/1X,
& '-----'/1X,
& '1: TAKE VELOCITY MEASUREMENT',/1X,
& '2: TAKE BL PRESSURE MEASUREMENT',/1X,
& '3: CHANGE WIND TUNNEL CONFIGURATION',/1X,
& '4: TOGGLE WRITE TO FILE OPTION',/1X,
& '5: EXIT PROGRAM',/1X,
& 'ENTER MENU CHOICE (1-5)')
READ(*,20) CHOICE
20 FORMAT(12)
*
IF ((CHOICE.GE.1).AND.(CHOICE.LE.4)) THEN
IF (CHOICE.EQ.1) THEN
CALL VELMEAS
ELSEIF (CHOICE.EQ.2) THEN
CALL BLMEAS
ELSEIF (CHOICE.EQ.3) THEN
CALL CONFIG
ELSE
CALL TOGWRTFILE
ENDIF
ELSEIF (CHOICE.EQ.5) THEN
GOTO 1000
ELSE
TYPE 30
30 FORMAT(1X,'INVALID MENU CHOICE- ENTER ONLY INTEGERS
FROM 1 TO 5')
ENDIF
GOTO 1
*
1000 IF (FLAG) CLOSE(UNIT=9)
*
RETURN
END
*
*****
* SUBROUTINE TO MEASURE WIND VELOCITY IN THE CENTER OF EACH
* OF THE FOUR TUNNEL SEGMENTS
*****
*
SUBROUTINE VELMEAS
*
INCLUDE 'READPRESS.INC'
INTEGER CHOICE
*
1 WRITE(*,10) TS1$, TS2$, TS3$, TS4$
10 FORMAT(1X,'READPRESS: VELOCITY MEASUREMENT MENU',/
& '1X:-----'/,
& '1X:1: 'A20/,
& '1X:2: 'A20/,
& '1X:3: 'A20/,
& '1X:4: 'A20/,
& '1X:5: RETURN TO MAIN MENU',/
& '1X:ENTER MENU CHOICE (1-5)')
READ(*,20) CHOICE
20 FORMAT(12)
*
IF (CHOICE.EQ.1) THEN
CALL READVEL(TS1$)
ELSEIF (CHOICE.EQ.2) THEN
CALL READVEL(TS2$)
ELSEIF (CHOICE.EQ.3) THEN
CALL READVEL(TS3$)
ELSEIF (CHOICE.EQ.4) THEN
CALL READVEL(TS4$)
ELSEIF (CHOICE.EQ.5) THEN
GOTO 1000
ELSE
TYPE 30
30 FORMAT(1X,'INVALID MENU CHOICE- ENTER ONLY INTEGERS
FROM 1 TO 5')
ENDIF
GOTO 1
*
1000 RETURN
END
*
*****

```

```

*****
* SUBROUTINE TO TOGGLE THE WRITE TO FILE OPTION ON/OFF
*****
*
SUBROUTINE TOGWRTFILE
*
INCLUDE 'READPRESS.INC'
1 FLAG=.NOT.FLAG
*
IF (FLAG) THEN
OPT='ON'
OPEN(UNIT=9,STATUS='UNKNOWN')
ELSE
OPT='OFF'
CLOSE(UNIT=9)
ENDIF
*
WRITE(*,5) OPT
5 FORMAT(1X,'THE WRITE TO FILE OPTION IS TOGGLED 'A3/,
& '1X:ENTER R TO RETOGGLE, RETURN TO CONTINUE')
READ(*,10) DUMMY
10 FORMAT(A1)
IF (DUMMY.EQ.'R') GOTO 1
*
RETURN
END

```

## READPRESS2.FOR:

```

*****
* READPRESS2.FOR -
*
* WRITTEN BY TIM STONE 9/16/89
*
*****
*****
* SUBROUTINE TO READ THE NECESSARY PRESSURES AND OUTPUT
* RESULTING VELOCITY AS CHOSEN IN VELMEAS
*****
*
SUBROUTINE READVEL(TSEG)
*
IMPLICIT INTEGER*2 (I-N)
INCLUDE 'REGDEF.INC'
INCLUDE 'READPRESS.INC'
CHARACTER*20 TSEG
CHARACTER*6 PTYPE
*
I=25
WRITE(*,10) TSEG
10 FORMAT(1X,'OPEN THE PRESSURE VALVES FOR THE 'A20/,
& '1X:(PRESS RETURN TO CONTINUE)')
READ(*,15) DUMMY
15 FORMAT(A1)
*
16 CALL AVEPRESS(HEAD,SIGMAHEAD,SIGHEXP,SIGHSTAT)
*
IF (HEAD.LT.0.0) THEN
22 TYPE 25
25 FORMAT(1X,'ERROR READING VELOCITY- NEGATIVE DYNAMIC
HEAD',/
& '1X:ABORT, TRY AGAIN, OR CONTINUE? (A, T, OR C)')
READ(*,15) DUMMY
IF (DUMMY.EQ.'T') THEN
GOTO 16
ELSEIF (DUMMY.EQ.'A') THEN
RETURN
ELSEIF (DUMMY.EQ.'C') THEN
HEAD=ABS(HEAD)
ELSE
TYPE 30
30 FORMAT(1X,'ENTER A, T, OR C ONLY')
GOTO 22
ENDIF
ENDIF
*
VEL=SQRT(2.0*HEAD/RHO)
SIGMAVEL=SQRT(SIGMAHEAD**2+HEAD/(2.0*RHO**3))+
& SIGMAHEAD**2/(2.0*RHO*HEAD))
SIGHSTAT=100.*SIGHSTAT/HEAD
SIGHEXP=100.*SIGHEXP/HEAD
*
WRITE(*,35) TSEG, VEL, SIGMAVEL, SIGHSTAT, SIGHEXP
35 FORMAT(1X,'VELOCITY IN THE 'A20, ' = 'F8.4, ' +/- 'F7.4,
& ' M/S',/1X,'STAT. ERROR = 'F8.6, '%',/EXP. ERROR =,
& 'F8.6, '%',/1X,

```

```

* (ENTER R TO RETAKE THE MEASUREMENT, RETURN TO
CONTINUE)
READ(*,15) DUMMY
IF (DUMMY.EQ.'R') GOTO 16

IF (FLAG) WRITE(9,40) TSEG,HEAD,SIGMAHEAD,VEL,SIGMAVEL
40 FORMAT(1X, 'VELOCITY MEASUREMENT IN THE 'A20:',1X,
* 'DYNAMIC HEAD = 'E12.4,' +/- 'E12.4,' PASCALS',1X,
* 'VELOCITY = 'F8.4,' +/- 'F7.4,' M/S)
*
RETURN
END
*
*.....
* SUBROUTINE TO MAKE BOUNDARY LAYER VELOCITY MEASUREMENT *
*.....
SUBROUTINE BLMEAS
*
IMPLICIT INTEGER*2 (I-N)
INCLUDE 'REGDEF.INC'
INCLUDE 'READPRESS.INC'
REAL X,YM(0:99),YA(99),Z,SIGX,SIGYM,SIGYA,SIGZ
INTEGER NAVG
CHARACTER*1 SIDE
CHARACTER*20 PNAME
*
SIGX=0.005
SIGYM=0.005
SIGZ=0.005
SIGYA=SQRT(2)*SIGYM
*
TYPE 1
1 FORMAT(1X,'OPEN THE BL PROBE PRESSURE VALVE AND THE',
* 1X,'APPROPRIATE STATIC PRESSURE VALVE',
* 1X,'(PRESS RETURN TO CONTINUE)')
READ(*,140) DUMMY
*
IF (FLAG) THEN
TYPE 10
10 FORMAT(1X,'ENTER TBL VEL. DATA FILENAME')
READ(*,20) PNAME
20 FORMAT(A20)
OPEN(UNIT=10,FILE=PNAME,STATUS='NEW')
WRITE(10,30) PO,SIGMAPO,TO,SIGMATO,RHO,SIGMARHO
30 FORMAT(1X,'PO = 'E14.6,' +/- 'E14.6,' PA',1X,'TO = ',
+ 'F8.2,' +/- 'F4.2,' K',1X,'RHO = 'F8.6,' +/- 'F8.6,
+ ' KG/M^3')
ENDIF
*
40 TYPE 50
50 FORMAT(1X,'A(PLAT) OR B(RIBLETED) SIDE? (ENTER A OR B)')
READ(*,140) SIDE
IF ((SIDE.NE.'A').AND.(SIDE.NE.'B')) THEN
TYPE 60
60 FORMAT(1X,'ENTER A OR B ONLY')
GOTO 40
ENDIF
WRITE(*,70) SIDE
70 FORMAT(1X,'SIDE = 'A1',1X,
* '(ENTER C TO CHANGE, RETURN TO CONTINUE)')
READ(*,140) DUMMY
IF (DUMMY.EQ.'C') GOTO 40
IF (FLAG) THEN
WRITE(9,80) SIDE
WRITE(10,80) SIDE
ENDIF
80 FORMAT(1X,'** BL MEASUREMENTS ON SIDE 'A1,' **')
*
90 TYPE 100
100 FORMAT(1X,'ENTER X0,Y0,Z0 POS. OF THE BL PROBE IN CM.')
READ(*,110) X,YM(0),Z
110 FORMAT(3F10.5)
INUM=1
120 WRITE(*,130) X,YM(0),Z,SIGX,SIGYM,SIGZ
130 FORMAT(1X,'X0,Y0,Z0 = '3F10.5,' +/- '3F8.5,' CM.',
* 1X,'(ENTER R TO REDO, RETURN TO CONTINUE)')
READ(*,140) DUMMY
FORMAT(A1)
IF (DUMMY.EQ.'R') GOTO 90
IF (FLAG) THEN
WRITE(9,145) X,YM(0),Z,SIGX,SIGYM,SIGZ
WRITE(10,145) X,YM(0),Z,SIGX,SIGYM,SIGZ
ENDIF
145 FORMAT(1X,'X0,Y0,Z0 = '3F10.5,' +/- '3F8.5,' CM.')
*
150 TYPE 160
160 FORMAT(1X,'ENTER Y POS. IN CM.')
READ(*,170) YM(INUM)
170 FORMAT(F10.5)
YA(INUM)=YM(INUM)-YM(0)

```

```

WRITE(*,180) YM(INUM),YA(INUM),SIGYM,SIGYA
180 FORMAT(1X,'YM,YA = '2F10.6,' +/- '2F10.6,' CM.',
* 1X,'(ENTER R TO REDO, RETURN TO CONTINUE)')
READ(*,140) DUMMY
IF (DUMMY.EQ.'R') GOTO 150
*
190 CALL AVEPRESS(HEAD,SIGMAHEAD,SIGHEXP,SIGHSTAT)
IF (HEAD.LT.0.0) THEN
200 TYPE 210
210 FORMAT(1X,'ERROR READING VELOCITY- NEGATIVE DYNAMK
HEAD',
* 1X,'TRY AGAIN, NEW POSITION, ABORT OR CONTINUE?',
* (T,N,A OR C))
READ(*,140) DUMMY
IF (DUMMY.EQ.'T') THEN
GOTO 190
ELSEIF (DUMMY.EQ.'N') THEN
GOTO 150
ELSEIF (DUMMY.EQ.'A') THEN
CLOSE(10)
RETURN
ELSEIF (DUMMY.EQ.'C') THEN
HEAD=ABS(HEAD)
ELSE
TYPE 220
220 FORMAT(1X,'ENTER T, N, A, OR C ONLY')
GOTO 200
ENDIF
ENDIF
*
VEL=SQRT(2.0*HEAD/RHO)
SIGMAVEL=SQRT(SIGMARHO**2*HEAD/(2.*RHO**3)+
* SIGMAHEAD**2/(2.*RHO*HEAD))
SIGHSTAT=100.*SIGHSTAT/HEAD
SIGHEXP=100.*SIGHEXP/HEAD
*
WRITE(*,230) X,YA(INUM),Z,VEL,SIGHSTAT,SIGHEXP
230 FORMAT(1X,'BL VELOCITY AT '3F10.4,' INCHES = 'F8.4,' M/S',
* 1X,'STAT. ERROR = 'F8.6,' %',EXP. ERROR = 'F8.6,' %',
* 1X,'(ENTER R TO RETAKE, RETURN FOR NEW Y POSITION',1X,
* 'M FOR NEW X,Z POS., S FOR NEW SIDE, E TO END)')
READ(*,140) DUMMY
IF (DUMMY.EQ.'R') GOTO 190
IF (FLAG) THEN
WRITE(9,240) INUM,YM(INUM),SIGYM,YA(INUM),SIGYA,HEAD,
+ SIGMAHEAD,VEL,SIGMAVEL
240 FORMAT(1X,I2,4(2X,F8.6),2(2X,E12.4),2(2X,F8.4))
WRITE(10,250) INUM,YA(INUM),SIGYA,VEL,SIGMAVEL
250 FORMAT(1X,I2,2X,F8.6,2X,F8.6,2X,F7.4,2X,F7.4)
ENDIF
INUM=INUM+1
IF (DUMMY.EQ.'M') GOTO 90
IF (DUMMY.EQ.'S') GOTO 40
IF (DUMMY.EQ.'E') THEN
RETURN
ELSE
GOTO 150
ENDIF
ENDIF
END

```

## AVEPRESS.FOR:

```

*.....
* AVEPRESS.FOR
* A SUBROUTINE TO TAKE VARIOUS PRESSURE READINGS
* WITH THE MKS BARATRON, STORE THE DATA, AND CONVERT
* PROBE PRESSURE MEASUREMENTS TO VELOCITY
*.....
* SUBROUTINE TO TAKE AN AVERAGE PRESSURE READING
*.....
SUBROUTINE AVEPRESS(HEAD,SIGMAHEAD,SIGHEXP,SIGHSTAT)
*
IMPLICIT INTEGER*2 (I-N)
REAL PRESS(35)
INTEGER ITER,IOAL
CHARACTER*1 TEST,DP
INCLUDE 'READPRESS.INC'
INCLUDE 'REGDEF.INC'
CALL MAPQB()
*
ITER=0
IOAL=1
PRESS(1)=0.
DO 10 I=1,10
CALL BARATN(ISTAT,IREMOT,IOUT,IEXPON)

```

```

      PRESS(1)=PRESS(1)+1000.*FLOAT(IOUT)*10.***(FLOAT(IEXPON)/10.
10  CONTINUE
      V1=SQRT(ABS(2.0*PRESS(1)/RHO))
15  PRESS(1)=0.
      DO 20 I=1,10
          CALL BARATN(ISTAT,IREMOT,IOUT,IEXPON)
          PRESS(1)=PRESS(1)+1000.*FLOAT(IOUT)*10.***(FLOAT(IEXPON)/10.
20  CONTINUE
      VEL=SQRT(ABS(2.0*PRESS(1)/RHO))
      V2=(VEL-V1)/VEL
      V2=100.*V2
      WRITE(*,30) VEL,V2
30  FORMAT(1X,'BARATRON VELOCITY READING = ',"P8.4," m/s"/,1X,
      + ' DELTAV = ',"P7.3," %"/,1X,'RETURN=1 SAMPLE,S=10,T=TAKE DATA')
      ITER=ITER+1
      IF (ITER.GE.100AL) THEN
          READ(*,A1) DF
      ELSE
          V1=VEL
          GOTO 15
      ENDIF
      IF (DF.EQ.'T') THEN
          HEAD=0.
          SIGHSTAT=0.
          SIGHEXP=0.
          DO 40 I=1,31
              CALL BARATN(ISTAT,IREMOT,IOUT,IEXPON)
              PRESS(1)=1000.*FLOAT(IOUT)*10.***(FLOAT(IEXPON))
              HEAD=HEAD+ABS(PRESS(1))/31.
              SIGHEXP=SIGHEXP+(0.001*PRESS(1)/31.)*2
40  CONTINUE
          SIGHEXP=SQRT(SIGHEXP)
          DO 50 I=1,31
              SIGHSTAT=SIGHSTAT+(PRESS(1)-HEAD)**2/30.
50  CONTINUE
          SIGHSTAT=SQRT(SIGHSTAT)
          SIGMAHEAD=2.04*SIGHSTAT*SIGHEXP
          ELSE
              V1=VEL
              IF (DF.EQ.'S') THEN
                  100AL=10
              ELSE
                  100AL=1
              ENDIF
              ITER=0
              GOTO 15
          ENDIF
      RETURN
      END

```

## BARATN.FOR:

```

      SUBROUTINE BARATN(ISTAT,IREMOT,IOUT,IEXPON)
      C SUBROUTINE TO READ MKS INSTRUMENTS BARATRON PRESSURE
      C READOUT VIA THE DRV11J HIGH DENSITY PARALLEL INTERFACE
      C-----C
      C WRITTEN BY PHILIP L. LAVRICH 2/19/85
      C-----C
      IMPLICIT INTEGER*2 (I-N)
      INCLUDE 'REGDEF.INC'
      C Definitions for mapping to device registers
      INTEGER*4 STATUS,LIB$WAIT
      C
      C SET CONTROL STATUS CODE FOR ALL REGISTERS
      C
      I  ISTAT = 0
          CALL CLRREG(HCSRA)
          CALL CLRREG(HCSRB)
          CALL CLRREG(HCSRC)
          CALL CLRREG(HCSRd)
      C
      C CHECK IF MKS NEEDS PULSE TO INITIATE DATA CONVERSION
      C
      IF (IREMOT.NE.1) THEN
          ! PULSE TO INITIATE CONVERSION
          CALL PUTREG(1,HDBRC)
          STATUS = LIB$WAIT(0.1)
      ! 0.1 Second
          CALL PUTREG(0,HDBRC)
          END IF
      C
      C GET DATA IN REGISTERS A AND B
      C
      C WAIT FOR DATA READY STROBE TO GO LO, THEN WAIT FOR HIGH
      C THIS ENSURES NOT TAKING THE SAME READING OVER AND OVER
      C

```

```

10  IN = GETREG(HDBRB)
      IF ((4000'0 AND. IN).NE.0) GO TO 10
      ! FIRST WAIT FOR LOW ON B-11
11  IN = GETREG(HDBRB)
      ! TEST BIT B-11 FOR DATA READY PULSE
      IF ((4000'0 AND. IN).EQ.0) GO TO 11
      ! WAIT TILL B-11 IS HIGH
      IBUFA = GETREG(HDBRA)
      ! READ DATA FROM DATA BUFFER A
      IBUFB = GETREG(HDBRB)
      ! READ DATA FROM DATA BUFFER B
      C
      C CONVERT THE DATA FROM BUFFER A
      C
      IACC = 'PX AND. IBUFA
      ! 4 LSB are the cm's digit
      IBUFA = IBUFA/10'X
      ! Shift right 4 bits
      IACC = IACC + 10*(PX AND. IBUFA)
      ! Next 4 bits are 10's digit
      IBUFA = IBUFA/10'X
      ! Shift right 4 bits
      IACC = IACC + 100*(PX AND. IBUFA)
      ! Next 4 bits are 100's digit
      IBUFA = IBUFA/10'X
      ! Shift right 4 bits
      IACC = IACC + 1000*(PX AND. IBUFA)
      ! Next 4 bits are 1000's digit
      C
      C CONVERT THE DATA FROM REGISTER B
      C
      C TEST BIT B-14 (10K BIT)
      C
      IF ((40000'0 AND. IBUFB).NE.0) IACC = IACC + 10000
      C
      C TEST POLARITY (BIT 10, 1=+)
      C IF NEGATIVE POLARITY, NEGATE RESULT
      C
      IF ((2000'0 AND. IBUFB).EQ.0) IACC = -IACC
      C
      C PUT RESULT IN IOUT
      C
      IOUT = IACC
      C
      C CHECK IF THERE IS AN ENCOUNTER OF OVERRANGE
      C
      IF ((100000'0 AND. IBUFB).NE.0) ISTAT = ISTAT + 2
      C
      C CHECK IF GOOD DATA BIT B-12 IS HIGH
      C
      IF ((10000'0 AND. IBUFB).EQ.0) ISTAT = ISTAT + 1
      C
      C NOW DECODE EXPONENT
      C
      IBUFB = IBUFB AND. '1777'0 ! ONLY LOOK AT BITS 0-9
      IF (IBUFB.EQ.'1776'0) THEN
          EXPON = -8
      ELSE IF (IBUFB.EQ.'1775'0) THEN
          EXPON = -7
      ELSE IF (IBUFB.EQ.'1773'0) THEN
          EXPON = -6
      ELSE IF (IBUFB.EQ.'1767'0) THEN
          EXPON = -2
      ELSE IF (IBUFB.EQ.'1757'0) THEN
          EXPON = -1
      ELSE IF (IBUFB.EQ.'1737'0) THEN
          EXPON = 0
      ELSE IF (IBUFB.EQ.'1677'0) THEN
          EXPON = -9
      ELSE IF (IBUFB.EQ.'1577'0) THEN
          EXPON = -5
      ELSE IF (IBUFB.EQ.'1377'0) THEN
          EXPON = -4
      ELSE IF (IBUFB.EQ.'777'0) THEN
          EXPON = -3
      ELSE
          ! ERROR CODE 4, EXPONENT NOT RECOGNIZED, SET EQUAL TO 0
          EXPON = 0 ! SET EXPONENT=0
          ISTAT = ISTAT + 4 ! SET ERROR CODE 4
          END IF
      C
      RETURN
      END

```

## DRV11.MAR:

```

      .TITLE      DRV11_HANDLER
      .LIBRARY    /SYS$LIBRARY:LIB/ ;NEEDED FOR $IO730DEF

```

```

; HIS DEFINES THE COMMON BLOCK WITH DEVICE ADDRESS
; AND CONTENTS
.PSECT QBUS
PIC,OVR,REL,GBL,SHR,NOEXE,RD,WRT,LONG
DR1ADD: .BLKL 1 ; Scan valve interface
DR2ADD: .BLKL 1 ; Scan valve interface
DRVADD: .BLKL 1 ; Traverser interface
DRJADD: .BLKL 1 ; Baratron interface
;
; These are the mapped addresses for the device register
;
.PSECT REGS
PIC,OVR,REL,GBL,SHR,NOEXE,RD,WRT,LONG
$DR1CS: .BLKL 1 ; Scan valve interface
$DR1OU: .BLKL 1
$DR1IN: .BLKL 1
$DR2CS: .BLKL 1 ; Scan valve interface
$DR2OU: .BLKL 1
$DR2IN: .BLKL 1
$DRVCS: .BLKL 1 ; Traverser interface
$DRVOU: .BLKL 1
$DRVIN: .BLKL 1
$HCSRA: .BLKL 1 ; Baratron interface
$HDBRA: .BLKL 1
$HCSRB: .BLKL 1
$HDBRB: .BLKL 1
$HCSRC: .BLKL 1
$HDBRC: .BLKL 1
$HCSR D: .BLKL 1
$HDBRD: .BLKL 1
;
.PSECT CODE GBL,NOSHR,LONG
;
; MACRO LIBRARY CALLS TO DEFINE SYSTEM PARAMETERS
;
$SSDEF GLOBAL
$SECDDEF GLOBAL
$IIOUV2DEF GLOBAL
;
; DEFINE LOCAL SYMBOLS
DR1_QBA=^0771770 ; QBUS ADDRESS FOR DRV11 TO Scan Valve
DR2_QBA=^0771760 ; QBUS ADDRESS FOR DRV11 TO Scan Valve #2
DRV_QBA=^0770000 ; QBUS ADDRESS FOR DRV11 TO Traverser
DRJ_QBA=^0770100 ; QBUS ADDRESS FOR DRV11-J TO Baratron
MAP_QBA=^0770000 ; QBUS BASE ADDRESS FOR MAPPING
qbus_io_base = ^0760000 ; beginning of io space on Q bus
;
; STORAGE FOR IN AND OUT ADDRESSES FOR CALL TO CRMPSC
AREAP0: LONG ^01000[2] ; ANY ADDRESS IN P0
BASEAD: .BLKL 2; VIRTUAL ADDRESS OF SECTION ON RETURN
;
; ROUTINE TO MAP A SECTION OF QBUS I/O SPACE TO USER
; ADDRESS SPACE
; NO ARGUMENTS
; RETURNS: DR1 CSR ADDRESS IN DR1ADD
; DR1 CSR CONTENTS IN DR1CS
; DR1 OUT CONTENTS IN DR1OU
; DR1 IN CONTENTS IN DR1IN
; DRV CSR ADDRESS IN DRVADD
; DRV CSR CONTENTS IN DRVCS
; DRV OUT CONTENTS IN DRVOU
; DRV IN CONTENTS IN DRVIN
;
.ENTRY MAPQB,^M<R4,R5>
$CRMPSC $ INADR=AREAP0, -
RETADR=BASEAD, -
FLAGS=#<SECSM_EXPREG!SECSM_WRT!SECSM_PFNMAP>, -
PAGCNT=#8, -
VBN=#<IIOUV2$AL_QBOSP+MAP_QBA-qbus_io_base>@-9>
BLBS R0,OKAY
; HANDLE ERROR ON CALL TO CRMPSC
PUSHAL (R0)
CALLS #1,C^LIB$STOP
OKAY: BICL3 #^XFFFFF000,DR1_QBA,R4 ; 12 LSB OF DR1 CSR address
ADDL2 BASEAD,R4 ; ADD BASE ADDRESS OF SECTION
MOVL R4,$DR1CS ; STORE VIRTUAL ADDRESS FOR CSR
MOVW #0,(R4) ; INITIALIZE DR1 CSR
ADDL3 #2,R4,$DR1OU ; STORE VIRTUAL ADDRESS FOR BUFFER
MOVW #0,(R4) ; INITIALIZE DR1 OUTPUT REGISTER
ADDL3 #4,R4,$DR1IN ; STORE VIRTUAL ADDRESS FOR IN BUFFER
BICL3 #^XFFFFF000,DR2_QBA,R4
; 12 LSB OF DR2 CSR address
ADDL2 BASEAD,R4 ; ADD BASE ADDRESS OF SECTION
MOVL R4,$DR2CS ; STORE VIRTUAL ADDRESS FOR CSR
ADDL3 #2,R4,$DR2OU ; STORE VIRTUAL ADDRESS FOR BUFFER
ADDL3 #4,R4,$DR2IN ; STORE VIRTUAL ADDRESS FOR IN BUFFER
BICL3 #^XFFFFF000,DRV_QBA,R4
; Repeat for DRV
ADDL2 BASEAD,R4
MOVL R4,$DRVCS

```

```

ADDL3 #2,R4,$DRVOU
ADDL3 #4,R4,$DRVIN
BICL3 #^XFFFFF000,DRJ_QBA,R4
; Again for DRV11-J
ADDL2 BASEAD,R4
MOVL R4,$HCSRA ; STORE VIRTUAL ADDRESS FOR CSRA
ADDL3 #2,R4,$HDBRA ; STORE VIRTUAL ADDRESS FOR IO BUF. A
ADDL3 #4,R4,$HCSRB ; STORE VIRTUAL ADDRESS FOR CSRB
ADDL3 #6,R4,$HDBRB ; STORE VIRTUAL ADDRESS FOR IO BUF. B
ADDL3 #8,R4,$HCSRC ; STORE VIRTUAL ADDRESS FOR CSRC
ADDL3 #10,R4,$HDBRC ; STORE VIRTUAL ADDRESS FOR IO BUF. C
ADDL3 #12,R4,$HCSR D ; STORE VIRTUAL ADDRESS FOR CSR D
ADDL3 #14,R4,$HDBRD ; STORE VIRTUAL ADDRESS FOR IO BUF. D
;
MOVL #DR1_QBA,DR1ADD
MOVL #DR2_QBA,DR2ADD
MOVL #DRV_QBA,DRVADD
MOVL #DRJ_QBA,DRJADD
MOVL #SS$ _NORMAL,R0
RET
;
; ROUTINE TO GET CONTENTS OF DRV11 REGISTERS
; Usage: VALUE = GETREG(REGADD)
; ARGUMENTS: REGADD is mapped address of register
; VALUE is returned in R0
;
.ENTRY GETREG,^M<R3,R4,R5,R6>
movl 4(sp),r3 ; address of register supplied in arg
movw @(r3),r0
RET
;
; ROUTINE TO PUT WORD SUPPLIED AS ARG. TO DRV11 REG.
; Usage: CALL PUTREG(VALUE,REGADD)
; ARGUMENTS: VALUE Word to put in dr1 out
; REGADD mapped address of register
; NO RETURNS
;
.ENTRY PUTREG,^M<R3,R4>
MOVL 4(AP),R3
MOVL 8(AP),R4
MOVW (R3),@(R4)
MOVL #SS$ _NORMAL,R0
RET
;
; ROUTINE TO CLEAR A DRV11 REGISTER
; Usage: CALL CLRREG(REGADD)
; ARGUMENTS: REGADD mapped address of register
; NO RETURNS
;
.ENTRY CLRREG,^M<R3,R4>
MOVL 4(AP),R3
CLRW @(R3)
MOVL #SS$ _NORMAL,R0
RET
;
; ROUTINE TO SET BITS ON A DRV11 REGISTER
; Usage: CALL BISREG(MASK,REGADD)
; ARGUMENTS: MASK Mask with bits to set
; REGADD mapped address of register
; NO RETURNS
;
.ENTRY BISREG,^M<R3,R4,R5>
MOVL 4(AP),R3
MOVL 8(AP),R4
MOVL (R4),R5
bimw 2,(R3),R5
MOVL #SS$ _NORMAL,R0
RET
;
; ROUTINE TO CLEAR BITS ON A DRV11 REGISTER
; Usage: CALL BICREG(MASK,REGADD)
; ARGUMENTS: MASK Mask with bits to clear
; REGADD Mapped address of register
; NO RETURNS
;
.ENTRY BICREG,^M<R3,R4,R5>
MOVL 4(AP),R3
MOVL 8(AP),R4
MOVL (R4),R5
bicw 2,(R3),R5
MOVL #SS$ _NORMAL,R0
RET
;
END

```

**B. Momentum Transfer Analysis Program.** Below is listed the units of VPFIT7, the momentum transfer analysis program used to interpolate for  $\delta$ , integrate numerically for  $\theta$  and  $\delta^*$ , calculate  $C_f$  from a nonlinear fit of the wake law equation to velocity profile data, and integrate  $C_f$  for  $C_d$ . The program units include:

- COMMONBLK1.FOR through COMMONBLK3.FOR, the program common block include files;
- VPFIT7.FOR, the main program unit including the menu driver;
- BLCALC.FOR, the main calculation unit which drives the numerical integration, the nonlinear least squares fits, and the miscellaneous newton solving;
- WRTOFILE.FOR, the subroutine to write the analysis results to file;
- CALCDRAG.FOR, the subroutines to store the necessary  $C_f$  data and integrate for  $C_d$ ;
- AIR.FOR, the subroutine to calculate air properties as a function of ambient temperature;
- MRQMIN.FOR, MRQCOF.FOR, COVSRT.FOR, and GAUSSJ.FOR, the subroutines from Press et al. (1986) used to perform the nonlinear least squares fit; and,
- RTNEWT.FOR, the newton solver subroutine also from Press et al. (1986).

#### COMMONBLK1.FOR;5:

```
*****
* commonblk1.for- parameter statement for tbi vp analysis *
*****
*
*   parameter(tk=0.41, tbs=5., tp=0.5, pi=3.141592654)
*
*****
```

#### COMMONBLK2.FOR;11:

```
*****
* commonblk2.for- common block file for tbi calculations *
*****
*
*   parameter(nmax=99)
*
*   common/loval/ rho, sigrho, ue, sigue, to, sigto, po, sigpo,
*   + cp, sigcp, gmu, siggmu, ka, sigka, pr, sigpr, y, sigy, u, sigu
*   common/vpanel/ yk, sigyk, yb, sigyb, yplus, sigyplus,
*   + ub, sigub, sigtoth, ubfit, sigubfit, uk, sigtok, uplus,
*   + siguplus, upw1, sigupw1, tpfit, sigtpfit
*   common/couat/ nk, npts, ndel, nd1, nd2, ikf, ikd
*   common/tblval/ theta, sigtheta, retheta, sigretheta,
*   + delta, sigdelta, retheta, sigretheta, dstar, sigdstar,
*   + cfks, sigcfks, cfch, sigcfch, utau, sigutau, jtau, sigjtau,
*   + xt, utogmu, xtrip, xot, rext, cfwh, delwh, delcheck,
*   + delorig, sigdelo
*   common/calc1/ f, sigf, g, sigg, h, sigh, chisqr, chisqr1, chisqr2,
*   + gamma
*   common/calc3/ sd1, sd2, sd3, sd4, sd5, mh, ms, mhplus, msplus, sigmh,
*   + sigmhplus, sigms, sigmsplus
*   common/calc4/ var, var1, var2, var3, var4, alpha, dyda, a,
*   + covar, siga, v1, v2, v3, jista
*   common/filing/ fnum, fname1, fname2, fname3, tab, dummy, choice,
*   + chindex
*
*   real rho, sigrho, ue, sigue, to, sigto, po, sigpo, cp, sigcp
*   real gmu, siggmu, ka, sigka, pr, sigpr, y(nmax), sigy(nmax)
*   real u(nmax), sigu(nmax), yk(nmax), sigyk(nmax), yb(nmax), sigyb(nmax)
*   real sigyb(nmax), yplus(nmax), sigyplus(nmax)
*   real ub(nmax), sigub(nmax), sigtoth(nmax), ubfit(nmax),
*   real sigubfit(nmax), uk(nmax), sigtok(nmax)
```

```
real uplus(nmax), siguplus(nmax), upw1(nmax)
real sigupw1(nmax), theta, sigtheta, retheta, sigretheta
real delta(nmax), sigdelta(nmax), retheta, sigretheta, dstar, sigdstar
real cfks, sigcfks, cfch(nmax), sigcfch(nmax), utau(nmax), sigutau(nmax)
real ka(nmax), sigka(nmax), pr(nmax), sigpr(nmax), g(nmax), sigg(nmax)
real h(nmax), sigh(nmax), chisqr(nmax), chisqr1, chisqr2, gamma
real sd1, sd2, sd3, sd4, sd5, mh, ms, mhplus(nmax), msplus(nmax), sigmh
real sigmhplus(nmax), sigms, sigmsplus(nmax), var, var1, var2, var3, var4
real alpha(nmax), dyda(nmax), covar(nmax), siga(nmax), v1, v2, v3
real tpfit, sigtpfit, xt, utogmu, xtrip, xot, rext, cfwh, delwh
real delcheck, delorig, sigdelo
integer nk, npts, ndel, nd1, nd2, ikf, ikd, jista(nmax), chisindex
character*1 tab, dummy, choice
character*4 fname
character*6 fname1
character*40 fname2
character*80 fname3
```

#### COMMONBLK3.FOR;7:

```
*****
* commonblk3.for- common block file for tbi calculations *
*****
*
*   common/dragvar/ savecf, savecf, cfd, sigcfd,
*   + af, saf, bfbf, cfdat, sigcfd, savevt
*
*   real savecf(2,2,5), savecf(2,2,5), cfd(2,2,5), sigcfd(2,2,5)
*   real af(5), saf(5), bfbf(5), cfdat(2,5), sigcfd(2,5)
*   real nd1, nd2, nd3, savevt(2,2)
```

#### VPFIT7.FOR;7:

```
*****
* vpf7.for- program to calculate tbi characteristics from *
*   tbi velocity data *
*****
*
```

```

*****
* main program section: drives menu *
*****

      include 'commonblk2.for'

1   type 10
10  format(/,1x,TBL Velocity Profile Analysis',1x,
      '-----',1x,
      '1: Analyze One Profile',1x,
      '2: Analyze a Set of Two Profiles',1x,
      '3: Analyze a Full Set of Four',1x,
      '4: Generate a Dummy Test Case and Analyze',1x,
      '5: Exit Program',1x,
      '(enter 1, 2, 3, 4, or 5)')
      read(*,20) choice
20  format(a1)
      if ((choice.eq.'1').or.(choice.eq.'2').or.
          (choice.eq.'3').or.(choice.eq.'4')) then
          call vpdtrnal
      elseif (choice.eq.'5') then
          stop
          endif
      goto 1

      end

*****
* vp analysis drives subroutine *
*****

      subroutine vpdtrnal

      include 'commonblk2.for'

1   type 10
10  format(1x,'enter code for data dir (MDD#)')
      read(*,20) fnum
20  format(a4)
      write(*,30) fnum
30  format(1x,'data dir. =',a4,
      ' (enter r to redo, return to cont.)')
      read(*,40) dummy
40  format(a1)
      if ((dummy.eq.'Y').or.(dummy.eq.'R')) goto 1
      frame2='stone.tbl.dred.data'//fnum//T
      frame3=frame2//vpfit//choice//.dat'
      open(11,file=frame3,status='new',recl=1000)
      frame3=frame2//vpfit//choice//.dat2'
      open(12,file=frame3,status='new',recl=1000)

      if (choice.eq.'1') then
95  type 60
100 format(1x,'enter 6 char. name of data file')
      read(*,70) fname1
70  format(a6)
      write(*,80) fname1
80  format(1x,'input data file name =',a4,
      ' (enter r to redo, return to cont.)')
      read(*,90) dummy
90  format(a1)
      if ((dummy.eq.'Y').or.(dummy.eq.'R')) goto 50
          call vpanel
          call wrtofile
      elseif (choice.eq.'2') then
95  type 100
100 format(1x,'enter a or b for side of s.t. to analyze')
      read(*,110) dummy
110 format(a1)
      if ((dummy.ne.'a').and.(dummy.ne.'b')) goto 95
          chindex=1
          frame1=dummy//1'
          call vpanel
          call wrtofile
          call cstore
          chindex=2
          frame1=dummy//2'
          call vpanel
          call wrtofile
          call cstore
          call drgcalc
      elseif (choice.eq.'3') then
          chindex=1
          frame1='a1'
          call vpanel
          call wrtofile
          call cstore

          chindex=2
          frame1='a2'
          call vpanel
          call wrtofile

```

```

          call cstore
          call drgcalc

          chindex=3
          frame1='b1'
          call vpanel
          call wrtofile
          call cstore

          chindex=4
          frame1='b2'
          call vpanel
          call wrtofile
          call cstore
          call drgcalc
      elseif (choice.eq.'4') then
          chindex=1
          call vpanel
          call wrtofile
      else
          write(*,*) 'routing error in vpdtrnal'
          endif

          close(11)
          close(12)

          return
          end

*****
* main vp analysis subroutine *
*****

      subroutine vpanel

      include 'commonblk2.for'

      * initialize variables

          call init
          mth=0.0254*1.5e-3
          sigmth=0.0254*0.8e-3
          ms=0.0254*21.03e-3
          sigma=0.0254*0.8e-3
          tab=char(9)

      * read in experimental data

          if (choice.eq.'4') then
              call genprof
              call rdprof
          endif

      * calculate delta1 and its error

          do 40 i=npts,1,-1
              if (u(i).gt.(0.99*ue)) nd1=i
40  continue
              ndel=nd1
              nd2=1
              do 50 i=2,npts
                  if (u(i).lt.(0.99*ue)) nd2=i
50  continue
              delta1=y(nd2)+(0.99*ue-u(nd2))*(y(nd1)-y(nd2))/(u(nd1)-u(nd2))
              sd1=sig(y(nd1))*(0.99*ue-u(nd2))/(u(nd1)-u(nd2))
              sd2=sig(y(nd2))*(1.-(0.99*ue-u(nd2))/(u(nd1)-u(nd2)))
              sd3=sig(u(nd1))*(0.99*ue-u(nd2))*(y(nd1)-y(nd2))/
              + (u(nd1)-u(nd2))**2
              sd4=sig(u(nd2))*((0.99*ue-u(nd2))*
              + (y(nd1)-y(nd2))/(u(nd1)-u(nd2))**2-(y(nd1)-y(nd2))/
              + (u(nd1)-u(nd2)))
              sd5=sig(ue)*(y(nd1)-y(nd2))/(u(nd1)-u(nd2))
              sigdelta1=sqrt(sd1**2+sd2**2+sd3**2+sd4**2+sd5**2)

      * call subroutines to perform calculations

          call blcalc

      * calculate h+, s+

          do 60 i=1,3
              mthp(i)=mth*atan(i/gm)
              sigmthp(i)=sqrt((sigmth*atan(i/gm))**2+
              + (sigu(i)*mth/gm)**2+(siggm*nmh*atan(i/gm)**2)**2)
              mthsp(i)=mth*atan(i/gm)
              sigmthsp(i)=sqrt((sigmth*atan(i/gm))**2+
              + (sigu(i)*mth/gm)**2+(siggm*nmh*atan(i/gm)**2)**2)
60  continue

          return
          end

```

```

*
*****
* subr. to read in vel. prof. from a data file *
*****
*
subroutine rdgprof
*
include 'commonblk1.f'
*
fname3=fname2//fname1//.dat
write(*,*) reading data & calculating freestream properties
open(10,file=fname3,status='old')
read(10,10) po,sigpo,to,sigto,rho,sigrho,us,sigue,npts
write(*,10) po,sigpo,to,sigto,rho,sigrho,us,sigue,npts
10 format(6x,e14.6,5x,e14.6/6x,f8.2,5x,f4.2/,
+ 7x,f8.6,5x,f8.6/6x,f5.2,5x,f4.2/,13x,i2)
*
call air(to,sigto,cp,sigcp,gnu,siggnu,ka,sigka,pr,sigpr)
*
y(1)=0.0
sigy(1)=1.e-6
u(1)=0.0
sigu(1)=1.e-6
nd1=npts+2
npts=nd1
do 20 i=2,(npts-1)
  read(10,30) j,y(i),sigy(i),u(i),sigu(i)
  write(*,30) j,y(i),sigy(i),u(i),sigu(i)
  y(i)=(y(i)+0.013)/100.
  sigy(i)=sigy(i)/100.
20 continue
30 FORMAT(1X,I2,2X,F8.6,2X,F8.6,2X,F7.4,2X,F7.4)
close(10)
y(npts)=1.1*y(npts-1)
sigy(npts)=0.1/100.
u(npts)=us
sigu(npts)=sigue
*
return
end
*
*****
* subr. to generate a vel. prof. from the wake law *
*****
*
subroutine genprof
*
include 'commonblk1.f'
include 'commonblk2.f'
real uplf(nmax),yplf(nmax),ybf(nmax),ubf(nmax)
real cf,thet,delta,ut,rendel,varist
integer nased
character*1 fake
*
po=1.0217e+5
sigpo=20.434
to=294.85
sigto=0.05
rho=1.207211
sigrho=0.00032
*
1 write(*,*) 'enter desired freestream velocity in m/s'
read(*,*) us
write(*,*) 'us = ',us, ' (enter r to change, return to cont.)'
read(*,1) fake
if (((fake.eq.'Y').or.(fake.eq.'R')) goto 1
sigue=0.005*us
2 write(*,*) 'enter desired npts'
read(*,12) npts
write(*,*) 'npts = ',npts, ' (enter r to change, return to cont.)'
read(*,1) fake
if (((fake.eq.'Y').or.(fake.eq.'R')) goto 2
3 write(*,*) 'enter streamwise dist. in in. (38 or 46)'
read(*,*) xt
write(*,*) 'Xdist = ',xt, ' (enter r to change, return to cont.)'
read(*,1) fake
if (((fake.eq.'Y').or.(fake.eq.'R')) goto 3
*
call air(to,sigto,cp,sigcp,gnu,siggnu,ka,sigka,pr,sigpr)
*
utognu=us/gnu
xtrip=4.5*0.0254
call tripcalv(0.,xtrip,0.01,xtrip,utognu,xot)
xt=0.0254*xt
xt=xt-xot
write(*,*) 'Xt,Xot = ',xt,xot
*
returnus=xt/gnu
cf=0.455/(log(0.06*returnus))**2
call fnddel(1.e+3,1.e+4,0.1,cf,rendel)
delta=rendel*gnu/us
delcheck=0.14*gnu*(returnus**(6./7.))/us

```

```

thet=0.036*del/0.37
delta=0.046*del/0.37
write(*,4) cf,delta,delcheck
4 format(1x,'CF,delta,delcheck = ',g16.9,g16.9,g16.9/,
+ ' (enter r to re-enter thl param.s, return to cont.)')
read(*,1) fake
if (((fake.eq.'Y').or.(fake.eq.'R')) goto 1
*
write(*,5)
5 format(1x,'enter p to perturb generated profile, ret. to cont.')
read(*,1) fake
if (((fake.eq.'Y').or.(fake.eq.'P')) then
  pert=1.
  write(*,7)
  7 format(1x,'enter % magnitude of random perturbation')
  read(*,*) varist
  write(*,*) '%pert. = ',varist,
  + ' (enter r to redo, ret. to cont.)'
  read(*,1) fake
  if (((fake.eq.'Y').or.(fake.eq.'R')) goto 6
  fake='Y'
  else
    pert=0.
  endif
*
nased=10*npts-1
ut=us*sqrt(0.5*cf)
nd1=del/dcost(npts-2)
do 8 i=1,(npts-1)
  y(i)=(i-1)*nd1+0.013e-2
  sigy(i)=0.7e-4
  ybf(i)=y(i)/del
  yplf(i)=y(i)*ut/gnu
  uplf(i)=(log(yplf(i)))+2.*tp*(sin(0.5*pi*ybf(i)))**2)/tk+th
  uplf(i)=(100.+pert*varist*2.*(0.5-ran(nased)))*uplf(i)/100.
  u(i)=uplf(i)*ut
  ubf(i)=u(i)/uc
  if (((u(i).gt.us).and.(fake.ne.'Y')) then
    write(*,*) 'generation error in genprof'
    npts=i
    goto 9
  endif
  8 sigu(i)=0.005*u(i)
9 continue
y(npts)=1.05*del
sigy(npts)=0.1/100.
ybf(npts)=1.1
yplf(npts)=y(npts)*ut/gnu
u(npts)=us
sigu(npts)=sigue
ubf(npts)=1.
uplf(npts)=u(npts)/ut
*
pert=pert*varist
write(11,10)
10 format(//,
+ 1x,'*****',
+ 1x,'* Wake Law Generated TBL Vel. Prof. & Anal.',
+ 1x,'*****')
*
write(11,20) to,sigto,po,sigpo,rho,sigrho,cp,sigcp,gnu,siggnu,
+ ka,sigka,pr,sigpr,us,sigue,delta,thet,delta,delcheck,xot,xt,
+ xet,cf,ut,npts,pert
20 format(1x,'To = ',f6.2,' +/- ',f5.3,' K',1x,'Po = ',
+ e12.6,' +/- ',e12.6,' n/m^2',1x,'density = ',f8.6,' +/- ',
+ f8.6,' kg/m^3',1x,'Cp = ',e12.6,' +/- ',e12.6,' 1/kg K',1x,
+ 'gm = ',e12.6,' +/- ',e12.6,' N s/m^2',1x,'k = ',e12.6,
+ ' +/- ',e12.6,' W/m K',1x,'Pr = ',f5.3,' +/- ',e10.4,1x,
+ 'Ue = ',f8.5,' +/- ',f8.6,' m/s',1x,'delta = ',e11.5,' m'
+ '/1x,theta = ',e11.5,' m',1x,'dstar = ',e11.5,' m',
+ 1x,'del check = ',g16.9,' m',1x,'Xoturb = ',g16.9,' m',
+ 1x,'Xturb = ',g16.9,' m',1x,'Xet = ',g16.9,1x,'CF = ',
+ g16.9,1x,'Utus = ',g16.9,' m/s',1x,'% of pts = ',i2,1x,
+ '% random velocity perturbation introduced = ',f5.1//)
*
tab=char(9)
write(12,40) 'i',tab, ' y ',tab,
+ ' sigy ',tab, ' u ',tab,
+ ' sigu ',tab, ' y/d ',tab,
+ ' u/uc ',tab, ' yplus ',tab,
+ ' uplus '
40 format(1x,i2,8(a1,f15.8))
do 30 i=1,npts
  write(12,60) i,tab,y(i),tab,sigy(i),tab,u(i),tab,sigu(i),
  + tab,ybf(i),tab,ubf(i),tab,yplf(i),tab,uplf(i)
30 continue
60 format(1x,i2,8(a1,f15.8))
*
return
end

```



```

*****
* subr. to initialize arrays *
*****

```

```

*
* subroutine init
*
* include 'commonblk2.for'
* include 'commonblk3.for'

```

```

*
do 100 i=1,nmax
  y(i)=0.
  sigy(i)=0.
  u(i)=0.
  sigu(i)=0.
  yb(i)=0.
  sigyb(i)=0.
  yb(i)=0.
  sigyb(i)=0.
  do 10 j=1,3
    yplu(j,i)=0.
    sigyplu(j,i)=0.
    ubf(j,i)=0.
    sigubf(j,i)=0.
    uplu(j,i)=0.
    siguplu(j,i)=0.
    upw(j,i)=0.
    sigupw(j,i)=0.
10 continue
  ub(i)=0.
  sigub(i)=0.
  sigotb(i)=0.
  ub(i)=0.
  sigotb(i)=0.
100 continue

```

```

*
return
end

```

## BLCALC.FOR;146:

```

*****
* b1calc.for - subroutines to calculate momentum and displacement *
* thickness, and local skin-friction coefficient *
* given turbulent boundary layer velocity data *
*****

```

```

*
* main subr.
*
*****

```

```

*
* subroutine b1calc

```

```

*
* include 'commonblk1.for'
* include 'commonblk2.for'
real ubf(nmax),sigubf(nmax),uplf(nmax),siguplf(nmax)
real upwlf(nmax),sigupwlf(nmax),yplf(nmax),sigyplf(nmax)
character*1 fake

```

```

* initialize the values

```

```

*
deltac=delta(1)
sigdeltac=sigdelta(1)
fake='y'
niter=0
dstar=0.
sigdstar=0.
thetas=0.
sigthetas=0.
delta(2)=0.

```

```

* numerically integrate to find thetas and dstar

```

```

*
write(*,*) 'integrating the'
do 10 i=1,nch1
  j=i-1
  if (i.lt.ndb1) then
    f(i)=1-u(i)/u0
    sigf(i)=sqrt((sigu(i)/u0)**2+(sigu0*u(i)/u0)**2)
    g(i)=f(i)*u(i)/u0
    sigg(i)=sqrt((sigf(i)*u(i)/u0)**2+(sigu(i)*f(i)/u0)**2)
    + (sigu0*u(i)*f(i)/u0)**2)
    if (j.gt.0) then
      h(j)=(y(i)-y(j))/delta(1)
      sigthetas(j)=sqrt((sigy(i)/delta(1))**2+(sigy(j)/delta(1))**2)
      + (sigdeltac(1)*y(i)-y(j))/delta(1)**2)
      dstar=dstar+0.5*h(j)*(f(i)+f(j))
      sigdstar=sigdstar+(0.5*sigthetas(j)*(f(i)+f(j)))**2
    +

```

```

      thetas=thetas+0.5*h(j)*(g(i)+g(j))
      sigthetas=sigthetas+(0.5*sigthetas(j)*(g(i)+g(j)))**2
    endif
  else

```

```

    f(i)=0.01
    sigf(i)=sigf(j)
    g(i)=f(i)*0.99
    sigg(i)=sigg(j)
    h(j)=1.-y(j)/delta(1)
    sigthetas(j)=sqrt((sigy(j)/delta(1))**2
    + (sigdeltac(1)*y(j)/delta(1)**2)
    + (sigdeltac(1)*h(j)*(f(i)+f(j)))**2)
    dstar=dstar+0.5*h(j)*(f(i)+f(j))
    sigdstar=sigdstar+(0.5*sigthetas(j)*(f(i)+f(j)))**2
    thetas=thetas+0.5*h(j)*(g(i)+g(j))
    sigthetas=sigthetas+(0.5*sigthetas(j)*(g(i)+g(j)))**2
  endif

```

```

  if (j.gt.1) then
    sigdstar=sigdstar+(0.5*sigf(j)*(h(j)+h(j-1)))**2
    sigthetas=sigthetas+(0.5*sigg(j)*(h(j)+h(j-1)))**2
  endif
10 continue

```

```

*
sigdstar=sqrt(sigdstar+(0.5*sigf(1)*h(1))**2
+ (0.5*sigf(npts)*h(npts-1))**2)
sigdstar=sqrt((sigdeltac(1)*dstar)**2+(sigdstar*delta(1))**2)
sigthetas=sqrt(sigthetas+(0.5*sigg(1)*h(1))**2
+ (0.5*sigg(npts)*h(npts-1))**2)
sigthetas=sqrt((sigdeltac(1)*thetas)**2+(sigthetas*delta(1))**2)
dstar=dstar*delta(1)
thetas=thetas*delta(1)

```

```

* non-dimensionalize profile data

```

```

*
write(*,*) 'non-dimensionalizing velocity profile data'
do 20 i=1,npts
  ub(i)=u(i)/u0
  sigub(i)=sqrt((sigu(i)/u0)**2+(sigu0*u(i)/u0)**2)
  yb(i)=y(i)/delta(1)
  sigyb(i)=sqrt((sigy(i)/delta(1))**2+(sigdeltac(1)*y(i)/
  + delta(1)**2)**2)
  sigotb(i)=sqrt(sigub(i)**2+sigyb(i)**2)
20 continue
redel=u0*delta(1)/gru
sigredel=sqrt((sigu0*delta(1)/gru)**2+(sigdeltac(1)*u0/gru)**2+
+ (siggru*u0*delta(1)/gru)**2)

```

```

* check delta calculation with vel. prof. power fit

```

```

23 format(1x,'no convergence within iteration limit',/
+ 1x,'proceeding w/ calc.')
write(*,*) 'calculating 2nd delta from power fit'
chisqr2=0.
chisqr1=0.
a1=1./20.
a2=1./2.
da=a2-a1
a(1)=a1
chisqr1=del fit(yb,ub,sigotb,npts,a(1))
var1=.4a(1)
write(*,*) 'Xaqr,m,l/m = ',chisqr1,a(1),var
a(1)=a2
chisqr2=del fit(yb,ub,sigotb,npts,a(1))
var2=chisqr2

```

```

*
nave=0
var1=.4a(1)
write(*,*) 'Xaqr,m,l/m = ',var2,a(1),var
var=100.*2.*abs(chisqr2-chisqr1)/(chisqr1+chisqr2)
if (var.gt.0.1) then
  da=0.8*da
  if (chisqr2.gt.chisqr1) then
    a2=a1+da
    a(1)=a2
    chisqr2=del fit(yb,ub,sigotb,npts,a(1))
    var2=chisqr2
  else
    a1=a2-da
    a(1)=a1
    chisqr1=del fit(yb,ub,sigotb,npts,a(1))
    var2=chisqr1
  endif
  nave=nave+1
  if (nave.lt.25) then
    goto 30
  else
    type 23
  endif
endif
if (chisqr2.gt.chisqr1) then
  a(1)=a1
  var2=chisqr1
else

```

```

a(1)=a2
var2=chinqr2
endif
var=1./a(1)
write(*,*) 'Final Xsq, s, 1/n = ', var2, a(1), var
*
delta(2)=(a(1)+1.)**delta(1)
sign(1)=sqrt(covar(1,1))
sigdelta(2)=sqrt((sigdelta*(a(1)+1.)/a(1))**2+
+ (sign(1)**delta(1))**2)**2)
write(*,*) 'm = ', a(1), ' chinqr = ', chinqr2
write(*,*) 'd0 = ', delorig, '+/- ', sigdolo
write(*,*) 'd1 = ', delta(1), '+/- ', sigdelta(1)
write(*,*) 'd2 = ', delta(2), '+/- ', sigdelta(2)
var=100.*2.*(delta(2)-delta(1))/(delta(1)+delta(2))
if (abs(var).gt.0.5) then
write(*,*) 'discrepancy in delta values'
if (false.eq.T) then
niter=niter+1
if (niter.lt.25) then
write(*,*) 'iterating for delta'
delta(1)=delta(1)*(100.+var/6.)/100.
sigdelta(1)=sigdelta(2)/2.
goto 1
else
type 23
goto 36
endif
else
write(*,*) 'enter i to iterate, return to continue calc.'
read(*,*) i
if (false.eq.T) goto 35
endif
elseif (false.eq.T) then
write(*,*) 'converged after ', niter, ' iterations'
write(*,*)
+ 'use original interp. delta or most rec. iter.? (o or m)'
read(*,*) i
if (false.eq.o) then
delta(1)=delorig
sigdelta(1)=sigdolo
elseif (false.eq.m) then
delta(1)=0.5*(delta(1)+delta(2))
sigdelta(1)=0.5*(sigdelta(1)+sigdelta(2))
else
write(*,*) 'enter o or m only'
goto 36
endif
endif
*
* select only data from [0.1<(y/delta)<0.9] for use in fits
*
nk=0
do 40 i=1,npts
if ((yb(i).gt.0.1).and.(yb(i).lt.0.9)) then
nk=nk+1
if (nk.eq.1) ikf=i
ikl=i
yk(nk)=y(i)
sigyk(nk)=sigy(i)
uk(nk)=ub(i)
sigtok(nk)=sigy(i)
endif
40 continue
*
* calculate White formula estimate of Cf
*
write(*,*) 'calc. Cf White'
if (((chindex.eq.1).or.(chindex.eq.3)) then
xt=38.
else
xt=46.
endif
utogm=us/gmu
xtrip=4.5*0.0254
call tripactv(0., xtrip, 0.01, xtrip, utogm, xot)
xt=0.0254*xt
xt=xot-xot
*
rest=us*x/gmu
cfwh=0.455/(log(0.06*rest))**2
sigcfwh=0.04*cfwh
call finddel(1., a+3, 1., a+4, 0.1, cfwh, rendl)
delwh=rendl*gm/uo
delchck=0.14*gm*(rest**(6./7.))/uo
write(*,*) 'Cf Wh = ', cfwh, '+/- ', sigcfwh
*
* use Cf (White) to calc. 1st vel. fit
*
write(*,*) 'calc. 1st set of vel. fits from Cf White'
a(1)=cfwh
sign(1)=sigcfwh

```

```

a(2)=delta(1)
sign(2)=sigdelta(1)
a(3)=us/gmu
sign(3)=sqrt((sign/gmu)**2+(siggm*us/gmu)**2)
a(4)=up
sign(4)=0.
call calcakfit(y, sigy, uk, xpts, a, sign,
+ ub, signub, chinqr(1))
write(*,*) 'Final Xsq1 = ', chinqr(1)
*
utau(1)=us*sqrt(0.5*cfwh)
sign(1)=sqrt(0.5*cfwh*sign**2+((0.25*sigcfwh*us)**2)/
+ (0.5*cfwh))
itau(1)=gm/utau(1)
sign(1)=sqrt((sign(1)*itau(1)/utau(1))**2
+ (siggm*itau(1)/gm)**2)
a(1)=utau(1)
sign(1)=sign(1)
a(2)=itau(1)
sign(2)=sign(1)
a(3)=delta(1)
sign(3)=sigdelta(1)
call calcupfit(y, sigy, u, sign, xpts, a, sign,
+ yplf, sigypfl, uplf, sigupfl, upwlf, sigupwlf)
*
i=1
do 45 j=1,npts
ubfit(j)=ubf(j)
sigubfit(j)=sigubf(j)
ypfit(j)=ypf(j)
sigypfit(j)=sigypf(j)
upfit(j)=upf(j)
sigupfit(j)=sigupf(j)
upwfit(j)=upwlf(j)
sigupwfit(j)=sigupwlf(j)
45 continue
*
* calculate karmon-schoenberg estimate of cf
*
write(*,*) 'calculating Cf (K-S)'
rotheta=us*theta/gmu
sigrotheta=sqrt((sign*theta/gmu)**2+(sigtheta*us/gmu)**2+
+ (siggm*us*theta/gmu)**2)**2)
cfks=0.0586*((log10(2.*rotheta))**2+0.8686*log10(2.*rotheta))
sigcfks=cfks*(2.*log10(2.*rotheta)+0.8686)/(rotheta*
+ ((log10(2.*rotheta))**2+0.8686*log10(2.*rotheta)))
sigcfks=sqrt((0.02*cfks)**2+(sigrotheta*sigcfks)**2)
write(*,*) 'Cfks = ', cfks, '+/- ', sigcfks
*
* calc. 1st Cf (C-H)
*
write(*,*) 'calculating 1st Cf (C-H)'
a(1)=delta(1)*us/gmu
cfch(1)=rtnow(1., a-2, 1., a-6, a(1))
v1=sigdelta(1)*4.*sqrt(0.5*cfch(1))/(tk*delta(1)*
+ (log(delta(1)*us/gmu)/tk+log(sqrt(0.5*cfch(1))))/tk+
+ tb+2.*tp/tk)
v2=sign**4.*sqrt(0.5*cfch(1))/(tk*us*(log(delta(1)*us/gmu)/tk+
+ log(sqrt(0.5*cfch(1))))/tk+tb+2.*tp/tk)
v3=siggm**4.*sqrt(0.5*cfch(1))/(tk*gm*(log(delta(1)*us/gmu)/tk+
+ log(sqrt(0.5*cfch(1))))/tk+tb+2.*tp/tk)
sigcfch(1)=sqrt(v1**2+v2**2+v3**2)
write(*,*) 'cfch1 = ', cfch(1), '+/- ', sigcfch(1)
*
* calc. 2nd Cf (C-H)
*
write(*,*) 'iterating to calc. 2nd Cf (C-H)'
chinqr(2)=0.
chinqr1=0.
a(1)=cfks
a(2)=delta(1)
a(3)=us/gmu
gmama=1.
lista(1)=1
*
* call fitting subr. first w/ Cf as the only coefficient
*
call mrgmin(yk, uk, sigtok, nk, a, 4, lista, 1, covar, alpha, 4,
+ chinqr(2), gmama)
if (abs(chinqr(2)-chinqr1).gt.0.000001) then
chinqr1=chinqr(2)
goto 50
endif
gmama=0.
call mrgmin(yk, uk, sigtok, nk, a, 4, lista, 1, covar, alpha, 4,
+ chinqr(2), gmama)
cfch(2)=a(1)
sigcfch(2)=sqrt(covar(1,1))
write(*,*) 'Xsq2, CfCH2 = ', chinqr(2), a(1)
*
* use 2nd Cf (C-H) to calc. 2nd vel. fit
*

```

```

write(*,*) 'calc. 2nd vel. fit from 2nd Cf CH'
a(1)=cfch(2)
sign(1)=sigcfch(2)
a(2)=delta(1)
sign(2)=sigdelta(1)
a(3)=ua/gm
sign(3)=sqrt((signa/gm)**2+(siggm*ua/gm)**2)
call calcukfit(y,sign,ub,npts,a,signa,
+ ubf,sigubf,chiqr(2))
write(*,*) 'final Xacr2 = ',chiqr(2)

+
utau(2)=ua*sqrt(0.5*cfch(2))
sigut(2)=sqrt(0.5*cfch(2)*signa**2+((0.25*sigcfch(2)*ua)**2)/
+ (0.5*cfch(2)))
ltau(2)=gm*utau(2)
sign(2)=sqrt((sigut(2)*ltau(2)/utau(2))**2+
+ (siggm*ltau(2)/gm)**2)
a(1)=utau(2)
sign(1)=sigut(2)
a(2)=ltau(2)
sign(2)=sign(2)
a(3)=delta(1)
sign(3)=sigdelta(1)
call calcukfit(y,sign,ub,npts,a,signa,
+ yplf,sigypf,uplf,siguplf,upwlf,sigupwlf)

+
i=2
do 55 j=1,npts
  ubfit(j)=ubf(j)
  sigubfit(j)=sigubf(j)
  yplu(j)=yplf(j)
  sigypu(j)=sigypf(j)
  uplu(j)=uplf(j)
  sigupu(j)=siguplf(j)
  upw(j)=upwlf(j)
  sigupw(j)=sigupwlf(j)
55 continue
+
* calc. 3rd Cf (C-H)
+
write(*,*) 'iterating to calc. 3rd Cf (C-H)'
chiqr(3)=0.
chiqr1=0.
a(1)=cfch(2)
a(2)=delta(1)
a(3)=ua/gm
gamma=1.
lista(1)=1
lista(2)=4
+
* call fitting subr. w/ Cf and tp as coefficients
60 call mrcmin(yk,nk,sigotk,nk,a,4,lista,2,covar,alpha,4,
+ chiqr(3),gamma)
if (abs(chiqr(3)-chiqr1).gt.0.00001) then
  chiqr1=chiqr(3)
  goto 60
endif
gamma=0.
call mrcmin(yk,nk,sigotk,nk,a,4,lista,2,covar,alpha,4,
+ chiqr(3),gamma)
cfch(3)=a(1)
sigcfch(3)=sqrt(covar(1,1))
tpfit=4
sigtpfit=sqrt(covar(4,4))
write(*,*) 'Xacr3,CfCH3 = ',chiqr(3),a(1)
+
* use 3rd Cf (C-H) to calc. 3rd vel. fit
+
write(*,*) 'calc. 3rd set of vel. fits from 3rd Cf CH'
sign(1)=sigcfch(3)
a(2)=delta(1)
sign(2)=sigdelta(1)
a(3)=ua/gm
sign(3)=sqrt((signa/gm)**2+(siggm*ua/gm)**2)
sign(4)=sigtpfit
call calcukfit(y,sign,ub,npts,a,signa,
+ ubf,sigubf,chiqr(3))
write(*,*) 'final Xacr3 = ',chiqr(3)

+
utau(3)=ua*sqrt(0.5*cfch(3))
sigut(3)=sqrt(0.5*cfch(3)*signa**2+((0.25*sigcfch(3)*ua)**2)/
+ (0.5*cfch(3)))
ltau(3)=gm*utau(3)
sign(3)=sqrt((sigut(3)*ltau(3)/utau(3))**2+
+ (siggm*ltau(3)/gm)**2)
a(1)=utau(3)
sign(1)=sigut(3)
a(2)=ltau(3)
sign(2)=sign(3)
a(3)=delta(1)
sign(3)=sigdelta(1)

```

```

call calcukfit(y,sign,ub,npts,a,signa,
+ yplf,sigypf,uplf,siguplf,upwlf,sigupwlf)
+
i=3
do 65 j=1,npts
  ubfit(j)=ubf(j)
  sigubfit(j)=sigubf(j)
  yplu(j)=yplf(j)
  sigypu(j)=sigypf(j)
  uplu(j)=uplf(j)
  sigupu(j)=siguplf(j)
  upw(j)=upwlf(j)
  sigupw(j)=sigupwlf(j)
65 continue
+
do 70 i=1,3
  chiqr(i)=chiqr(i)/float(npts-2)
70 continue
+
return
end
+
* calc. u/ue from wake law fit, error and chiqr *
+
subroutine calcukfit(xp,sigxp,yp,nk,a,signa,
+ yplf,sigypfit,chiqr)
+
* inputs: xp=yp, yp=ua/ue, a(1)=Cf, a(2)=delta, a(3)=ua/gm,
+ a(4)=tp
* outputs: yplf=ua/ue from wake law fit
+
real xp(nk),sigxp(nk),yp(nk),a(4),signa(4),
+ dyda(4),yplf(nk),sigypfit(nk),chiqr,var
+
chiqr=0.
do 10 i=2,nk
  call wakelaw(xp(i),a,yplf(i),dyda)
  call fiter(xp(i),sigxp(i),a,signa,sigypfit(i))
  var=(yp(i)-yplf(i))
  chiqr=chiqr+(var/sigypfit(i))**2
10 continue
+
return
end
+
* calc. error in u/ue from wake law fit *
+
subroutine fiter(xp,sigxp,a,signa,sigyp)
+
* inputs: xp=yp, a(1)=Cf, a(2)=delta, a(3)=ua/gm, a(4)=tp
* output: sigyp=sigma(u/ue) from wake law fit
+
include 'commonblk1.for'
real xp,sigxp,a(4),signa(4),var,dydx,dyda(4),sigyp
+
dyda=sqrt(0.5*a(1))*(1/(tk*xp)+2.*pi*a(4)*
+ sin(0.5*pi*xp/a(2))*cos(0.5*pi*xp/a(2))/
+ (tk*a(2)))
call wakelaw(xp,a,var,dyda)
sigyp=(sigxp*dyda)**2
do 10 i=1,4
  sigyp=sigyp+(signa(i)*dyda(i))**2
10 continue
sigyp=sqrt(sigyp)
+
return
end
+
* calculate y+, u+, and u+ from wake law *
+
subroutine calcukfit(x,sign,y,signa,npts,a(4),sign(4),
+ xp(npts),sigxp(npts),y(npts),sigyp(npts),
+ ypw(npts),sigypw(npts),y1,y2,y3,y4
+
xp(1)=0.
yp(1)=0.
ypw(1)=0.
do 10 i=2,npts
  xp(i)=a(i)/a(2)

```

```

      sigyp(i)=sqrt((sign(1)/u(2))**2+(sign(2)*x(i)/u(2)**2)**2)
      yp(i)=y(i)/u(1)
      sigyp(i)=sqrt((sigy(i)/u(1))**2+(sign(1)*y(i)/u(1)**2)**2)
      y1=0.5*pi*u(1)/u(3)
      sy1=sqrt((sign(i)*y1/u(i))**2+(sign(3)*y1/u(3))**2)
      y2=(sin(y1))**2
      sy2=sqrt((sy1**2*sin(y1)*cos(y1))**2)
      ypw(i)=(log(xp(i))+2.*u(4)*y2)/tk+tb
      y3=2.*u(4)*y2/tk
      sy3=sqrt((sign(4)*y3/u(4))**2+(sy2**2*y3/y2)**2)
      sy4=sigyp(i)/(xp(i)*tk)
      sigypw(i)=sqrt(sy3**2+sy4**2)
10  continue
      sigxp(1)=sigxp(2)
      sigyp(1)=sigyp(2)
      sigypw(1)=sigypw(2)
      return
    end
    .....
* Subr. to evaluate the wake law and deriv. for merqmin fit subr.
* .....
    subroutine wakela(xp,a,yp,dydx)
    * inputs: xp=y, a(1)=Cf, a(2)=delta, a(3)=u0/gnu, a(4)=ep
    * outputs: yp=u/u0, dydx=d(u/u0)/dx
    .....
    include 'commonblk1.for'
    real xp,a(4),yp,dydx(4),y1,y2,y3,y4
    .....
      y1=sqrt(0.5*a(1))
      y2=log(xp*a(3))
      y3=log(y1)
      y4=(sin(0.5*pi*xp/a(2)))**2
      ypw1=((y2+y3+2.*a(4)*y4)/tk+tb)
      dydx(1)=((y2+y3+2.*a(4)*y4+1.)/tk+tb)/(4.*y1)
      dydx(2)=-2.*a(4)*y1*pi*xp*sin(0.5*pi*xp/a(2))*
      + cos(0.5*pi*xp/a(2))/(tk*a(2)**2)
      dydx(3)=0.
      dydx(4)=y1**2.*y4/tk
    .....
    return
    end
    .....
* Subroutine to fit u/u0=(y/delta)**n
* .....
    function delfit(xp,yp,sigxp,npts,a)
    .....
    real xp(npts),a,yp(npts),sigyp(sigxp(npts))
    .....
      delfit=0.
      do 10 i=2,npts
        var=(yp(i)-xp(i)**a)
        sigypf=sigyp(i)**(a-1.)
        delfit=delfit+(var/sigypf)**2
10  continue
    .....
    return
    end
    .....
* newton solver subr. to find Cf from wake law eval. @ delta
* .....
    FUNCTION RTNEWT(X1,X2,XACC,var)
    PARAMETER (JMAX=20)
    RTNEWT=.5*(X1+X2)
    DO 11 J=1,JMAX
      CALL wakesolv(RTNEWT,F,DF,var)
      DX=F/DF
      RTNEWT=RTNEWT-DX
      IF(X1-RTNEWT)*(RTNEWT-X2).LT.0.)
      + write(*,*) 'jumped out of brackets in rtnewt'
      IF(ABS(DX).LT.XACC) RETURN
11  CONTINUE
      write(*,*) 'RTNEWT exceeded maximum iterations'
      END
    .....
* Subroutine to evaluate the wake law solution at delta
* .....
    subroutine wakesolv(xp,yp,dyp,var)
    .....
    include 'commonblk1.for'
    real xp,yp,dyp,y1,y2,y3,var

```

```

      y1=sqrt(0.5*xp)
      y2=log(var)
      y3=log(y1)
      ypw1=((y2+y3+2.*tp)/tk+tb)-0.99
      dyp=((y2+y3+2.*tp+1.)/tk+tb)/(4.*y1)
      write(*,*) 'wakesolv: Cf,y,Radel = ',xp,yp,var
    .....
    return
    end
    .....
* newton solver to calc. delta from wake law given Cf & u0/gnu
* .....
    subroutine finddel(X1,X2,XACC,var,rtnewt)
    PARAMETER (JMAX=20)
    RTNEWT=.5*(X1+X2)
    DO 11 J=1,JMAX
      CALL delasolv(RTNEWT,F,DF,var)
      DX=F/DF
      RTNEWT=RTNEWT-DX
      IF(X1-RTNEWT)*(RTNEWT-X2).LT.0.) write(*,*)
      + 'jumped out of brackets in finddel newton solver'
      IF(ABS(DX).LT.XACC) RETURN
11  CONTINUE
      write(*,*) 'finddel exceeded maximum iterations'
      END
    .....
* Subr. to eval. wake law for subr. finddel
* .....
    subroutine delasolv(xp,yp,dyp,var)
    .....
    include 'commonblk1.for'
    real xp,yp,dyp,y1,y2,y3,var
    .....
      y1=sqrt(0.5*var)
      y2=log(xp)
      y3=log(y1)
      ypw1=((y2+y3+2.*tp)/tk+tb)-0.99
      dyp=y1/(tk*xp)
      write(*,*) 'delasolv: Radel,y,Cf = ',xp,yp,var
    .....
    return
    end
    .....
* subr. to solve for apparent tbl origin
* .....
    subroutine tripsolv(X1,X2,XACC,xtrip,utognu,rtnewt)
    PARAMETER (JMAX=20)
    RTNEWT=.5*(X1+X2)
    DO 11 J=1,JMAX
      CALL tripseq(RTNEWT,F,DF,xtrip,utognu)
      write(*,*) 'tripsolv: Xot,y = ',rtnewt,f
      DX=F/DF
      RTNEWT=RTNEWT-DX
      IF(X1-RTNEWT)*(RTNEWT-X2).LT.0.)
      + write(*,*) 'jumped out of brackets in tripsolv newton solver'
      IF(ABS(DX).LT.XACC) RETURN
11  CONTINUE
      write(*,*) 'tripsolv exceeded maximum iterations'
      END
    .....
* subr. to eval. tripsolv formula
* .....
    subroutine tripseq(xp,yp,dyp,xtrip,utognu)
    .....
    include 'commonblk1.for'
    real xp,yp,dyp,y1,y2,y3,xtrip,utognu
    .....
      y1=xtrip*xp
      y2=0.37*y1/(y1*utognu)**0.2
      y3=3.5*sqrt(2.)*xtrip*(xtrip*utognu)**0.5
      ypy2=y3
      dyp=y2/y1
      write(*,*) 'tripsq: Xot,y,Xtrip,utognu = ',xp,yp,xtrip,utognu
    .....
    return
    end

```

WRTOFILE.FOR;29:

```

*****
* writefile.for: subroutine to write tbl velocity profile *
* analysis results to file *
*****
subroutine writefile
include 'commonblk1.for'
include 'commonblk2.for'

tab=char(9)

write(*,*) 'writing results to file'

write(11,10)
write(12,10)
10 format(/,
+ 1x,'*****',/,
+ 1x,'* Analysis of TBL velocity profile *',/,
+ 1x,'*****')

write(11,20) npts,to,sigto,po,sigpo,rho,sigrho,cp,sigcp,gmu,
+ siggmu,ks,sigks,pr,sigpr,ue,sigue,delta(1),sigdelta(1),redel,
+ sigredel,theta,sigtheta,theta2,sigtheta2,dstar,sigdstar,
+ st,delsig,delsig,delta(2),sigdelta(2),delwh,delcheck
20 format(1x,'# of data pts. =',i2,1x,'To =',f6.2,' +/- ',
+ f5.3,' K',1x,'Po =',e12.6,' +/- ',e12.6,' n/m^2',1x,
+ 'density =',f8.6,' +/- ',f8.6,' kg/m^3',1x,'Cp =',e12.6,
+ ' +/- ',e12.6,' J/kg K',1x,'gmu =',e12.6,' +/- ',e12.6,
+ ' N s/m^2',1x,'k =',e12.6,' +/- ',e12.6,' W/m K',1x,
+ 'Pr =',f5.3,' +/- ',e10.4,1x,'ue =',f8.5,' +/- ',f8.6,
+ ' m/s',1x,'delta =',e11.5,' +/- ',e11.5,' m',1x,
+ 'Redelta =',e11.5,' +/- ',e11.5,1x,'theta =',e11.5,' +/- ',
+ e11.5,' m',1x,'theta2 =',e11.5,' +/- ',e11.5,1x,
+ 'dstar =',e11.5,' +/- ',e11.5,' m',1x,'Xt =',g16.9,' m',1x,
+ 1x,'delta from interpo. =',g16.9,' +/- ',g16.9,' m',1x,
+ 'delta from pow. fit =',g16.9,' +/- ',g16.9,' m',1x,
+ 'delta from Cf (Wh.) =',g16.9,' m',1x,
+ 'delta from Wh. for. =',g16.9,' m')

if (choice.ne.'4') then
write(12,21) 'i',tab,' y',tab,
+ ' sigy',tab,' u',tab,
+ ' sigu',tab,' u/ue',tab,
+ ' u/ue'
21 format(/,1x,a2,6(a1,a16))
do 25 i=1,npts
write(12,26) i,tab,y(i),tab,sigy(i),tab,u(i),tab,sigu(i),
+ tab,ub(i),tab,sigub(i)
25 continue
26 format(1x,i2,6(a1,g16.9))
endif

do 100 i=1,5

write(11,(/))
write(12,(/))
if (i.eq.1) then
write(11,30) 'Wh.',1,cfwh,sigcfwh,chiqr(1)
elseif (i.eq.2) then
write(11,31) 'K-S',1,cfks,sigcfks
elseif (i.eq.3) then
write(11,31) 'C-H',(i-2),cfch(i-2),sigcfch(i-2)
else
write(11,30) 'C-H',(i-2),cfch(i-2),sigcfch(i-2),chiqr(i-2)
endif
30 format(1x,'Cf (a3,,;i1,)=',e14.7,' +/- ',e14.7,
+ ',1x,'Reduced Chi-squared =',g16.9)
31 format(1x,'Cf (a3,,;i1,)=',e14.7,' +/- ',e14.7)

if (i.lt.5) then
write(11,40) tk,th,tp
else
write(11,50) tk,th,tpfit,sigtpfit
endif
40 format(1x,'tbl const. k =',f4.2,1x,'tbl const. B =',
+ f3.1,1x,'tbl const. P =',f3.1)
50 format(1x,'tbl const. k =',f4.2,1x,'tbl const. B =',
+ f3.1,1x,'tbl const. P(from fit) =',f10.8,' +/- ',
+ f10.8)

if ((i.eq.1).or.(i.eq.4).or.(i.eq.5)) then
if (i.eq.1) then
k=1
else
k=i-2
endif
write(11,60) utau(k),sigutau(k),ltau(k),sigltau(k),
+ mltplus(k),sigmltplus(k),mplus(k),sigmplus(k)
60 format(1x,'Utau =',f9.4,' +/- ',f8.4,' m/s',1x,
+ 'ltau =',e14.7,' +/- ',e14.7,' m',1x,
+ 'ltau =',f4.1,' +/- ',f3.1,' wall units')

```

```

+ 1x,'u+ =',f4.1,' +/- ',f3.1,' wall units')

write(12,70) 'i',tab,' y/d',tab,
+ ' sy/d',tab,' yplus',tab,
+ ' syplus',tab,' u/uef',tab,
+ ' ue/uef',tab,' uplus',tab,
+ ' uplus'
70 format(/,1x,a2,8(a1,a15))

write(*,*) 'usef'
do 80 j=1,npts
write(12,90) j,tab,yb(j),tab,sigyb(j),tab,yplus(k,j),
+ tab,sigyplus(k,j),tab,ubfb(k,j),tab,sigubfb(k,j),tab,
+ uplus(k,j),tab,siguplus(k,j)
80 continue
90 format(1x,i2,8(a1,g15.8))
endif

100 continue

return
end

```

## CALCDRAG.FOR;16:

```

*****
* calcdrag.for: subroutine to store calculated Cf's and
* use them to calculate Cd and Cd ratios
*****
subroutine cstore
include 'commonblk2.for'
include 'commonblk3.for'

write(*,*) 'storing Cf data'

if (chindex.lt.3) then
nside=1
else
nside=2
endif
if ((chindex.eq.1).or.(chindex.eq.3)) then
nspot=1
else
nspot=2
endif

sevx(nside,nspot)=xt
do 10 i=1,5
if (i.eq.1) then
savecf(nside,nspot,i)=cfwh
savecf(nside,nspot,i)=sigcfwh
elseif (i.eq.2) then
savecf(nside,nspot,i)=cfks
savecf(nside,nspot,i)=sigcfks
else
savecf(nside,nspot,i)=cfch(i-2)
savecf(nside,nspot,i)=sigcfch(i-2)
endif
10 continue

return
end

*****
* subr. to calculate Cf's and Cd1/Cd2
*****
subroutine dragcalc
include 'commonblk2.for'
include 'commonblk3.for'

write(*,*) 'calculating Cd'

write(11,(/))

if (chindex.lt.3) then
nside=1
else
nside=2
endif

```

```

*
* calc. Cd using trapezoidal approx.
*
do 10 i=1,5
  sd1=(savgf(nside,2,i)+savgf(nside,1,i))/2.
  sd1=sqrt((0.5*savgf(nside,2,i))**2+
    + (0.5*savgf(nside,1,i))**2)
  sd2=(savgf(nside,2)+savgf(nside,1))
  sd2=sqrt(2)*0.005
  cfd(1,nside,i)=sd1*sd2
  sigcfd(1,nside,i)=sqrt((sd1*sd2)**2+(sd2*sd1)**2)
  write(*,*) i,'trap. Cd = ',cfd(1,nside,i), ' +/- ',
    + sigcfd(1,nside,i)
  write(11,15) 1,nside,i,cfd(1,nside,i),sigcfd(1,nside,i)
10 continue
15 format(1x,'Cd(1,1,1,1,1) = ',g16.9,' +/- ',g16.9)
*
* using Cf=mu/x**b assumption
*
write(11,17)
*
do 20 i=1,5
  sd1=savgf(nside,1,i)/savgf(nside,2,i)
  sd1=sqrt((savgf(nside,1,i)*sd1/savgf(nside,1,i))**2+
    + (savgf(nside,2,i)*sd1/savgf(nside,2,i))**2)
  sd1=sd1/sd1
  sd1=log(sd1)
  sd2=savgf(nside,2)/savgf(nside,1)
  sd2=sqrt((0.005*sd2/savgf(nside,1))**2+
    + (0.005*sd2/savgf(nside,2))**2)
  sd2=sd2/sd2
  sd2=log(sd2)
  bff(i)=sd1/sd2
  sbf(i)=sqrt((sd1**b/sd1)**2+(sd2**b/sd2)**2)
  alf(i)=savgf(nside,1,i)*savgf(nside,1)**bfff(i)
  saf(i)=sqrt((savgf(nside,1,i)*alf(i)/savgf(nside,1,i))**2+
    + (0.005*bff(i)*alf(i)/savgf(nside,1))**2)
  + (sbf(i)*alf(i)*log(savgf(nside,1)))**2)
  c=1.-bff(i)
  sc=sbf(i)
  sd1=alf(i)/c
  sd1=sqrt((saf(i)*sd1/alf(i))**2+(sc*sd1/c)**2)
  sd2=savgf(nside,2)**c
  sd2=sqrt((0.005*c*sd2/savgf(nside,2))**2+
    + (sc*sd2*log(savgf(nside,2)))**2)
  sd3=savgf(nside,1)**c
  sd3=sqrt((0.005*c*sd3/savgf(nside,1))**2+
    + (sc*sd3*log(savgf(nside,1)))**2)
  cfd(2,nside,i)=sd1*(sd2-sd3)
  sigcfd(2,nside,i)=sqrt((sd1*(sd2-sd3))**2+
    + (sd2*sd1)**2+(sd3*sd1)**2)
  write(*,*) i,'a/x**b Cd = ',cfd(2,nside,i), ' +/- ',
    + sigcfd(2,nside,i)
  write(11,22) 2,nside,i,cfd(2,nside,i),sigcfd(2,nside,i),
    + alf(i),sbf(i),bff(i),sbf(i))
20 continue
22 format(1x,'Cd(2,1,1,1,1) = ',g16.9,' +/- ',g16.9,
  + ',1x,' with a = ',g16.9,' +/- ',g16.9, and b = ',
  + g16.9,' +/- ',g16.9)
*
* if nec., calc. drag
*
if (chindex.eq.4) then
  do 30 i=1,2
    do 25 j=1,5
      cfdnat(i,j)=cfd(2,j)/cfd(1,i,j)
      sigcfdnat(i,j)=sqrt((sigcfd(1,i,j)*cfdnat(i,j)/cfd(1,i,j))**2+
        + (sigcfd(2,j)*cfdnat(i,j)/cfd(2,j))**2)
      write(*,*) i,j,'Cd2/Cd1 = ',cfdnat(i,j), ' +/- ',
        + sigcfdnat(i,j)
      sigcfdnat(i,j)
    write(11,35) i,j,cfdnat(i,j),sigcfdnat(i,j)
25 continue
30 continue
endif
35 format(1x,'Cd2/Cd1(1,1,1,1,1) = ',g16.9,' +/- ',g16.9)
*
return
end

```

## AIR.FOR;14:

```

*****
* SUBROUTINE AIR(T,MA,RA,CPA,GA,MUA,KA,PRA)
*
* THIS SUBROUTINE PROVIDES THE THERMODYNAMIC AND TRANSPORT*
* PROPERTIES OF AIR
*
* T = TEMPERATURE, K

```

```

*
* CP = SPECIFIC HEAT AT CONSTANT PRESSURE, J/(KG K)*
* GNU = DYNAMIC VISCOSITY, (N S)/(m**2)
* K = THERMAL CONDUCTIVITY, W/(m K)
* PR = PRANDTL NUMBER
* DATA FOR AIR AT 1 ATMOSPHERE
* SOURCE: HILSENDRATH,NBS CTR 564
* QC286.JH635
* WRITTEN GERRY GUENNETTE/ MODIFIED BY TIM STONE
*****

```

```

C
SUBROUTINE
AIR(TO,SIGTO,CP,SIGCP,GNU,SIGGNU,KA,SIGKA,PR,SIGPR)
C
DIMENSION TK(75),CPTAB(75),GNUTAB(53),KTAB(35)
REAL*4 GNU,GNUTAB,GNUO,KA,KTAB,KO,KK
CHARACTER*12 GAS

```

### TABULATED DATA

#### Temperature values for tables

DATA TK/	200	220	240	260	280
2	300	320	340	360	380
3	400	420	440	460	480
4	500	520	540	560	580
5	600	620	640	660	680
6	700	720	740	760	780
7	800	850	900	950	1000
8	1050	1100	1150	1200	1250
9	1300	1350	1400	1450	1500
1	1550	1600	1650	1700	1750
1	1800	1850	1900	1950	2000
1	2050	2100	2150	2200	2250
1	2300	2350	2400	2450	2500
1	2550	2600	2650	2700	2750
1	2800	2850	2900	2950	3000

#### Specific heat at constant pressure table for AIR at 1 atmosphere for 200K TO 3000K

DATA CPTAB/	3.5062	3.5038	3.5028	3.5028	3.5038
2	3.5059	3.5091	3.5134	3.5188	3.5255
3	3.5333	3.5422	3.5523	3.5634	3.5754
4	3.5882	3.6019	3.6163	3.6313	3.6468
5	3.6626	3.6788	3.6953	3.7120	3.7288
6	3.7455	3.7621	3.7789	3.7954	3.8118
7	3.828	3.869	3.906	3.944	3.979
8	4.013	4.046	4.078	4.109	4.140
9	4.171	4.201	4.230	4.260	4.289
1	4.321	4.352	4.385	4.418	4.451
1	4.487	4.524	4.566	4.611	4.662
1	4.719	4.781	4.856	4.947	5.055
1	5.179	5.321	5.484	5.670	5.882
1	6.12	6.40	6.71	7.06	7.45
1	7.87	8.35	8.86	9.40	9.96

#### Viscosity table for air at 1 atmosphere for 200K TO 1900K

DATA GNUTAB/	0.7742	0.8391	0.9015	0.9617	1.020
2	1.076	1.130	1.183	1.234	1.283
3	1.332	1.379	1.425	1.470	1.513
4	1.556	1.598	1.640	1.680	1.720
5	1.758	1.796	1.834	1.870	1.906
6	1.942	1.977	2.012	2.046	2.080
7	2.112	2.193	2.271	2.346	2.420
8	2.492	2.562	2.629	2.696	2.760
9	2.824	2.886	2.947	3.007	3.066
1	3.123	3.180	3.235	3.290	3.344
1	3.397	3.449	3.501		

#### Thermal conductivity table for air at 1 atmosphere for 200K TO 1000K

DATA KTAB/	0.7494	0.8196	0.8885	0.9561	1.022
2	1.087	1.151	1.213	1.275	1.335
3	1.394	1.452	1.509	1.565	1.620
4	1.674	1.727	1.779	1.831	1.881
5	1.931	1.980	2.028	2.076	2.123
6	2.169	2.214	2.259	2.304	2.348
7	2.392	2.498	2.600	2.701	2.798

### LINEAR INTERPOLATION ON INPUT TEMPERATURE

```

DO 100 I=1,75
  IF(TO.LE.TK(I)) GO TO 200
100 CONTINUE
  WRITE(5,*) 'INPUT TEMP TOO LARGE'
  STOP
200 IF(LEQ.1) THEN
  WRITE(5,*) 'INPUT TEMP TOO SMALL'
  STOP
  END IF
  TFACT=(TO-TK(I-1))/(TK(I)-TK(I-1))

```

```

* AIR SPECIFIC HEAT, (J/(KG K))
*
  CPO=287.041
  CP=CPO*(CPTAB(I-1)+TFACT*(CPTAB(I)-CPTAB(I-1)))
  SIGCP=ABS(SIGTO*CPO*(CPTAB(I)-CPTAB(I-1)))/(TK(I)-TK(I-1)))
*
* AIR VISCOSITY, (KG/(M S))
*
  GNU=1.458E-6*SQRT(TO)/(1.+110.4/TO)
  SIGGNU=ABS(SIGTO*0.5*1.458E-6*(1./SQRT(TO)+3.*110.4/TO**1.5)/
  + (1.+110.4/TO)**2)
*
* AIR THERMAL CONDUCTIVITY, (W/(M K))
*
  K0=2.414E-2
  AK=0.6325E-5
  BK=245.4
  CK=12
  KK=5.77E-5
  KA=K0*(AK/KK)*SQRT(TO)/(1.+(BK*10.**(-1.*CK/TO))/TO)
  v1=0.5*K0*AK*(1.+BK*10.**(-1.*CK/TO))/TO/(KK*SQRT(TO))
  v2=K0*(AK/KK)*SQRT(TO)*BK*10.**(-1.*CK/TO)*(CK*LOG(10./TO)-1)
  + /TO**2
  v3=(1.+BK*10.**(-1.*CK/TO))/TO**2
  SIGKA=ABS(SIGTO*(v1-v2)/v3)
*
* AIR PRANDTL NUMBER
*
  PR=GNU*CP/KA
  SIGPR=SQRT((SIGGNU*CP/KA)**2+(SIGCP*GNU/KA)**2+(SIGKA*
  + CP*GNU/KA**2)**2)
*
  RETURN
  END

```

## MRQMIN.FOR:

```

SUBROUTINE MRQMIN(X,Y,SIG,NDATA,A,MA,LISTA,MFTT,
* COVAR,ALPHA,NCA,CHISQ,ALAMDA)
PARAMETER (MMAX=20)
DIMENSION X(NDATA),Y(NDATA),SIG(NDATA),A(MA),LISTA(MFTT),
*
COVAR(NCA,NCA),ALPHA(NCA,NCA),ATRY(MMAX),BETA(MMAX),DA(MM
AX)
IF (ALAMDA.LT.0.) THEN
  KK=MFTT+1
  DO 12 J=1,MA
    IHIT=0
    DO 11 K=1,MFTT
      IF (LISTA(K).EQ.J) IHIT=IHIT+1
    CONTINUE
    IF (IHIT.EQ.0) THEN
      LISTA(KK)=J
      KK=KK+1
    ELSE IF (IHIT.GT.1) THEN
      PAUSE 'Improper permutation in LISTA'
    ENDIF
  CONTINUE
  IF (KK.NE.(MA+1)) PAUSE 'Improper permutation in LISTA'
  ALAMDA=0.001
  CALL MRQCOF(X,Y,SIG,NDATA,A,MA,LISTA,MFTT,ALPHA,BETA,NCA,
  * CHISQ)
  OCHISQ=CHISQ
  DO 13 J=1,MA
    ATRY(J)=A(J)
  CONTINUE
13 CONTINUE
ENDIF
DO 15 J=1,MFTT
  DO 14 K=1,MFTT
    COVAR(J,K)=ALPHA(J,K)
  CONTINUE
14 CONTINUE
COVAR(J,J)=ALPHA(J,J)*(1.+ALAMDA)
DA(J)=BETA(J)
15 CONTINUE
CALL GAUSS(COVAR,MFTT,NCA,DA,1,1)
IF (ALAMDA.EQ.0.) THEN
  CALL COVSRT(COVAR,NCA,MA,LISTA,MFTT)
  RETURN
ENDIF
DO 16 J=1,MFTT
  ATRY(LISTA(J))=ATRY(LISTA(J))+DA(J)
16 CONTINUE
CALL MRQCOF(X,Y,SIG,NDATA,ATRY,MA,LISTA,MFTT,COVAR,DA,NCA,
* CHISQ)
IF (CHISQ.LT.OCHISQ) THEN
  ALAMDA=0.1*ALAMDA
  OCHISQ=CHISQ

```

```

DO 18 J=1,MFTT
  DO 17 K=1,MFTT
    ALPHA(J,K)=COVAR(J,K)
  CONTINUE
  BETA(J)=DA(J)
  A(LISTA(J))=ATRY(LISTA(J))
18 CONTINUE
ELSE
  ALAMDA=10.*ALAMDA
  CHISQ=OCHISQ
ENDIF
RETURN
END

```

## MRQCOF.FOR:

```

SUBROUTINE
MRQCOF(X,Y,SIG,NDATA,A,MA,LISTA,MFTT,ALPHA,BETA,NALP,
+ CHISQ)
PARAMETER (MMAX=20)
DIMENSION
X(NDATA),Y(NDATA),SIG(NDATA),ALPHA(NALP,NALP),BETA(MA),
* DYDA(MMAX),LISTA(MFTT)
DO 12 J=1,MFTT
  DO 11 K=1,J
    ALPHA(J,K)=0.
  CONTINUE
  BETA(J)=0.
12 CONTINUE
CHISQ=0.
DO 15 I=1,NDATA
  CALL wakslaw(X(I),A,YMOD,DYDA)
  SIG2I=1./SIG(I)*SIG(I)
  DY=Y(I)-YMOD
  DO 14 J=1,MFTT
    WT=DYDA(LISTA(J))*SIG2I
    K=1,J
    ALPHA(J,K)=ALPHA(J,K)+WT*DYDA(LISTA(K))
  CONTINUE
  BETA(J)=BETA(J)+DY*WT
14 CONTINUE
CHISQ=CHISQ+DY*DY*SIG2I
15 CONTINUE
DO 17 J=2,MFTT
  DO 16 K=1,J-1
    ALPHA(K,J)=ALPHA(J,K)
  CONTINUE
17 CONTINUE
RETURN
END

```

## COVSRT.FOR:

```

SUBROUTINE COVSRT(COVAR,NCVM,MA,LISTA,MFTT)
DIMENSION COVAR(NCVM,NCVM),LISTA(MFTT)
DO 12 J=1,MA-1
  DO 11 I=J+1,MA
    COVAR(I,J)=0.
  CONTINUE
12 CONTINUE
DO 14 I=1,MFTT-1
  DO 13 J=I+1,MFTT
    IF (LISTA(I).GT.LISTA(J)) THEN
      COVAR(LISTA(I),LISTA(I))=COVAR(I,J)
    ELSE
      COVAR(LISTA(I),LISTA(J))=COVAR(I,J)
    ENDIF
  CONTINUE
13 CONTINUE
14 CONTINUE
SWAP=COVAR(1,1)
DO 15 J=1,MA
  COVAR(1,J)=COVAR(J,J)
  COVAR(J,J)=0.
15 CONTINUE
COVAR(LISTA(1),LISTA(1))=SWAP
DO 16 J=2,MFTT
  COVAR(LISTA(J),LISTA(J))=COVAR(1,J)
16 CONTINUE
DO 18 J=2,MA
  DO 17 I=1,J-1
    COVAR(I,J)=COVAR(J,I)

```

```

17 CONTINUE
18 CONTINUE
RETURN
END

```

## GAUSSJ.FOR:

```

SUBROUTINE GAUSS(A,N,NP,B,M,MP)
PARAMETER (NMAX=50)
DIMENSION
A(NP,NP),B(NP,MP),IPTV(NMAX),INDXR(NMAX),INDXC(NMAX)
DO 11 J=1,N
IPTV(J)=0
11 CONTINUE
DO 22 I=1,N
BIG=0.
DO 13 J=1,N
IF(IPTV(J).NE.1)THEN
DO 12 K=1,N
IF (IPTV(K).EQ.0) THEN
IF (ABS(A(J,K)).GE.BIG)THEN
BIG=ABS(A(J,K))
IROW=J
ICOL=K
ENDIF
ELSE IF (IPTV(K).GT.1) THEN
write(*,*) 'singular matrix'
RETURN
ENDIF
12 CONTINUE
ENDIF
13 CONTINUE
IPTV(ICOL)=IPTV(ICOL)+1
IF (IROW.NE.ICOL) THEN
DO 14 L=1,N
DUM=A(IROW,L)
A(IROW,L)=A(ICOL,L)
A(ICOL,L)=DUM
14 CONTINUE
DO 15 L=1,M
DUM=B(IROW,L)
B(IROW,L)=B(ICOL,L)
B(ICOL,L)=DUM
15 CONTINUE
ENDIF
INDXR(I)=IROW
INDXC(I)=ICOL
IF (A(ICOL,ICOL).EQ.0.) THEN
write(*,*) 'singular matrix'

```

```

RETURN
endif
PTVINV=1./A(ICOL,ICOL)
A(ICOL,ICOL)=1.
DO 16 L=1,N
A(ICOL,L)=A(ICOL,L)*PTVINV
16 CONTINUE
DO 17 L=1,M
B(ICOL,L)=B(ICOL,L)*PTVINV
17 CONTINUE
DO 21 LL=1,N
IF(LL.NE.ICOL)THEN
DUM=A(LL,ICOL)
A(LL,ICOL)=0.
DO 18 L=1,N
A(LL,L)=A(LL,L)-A(ICOL,L)*DUM
18 CONTINUE
DO 19 L=1,M
B(LL,L)=B(LL,L)-B(ICOL,L)*DUM
19 CONTINUE
ENDIF
21 CONTINUE
22 CONTINUE
DO 24 L=N,1,-1
IF(INDXR(L).NE.INDXC(L))THEN
DO 23 K=1,N
DUM=A(K,INDXR(L))
A(K,INDXR(L))=A(K,INDXC(L))
A(K,INDXC(L))=DUM
23 CONTINUE
ENDIF
24 CONTINUE
RETURN
END

```

## RTNEWT.FOR:

```

FUNCTION RTNEWT(X1,X2,XACC,a)
PARAMETER (JMAX=20)
RTNEWT=.5*(X1+X2)
DO 11 J=1,JMAX
CALL wksolvev(RTNEWT,F,DP,a)
DX=F/DP
RTNEWT=RTNEWT-DX
IF(X1-RTNEWT)*(RTNEWT-X2).LT.0.)PAUSE 'jumped out of brackets'
IF(ABS(DX).LT.XACC) RETURN
11 CONTINUE
PAUSE 'RTNEWT exceeding maximum iterations'
END

```

## C.4. Momentum Transfer Analysis Results

**A. Freestream Turbulence.** The root-mean-square freestream turbulence was measured to be below 1 percent for freestream velocities above 8.5 m/s and below 0.8 percent for freestream velocities above 12.5 m/s.

**B. Streamwise Pressure Gradient.** The streamwise pressure gradients were small enough that their effect upon riblet performance was negligible. For freestream velocities below 15 m/s, the drag and heat transfer reduction range, the streamwise pressure gradients measured with the pitot-static probes were all less than 8 Pa/m and the majority were less than 3 Pa/m. In terms of the Clauser pressure gradient parameter, all  $\beta$  were less than 0.07 and the majority were less than 0.02. The results of the research into the effect of pressure gradient on riblet performance summarized in Coustols and Savill (1989) indicate that, for these values of  $\beta$ , the degradation in drag reduction should be less than 1 percent.



**C. Boundary Layer Thickness.** The boundary layer thicknesses calculated via interpolation from the velocity profiles measured over the flat and ribleted plates as well as the thickness calculated from the empirical formula 2.41 are shown in Figure C.1, Boundary Layer Thickness versus Reynolds Number for Flat and Ribleted Plates. The trends apparent in the graph are fairly close similarity between the flat and ribleted plate results, wide scatter of the data at low Reynolds numbers, and fairly large discrepancies between the measured and empirically predicted values. Indeed, for 90 percent of the cases, the calculated values were lower, in most cases significantly so, than the values predicted with the empirical formula. The results seem to indicate a fairly serious deficiency in the calculation methodology. Unfortunately, time did not permit resolution of this particular problem.

Although these results raise questions as to the accuracy and validity of the momentum transfer results, the particular method of calculating skin friction was insensitive to even large error in boundary layer thickness and so its accuracy and validity are unaffected by the problems in  $\delta$  calculation. The Coles Hirst 3 method of calculating  $C_f$  depends primarily upon the slope of the profile in the lower and middle regions of the boundary layer. In addition, the fit coefficients used in this method include a parameter to account for inaccuracies in the boundary layer estimate. Indeed, during attempts to improve the boundary layer thickness calculation methodology, the author noted that changes in  $\delta$  of up to 50 percent affected the resulting  $C_f$  calculation by less than 1.5 percent!

The deficiencies apparent in the calculation of  $\delta$  propagated through the calculation of the displacement and momentum thicknesses. The displacement thicknesses calculated via numerical integration of the velocity profiles measured over the flat and ribleted plates as well as the thickness calculated from the empirical formula 2.43 are shown in Figure C.2, Displacement Thickness versus Reynolds Number for Flat and Ribleted Plates. The results echo the trends of the  $\delta$  calculations almost exactly since  $d$  directly affects the amount of profile integrated. The momentum thicknesses calculated via numerical integration of the velocity profiles measured over the flat and ribleted plates as well as the thickness calculated from the empirical formula 2.42 are shown in Figure C.3, Momentum Thickness versus Reynolds Number for Flat and Ribleted Plates. As with  $\delta^*$ , the results echo the trends of the boundary layer thickness variation with Reynolds number very closely.

**D. Velocity Profiles and  $C_f$  Calculation Curve Fits.** The results of three separate boundary layer traversals performed at the same freestream velocity are shown together for comparison in Figure C.4, Test of Velocity Profile Repeatability. The three traversals were each taken on separate days at the same streamwise location but at different spanwise locations, yet, as

can be seen, the results show very low scatter and excellent repeatability. Indeed, the skin friction coefficients calculated from the profiles were within a 2 percent range (i.e., they agreed to  $\pm 1$  percent), which is actually about 1.5 to 2 times more accurate than would be expected based on studies such as Harotinidis (1989).

Although the possible presence of differences in the boundary layers was not ruled out with measurements specifically aimed at detecting them nor accounted for in the data analysis, the values of coefficient of skin friction calculated from velocity profiles fore of the test sections suggest that the momentum aspects of the boundary layers were similar enough not to degrade seriously the accuracy of the experiment. Due to time constraints, the velocity profile repeatability test was performed only upon the flat plate test section side. Thus, an unquantifiable amount of error could be present in the results due to differences between the boundary layers over the flat plate test section side and that of the ribletted test section. However, in all test runs, the coefficients of friction calculated from the velocity profiles fore of the test sections agreed to within their uncertainties: all were less than 8 percent different, and the majority were less than 5 percent different. That the values on the ribletted side tended to be lower might indicate that this difference was due to the 2 inches of ribletted wall upstream of the riblet test section. No attempt was made adjust the calculation of drag or heat transfer reduction for these possible differences in wall boundary layers.

One of the many test case validations of the Coles Hirst 3 method of calculating  $C_f$  is shown in Figure C.5, Validation of Profile Analysis Program. A dummy data file was created using the wake law and analyzed with the VPFIT7 program. These data are plotted as squares. The resulting curve fit, which predicted the  $C_f$  used to generate the data to within 0.005 percent, is plotted as a solid line.

The complete set of velocity profile measurements from which skin friction was calculated is shown in Figures C.6 through C.15. The velocity measurements versus distance from the wall are plotted in wall units along with the curve fits calculated according to Coles Hirst method 3. The top graph in each figure shows the profile just fore of the test section and the one below the profile just aft. The figures come in pairs, the even numbered ones being the flat plate results and the odd ones being the ribletted results. Thus, Figure C.6 shows the profiles fore and aft of the flat test section at a freestream velocity of 8.41 m/s, while Figure C.7 shows the profiles fore and aft of the ribletted test section at that freestream velocity.

Several trends are apparent from the graphs: fairly good fits, some scatter at lower velocities, and some periodicity to the scatter. In general, the fits seem to follow the trends accurately throughout the entire boundary layer. For the most part the fits are quite good except that at lower velocities some scatter is apparent. Indeed, only for freestream values of 15 m/s and above are the magnitudes of the reduced chi-squared in the region where the fits would be

considered good. However, the size of the chi-squared does seem to be from normally distributed error and not from coherent trends in the data unaccounted for in the fitting equation. Thus, the only real discrepancy in the results is that at lower velocities an unaccounted for source of normally distributed error seems to be present. One possible cause might be some form of periodic compressor disturbance.

At freestream velocities lower than 8.5 m/s, periodic disturbances in the mean velocity profile were present. The most likely cause is that at these lower speeds, the layers of gauze across the inlet were blocking enough flow to cause the compressor to enter some type of low frequency stall mode. Indeed, the velocity data taken up to 10 m/s show periodic fluctuation of the velocity with distance from the wall. Since the data were taken in order of distance away from the wall, this trend could be indication of periodic flow disturbances at low velocities. Other less likely possibilities include the effect of periodic variation in ambient temperature or pressure on the density and periodic sticking and slipping of the boundary layer probe apparatus.

**E. Effect of Riblets on Wall Shear.** The full effects of riblets on skin friction and drag are treated in Sections 6.4.B and C.

## **APPENDIX D - HEAT TRANSFER ANALYSIS, ERROR ANALYSIS, PROGRAMS, AND RESULTS**

### **D.1. Heat Transfer Measurement Equipment**

**A. Ambient Conditions.** Ambient temperature was measured with four liquid-in-glass, partial immersion, mercury thermometers. Two of these were 0.1°C gradation, 0°C to 100°C range; the other two were 0.2°C gradation, 0°C to 200°C range. They were suspended via 1.27-cm-wide, Styrofoam-insulated, thermometer clamps and shielded from radiation and convection heat loss with cylindrical shields, 20 cm in length and 7 cm in diameter, constructed of 1.5-mm Aluminum sheeting. Readings were taken using thermometer-attachable, magnifying eyepieces. Because the thermometers were readable to at least half their gradation spacing, this was taken as their accuracy. Compared to the estimates of liquid-in-glass thermometer accuracy outlined in Goldstein and Chiang (1985), this value is slightly conservative. The average of the readings of the four thermometers was taken as ambient temperature. With the air in the lab sufficiently mixed with fans, the four thermometers placed around the room showed the same temperature to within their readability. The uncertainty of the ambient temperature is thus just half the root mean square of the readabilities.

Ambient density was determined from the ambient pressure and temperature via the equation of state as described in Appendix C.2.B. Ambient pressure was measured as described in Appendix C.1.A.

**B. Tunnel Wall Temperature.** Test plate temperature was measured with 140 Omega, type F3105, thin-film, platinum, RTD's potted in 9.91-mm long, 3.23-mm-diameter cylinders of Eccobond 285 epoxy. Detailed description of these sensors and their use may be found in Sections 3.2.I. and 4.2.A., and Appendix B.1.A., and B.1.C. A detailed analysis of the uncertainty in their readings may be found in Appendix B.1.D. and B.3. and Table B.1.

**C. Test Section Heater and Shunt Resistor Voltage.** The power output of the 20 heaters in the test segment was determined by directly measuring the voltage drop across each of the heaters ( $V_h$ ) and by indirectly measuring the current via the voltage measurement across shunt resistors ( $V_{sh}$ ) with known resistances. The 20 channels of voltage input on the Helios I were used to read the voltage drop across the heaters directly by connecting a pair of 3-m leads from the front end in parallel with each heater. The 20 channels of current input were modified to allow the measurement of large currents. The shunt resistors originally wired into the current input connector were removed. Six-inch lengths of Inconel wire, used for its extremely low resistance

sensitivity to temperature, were connected in the test segment interface boxes in series with each heater and a set of two 3-m leads were then connected to the front end in parallel with each of these new shunt resistors. Four-wire resistance measurements of the new shunt resistors over the range of test currents showed no detectable change in resistance due to temperature effects.

## **D.2. Heat Transfer Analysis and Error Analysis Methodology**

**A. Determining Stanton Number.** Stanton number, nondimensionalized convective heat flux at the wall, was calculated from direct measurements of heater heat flux and adjusted to account for back, side, and radiation losses and wall temperature variation based on an energy balance of the test sections. Interpolation, extrapolation, and splines were used to calculate the temperature in the pretest plate at three spanwise positions at the streamwise midpoint of each heater and in the test plate at four spanwise positions. These temperatures were used to estimate the radiation heat loss via equation 3.8, the side losses via Fourier's law of heat conduction, and using the temperatures at the back guard heaters, the back losses again using Fourier's Law. These values were then used to calculate the convective turbulent heat flux at the wall with equation 3.6. Definition 2.29 was used to calculate Stanton number from this. The solution for the effect of a step rise in temperature on Stanton number was used to correct these values for the variation in upstream wall temperature.

The choice of the method of measurement was a design decision because of its effect on test plate configuration. For this reason, the background of and reasoning behind the choice are discussed in the design Sections 3.2.A., E., and F.

The heat transfer equivalents of local skin friction and total test section drag can be calculated from the calculated values of convective heat fluxes from the test sections into the flow. The local Stanton number is the nondimensionalized form of the local, convective heat flux at the wall,  $q_w$ , given by equation 6.14. The error in Stanton number due to error propagation is given by:

$$u_{St} \approx \sqrt{u_{q_w}^2 \left( \frac{St}{q_w} \right)^2 + u_{\rho}^2 \left( \frac{St}{\rho} \right)^2 + u_{U_{\infty}}^2 \left( \frac{2 St}{U_{\infty}} \right)^2 + u_{C_p}^2 \left( \frac{St}{C_p} \right)^2 + (u_{T_w}^2 + u_{T_e}^2) \left( \frac{St}{(T_w - T_e)} \right)^2}. \quad (D.1)$$

A similar coefficient analogous to the coefficient of drag may be calculated based on the convective heat flux over the entire test section,  $Q_w$ , as given by equation 6.15. The error propagation through this equation is the same as D.1 with  $q_w$  replaced by  $(Q_w/A)$ . The local and total convective heat fluxes may be found from an energy balance of the test sections.

The total convective heat transfer out of the test sections was calculated by considering

them as control volumes and performing an energy balance. The Aluminum plate test section and the test section heaters were taken as the control volume on which the energy balance was performed. The heat flux from these heaters was treated as uniform heat generation in an infinitesimally thin plane located on the surface of the heaters closer to the flow. The heat transfer out of this control volume consisted of:

- loss out of the sides, through the strip of foam epoxy insulation into the surrounding plate, via conduction, noted as  $Q_s$ ;
- loss out of the front, into the flow, via forced convection, termed  $q_w$  locally and  $Q_w$  in total;
- loss out of the front, into the flow, via radiation,  $q_r$ ; and,
- loss out of the rear into the insulation via conduction,  $Q_b$ .

The heater heat flux was calculated from heater voltage and current. The conduction losses were calculated via Fourier's law of heat conduction from the test section and surrounding plate and insulation temperatures and conductivities. The radiation loss was calculated from Stefan-Boltzmann's Law of Radiation. This balance may be rephrased in equation form as equation 6.16. The error propagation through this equation when used to calculate the wall heat flux is given by:

$$u_{Q_w} \approx \sqrt{\sum_{i=1}^4 u_{Q_{hi}}^2 + u_{Q_{si}}^2 + u_{Q_{bi}}^2 + u_{q_{ri}}^2 A_i^2 + u_{A_i}^2 q_{ri}^2}, \quad (D.2)$$

where  $Q_{hi}$  are the heater flux inputs,  $Q_{si}$  are the losses out of the sides of each subsection,  $q_{wi}$  and  $q_{ri}$  are the convective and radiative losses out of the front of each subsection,  $A_i$  are the subsection areas, and  $Q_{bi}$  are the back losses out of the subsections. The uncertainty in radiated heat flux may be found via equation 3.10. An equation similar to D.2 may be derived for  $q_{wi}$ , the wall heat flux in each subsection of the test sections quite easily.

**B. Heater Input.** Heater heat fluxes were calculated from direct measurements of heater voltage drops,  $V_{hi}$ , and indirect measurements of heater current,  $I_{hi}$ . The heater currents were calculated from measurements of the voltage drops,  $V_{shi}$ , across the shunt resistors, of known resistance  $R_{shi}$ , in series with the heaters. The two voltage measurements for each heater are shown in Figure 3.7. The  $i$ -th heater heat flux is given by equation 6.17, the uncertainty in which is:

$$u_{Q_{hi}} \approx \sqrt{u_{V_{hi}}^2 \left( \frac{Q_{hi}}{V_{hi}} \right)^2 + u_{V_{shi}}^2 \left( \frac{Q_{hi}}{V_{shi}} \right)^2 + u_{R_{shi}}^2 \left( \frac{Q_{hi}}{R_{shi}} \right)^2}. \quad (D.3)$$

**C. Conduction Heat Loss.** The heat losses through the back of the test sections were

calculated via a one-dimensional solution of Fourier's law of heat conduction through three materials from test plate temperature and insulation temperature measurements. Fourier's law of heat conduction can be solved for the case of one-dimensional heat transfer through three materials a, b, and c, given their conductivities and the temperature before material a,  $T_1$ , and after material c,  $T_4$ , to give:

$$q_{b_i} = -k_a \frac{T_2 - T_1}{y_2 - y_1}, \quad (D.4)$$

where  $T_2$  is given by equation 6.20. The total conduction heat loss may be found by multiplying equation 6.17 by the area of the loss plane. The uncertainty in this value may be estimated roughly via error propagation analysis. However, some unquantifiable error is introduced by the fact that the solution is two dimensional and the real case is not. Due to this, a set estimate of 5 percent based upon the error propagation limits was taken. The formulae used may be found in the HEATCALC program listout. The same analysis procedure was followed for the side conduction losses.

**C. Radiation Heat Loss.** Radiation heat loss was estimated from Stefan-Boltzmann's Law of Radiation, equation 3.8. An emissivity of 0.05 was used based on the experimental results described in Singham (1962). The difference between the temperature of the RTD's near the test wall surface and the actual surface, in general less than  $0.05^\circ\text{C}$ , due to the 0.1-in depth of the RTD sensing element beneath the surface, can be included in addition to the uncertainty in the emissivity, estimated to be 5 percent, in the evaluation of the radiation heat flux uncertainty.

**D. Adjusting for Wall Temperature Variation.** The solution for the effect of a step rise in temperature on Stanton number, as given in, among others, Kays and Crawford (1980), was used to correct the coefficient of heat transfer values for the variation in upstream wall temperature via a discrete approximation of the standard formula 6.21. This equation is very easily translated to the discrete case by substituting sum for integral and  $\Delta$  for  $d$ , from which the error propagation formula follows.

### **D.3. Heat Transfer Analysis Program**

Listed below are the various program units which comprise the heat transfer calculation program HEATCALC. The various units include:

- HEATCALC.FOR, the main program to perform the calculations and write the results to file;

- CALCFLUX.FOR, the subroutine to perform calculation of the two dimensional heat flux through three materials;
- SPLINE.FOR and SPLINT.FOR, the subroutines from Press et al. (1986) used to perform the spline interpolation of wall temperature; and,
- AIR.FOR, the subroutine to calculate air properties as a function of ambient temperature, listed in Appendix C.3.B.

## HEATCALC.FOR

```

program heatcalc
  real emiss,sam,sbconst,to,sto,rho,srho,ue,sue,cp,scp,sweight,
    k1,k2,k3,k4
  real rsh(2,10),srsh(2,10),lmeas(2,10),sim(2,10)
  real vmeas(2,10,31),svmexp(2,10,31),svmstat(2,10),svmtot(2,10)
  real vsh(2,10,31),svshexp(2,10,31),svshstat(2,10),svshtot(2,10)
  real lmeas(2,30,31),stmot(2,30),stmat(2,30),stmexp(2,30),
    tdist(2,6,5),stdstat(2,6,5),stdexp(2,6,5),stdtot(2,6,5),
    tave(2,6),sta(2,6),tcalerr(129),tback(2),stback(2)
  real t3fm(30,31),st3fmot(30),st3fmat(30),st3fmexp(30),
    t3fd(2,12,3),st3fdstat(2,12,3),st3fdexp(2,12,3),
    st3fdtot(2,12,3),t3fave(2,12)
  real t1fm(39,31),st1fmot(39),st1fmat(39),st1fmexp(39),
    t1fd(2,4,3),st1fdstat(2,4,3),st1fdexp(2,4,3),
    st1fdtot(2,4,3),savechrat
  real qmeas(2,10),sqm(2,10),grad(2,4),sqr(2,4),qloss(2,4),
    sq(2,4),qconv(2,4),sqc(2,4),qtot(2),sq(2),ch(2,4),
    sch(2,4),chrat(2,4),schrat(2,4),chrave(2),schrave(2),
    qlloss(2),sqtl(2),qrat,sqrat,persch(2,4),avechrat
  real area,length(12),ya(10),xa(10),ya,x,z(17),x1,x2,x3,x4,x5
  real delt,sdelt,delt1,delt2,delt3,delt4,
    delt5,delt6,delt7,delt8,delt9,delt10,delt11,delt12,delt13,
    delt14,delt15,delt16,delt17,delt18,delt19,delt20,delt21,
    delt22,delt23,delt24,delt25,delt26,delt27,delt28,delt29,
    delt30,delt31,delt32,delt33,delt34,delt35,delt36,delt37,
    delt38,delt39,delt40,delt41,delt42,delt43,delt44,delt45,
    delt46,delt47,delt48,delt49,delt50,delt51,delt52,delt53,
    delt54,delt55,delt56,delt57,delt58,delt59,delt60,delt61,
    delt62,delt63,delt64,delt65,delt66,delt67,delt68,delt69,
    delt70,delt71,delt72,delt73,delt74,delt75,delt76,delt77,
    delt78,delt79,delt80,delt81,delt82,delt83,delt84,delt85,
    delt86,delt87,delt88,delt89,delt90,delt91,delt92,delt93,
    delt94,delt95,delt96,delt97,delt98,delt99,delt100,delt101,
    delt102,delt103,delt104,delt105,delt106,delt107,delt108,
    delt109,delt110,delt111,delt112,delt113,delt114,delt115,
    delt116,delt117,delt118,delt119,delt120,delt121,delt122,
    delt123,delt124,delt125,delt126,delt127,delt128,delt129,
    delt130,delt131,delt132,delt133,delt134,delt135,delt136,
    delt137,delt138,delt139,delt140,delt141,delt142,delt143,
    delt144,delt145,delt146,delt147,delt148,delt149,delt150,
    delt151,delt152,delt153,delt154,delt155,delt156,delt157,
    delt158,delt159,delt160,delt161,delt162,delt163,delt164,
    delt165,delt166,delt167,delt168,delt169,delt170,delt171,
    delt172,delt173,delt174,delt175,delt176,delt177,delt178,
    delt179,delt180,delt181,delt182,delt183,delt184,delt185,
    delt186,delt187,delt188,delt189,delt190,delt191,delt192,
    delt193,delt194,delt195,delt196,delt197,delt198,delt199,
    delt200,delt201,delt202,delt203,delt204,delt205,delt206,
    delt207,delt208,delt209,delt210,delt211,delt212,delt213,
    delt214,delt215,delt216,delt217,delt218,delt219,delt220,
    delt221,delt222,delt223,delt224,delt225,delt226,delt227,
    delt228,delt229,delt230,delt231,delt232,delt233,delt234,
    delt235,delt236,delt237,delt238,delt239,delt240,delt241,
    delt242,delt243,delt244,delt245,delt246,delt247,delt248,
    delt249,delt250,delt251,delt252,delt253,delt254,delt255,
    delt256,delt257,delt258,delt259,delt260,delt261,delt262,
    delt263,delt264,delt265,delt266,delt267,delt268,delt269,
    delt270,delt271,delt272,delt273,delt274,delt275,delt276,
    delt277,delt278,delt279,delt280,delt281,delt282,delt283,
    delt284,delt285,delt286,delt287,delt288,delt289,delt290,
    delt291,delt292,delt293,delt294,delt295,delt296,delt297,
    delt298,delt299,delt300,delt301,delt302,delt303,delt304,
    delt305,delt306,delt307,delt308,delt309,delt310,delt311,
    delt312,delt313,delt314,delt315,delt316,delt317,delt318,
    delt319,delt320,delt321,delt322,delt323,delt324,delt325,
    delt326,delt327,delt328,delt329,delt330,delt331,delt332,
    delt333,delt334,delt335,delt336,delt337,delt338,delt339,
    delt340,delt341,delt342,delt343,delt344,delt345,delt346,
    delt347,delt348,delt349,delt350,delt351,delt352,delt353,
    delt354,delt355,delt356,delt357,delt358,delt359,delt360,
    delt361,delt362,delt363,delt364,delt365,delt366,delt367,
    delt368,delt369,delt370,delt371,delt372,delt373,delt374,
    delt375,delt376,delt377,delt378,delt379,delt380,delt381,
    delt382,delt383,delt384,delt385,delt386,delt387,delt388,
    delt389,delt390,delt391,delt392,delt393,delt394,delt395,
    delt396,delt397,delt398,delt399,delt400,delt401,delt402,
    delt403,delt404,delt405,delt406,delt407,delt408,delt409,
    delt410,delt411,delt412,delt413,delt414,delt415,delt416,
    delt417,delt418,delt419,delt420,delt421,delt422,delt423,
    delt424,delt425,delt426,delt427,delt428,delt429,delt430,
    delt431,delt432,delt433,delt434,delt435,delt436,delt437,
    delt438,delt439,delt440,delt441,delt442,delt443,delt444,
    delt445,delt446,delt447,delt448,delt449,delt450,delt451,
    delt452,delt453,delt454,delt455,delt456,delt457,delt458,
    delt459,delt460,delt461,delt462,delt463,delt464,delt465,
    delt466,delt467,delt468,delt469,delt470,delt471,delt472,
    delt473,delt474,delt475,delt476,delt477,delt478,delt479,
    delt480,delt481,delt482,delt483,delt484,delt485,delt486,
    delt487,delt488,delt489,delt490,delt491,delt492,delt493,
    delt494,delt495,delt496,delt497,delt498,delt499,delt500,
    delt501,delt502,delt503,delt504,delt505,delt506,delt507,
    delt508,delt509,delt510,delt511,delt512,delt513,delt514,
    delt515,delt516,delt517,delt518,delt519,delt520,delt521,
    delt522,delt523,delt524,delt525,delt526,delt527,delt528,
    delt529,delt530,delt531,delt532,delt533,delt534,delt535,
    delt536,delt537,delt538,delt539,delt540,delt541,delt542,
    delt543,delt544,delt545,delt546,delt547,delt548,delt549,
    delt550,delt551,delt552,delt553,delt554,delt555,delt556,
    delt557,delt558,delt559,delt560,delt561,delt562,delt563,
    delt564,delt565,delt566,delt567,delt568,delt569,delt570,
    delt571,delt572,delt573,delt574,delt575,delt576,delt577,
    delt578,delt579,delt580,delt581,delt582,delt583,delt584,
    delt585,delt586,delt587,delt588,delt589,delt590,delt591,
    delt592,delt593,delt594,delt595,delt596,delt597,delt598,
    delt599,delt600,delt601,delt602,delt603,delt604,delt605,
    delt606,delt607,delt608,delt609,delt610,delt611,delt612,
    delt613,delt614,delt615,delt616,delt617,delt618,delt619,
    delt620,delt621,delt622,delt623,delt624,delt625,delt626,
    delt627,delt628,delt629,delt630,delt631,delt632,delt633,
    delt634,delt635,delt636,delt637,delt638,delt639,delt640,
    delt641,delt642,delt643,delt644,delt645,delt646,delt647,
    delt648,delt649,delt650,delt651,delt652,delt653,delt654,
    delt655,delt656,delt657,delt658,delt659,delt660,delt661,
    delt662,delt663,delt664,delt665,delt666,delt667,delt668,
    delt669,delt670,delt671,delt672,delt673,delt674,delt675,
    delt676,delt677,delt678,delt679,delt680,delt681,delt682,
    delt683,delt684,delt685,delt686,delt687,delt688,delt689,
    delt690,delt691,delt692,delt693,delt694,delt695,delt696,
    delt697,delt698,delt699,delt700,delt701,delt702,delt703,
    delt704,delt705,delt706,delt707,delt708,delt709,delt710,
    delt711,delt712,delt713,delt714,delt715,delt716,delt717,
    delt718,delt719,delt720,delt721,delt722,delt723,delt724,
    delt725,delt726,delt727,delt728,delt729,delt730,delt731,
    delt732,delt733,delt734,delt735,delt736,delt737,delt738,
    delt739,delt740,delt741,delt742,delt743,delt744,delt745,
    delt746,delt747,delt748,delt749,delt750,delt751,delt752,
    delt753,delt754,delt755,delt756,delt757,delt758,delt759,
    delt760,delt761,delt762,delt763,delt764,delt765,delt766,
    delt767,delt768,delt769,delt770,delt771,delt772,delt773,
    delt774,delt775,delt776,delt777,delt778,delt779,delt780,
    delt781,delt782,delt783,delt784,delt785,delt786,delt787,
    delt788,delt789,delt790,delt791,delt792,delt793,delt794,
    delt795,delt796,delt797,delt798,delt799,delt800,delt801,
    delt802,delt803,delt804,delt805,delt806,delt807,delt808,
    delt809,delt810,delt811,delt812,delt813,delt814,delt815,
    delt816,delt817,delt818,delt819,delt820,delt821,delt822,
    delt823,delt824,delt825,delt826,delt827,delt828,delt829,
    delt830,delt831,delt832,delt833,delt834,delt835,delt836,
    delt837,delt838,delt839,delt840,delt841,delt842,delt843,
    delt844,delt845,delt846,delt847,delt848,delt849,delt850,
    delt851,delt852,delt853,delt854,delt855,delt856,delt857,
    delt858,delt859,delt860,delt861,delt862,delt863,delt864,
    delt865,delt866,delt867,delt868,delt869,delt870,delt871,
    delt872,delt873,delt874,delt875,delt876,delt877,delt878,
    delt879,delt880,delt881,delt882,delt883,delt884,delt885,
    delt886,delt887,delt888,delt889,delt890,delt891,delt892,
    delt893,delt894,delt895,delt896,delt897,delt898,delt899,
    delt900,delt901,delt902,delt903,delt904,delt905,delt906,
    delt907,delt908,delt909,delt910,delt911,delt912,delt913,
    delt914,delt915,delt916,delt917,delt918,delt919,delt920,
    delt921,delt922,delt923,delt924,delt925,delt926,delt927,
    delt928,delt929,delt930,delt931,delt932,delt933,delt934,
    delt935,delt936,delt937,delt938,delt939,delt940,delt941,
    delt942,delt943,delt944,delt945,delt946,delt947,delt948,
    delt949,delt950,delt951,delt952,delt953,delt954,delt955,
    delt956,delt957,delt958,delt959,delt960,delt961,delt962,
    delt963,delt964,delt965,delt966,delt967,delt968,delt969,
    delt970,delt971,delt972,delt973,delt974,delt975,delt976,
    delt977,delt978,delt979,delt980,delt981,delt982,delt983,
    delt984,delt985,delt986,delt987,delt988,delt989,delt990,
    delt991,delt992,delt993,delt994,delt995,delt996,delt997,
    delt998,delt999,delt1000,delt1001,delt1002,delt1003,delt1004,
    delt1005,delt1006,delt1007,delt1008,delt1009,delt1010,delt1011,
    delt1012,delt1013,delt1014,delt1015,delt1016,delt1017,delt1018,
    delt1019,delt1020,delt1021,delt1022,delt1023,delt1024,delt1025,
    delt1026,delt1027,delt1028,delt1029,delt1030,delt1031,delt1032,
    delt1033,delt1034,delt1035,delt1036,delt1037,delt1038,delt1039,
    delt1040,delt1041,delt1042,delt1043,delt1044,delt1045,delt1046,
    delt1047,delt1048,delt1049,delt1050,delt1051,delt1052,delt1053,
    delt1054,delt1055,delt1056,delt1057,delt1058,delt1059,delt1060,
    delt1061,delt1062,delt1063,delt1064,delt1065,delt1066,delt1067,
    delt1068,delt1069,delt1070,delt1071,delt1072,delt1073,delt1074,
    delt1075,delt1076,delt1077,delt1078,delt1079,delt1080,delt1081,
    delt1082,delt1083,delt1084,delt1085,delt1086,delt1087,delt1088,
    delt1089,delt1090,delt1091,delt1092,delt1093,delt1094,delt1095,
    delt1096,delt1097,delt1098,delt1099,delt1100,delt1101,delt1102,
    delt1103,delt1104,delt1105,delt1106,delt1107,delt1108,delt1109,
    delt1110,delt1111,delt1112,delt1113,delt1114,delt1115,delt1116,
    delt1117,delt1118,delt1119,delt1120,delt1121,delt1122,delt1123,
    delt1124,delt1125,delt1126,delt1127,delt1128,delt1129,delt1130,
    delt1131,delt1132,delt1133,delt1134,delt1135,delt1136,delt1137,
    delt1138,delt1139,delt1140,delt1141,delt1142,delt1143,delt1144,
    delt1145,delt1146,delt1147,delt1148,delt1149,delt1150,delt1151,
    delt1152,delt1153,delt1154,delt1155,delt1156,delt1157,delt1158,
    delt1159,delt1160,delt1161,delt1162,delt1163,delt1164,delt1165,
    delt1166,delt1167,delt1168,delt1169,delt1170,delt1171,delt1172,
    delt1173,delt1174,delt1175,delt1176,delt1177,delt1178,delt1179,
    delt1180,delt1181,delt1182,delt1183,delt1184,delt1185,delt1186,
    delt1187,delt1188,delt1189,delt1190,delt1191,delt1192,delt1193,
    delt1194,delt1195,delt1196,delt1197,delt1198,delt1199,delt1200,
    delt1201,delt1202,delt1203,delt1204,delt1205,delt1206,delt1207,
    delt1208,delt1209,delt1210,delt1211,delt1212,delt1213,delt1214,
    delt1215,delt1216,delt1217,delt1218,delt1219,delt1220,delt1221,
    delt1222,delt1223,delt1224,delt1225,delt1226,delt1227,delt1228,
    delt1229,delt1230,delt1231,delt1232,delt1233,delt1234,delt1235,
    delt1236,delt1237,delt1238,delt1239,delt1240,delt1241,delt1242,
    delt1243,delt1244,delt1245,delt1246,delt1247,delt1248,delt1249,
    delt1250,delt1251,delt1252,delt1253,delt1254,delt1255,delt1256,
    delt1257,delt1258,delt1259,delt1260,delt1261,delt1262,delt1263,
    delt1264,delt1265,delt1266,delt1267,delt1268,delt1269,delt1270,
    delt1271,delt1272,delt1273,delt1274,delt1275,delt1276,delt1277,
    delt1278,delt1279,delt1280,delt1281,delt1282,delt1283,delt1284,
    delt1285,delt1286,delt1287,delt1288,delt1289,delt1290,delt1291,
    delt1292,delt1293,delt1294,delt1295,delt1296,delt1297,delt1298,
    delt1299,delt1300,delt1301,delt1302,delt1303,delt1304,delt1305,
    delt1306,delt1307,delt1308,delt1309,delt1310,delt1311,delt1312,
    delt1313,delt1314,delt1315,delt1316,delt1317,delt1318,delt1319,
    delt1320,delt1321,delt1322,delt1323,delt1324,delt1325,delt1326,
    delt1327,delt1328,delt1329,delt1330,delt1331,delt1332,delt1333,
    delt1334,delt1335,delt1336,delt1337,delt1338,delt1339,delt1340,
    delt1341,delt1342,delt1343,delt1344,delt1345,delt1346,delt1347,
    delt1348,delt1349,delt1350,delt1351,delt1352,delt1353,delt1354,
    delt1355,delt1356,delt1357,delt1358,delt1359,delt1360,delt1361,
    delt1362,delt1363,delt1364,delt1365,delt1366,delt1367,delt1368,
    delt1369,delt1370,delt1371,delt1372,delt1373,delt1374,delt1375,
    delt1376,delt1377,delt1378,delt1379,delt1380,delt1381,delt1382,
    delt1383,delt1384,delt1385,delt1386,delt1387,delt1388,delt1389,
    delt1390,delt1391,delt1392,delt1393,delt1394,delt1395,delt1396,
    delt1397,delt1398,delt1399,delt1400,delt1401,delt1402,delt1403,
    delt1404,delt1405,delt1406,delt1407,delt1408,delt1409,delt1410,
    delt1411,delt1412,delt1413,delt1414,delt1415,delt1416,delt1417,
    delt1418,delt1419,delt1420,delt1421,delt1422,delt1423,delt1424,
    delt1425,delt1426,delt1427,delt1428,delt1429,delt1430,delt1431,
    delt1432,delt1433,delt1434,delt1435,delt1436,delt1437,delt1438,
    delt1439,delt1440,delt1441,delt1442,delt1443,delt1444,delt1445,
    delt1446,delt1447,delt1448,delt1449,delt1450,delt1451,delt1452,
    delt1453,delt1454,delt1455,delt1456,delt1457,delt1458,delt1459,
    delt1460,delt1461,delt1462,delt1463,delt1464,delt1465,delt1466,
    delt1467,delt1468,delt1469,delt1470,delt1471,delt1472,delt1473,
    delt1474,delt1475,delt1476,delt1477,delt1478,delt1479,delt1480,
    delt1481,delt1482,delt1483,delt1484,delt1485,delt1486,delt1487,
    delt1488,delt1489,delt1490,delt1491,delt1492,delt1493,delt1494,
    delt1495,delt1496,delt1497,delt1498,delt1499,delt1500,delt1501,
    delt1502,delt1503,delt1504,delt1505,delt1506,delt1507,delt1508,
    delt1509,delt1510,delt1511,delt1512,delt1513,delt1514,delt1515,
    delt1516,delt1517,delt1518,delt1519,delt1520,delt1521,delt1522,
    delt1523,delt1524,delt1525,delt1526,delt1527,delt1528,delt1529,
    delt1530,delt1531,delt1532,delt1533,delt1534,delt1535,delt1536,
    delt1537,delt1538,delt1539,delt1540,delt1541,delt1542,delt1543,
    delt1544,delt1545,delt1546,delt1547,delt1548,delt1549,delt1550,
    delt1551,delt1552,delt1553,delt1554,delt1555,delt1556,delt1557,
    delt1558,delt1559,delt1560,delt1561,delt1562,delt1563,delt1564,
    delt1565,delt1566,delt1567,delt1568,delt1569,delt1570,delt1571,
    delt1572,delt1573,delt1574,delt1575,delt1576,delt1577,delt1578,
    delt1579,delt1580,delt1581,delt1582,delt1583,delt1584,delt1585,
    delt1586,delt1587,delt1588,delt1589,delt1590,delt1591,delt1592,
    delt1593,delt1594,delt1595,delt1596,delt1597,delt1598,delt1599,
    delt1600,delt1601,delt1602,delt1603,delt1604,delt1605,delt1606,
    delt1607,delt1608,delt1609,delt1610,delt1611,delt1612,delt1613,
    delt1614,delt1615,delt1616,delt1617,delt1618,delt1619,delt1620,
    delt1621,delt1622,delt1623,delt1624,delt1625,delt1626,delt1627,
    delt1628,delt1629,delt1630,delt1631,delt1632,delt1633,delt1634,
    delt1635,delt1636,delt1637,delt1638,delt1639,delt1640,delt1641,
    delt1642,delt1643,delt1644,delt1645,delt1646,delt1647,delt1648,
    delt1649,delt1650,delt1651,delt1652,delt1653,delt1654,delt1655,
    delt1656,delt1657,delt1658,delt1659,delt1660,delt1661,delt1662,
    delt1663,delt1664,delt1665,delt1666,delt1667,delt1668,delt1669,
    delt1670,delt1671,delt1672,delt1673,delt1674,delt1675,delt1676,
    delt1677,delt1678,delt1679,delt1680,delt1681,delt1682,delt1683,
    delt1684,delt1685,delt1686,delt1687,delt1688,delt1689,delt1690,
    delt1691,delt1692,delt1693,delt1694,delt1695,delt1696,delt1697,
    delt1698,delt1699,delt1700,delt1701,delt1702,delt1703,delt1704,
    delt1705,delt1706,delt1707,delt1708,delt1709,delt1710,delt1711,
    delt1712,delt1713,delt1714,delt1715,delt1716,delt1717,delt1718,
    delt1719,delt1720,delt1721,delt1722,delt1723,delt1724,delt1725,
    delt1726,delt1727,delt1728,delt1729,delt1730,delt1731,delt1732,
    delt1733,delt1734,delt1735,delt1736,delt1737,delt1738,delt1739,
    delt1740,delt1741,delt1742,delt1743,delt1744,delt1745,delt1746,
    delt1747,delt1748,delt1749,delt1750,delt1751,delt1752,delt1753,
    delt1754,delt1755,delt1756,delt1757,delt1758,delt1759,delt1760,
    delt1761,delt1762,delt1763,delt1764,delt1765,delt1766,delt1767,
    delt1768,delt1769,delt1770,delt1771,delt1772,delt1773,delt1774,
    delt1775,delt1776,delt1777,delt1778,delt1779,delt1780,delt1781,
    delt1782,delt1783,delt1784,delt1785,delt1786,delt1787,delt1788,
    delt1789,delt1790,delt1791,delt1792,delt1793,delt1794,delt1795,
    delt1796,delt1797,delt1798,delt1799,delt1800,delt1801,delt1802,
    delt1803,delt1804,delt1805,delt1806,delt1807,delt1808,delt1809,
    delt1810,delt1811,delt1812,delt1813,delt1814,delt1815,delt1816,
    delt1817,delt1818,delt1819,delt1820,delt1821,delt1822,delt1823,
    delt1824,delt1825,delt1826,delt1827,delt1828,delt1829,delt1830,
    delt1831,delt1832,delt1833,delt1834,delt1835,delt1836,delt1837,
    delt1838,delt1839,delt1840,delt1841,delt1842,delt1843,delt1844,
    delt1845,delt1846,delt1847,delt1848,delt1849,delt1850,delt1851,
    delt1852,delt1853,delt1854,delt1855,delt1856,delt1857,delt1858,
    delt1859,delt1860,delt1861,delt1862,delt1863,delt1864,delt1865,
    delt1866,delt1867,delt1868,delt1869,delt1870,delt1871,delt1872,
    delt1873,delt1874,delt1875,delt1876,delt1877,delt1878,delt1879,
    delt1880,delt1881,delt1882,delt1883,delt1884,delt1885,delt1886,
    delt1887,delt1888,delt1889,delt1890,delt1891,delt1892,delt1893,
    delt1894,delt1895,delt1896,delt1897,delt1898,delt1899,delt1900,
    delt1901,delt1902,delt1903,delt1904,delt1905,delt1906,delt1907,
    delt1908,delt1909,delt1910,delt1911,delt1912,delt1913,delt1914,
    delt1915,delt1916,delt1917,delt1918,delt1919,delt1920,delt1921,
    delt1922,delt1923,delt1924,delt1925,delt1926,delt1927,delt1928,
    delt1929,delt1930,delt1931,delt1932,delt1933,delt1934,delt1935,
    delt1936,delt1937,delt1938,delt1939,delt1940,delt1941,delt1942,
    delt1943,delt1944,delt1945,delt1946,delt1947,delt1948,delt1949,
    delt1950,delt1951,delt1952,delt1953,delt1954,delt1955,delt1956,
    delt1957,delt1958,delt1959,delt1960,delt1961,delt1962,delt1963,
    delt1964,delt1965,delt1966,delt1967,delt1968,delt1969,delt1970,
    delt1971,delt1972,delt1973,delt1974,delt1975,delt1976,delt1977,
    delt1978,delt1979,delt1980,delt1981,delt1982,delt1983,delt1984,
    delt1985,delt1986,delt1987,delt1988,delt1989,delt1990,delt1991,
    delt1992,delt1993,delt1994,delt1995,delt1996,delt1997,delt1998,
    delt1999,delt2000,delt2001,delt2002,delt2003,delt2004,delt2005,
    delt2006,delt2007,delt2008,delt2009,delt2010,delt2011,d
```



```

      read(9,210,end=200) (tmeas(2,j),j=1,30)
200 continue
210 format(18.3,29(1x,18.3))
close(9)
*
fname='stone.flux.data://numr/'31rdrun.dat'
open(9,file=fname,status='old')
do 220 i=1,4
  read(9,'a8') flag
220 continue
do 230 i=1,nsam
  read(9,240,end=230) (t3fm(j,i),j=1,30)
230 continue
240 format(18.3,29(1x,18.3))
close(9)
*
fname='stone.flux.data://numr/'11rdrun.dat'
open(9,file=fname,status='old')
do 250 i=1,4
  read(9,'a8') flag
250 continue
do 260 i=1,nsam
  read(9,270,end=260) (t1fm(j,i),j=1,39)
260 continue
270 format(18.3,29(1x,18.3))
close(9)
*
read in T indices data
*
fname='stone.flux.data/tpkindices.dat'
open(9,file=fname,status='old')
do 280 i=1,2
  do 290 j=1,6
    do 280 k=1,5
      read(9,310,end=280) ntm(i,j,k)
280 continue
290 continue
300 continue
310 format(1x,12)
close(9)
*
fname='stone.flux.data/tpkindices.dat'
open(9,file=fname,status='old')
do 320 i=1,2
  do 330 j=1,12
    do 320 k=1,3
      read(9,'s0,end=320) nt3fm(i,j,k)
320 continue
330 continue
340 continue
350 format(1x,12)
close(9)
*
fname='stone.flux.data/11findices.dat'
open(9,file=fname,status='old')
do 360 i=1,2
  do 370 j=1,4
    do 360 k=1,3
      read(9,390,end=360) nt1fm(i,j,k)
360 continue
370 continue
380 continue
390 format(1x,12)
close(9)
*
read in T error
*
fname='stone.flux.data/calerr.dat'
open(9,file=fname,status='old')
do 400 i=1,129
  read(9,420,end=400) tcalerr(i)
400 continue
420 format(57x,f7.5)
close(9)
*
read in freestream properties
*
fname='stone.flux.data://numr/'ftrprop.dat'
open(9,file=fname,status='old')
read(9,470,end=471) to,sto,rho,srho,ue,sue
470 format(1x,f8.2,1x,f4.2,1x,f8.6,1x,f8.6,1x,f7.4,1x,f7.4)
471 continue
close(9)
*
calculate Cp
*
call air(to,sto,cp,scp,dcl1,sdel1,dcl2,sdel2,dcl3,sdel3)
*
calculate T averages and errors
*
write(*,*) 'Performing temperature analysis'
nfree=nsam-1
nave=nsam+1
do 510 i=1,2
  do 500 j=1,30
    tmeas(i,j,nave)=0.
    st1mstat(i,j)=0.
    k=i*30+j
    st1mexp(i,j)=tcalerr(k)/sqrt(float(nsam))
    if (i.eq.1) then
      t3fm(j,nave)=0.
      st3mstat(j)=0.
      st3mexp(j)=tcalerr(j)/sqrt(float(nsam))
    endif
    do 480 k=1,nsam
      tmeas(i,j,nave)=tmeas(i,j,nave)+tmeas(i,j,k)/float(nsam)
      if (i.eq.1) t3fm(j,nave)=t3fm(j,nave)
      +t3fm(j,k)/float(nsam)
480 continue
do 490 k=1,nsam
  st1mstat(i,j)=st1mstat(i,j)
  + (tmeas(i,j,k)-tmeas(i,j,nave))**2
  if (i.eq.1) st3mstat(j)=st3mstat(j)
  + (t3fm(j,k)-t3fm(j,nave))**2
490 continue
st1mstat(i,j)=sqrt(st1mstat(i,j)/float(nfree))
st1mot(i,j)=st1mexp(i,j)+sweight*st1mstat(i,j)
if (i.eq.1) then
  st3mstat(j)=sqrt(st3mstat(j)/float(nfree))
  st3mot(j)=st3mexp(j)+sweight*st3mstat(j)
endif
500 continue
510 continue
*
do 525 j=1,39
  t1fm(j,nave)=0.
  st1fmstat(j)=0.
  k=j+90
  st1fmexp(j)=tcalerr(j)/sqrt(float(nsam))
  do 515 k=1,nsam
    t1fm(j,nave)=t1fm(j,nave)+t1fm(j,k)/float(nsam)
515 continue
do 520 k=1,nsam
  st1fmstat(j)=st1fmstat(j)+(t1fm(j,k)-t1fm(j,nave))**2
520 continue
st1fmstat(j)=sqrt(st1fmstat(j)/float(nfree))
st1fmot(j)=st1fmexp(j)+sweight*st1fmstat(j)
525 continue
*
rearrange test plate T indexing by position
*
do 550 i=1,2
  do 540 j=1,6
    do 530 k=1,5
      tdist(i,j,k)=tmeas(i,ntm(i,j,k),11)
      stdex(i,j,k)=st1mexp(i,ntm(i,j,k))
      stdest(i,j,k)=st1mstat(i,ntm(i,j,k))
      stdot(i,j,k)=st1mot(i,ntm(i,j,k))
530 continue
540 continue
550 continue
*
tback(1)=tmeas(1,28,nave)
stback(1)=tcalerr(58)
tback(2)=tmeas(2,28,nave)
stback(2)=tcalerr(88)
*
estimate T in test plate corners
*
do 555 i=1,2
  tdist(i,1,1)=tdist(i,1,2)*tdist(i,2,1)/tdist(i,2,2)
  tdist(i,1,5)=tdist(i,1,4)*tdist(i,2,5)/tdist(i,2,4)
  tdist(i,6,1)=tdist(i,6,2)*tdist(i,5,1)/tdist(i,5,2)
  tdist(i,6,5)=tdist(i,6,4)*tdist(i,5,5)/tdist(i,5,4)
555 continue
*
rearrange 3' T indexing
*
do 580 i=1,2
  do 570 j=1,12
    do 560 k=1,3
      t3fd(i,j,k)=t3fm(nt3fm(i,j,k),nave)
      st3dex(i,j,k)=st3mexp(nt3fm(i,j,k))
      st3dest(i,j,k)=st3mstat(nt3fm(i,j,k))
      st3dot(i,j,k)=st3mot(nt3fm(i,j,k))
560 continue
570 continue
580 continue
*
estimate T of broken side-RTDs (assuming symmetry about midline)
from average percent spanwise variation in 3' plate
*
t3fd(1,3,1)=t3fd(1,3,3)
st3dex(1,3,1)=st3dex(1,3,3)

```

```

st3dstat(1,3,1)=st3dstat(1,3,3)
st3drot(1,3,1)=st3drot(1,3,3)
t3d(1,9,1)=t3d(1,9,2)*(1-0.5)*(t3d(1,3,2)+t3d(1,3,3))
t3d(1,3,2)=t3d(1,12,2)-t3d(1,12,3)/t3d(1,12,2))
st3dexp(1,9,1)=2.*st3dexp(1,9,2)
st3dstat(1,9,1)=2.*st3dstat(1,9,2)
st3drot(1,9,1)=2.*st3drot(1,9,2)
t3d(1,9,3)=t3d(1,9,1)
st3dexp(1,9,3)=2.*st3dexp(1,9,2)
st3dstat(1,9,3)=2.*st3dstat(1,9,2)
st3drot(1,9,3)=2.*st3drot(1,9,2)
t3d(1,12,1)=t3d(1,12,3)
st3dexp(1,12,1)=st3dexp(1,12,3)
st3dstat(1,12,1)=st3dstat(1,12,3)
st3drot(1,12,1)=st3drot(1,12,3)

```

```

t3d(2,9,1)=t3d(2,9,3)
st3dexp(2,9,1)=st3dexp(2,9,3)
st3dstat(2,9,1)=st3dstat(2,9,3)
st3drot(2,9,1)=st3drot(2,9,3)
t3d(2,12,1)=t3d(2,12,3)
st3dexp(2,12,1)=st3dexp(2,12,3)
st3dstat(2,12,1)=st3dstat(2,12,3)
st3drot(2,12,1)=st3drot(2,12,3)

```

use spline to estimate T of damaged midline RTDs

```

ya(1)=t3d(1,1,2)
ya(2)=t3d(1,2,2)
ya(3)=t3d(1,3,2)
ya(4)=t3d(1,4,2)
ya(5)=t3d(1,5,2)
ya(6)=t3d(1,6,2)
ya(7)=t3d(1,9,2)
ya(8)=t3d(1,10,2)
ya(9)=t3d(1,11,2)
ya(10)=t3d(1,12,2)
xa(1)=0.125
xa(2)=0.625
xa(3)=1.625
xa(4)=3.375
xa(5)=5.75
xa(6)=8.5
xa(7)=19.75
xa(8)=24.25
xa(9)=28.75
xa(10)=33.5
n=10
call spline(xa, ya, n, y2a)
x=11.75
call splint(xa, ya, y2a, n, x, t3d(1,7,2))
x=15.5
call splint(xa, ya, y2a, n, x, t3d(1,8,2))

```

```

ya(1)=t3d(2,1,2)
ya(2)=t3d(2,2,2)
ya(3)=t3d(2,3,2)
ya(4)=t3d(2,4,2)
ya(5)=t3d(2,7,2)
ya(6)=t3d(2,8,2)
ya(7)=t3d(2,9,2)
ya(8)=t3d(2,10,2)
ya(9)=t3d(2,11,2)
ya(10)=t3d(2,12,2)
xa(1)=0.125
xa(2)=0.625
xa(3)=1.625
xa(4)=3.375
xa(5)=11.75
xa(6)=15.5
xa(7)=19.75
xa(8)=24.25
xa(9)=28.75
xa(10)=33.5
call spline(xa, ya, n, y2a)
x=5.75
call splint(xa, ya, y2a, n, x, t3d(2,5,2))
x=8.5
call splint(xa, ya, y2a, n, x, t3d(2,6,2))

```

estimate side T in heater sections w/out side RTDs

```

do 590 i=1,2
dt3dave=1-0.5*(t3d(1,3,2)-t3d(1,3,3))/t3d(1,3,2)
+ (t3d(1,9,2)-t3d(1,9,3))/t3d(1,9,2))
t3d(1,1,1)=dt3dave*t3d(1,1,2)
t3d(1,1,3)=dt3dave*t3d(1,1,2)
t3d(1,2,1)=dt3dave*t3d(1,2,2)
t3d(1,2,3)=dt3dave*t3d(1,2,2)
t3d(1,4,1)=dt3dave*t3d(1,4,2)
t3d(1,4,3)=dt3dave*t3d(1,4,2)
t3d(1,5,1)=dt3dave*t3d(1,5,2)

```

```

t3d(1,5,3)=dt3dave*t3d(1,5,2)
t3d(1,6,1)=dt3dave*t3d(1,6,2)
t3d(1,6,3)=dt3dave*t3d(1,6,2)
t3d(1,7,1)=dt3dave*t3d(1,7,2)
t3d(1,7,3)=dt3dave*t3d(1,7,2)
t3d(1,8,1)=dt3dave*t3d(1,8,2)
t3d(1,8,3)=dt3dave*t3d(1,8,2)
dt3dave=1-0.5*(t3d(1,9,2)-t3d(1,9,3))/t3d(1,9,2)
+ (t3d(1,12,2)-t3d(1,12,3))/t3d(1,12,2))
t3d(1,10,1)=dt3dave*t3d(1,10,2)
t3d(1,10,3)=dt3dave*t3d(1,10,2)
t3d(1,11,1)=dt3dave*t3d(1,11,2)
t3d(1,11,3)=dt3dave*t3d(1,11,2)

```

590 continue

calculate 3' section average Ts

```

do 598 i=1,2
do 598 j=1,12
t3dave(i,j)=(t3d(i,j,1)+t3d(i,j,2)+t3d(i,j,3))/3.

```

598 continue

598 continue

rearrange 1' T indexing

```

do 620 i=1,2
do 610 j=1,4
do 600 k=1,3
t1fd(i,j,k)=t1fm(t1fm(i,j,k), nave)
st1fdexp(i,j,k)=st1fmaxp(t1fm(i,j,k))
st1fdstat(i,j,k)=st1fmaxst(t1fm(i,j,k))
st1fdrot(i,j,k)=st1fmaxrot(t1fm(i,j,k))
600 continue
610 continue
620 continue
t1fd(1,4,1)=t1fd(1,4,3)
st1fdrot(1,4,1)=st1fdrot(1,4,3)

```

calculate test section average Ts

```

do 640 i=1,2
do 630 j=1,6
tave(i,j)=(t1stat(i,j,2)+t1stat(i,j,3)+t1stat(i,j,4))/3.
sta(i,j)=sqrt((st1drot(i,j,2)/3.)**2
+(st1drot(i,j,3)/3.)**2+(st1drot(i,j,4)/3.)**2)
630 continue
640 continue

```

heat flux estimation

```

write(*,*) 'Performing heat flux analysis'
do 680 i=1,2
do 670 j=1,10

```

calculate measured heat flux

```

vmeas(i,j,nave)=0.
svmexp(i,j,nave)=0.
svmstat(i,j)=0.
vsh(i,j,nave)=0.
svshexp(i,j,nave)=0.
svshstat(i,j)=0.
do 650 k=1,nsam
vmeas(i,j,nave)=vmeas(i,j,nave)+vmeas(i,j,k)/float(nsam)
svmexp(i,j,k)=9.e-5*vmeas(i,j,k)+3.e-3
svmexp(i,j,nave)=svmexp(i,j,nave)
+(svmexp(i,j,k)/float(nsam))**2
vsh(i,j,nave)=vsh(i,j,nave)+vsh(i,j,k)/float(nsam)
svshexp(i,j,k)=5.e-5*vsh(i,j,k)+3.e-5
svshexp(i,j,nave)=svshexp(i,j,nave)
+(svshexp(i,j,k)/float(nsam))**2
650 continue
svmexp(i,j,nave)=sqrt(svmexp(i,j,nave))
svshexp(i,j,nave)=sqrt(svshexp(i,j,nave))
do 660 k=1,nsam
svmstat(i,j)=svmstat(i,j)
+(vmeas(i,j,k)-vmeas(i,j,nave))**2
svshstat(i,j)=svshstat(i,j)
+(vsh(i,j,k)-vsh(i,j,nave))**2
660 continue
svmstat(i,j)=sqrt(svmstat(i,j)/float(nfree))
svshstat(i,j)=sqrt(svshstat(i,j)/float(nfree))
svmrot(i,j)=svmexp(i,j,11)+sweight*svmstat(i,j)
svshrot(i,j)=svshexp(i,j,11)+sweight*svshstat(i,j)

rsh(i,j)=0.001*rsh(i,j)
lmeas(i,j)=vsh(i,j,11)/rsh(i,j)
smx(i,j)=sqrt((svshrot(i,j)/rsh(i,j))**2+
(rsh(i,j)*vsh(i,j,11)/rsh(i,j))**2)
qmeas(i,j)=vmeas(i,j,11)*lmeas(i,j)
sqm(i,j)=sqrt((svmrot(i,j)*lmeas(i,j))**2+
(smx(i,j)*vmeas(i,j,11))**2)

```

```

    if ((j.ge.2).and.(j.le.5)) then
        k=1
        l=1
    calculate radiation loss heat flux
        delt=((tave(i,j)+273.15)**4-(to)**4)
        grad(i,k)=emiss*sbconst*area*delt
        sq(i,k)=sqrt((emiss*sbconst*area*delt)**2
        + (sta(i,j)**4*emiss*sbconst*area*tave(i,j)**3)**2
        + (sto**4*emiss*sbconst*area*to**3)**2)
    calculate side loss heat flux for each test heater section
    out of the front
        if (j.eq.2) then
            dy1=(1.-1./32.)*0.0254
            dy2=0.0254/16.
            dy3=(1.-1./32.)*0.0254
            call calcflux(dy1,dy2,dy3,k1,k2,k1,
                tave(i,j),tave(i,k),del1)
        else
            del1=225.*(tave(i,j)-tave(i,k))/(2.*0.0254)
            endif
    out of the rear
        if (j.eq.5) then
            dy1=(1.25-1./32.)*0.0254
            dy2=0.0254/16.
            dy3=(1.-1./32.)*0.0254
            call calcflux(dy1,dy2,dy3,k1,k2,k1,
                tave(i,j),tave(i,l),del2)
        else
            del2=225.*(tave(i,j)-tave(i,l))/(2.*0.0254)
            endif
    out of the left side
        dy1=(1.25-1./32.)*0.0254
        dy2=0.0254/16.
        dy3=(1.-1./32.)*0.0254
        call calcflux(dy1,dy2,dy3,k1,k2,k1,
            tdist(i,j,2),tdist(i,j,1),del3)
    out of the right side
        call calcflux(dy1,dy2,dy3,k1,k2,k1,
            tdist(i,j,4),tdist(i,j,5),del4)
    out of the back
        dy1=(0.5-0.135)*0.0254
        dy2=(3./16.)*0.0254
        dy3=0.0254
        call calcflux(dy1,dy2,dy3,k1,k4,k3,
            tdist(i,j,3),tback(i),del5)
    total loss
        qloss(i,k)=(0.5*7.*(del1+del2)+0.5*2.*(del3+del4)
            +7.*2.*del5)*0.0254**2
        sq(i,k)=0.1*qloss(i,k)
    calculate convection heat flux and Ch (Stanton #)
        qconv(i,k)=qmeas(i,j)-grad(i,k)-qloss(i,k)
        sqc(i,k)=sqrt((sqm(i,j)**2+sq(i,k)**2+sq(i,k)**2)
        textra=0.1*qconv(i,k)/(225.*2.*0.0254**7.)
        write(*,*) 'delTextra = ',textra
        tdel(i,j)=tave(i,j)-to+273.15-textra
        tsdel(i,j)=sqrt((sta(i,j)**2+sto**2)+0.1*textra
        ch(i,k)=(qconv(i,k)/area)/(rho*ue*cp*tdel(i,j))
        sch(i,k)=sqrt(((sqc(i,k)*ch(i,k)/qconv(i,k))**2
        + (srho*ch(i,k)/rho)**2+(tsdel(i,j)*ch(i,k)/tdel(i,j))**2
        + (sue*ch(i,k)/ue)**2+(scp*ch(i,k)/cp)**2)
        endif
670 continue
680 continue
    adjust Ch for variation in T in starting length
        z(1)=0.25
        z(2)=1.
        z(3)=2.25
        z(4)=4.5
        z(5)=7.
        z(6)=10.
        z(7)=13.5
        z(8)=17.5

```

```

        z(9)=22.
        z(10)=26.5
        z(11)=31.
        z(12)=36.
        z(13)=38.
        z(14)=40.
        z(15)=42.
        z(16)=44.
        z(17)=46.
        do 710 i=1,2
            chrave(i)=0.
            schrave(i)=0.
            do 700 j=1,4
                k=j+1
                dtave=tave(i,k)-to
                dtl=(tave(i,k)-t3tave(i,1))/dtave
                chrat(i,j)=1.-dtl
                x1=z(13)+1.
                do 690 l=2,12
                    dtl=(t3tave(i,l)-t3tave(i,l-1))/dtave
                    var=1./9.
                    tbletpctn=1./((1.-z(l-1)/x1)**0.9)**var
                    chrat(i,j)=chrat(i,j)+tbletpctn*dtl
                690 continue
                schrat(i,j)=sqrt((0.05*(1.-chrat(i,j)))**2)
                ch(i,j)=ch(i,j)/chrat(i,j)
                sch(i,j)=sqrt(sch(i,j)**2
                    + (schrat(i,j)*ch(i,j)/chrat(i,j))**2)
                persch(i,j)=100.*sch(i,j)/ch(i,j)
                write(*,695) i,j,ch(i,j),persch(i,j)
                695 format(1x,'Ch','i1','j1',' = ',e10.4,' +/- ',f8.4,'%')
                chrave(i)=chrave(i)+chrat(i,j)/4.
                schrave(i)=sqrt(schrave(i)**2+(schr(i,j)/4.))**2)
            700 continue
            710 continue
    calculate side loss heat flux for whole test section
        do 720 i=1,2
            qtot(i)=0.
            sq(i)=0.
            do 715 j=1,4
                qtot(i)=qtot(i)+qconv(i,j)
                sq(i)=sqrt(sq(i)**2+sqc(i,j)**2)
            715 continue
            qtot(i)=qtot(i)/chrave(i)
            sq(i)=sqrt((sq(i)/chrave(i))**2
                + (schrave(i)*qtot(i))**2)
        720 continue
    calculate variation of delta T across test sections
        do 728 i=1,2
            avetdel(i)=0.
            atsdstat(i)=0.
            atsdexp(i)=0.
            do 726 j=2,5
                avetdel(i)=avetdel(i)+tdel(i,j)/4.
                atsdexp(i)=atsdexp(i)+(tsdel(i,j)/4.))**2
            726 continue
            atsdexp(i)=sqrt(atsdexp(i))
            do 727 j=2,5
                atsdstat(i)=atsdstat(i)+(tdel(i,j)-avetdel(i))**2
            727 continue
            atsdstat(i)=sqrt(atsdstat(i)/4.)
            atsdct(i)=atsdexp(i)+atsdstat(i)
        728 continue
    calculate heat flux ratio
        avechrat=(ch(2,1)/ch(1,1)+ch(2,2)/ch(1,2)+
            ch(2,3)/ch(1,3)+ch(2,4)/ch(1,4))/4.
        x1=sqrt((sch(2,1)/ch(1,1))**2+(sch(1,1)*ch(2,1)/ch(1,1))**2)
        x2=sqrt((sch(2,2)/ch(1,2))**2+(sch(1,2)*ch(2,2)/ch(1,2))**2)
        x3=sqrt((sch(2,3)/ch(1,3))**2+(sch(1,3)*ch(2,3)/ch(1,3))**2)
        x4=sqrt((sch(2,4)/ch(1,4))**2+(sch(1,4)*ch(2,4)/ch(1,4))**2)
        savechrat=sqrt((x1/4.))**2+(x2/4.))**2+(x3/4.))**2+(x4/4.))**2)
        qrat=qtot(2)*avetdel(1)/(qtot(1)*avetdel(2))
        sqrat=sqrt((sq(2)/qtot(1))**2+(sq(1)*qtot(2)/qtot(1))**2)
        + (atsdct(1)*qrat/avetdel(1))**2+
        + (atsdct(2)*qrat/avetdel(2))**2)
        write(*,725) qrat,sqrat
        725 format(1x,'Q/Qrp = ',f7.5,' +/- ',f7.5)
    write data to file
        write(*,*) 'Writing results to file'
        write(11,745) to,sto,rho,srho,ue,sue
        745 format(1x,'To = ',f6.2,' +/- ',f4.2/,1x,'rho = ',f8.6,
            ' +/- ',f8.6/,1x,'Ue = ',f7.4,' +/- ',f7.4/)

```

```

do 770 i=1,2
do 780 j=1,10
write(11,780) i,j,vmeas(i,j,nave),svmtot(i,j),
svmaxp(i,j,nave),svmstat(i,j)
780 continue
write(11,770)
770 continue
790 format(1x,'Vave(h',i1',',i2,') = ',f10.5,' +/- ',f10.5,
' w/b = ',f10.5,' & s = ',f10.5)

write(11,770)
do 820 i=1,2
do 810 j=1,10
write(11,810) i,j,vsh(i,j,nave),svshtot(i,j),
svshexp(i,j,nave),svshstat(i,j)
810 continue
write(11,770)
820 continue
840 format(1x,'Vave(sh',i1',',i2,') = ',f10.5,' +/- ',f10.5,
' w/b = ',f10.5,' & s = ',f10.5)

write(11,770)
do 860 i=1,2
do 850 j=1,10
write(11,870) i,j,rsh(i,j),srsh(i,j)
850 continue
write(11,770)
860 continue
870 format(1x,'R(sh',i1',',i2,') = ',f10.5,' +/- ',f10.5)

write(11,770)
do 890 i=1,2
do 880 j=1,10
write(11,900) i,j,lmeas(i,j),sim(i,j)
880 continue
write(11,770)
890 continue
900 format(1x,'l(h',i1',',i2,') = ',f10.5,' +/- ',f10.5)

write(11,770)
do 920 i=1,2
do 910 j=1,10
write(11,930) i,j,qmeas(i,j),sqm(i,j)
910 continue
write(11,770)
920 continue
930 format(1x,'Qm(h',i1',',i2,') = ',f10.5,' +/- ',f10.5)

write(11,770)
do 1010 i=1,2
do 935 j=1,12
if (i.eq.1) write(11,960) j,((i3fd(i,j,k),k=1,3),i=1,2)
935 continue
if (i.eq.1) write(11,770)
do 940 j=1,12
write(11,950) (i,j,k,i3fd(i,j,k),st3fdtot(i,j,k),
st3fdexp(i,j,k),st3fdstat(i,j,k),k=1,3)
940 continue
950 format(1x,'T(3fh',i1',',i2,') = ',f10.5,' +/- ',
f10.5,' w/b = ',f10.5,' & s = ',f10.5,' 1x,T(3fh',i1',',
i2,') = ',f10.5,' +/- ',f10.5,' w/b = ',f10.5,
' & s = ',f10.5,' 1x,T(3fh',i1',',i2,') = ',f10.5,
' +/- ',f10.5,' w/b = ',f10.5,' & s = ',f10.5)
960 format(1x,'T(3fh',i2,') = ',f6.2,3x,f6.2,3x,f6.2,3x,
',3x,f6.2,3x,f6.2,3x,f6.2)
write(11,770)
do 965 j=1,6
if (i.eq.1) write(11,990) j,((i1dist(i,j,k),k=1,5),i=1,2)
965 continue
if (i.eq.1) write(11,770)
do 970 j=1,6
write(11,980) (i,j,k,i1dist(i,j,k),stdtot(i,j,k),
stdexp(i,j,k),stdstat(i,j,k),k=1,5)
970 continue
980 format(1x,'T(tph',i1',',i1,') = ',f10.5,' +/- ',
f10.5,' w/b = ',f10.5,' & s = ',f10.5,' 1x,T(tph',i1',',
i1,') = ',f10.5,' +/- ',f10.5,' w/b = ',f10.5,
' & s = ',f10.5,' 1x,T(tph',i1',',i1,') = ',f10.5,
' +/- ',f10.5,' w/b = ',f10.5,' & s = ',f10.5,' 1x,
T(tph',i1',',i1,') = ',f10.5,' +/- ',f10.5,' w/b = ',
f10.5,' & s = ',f10.5,' 1x,T(tph',i1',',i1,') = ',
f10.5,' +/- ',f10.5,' w/b = ',f10.5,' & s = ',f10.5)
990 format(1x,'T(tph',i1,') = ',f6.2,2x,f6.2,2x,f6.2,2x,f6.2,2x,
f6.2,1x,',1x,f6.2,2x,f6.2,2x,f6.2,2x,f6.2,2x,f6.2)
write(11,770)
do 995 j=1,4
if (i.eq.1) write(11,1030) j,(i3fd(i,j,k),k=1,3),i=1,2)
995 continue
if (i.eq.1) write(11,770)
do 1000 j=1,4
write(11,1020) (i,j,k,i3fd(i,j,k),st3fdtot(i,j,k),
st3fdexp(i,j,k),st3fdstat(i,j,k),k=1,3)
1000 continue
1010 continue
1020 format(1x,'T(1fh',i1',',i1,') = ',f10.5,' +/- ',
f10.5,' w/b = ',f10.5,' & s = ',f10.5,' 1x,T(1fh',i1',',
i1,') = ',f10.5,' +/- ',f10.5,' w/b = ',f10.5,
' & s = ',f10.5,' 1x,T(1fh',i1',',i1,') = ',f10.5,
' +/- ',f10.5,' w/b = ',f10.5,' & s = ',f10.5)
1030 format(1x,'T(1fh',i1,') = ',f6.2,3x,f6.2,3x,f6.2,3x,
',3x,f6.2,3x,f6.2,3x,f6.2)

write(11,770)
do 1031 i=1,2
write(11,1032) i,tback(i),stback(i)
1031 continue
1032 format(1x,'Tback',i1,') = ',f6.2,' +/- ',f6.4)

write(11,770)
do 1080 i=1,2
do 1035 j=1,12
if (i.eq.1) write(11,1060) j,(i3fave(k,j),k=1,2)
1035 continue
if (i.eq.1) write(11,770)
do 1040 j=1,12
write(11,1050) i,j,i3fave(i,j)
1040 continue
1050 format(1x,'Tave(3fh',i1',',i2,') = ',f6.2)
1060 format(1x,'Tave(3fh',i2,') = ',f6.2,3x,',3x,f6.2)
write(11,770)
do 1065 j=1,6
if (i.eq.1) write(11,2000) j,(iave(k,j),k=1,2)
1065 continue
if (i.eq.1) write(11,770)
do 1070 j=1,6
write(11,1090) i,j,iave(i,j),sta(i,j)
1070 continue
1080 continue
1090 format(1x,'Tave(tps',i1',',i2,') = ',f6.2,' +/- ',f6.4)
2000 format(1x,'Tave(tps',i1,') = ',f6.2,3x,',3x,f6.2)

write(11,770)
do 2005 i=1,2
if (i.eq.1) then
do 2004 j=2,5
write(11,2006) j,tdelt(1,j),tsdelt(1,j,j),
tdelt(2,j),tsdelt(2,j)
2004 continue
endif
write(11,2007) i,avetdelt(i),atsdexp(i),atsdstat(i),
atsdtot(i)
2005 continue
2006 format(1x,'deltaT(1',i1,') = ',e10.4,' +/- ',e10.4,
' ; deltaT(2',i1,') = ',e10.4,' +/- ',e10.4)
2007 format(1x,'delTave',i1,') = ',e10.4,' (B= ',e10.4,', S= ',
e10.4,') +/- ',e10.4)

write(11,770)
do 2020 i=1,2
do 2010 j=1,4
write(11,2030) i,j,grad(i,j),sq(i,j)
2010 continue
write(11,770)
2020 continue
2030 format(1x,'Qr(tps',i1',',i2,') = ',f10.5,' +/- ',f10.5)

write(11,770)
do 2050 i=1,2
do 2040 j=1,4
write(11,2060) i,j,qloss(i,j),sq(i,j)
2040 continue
write(11,770)
2050 continue
2060 format(1x,'Qloss(tps',i1',',i2,') = ',f10.5,' +/- ',f10.5)

write(11,770)
do 2080 i=1,2
do 2070 j=1,4
write(11,2090) i,j,qconv(i,j),sq(i,j)
2070 continue
write(11,770)
2080 continue
2090 format(1x,'Qconv(tps',i1',',i2,') = ',f10.5,' +/- ',f10.5)

write(11,770)
do 2110 i=1,2
do 2100 j=1,4
write(11,2120) i,j,ch(i,j),sch(i,j)
2100 continue
write(11,770)
2110 continue
2120 format(1x,'Ch(tps',i1',',i2,') = ',f10.5,' +/- ',f10.5)

write(11,770)

```

```

do 2140 i=1,2
do 2130 j=1,4
write(11,2150) i,j,chrat(i,j),schrat(i,j)
2130 continue
write(11,'//')
2140 continue
2150 format(1x,'[ChCh(di=0)](tps',i1,';',i2,') = ',f7.5,' +/- ',
.      f7.5)

write(11,'//')
do 2160 i=1,2
write(11,2170) i,chrave(i),schrave(i)
2160 continue
2170 format(1x,'[ChCh(di=0)]ave(',i1,') = ',f7.5,' +/- ',f7.5)

write(11,'//')
write(11,2175) avechrat,savechrat
2175 format(1x,'[ChCh(tp)]ave = ',f10.5,' +/- ',f10.5)

write(11,'//')
do 2180 i=1,2
write(11,2190) i,qtot(i),sq(i)
2180 continue
2190 format(1x,'Qt(',i1,') = ',f10.5,' +/- ',f10.5)

write(11,'//')
write(11,2200) qrat,sqrat
2200 format(1x,'Q/Qtp = ',f10.5,' +/- ',f10.5)

close(11)
close(12)
end

```

## SPLINE.FOR

```

SUBROUTINE SPLINE(X,Y,N,Y2)
PARAMETER (NMAX=100)
DIMENSION X(N),Y(N),Y2(N),U(NMAX)
Y2(1)=0.
U(1)=0.
DO 11 I=2,N-1
SIG=(X(I)-X(I-1))/(X(I+1)-X(I-1))
P=SIG*Y2(I-1)+2.
Y2(I)=(SIG-1.)/P
U(I)=(6.*((Y(I+1)-Y(I))/(X(I+1)-X(I))-(Y(I)-Y(I-1))/
* (X(I)-X(I-1)))/(X(I+1)-X(I-1))-SIG*U(I-1))/P
11 CONTINUE
QN=0.
UN=0.
Y2(N)=(UN-QN*U(N-1))/(QN*Y2(N-1)+1.)
DO 12 K=N-1,1,-1
Y2(K)=Y2(K)*Y2(K+1)+U(K)
12 CONTINUE
RETURN
END

```

## CALCFLUX.FOR

```

* calcflux.for
* subroutine to calculate 2-D heat flux thru three layers
* of materials
*
* subroutine calcflux(dy1,dy2,dy3,k1,k2,k3,
* t1,t4,flux)
*
* real dy1,dy2,dy3,t1,t2,t4,k1,k2,k3,r31,r32,a,b,c,
* delt,flux
*
* r31=(k3/dy3)/(k1/dy1)
* r32=(k3/dy3)/(k2/dy2)
* a=1.+r32
* b=r31
* c=a+b
* t2=(a*t1+b*t4)/c
* delt=t1-t2
* flux=k1*delt/dy1
*
* return
end

```

## SPLINT.FOR

```

SUBROUTINE SPLINT(XA,YA,Y2A,N,X,Y)
DIMENSION XA(N),YA(N),Y2A(N)
KLO=1
KHI=N
1 IF (KHI-KLO.GT.1) THEN
K=(KHI+KLO)/2
IF(XA(K).GT.X)THEN
KHI=K
ELSE
KLO=K
ENDIF
GOTO 1
ENDIF
H=XA(KHI)-XA(KLO)
IF (H.EQ.0.) PAUSE 'Bad XA input.'
A=(XA(KHI)-X)/H
B=(X-XA(KLO))/H
Y=A*YA(KLO)+B*YA(KHI)+
* ((A**3-A)*Y2A(KLO)+(B**3-B)*Y2A(KHI))/(H**2)/6.
RETURN
END

```

## D.4. Heat Transfer Analysis Results

**A. Tunnel Wall Temperature.** The tunnel wall temperatures were manipulated successfully to within  $\pm 1$  to  $1.5^\circ\text{C}$  overall and within  $\pm 0.1$  to  $0.15^\circ\text{C}$  over the test plate sections. The tunnel wall temperatures are shown in Figures D.1 through D.6. A distribution of temperature is shown from one representative run at each of the test freestream velocities, 8.48, 9.95, 10.03, 12.47, 14.88, and 20.06 m/s. The temperature distributions during the other test runs were not different from the ones shown in any significant way. The temperature distribution in these plots is shown with gray scale contours, lighter for higher temperatures and darker for lower

temperatures. The distribution is shown for both of the entire, heated tunnel walls, the flat plate test section side A on the left and the ribletted test section side B on the right. The test sections themselves are outlined with rectangles. It should be noted that the physical dimensions of the walls are not shown to scale. The plots show that the temperature of the test sections were of a uniform temperature to within  $\pm 0.1$  to  $0.15^{\circ}\text{C}$  and that the heated starting lengths were of a uniform temperature to within  $\pm 1$  to  $1.5^{\circ}\text{C}$ .

**B. Stanton Number.** The local Stanton number measurements were subject to fairly large conduction loss experimental error and showed fairly wide scatter but were reasonably close to the values predicted with empirical formulae 2.56 and 2.64. The local Stanton numbers calculated from energy balances of the heated subsections of the two test sections are shown in Figures D.7 and D.8. The values over the flat plate test section are shown versus turbulent Reynolds number in Figure D.7, Local Stanton Number over the Flat Plate. For clarity, the uncertainty bars, which were in the 4 to 5 percent range are not shown. The magnitude of this uncertainty was due to the fact that the test plate subsections were not insulated from one another, merely from the surrounding plate. The values predicted using equations 2.56 and 2.64 are plotted as a solid line and the upper and lower limits of the uncertainty range of this prediction are shown as dotted lines. The results agree within the uncertainty ranges except for Reynolds numbers below 50,000. The values over the ribletted test section are shown in Figure D.8, Local Stanton Number over the Ribletted Plate. The values predicted using equations 2.56 and 2.64 are again plotted as a solid line and the upper and lower limits of the uncertainty range of this prediction as dotted lines. The scatter in this set of data is almost 1.5 times larger than that of the flat plate data. However, this difference could very well have been caused by the effects of the adjustment of the heat transfer characteristics of the flow to the shortness of the length of the ribletted wall upstream of the test section. The broad trend of increasing Stanton number with increasing Reynolds rather than the flat plate trend of decreasing Stanton number with increasing Reynolds number is evident.

The much more accurate measurements of average or integral Stanton number, the calculations of the effect of riblets on which had uncertainties of 1.1 percent on average and less than 1.3 percent in all cases, showed reduction in heat transfer due to riblets for Reynolds number below 650,000 and  $s^+$  below 20. The effect of riblets on Stanton number versus turbulent Reynolds number is presented via the integral or average test section Stanton number in Figure 6.3, Integral Test Section Stanton Number versus Turbulent Reynolds Number for the Flat and Ribletted Plates. The effect of riblets on the integral Stanton number versus riblet spacing in wall units calculated from the curve fits shown in Figure 6.1 is shown in Figure 6.4, Effect of Riblets on Integral Stanton Number. The results shown in these plots are discussed in Section 6.4.D.

## **BIBLIOGRAPHY**

- Abernathy, R.B., Thompson, J.W., et al. (1980), "Uncertainty in Gas Turbine Measurements Handbook," AEDC-TR-73-5.
- Alfredsson, H., Johansson, A.V., Haritonidis, J.H., and Eckelmann, H. (1988), "The Fluctuating Wall-shear Stress and the Velocity Field in the Viscous Sublayer," *Phys. Fluids*, vol. 31, pp. 1026-1033.
- Anon. (1979), "Eccobond SF-40 Technical Data," Technical Bulletin 3-2-2A, rev. 10/79 (Woburn, MA: Emerson and Cuming, 1979).
- Anon. (1984), *Model 1050 Constant Temperature Anemometer Instruction Manual*, rev. B (St. Paul, MN: TSI, 1984).
- Anon. (1985), "Eccobond 285 Technical Data," Technical Bulletin 3-12-17, rev. 12/85 (Woburn, MA: Emerson and Cuming, 1985).
- Anon. (1987a), "Mission Accomplished," *NASA Tech. Briefs*, vol. 11, no. 3, pp. 82-83.
- Anon. (1987b), *56C17 CTA Bridge Instruction Manual* (Skovlunde, Den.: Dantec Elektronik, 1987).
- Anon. (1988a), *OMEGA Complete Temperature Measurement Handbook and Encyclopedia* (Stamford, CT: OMEGA Engineering, 1988).
- Anon. (1988b), "Thermo-12/Blue Pipe and Block Insulation Specification Data," Product Report R-611 (Denver, CO: Manville Industrial Products Div., 1988).
- Anselmet, F., Fulachier, L., Coustols, E., and Coustieux, J. (1986), "Flow Visualization and Laser Measurements in a Turbulent Boundary Layer over a Riblet Surface," *Euro. Meeting on Turbulent Drag Reduction, Lausanne, Switz.*
- Anselmet, F., Djenidi, L., and Fulachier, L. (1987), "Turbulent and Laminar Boundary Layers over a Riblet Surface," *6th Sym. on Turbulent Shear Flows, Toulouse, Fr.*
- Antonia, R.A., Danh, H.Q., and Prabhu, A. (1977), "Response of a Turbulent Boundary Layer to a Step Change in Surface Heat Flux," *J. of Fluid Mech.*, vol. 80, part 1, pp. 153-177.
- Arpaci, V.S. (1966), *Conduction Heat Transfer* (Reading, MA: Addison-Wesley, 1966).
- Aubrey, N., Holmes, P., Lumley, J.L., and Stone, E. (1988), "The Dynamics of Coherent Structures in the Wall Region of a Turbulent Boundary Layer," *J. Fluid Mech.*, vol. 192, pp. 115-173.
- Bacher, E.V. and Smith, C.R. (1985a), "A Combined Visualization-anemometry Study of the Turbulent Drag Reducing Mechanisms of Triangular Micro-groove Surface Modifications," AIAA Paper 85-0548.
- Bacher, E.V. and Smith, C.R. (1985b), "Turbulent Boundary Layer Modification by Surface Riblets," *AIAA Journal*, vol. 24, pp. 1382-1385.
- Baker, N.H., Baker, D.H., and Ryder, E.A. (1953), *Temperature Measurements in Engineering*, vol. 1 (New York: Wiley and Sons, 1953).
- Bandyopadhyay, P.R. (1986), "Review- Mean Flow in Turbulent Boundary Layers Disturbed to Alter Skin Friction," *J. of Fluids Eng.*, vol. 108, pp. 127-140.
- Barnes, J.F. and Fray, D.E. (1965), "An Experimental Investigation of a High-temperature Turbine (No. 126)," *H.M.S.O., A.R.C., R. & M.* 3405.
- Bartenwerfer, M. and Bechert, D.W. (1987), "Die Viskose Strömung über Oberflächen mit Längsgrippen," DFVLR-FB 87-21 (trans. as "The Viscous Flow on Surfaces with Streamwise Aligned Riblets," ESA-TT-1091).
- Batchelor, G.K. (1967), *An Introduction to Fluid Mechanics* (Cambridge, UK: Cambridge U., 1967).
- Bath, T.D. (1968), "Channeled Flow at the Pipe Surface in Gas Transmission Pipelines," *Final Report Phase I, MRI Project No. 3123-C*, MRI, Kansas City, MO.

- Beauchamp, C.H. and Phillips, R.B. (1988), "Riblet and Polymer Drag Reduction on an Axisymmetric Body," *Proc. Sym. on Hydrodynamic Performance Enhancement for Marine Applications, Newport, RI*.
- Bechert, D.W. (1987), "Experiments on Three-dimensional Riblets," *Turbulent Drag Reduction by Passive Means: Proc. Int. Conf., London, UK*, vol. 2, pp. 425-431.
- Bechert, D.W. and Bartenwerfer, M. (1989), "The Viscous Flow on Surfaces with Longitudinal Ribs," *J. Fluid Mech.*, vol. 206, pp. 105-129.
- Bechert, D.W., Bartenwerfer, M., Hoppe, G., and Reif, W.-E. (1987), "Drag Reduction Mechanisms Derived from Shark Skin," *Proc. 15th Congress of the Int. Council of the Aeronautical Sci., London, UK*, Paper ICAS-86-1.8.3.
- Bechert, D.W., Hoppe, G., and Reif, W.-E. (1985), "On the Drag Reduction of the Shark Skin," AIAA Paper 85-0546.
- Benedict, R.P. (1984), *Fundamentals of Temperature, Pressure, and Flow Measurements*, 3rd ed. (New York: John Wiley & Sons, 1984).
- Bevington, P.R. (1969), *Data Reduction and Error Analysis for the Physical Sciences* (New York: McGraw-Hill, 1969).
- Blackwelder, R.F. (1988), "Coherent Structures Associated with Turbulent Transport," *Transport Phenomena in Turbulent Flows* (New York: Hemisphere, 1988), eds. M. Hirata and N. Kasagi, pp. 69-88.
- Blackwelder, R.F. and Eckelmann, H. (1978), "Streamwise Vortices Associated with the Bursting Phenomenon," *J. Fluid Mech.*, vol. 94, part 3, pp. 577-594.
- Blackwelder, R.F. and Kaplan, R.E. (1976), "On the Wall Structure of the Turbulent Boundary Layer," *J. of Fluid Mech.*, vol. 76, part 1, pp. 89-112.
- Blakewell, H.P. and Lumley, J.L. (1967), "Viscous Sublayer and Adjacent Wall Region in Turbulent Pipe Flows," *Phys. Fluids*, vol. 10, p. 1880.
- Blasius, H. (1908), *Z. Angew. Math. Phys.*, vol. 56, pp. 1-37.
- Bodenhorn, A. (1982), "Determining the Overall Performance and the Regions of Instability of a Centrifugal Fan," MIT 16.62 Project Lab Final Report.
- Borishanskii, V.M. and Kutateladze, S.S. (1965), *A Concise Encyclopedia of Heat Transfer* (London, UK: Pergamon, 1965), trans. J.B. Arthur, ed. H. Cohen.
- Bragg, G.M. (1969), "The Turbulent Boundary Layer in a Corner," *J. Fluid Mech.*, vol. 36, pt. 3, pp. 485-503.
- Brinich, P.F. and Graham, R.W. (1977), "Flow and Heat Transfer in a Curved Channel," NASA TN D-8464.
- Burdak, V.D. (1969), "Function of the Etenoid Apparatus of Fish in the Presence of a Turbulent Boundary Layer," *Zoologicheskii Zhurnal*, vol. 48, pp. 1053-1055.
- Bushnell, D.M. (1983), "Turbulent Drag Reduction for External Flows," AIAA Paper 83-0227.
- Bushnell, D.M. (1984), "Body-Turbulence Interaction," AIAA Paper 84-1527.
- Bushnell, D.M. and McGinley, C.B. (1989), "Turbulence Control in Wall Flows," *Ann. Rev. of Fluid Mech.*, vol. 21, pp. 1-20.
- Callendar, H.L. (1887), "On the Practical Measurement of Temperature," *Phil. Trans. R. Soc. London*, vol. 178, p. 160.
- Caram, J.M. and Ahmed, A. (1989), "Effects of Riblets on the Wake of an Airfoil," AIAA Paper 89-2199.



- Carslaw, H.S. and Jaeger, J.C. (1947), *Conduction of Heat in Solids* (New York: Oxford U., 1947).
- Chen, J.J.J., Leung, Y.-C., and Ko, N.W.M. (1986), "Drag Reduction in a Longitudinally Grooved Flow Channel," *Ind. Eng. Chem. Fundam.*, vol. 25.
- Chen, T.S., Mucoglu, A., and Sparrow, E.M. (1977), "Mixed Convection in Boundary Layer Flow on a Horizontal Plate," *ASME Trans., J. of Heat Transfer*, vol. 99, pp. 66-71.
- Chernyshov, O.B. and Zayets, V.A. (1970), "Some Peculiarities of the Structure of the Skin of Sharks," *Hydrodynamic Problems of Bionics*, no. 4, pp. 77-83.
- Childs, G.E., Ericks, L.J., and Powell, R.L. (1973), "Thermal Conductivity of Solids at Room Temperature and Below: A Review and Compilation of the Literature," NBS Monograph 131.
- Choi, K.-S. (1984), "A Survey of the Turbulent Drag Reduction Using Passive Devices," NMI Rep. R-193, NMI, Feltham, UK.
- Choi, K.-S. (1985), "Near Wall Turbulence Structure on a Riblet Wall," BMT Rep., BMT, Feltham, UK.
- Choi, K.-S. (1986), "Drag Reduction by Manipulation of Near-wall Structure," *Proc. European Meeting on Turbulent Drag Reduction, Lausanne, Switz.*
- Choi, K.-S. (1988a), "The Wall-pressure Fluctuation of Modified Turbulent Boundary Layer with Riblets," *Turbulence and Relaminarization: Proc. of the IUTAM Sym., Bangalore, India* (New York: Springer-Verlag, 1988), pp. 149-160.
- Choi, K.-S. (1988b), "On Physical Mechanisms of Turbulent Drag Reduction Using Riblets in Transport Phenomena," *Turbulent Flows: Theory, Experiment, and Numerical Simulation*, eds. M. Hirata and N. Kasagi, pp. 185-198.
- Choi, K.-S. (1989), "Near-wall Structure of a Turbulent Boundary Layer with Riblets," *J. Fluid Mech.*, vol. 208, pp. 417-458.
- Choi, K.-S., and Johnson, R. (1989), "Effects of Pressure Gradients on the Near-wall Turbulence Structure with Riblets," BMT Rep., BMT, Teddington, UK.
- Choi, K.-S., Gadd, G.E., Pearcey, H.H., Savill, A.M., and Svensson, S. (1989), "Tests of Drag-reducing Polymer Coated on a Riblet Surface," *Appl. Sci. Research*, vol. 46, pp. 209-216.
- Choi, K.S., Pearcey, H.H., and Savill, A.M. (1987), "Test of Drag Reducing Riblets on a One-third Scale Racing Yacht," *Turbulent Drag Reduction by Passive Means: Proc. Int. Conf., London, UK*, vol. 2, pp. 377-391.
- Clauser, F.H. (1954), "Turbulent Boundary Layers in Adverse Pressure Gradients," *J. Aero. Sci.*, vol. 21, pp. 91-180.
- Clauser, F.H. (1956), *Adv. Appl. Mech.*, vol. 4, pp. 1-51.
- Cohen, H., Rogers, G.F.C., and Saravanamuttoo, H.I.H. (1987), *Gas Turbine Theory*, 3rd ed. (New York: J. Wiley & Sons, 1987).
- Coleman, H.W., Hosni, M.H., Taylor, R.P., and Brown, G.B. (1988), "Smooth Wall Qualification of a Turbulent Heat Transfer Test Facility," TFD-88-2, Mech. and Nuclear Eng. Dept., Miss. State U.
- Coles, D.E. (1955), "The Law of the Wall in Turbulent Shear Flow," *Fifty Years of Boundary Layer Research*, eds. W. Tollmien and W. Görtler, p.133.
- Coles, D.E. (1956), "The Law of the Wake in the Turbulent Boundary Layer," *J. Fluid Mech.*, vol. 1, pp. 191-226.
- Coles, D.E. and Hirst, E.A., eds., (1969), *Proc. Computation of Turbulent Boundary Layers- 1968 AFOSR-IFP-Stanford Conf., Vol II- Compiled Data* (Stanford, CA: Stanford U., 1969).
- Coustols, E. (1989), "Behaviour of Internal Manipulators: 'Riblet' Models in Subsonic and Transonic Flows," AIAA Paper 89-0963.

Coustols, E. and Savill, A.M. (1989), "Résumé of Important Results Presented at the Third Turbulent Drag Reduction Working Party," *Appl. Sci. Research*, vol. 46, pp. 183-196.

Coustols, E., Cousteix, J., and Belanger, J. (1987), "Drag Reduction on Riblet Surfaces and Through Outer Layer Manipulators," *Turbulent Drag Reduction by Passive Means: Proc. Int. Conf., London, UK*, vol. 2, pp. 250-289.

Dinkelacker, A., Nitschke-Kowsky, P., and Reif, W.-E. (1988), "On the Possibility of Drag Reduction with the Help of Longitudinal Ridges in the Walls," *Turbulence and Relaminarization: Proc. of the IUTAM Sym., Bangalore, India* (New York: Springer-Verlag, 1988), pp. 109-120.

Djenidi, L., Anselmet, F., and Fulachier, L.L. (1987a), "Influence of a Riblet Wall on Boundary Layers," *Proc. 1st European Turbulence Conf., Lyons, France*.

Djenidi, L., Anselmet, F., and Fulachier, L. (1987b), "Influence of a Riblet Wall on Boundary Layers," *Turbulent Drag Reduction by Passive Means: Proc. Int. Conf., London, UK*, vol. 2, pp. 310-329.

Djenidi, L., Anselmet, F., and Fulachier, L. (1988), "About the Mechanism Involved in a Turbulent Boundary Layer Over Riblets," *Proc. of the 2nd European Turbulence Conf., Berlin*.

Djenidi, L., Liandrat, J., Anselmet, F., and Fulachier, L. (1989), "Numerical and Experimental Investigation of the Laminar Boundary Layer Over Riblets," *Appl. Sci. Research*, vol. 46, pp. 263-270.

Eckert, E.R.G. and Drake, R.M. (1987), *Analysis of Heat and Mass Transfer* (New York: Hemisphere, 1987).

Eckert, E.R.G. and Goldstein, R.J., eds. (1976), *Measurements in Heat Transfer*, 2nd ed. (New York: McGraw-Hill, 1976).

Eilers, R.E., Koper, C.A., McLean, J.D., and Coder, D.W. (1985), "An Application of Riblets for Turbulent-skin-friction Reduction," *Proc. 12th AIAA Sym. on the Aeronautics/Hydronautics of Sailing*, pp. 133-139.

Emmerling, R. (1973), "Die Momentane Struktur des Wanddruckes einer Turbulenten Grenzschichtströmung," *Mitt., MPI, Strömungsforschung, Göttingen*, no. 56.

Enyutin, G.V., Fadeev, I.V., Lashkov, Y.A., Samoilova, N.V., and Shumilkina, E.A. (1987), "Experimental Investigation of the Effect of Longitudinal Riblets on the Friction Drag of a Flat Plate," *Fluid Dynamics*, vol. 22, no. 2, pp. 284-289.

Fage, A., and Townend, H.C.H. (1932), "An Examination of Turbulent Flow with an Ultramicroscope," *Proc. Roy. Soc., ser. A*, vol. 135, pp. 656-677.

Falco, R.E. (1979), "Structural Aspects of Turbulence in Boundary Layers," *6th Biennial Sym. on Turbulence, Rolla, MO*, eds. G.K. Patterson and J.L. Zakin.

Fulachier, L., Djenidi, L., and Anselmet, F. (1987), "Premieres Résultats Concernant les Couches Limites Turbulentes ou Laminaires sur Riblets," *Note IMST*, No. 5-87.

Gallagher, J.A. and Thomas, A.S.W. (1984), "Turbulent Boundary Layer Characteristics over Streamwise Grooves," *AIAA Paper 84-2185*.

Gatski, T.B. and Grosch, C.E. (1984), "Embedded Cavity Drag in Steady and Unsteady Flows," *AIAA Paper 84-0436*.

Gaudet, L. (1987), "An Assessment of the Drag Reduction Properties of Riblets and the Penalties of Off-design Conditions," *Turbulent Drag Reduction by Passive Means: Proc. Int. Conf., London, UK*, vol. 2, pp. 363-376.

Gaudet, L. (1989), "Properties of Riblets at Supersonic Speeds," *Appl. Sci. Research*, vol. 46, pp. 245-254.

Grass, A.J. (1971), "Structural Features of Turbulent Flow over Smooth and Rough Boundaries," *J Fluid Mech.*, vol. 50, part 2, p. 233.

Goldstein, R.J. and Chiang, H.D. (1985), "Measurement of Temperature and Heat Transfer," *Handbook of Heat Transfer Applications*, 2nd ed. (New York: McGraw-Hill, 1985), eds. W.M. Rohsenow, J.P. Hartnett, and E.N. Ganic, pp. 12.1-12.94.

Guezennec, Y.G. and Nagib, H.M. (1985), "Documentation of Mechanisms Leading to Net Drag Reduction in Manipulated Turbulent Boundary Layers," AIAA Paper 85-0519.

Haritonidis, J.H. (1989), "The Measurement of Wall Shear Stress," *Lecture Notes in Engineering*, Vol. 45-*Advances in Fluid Mechanics Measurement* (New York: Springer-Verlag, 1989), ed. M. Gad-el-Hak, pp.229-261.

Hausen, H. (1983), *Heat Transfer in Counterflow, Parallel Flow and Crossflow* (New York: McGraw-Hill Book Co., 1983).

Hawthorne, W.R. (1956), "Thermodynamics of Cooled Turbines," *Trans. ASME*, vol. 78, p. 1765.

Head, M.R. and Bandyopadhyay, P. (1981), "New Aspects of Turbulent Boundary Layer Structure," *J. Fluid Mech.*, vol. 107, p. 297.

Hefner, J.N. and Bushnell, D.M. (1977), "An Overview of Concepts for Aircraft Drag Reduction," *Special Course On Concepts for Drag Reduction*, AGARD-R-654, pp. 1.1-1.30.

Hefner, J.N., Bushnell, D.M., and Anders, J.B. (1983), "Alteration of Outer Flow Structures for Turbulent Drag Reduction," AIAA Paper 83-0293.

Hilsenrath, J., et al. (1960), *Tables of Thermodynamics and Transport Properties of Air, Argon, et al.* (New York: Pergamon, 1960), revision of NBS Cir. 564.

Hinze, J.O. (1959), *Turbulence- An Introduction to Its Mechanisms and Theory* (New York: McGraw-Hill, 1959).

Holman, J.P. (1966), *Experimental Methods for Engineers* (New York: McGraw-Hill, 1966).

Hooshmand, A., Youngs, R.A., Wallace, J.M., and Balint, J.-L. (1983), "An Experimental Study of Changes in the Structure of a Turbulent Boundary Layer Due to Surface Geometry Changes," AIAA Paper 83-0230.

Hooshmand, A. (1985), "An Experimental Investigation of the Influence of a Drag Reducing, Longitudinally Aligned, Triangular, Riblet Surface on the Velocity and Streamwise Vorticity Fields of a Zero-Pressure Gradient Turbulent Boundary Layer," Ph.D. Thesis, U. of Maryland.

Hussain, A.K.M.F. (1983), "Coherent Structures- Reality and Myth," *Phys. Fluids*, vol. 26, pp. 2816-2850.

Iritani, Y., Kasagi, N. and Hirata, M. (1983), "Heat Transfer and Associated Turbulence Structure in the Near-wall Region of a Turbulent Boundary Layer," *4th Sym. on Turbulent Shear Flows*, p. 17.31-36.

Jang, P.S., Benney, D.J., and Gran, R.L. (1986), "On the Origin of Streamwise Vortices in a Turbulent Boundary Layer," *J. Fluid Mech.*, vol. 169, pp. 109-123.

Johansson, A.V. and Alfredsson, P.H. (1985), "Recent Developments of Drag Reduction Methods for Ships," *Proc. 2nd Int. Sym. on Ship Viscous Reduction, Sweden*.

Kakaç, S. and Yener, Y. (1985), *Heat Conduction* (New York: Hemisphere, 1985).

Kármán, T. von (1921), "Über Laminare und Turbulente Reibung," *Z. Angew. Math. Mech.*, vol. 1, pp. 233-252 (trans. as "On Laminar and Turbulent Friction," NACA Tech. Mem. 1092).

Kármán, T. von (1930), "Mechanische Ähnlichkeit und Turblenz," *Nachr. Ges. Wiss. Goett. Math.-Phys. Kl.*, pp. 58-76.

Kármán, T. von (1931), *Proc. 3d Int. Congr. Appl. Mech., Stockholm, Sweden*, p. 85.

Kármán, T. von (1939), "The Analogy Between Fluid Friction and Heat Transfer," *ASME Trans.*, vol. 61, pp. 705-710.

Kasagi, N. (1988), "Structural Study of Near Wall Turbulence and Its Heat Transfer Mechanism," *Zaric*

*Mem. Conf. on Near Wall Turbulence*, Dubrovnik, Croatia, p. 596.

Kays, W.M. and Crawford, M.E. (1980), *Convective Heat and Mass Transfer*, 2nd ed. (New York: McGraw-Hill, 1980).

Kays, W.M. and Moffat, R.J. (1988), "The Near Wall Region of the Turbulent Boundary Layer: Some Results from Heat Transfer Measurements," *Zaric Mem. Conf. on Near Wall Turbulence*, Dubrovnik, Croatia, p. 630.

Kennedy, J.F., Hsu, S.-T., and Lin, J.-T. (1973), "Turbulent Flows Past Boundaries with Small Streamwise Fins," *Proc. of the ASCE, J. Hydr. Div.*, vol. 99, no. HY4, pp. 605-616.

Kerrebrock, J.L. (1984), *Aircraft Engines and Gas Turbines* (Cambridge, MA: MIT Press, 1984).

Kestin, E.H. and Persen, L.N. (1962), "The Transfer of Heat Across a Turbulent Boundary Layer at Very High Prandtl Numbers," *Int. J. Heat Mass Transfer*, vol. 5, pp. 355-372.

Kestin, J. and Richardson, P.D. (1963), "Heat Transfer Across Turbulent Incompressible Boundary Layers," *Int. J. Heat Mass Transfer*, vol. 6, pp. 147-189.

Khabakhpasheva, E.M. (1986), "Experimental Investigation of Turbulent Momentum and Heat Transfer in the Proximity of the Wall," *Proc. 8th Int. Conf. of Heat and Mass Transfer*, vol. 1, p. 79.

Khabakhpasheva, E.M. (1986), "Structure of Turbulence in Heat Transfer," *Zaric Mem. Conf. on Near Wall Turbulence*, Dubrovnik, Croatia, p. 544.

Khalid, M. (1986), "An Experimental Investigation of Skin Friction on Smooth Surfaces Supporting Air Bearing Channels," NAE-AN-391, NRC No. 26163, Nat. Aero. Est., Ottawa.

Khan, M.M.S. (1986), "A Numerical Investigation of the Drag Reduction by Riblet-surfaces," AIAA Paper 86-1127.

Kim, H.T., Kline, S.J., and Reynolds, W.C. (1971), "The Production of Turbulence Near a Smooth Wall in a Turbulent Boundary Layer," *J. Fluid Mech.*, vol. 50, part 1, pp. 133-160.

Kim, J. and Moin, P. (1979), "Large Eddy Simulation of Turbulent Channel Flow- Illiac IV Calculations," AGARD CP 271.

Kim, J., Moin, P., and Moser, R.D. (1987), "Turbulence Statistics in Fully-developed Channel Flow at Low Reynolds Numbers," *J. Fluid Mech.*, vol. 177, pp. 133-166.

Klebanoff, P.S. (1954), NACA TN 3178.

Kleinstein, G. (1967), "Generalized Law of the Wall and Eddy-Viscosity Model for Wall Boundary Layers," *AIAA J.*, vol. 5, no. 8, pp. 1402-1407.

Kline, S.J., Reynolds, W.C., Schraub, F.A., and Runstadler, P.W. (1967), "The Structure of Turbulent Boundary Layers," *J. Fluid Mech.*, vol. 30, part 4, pp. 741-773.

Kline, S.J. and Robinson, S.K., "Quasi-Coherent Structures in the Turbulent Boundary Layer: Part I, Status Report on a Community-Wide Summary of the Data," *Zaric Mem. Conf. on Near Wall Turbulence*, Dubrovnik, Croatia.

Kozlov, V.E. (1988), "The Influence of Free Stream Turbulence and Surface Ribbing on the Characteristics of a Transitional Boundary Layer," *Zaric Mem. Conf. on Near Wall Turbulence*, Dubrovnik, Croatia.

Launder, B.E. and Li, S. (1989), "A Numerical Study of Riblet Effects On Laminar Flow Through a Plane Channel," *Appl. Sci. Research*, vol. 46, pp. 271-279.

Lazos, B.S. (1989), "Effects of Contamination on Riblet Performance," *J. of Aircraft*, vol. 26, no. 7, pp. 684-686.

Lazos, B.S. and Wilkinson, S.P. (1987), "Turbulent Viscous Drag Reduction with Thin-element Riblets," *AIAA Journal*, vol. 26, no. 4, pp. 496-498.

Lazos, B.S. and Wilkinson, S.P. (1987), "Direct Drag and Hot-Wire Measurements on Thin-element Riblet Arrays," *Turbulence and Relaminarization: Proc. of the IUTAM Sym., Bangalore, India* (New York: Springer-Verlag, 1988), pp. 121-131.

Leuthesser (1963), *Proc. Am. Civil Eng., J. Hydraulics Div.*, vol. 89, no. HY3, pp. 1-19.

Lewkowicz, A.K. and Das, D.K. (1978), "Some Exploratory Tests on a Turbulent Boundary Layer with Pressure Gradient on an Irregularly Roughened Plate with Distributed Flexible Tufts," Rep. FM/42/78, U. of Liverpool.

Lin, J.C., Howard, F.G., and Selby, G.V. (1990), "Control of Turbulent Separated Flow Over a Rearward-Facing Ramp Using Longitudinal Grooves," *J. Aircraft*, vol. 27, no. 3, pp. 283-285.

Lindemann, A.M. (1985), "Turbulent Reynolds Analogy Factors for Nonplanar Surface Microgeometries," *J. of Spacecraft and Rockets*, vol. 22, no. 5, pp. 581-582.

Liu, C.-K. (1966), "An Experimental Study of Turbulent Boundary Layer on Rough Walls," Ph.D., Stanford U., Dept. Mech. Eng.

Liu, C.-K., Kline, S.J., and Johnston, J.P. (1966), "An Experimental Study of Turbulent Boundary Layer on Rough Walls," Report MD-15, Stanford U., Dept. Mech. Eng.

Lumley, J.L. and Tenckes, H. (1972), *A First Course in Turbulence* (Cambridge, MA: MIT, 1972).

Lykoudis, P.S. (1980), "Damping of Shear Turbulence in the Presence of Magnetic Fields: a Semi-empirical Approach," *MHD Flows and Turbulence II: Proc. 2nd Bat-Sheva Int. Sem., Beersheva, Israel*.

Marquardt, D.W. (1963), "An Algorithm for Least-Squares Estimation of Nonlinear Parameters," *J. Soc. Ind. Appl. Math.*, vol. 11 no. 2, pp. 431-441.

McLean, J.D., George-Falvy, D.N., and Sullivan, P.P. (1987), "Flight Test of Turbulent Skin-friction Reduction by Riblets," *Turbulent Drag Reduction by Passive Means: Proc. Int. Conf., London, UK, 1987*, vol. 2, pp. 408-424.

Metcalf, M. (1985), *Effective Fortran 77* (Oxford, UK: Clarendon, 1985).

Millikan, C.B. (1938), "A Critical Discussion of Turbulent Flows in Channels and Circular Tubes," *Proc. 5th Int. Congr. Appl. Mech., Camb., MA*, pp. 386-392.

Moffat, R.J. (1982), "Contributions to the Theory of Single-Sample Uncertainty Analysis," *ASME Trans., J. of Fluids Eng.*, vol. 104, pp. 250-260.

Moffat, R.J. and Kays, W.M. (1984), "A Review of Turbulent Boundary Layer Heat Transfer Research at Stanford, 1958-1983," *Advances in Heat Transfer, Vol. 16* (New York: Academic Press, 1984), ed. J.P. Hartnett and T.F. Irvine, pp. 241-365.

Mori, Y. (1961), "Buoyancy Effects in Forced Convection Flow Over a Horizontal Flat Plate," ASME Paper 60-WA-220.

Nagano, Y. and Hishida, M. (1988), "Turbulent Heat Transfer Associated with Coherent Structures Near the Wall," *Zaric Mem. Conf. on Near Wall Turbulence*, Dubrovnik, Croatia, p. 568.

Nakagawa, H. and Nezu (1981), "Structure of Space-time correlation in Open Channel Flow," *J. Fluid Mech.*, vol. 104, p. 1.

Nieuwstadt, F.T.M., Dam, W. van, Leijdens, H., and Pulles, C.J.A. (1986), "Some Turbulence Measurements above a Grooved Wall," *Proc. European Drag Reduction Conf., Lausanne, Switz.*

Nikuradse, J. (1926), "Untersuchungen ueber die Geschwindigkeitsverteilung in Turbulenten Stromingen," *Forschungsarbeiten auf dem Gebeite des Ingenieurwesens*, vol. 281.

Nikuradse, J. (1930), "Widerstandsgesetz und Geschwindigkeitsverteilung von turbulenten Wasserströmung in glatten und rauhen Rohren," *Ing.-Arch.*, vol. 1, pp. 306-332.

Nitschke, P. (1983), "Experimentelle Untersuchung der Turbulenten Strömung in Glatten und Längsgerillten Röhren," Bericht 3, Max-Planck-Institut für Strömungsforschung, Göttingen (trans. as "Experimental Investigation of the Turbulent Flow in Smooth and Longitudinally Grooved Tubes," NASA TM 77 480).

Nouse, H. et al. (1975), "Experimental Results of Full Scale Air-Cooled Turbine Test," ASME Paper 75-GT-116.

Offen, G. and Kline, S.J. (1974), "Combined Dye-streak and Hydrogen Bubble Visual Observations of the Turbulent Boundary Layer," *J. Fluid Mech.*, vol. 62, p. 223.

Oldaker, D.K. and Tiederman, W.G. (1977), "Spatial Structure of the Viscous Sub-layer in Drag-reducing Channel Flows," *Phys. Fluids*, vol. 20, S133.

Patel, V.C. (1965), "Calibration of the Preston Tube and Limitations on its Use in Pressure Gradients," *J. Fluid Mech.*, vol. 23, part 1, pp. 185-208.

Pearson, C.F. (1989), "Interaction of Streamwise Vorticity with a Grooved Boundary," *Bull. Am. Phys. Soc.*, vol. 33, no. 2233.

Pearson, C.F. and Abernathy, F.H. (1984), "Evolution of the Flow Field Associated with a Streamwise Diffusing Vortex," *J. Fluid Mech.*, vol. 146, pp. 271-283.

Perepelitsa, B.V. (1988), "Effect of Turbulent Flow Structure on Temperature Field Formation in Near Wall Region," *Zaric Mem. Conf. on Near Wall Turbulence*, Dubrovnik, Croatia, p. 582.

Perry, A.E. and Chong, M.S. (1982), "On the Mechanism of Wall Turbulence," *J. of Fluid Mech.*, vol. 119, pp. 173-217.

Perry, A.E. and Hoffman, P.H. (1976), "An Experimental Study of Turbulent Convective Heat Transfer from a Flat Plate," *J. Fluid Mech.*, vol. 77, p. 335.

Prandtl, L. (1927), *Ergeb. AVA Goett.*, ser. III, pp. 1-5.

Prandtl, L. (1933), *Z. Ver. Dtsch. Ing.*, vol. 7, no. 5, pp. 105-114 (trans. as "Recent Results of Turbulence Research," NACA Tech. Mem. 720).

Press, W.H., Flannery, B.P., Teukolsky, S.A., and Vetterling, W.T. (1986), *Numerical Recipes: The Art of Scientific Computing* (New York: Cambridge U., 1986).

Preston, J.H. (1954), "The Determination of Turbulent Skin Friction by Means of Pitot Tubes," *J. Roy. Aero. Soc.*, vol. 58, pp. 109-121.

Pulles, C.J.A. (1988), "Drag Reduction of Turbulent Boundary Layers by Means of Grooved Surfaces," Ph.D. Thesis, Technical U. of Eindhoven.

Pulles, C.J.A., Krishna Prasad, K., and Nieuwstadt, F.T.M (1989), "Turbulence Measurements Over Longitudinal Micro-Grooved Surfaces," *Appl. Sci. Research*, vol. 46, pp. 197-208.

Raschi, W.G. and Musick, J.A. (1984), "Hydrodynamic Aspects of Shark Scales," Report 272, Virginia Institute of Marine Science, Gloucester Point, VA.

Reed, C.B. and Lykoudis, P.S. (1978), "The Effect of a Transverse Magnetic Field on Shear Turbulence," *J. of Fluid Mech.*, vol. 89, part 1, pp. 147-171.

Reidy, L.W. (1987), "Flat Plate Drag Reduction in a Water Tunnel Using Riblets," Naval Ocean Systems Center TR 1169.

Reidy, L.W. and Anderson, G.W. (1988), "Drag Reduction for External and Internal Boundary Layers Using Riblets and Polymers," AIAA Paper 88-0138.

Reif, W.-E. (1982), "Morphogenesis and Function of the Squamation in Sharks," *Neues Jahrbuch für Geologie und Paläontologie, Abhandlungen Band*, vol. 164, pp. 172-183.

Reif, W.-E. (1985), "Squamation and Ecology of Sharks," *Courier Forschungsinstitut Senckenberg*, no. 78,

Reif, W.-E. and Dinkelacker, A. (1982), "Hydrodynamics of the Squamation in Fast Swimming Sharks," *Neues Jahrbuch für Geologie und Paläontologie, Abhandlungen Band*, vol. 164, pp. 184-187.

Reynolds, O. (1874), "On the Extent and Action of the Heating Surface for Steam Boilers," *Proc. Manch. Lit. Phil. Soc.*, vol. 14, pp. 7-12.

Reynolds, O. (1895), *Phil. Trans. R. Soc.*, ser. A, vol. 186, pp. 123-164.

Reynolds, W.C. (1958), "Heat Transfer in the Turbulent Incompressible Boundary Layer with Constant and Variable Wall Temperature," Ph.D. Thesis, Stanford U., Dept. of Mech. Eng.

Reynolds, W.C., Kays, W.M., and Kline, S.J. (1958a), "Heat Transfer in the Turbulent Boundary Layer I-Constant Wall Temperature," NASA Mem. 12-1-58W.

Reynolds, W.C., Kays, W.M., and Kline, S.J. (1958b), "Heat Transfer in the Turbulent Boundary Layer II-Step Wall-Temperature Distribution," NASA Mem. 12-1-58W.

Riddle, J.L., Furukawa, G.T., and Plumb, H.H. (1973), "Platinum Resistance Thermometry," NBS Monograph 126.

Riddle, J.L., Furukawa, G.T., and Plumb, H.H. (1976), "Platinum Resistance Thermometry," *Measurements in Heat Transfer*, 2nd ed. (New York: Springer-Verlag, 1976), eds. E.R.G. Eckert and R.J. Goldstein, pp. 25-104.

Rohr, J.J., Reidy, L.W., and Anderson, G.W. (1989), "An Experimental Investigation of the Drag Reducing Benefits of Riblets and Polymers in Pipes," *Proc. of the IAUR Drag Reduction Sym.*

de Saint Victor, X. (1987), "Résolution des Équations de Navier-Stokes Appliquées à L'étude de L'écoulement Laminaire dans des Riblets," Rapport Technique OA No. 18/5025 AYD, ONERA/CERT.

Sami, S. (1967), "The Pitot Tube in Turbulent Shear Flow," *Proc. 11th Midwestern Mech. Conf., Dev. in Mech.*, vol. 5, p. 191.

Sant, J. H. van (1983), *Conduction Heat Transfer Solutions* (Livermore, CA: Lawrence Livermore National Laboratory, 1983).

Satterlee, H.M. (1955), "An Experimental Investigation of Heat Transfer in the Turbulent Boundary Layer of a Flat Plate: Design of Apparatus," Eng. Thesis, Stanford U., Dept. of Mech. Eng.

Savill, A.M. (1987), "Effects on Turbulent Boundary Layer Structure of Longitudinal Riblets Alone and in Combination with Outer Layer Devices," *Flow Visualization IV: Proc 4th Int. Sym. Paris*, pp. 303-308.

Savill, A.M., Truong, T.V., and Ryhming, I.L. (1988), "Turbulent Drag Reduction by Passive Means," *J. of Th. and Appl. Mech.*, vol. 7, pp. 353-378.

Sawyer, W.G. and Winter, K.G. (1987), "An Investigation of the Effect on Turbulent Skin Friction of Surfaces with Streamwise Grooves," *Turbulent Drag Reduction by Passive Means: Proc. Int. Conf., London, UK*, vol. 2, pp. 330-362.

Schoenherr, K.E. (1932), *Trans. Soc. Nav. Arch. Marine Eng.*, vol. 40, p. 279.

Schubauer, G.B. (1954), *J. Appl. Phys.*, vol. 23, p. 191.

Schultz-Grunow, F. (1940), *Luftfahrtforschung*, vol. 17, no. 8, pp. 239-246 (trans. as "New Frictional Resistance Law for Smooth Plates," NACA Tech. Mem. 986).

Singham, J.R. (1962), "Tables of Emissivity of Surfaces," *Int. J. Heat Mass Transfer*, vol. 5, pp. 67-76.

Slanciauskas, A. (1988), "Spatial Correlations of the Temperature Fluctuation in Boundary Layers," *Zaric Mem. Conf. on Near Wall Turbulence*, Dubrovnik, Croatia, p. 620.

Smith, C.R. and Metzler, S.P. (1983), "The Characteristics of Low-speed Streaks in the Near-wall Region of a Turbulent Boundary Layer," *J. Fluid Mech.*, vol. 129, pp. 27-54.

- Smith, C.R. and Schwartz, S.P. (1983), "Observation of Streamwise Rotation in the Near Wall Region of a Turbulent Boundary Layer," *Phys. Fluids*, vol. 26, p. 641.
- Spalart, D.B. (1986), "Direct Simulation of a Turbulent Boundary Layer up to  $Re_\theta = 1410$ ," NASA TM 89407.
- Spalding, D.B. (1961), "A Single Formula for the 'Law of the Wall,'" *J. Appl. Mech.*, vol. 28, pp. 455-457.
- Sparrow, E.M. (1976), "Error Estimates in Temperature Measurements," *Measurements in Heat Transfer*, 2nd ed. (New York: Springer-Verlag, 1976), eds. E.R.G. Eckert and R.J. Goldstein, pp. 1-24.
- Sparrow, E.M., and Minkowycz, W.J. (1962), "Buoyancy Effects on Horizontal Boundary Layer Flow," *Int. J. Heat Mass Transfer*, vol. 5, pp. 505-511.
- Squire, L.C. and Savill, A.M. (1987), "Some Experiences of Riblets at Transonic Speeds," *Turbulent Drag Reduction by Passive Means: Proc. Int. Conf., London, UK*, vol. 2, pp. 392-407.
- Squire, L.C. and Savill, A.M. (1989), "Drag Measurements on Planar Riblet Surfaces at High Subsonic Speeds," *Appl. Sci. Research*, vol. 46, pp. 229-243.
- Taylor, R.P., Love, P.H., Coleman, H.W., and Hosni, M.H. (1990), "Heat Transfer Measurements in Incompressible Turbulent Flat Plate Boundary Layers with Step Wall Temperature Boundary Conditions," *J. Heat Transfer*, vol. 112, pp. 245-247.
- Theodorsen, T. (1952), "Mechanism of Turbulence," *Proc. 2nd Midwestern Conf. Fluid Mech.*, OSU, Columbus, OH.
- Truong, T.V. and Pulvin, P.H. (1989), "Influence of Wall Riblets on Diffuser Flow," *Appl. Sci. Research*, vol. 46, pp. 217-227.
- Valkenburg, P. van (1988), "The Aerodynamics of the Bobsled," *Sci. Am.*, Feb. 1988, pp. 110-114.
- VanDusen, M.S. (1925), *J. Am. Chem. Soc.*, vol. 47, p. 3326.
- Vukoslavcevic, P., Balint, J.-L., and Wallace, J.M. (1987), "On the Mechanism of Viscous Drag Reduction Using Streamwise Aligned Riblets," *Turbulent Drag Reduction by Passive Means: Proc. Int. Conf., London, UK*, vol. 2, pp. 290-309.
- Wallace, J.M. (1982), "On the Structure of Bounded Turbulent Shear Flow," *Developments in Theoretical and Applied Mechanics*, vol. 11, pp. 509-521.
- Wallace, J.M. and Balint, J.-L. (1987), "Viscous Drag Reduction Using Streamwise Aligned Riblets: Survey and New Results," *Turbulence and Relaminarization: Proc. of the IUTAM Sym., Bangalore, India* (New York: Springer-Verlag, 1988), pp. 133-147.
- Walsh, M.J. (1980), "Drag Characteristics of V-Grooved and Transverse Curvature Riblets," in *Progress in Aeronautics and Astronautics*, Vol. 72, *Viscous Flow Drag Reduction* (New York: AIAA, 1980), ed. G. Hough, pp. 168-184.
- Walsh, M.J. (1982), "Turbulent Boundary Layer Drag Reduction Using Riblets," AIAA Paper 82-0169.
- Walsh, M.J. (1983), "Riblets as a Viscous Drag Reduction Technique," *AIAA Journal*, vol. 21, no. 4, pp. 485-486.
- Walsh, M.J. (1985), "Riblets for Aircraft Skin-Friction Reduction," *Proc. Langley Sym. on Aerodynamics*, Hampton, VA, vol. 1, pp. 557-571.
- Walsh, M.J. (1990a), "Effect of Detailed Surface Geometry on Riblet Drag Reduction Performance," *J. Aircraft*, vol. 27, no. 6, pp. 572-573.
- Walsh, M.J. (1990b), "Riblets," in *AIAA Progress in Aeronautics and Astronautics: Viscous Drag Reduction in Boundary Layers*, vol. 123 (New York: AIAA, 1990), eds. D.M. Bushnell and J.N. Hefner, pp. 203-261.



Walsh, M.J. and Anders, J.B., Jr., (1989), "Riblet/LEBU Research at NASA Langley," *Appl. Sci. Res.*, vol. 46, pp. 255-262.

Walsh, M.J. and Lindemann, A.M. (1984), "Optimization and Application of Riblets for Turbulent Drag Reduction," AIAA Paper 84-0347.

Walsh, M.J. and Weinstein, L.M. (1978), "Drag and Heat Transfer on Surfaces with Small Longitudinal Fins," AIAA Paper 78-1161.

Walsh, M.J. and Weinstein, L.M. (1979), "Drag and Heat Transfer Characteristics of Small Longitudinally Ribbed Surfaces," *AIAA J.*, vol. 17, No. 7.

Walsh, M.J., Sellers, W.L., and McGinley, C.B. (1988), "Riblet Drag Reduction at Flight Conditions," AIAA Paper 88-2554.

Walsh, M.J., Sellers, W.L., and McGinley, C.B. (1989), "Riblet Drag Reduction at Flight Conditions," *J. of Aircraft*, vol. 26, no. 6, pp. 570-575.

White, F.M. (1969), *J. Basic Eng.*, vol. 91, pp. 371-378.

White, F.M. (1974), *Viscous Fluid Flow* (New York: McGraw-Hill, 1974).

Wilkinson, S.P. (1988), "Direct Drag Measurements on Thin-element Riblets with Suction and Blowing," AIAA Paper 88-3670.

Wilkinson, S.P., Bushnell, D.M., Lazos, B.S., and Anders, J.B. (1987), "Turbulent Drag Reduction Research at NASA Langley- Progress and Plans" *Turbulent Drag Reduction by Passive Means: Proc. Int. Conf., London, UK*, vol. 2, pp. 1-32.

Zaric, Z. (1972a), "Wall Turbulence Studies," *Adv. Heat Transfer*, vol. 8, p. 285.

Zaric, Z. (1972b), "Statistical Analysis of Near Wall Turbulence," *Heat Mass Transfer*, vol. 9.

Zaric, Z. (1974), "Statistical Analysis of Wall Turbulence Phenomena," *Adv. in Geophysics*, vol. 1, Pt. 18A, p. 249.

Zaric, Z. (1975), "Wall Turbulence Structure and Convection Heat Transfer," *Int. J. Heat Mass Transfer*, vol. 18, p. 831.

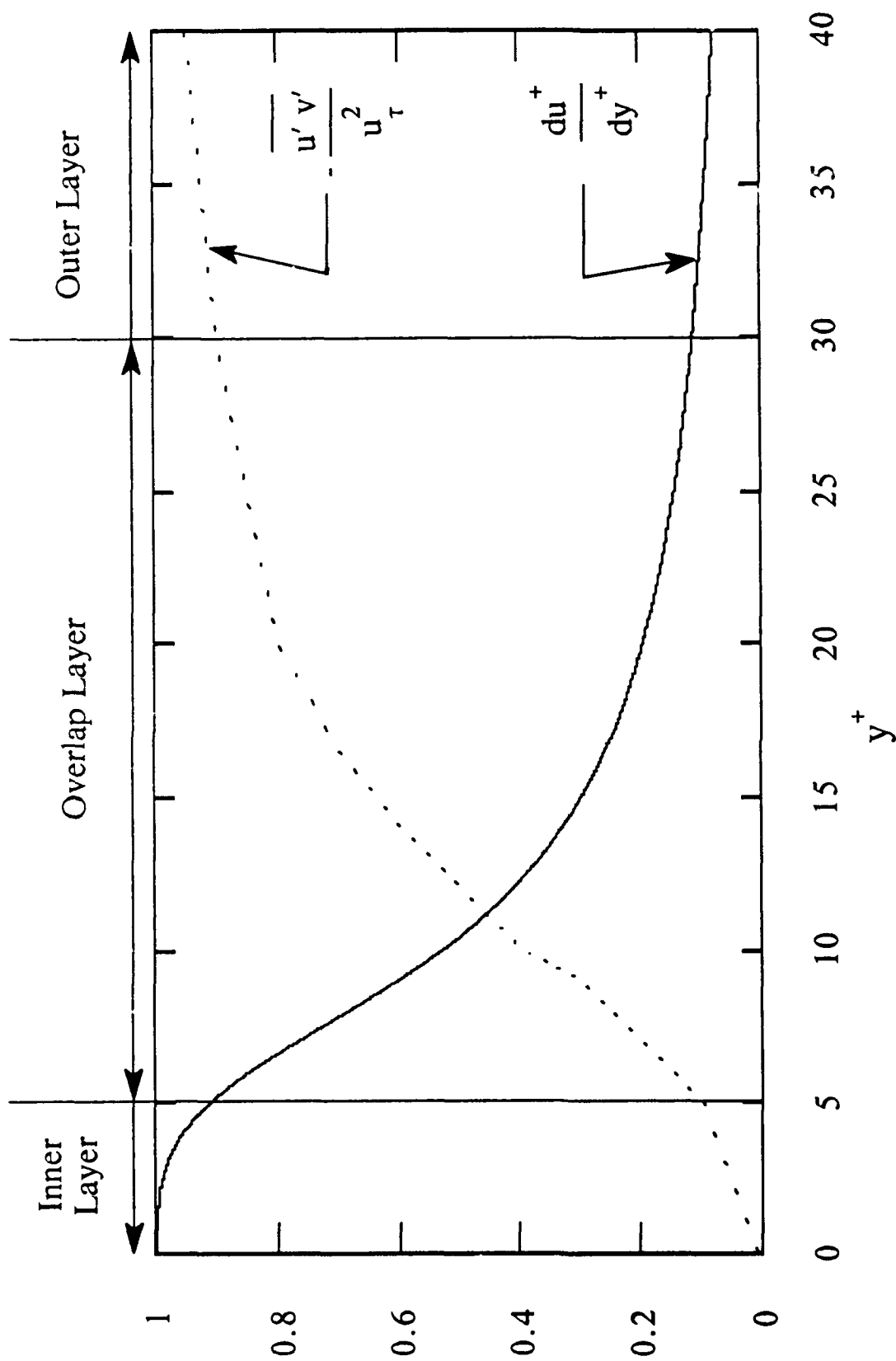


Figure 2.1. The Distribution of Stress in the Wall Region of a Turbulent Boundary Layer. The distribution of the Reynolds stress [from Schubauer (1954)] and the viscous stress [derived numerically from formula 2.23] in the wall region of a turbulent boundary layer shows three regions: the inner, where viscous stress dominates; the outer, where the Reynolds stress dominates; and the overlap layer, where they are approximately equal.

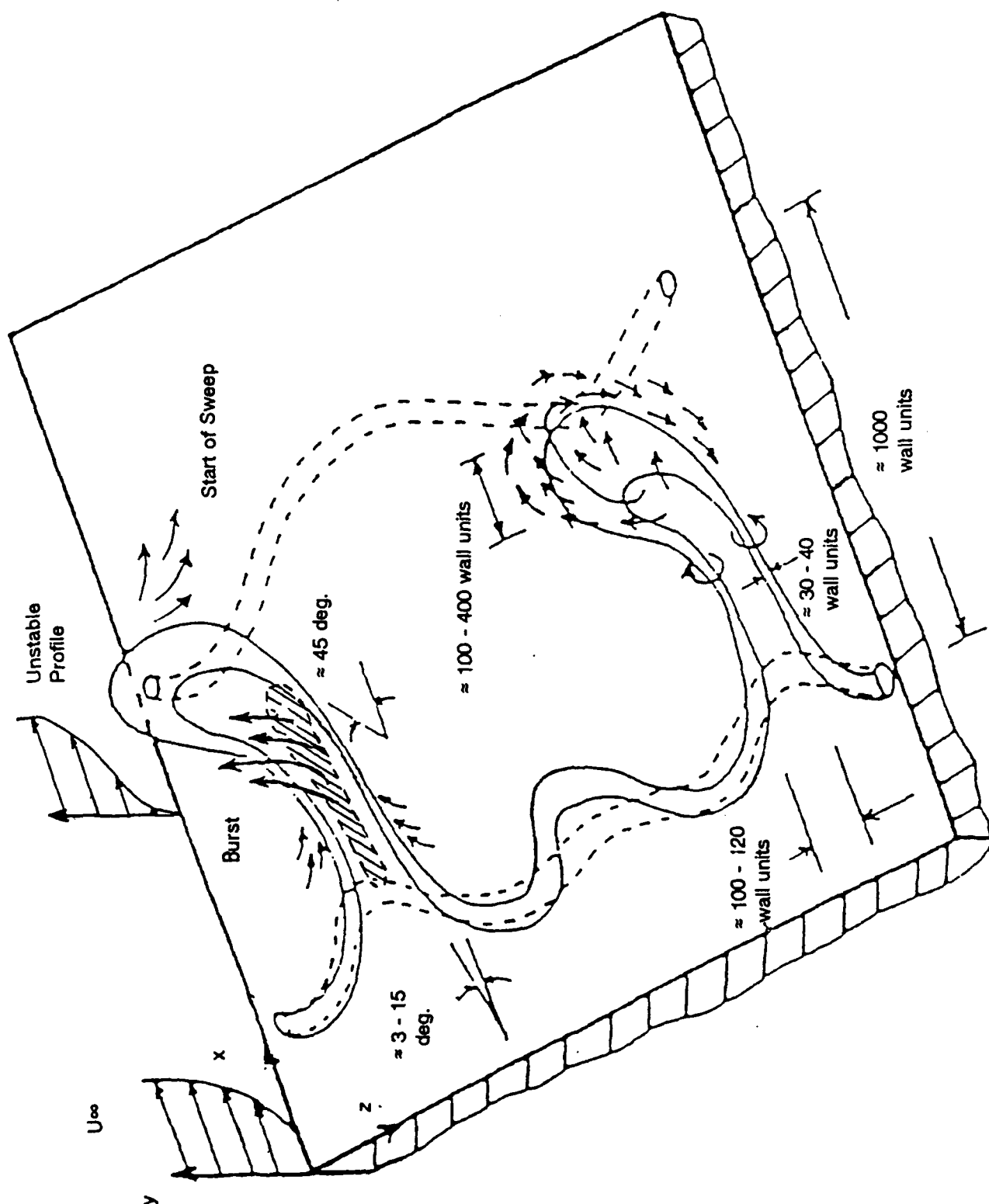


Figure 2.2. **The Bursting Process.** This conceptual model of the bursting process in the turbulent boundary layer shows the hairpin vortices formed from warped sheets of diffusing vorticity, the low speed streaks formed between the vortices, the unstable inflectional profiles near the streaks, the bursting of these streaks, and the start of a sweep [after Wallace (1982)].

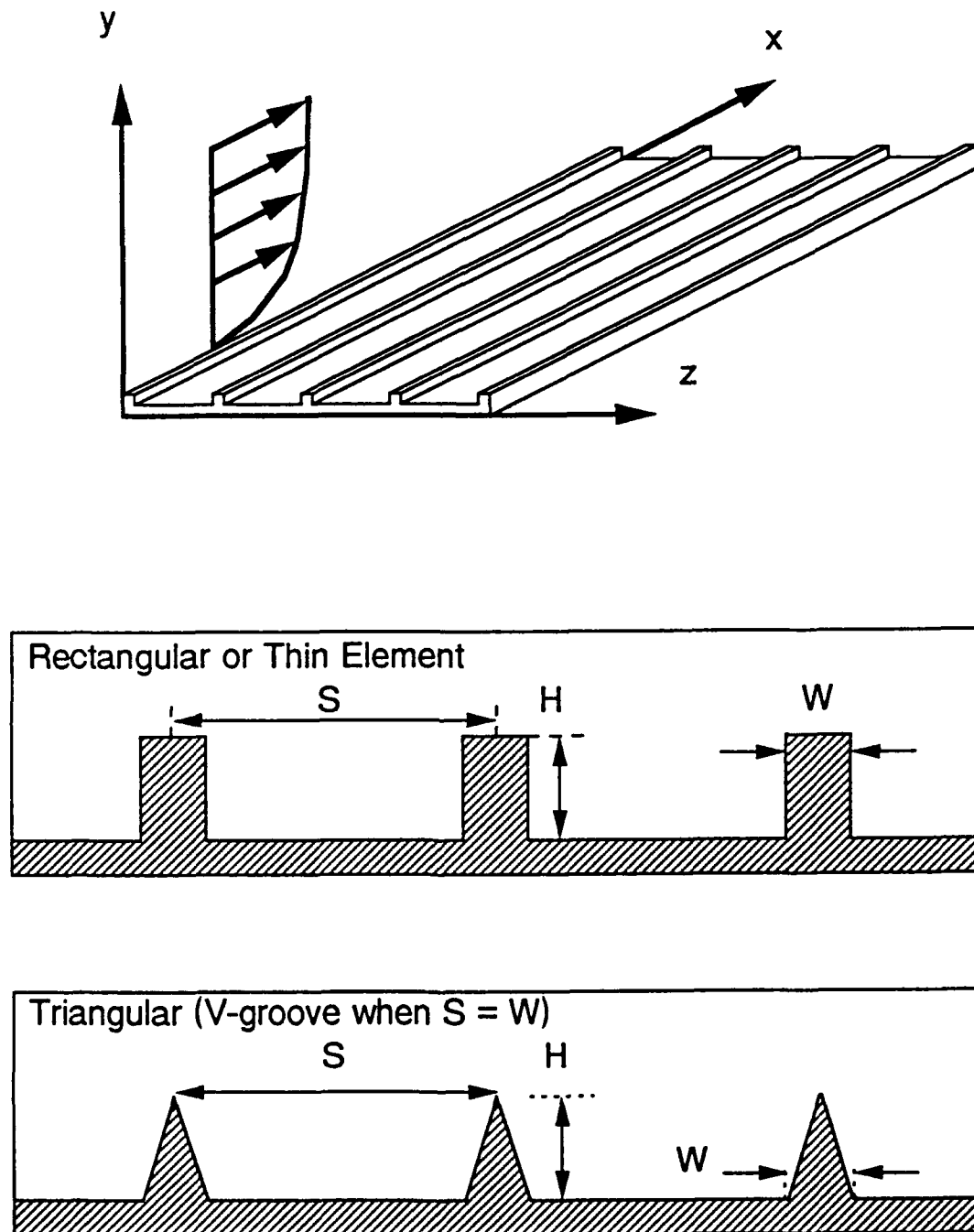


Figure 2.3. Riblet Placement and Terminology. Top: placement of riblets in a flow; Middle: terminology of rectangular or thin-element riblets; Bottom: terminology of triangular riblets or V-groove riblets.

## Drag Reduction of Thin Element Riblets

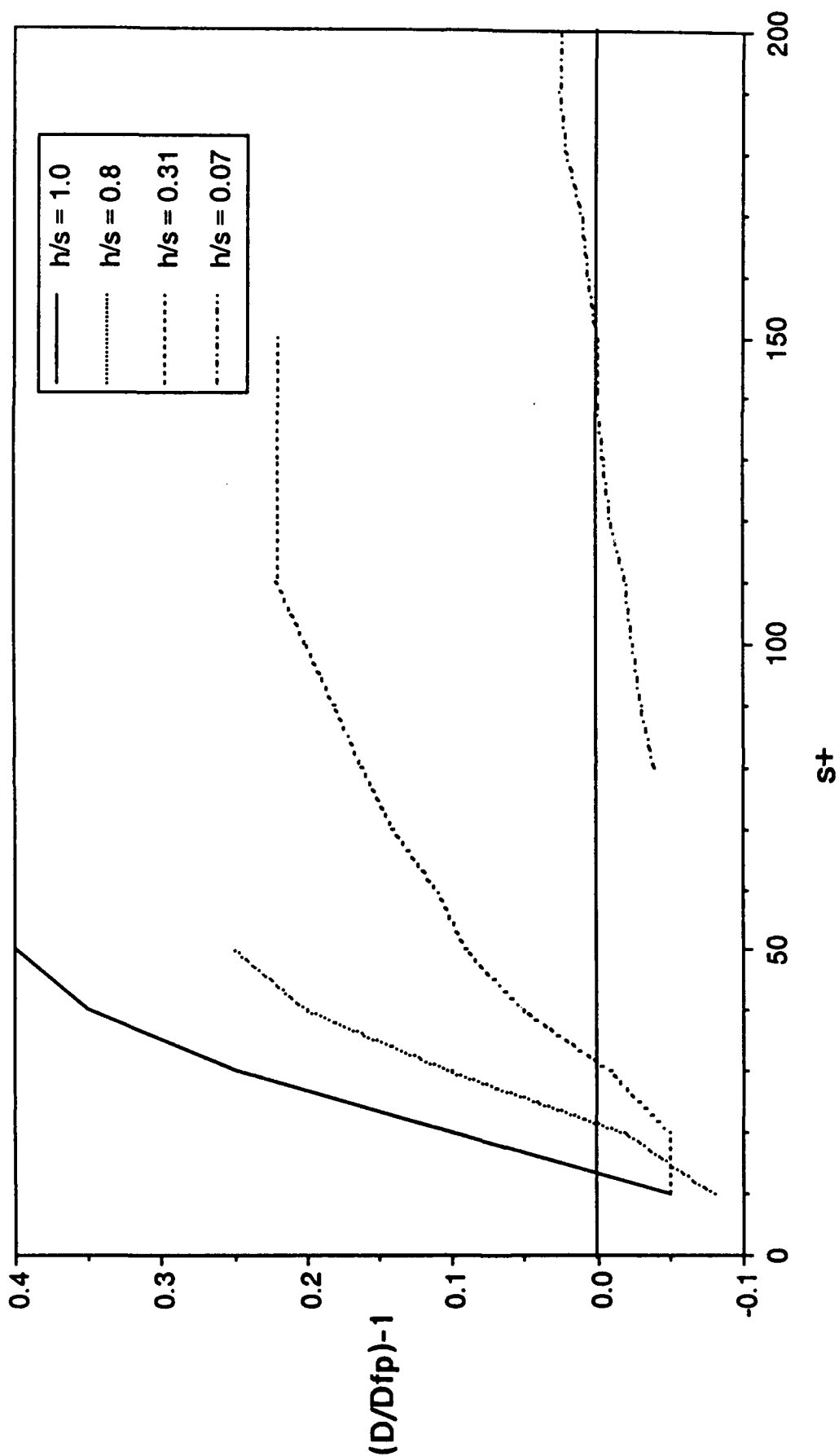


Figure 2.4. Drag Reduction of Thin Element Riblets. The drag reduction of thin element riblets versus spacing in wall units,  $s^+$ , shows the "drag bucket" region for  $s^+$  below 30, the drag rise region above this, and the increase in slope with increasing aspect ratio,  $h/s$  [after Wilkinson et. al. (1987)].

# Stanton Number Measurement Error

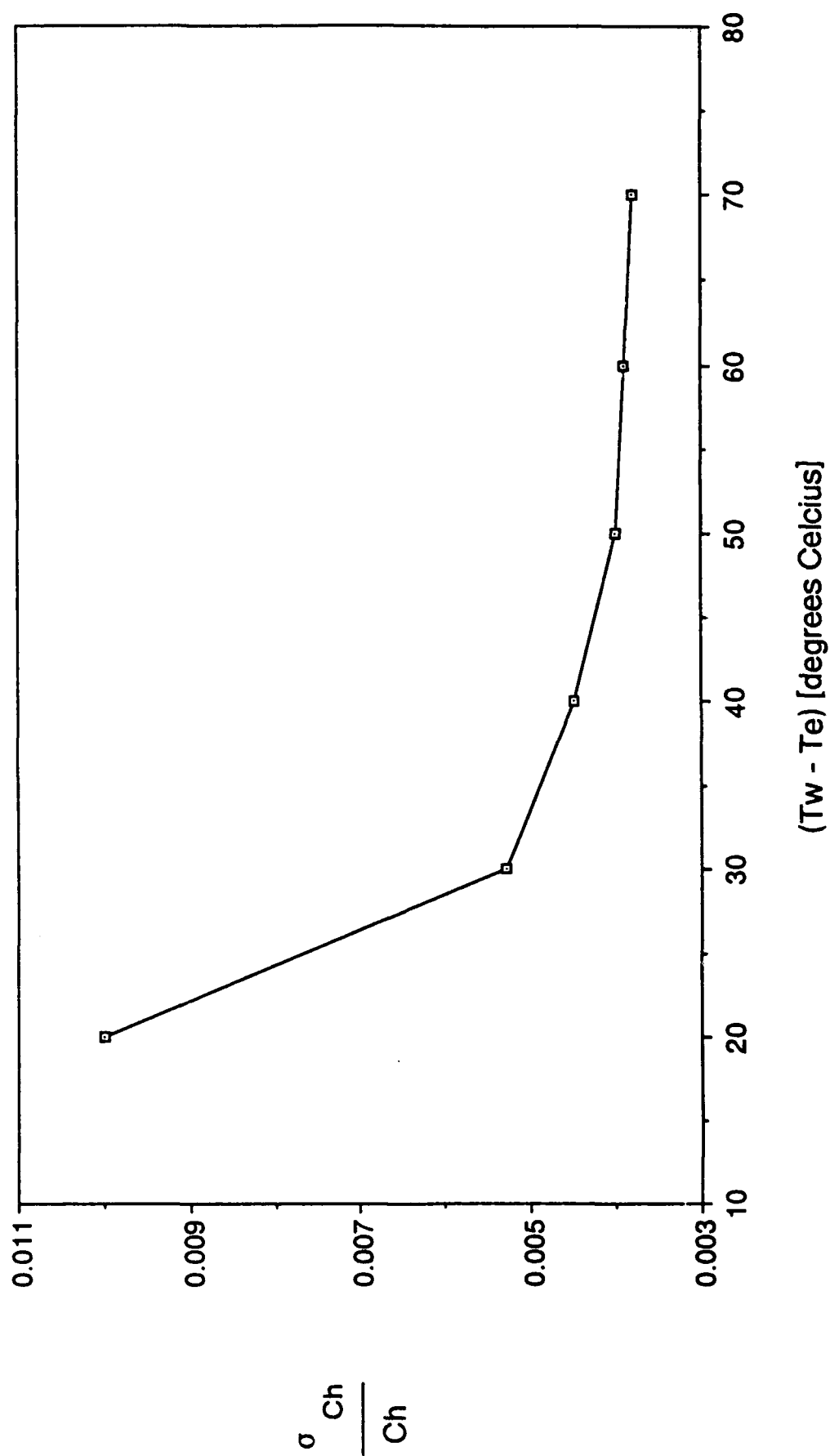
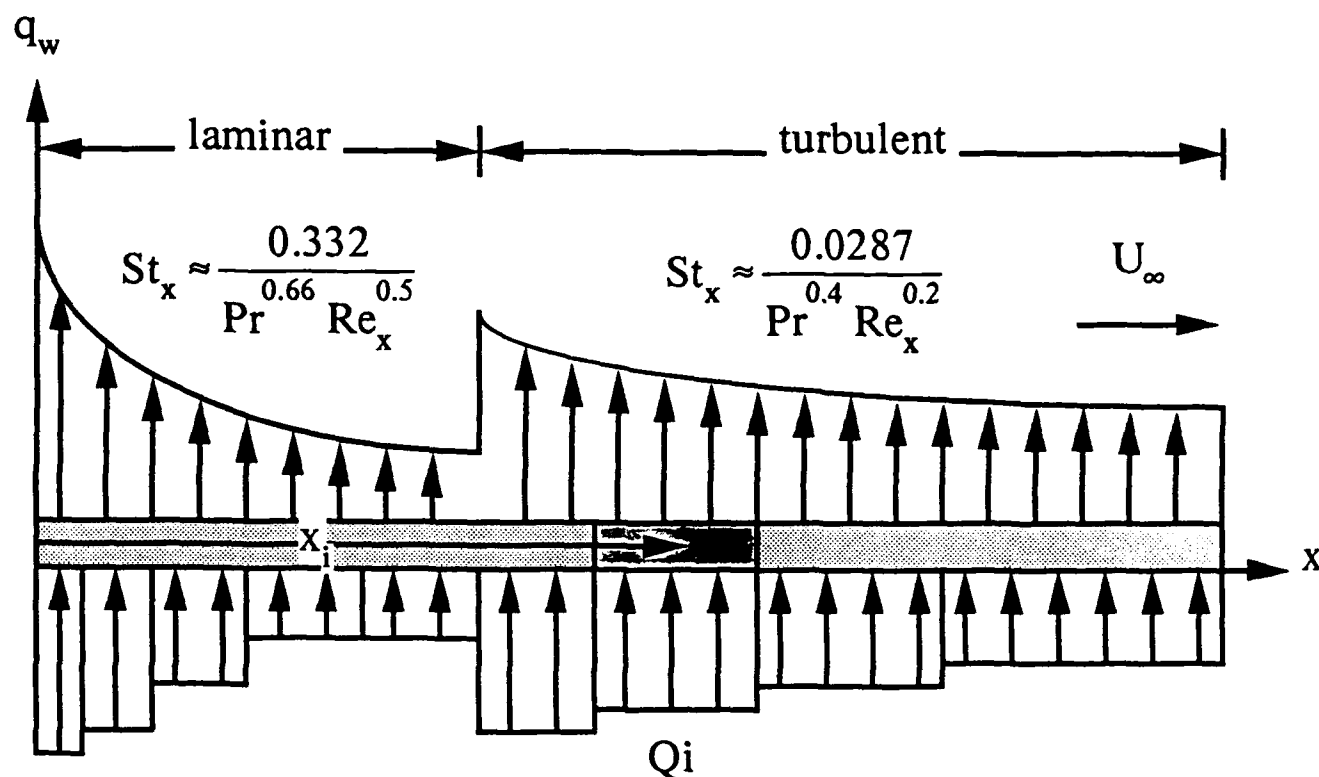


Figure 3.1. Stanton Number Measurement Error. Graph of relative error in Stanton number due to wall temperature measurement error as a function of driving temperature differential shows that reduction in error with rising differential levels off beyond 50 degrees.



Above- Actual BCs; Below- Simplified BCs.

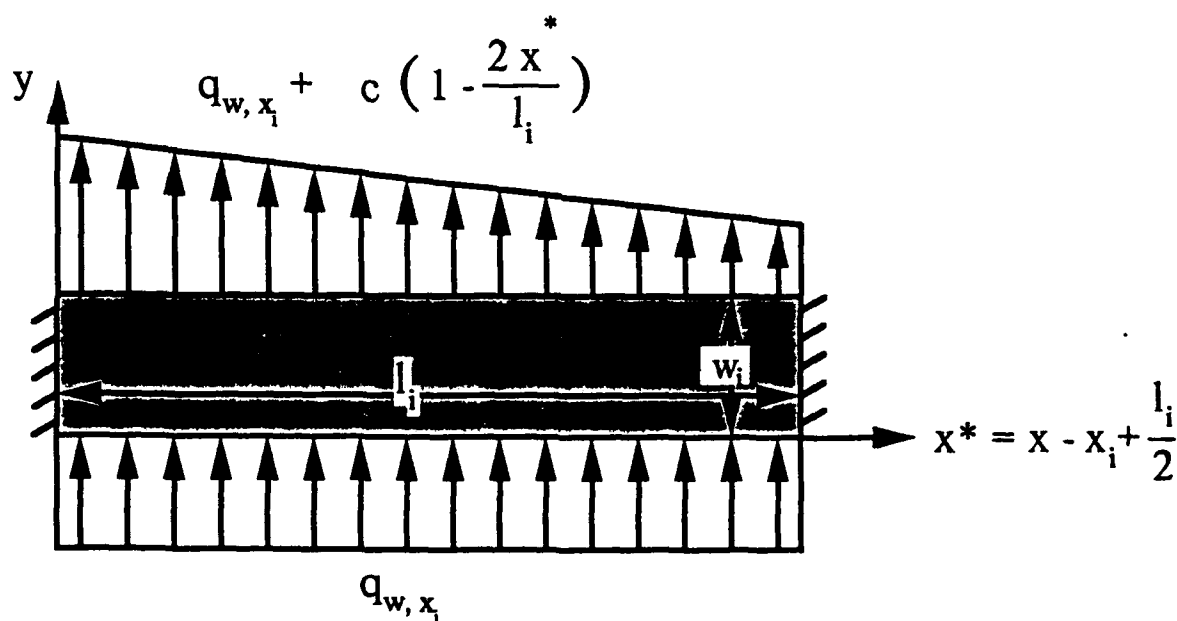
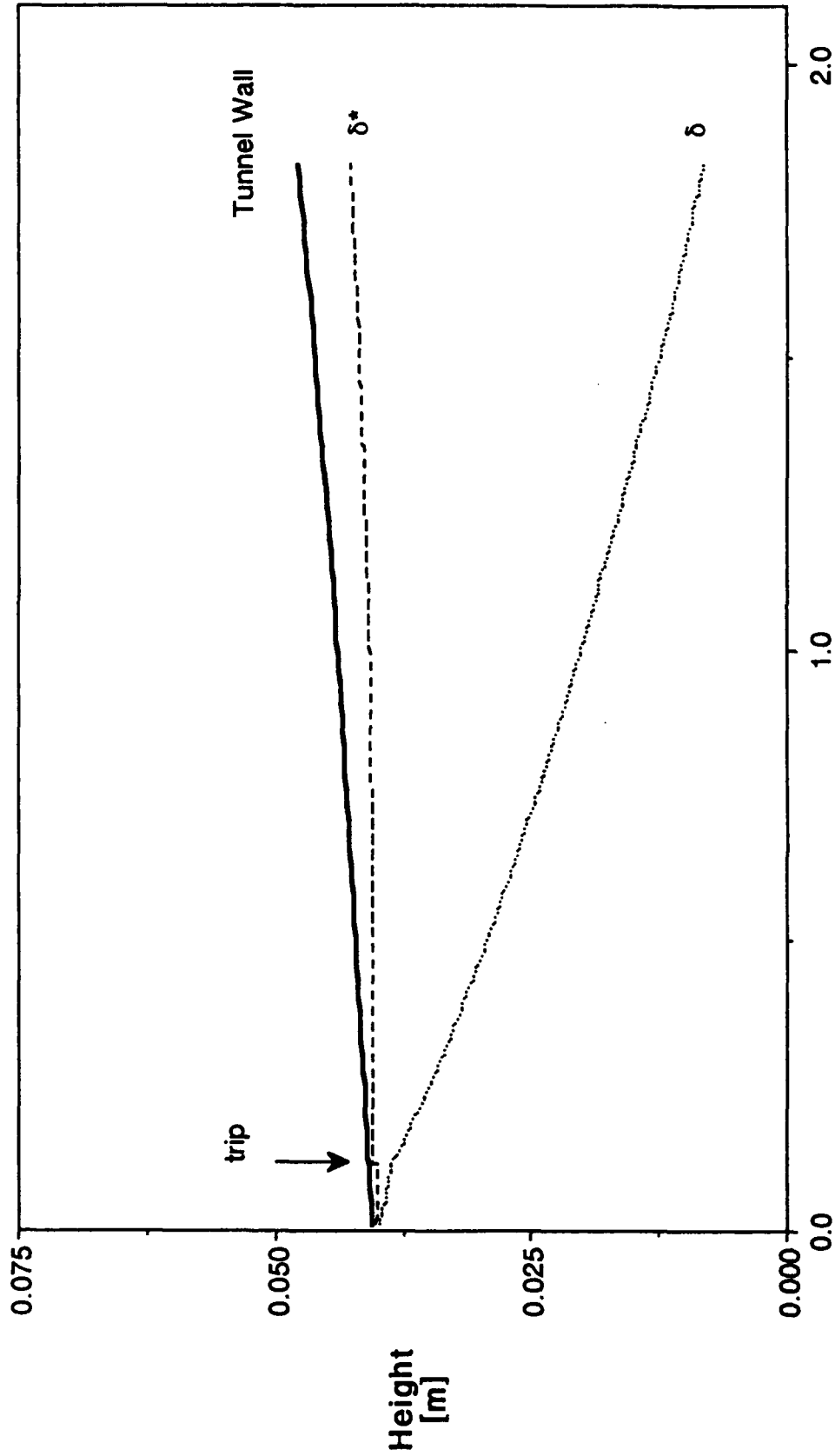


Figure 3.2. Actual and Simplified Tunnel Wall Boundary Conditions. The actual boundary conditions show the complexity of the tunnel wall heat transfer. The simplified boundary conditions are a good approximation of very small segments of the tunnel wall.

# Tunnel Height Setting and Predicted Boundary Layer Thicknesses @ 10 m/s

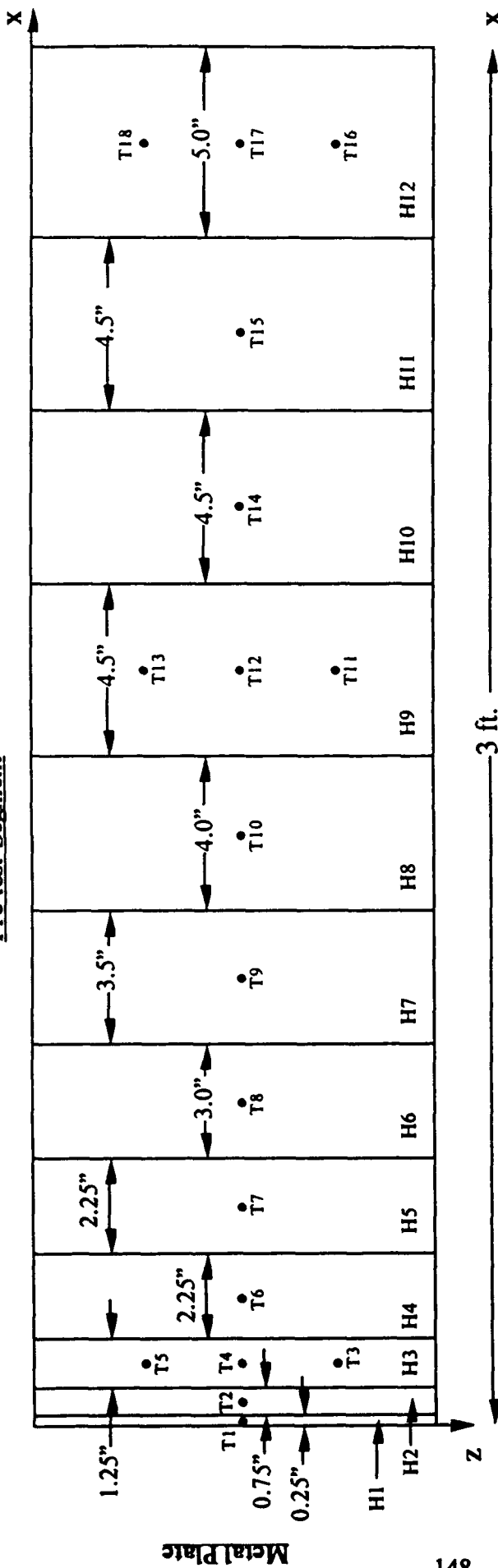


Streamwise Distance [m]

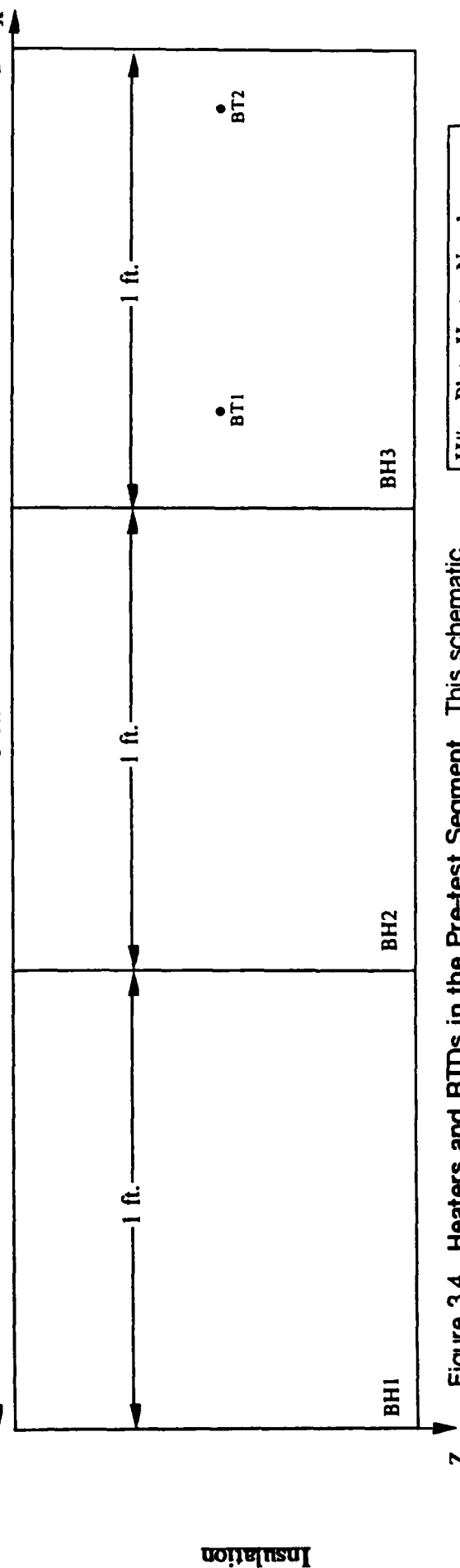
Figure 3.3. Tunnel Height Setting and Predicted Boundary Layer Thickness @ 10 m/s. The above plot shows the tunnel wall height above the centerline and the predicted boundary layer thickness and displacement thickness at that setting for a freestream velocity of 10 m/s.



# Pre-test Segment



148

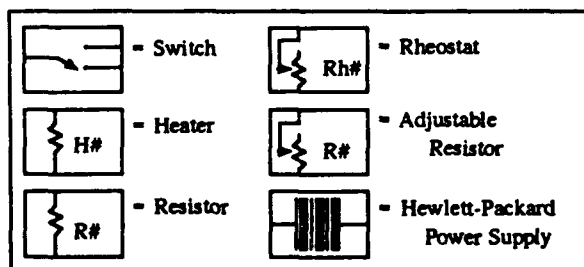
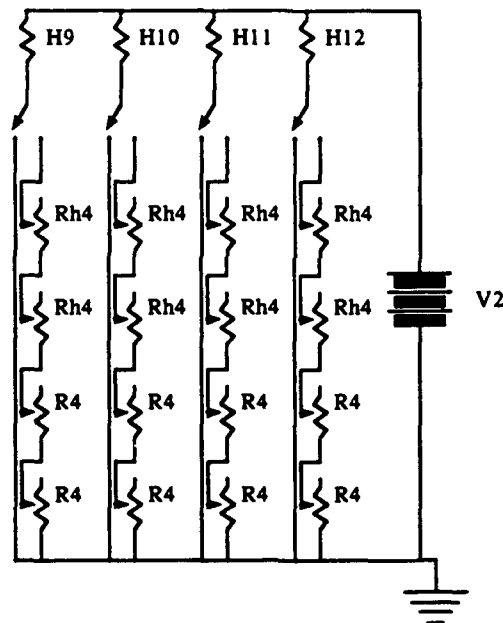
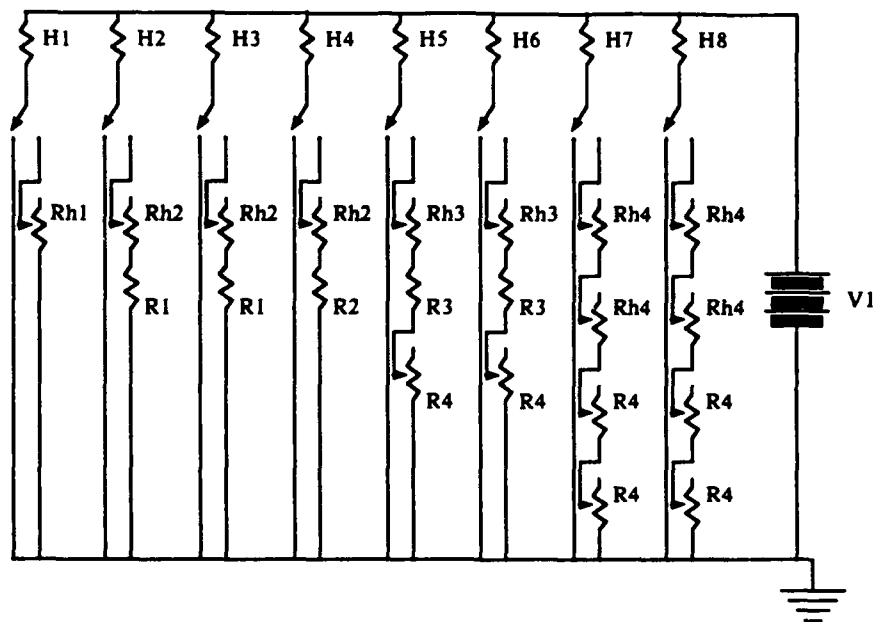


Insulation

Figure 3.4. Heaters and RTDs in the Pre-test Segment. This schematic shows heater labelling and sizes and RTD labelling and placement for the metal plate and insulation layers of the pre-test segment.

H# = Plate Heater Number;  
T# = Plate RTD Number;  
BH# = Guard Heater Number;  
BT# = Insulation RTD Number.





Rh1: Ohmite H-6 RH770, 0-6 Ohms, <2 Amps  
 Rh2: Ohmite G RH9915, 0-75 Ohms, <1 Amp  
 Rh3: Hardwick-Hindle O-3A, 0-30 Ohms, <1.8 Amps  
 Rh4: Ohmite L RH885, 0-15 Ohms, <3.2 Amps  
 R1: Ohmite RS8753, 75 Ohms, <0.8 Amps  
 R2: RCLAL-50 RS8900, 50 Ohms, <1 Amp  
 R3: Ohmite RS8202, 15 Ohms, <2.9 Amps  
 R4: Reon RS8201, 10 Ohms Adjustable, <3.2 Amps

**Figure 3.6. Pre-test Segment Heater Control Circuitry.** The schematics above show the heater control circuitry for the two circuits controlling and powering the pre-test segment heaters.

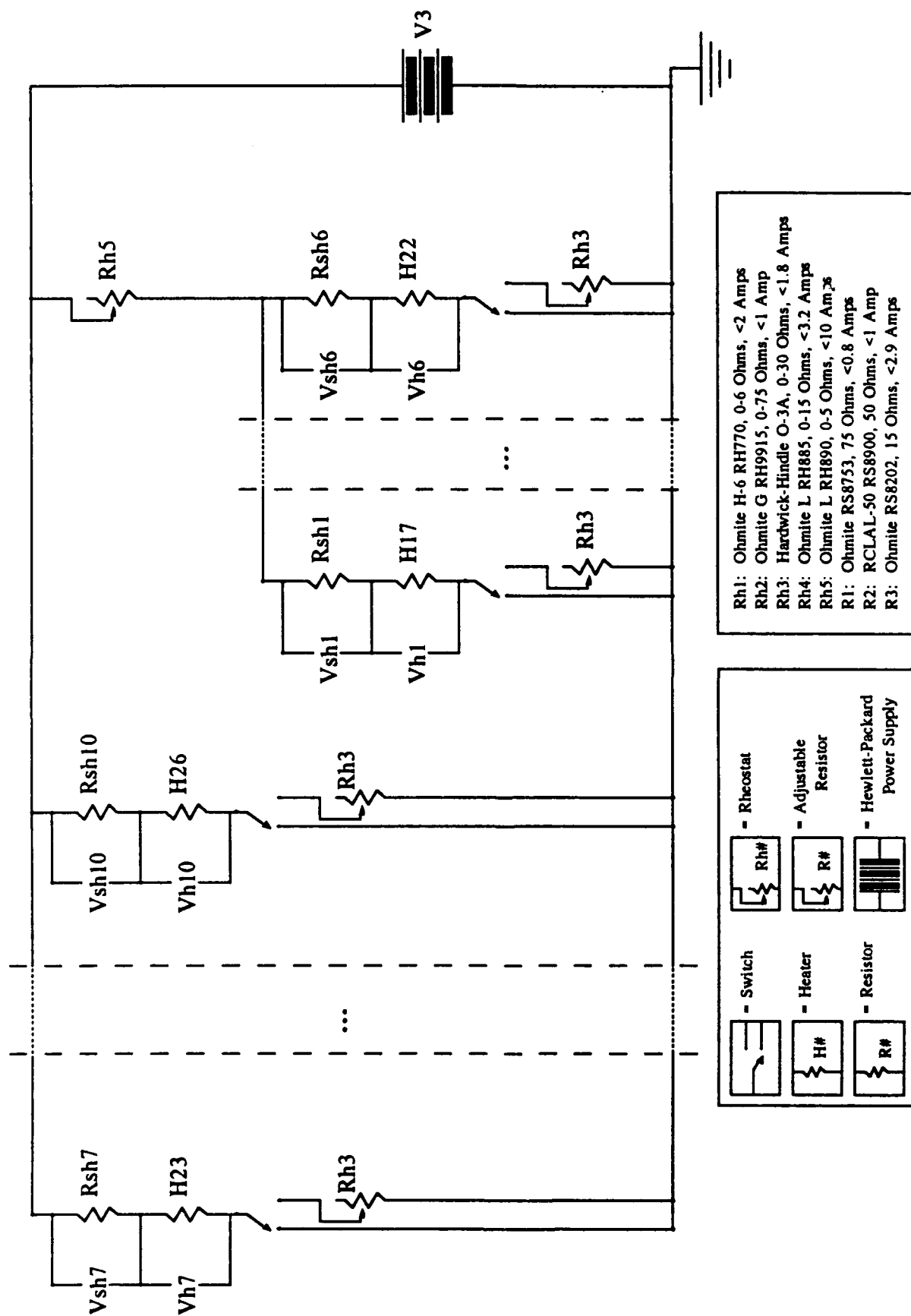
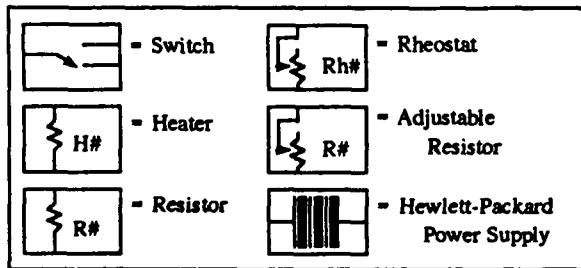
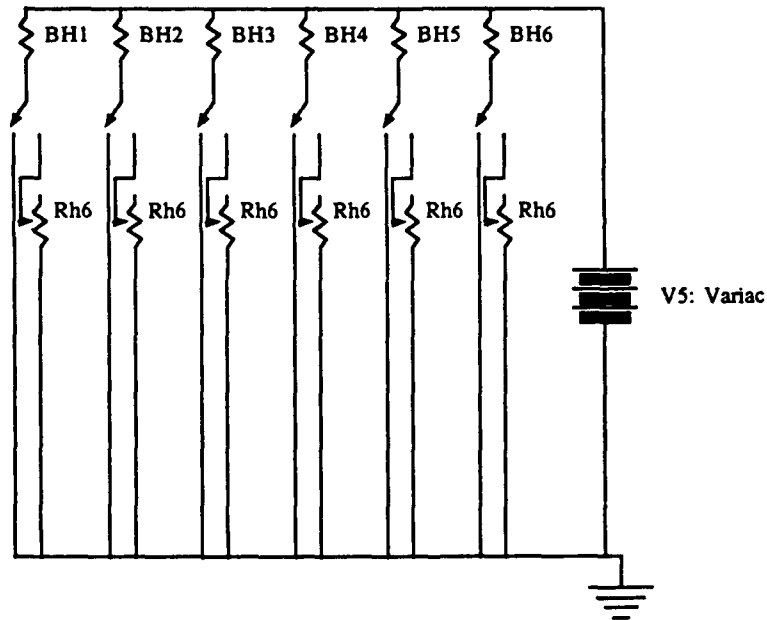
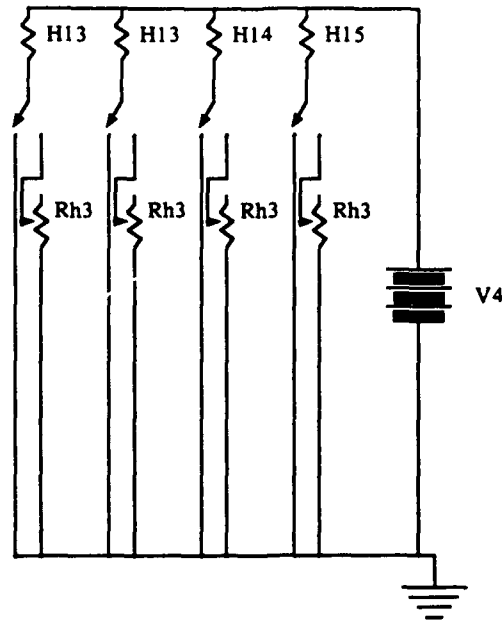


Figure 3.7. Test Segment Heater Control Circuitry. The schematic above shows the circuitry powering and controlling the test segment heaters in addition to the voltage measurements Vh and Vsh used in determining test section heater power.



Rh1: Ohmite H-6 RH770, 0-6 Ohms, <2 Amps  
 Rh2: Ohmite G RH9915, 0-75 Ohms, <1 Amp  
 Rh3: Hardwick-Hindle O-3A, 0-30 Ohms, <1.8 Amps  
 Rh4: Ohmite L RH885, 0-15 Ohms, <3.2 Amps  
 Rh5: Ohmite L RH890, 0-5 Ohms, <10 Amps  
 Rh6: Ohmite K RH312, 0-10 Ohms, <10 Amps  
 R1: Ohmite RS8753, 75 Ohms, <0.8 Amps  
 R2: RCLAL-50 RS8900, 50 Ohms, <1 Amp

**Figure 3.8. Spacer Segment and Guard Heater Control Circuitry.** The schematics above show the heater circuitry controlling and powering the heaters in the spacer segments (top) and the back insulation guard heaters (bottom).

# Positioning of RTD holes on the two 3' sections in (x, z) coordinates

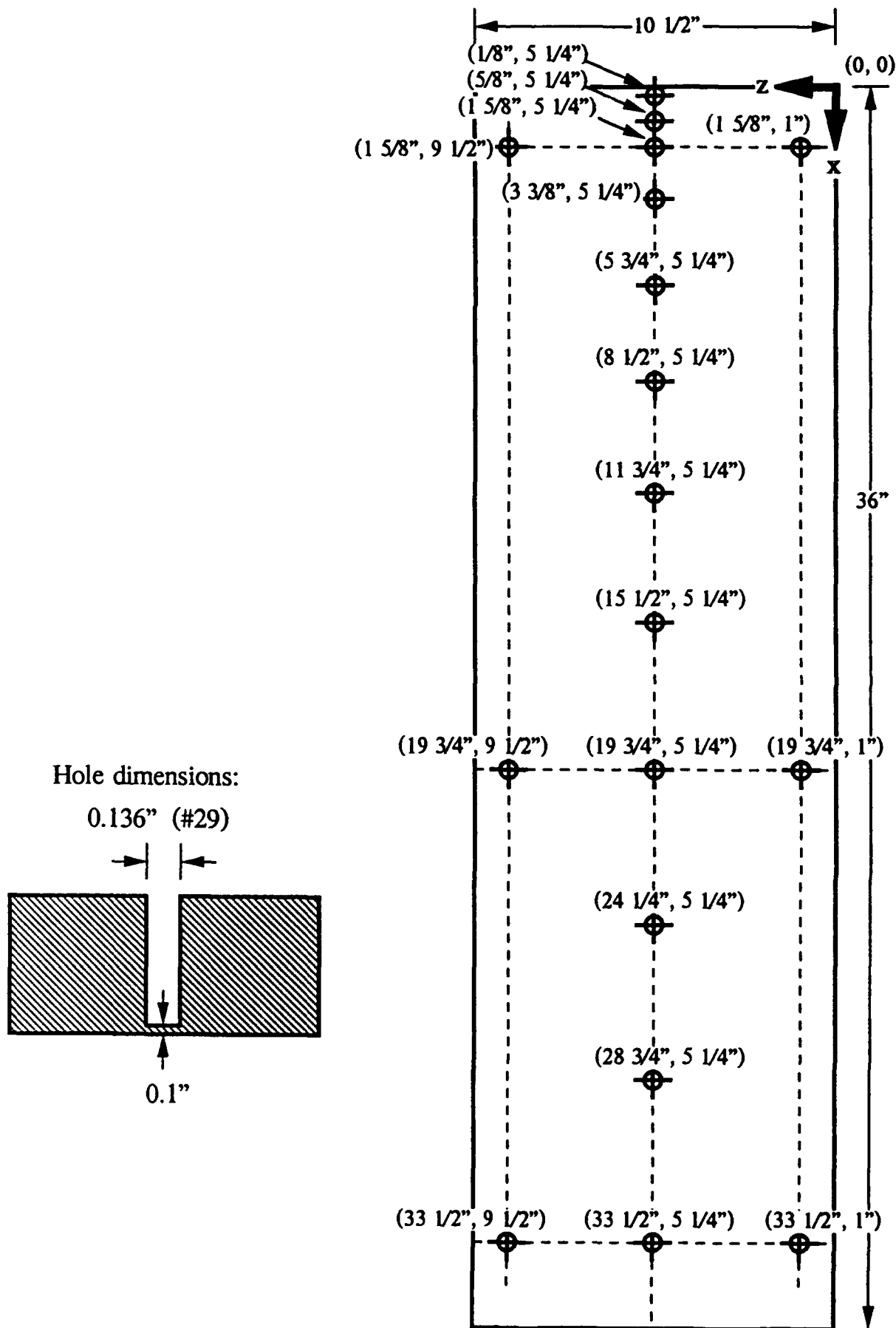
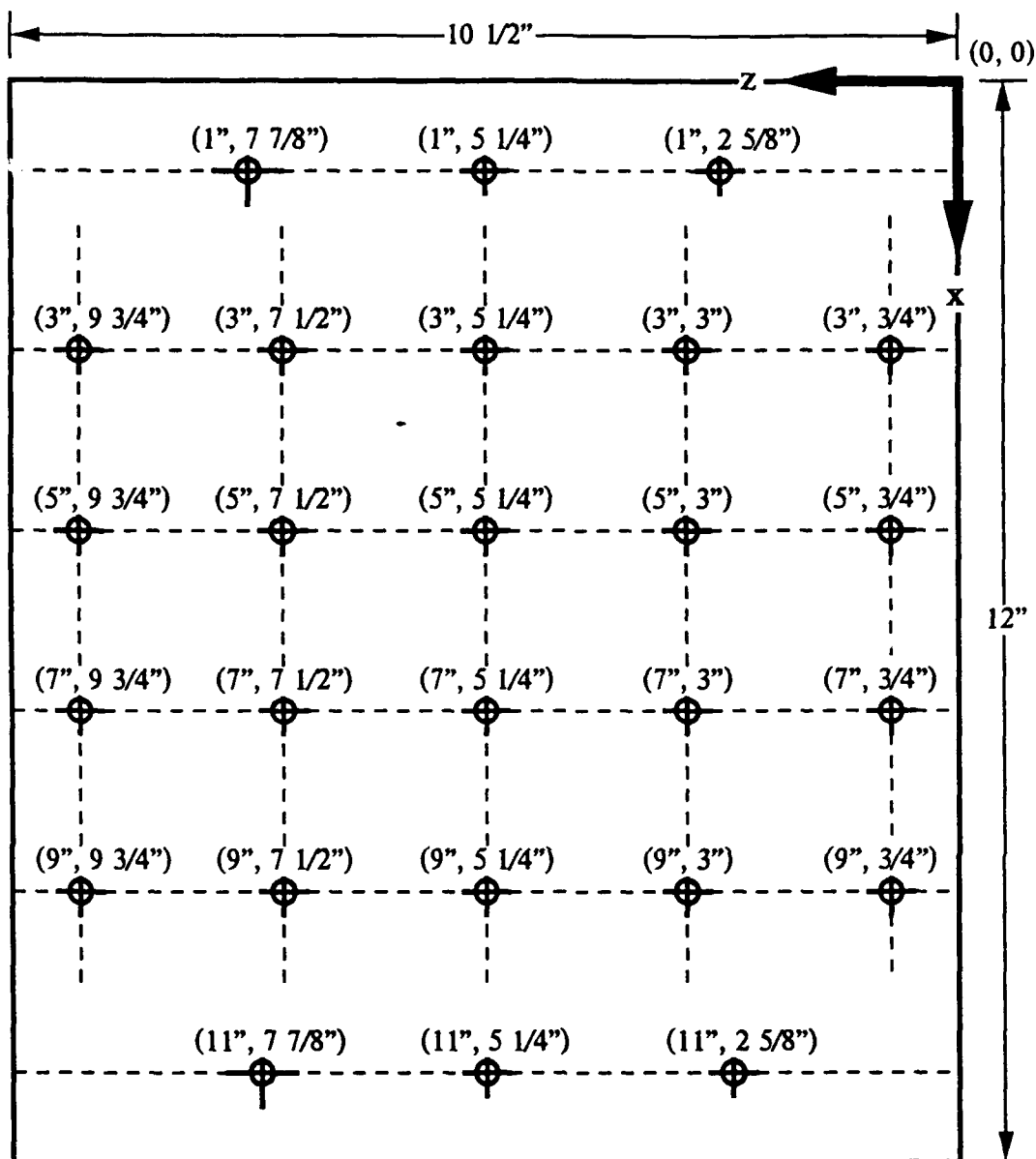


Figure 3.9. RTD Placement in the pre-test segment.

# Positioning of RTD holes on the two test sections in (x, z) coordinates



Hole dimensions: 0.136" (#29)

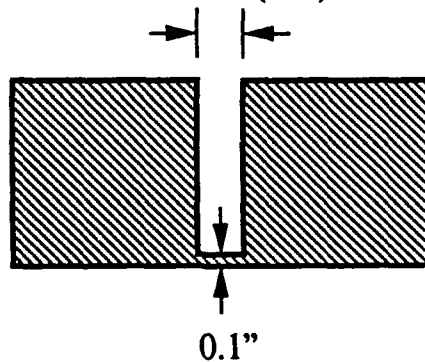
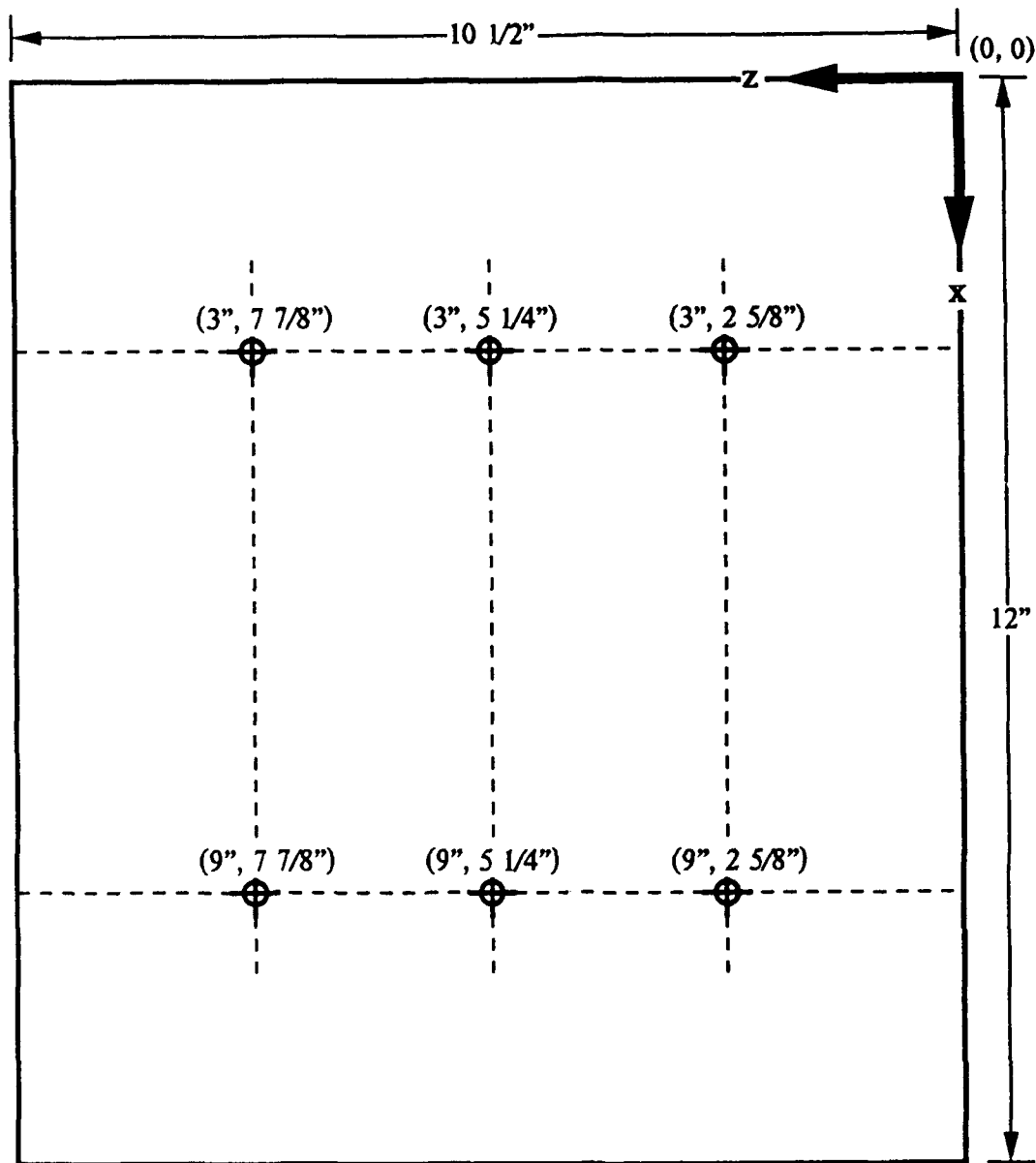


Figure 3. 10. RTD placement in the test section.

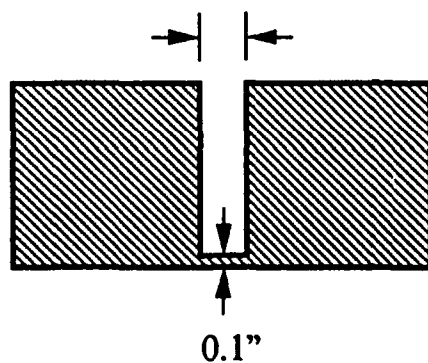
# Positioning of RTD holes on the four 1' sections in (x, z) coordinates



0.136" (#29)

scale: 1 inch = 2 inches

Hole dimensions:



scale: 1 inch = 1/2 inch

Figure 3.11. RTD Placement in the spacer segments.



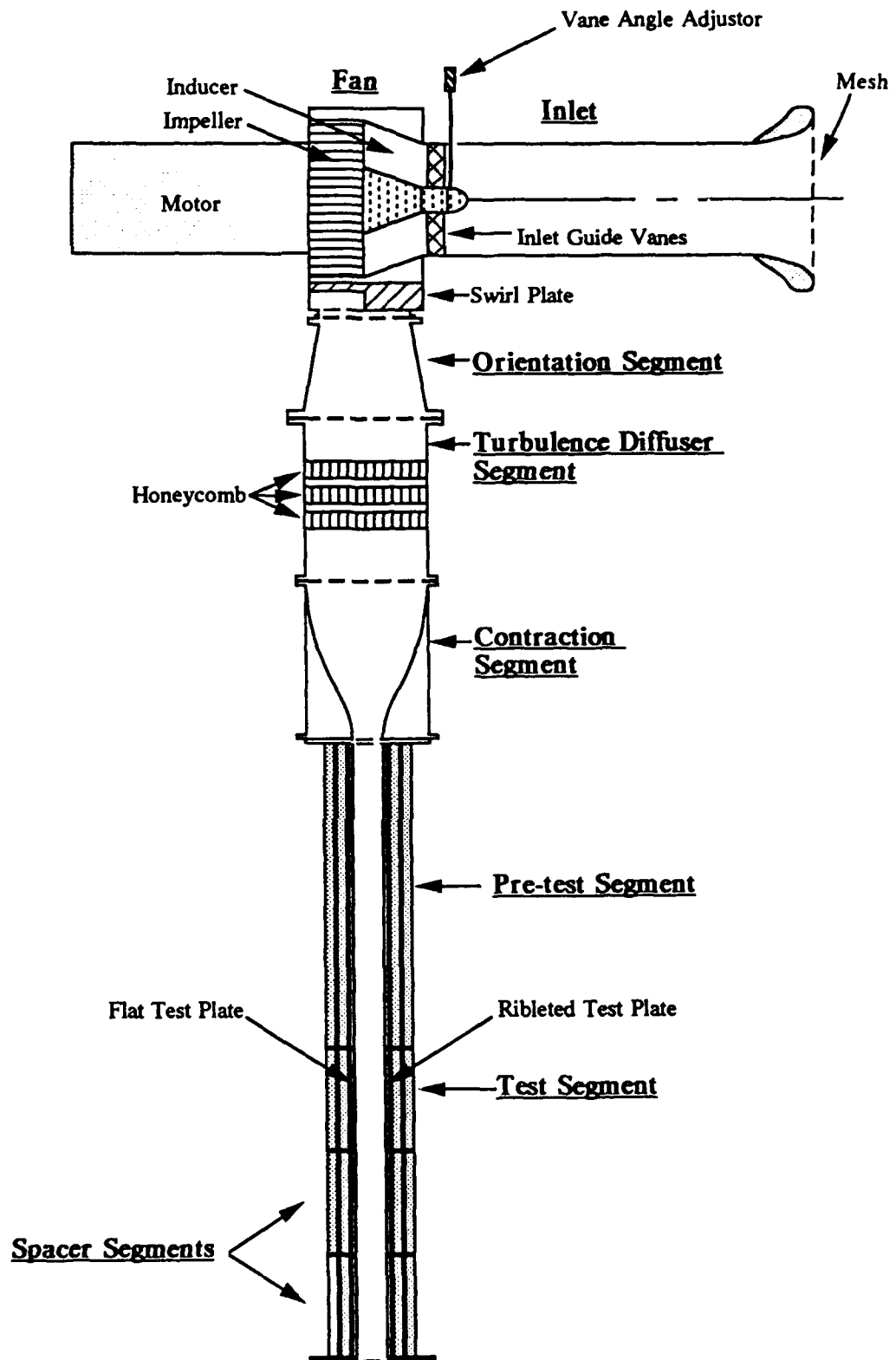
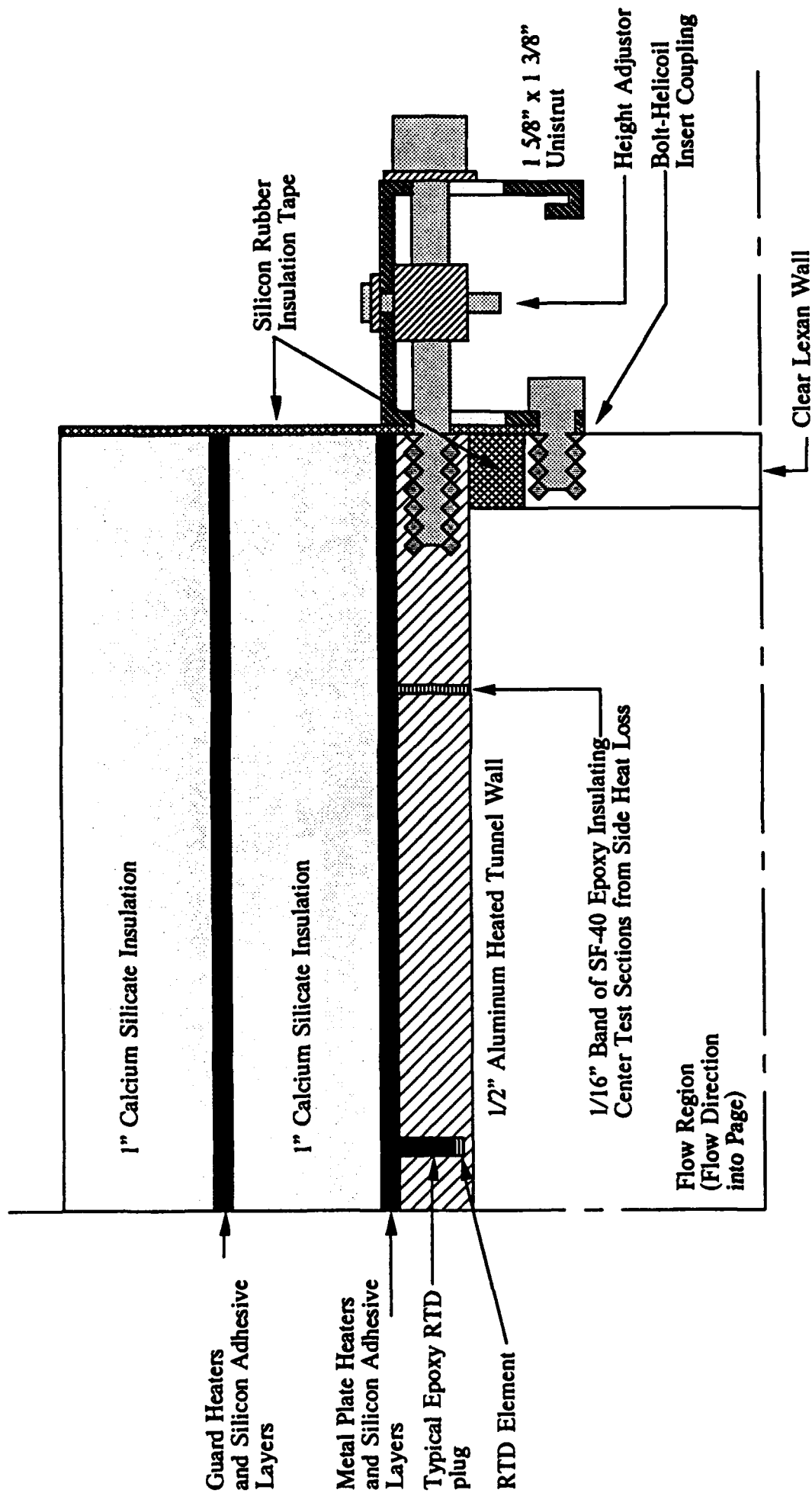


Figure 4.1. **Wind Tunnel Apparatus.** This plan view of the wind tunnel apparatus shows the inlet, the compressor, and the following segments: orientation, turbulence diffusion, contraction, pre-test, test, and the two spacer segments. The scale is 20:1.



Tunnel Quarter Cross Section: 1:1 Scale

Figure 4.2. Tunnel Quarter Cross Section. The above quarter cross section of the wind tunnel shows: the Unistrut tunnel frame, the clear Lexan wall, the Aluminum plate wall, and the two layers of heaters, insulation, and adhesive comprising its backing.

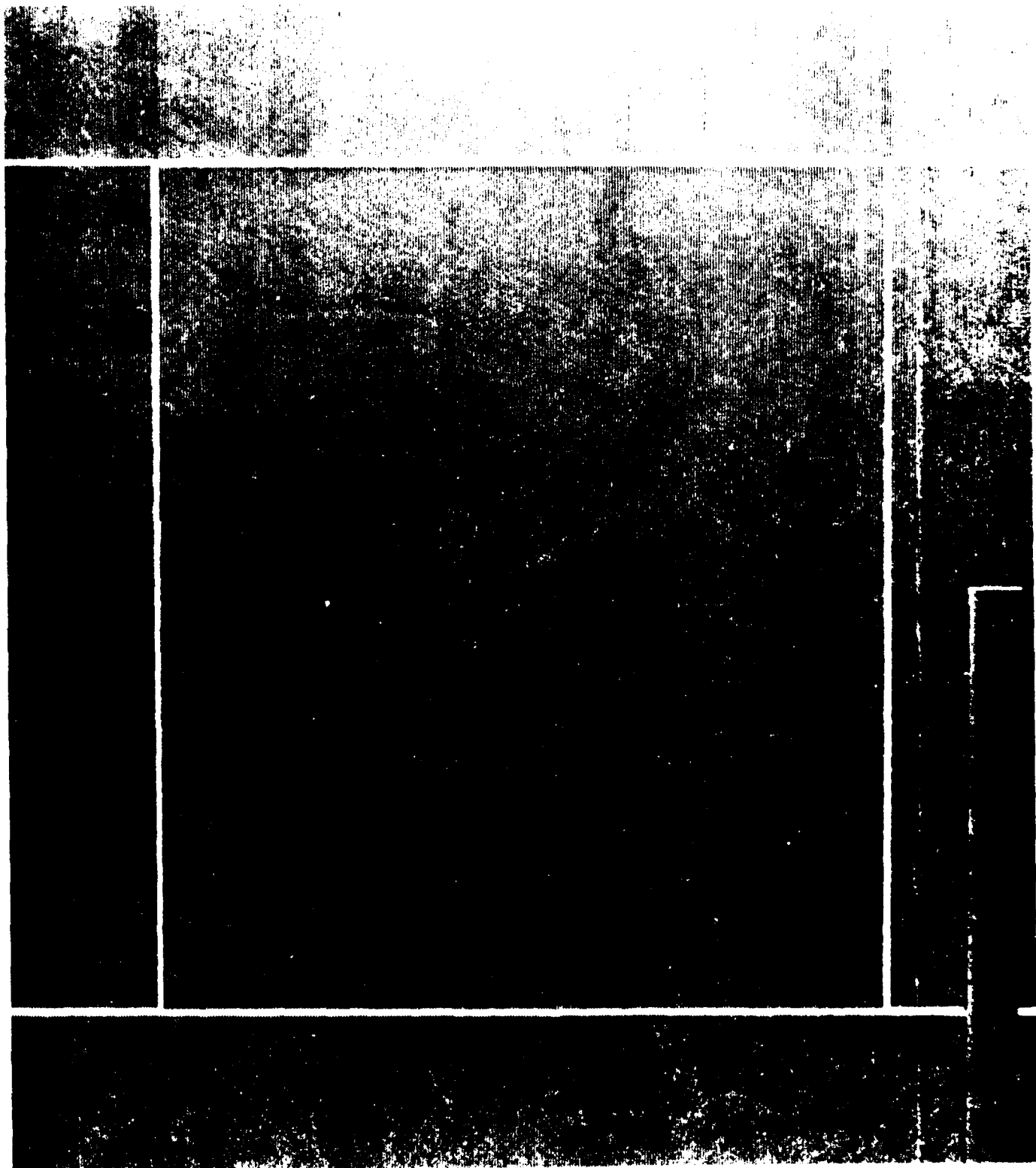


Figure 4.3. **Photograph of the Ribbled Test Plate.** This photograph shows a plan view of the ribbled test plate. The scale in inches can be seen on the ruler in the lower right. The thick white strips are the syntactic foam used to insulate the actual test section, the rectangular center section. All riblets were of uniformly good quality except for a row of three to the right of the test section, which show up as a wavy white line near the ruler.

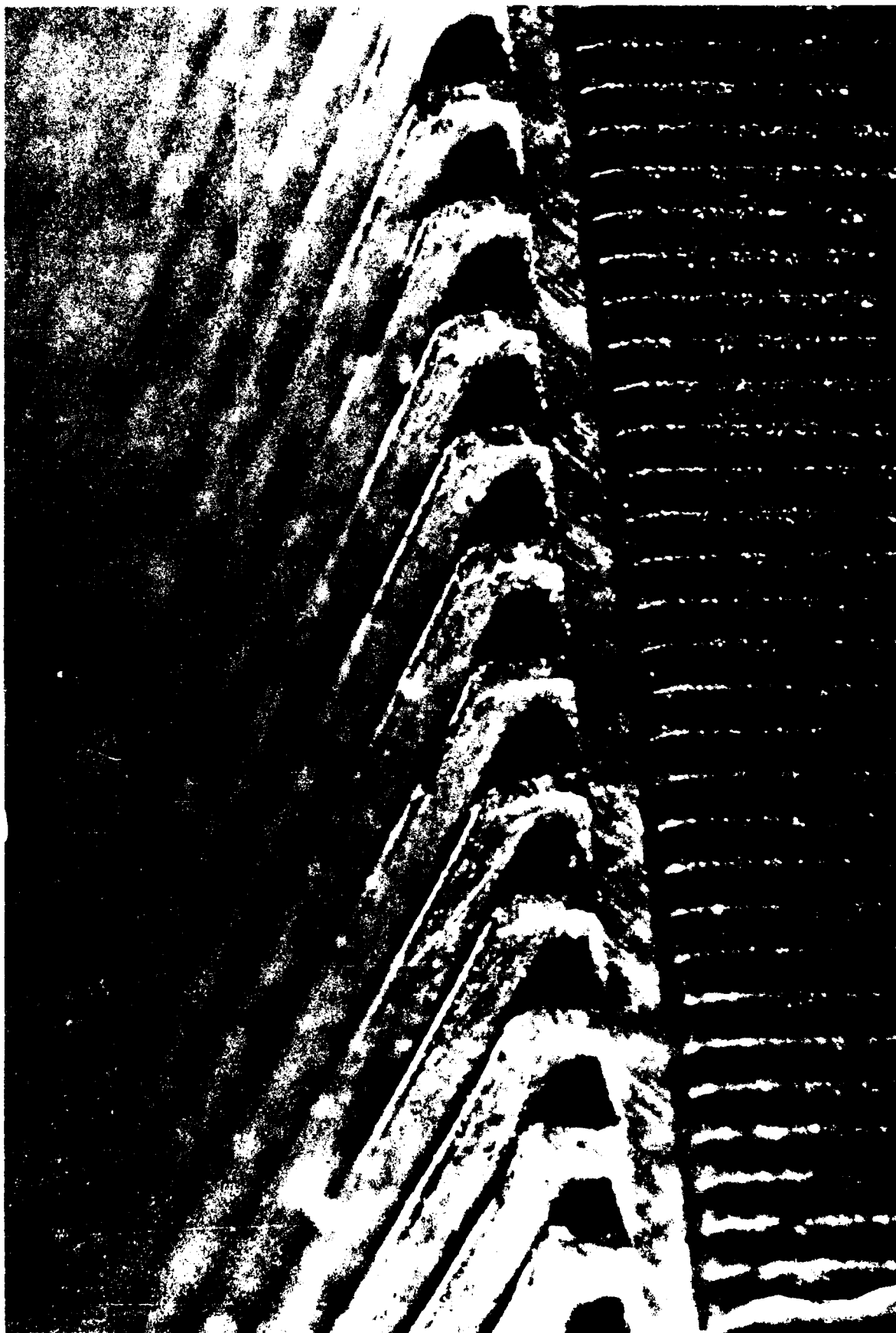


Figure 4.4. Photograph of the Leading Edge of the Ribbled Test Plate. This photograph of the riblets shows their uniformity. One ruler gradation is 10 mils.

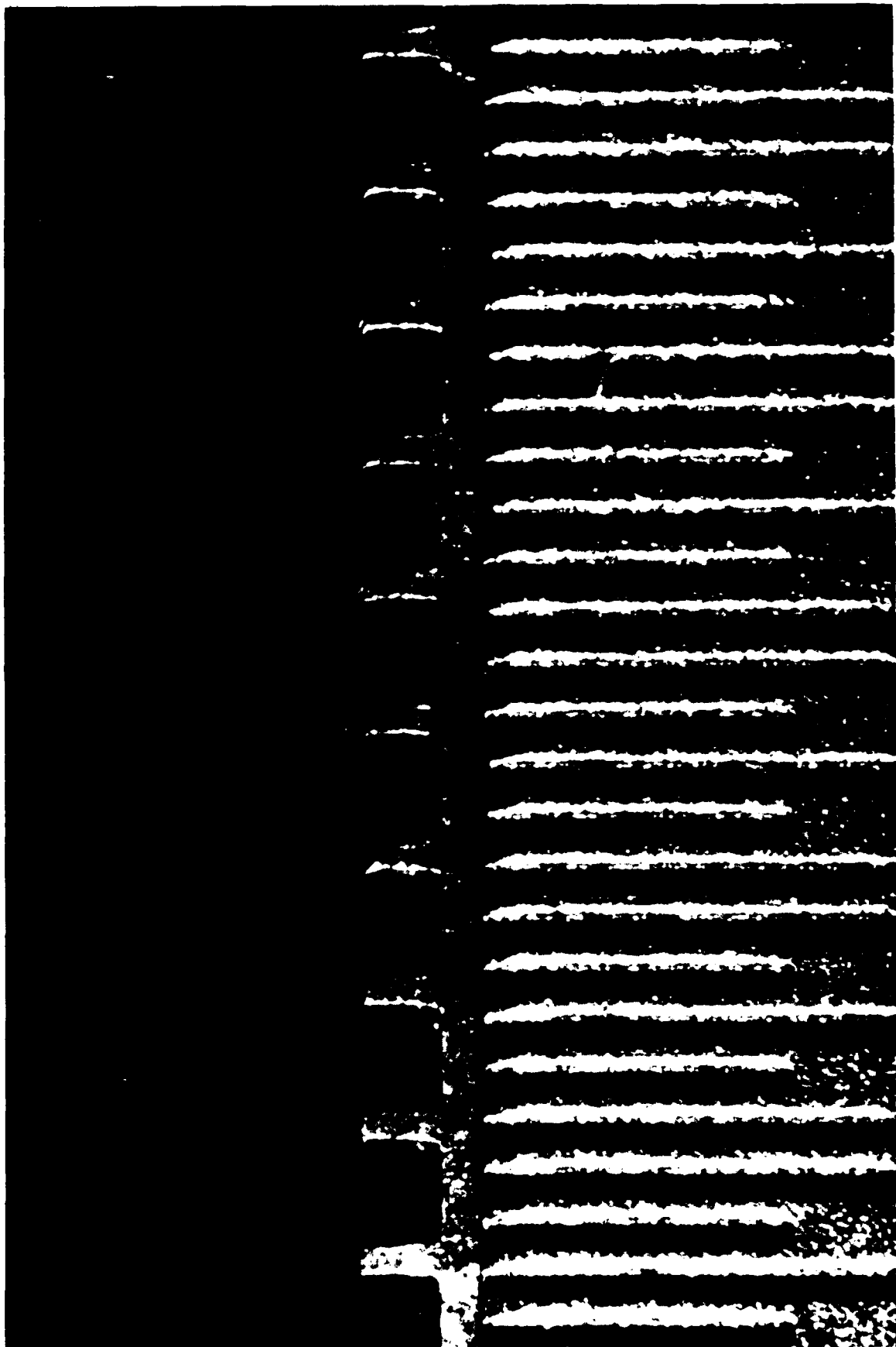


Figure 4.5. Photograph of the Riblet Cross Section. A cross section view of the leading edge of the ribleted test plate is seen above. One ruler gradation is 10 mils.

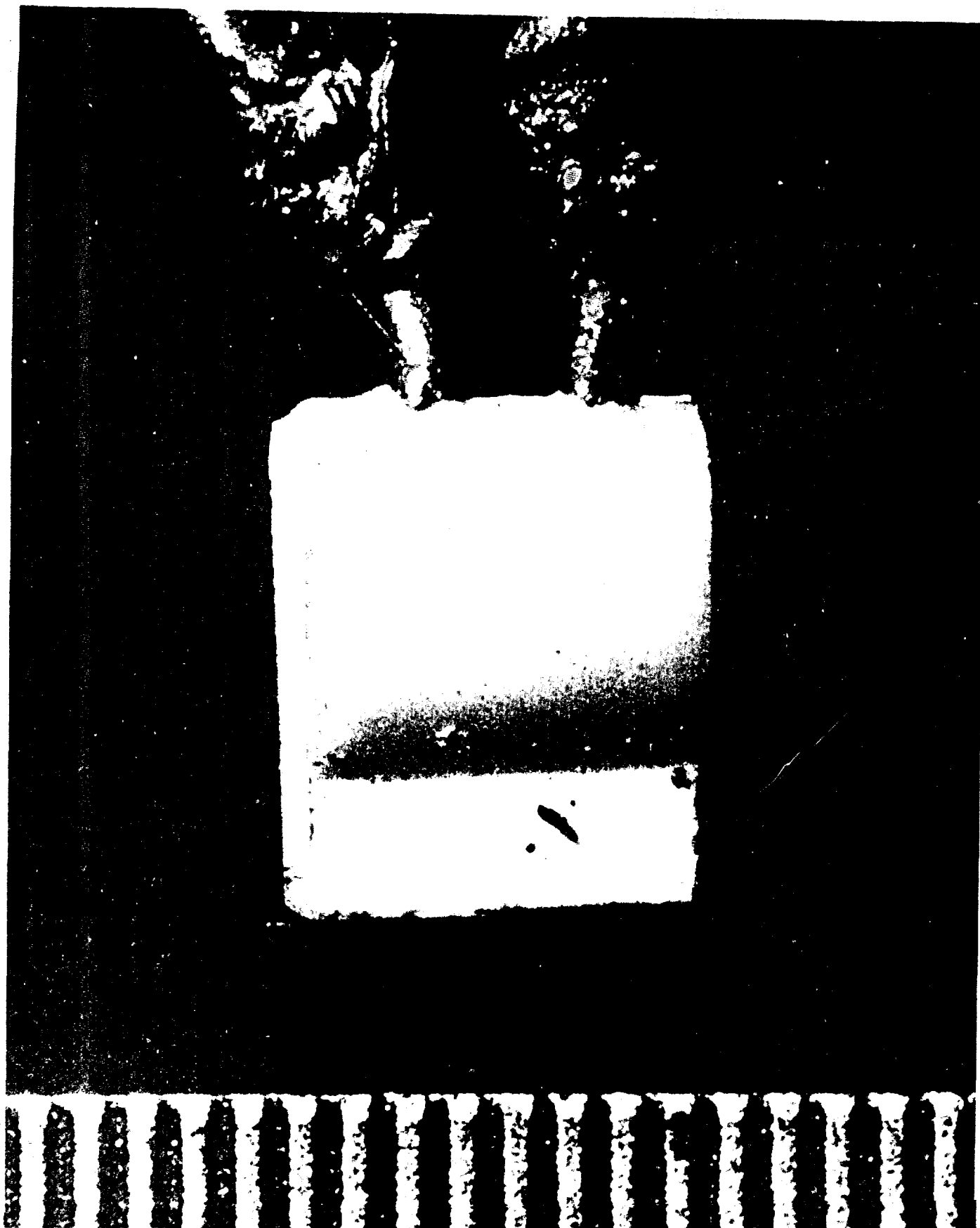


Figure 4.5 Thin Film RTD. This photograph shows one of the 140 thin film, platinum resistance temperature devices (RTDs) used in the experiment prior to its being set into an epoxy plug. One ruler gradation is 10 mils.

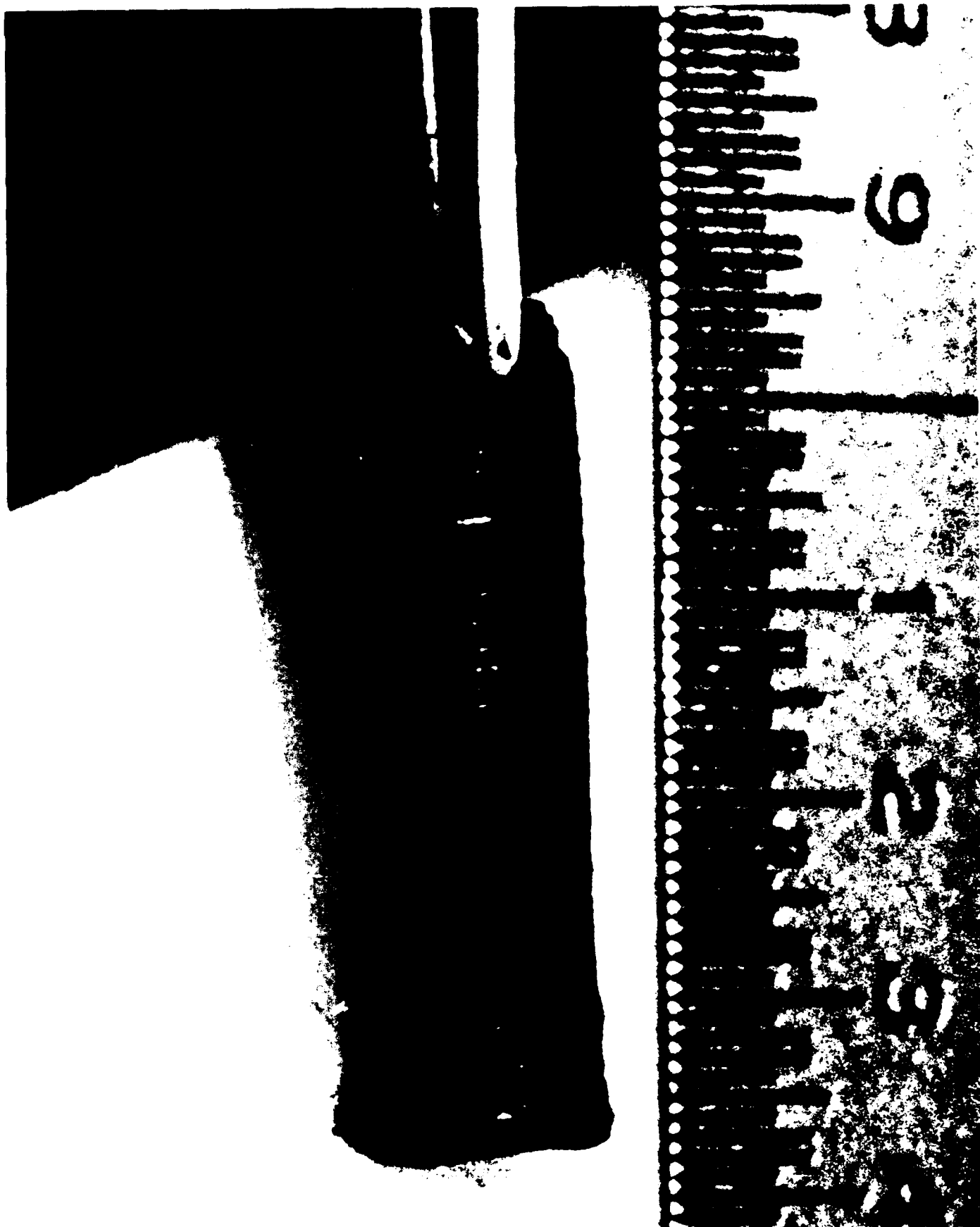


Figure 4.7. RTD in Epoxy Plug. This photograph shows one of the RTDs used in the experiment after being set into an epoxy plug. One ruler gradation is one tenth of an inch.

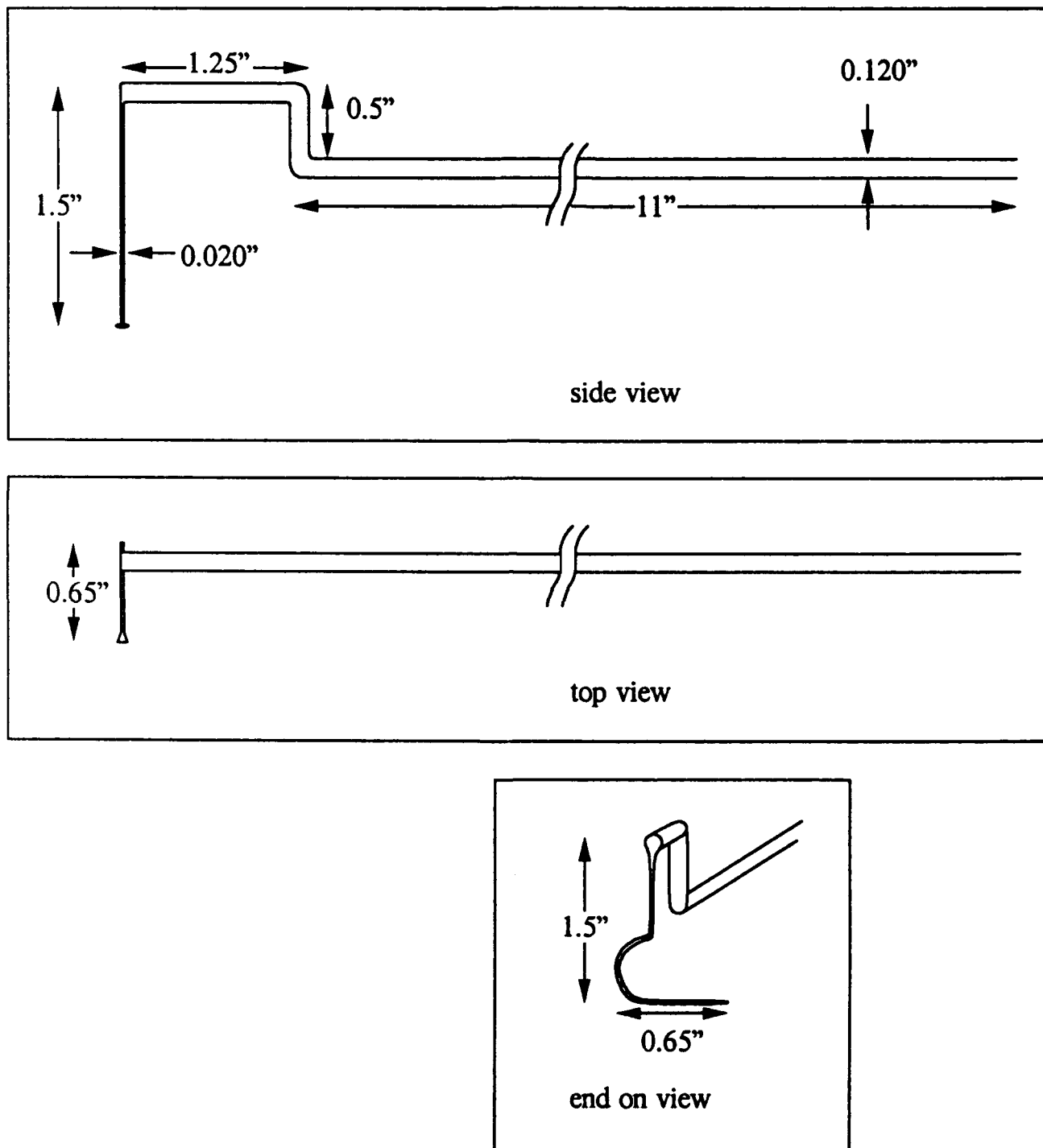


Figure 4.8. **Boundary Layer Probe.** The above three views show the dimensions of the total pressure probe used to measure boundary layer velocity. The probe was custom built to allow the possibility of accessing the boundary layer at any point in the tunnel cross section.



# Calibration Curve for RTD#1

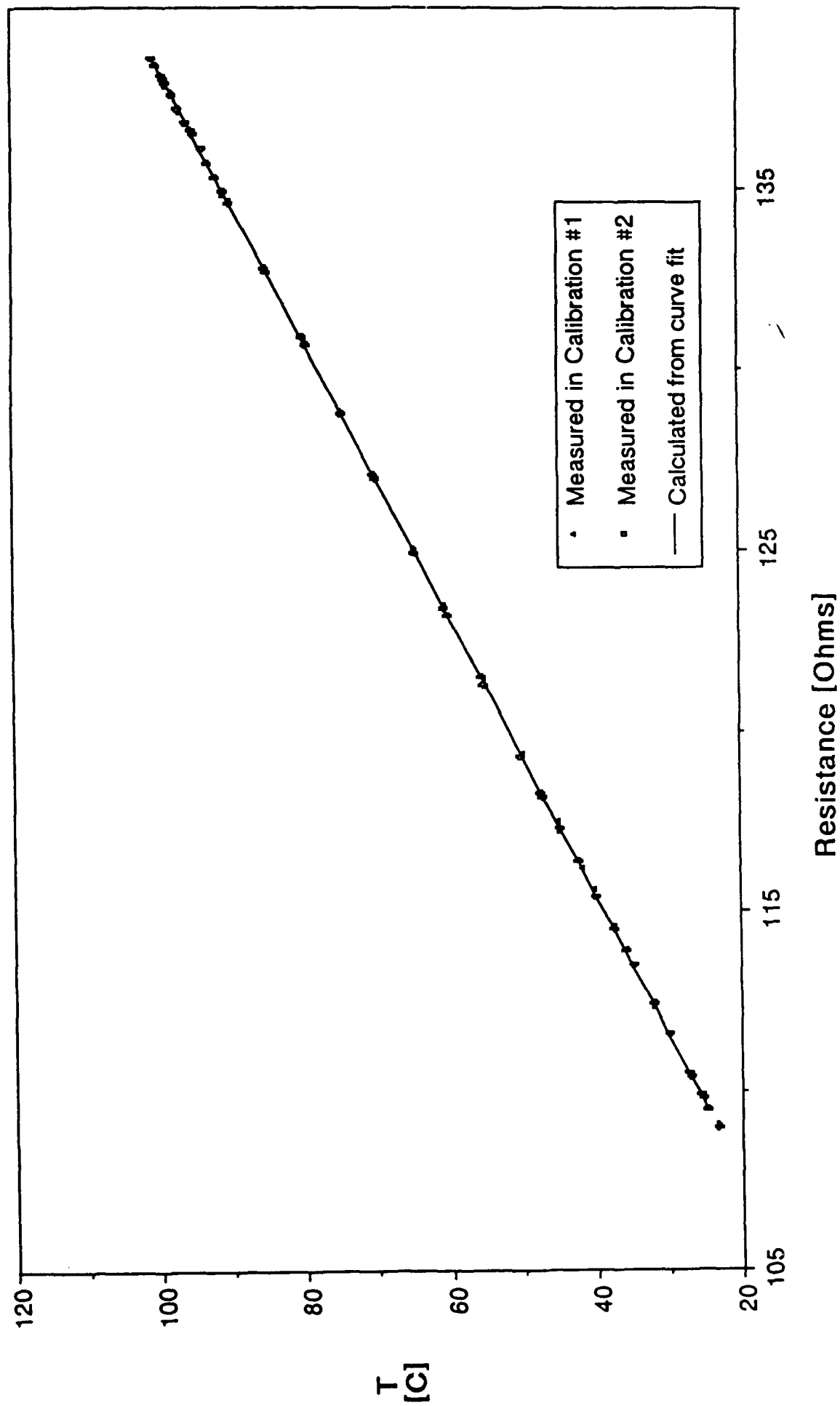


Figure 4.9. Calibration Curve for RTD #1. The above graph shows a typical RTD calibration. Both sets of calibration data are plotted along with the calibration curve as temperature in degrees Celsius versus sensor resistance in ohms. The results show no hysteresis, little scatter, strong repeatability, and good agreement of the data with the calibration curve.

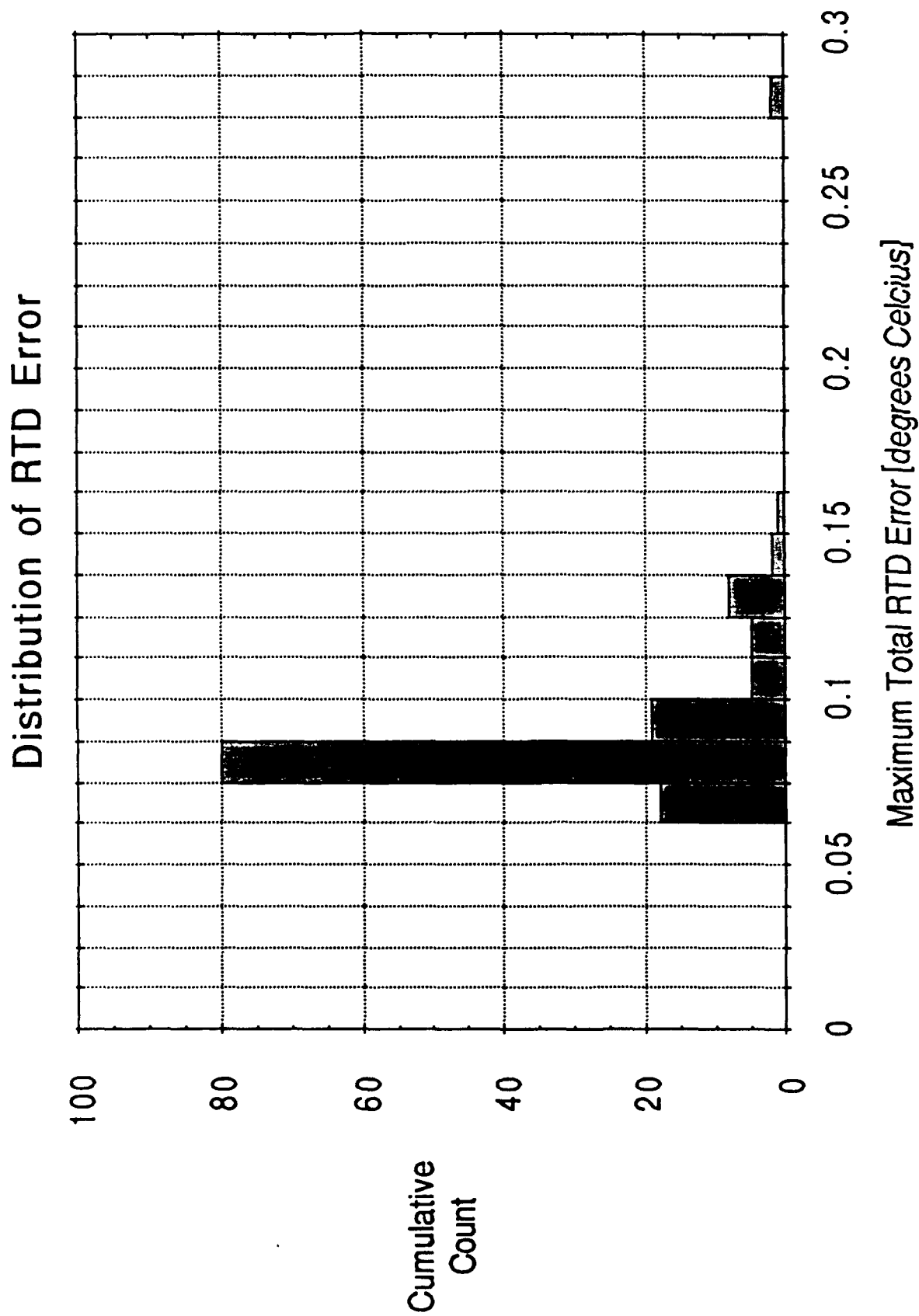


Figure 4.10. Distribution of RTD Error. The above graph shows the distribution of the maximum, total, combined experimental and statistical error in determining temperature from RTD resistance for each RTD based on the calibration results. As can be seen, the majority had error within the desired 0.1°C.

# Distribution of RTD Calibration Fit Reduced Chi-squared

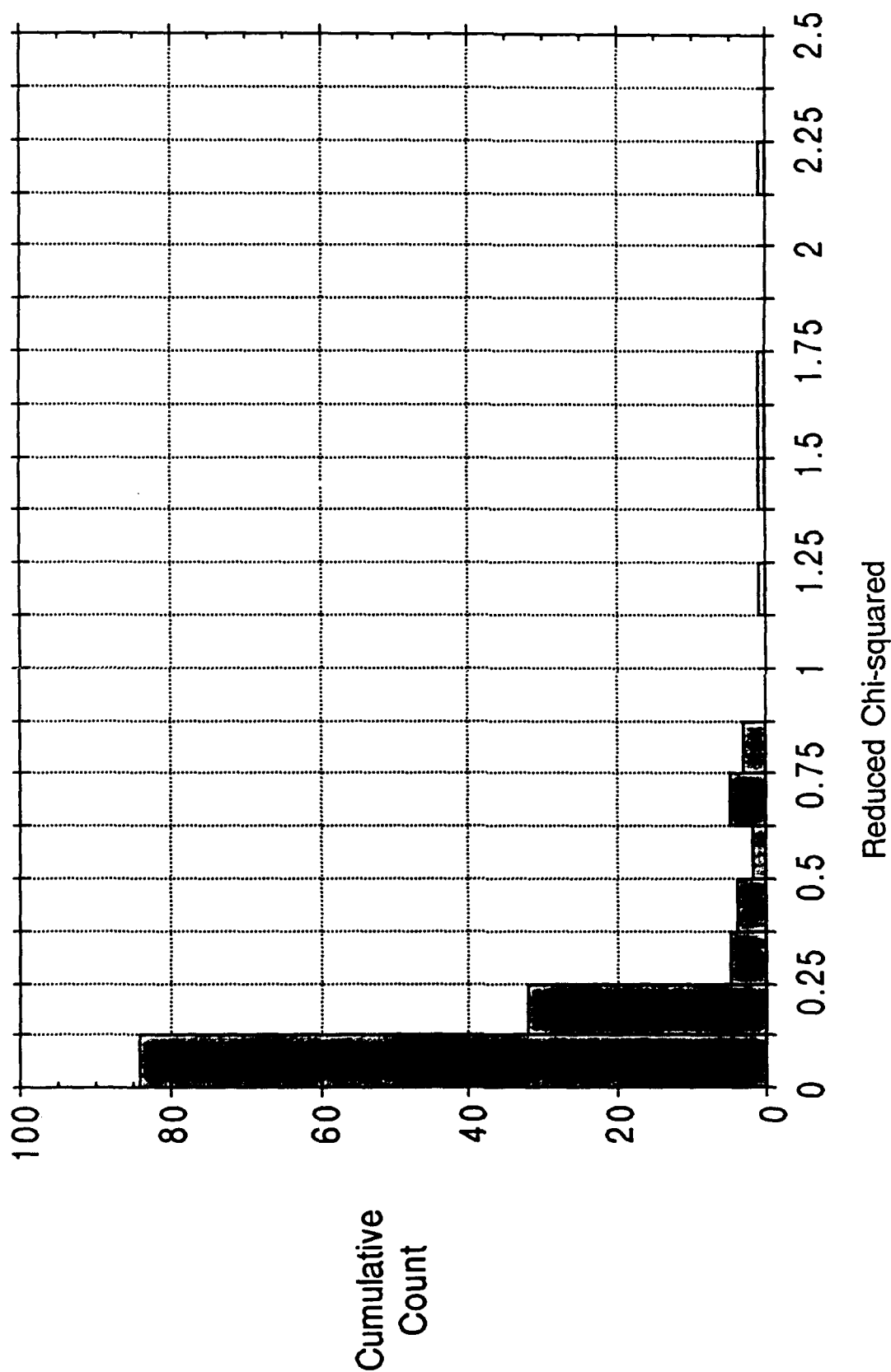


Figure 4.11. Distribution of RTD Chi-squared. The above graph shows the distribution of the reduced chi-squared of the calibration fits, a statistical test of the goodness of the fit. All but five RTDs had values less than one, the value usually taken as the benchmark near which a fit is considered statistically good.

## Coefficient of Friction versus Turbulent Reynolds Number over the Flat and Ribleted Test Plates

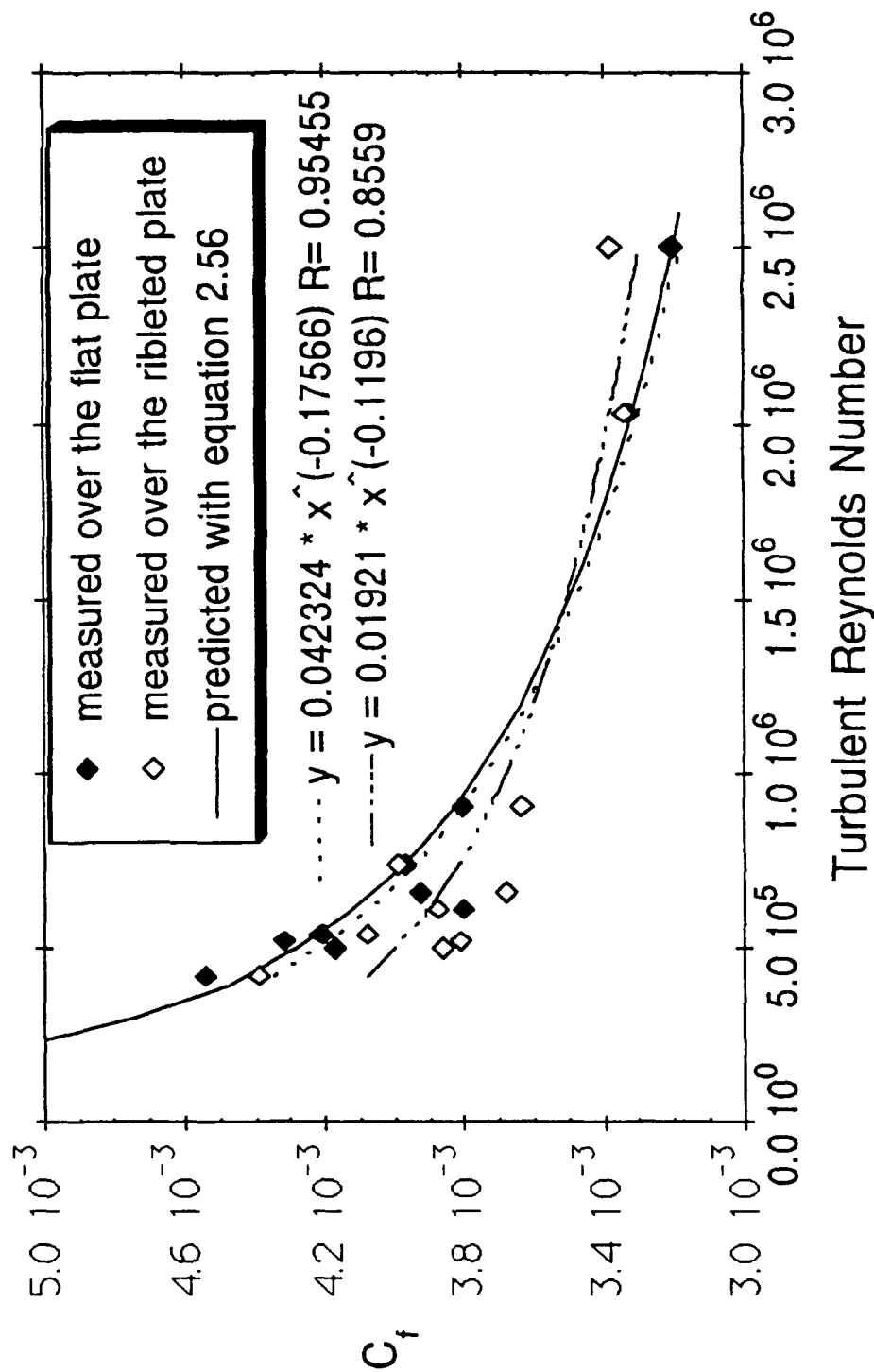


Figure 6.1. Effect of Riblets on Coefficient of Skin Friction. The above graph shows the effect of the riblets used in this experiment on the coefficient of skin friction versus turbulent Reynolds number. The measurements over the flat plate test section are plotted as black diamonds and those over the ribleted test section as clear diamonds. The values predicted by empirical formula 2.56 are plotted as the solid line. The values calculated from least squares fits of equation 6.10 to the flat plate and riblet data are plotted as dashed and dotted lines respectively. The results show good agreement of the flat plate values with predicted values, lower riblet skin friction for Reynolds numbers below 1.5 million and higher for above.

## Drag Reduction of Thin Element Riblets

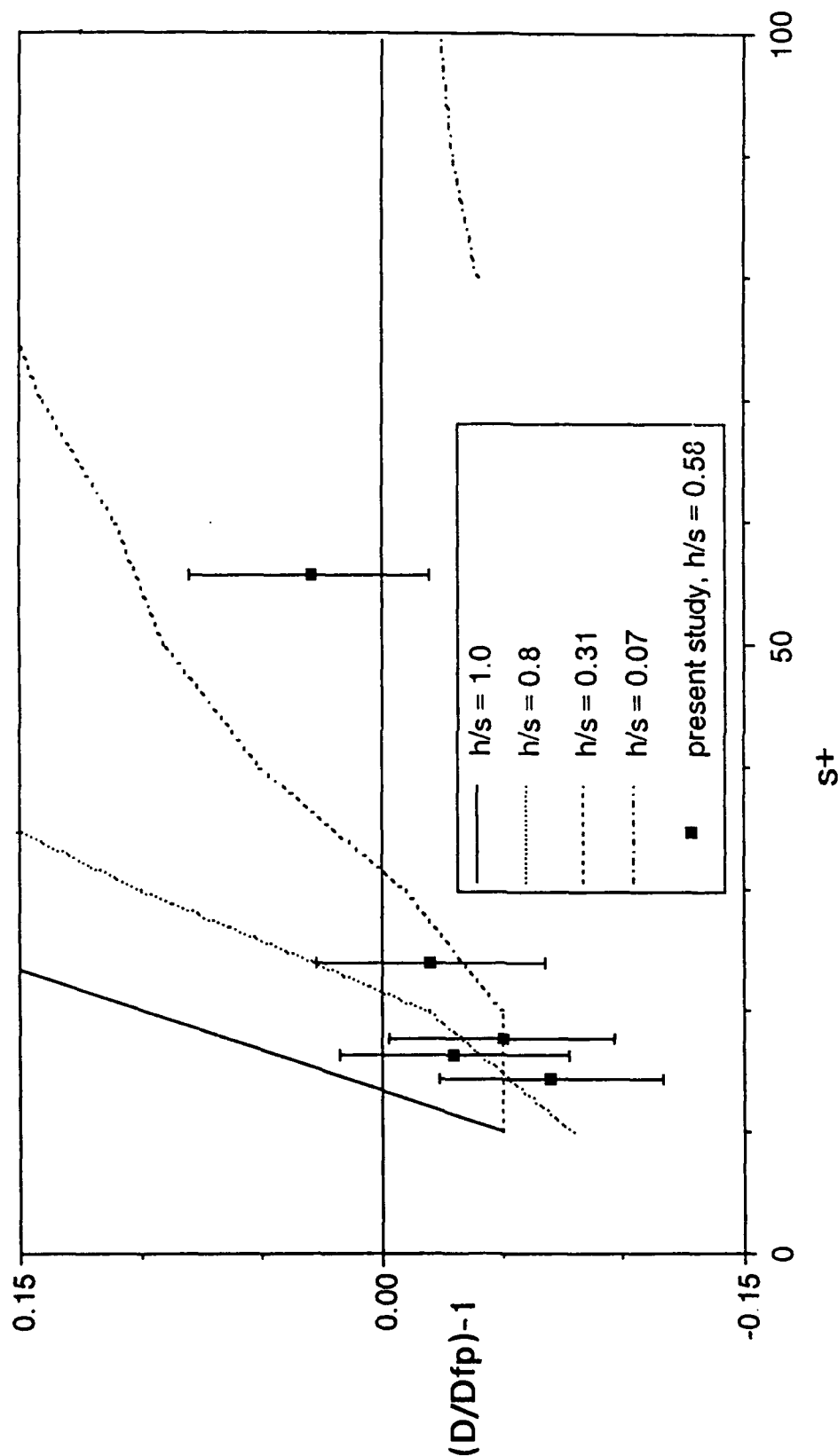


Figure 6.2. Drag Reduction of Thin Element Riblets. This graph shows the effect of the riblets used in this experiment on the coefficient of drag of the test sections versus riblet spacing in wall units. In addition, the four curves from Lazos and Wilkinson (1987) for thin element riblets of varying aspect ratio are plotted as in figure 2.4 for comparison. The results show drag reduction for spacing below 30, with maximum reduction of 7% at 15 wall units. The measurements in the drag reduction region agree closely with the results of Lazos and Wilkinson for riblets of comparable aspect ratio. However, in the region of drag increase the measured result was quite a bit lower than would be expected based on the prior results.

## Average Test Section Stanton Number versus Turbulent Reynolds Number for the Flat and Ribletted Plates

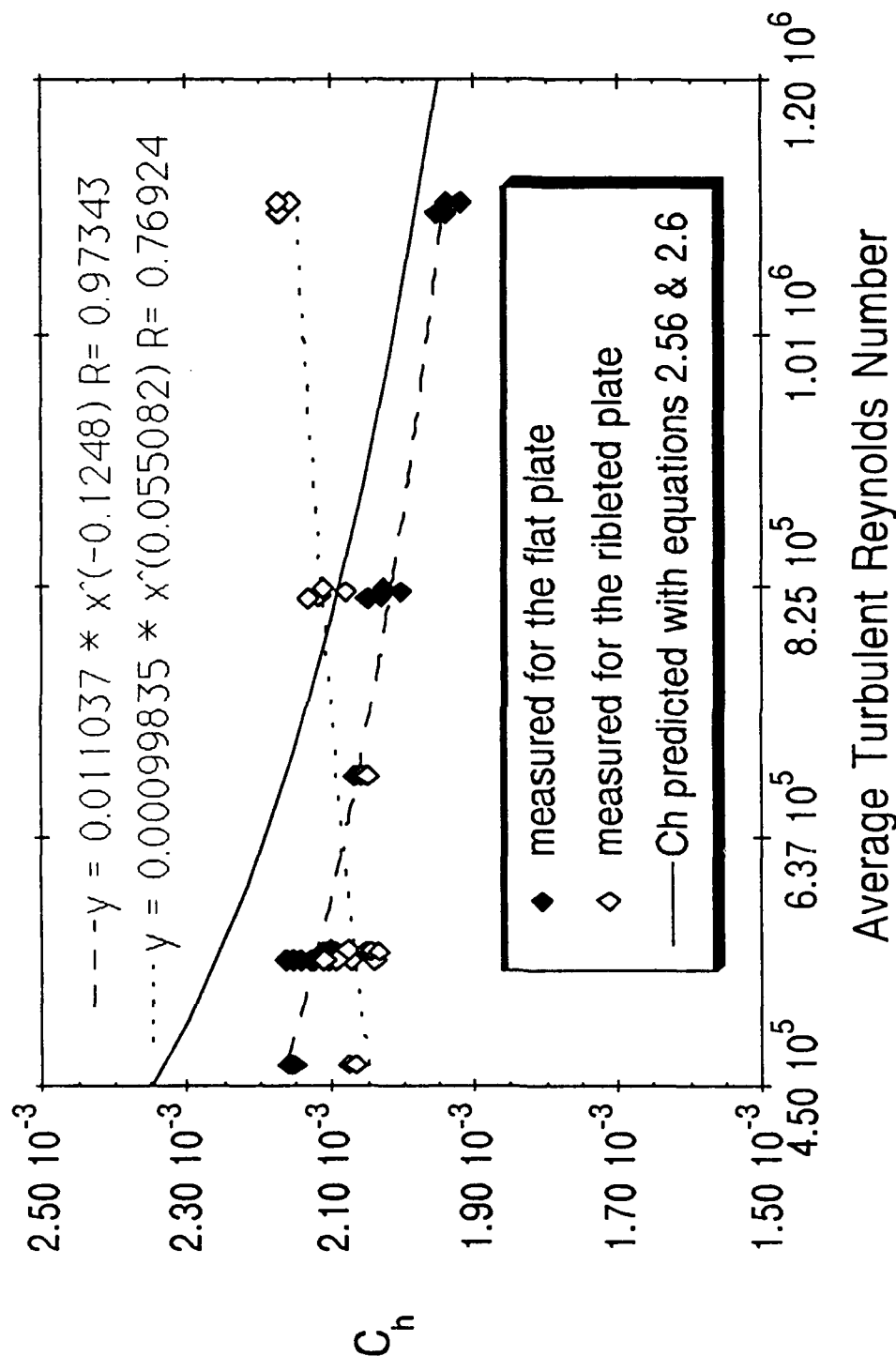


Figure 6.3. Average Test Section Stanton Number versus Turbulent Reynolds Number for the Flat and Ribletted Plates. This graph shows the effect of the riblets used in this experiment on the average coefficient of heat transfer of the test sections versus average turbulent Reynolds number. The values for the flat plate test section are plotted as black diamonds and the least squares power fit to them as a dashed line. Those over the ribletted test section are plotted as clear diamonds and the power fit to them as a dotted line. The values predicted by the use of equations 2.56 and 2.64 are plotted as a solid line. The results show that the flat plate measurements were uniformly lower than predicted values but within the 4% error margin of the predictions and that the ribletted plate had lower heat transfer for Reynolds number below 650,000 and higher for above.

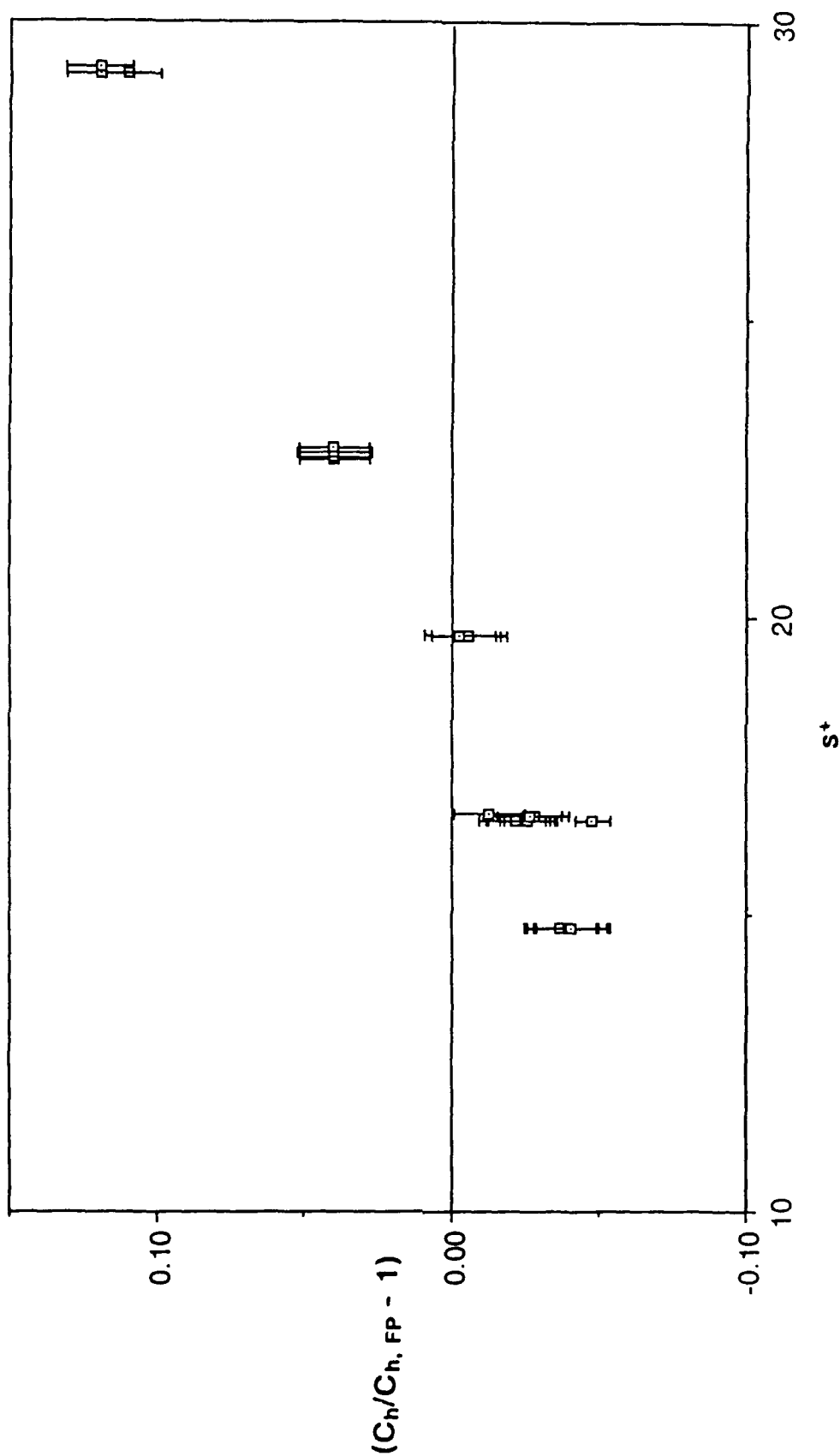


Figure 6.4. Effect of Riblets on Integral Stanton Number. The graph above shows the effect of the riblets used in this experiment on the total heat transfer coefficient of the test sections versus riblet spacing in wall units. The results show heat transfer reduction below  $s^+$  of 20 with maximum reduction of 5% at 15 wall units. The general trends of the effect of riblets on heat transfer are the same as those on drag.

## Reynolds Analogy Factor Variation with Reynolds Number

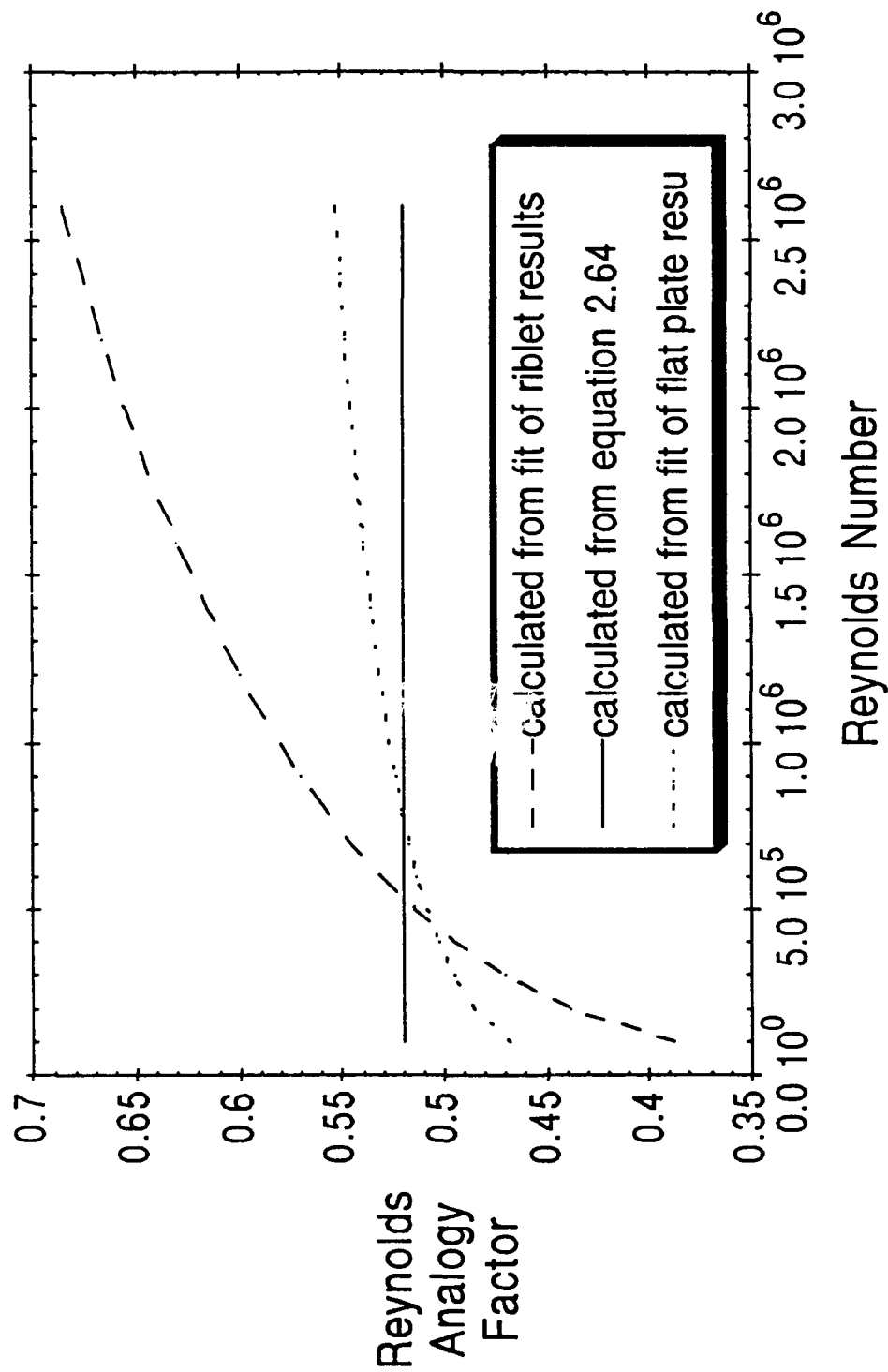


Figure 6.5. Reynolds Analogy Factor Variation with Reynolds Number. The graph above shows the variation of the Reynolds analogy factor, the ratio of the Stanton number to the coefficient of skin friction, calculated from the least squares power fits of the data for the coefficients over the flat and ribletted test sections as well as from equation 2.64. The variation of the flat plate factor is within its error range of the constant value calculated from equation 2.64. The factor over the ribletted test section rises strongly with Reynolds number. Below about 500,000, the factor is less for the ribletted plate than for the flat plate.



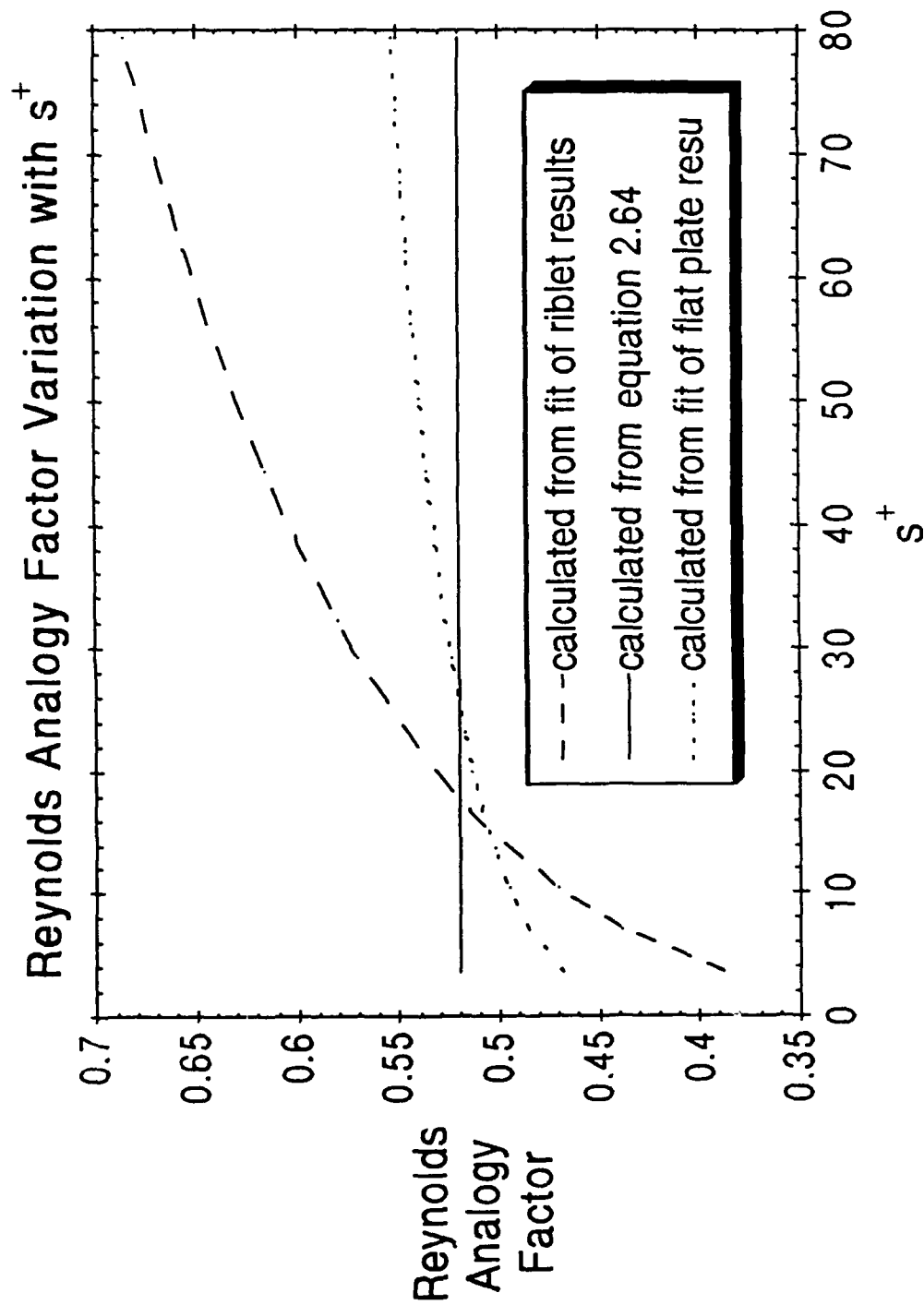


Figure 6.6. Reynolds Analogy Factor Variation with  $s^+$ . The graph above shows the variation of the Reynolds analogy factor, the ratio of the Stanton number to the coefficient of skin friction, calculated from the least squares power fits of the data for the coefficients over the flat and ribletted test sections as well as from equation 2.56 with riblet spacing in wall units. The riblet factor increases from approximately the flat plate value at  $s^+$  of 20 to almost 1.4 times the flat plate value at  $s^+$  of 80.

Boundary Layer Thickness versus Reynolds Number for Flat and Ribletted Plates

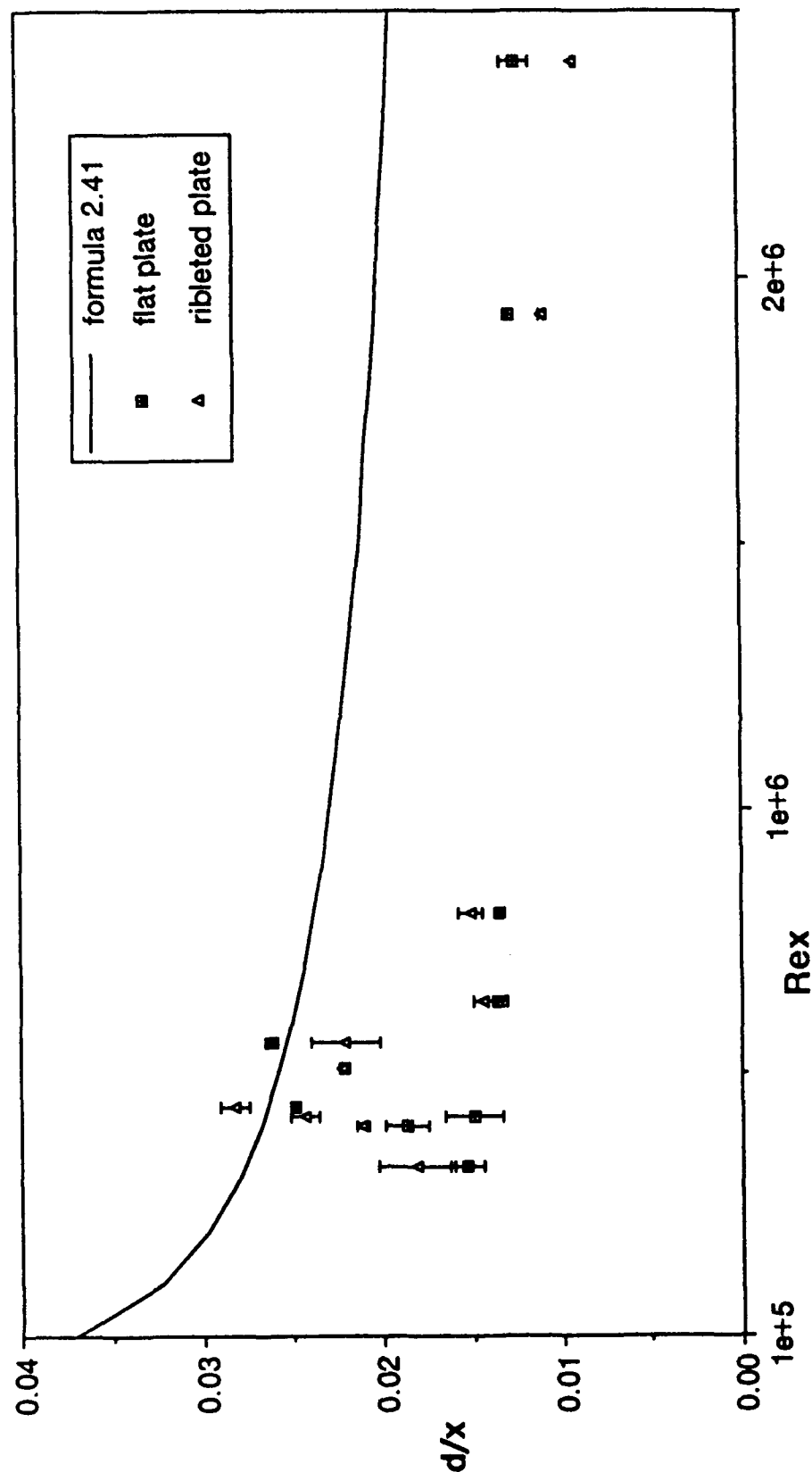


Figure 10.1. Boundary Layer Thickness versus Reynolds Number for Flat and Ribletted Plates. The graph above shows the boundary layer thickness calculated via interpolation from the mean velocity profiles versus Reynolds number for the flat and ribletted plates in addition to the empirical predictions of formula 2.41. As can be seen, the flat and ribletted plate results are quite close, the data show large scatter at low Reynolds number, and the measured and empirically predicted results differ by a substantial amount.

# Displacement Thickness versus Reynolds Number for Flat and Ribletted Plates

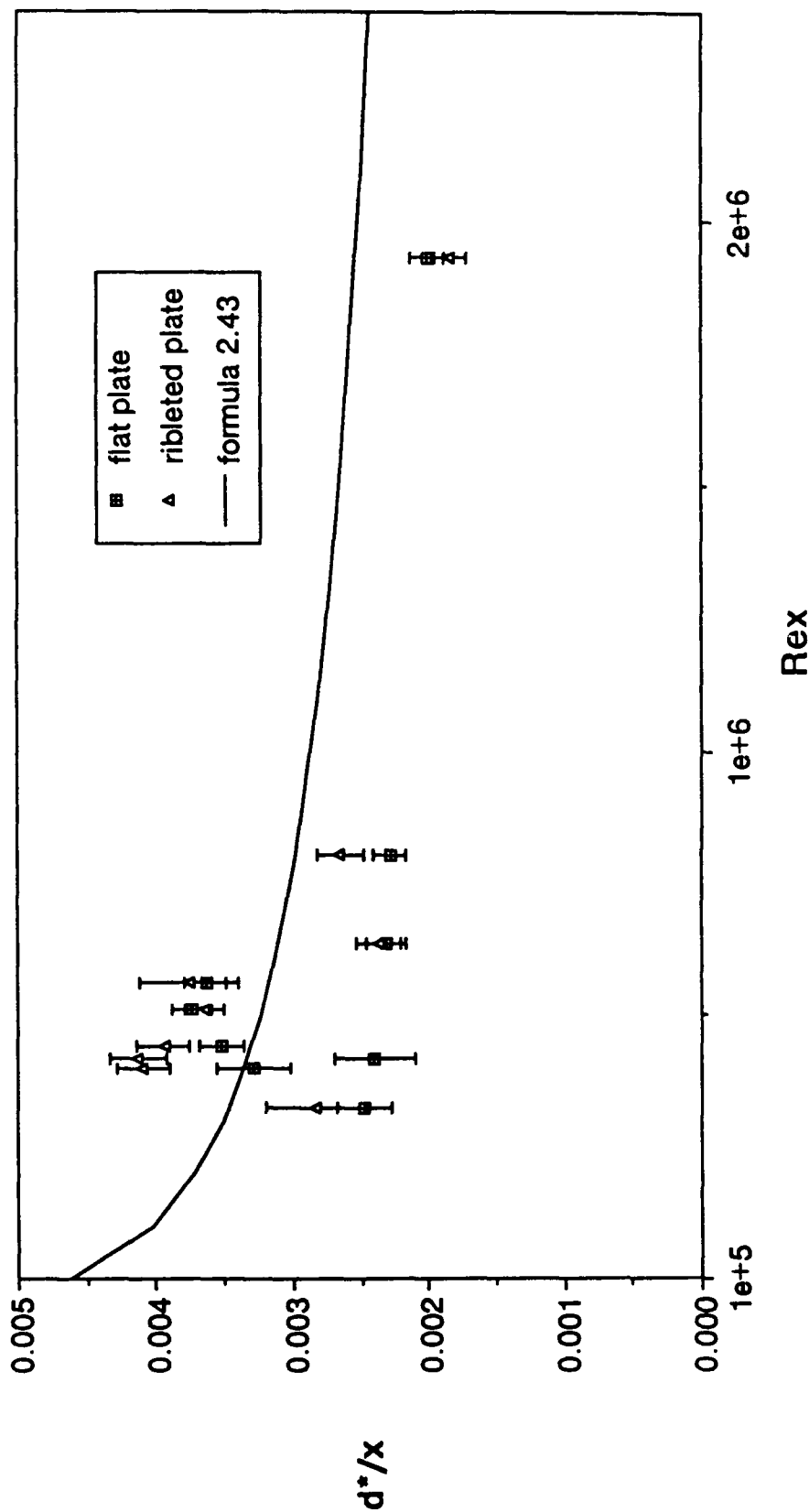


Figure 10.2. Displacement Thickness versus Reynolds Number for Flat and Ribletted Plates. The graph above shows the displacement thickness calculated via numerical integration of the mean velocity profiles versus Reynolds number for the flat and ribletted plates in addition to the empirical predictions of formula 2.43. The results echo the trends of the boundary layer thickness versus Reynolds number results almost exactly.

# Momentum Thickness versus Reynolds Number for Flat and Ribleted Plates

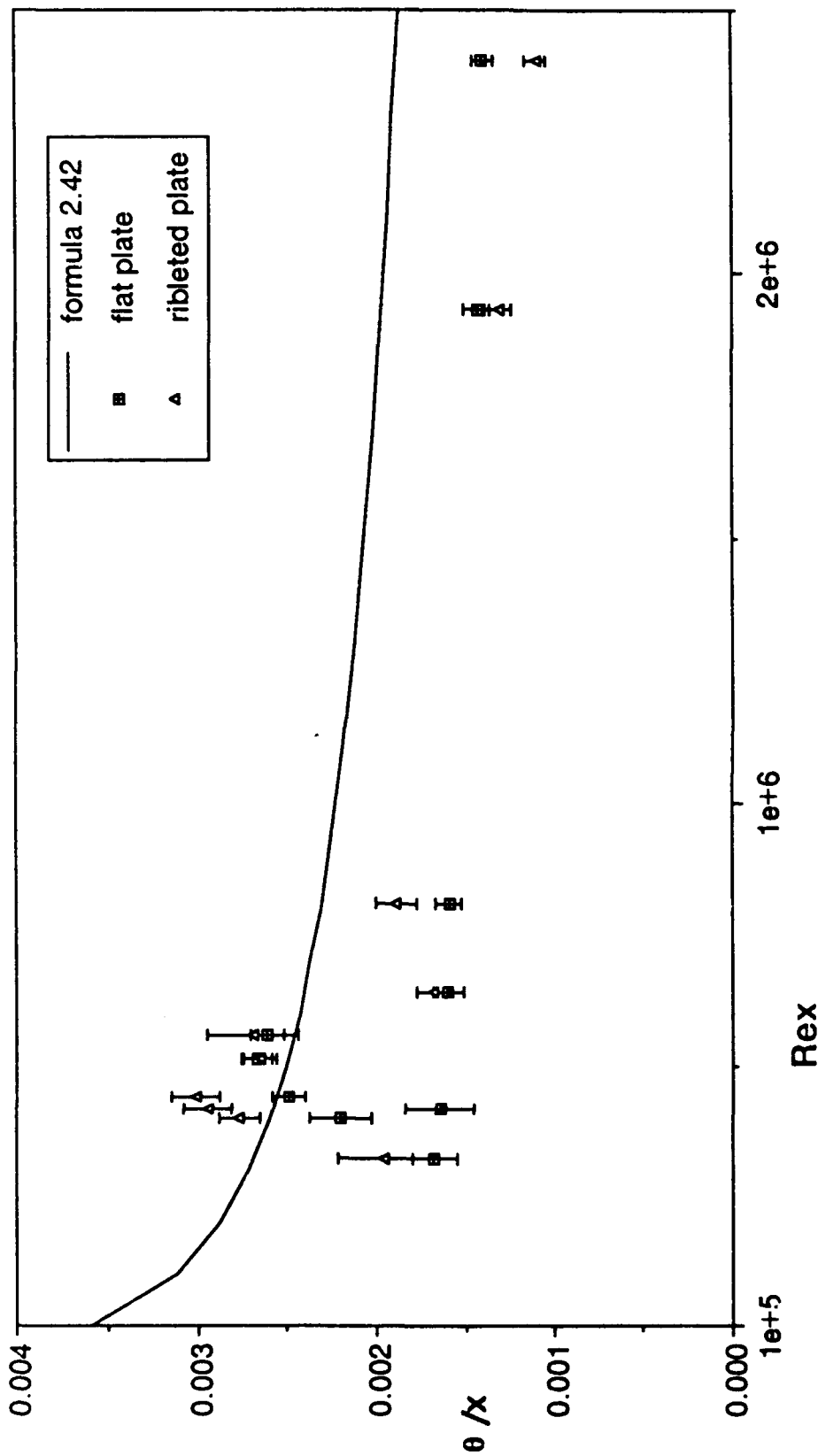


Figure 10.3. Momentum Thickness versus Reynolds Number for Flat and Ribleted Plates. The graph above shows the momentum thickness calculated via numerical integration of the mean velocity profiles versus Reynolds number for the flat and ribleted plates in addition to the empirical predictions of formula 2.42. The results echo the trends of the variation of the boundary layer and displacement thicknesses versus Reynolds number almost exactly.

# Test of Velocity Profile Repeatability @ a1, 10.88 m/s

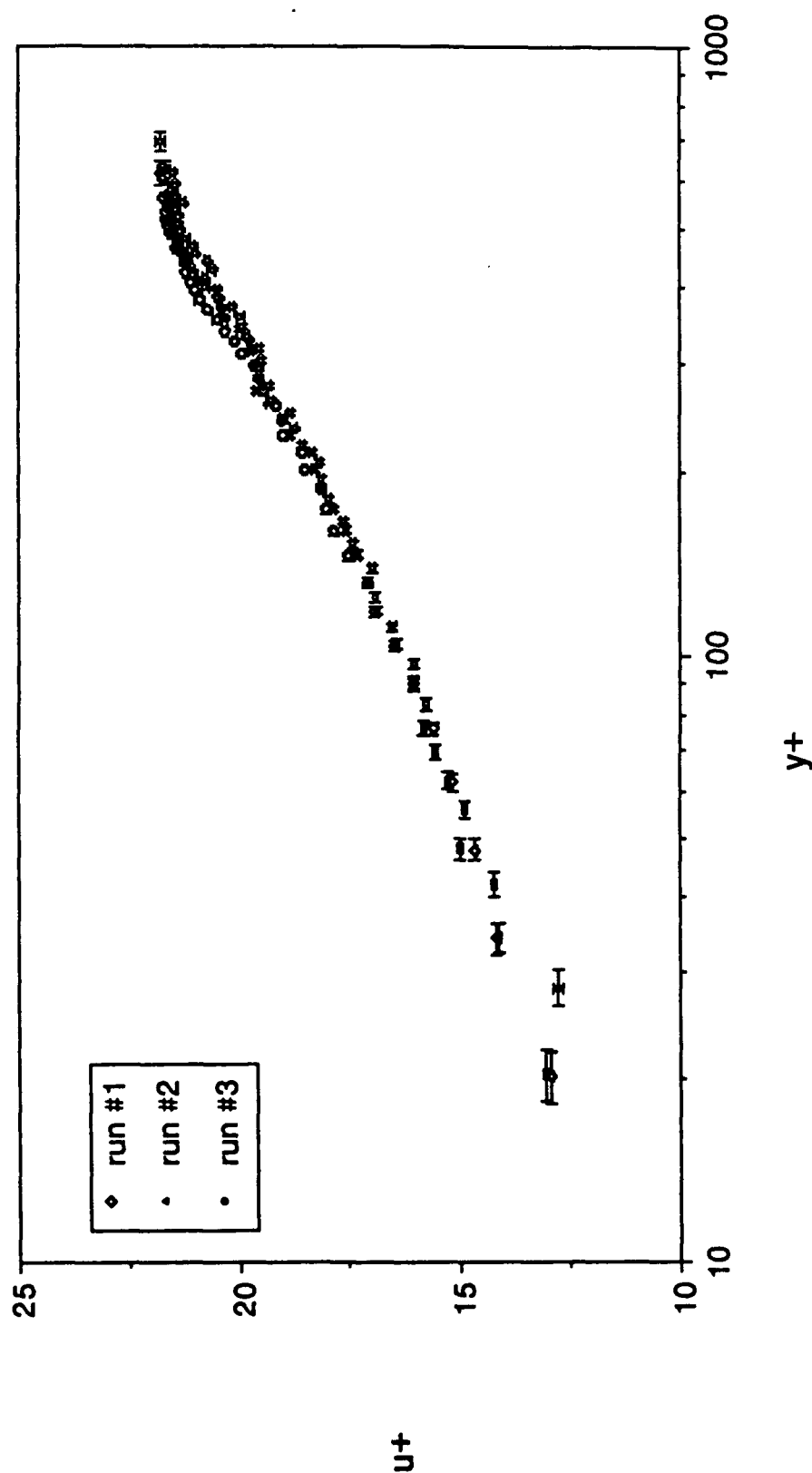


Figure 10.4. Test of Velocity Profile Repeatability. The graph above shows the results of three boundary layer traversals in the same position at the same freestream velocity but on different days plotted as velocity versus distance from the wall both in wall units. The results show low scatter and excellent repeatability.

### Validation of Velocity Profile Analysis Program: Comparison of Wake Law Generated Data and Curve Fit

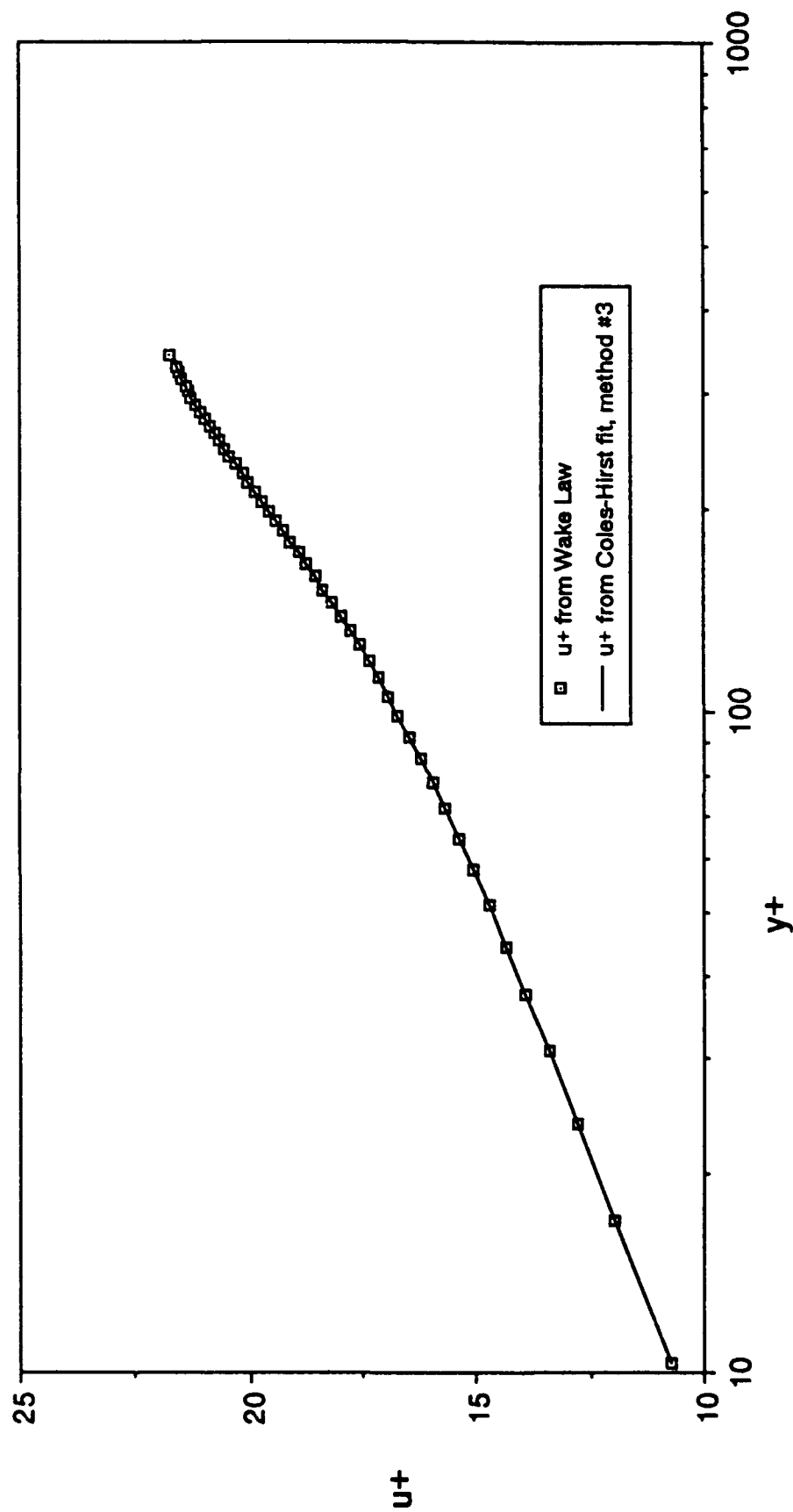
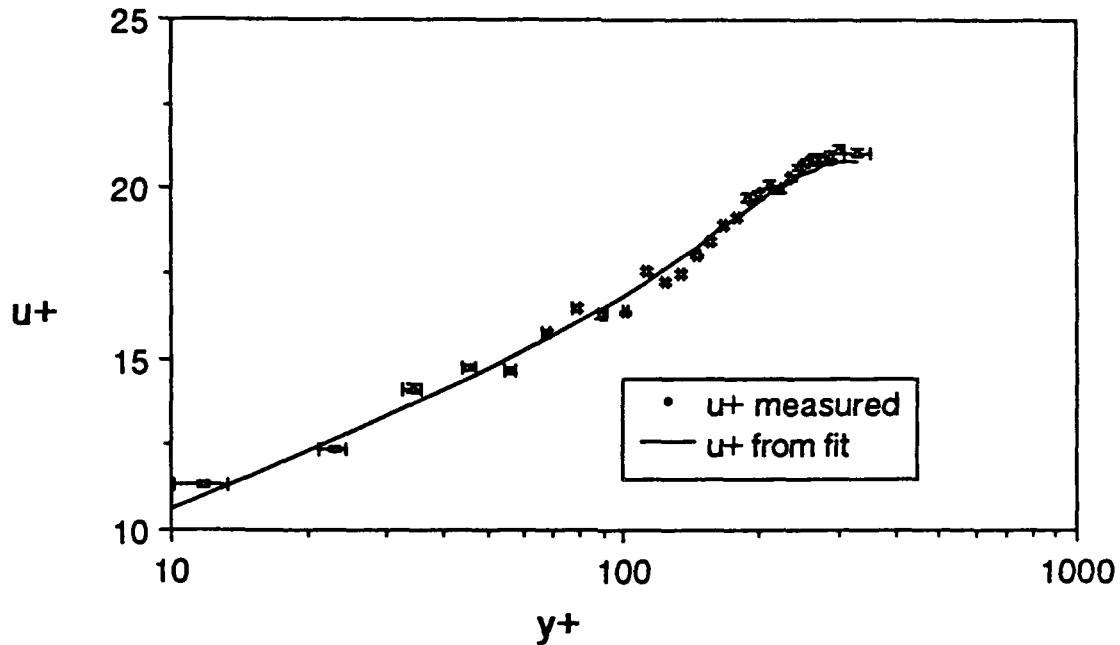
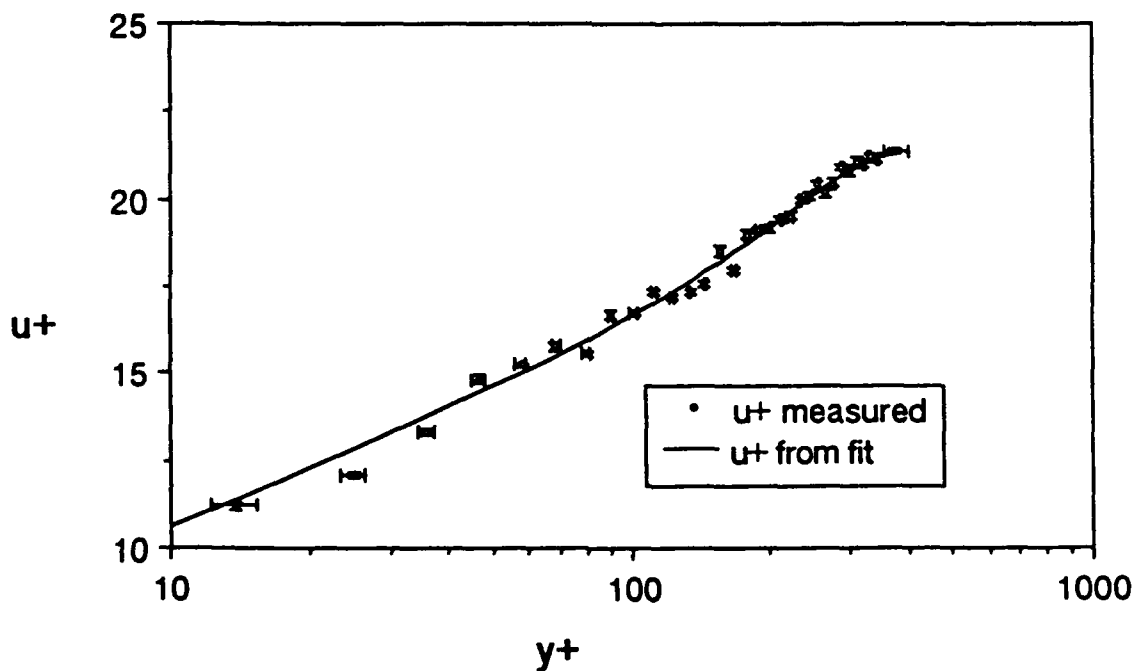


Figure 10.5. Validation of Velocity Profile Analysis Program. The above graph shows a plot of a dummy set of velocity profile data generated from the wake law and the curve fit calculated according to Coles-Hirst method 3 from this data. The results clearly validate the accuracy of the analysis program.

**Profile 3312.a1: Mean Velocity Profile Fore of the Flat Plate Test Section at Freestream Velocity of 8.41 m/s**

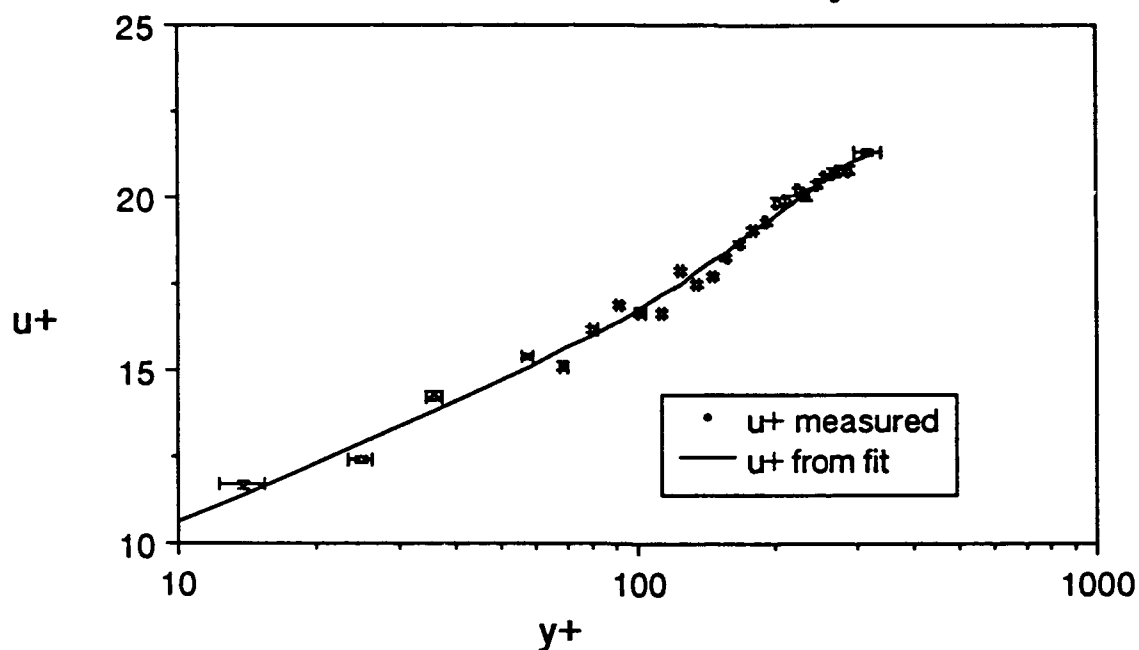


**Profile 3312.a2: Mean Velocity Profile Aft of the Flat Plate Test Section at Freestream Velocity of 8.41 m/s**



**Figure 10.6. Mean Velocity Profiles Fore and Aft of the Flat Test Section at 8.41 m/s.** The above two graphs show the mean velocity profiles measured fore and aft of the flat plate test section and their fits calculated according to Coles-Hirst method 3 at a freestream velocity of 8.41 m/s.

**Profile 3312.b1: Mean Velocity Profile Fore of the Ribleted Plate Test Section at Freestream Velocity of 8.41 m/s**



**Profile 3312.b2: Mean Velocity Profile Aft of the Ribleted Plate Test Section at Freestream Velocity of 8.41 m/s**

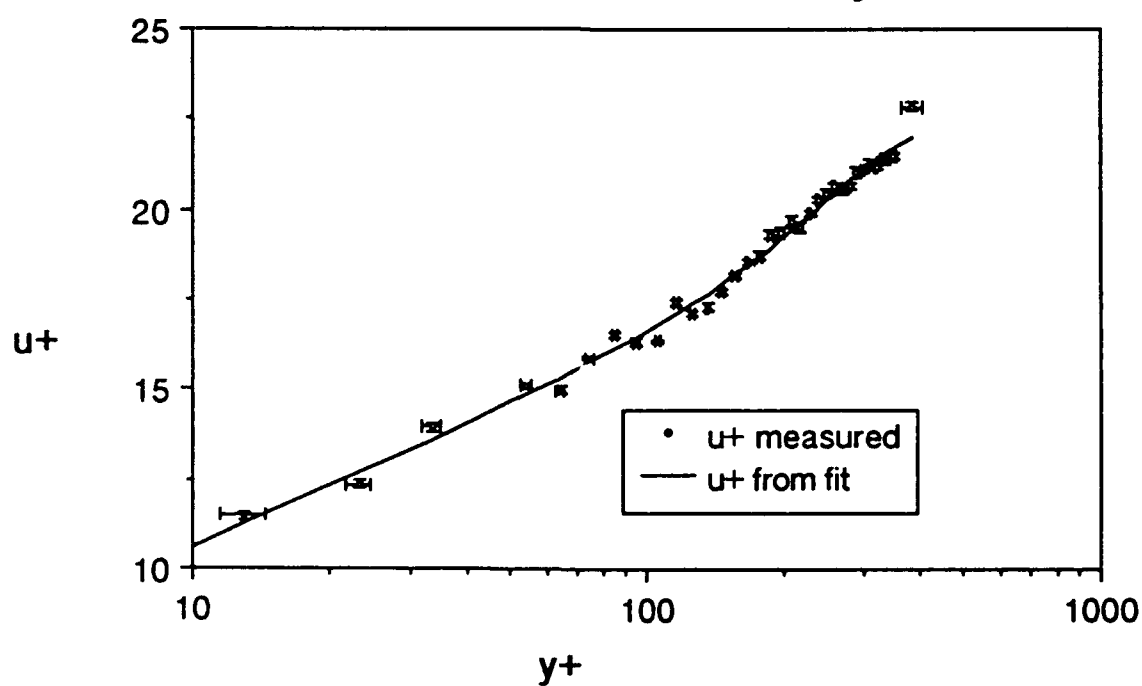
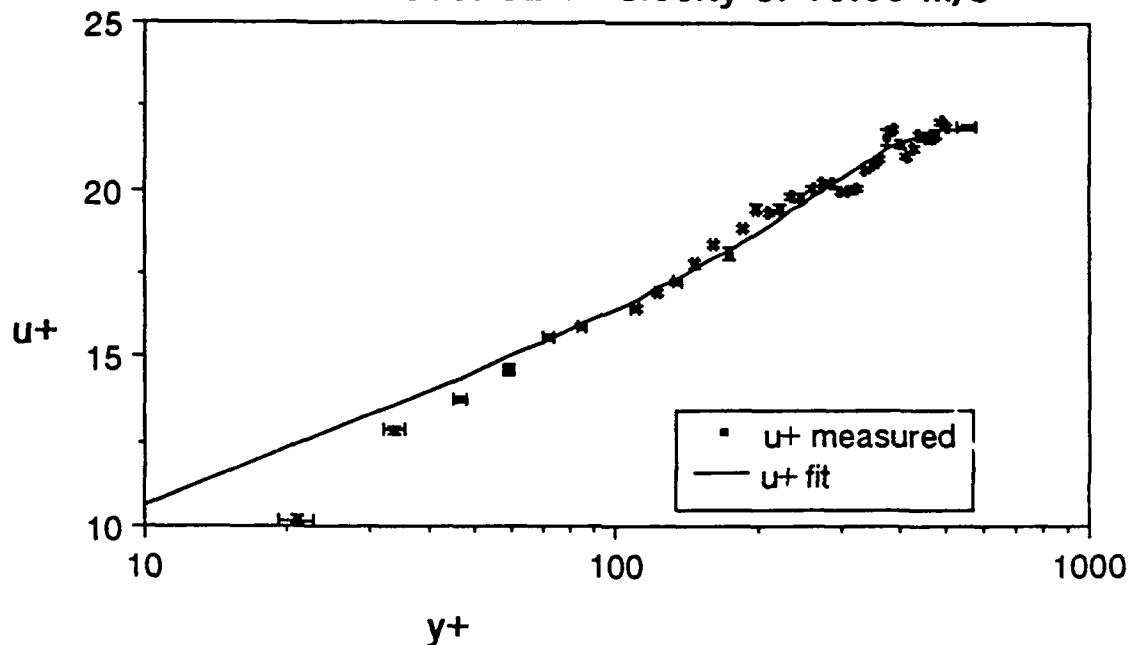


**Figure 10.7. Mean Velocity Profiles Fore and Aft of the Ribleted Test Section at 8.41 m/s.** The above two graphs show the mean velocity profiles measured fore and aft of the ribleted plate test section and their fits calculated according to Coles-Hirst method 3 at a freestream velocity of 8.41 m/s.



Profile 3051.a1: Mean Velocity Profile Fore of the Flat Plate Test Section at Freestream Velocity of 10.08 m/s



Profile 3051.a2: Mean Velocity Profile Aft of the Flat Plate Test Section at Freestream Velocity of 10.08 m/s

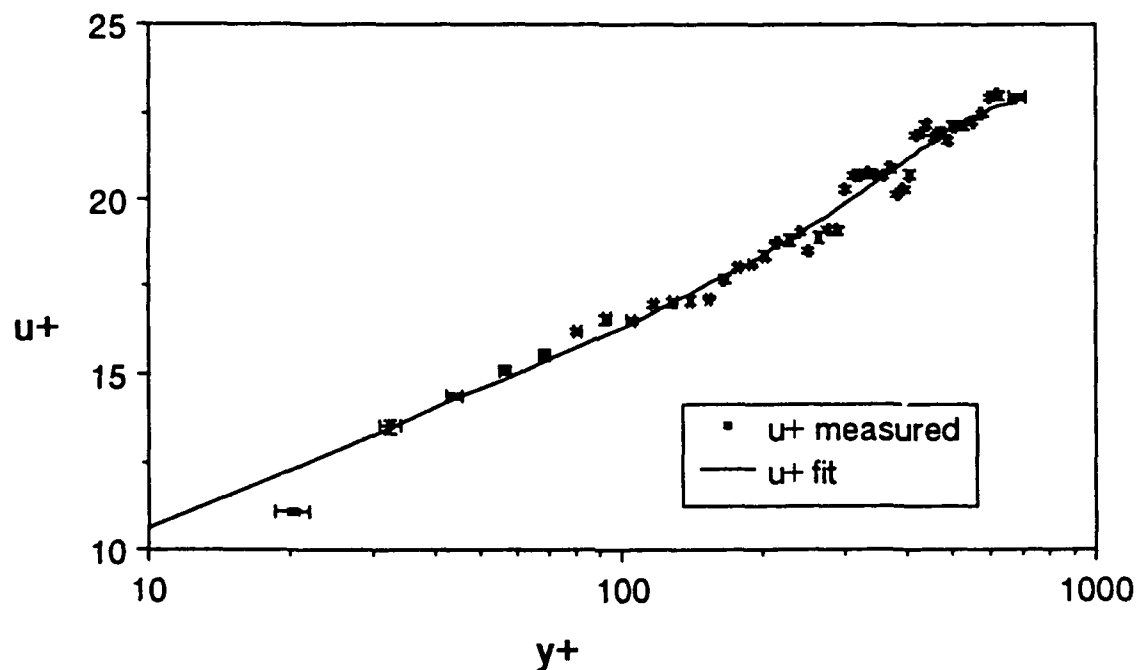
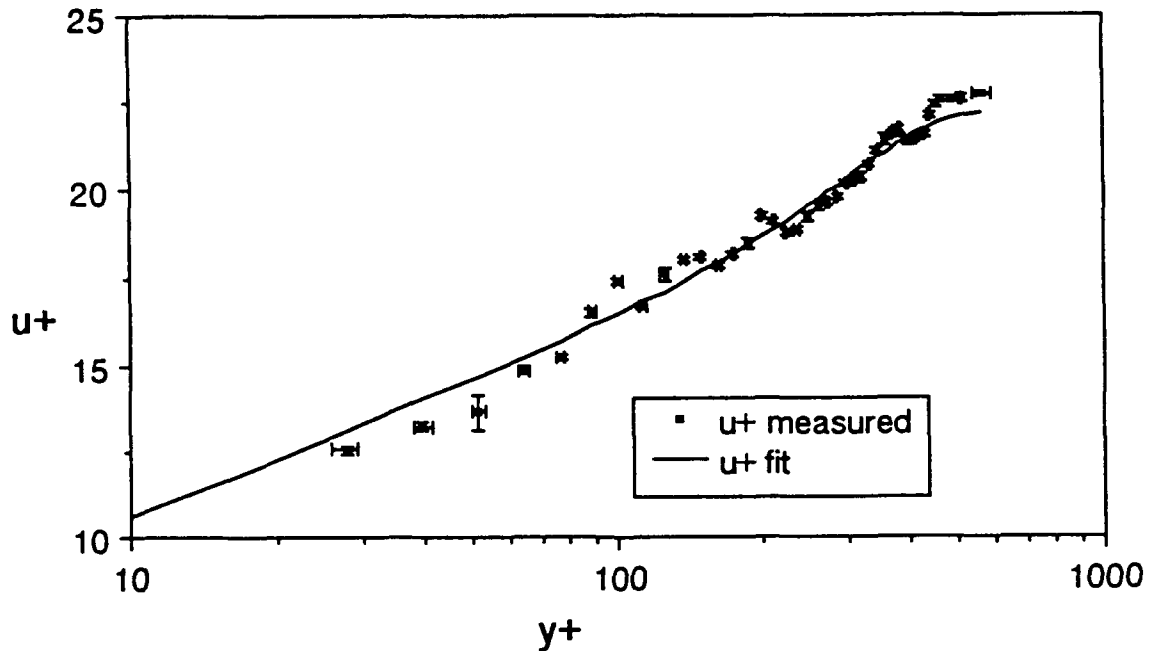
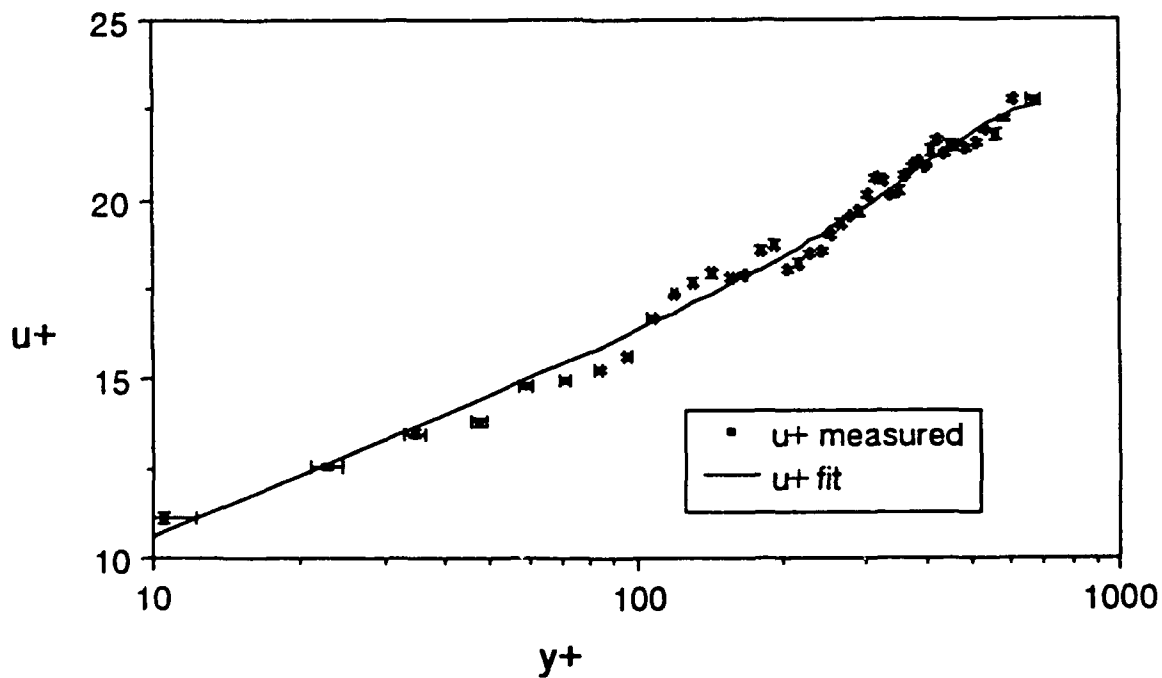


Figure 10.8. Mean Velocity Profiles Fore and Aft of the Flat Test Section at 10.08 m/s. The above two graphs show the mean velocity profiles measured fore and aft of the flat plate test section and their fits calculated according to Coles-Hirst method 3 at a freestream velocity of 10.08 m/s.

**Profile 3051.b1: Mean Velocity Profile Fore of the Ribletted Plate Test Section at Freestream Velocity of 10.08 m/s**

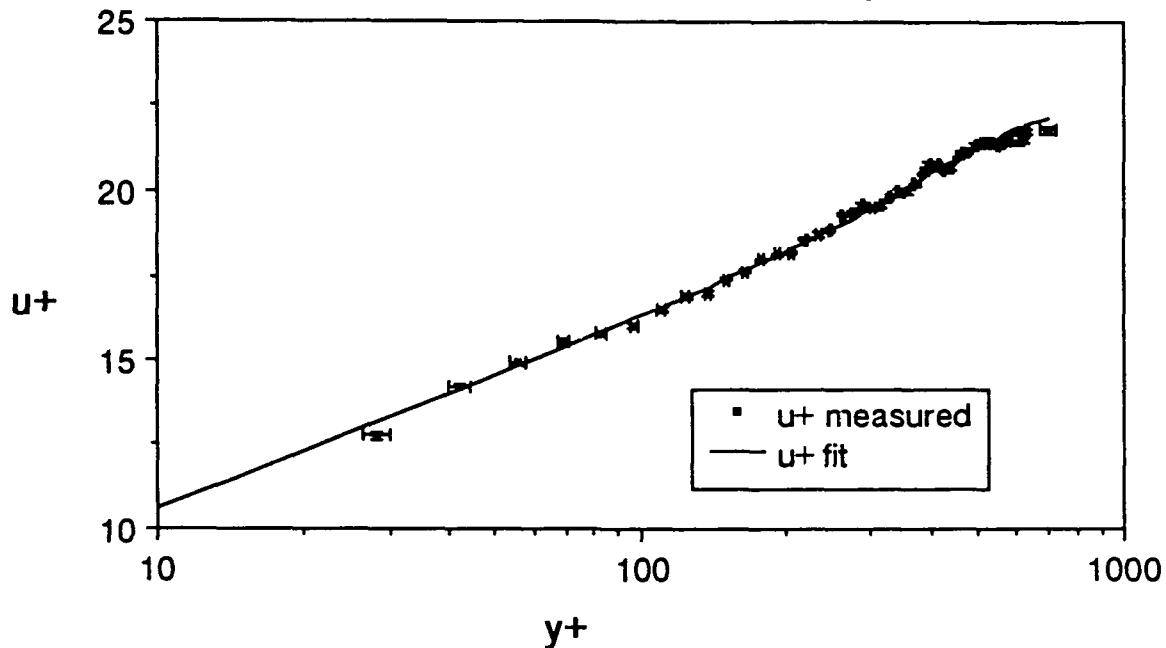


**Profile 3051.b2: Mean Velocity Profile Aft of the Ribletted Plate Test Section at Freestream Velocity of 10.08 m/s**



**Figure 10.9. Mean Velocity Profiles Fore and Aft of the Ribletted Test Section at 10.08 m/s.** The above two graphs show the mean velocity profiles measured fore and aft of the ribletted plate test section and their fits calculated according to Coles-Hirst method 3 at a freestream velocity of 10.08 m/s.

**Profile 2031.a1c: Mean Velocity Profile Fore of the Flat Plate Test Section at Freestream Velocity of 10.88 m/s**



**Profile 2031.a2: Velocity Profile Aft of the Flat Plate Test Section at a Freestream Velocity of 10.88 m/s**

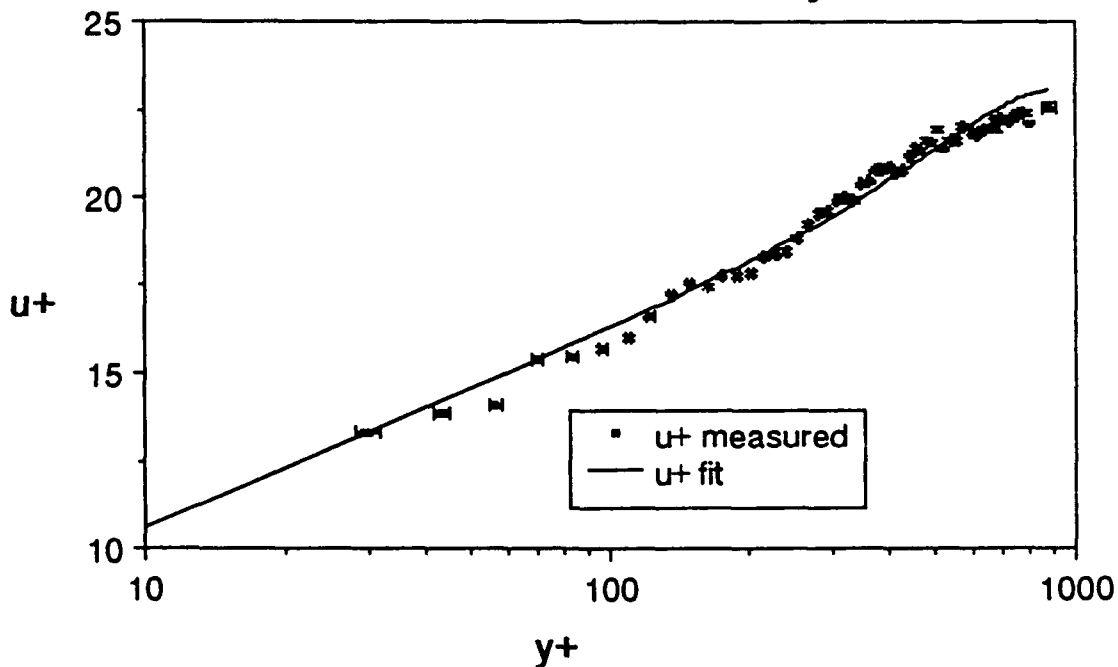
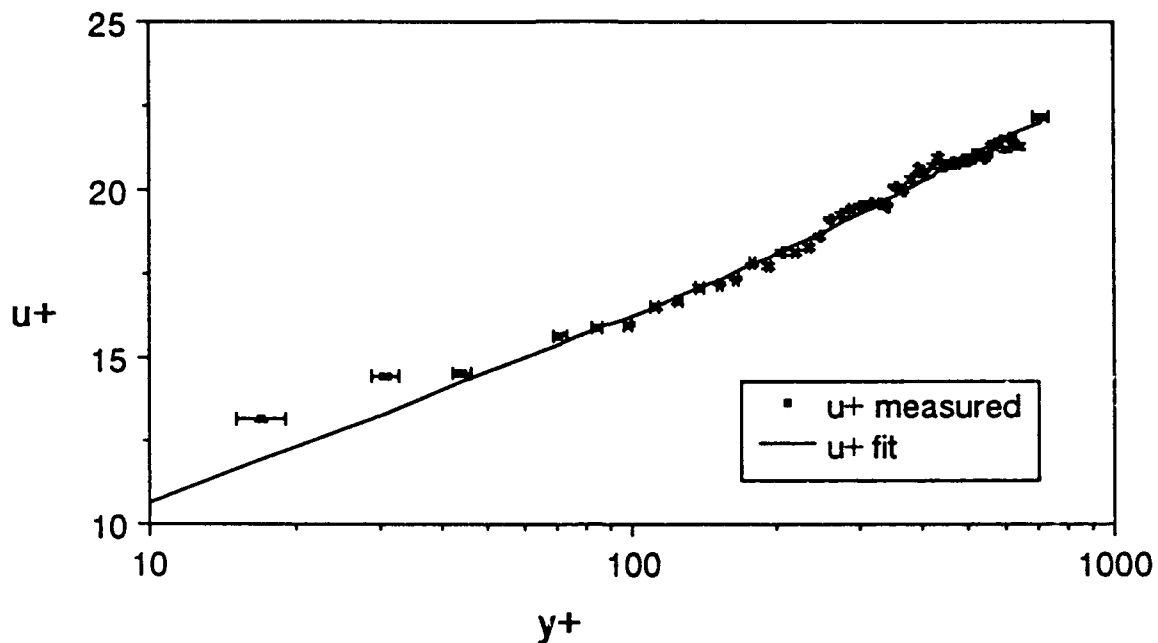


**Figure 10.10. Mean Velocity Profiles Fore and Aft of the Flat Test Section at 10.88 m/s.** The above two graphs show the mean velocity profiles measured fore and aft of the flat plate test section and their fits calculated according to Coles-Hirst method 3 at a freestream velocity of 10.88 m/s.

**Profile 2031.b1: Mean Velocity Profile Fore of the Ribletted Plate Test Section at Freestream Velocity of 10.88 m/s**



**Profile 2031.b2: Mean Velocity Profile Aft of the Ribletted Plate Test Section at Freestream Velocity of 10.88 m/s**

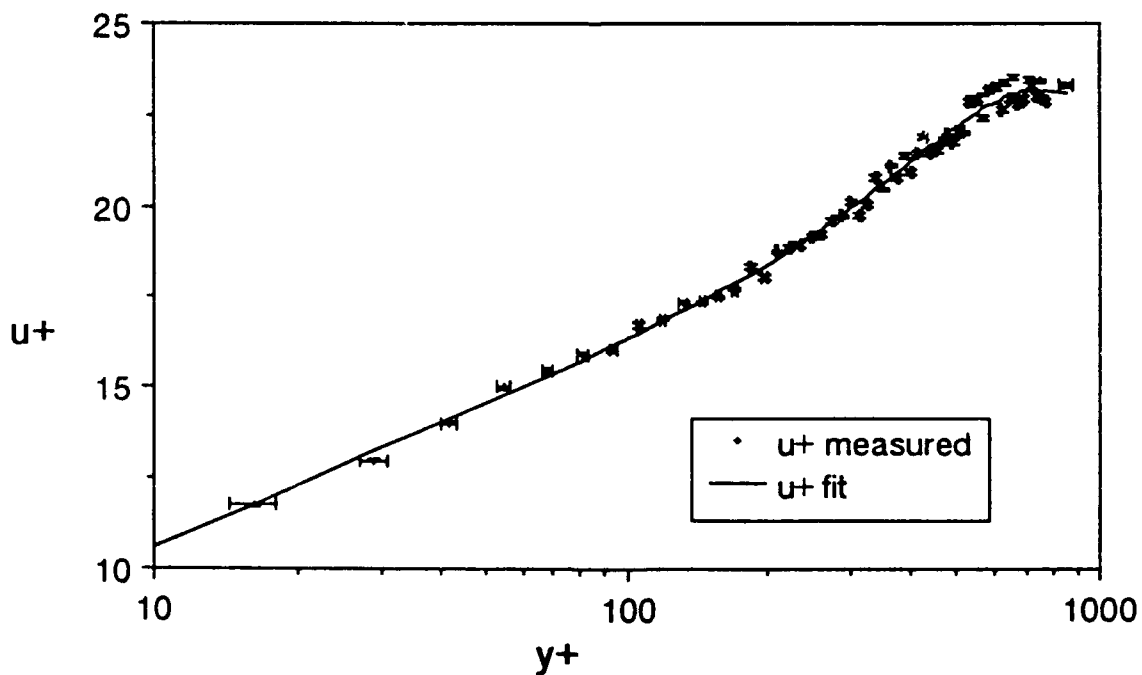
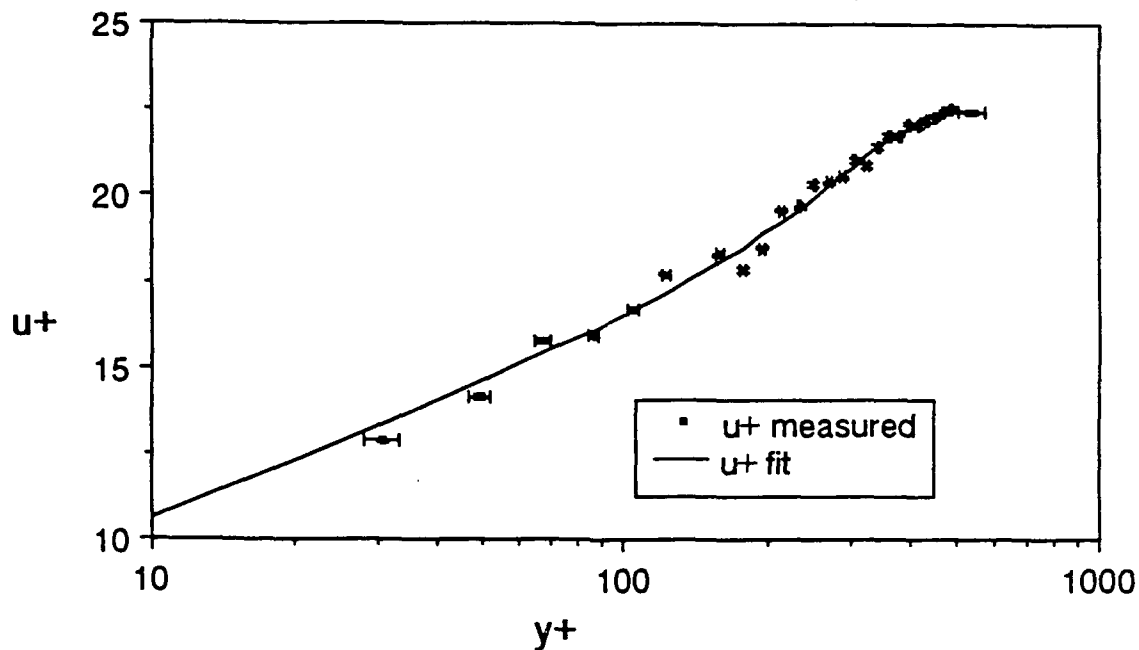


**Figure 10.11. Mean Velocity Profiles Fore and Aft of the Ribletted Test Section at 10.88 m/s.** The above two graphs show the mean velocity profiles measured fore and aft of the ribletted plate test section and their fits calculated according to Coles-Hirst method 3 at a freestream velocity of 10.88 m/s.

**Profile 3301.a1: Mean Velocity Profile Fore of the Flat Plate Test Section at Freestream Velocity of 15.02 m/s**



**Profile 3301.a2: Mean Velocity Profile Aft of the Flat Plate Test Section at Freestream Velocity of 15.02 m/s**

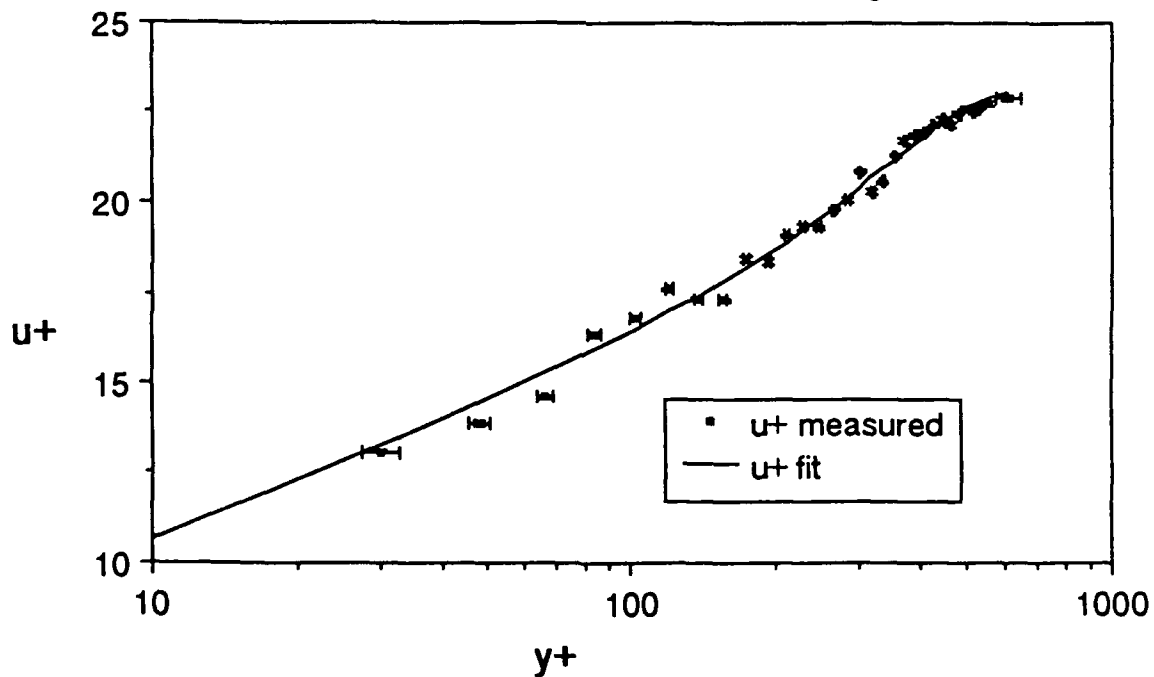
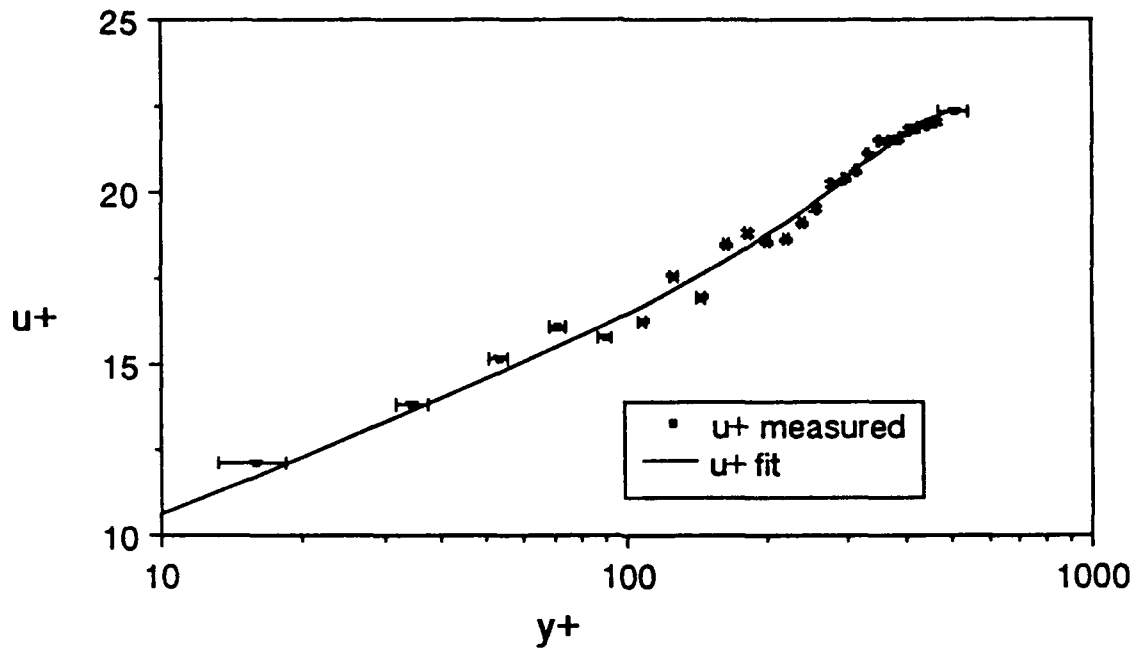


**Figure 10.12. Mean Velocity Profiles Fore and Aft of the Flat Test Section at 15.02 m/s.** The above two graphs show the mean velocity profiles measured fore and aft of the flat plate test section and their fits calculated according to Coles-Hirst method 3 at a freestream velocity of 15.02 m/s.

**Profile 3301.b1: Mean Velocity Profile Fore of the Ribleted Plate Test Section at Freestream Velocity of 15.02 m/s**



**Profile 3301.b2: Mean Velocity Profile Aft of the Ribleted Plate Test Section at Freestream Velocity of 15.02 m/s**

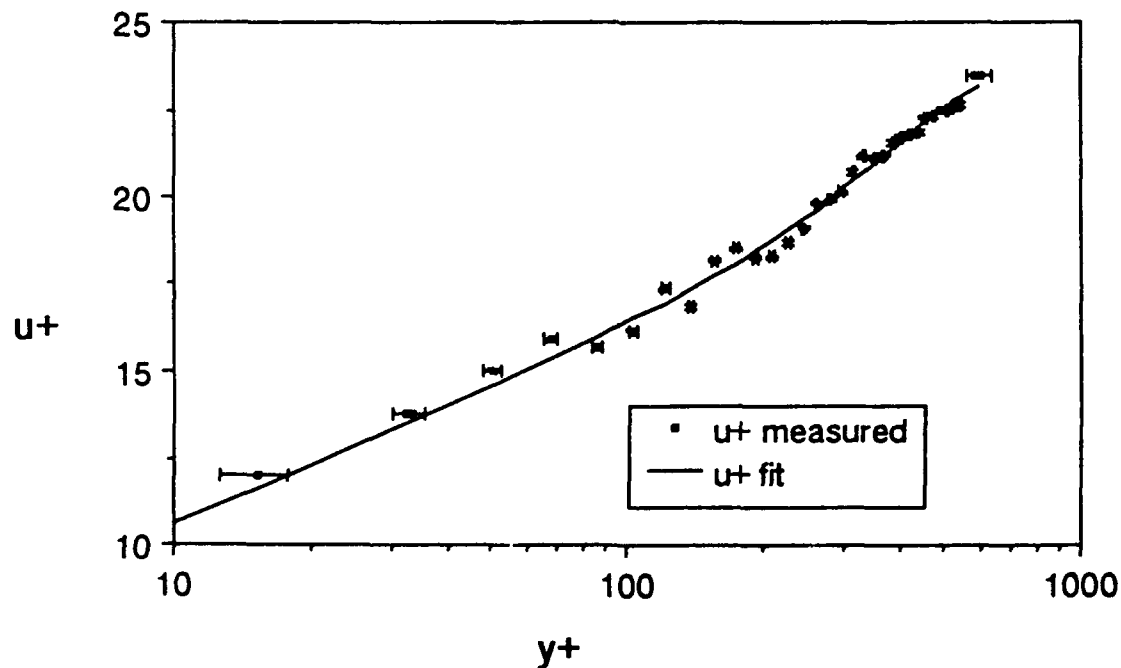
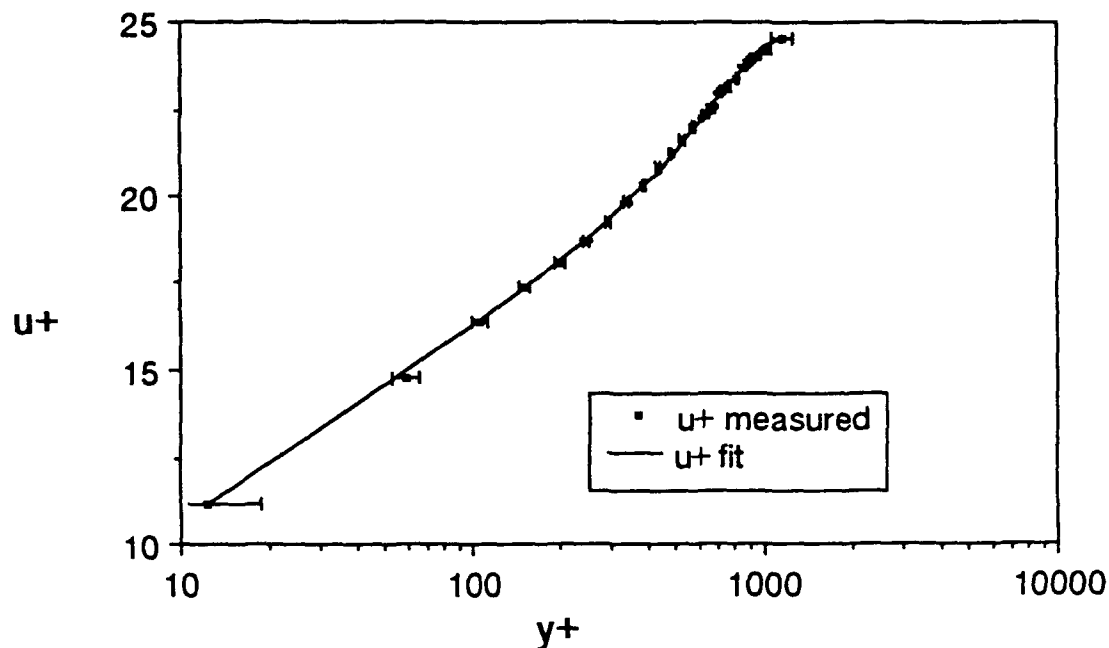


**Figure 10.13. Mean Velocity Profiles Fore and Aft of the Ribleted Test Section at 15.02 m/s.** The above two graphs show the mean velocity profiles measured fore and aft of the ribleted plate test section and their fits calculated according to Coles-Hirst method 3 at a freestream velocity of 15.02 m/s.

**Profile 3311.a1: Mean Velocity Profile Fore of the Flat Plate Test Section at Freestream Velocity of 41.65 m/s**



**Profile 3311.a2: Mean Velocity Profile Aft of the Flat Plate Test Section at Freestream Velocity of 41.65 m/s**

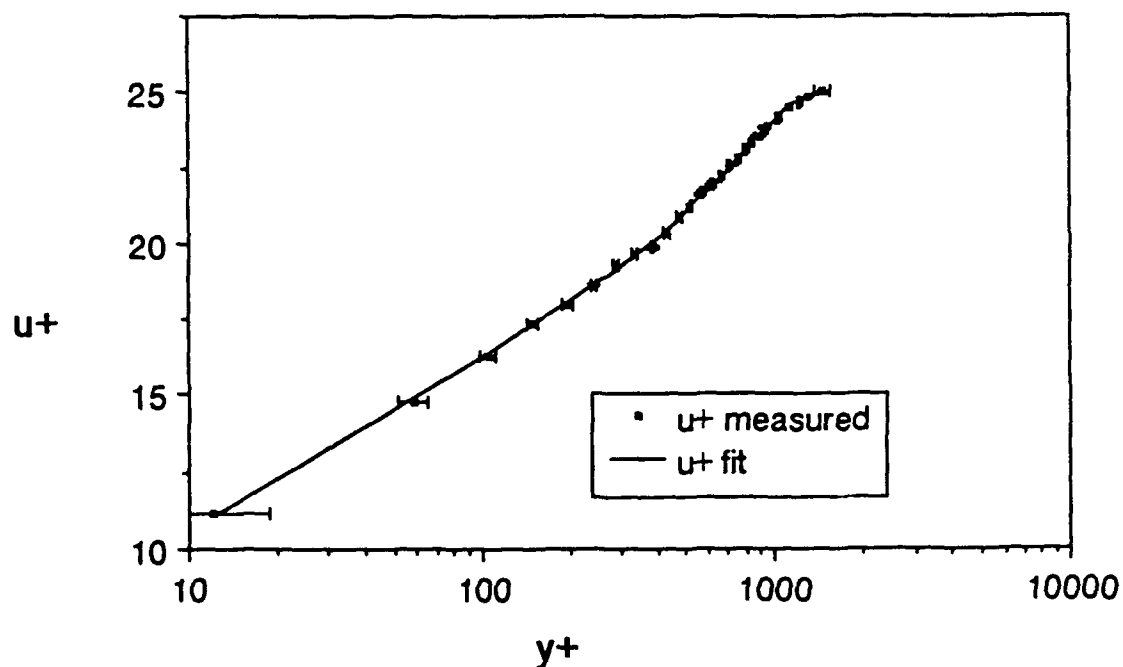
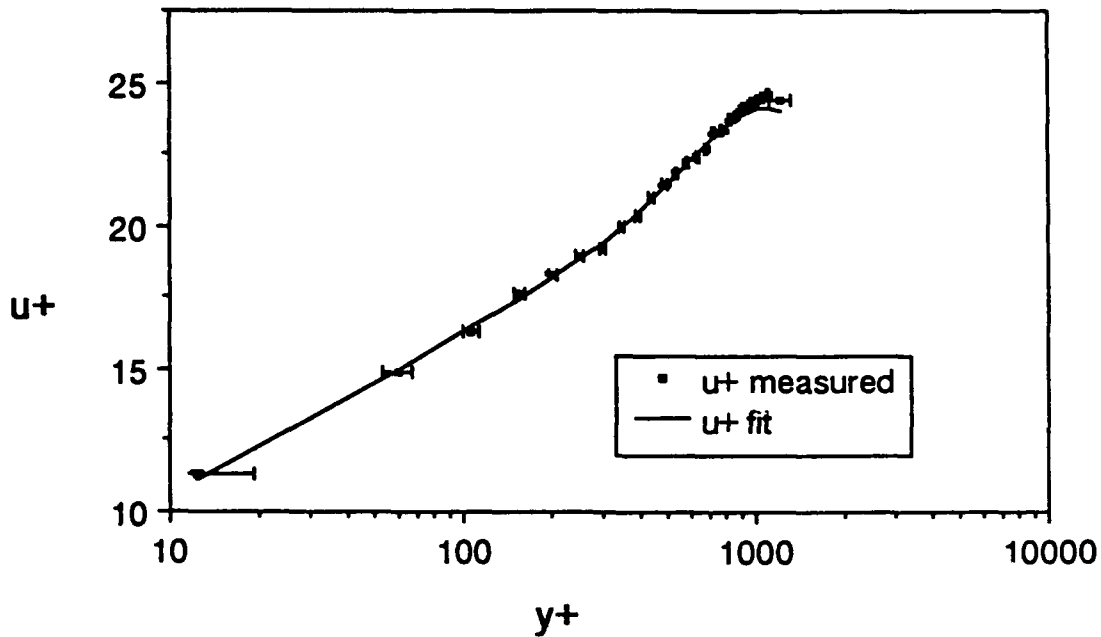


**Figure 10.14. Mean Velocity Profiles Fore and Aft of the Flat Test Section at 41.65 m/s.** The above two graphs show the mean velocity profiles measured fore and aft of the flat plate test section and their fits calculated according to Coles-Hirst method 3 at a freestream velocity of 41.65 m/s.

**Profile 3311.b1: Mean Velocity Profile Fore of the Ribletted Plate Test Section at Freestream Velocity of 41.65 m/s**



**Profile 3311.b2: Mean Velocity Profile Aft of the Ribletted Plate Test Section at Freestream Velocity of 41.65 m/s**

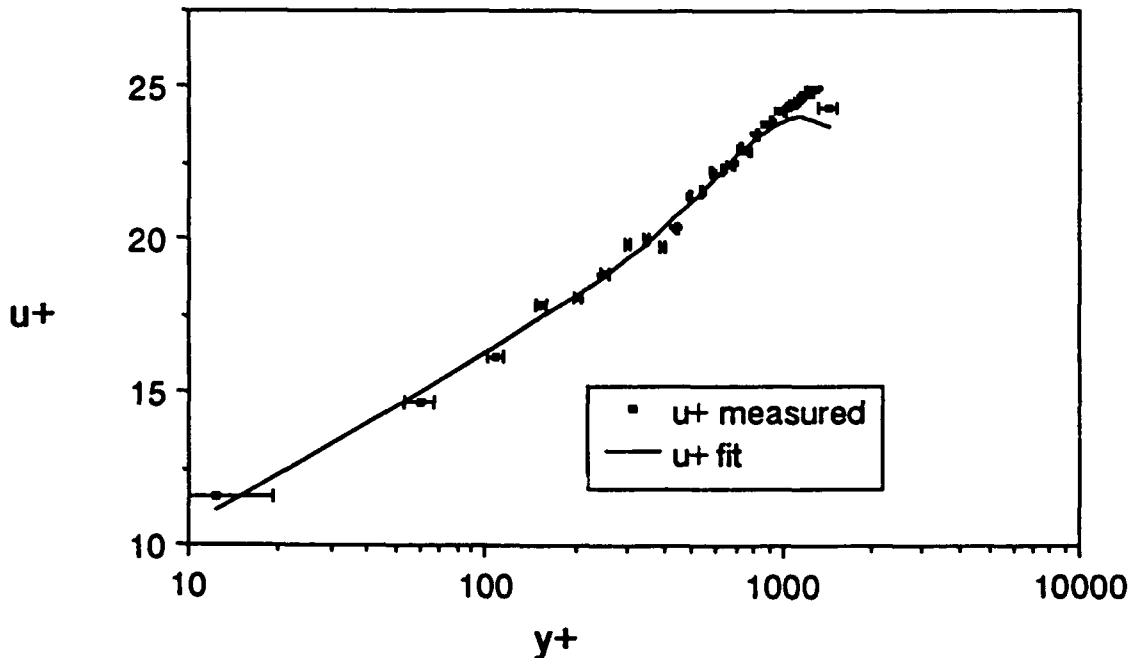


**Figure 10.15. Mean Velocity Profiles Fore and Aft of the Ribletted Test Section at 41.65 m/s.** The above two graphs show the mean velocity profiles measured fore and aft of the ribletted plate test section and their fits calculated according to Coles-Hirst method 3 at a freestream velocity of 41.65 m/s.



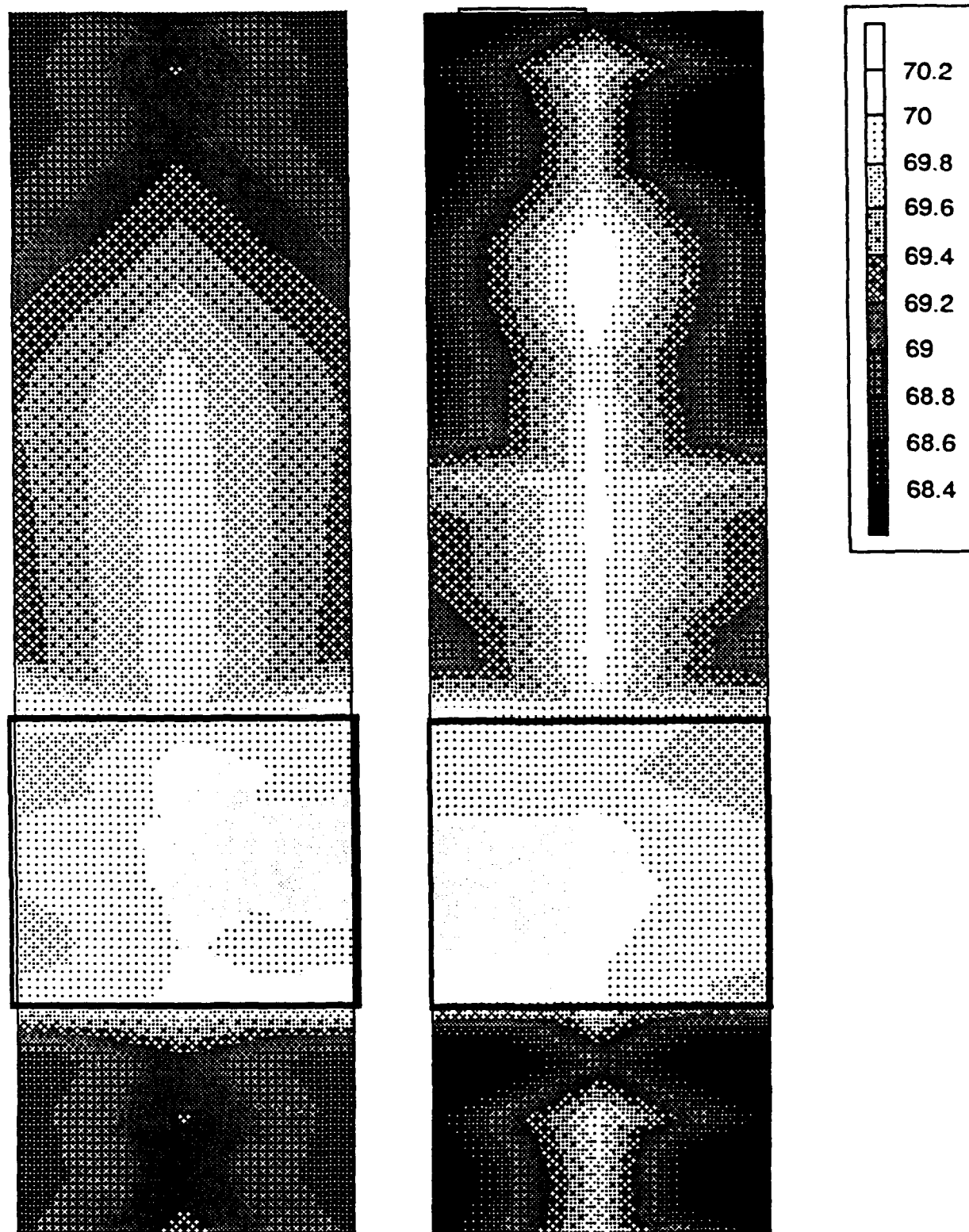


**Figure 11.1. Wall Temperature at 8.48 m/s.** The contour plots above show the wall temperature of the two tunnel walls during run 3171 at a freestream velocity of 8.48 m/s. The strip on the left is the A side, the flat plate test section side, and the right is the B side, the ribletted test section side. The test sections are outlined with rectangles. The walls are not drawn to scale.

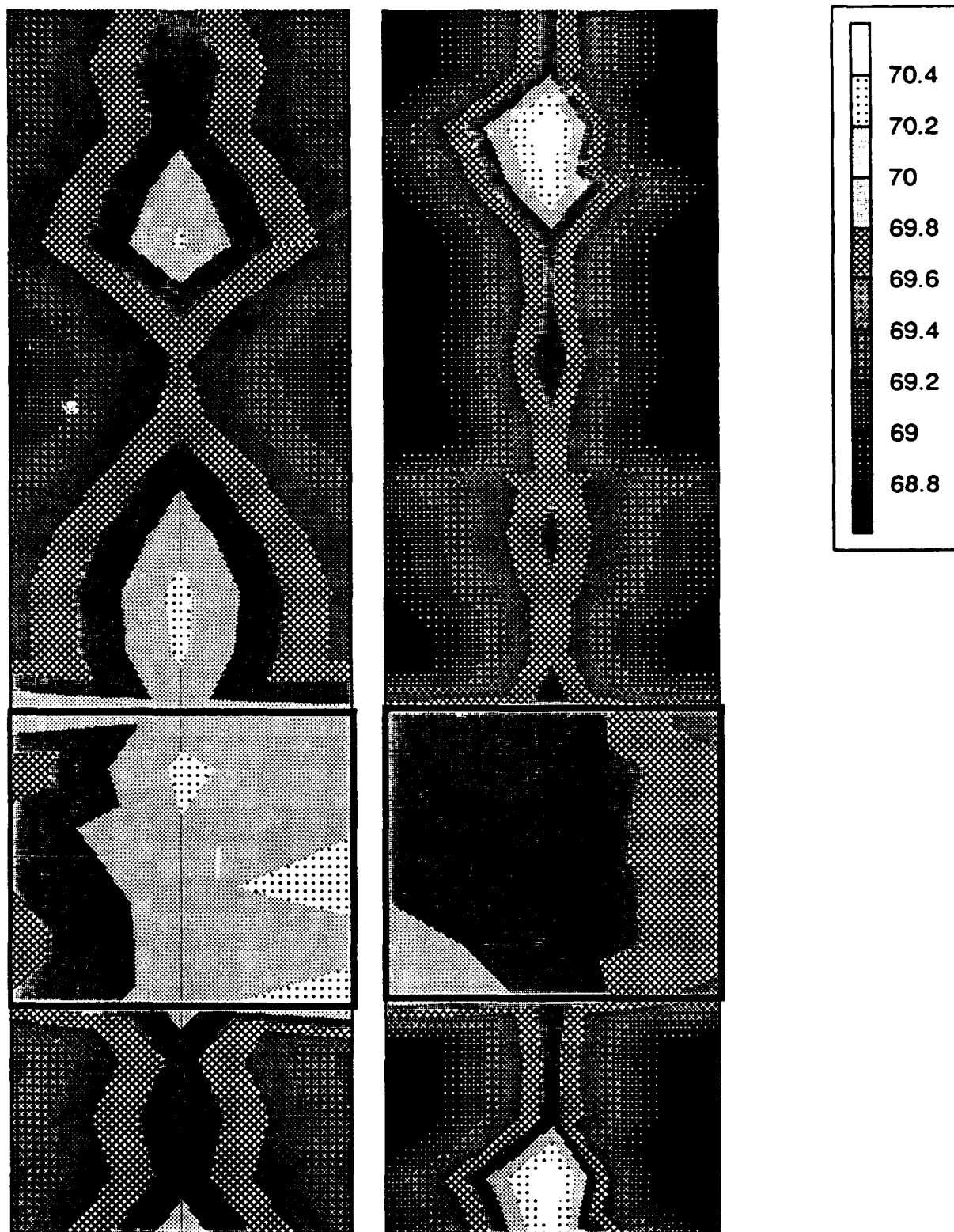


**Figure 11.2. Wall Temperature at 9.95 m/s.** The contour plots above show the wall temperature of the two tunnel walls during run 2161 at a freestream velocity of 9.95 m/s. The strip on the left is the A side, the flat plate test section side, and the right is the B side, the ribleted test section side. The test sections are outlined with rectangles. The walls are not drawn to scale.

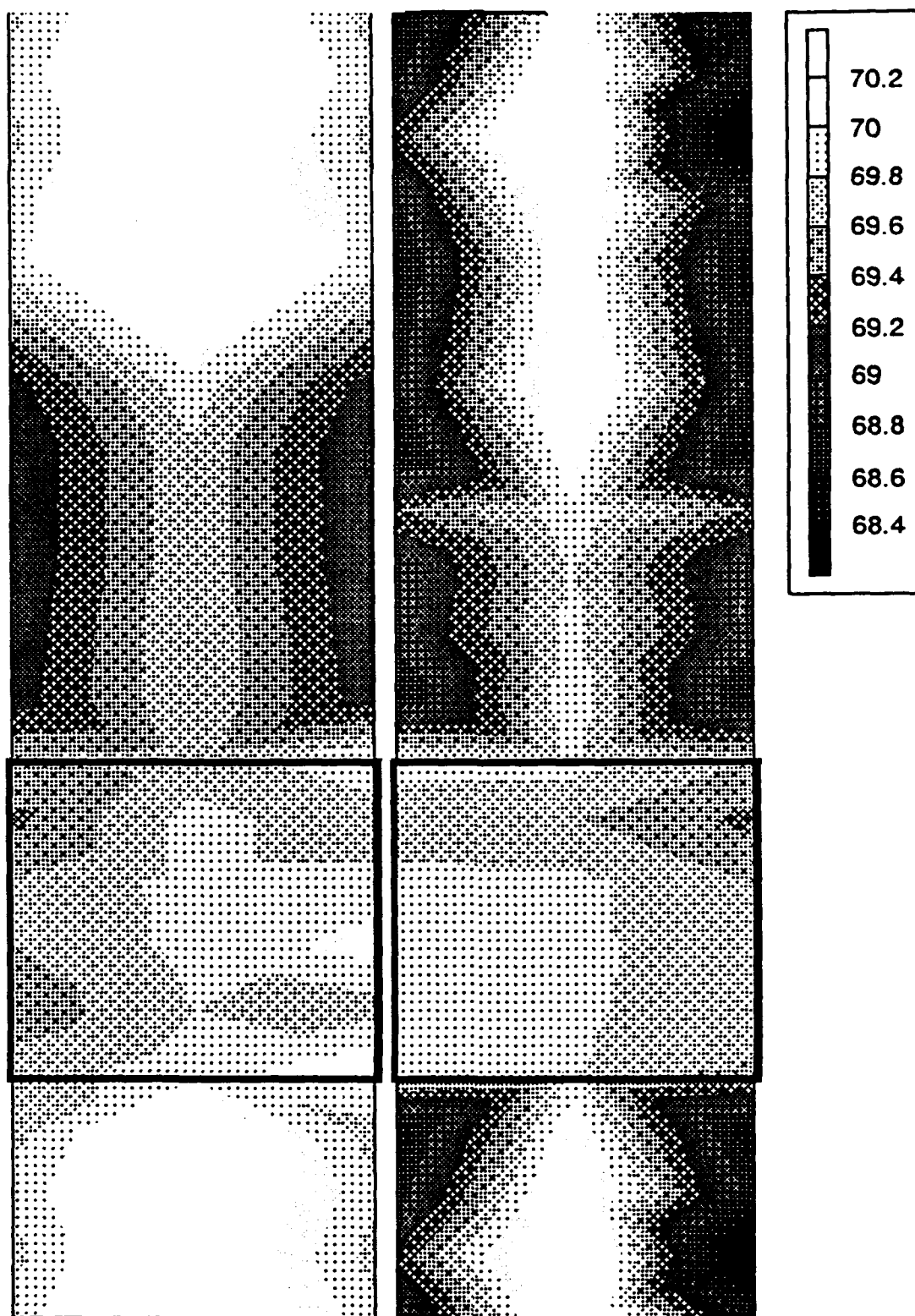


**Figure 11.3. Wall Temperature at 10.03 m/s.** The contour plots above show the wall temperature of the two tunnel walls during run 2281 at a freestream velocity of 10.03 m/s. The strip on the left is the A side, the flat plate test section side, and the right is the B side the ribleted test section side. The test sections are outlined with rectangles. The walls are not drawn to scale.

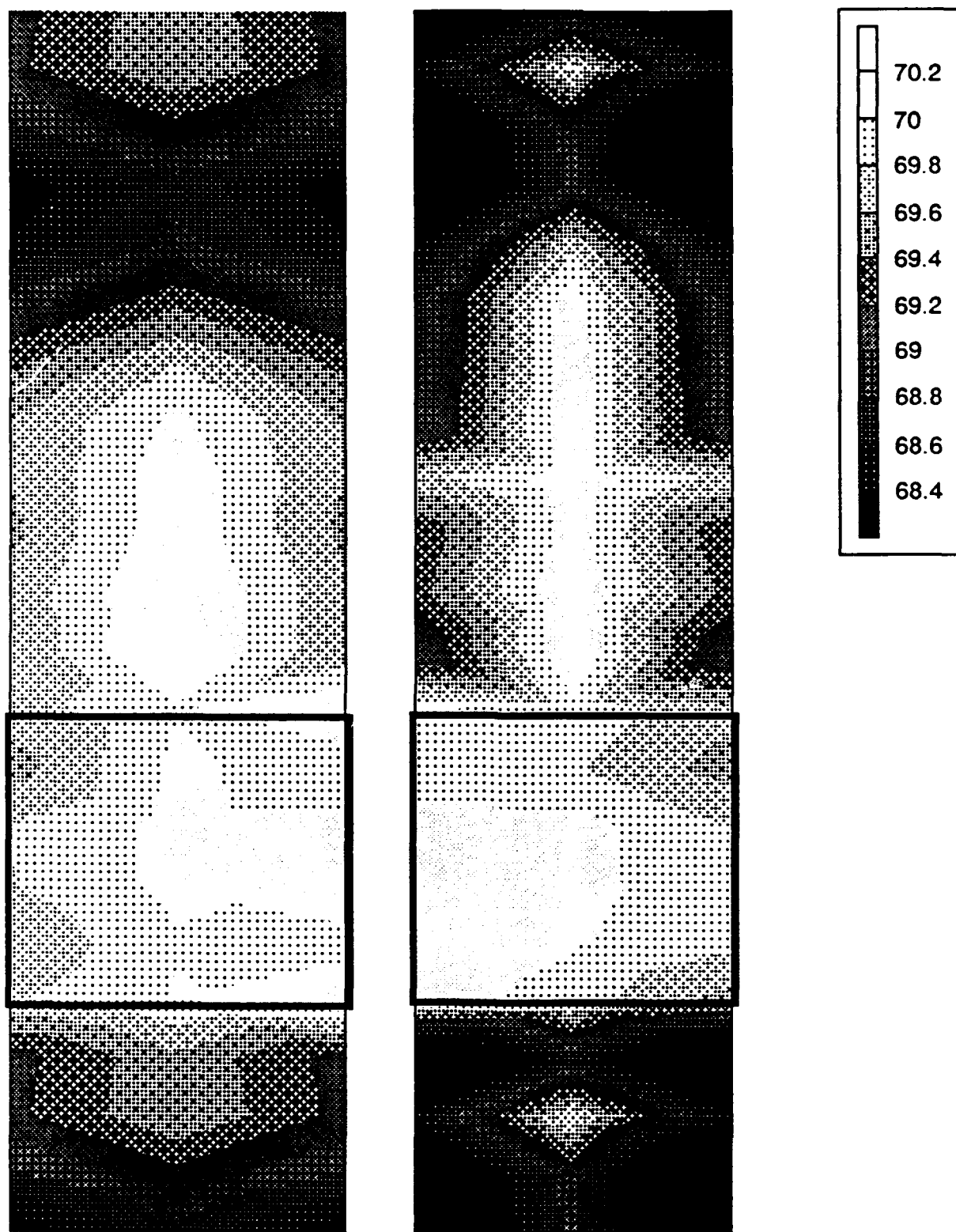


**Figure 11.4. Wall Temperature at 12.47 m/s.** The contour plots above show the wall temperature of the two tunnel walls during run 3111 at a freestream velocity of 12.47 m/s. The strip on the left is the A side, the flat plate test section side, and the right is the B side, the ribleted test section side. The test sections are outlined with rectangles. The walls are not drawn to scale.

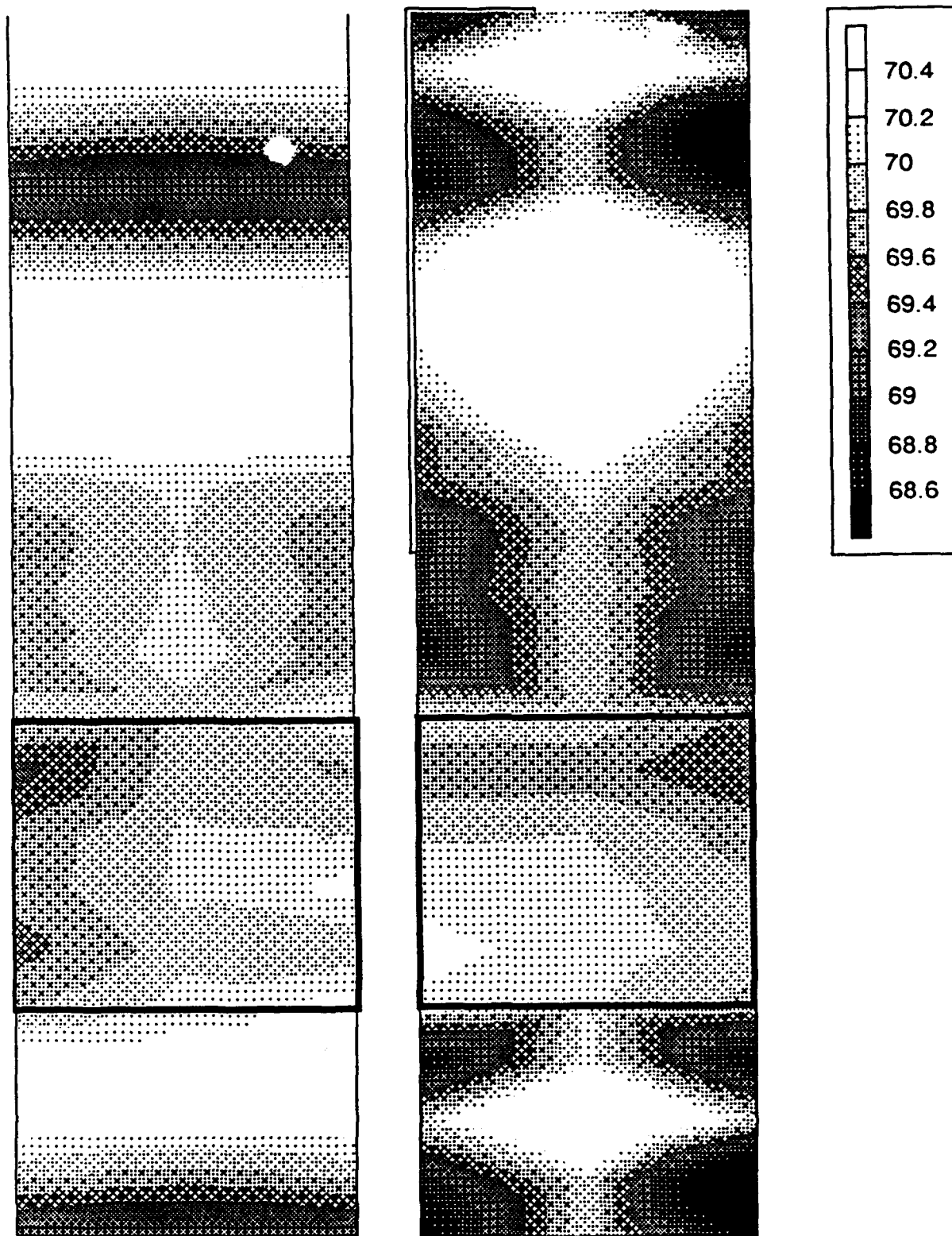


**Figure 11.5. Wall Temperature at 14.88 m/s.** The contour plots above show the wall temperature of the two tunnel walls during run 3181 at a freestream velocity of 14.88 m/s. The strip on the left is the A side, the flat plate test section side, and the right is the B side, the ribleted test section side. The test sections are outlined with rectangles. The walls are not drawn to scale.

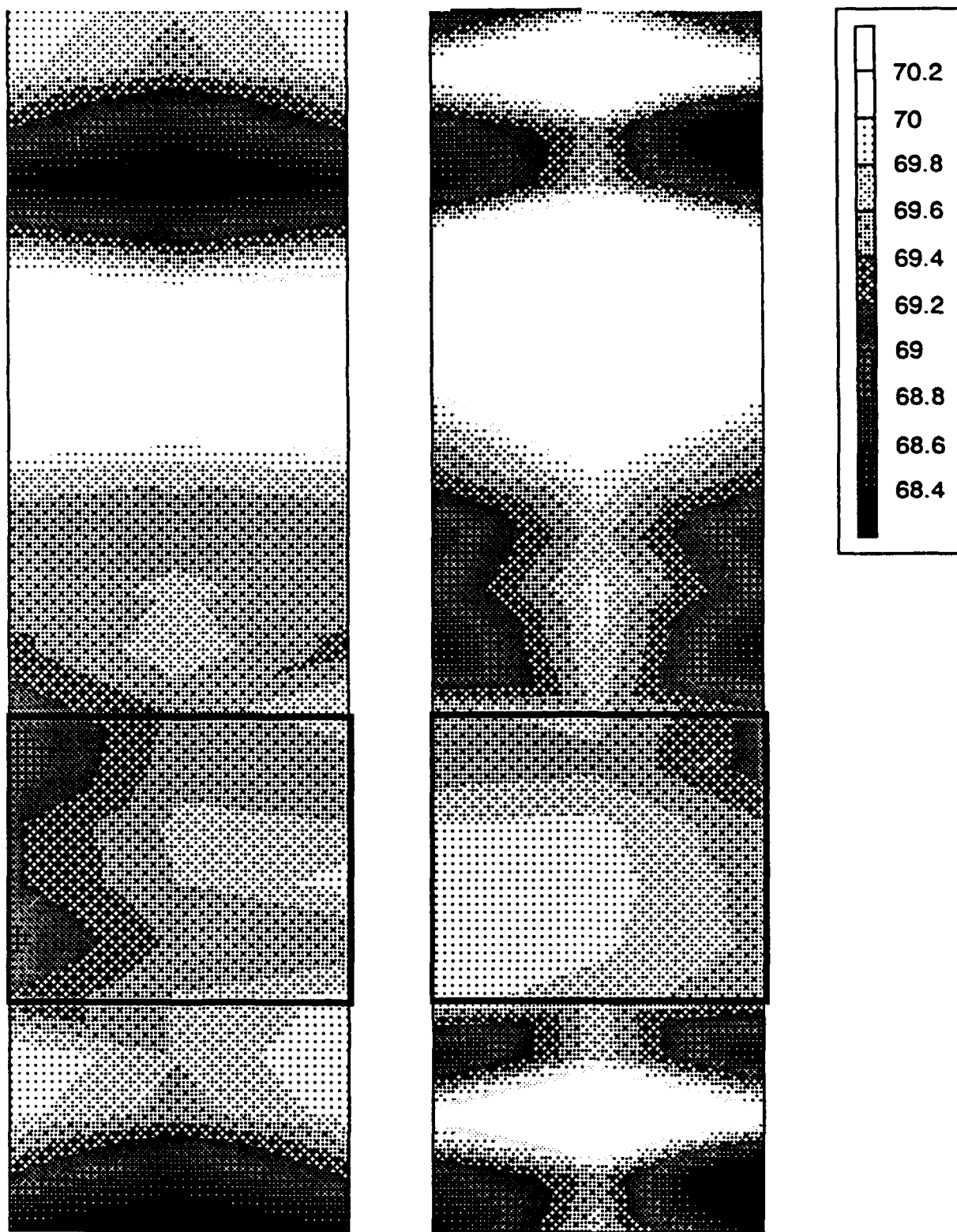


**Figure 11.6. Wall Temperature at 20.06 m/s.** The contour plots above show the wall temperature of the two tunnel walls during run 3185 at a freestream velocity of 20.06 m/s. The strip on the left is the A side, the flat plate test section side, and the right is the B side, the ribletted test section side. The test sections are outlined with rectangles. The walls are not drawn to scale.

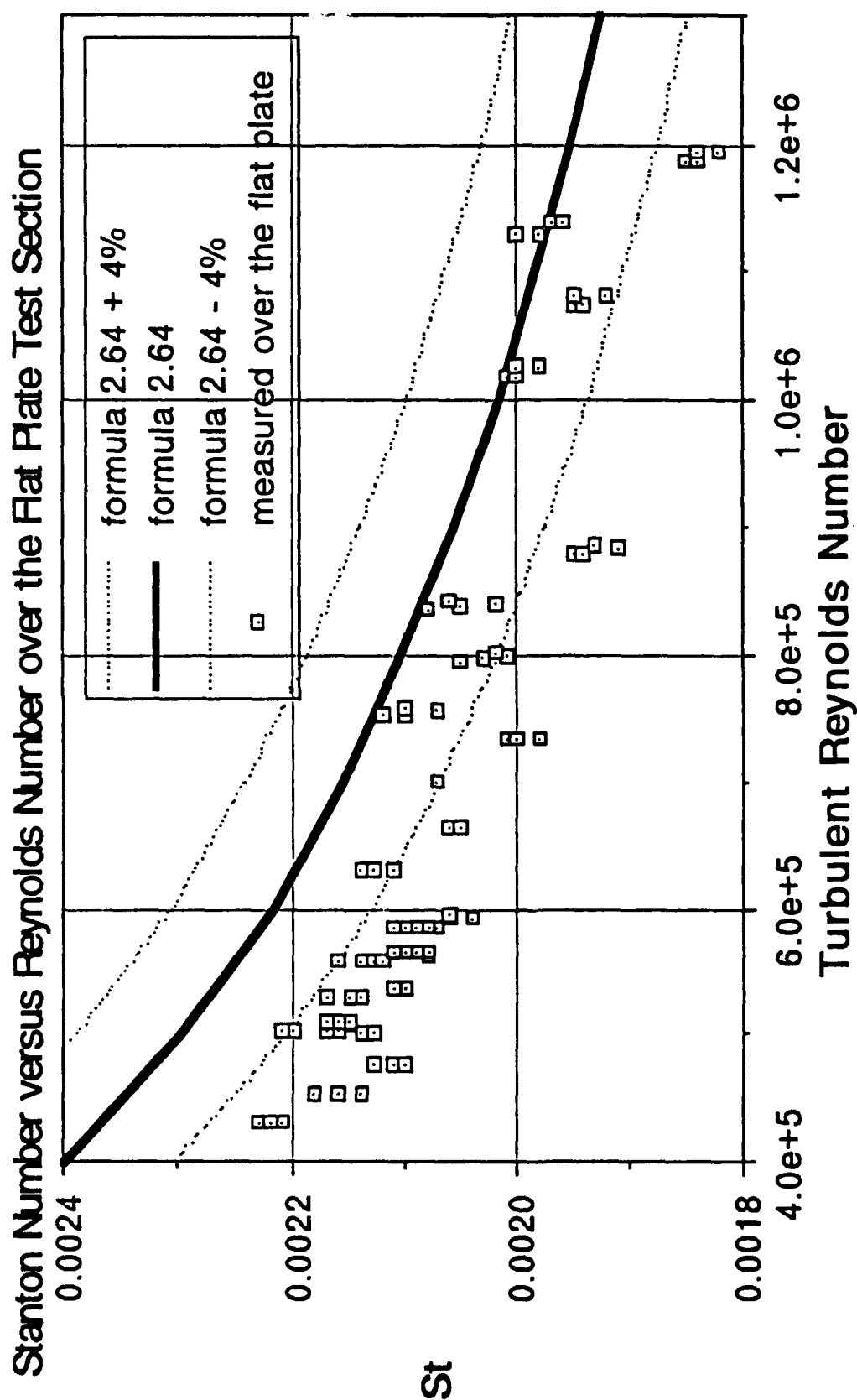


**Figure 11.7. Local Stanton Number over the Flat Plate.** The above graph shows local Stanton number versus turbulent Reynolds number measured over the flat plate test section. The heavy line shows the values predicted via formula 2.64, the upper and lower uncertainty ranges of which are plotted as dashed lines. The results compare quite well considering that the subsections within the test sections from which these Stanton numbers were calculated were not insulated from one another.

# Stanton Number versus Reynolds Number over the Ribletted Test Section

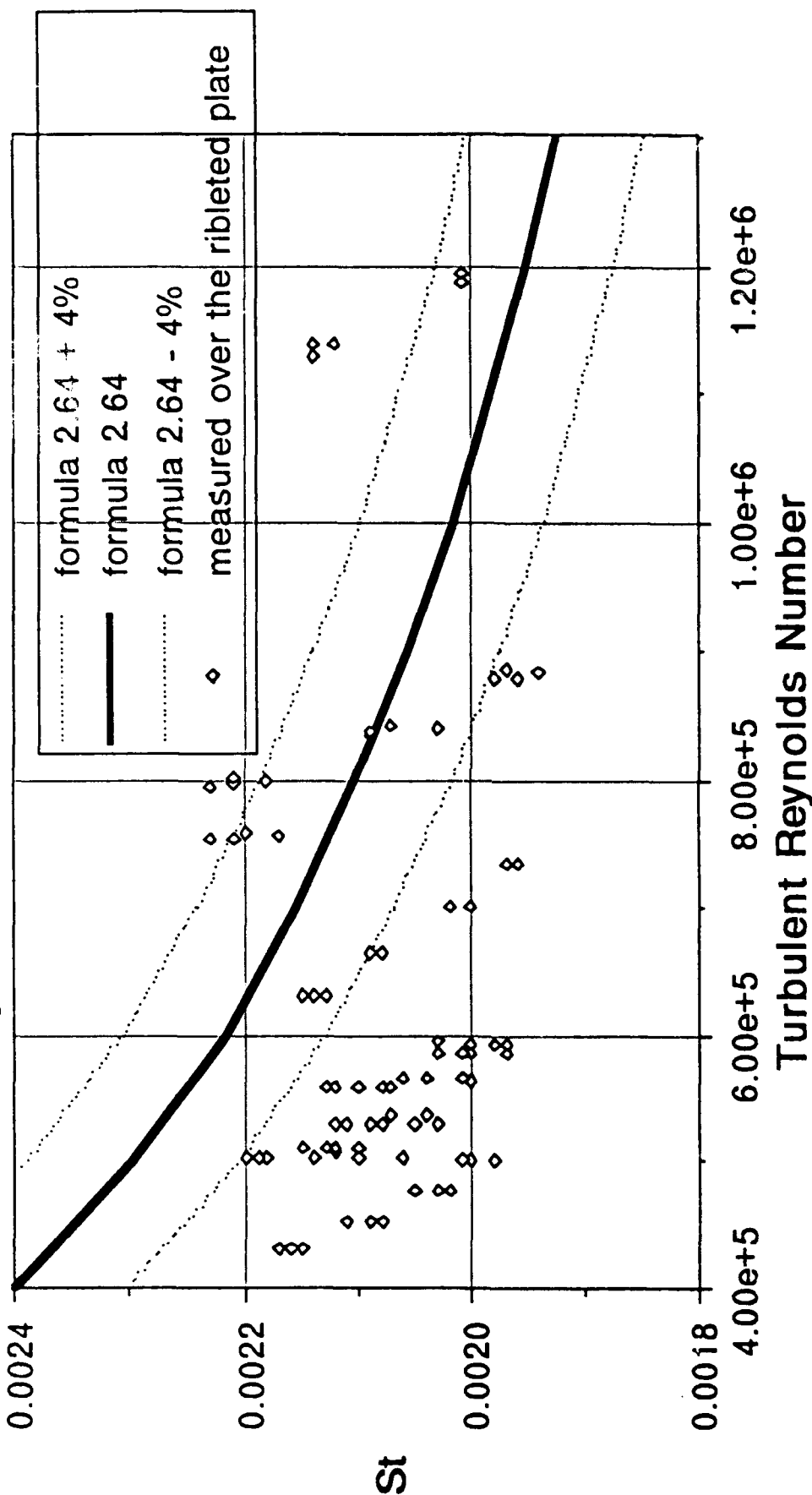


**Figure 11.8. Local Stanton Number over the Ribletted Plate.** The above graph shows local Stanton number measured over the flat plate test section. The heavy line shows the values predicted via formula 2.64, the upper and lower uncertainty ranges of which are plotted as dashed lines. The results compare fairly well considering that the subsections within the test sections from which these Stanton numbers were calculated were not insulated from one another, although the data scatter is larger than that of the flat plate side data.



Table 4.1- Size and room temperature resistances of the pre-test segment heaters

Pre-test Segment Heaters		
Heater [#]	Size [in. x in.]	Resistance [Ohms]
H1A	0.25 X 10.5	513.05
H1B	0.25 X 10.5	514.54
H2A	0.75 X 10.5	154.23
H2B	0.75 X 10.5	152.96
H3A	1.25 X 10.5	92.34
H3B	1.25 X 10.5	91.82
H4A	2.25 X 10.5	53.44
H4B	2.25 X 10.5	53.32
H5A	2.5 X 10.5	48.10
H5B	2.5 X 10.5	48.09
H6A	3.0 X 10.5	39.11
H6B	3.0 X 10.5	39.39
H7A	3.5 X 10.5	34.19
H7B	3.5 X 10.5	34.36
H8A	4.0 X 10.5	31.00
H8B	4.0 X 10.5	29.92
H9A	4.5 X 10.5	26.74
H9B	4.5 X 10.5	26.71
H10A	4.5 X 10.5	27.50
H10B	4.5 X 10.5	27.46
H11A	4.5 X 10.5	27.56
H11B	4.5 X 10.5	27.23
H12A	5.0 X 10.5	24.60
H12B	5.0 X 10.5	24.83

Table 4.2- Size and room temperature resistances of the test and spacers segment and back insulation heaters

**Spacer Segments Heaters**

Heater [#]	Size [in. x in.]	Resistance [Ohms]
H13A	6.0 x 10.5	20.70
H13B	6.0 x 10.5	20.47
H14A	6.0 x 10.5	20.43
H14B	6.0 x 10.5	20.74
H15A	6.0 x 10.5	20.45
H15B	6.0 x 10.5	20.66
H16A	6.0 x 10.5	20.63
H16B	6.0 x 10.5	20.78

**Test Segment Heaters**

Heater [#]	Size [in. x in.]	Resistance [Ohms]
H17A	2.0 X 7.0	91.70
H17B	2.0 X 7.0	91.60
H18A	2.0 X 7.0	95.88
H18B	2.0 X 7.0	97.97
H19A	2.0 X 7.0	91.11
H19B	2.0 X 7.0	91.45
H20A	2.0 X 7.0	91.71
H20B	2.0 X 7.0	90.95
H21A	2.0 X 7.0	91.74
H21B	2.0 X 7.0	91.77
H22A	2.0 X 7.0	97.00
H22B	2.0 X 7.0	91.94
H23A	1.75 X 6.	137.00
H23B	1.75 X 6.	135.45
H24A	1.75 X 6.	137.92
H24B	1.75 X 6.	136.98
H25A	1.75 X 6.	113.32
H25B	1.75 X 6.	114.75
H26A	1.75 X 6.	113.54
H26B	1.75 X 6.	114.88

**Back Insulation Guard Heaters**

Heater [#]	Size [in. x in.]	Resistance [Ohms]
BH1A	12.0 x 10.5	10.90
BH1B	12.0 x 10.5	10.83
BH2A	12.0 x 10.5	10.87
BH2B	12.0 x 10.5	11.07
BH3A	12.0 x 10.5	10.94
BH3B	12.0 x 10.5	10.97
BH4A	12.0 x 10.5	10.95
BH4B	12.0 x 10.5	10.92
BH5A	12.0 x 10.5	10.99
BH5B	12.0 x 10.5	10.91
BH6A	12.0 x 10.5	10.88
BH6B	12.0 x 10.5	11.00

Table 4.3- Shunt resistance values

Shunt Resistor [#]	Resistance [Ohms]
RshA,1	0.18
RshA,2	0.187
RshA,3	0.164
RshA,4	0.188
RshA,5	0.194
RshA,6	0.197
RshA,7	0.18
RshA,8	0.187
RshA,9	0.184
RshA,10	0.18
RshB,1	0.192
RshB,2	0.182
RshB,3	0.174
RshB,4	0.166
RshB,5	0.183
RshB,6	0.184
RshB,7	0.19
RshB,8	0.186
RshB,9	0.166
RshB,10	0.182

Table 9.1. RTD Calibration Results.

#	$\chi^2/\nu$	$\sigma_{T_{cal2}}$	$\sigma_{TCVD2}$	$\Delta T_2$	$\Delta T_{cal}$	$u_{T_{tot}}$	$R_o$	$\alpha$	$\delta$	$b_1$	$b_2$	$b_3$
1	0.12	0.072	0.068	-0.047	-0.003	0.075	99.7746	4.065E-03	2.44038	1.999E+03	5.004E+06	1.010E+04
2	0.09	0.072	0.068	-0.141	-0.009	0.081	99.7200	4.066E-03	2.44033	1.999E+03	5.004E+06	1.011E+04
3	1.45	0.079	0.115	-0.092	-0.002	0.081	99.6054	4.070E-03	2.44009	1.999E+03	5.003E+06	1.011E+04
4	0.41	0.072	0.061	-0.149	-0.034	0.106	99.7839	4.053E-03	2.44092	1.998E+03	5.004E+06	1.013E+04
5	0.07	0.071	0.061	-0.200	-0.011	0.082	99.8459	4.060E-03	2.44063	1.999E+03	5.004E+06	1.011E+04
6	2.24	0.071	0.061	-0.069	-0.063	0.134	99.5049	4.072E-03	2.43991	1.999E+03	5.003E+06	1.011E+04
7	0.11	0.071	0.060	-0.083	0.000	0.072	99.7220	4.062E-03	2.44043	1.999E+03	5.004E+06	1.012E+04
8	0.67	0.072	0.069	0.004	-0.022	0.094	99.6902	4.063E-03	2.44034	1.999E+03	5.004E+06	1.012E+04
9	0.11	0.079	0.115	0.033	0.003	0.082	99.7351	4.068E-03	2.43922	2.000E+03	5.007E+06	1.011E+04
10	0.14	0.071	0.060	-0.008	-0.012	0.083	99.8150	4.054E-03	2.43994	1.999E+03	5.008E+06	1.013E+04
11	0.86	0.071	0.061	-0.157	0.002	0.074	99.7480	4.061E-03	2.43959	2.000E+03	5.007E+06	1.012E+04
12	0.09	0.123	0.270	-0.098	-0.002	0.125	99.6839	4.054E-03	2.43983	1.999E+03	5.008E+06	1.014E+04
13	0.12	0.080	0.115	-0.016	-0.016	0.095	99.7335	4.055E-03	2.43980	1.999E+03	5.008E+06	1.013E+04
14	0.45	0.072	0.061	0.010	0.016	0.087	99.7909	4.042E-03	2.44051	1.999E+03	5.009E+06	1.016E+04
15	0.09	0.071	0.060	0.105	-0.012	0.083	99.7019	4.070E-03	2.43898	2.000E+03	5.008E+06	1.010E+04
16	0.40	0.071	0.061	0.037	-0.020	0.091	99.6898	4.061E-03	2.43949	2.000E+03	5.008E+06	1.013E+04
17	0.13	0.071	0.061	-0.010	-0.018	0.090	99.7377	4.070E-03	2.41790	2.001E+03	5.012E+06	1.011E+04
18	0.69	0.072	0.061	-0.069	-0.041	0.113	99.7677	4.051E-03	2.43891	2.000E+03	5.012E+06	1.014E+04
19	0.33	0.079	0.115	-0.187	-0.018	0.098	99.6859	4.059E-03	2.43850	2.000E+03	5.012E+06	1.013E+04
20	0.36	0.072	0.061	0.089	-0.005	0.076	99.7827	4.055E-03	2.43857	2.000E+03	5.013E+06	1.014E+04
21	0.75	0.072	0.061	-0.157	-0.053	0.125	99.7040	4.054E-03	2.43853	2.000E+03	5.013E+06	1.015E+04
22	0.07	0.072	0.069	-0.107	0.006	0.078	99.7529	4.057E-03	2.43774	2.001E+03	5.016E+06	1.014E+04
23	0.07	0.072	0.069	-0.077	-0.045	0.118	99.6695	4.056E-03	2.43777	2.001E+03	5.019E+06	1.015E+04
24	0.11	0.071	0.061	-0.191	-0.029	0.100	99.7841	4.056E-03	2.43703	2.002E+03	5.019E+06	1.014E+04
25	0.17	0.071	0.061	-0.063	-0.014	0.085	99.7967	4.061E-03	2.43671	2.002E+03	5.018E+06	1.013E+04
26	0.06	0.071	0.061	0.056	0.003	0.075	99.8471	4.060E-03	2.43679	2.002E+03	5.018E+06	1.012E+04
27	0.072	0.072	0.068	-0.088	-0.003	0.075	99.8005	4.062E-03	2.43670	2.002E+03	5.018E+06	1.012E+04
28	0.32	0.072	0.061	-0.087	-0.016	0.082	99.8398	4.038E-03	2.43802	2.001E+03	5.019E+06	1.017E+04
29	0.15	0.123	0.270	-0.003	-0.016	0.140	99.8263	4.052E-03	2.43726	2.001E+03	5.019E+06	1.014E+04
30	0.12	0.072	0.061	-0.023	-0.011	0.082	99.8299	4.052E-03	2.43724	2.002E+03	5.019E+06	1.014E+04
31	0.12	0.072	0.069	-0.041	0.020	0.093	99.7395	4.055E-03	2.43718	2.002E+03	5.018E+06	1.014E+04
32	0.62	0.072	0.069	-0.596	-0.030	0.103	99.7115	4.047E-03	2.43765	2.001E+03	5.018E+06	1.017E+04
33	0.08	0.072	0.061	-0.071	0.008	0.080	99.7699	4.051E-03	2.43697	2.002E+03	5.020E+06	1.015E+04
34	0.10	0.071	0.061	-0.131	0.006	0.077	99.7602	4.057E-03	2.43666	2.002E+03	5.020E+06	1.014E+04
35	0.11	0.072	0.068	-0.015	-0.008	0.080	99.7714	4.063E-03	2.43628	2.002E+03	5.019E+06	1.012E+04
36	0.12	0.072	0.061	-0.008	-0.013	0.085	99.8377	4.050E-03	2.43702	2.002E+03	5.020E+06	1.015E+04
37	0.13	0.079	0.115	-0.045	0.012	0.091	99.7207	4.059E-03	2.43653	2.002E+03	5.019E+06	1.014E+04
38	1.64	0.071	0.060	-0.274	-0.003	0.074	99.8619	4.053E-03	2.43672	2.002E+03	5.020E+06	1.016E+04
39	0.10	0.071	0.061	-0.088	-0.008	0.079	99.9006	4.058E-03	2.43673	2.002E+03	5.019E+06	1.012E+04
40	0.11	0.071	0.060	-0.042	0.008	0.080	99.9052	4.054E-03	2.43694	2.002E+03	5.019E+06	1.013E+04
41	0.08	0.080	0.115	-0.064	0.014	0.094	99.7715	3.990E-03	2.43709	1.999E+03	5.023E+06	1.015E+04
42	0.20	0.072	0.062	-0.193	0.082	0.154	100.5090	4.046E-03	2.44022	2.001E+03	5.020E+06	1.022E+04
43	0.31	0.072	0.061	-0.261	-0.044	0.115	99.7704	4.052E-03	2.43729	2.001E+03	5.020E+06	1.016E+04
44	0.14	0.071	0.061	0.000	-0.007	0.079	99.7888	4.059E-03	2.43659	2.002E+03	5.019E+06	1.013E+04
45	0.58	0.071	0.061	0.009	-0.008	0.079	99.8207	4.052E-03	2.43696	2.002E+03	5.020E+06	1.015E+04
46	0.13	0.072	0.061	-0.151	0.014	0.086	99.8443	4.041E-03	2.43757	2.001E+03	5.020E+06	1.017E+04
47	0.09	0.072	0.061	-0.078	0.004	0.076	99.7668	4.052E-03	2.43698	2.002E+03	5.020E+06	1.015E+04

Table 9.1. RTD Calibration Results.

#	$\chi^2/\nu$	$\sigma_{T_{cal2}}$	$\sigma_{TCVD2}$	$\Delta T_2$	$\Delta T_{cal}$	$u_{T_{tot}}$	$R_o$	$\alpha$	$\delta$	$b_1$	$b_2$	$b_3$
48	0.78	0.080	0.115	-0.159	0.003	0.083	99.7970	4.051E-03	2.43698	2.007E+03	5.020E+06	1.015E+04
49	0.17	0.071	0.061	-0.126	-0.012	0.083	99.6739	4.058E-03	2.43663	2.007E+03	5.020E+06	1.015E+04
50	0.66	0.080	0.115	-0.102	0.003	0.089	99.7005	4.051E-03	2.43700	2.007E+03	5.020E+06	1.016E+04
51	0.36	0.071	0.061	-0.099	-0.018	0.089	99.6951	4.068E-03	2.43605	2.003E+03	5.019E+06	1.012E+04
52	0.12	0.071	0.060	-0.085	0.000	0.072	99.7328	4.059E-03	2.43651	2.007E+03	5.020E+06	1.014E+04
53	0.13	0.079	0.115	-0.047	-0.002	0.081	99.7434	4.071E-03	2.43586	2.003E+03	5.019E+06	1.011E+04
54	0.12	0.072	0.069	-0.054	0.005	0.077	99.7352	4.057E-03	2.43664	2.007E+03	5.020E+06	1.014E+04
55	0.06	0.079	0.115	0.064	-0.026	0.105	99.7312	4.063E-03	2.43632	2.007E+03	5.019E+06	1.013E+04
56	0.12	0.072	0.069	-0.008	-0.012	0.084	99.7383	4.053E-03	2.43683	2.007E+03	5.020E+06	1.015E+04
57	0.24	0.071	0.060	0.131	-0.009	0.081	99.6905	4.071E-03	2.43590	2.003E+03	5.019E+06	1.012E+04
58	0.70	0.071	0.060	-0.072	-0.057	0.128	99.6543	4.074E-03	2.43570	2.003E+03	5.019E+06	1.011E+04
59	0.11	0.071	0.061	-0.057	-0.012	0.083	99.7745	4.065E-03	2.43616	2.007E+03	5.019E+06	1.012E+04
60	0.13	0.072	0.069	-0.080	-0.013	0.086	99.7332	4.055E-03	2.43673	2.007E+03	5.020E+06	1.015E+04
61	0.11	0.071	0.061	-0.086	-0.001	0.073	99.7058	4.065E-03	2.43620	2.007E+03	5.019E+06	1.013E+04
62	0.10	0.123	0.270	-0.114	0.008	0.131	99.7176	4.064E-03	2.43624	2.007E+03	5.019E+06	1.013E+04
63	0.14	0.072	0.068	-0.007	-0.012	0.085	99.7861	4.060E-03	2.43647	2.007E+03	5.020E+06	1.013E+04
64	0.12	0.071	0.060	-0.013	-0.009	0.080	99.7953	4.058E-03	2.43655	2.007E+03	5.020E+06	1.013E+04
65	1.51	0.079	0.115	-0.045	-0.005	0.092	99.8089	4.053E-03	2.43687	2.007E+03	5.020E+06	1.015E+04
66	0.21	0.072	0.069	0.046	-0.004	0.084	99.5174	4.068E-03	2.43599	2.003E+03	5.019E+06	1.014E+04
67	0.25	0.072	0.069	0.019	-0.007	0.076	99.8975	4.050E-03	2.43680	2.007E+03	5.021E+06	1.014E+04
68	0.08	0.072	0.069	-0.186	-0.011	0.080	99.7981	4.056E-03	2.43648	2.007E+03	5.021E+06	1.014E+04
69	0.07	0.072	0.061	-0.039	-0.008	0.083	99.8740	4.053E-03	2.43661	2.007E+03	5.021E+06	1.014E+04
70	0.07	0.072	0.061	0.048	-0.010	0.079	99.8672	4.045E-03	2.43704	2.007E+03	5.021E+06	1.016E+04
71	0.07	0.071	0.061	0.021	-0.010	0.081	99.7629	4.061E-03	2.43620	2.007E+03	5.020E+06	1.013E+04
72	0.11	0.080	0.115	-0.124	0.003	0.099	99.7329	4.053E-03	2.43667	2.007E+03	5.021E+06	1.015E+04
73	0.08	0.072	0.061	-0.077	-0.012	0.075	99.7104	4.050E-03	2.43678	2.007E+03	5.021E+06	1.016E+04
74	0.08	0.071	0.061	-0.077	-0.012	0.084	99.7898	4.063E-03	2.43617	2.007E+03	5.020E+06	1.012E+04
75	0.11	0.079	0.115	-0.141	0.001	0.080	99.7178	4.066E-03	2.43614	2.007E+03	5.019E+06	1.012E+04
76	0.71	0.072	0.068	0.017	0.001	0.073	99.7629	4.063E-03	2.43626	2.007E+03	5.020E+06	1.013E+04
77	0.42	0.071	0.060	-0.256	-0.025	0.097	99.6466	4.071E-03	2.43585	2.003E+03	5.019E+06	1.012E+04
78	0.09	0.072	0.061	0.013	-0.007	0.078	99.9133	4.049E-03	2.43698	2.007E+03	5.020E+06	1.014E+04
79	0.12	0.072	0.069	0.000	-0.010	0.083	99.7424	4.052E-03	2.43744	2.001E+03	5.018E+06	1.015E+04
80	0.07	0.071	0.061	-0.115	0.000	0.072	99.7385	4.060E-03	2.43700	2.007E+03	5.017E+06	1.013E+04
81	0.11	0.071	0.061	-0.161	0.004	0.075	99.7461	4.061E-03	2.43701	2.007E+03	5.017E+06	1.013E+04
82	0.09	0.072	0.061	-0.133	0.015	0.087	99.8798	4.049E-03	2.43766	2.001E+03	5.018E+06	1.014E+04
83	0.15	0.071	0.061	-0.022	-0.010	0.082	99.7084	4.060E-03	2.43707	2.007E+03	5.017E+06	1.014E+04
84	0.10	0.072	0.068	-0.088	-0.003	0.075	99.7013	4.066E-03	2.43677	2.007E+03	5.017E+06	1.012E+04
85	0.16	0.072	0.068	0.106	-0.037	0.110	99.7048	4.069E-03	2.43658	2.007E+03	5.017E+06	1.012E+04
86	0.15	0.072	0.068	-0.052	-0.014	0.086	99.7946	4.061E-03	2.43701	2.007E+03	5.017E+06	1.013E+04
87	0.10	0.080	0.115	0.083	-0.001	0.080	99.8004	4.051E-03	2.43754	2.001E+03	5.018E+06	1.015E+04
88	0.10	0.072	0.068	0.049	0.006	0.078	99.8208	4.066E-03	2.43675	2.007E+03	5.017E+06	1.011E+04
89	0.10	0.072	0.069	0.069	-0.003	0.075	99.7723	4.058E-03	2.43756	2.001E+03	5.016E+06	1.013E+04
90	0.09	0.072	0.061	-0.121	0.021	0.093	99.7805	4.052E-03	2.43790	2.001E+03	5.016E+06	1.015E+04
91	0.10	0.072	0.061	0.083	-0.009	0.080	99.8005	4.051E-03	2.43793	2.001E+03	5.016E+06	1.014E+04
92	0.10	0.071	0.061	0.015	-0.005	0.076	99.7956	4.057E-03	2.43764	2.001E+03	5.016E+06	1.013E+04
93	0.14	0.072	0.061	0.061	-0.012	0.084	99.8210	4.049E-03	2.43808	2.001E+03	5.016E+06	1.015E+04
94	0.15	0.071	0.060	-0.059	-0.009	0.080	99.7909	4.062E-03	2.43734	2.001E+03	5.016E+06	1.012E+04

Table 9.1. RTD Calibration Results.

#	$\chi^2/\nu$	$\sigma_{T_{cal2}}$	$\sigma_{TCVD2}$	$\Delta T_2$	$\Delta T_{cal}$	$u_{T_{tot}}$	$R_o$	$\alpha$	$\delta$	$b_1$	$b_2$	$b_3$
95	0.08	0.071	0.061	-0.154	0.003	0.074	99.7708	4.056E-03	2.43769	2.001E+03	5.016E+06	1.014E+04
96	0.09	0.072	0.061	-0.133	-0.001	0.073	99.7794	4.053E-03	2.43786	2.001E+03	5.016E+06	1.014E+04
97	0.11	0.072	0.068	-0.081	0.004	0.076	99.9263	4.052E-03	2.43789	2.001E+03	5.016E+06	1.014E+04
98	0.07	0.123	0.270	-0.159	-0.002	0.126	99.8723	4.052E-03	2.43796	2.001E+03	5.016E+06	1.014E+04
99	0.10	0.123	0.270	0.007	-0.005	0.128	99.8914	4.054E-03	2.43788	2.001E+03	5.016E+06	1.013E+04
100	0.07	0.071	0.060	-0.093	-0.010	0.081	99.8600	4.050E-03	2.43801	2.001E+03	5.016E+06	1.014E+04
101	0.11	0.079	0.115	-0.073	-0.004	0.083	99.8086	4.064E-03	2.43733	2.001E+03	5.016E+06	1.013E+04
102	0.11	0.071	0.061	-0.100	0.009	0.081	99.8016	4.062E-03	2.43742	2.001E+03	5.015E+06	1.012E+04
103	0.09	0.071	0.061	-0.052	-0.010	0.081	99.7631	4.067E-03	2.43721	2.002E+03	5.015E+06	1.011E+04
104	0.08	0.072	0.069	0.102	0.003	0.075	99.7714	4.056E-03	2.43783	2.001E+03	5.015E+06	1.014E+04
105	0.12	0.072	0.061	-0.016	-0.004	0.075	99.7338	4.055E-03	2.43795	2.001E+03	5.015E+06	1.014E+04
106	0.13	0.071	0.061	0.012	0.005	0.076	99.8579	4.060E-03	2.43770	2.001E+03	5.015E+06	1.012E+04
107	0.09	0.072	0.068	-0.118	0.004	0.076	99.8330	4.057E-03	2.43794	2.001E+03	5.015E+06	1.013E+04
108	0.13	0.072	0.061	-0.045	-0.019	0.090	99.9195	4.052E-03	2.43823	2.001E+03	5.015E+06	1.013E+04
109	0.14	0.071	0.061	-0.034	-0.023	0.095	99.8995	4.055E-03	2.43805	2.001E+03	5.015E+06	1.013E+04
110	1.14	0.071	0.060	-0.178	0.010	0.081	99.7875	4.054E-03	2.43800	2.001E+03	5.015E+06	1.014E+04
111	0.13	0.071	0.061	-0.073	-0.008	0.080	99.7864	4.064E-03	2.43746	2.001E+03	5.015E+06	1.012E+04
112	0.10	0.072	0.061	0.053	-0.007	0.078	99.8160	4.050E-03	2.43821	2.001E+03	5.015E+06	1.014E+04
113	0.09	0.072	0.069	-0.040	0.010	0.082	99.7635	4.050E-03	2.43819	2.001E+03	5.015E+06	1.013E+04
114	0.21	0.072	0.061	-0.200	0.059	0.131	99.8486	4.043E-03	2.43857	2.000E+03	5.016E+06	1.016E+04
115	0.11	0.071	0.061	-0.065	0.009	0.081	99.7363	4.057E-03	2.43788	2.001E+03	5.015E+06	1.014E+04
116	0.11	0.072	0.061	-0.103	0.008	0.079	99.8516	4.056E-03	2.43788	2.001E+03	5.015E+06	1.013E+04
117	0.16	0.072	0.061	-0.121	0.016	0.088	99.8958	4.045E-03	2.43864	2.000E+03	5.015E+06	1.015E+04
118	0.10	0.072	0.069	-0.103	0.012	0.085	99.8189	4.043E-03	2.43870	2.000E+03	5.015E+06	1.016E+04
119	0.13	0.072	0.068	0.096	-0.002	0.075	99.8243	4.062E-03	2.43765	2.001E+03	5.015E+06	1.012E+04
120	0.13	0.071	0.061	-0.045	0.004	0.075	99.8204	4.055E-03	2.43802	2.001E+03	5.015E+06	1.013E+04
121	0.10	0.071	0.061	-0.031	0.000	0.071	99.7933	4.060E-03	2.43778	2.001E+03	5.015E+06	1.012E+04
122	0.07	0.276	0.537	0.047	0.002	0.278	99.8619	4.057E-03	2.43787	2.001E+03	5.015E+06	1.012E+04
123	0.12	0.123	0.270	-0.026	-0.014	0.137	99.8916	4.056E-03	2.43795	2.001E+03	5.015E+06	1.012E+04
124	0.09	0.068	0.068	0.033	0.001	0.073	99.8640	4.058E-03	2.43785	2.001E+03	5.015E+06	1.012E+04
125	0.12	0.079	0.115	-0.012	-0.009	0.088	99.8958	4.054E-03	2.43804	2.001E+03	5.015E+06	1.013E+04
126	0.06	0.071	0.061	0.056	0.016	0.088	99.9465	4.056E-03	2.43800	2.001E+03	5.015E+06	1.012E+04
127	0.13	0.072	0.061	-0.061	0.003	0.074	99.8339	4.054E-03	2.43807	2.001E+03	5.015E+06	1.014E+04
128	0.13	0.072	0.061	-0.207	-0.007	0.079	99.8991	4.049E-03	2.43828	2.001E+03	5.015E+06	1.014E+04
129	0.08	0.072	0.061	-0.140	0.004	0.075	99.8682	4.052E-03	2.43817	2.001E+03	5.015E+06	1.014E+04
130	0.12	0.072	0.061	0.018	0.002	0.073	99.8262	4.050E-03	2.43815	2.001E+03	5.016E+06	1.014E+04
131	0.11	0.071	0.061	-0.104	0.009	0.081	99.8038	4.062E-03	2.43749	2.001E+03	5.015E+06	1.012E+04
132	0.09	0.072	0.061	0.045	0.004	0.076	99.8799	4.054E-03	2.43794	2.001E+03	5.015E+06	1.013E+04
133	0.10	0.072	0.069	0.015	-0.002	0.074	99.7954	4.057E-03	2.43785	2.001E+03	5.015E+06	1.013E+04
134	0.13	0.072	0.069	-0.045	-0.011	0.083	99.9204	4.051E-03	2.43812	2.001E+03	5.015E+06	1.013E+04
135	0.09	0.071	0.061	-0.123	0.012	0.083	99.9351	4.053E-03	2.43806	2.001E+03	5.015E+06	1.013E+04
136	0.08	0.123	0.270	0.025	0.009	0.133	99.8829	4.055E-03	2.43803	2.001E+03	5.015E+06	1.013E+04
137	0.07	0.072	0.061	-0.051	0.010	0.082	99.8982	4.040E-03	2.43883	2.000E+03	5.016E+06	1.016E+04
138	0.10	0.276	0.536	-0.034	-0.004	0.280	99.9039	4.035E-03	2.43914	2.002E+03	5.014E+06	1.009E+04
139	0.08	0.079	0.115	-0.012	-0.012	0.091	99.9007	4.071E-03	2.43713	2.002E+03	5.014E+06	1.009E+04
140	0.10	0.123	0.270	-0.106	-0.019	0.142	99.8542	4.068E-03	2.43766	2.001E+03	5.013E+06	1.010E+04

**SECTION 2**  
**INTEGRAL BOUNDARY LAYER HEAT TRANSFER**  
**PREDICTION ON TURBINE BLADES**

## Chapter 1

# Nomenclature

## 1.1 Subscripts

$()_{AW}$ : adiabatic wall quantity

$()_e$ : edge quantity

$()_0$ : stagnation quantity

$()_P$ : pressure surface quantity

$()_{REF}$ : reference quantity

$()_S$ : suction surface quantity

$()_w$ : wall quantity

$()_\infty$ : freestream quantity

## 1.2 Definitions

$A$  = area

$$C_D = \frac{1}{\rho_\infty U_\infty^2} \int \tau \frac{\partial u}{\partial \eta} d\eta$$

$$C_f = \frac{\tau_w}{\frac{1}{2} \rho_\infty U_\infty^2}$$

$C_p$  = specific heat at constant pressure

$D$  = Diameter, Diffusion Factor

$F_{1-2}$  = View Factor from object 1 to object 2

$$H = \frac{\delta^*}{\theta}$$

$$H^* = \frac{\theta^*}{\theta}$$

$$H^{**} = \frac{\delta^{**}}{\theta}$$

$$H_2 = \frac{\delta_2}{\theta}$$

$$H_k = \frac{\delta_k^*}{\theta_k}$$

$$H_w = \frac{T_w}{T_{0e}}$$

$k$  = coefficient of thermal conductivity

$L$  = streamwise arclength

$L_{MB}$  = Mean Beam Length

$M_e$  = Edge Mach Number

$p$  = partial pressure

$P$  = perturbation coefficient

$Pr$  = Prandtl Number

$q$  = local heat transfer

$$Q = \frac{q_w}{\rho_e U_e C_p T_{0e}}$$

$r$  = temperature recovery factor,  $\sqrt{Pr}$  in laminar flows

$R$  = Reaction

$Re$  = Reynolds Number

$St$  = Stanton Number,  $\frac{q_w}{\rho_e U_e C_p (T_{AW} - T_w)}$

$T$  = temperature

$$T_{AW} = T_e + \frac{\sqrt{Pr}}{2} \frac{U_e^2}{C_p}$$

TET = turbine entrance temperature

$u$  = local streamwise velocity

$U_\infty$  = freestream velocity

$v$  = radial velocity, normal velocity

$V$  = axial fluid velocity

$V_\theta$  = circumferential blade velocity



$\alpha$  = absorption

$\beta$  = Falkner-Skan wedge flow parameter

$\gamma$  = ratio of specific heats

$\delta^\circ$  = deviation angle, the angle between the trailing edge angle of the turbine blade, and the fluid departure angle in the blade reference frame

$$\delta^* = \int (1 - \frac{\rho u}{\rho_* U_*}) dy$$

$$\delta^{**} = \int \frac{u}{U_*} (1 - \frac{\rho}{\rho_*}) dy$$

$$\delta_2 = \int \frac{\rho u}{\rho_* U_*} (1 - \frac{T_0}{T_{0*}}) dy$$

$$\delta_k^* = \int (1 - \frac{u}{U_*}) dy$$

$\delta_T$  = thermal boundary layer thickness

$\delta_U$  = velocity boundary layer thickness

$\Delta W$  = work across turbine stage

$\epsilon$  = emmittance

$\zeta$  = efficiency

$\eta$  = normalized normal boundary layer coordinate  $\frac{y}{\delta_U}$

$$\theta = \int \frac{\rho u}{\rho_* U_*} (1 - \frac{u}{U_*}) dy$$

$$\theta^* = \int \frac{\rho u}{\rho_* U_*} (1 - \frac{u^2}{U_*^2}) dy$$

$$\theta_k = \int \frac{u}{U_*} (1 - \frac{u}{U_*}) dy$$

$\mu$  = viscosity

$\rho$  = local density

$\sigma$  = solidity ( $\frac{\text{circumferencial spacing}}{\text{axial chord}}$ ) or Stefan-Boltzman constant

$\Phi$  = non-dimensional flow coefficient

$\Psi$  = non-dimensional work coefficient

$\omega$  = pressure loss coefficient ( $\frac{\Delta \text{ total pressure across the blade}}{\text{total} - \text{static pressure upstream of blade}}$ )

## Chapter 2

# Introduction

A turbine blade design involves a series of tradeoffs. Aerodynamic efficiency, heat transfer, performance and structural concerns affect the final design. In the turbine, like the rest of the engine, overall efficiency is the guiding design principle. Historically, the aerodynamic efficiency of the blades has been the first criteria [17]. Secondly, structural constraints are imposed to insure that the blade will stand up to the hostile gas turbine environment. High turbine entry temperature (TET), pressure, and rotational speed combine to make this a very hostile environment indeed. Yet this environment is getting more hostile due to increasing TET. By increasing TET specific thrust in a turbofan can be increased [14].

Since cooling is treated almost as an afterthought it is not well represented in the initial design process. Cooling is accomplished by channelling high pressure air from the compressor through ducts in the blades and endwalls of the turbine (Fig. 2.1). On the first stages of the turbine, some of the cooling air is vented through small holes or slots on to the surface of the blade providing an insulating film to further reduce heat transfer. Since this cooling air is not at the same temperature as the main flow, less energy can be removed from it in the turbine stage than had it passed through the combustor [14]. The film cooling also reduces the efficiency of the turbine by mixing with the boundary layer flow and increasing drag on the blades. These losses can be termed cooling losses.

It is difficult to predict the heat transfer in a turbine stage due to several factors including high freestream turbulence, pressure gradients, uncertainty in the blade temperature, and three dimensional effects. Prediction of the transition point, heat transfer in the transitional flow, separation bubbles, separated flow and unsteady effects all combine to make heat transfer prediction something of a black art. In fact, the limit on TET is set by the precision of blade-

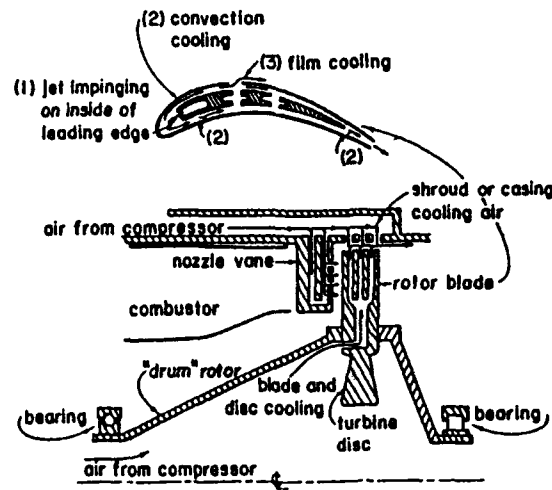


Figure 2.1: Schematic of air-cooled turbine, with cross section of cooled airfoil section at top [14, pg. 176]

cooling design techniques [14, pg. 197]. All modes of heat transfer must be considered when the total heat transfer, and therefore total heat to be removed is calculated.

Since the amount of cooling air needed for the design depends on the heat transfer predicted, uncertainty in the design is involved. Errors in the local heat transfer prediction and hence the surface temperature prediction can cause additional thermal stresses and shorten blade life. If the error is large, blade life could be short. In order to meet contractual obligations to blade life and efficiency several iterations of the build-test-teardown cycle are often necessary. Since each cycle can cost millions of dollars, it is useful to have a design tool that can accurately predict heat transfer and aerodynamic losses thereby reducing the number of necessary cycles.

What would happen if heat transfer were considered first, before the demands of aerodynamic efficiency? If the decrease in aerodynamic efficiency were low compared to the decrease in heat transfer, the tradeoff might raise the total cycle efficiency. The ISES airfoil design code written by Drela and Giles [6] uses integral boundary layer techniques and solves the inviscid

Euler equations for two-dimensional transonic cases. It can act as an analysis tool in which case it takes as input an airfoil shape and performs analysis at the desired conditions. It can also act as a design tool in which case it takes an airfoil and manipulates it toward achieving the specified criteria, be that drag, lift, or other parameter. With some modification ISES could be used to analyze heat transfer, and in the design mode manipulate an airfoil toward a specified heat transfer. From this, one could see how the tradeoff between aerodynamic efficiency and heat transfer would work, and reduce the number of build cycles required.

ISES has been shown to work well at designing and analyzing airfoils [6]. However, ISES boundary layer equations' boundary conditions specify that the wall be adiabatic. Since this is not the case on turbine airfoils this condition must be modified. By allowing heat transfer, lift and drag analysis can be done on non-adiabatic airfoils. In addition, to show the total heat transferred to the blade, a prediction of the local heat transfer based on the boundary layer must be made. Green [9] proposed a method of boundary layer and hence total heat transfer prediction based on forward integration of *three* simultaneous equations as opposed to the two used in ISES: the momentum-integral equation, the entrainment equation, and the total-energy equation [9, Eqns. 17, 19, and A-1]. In BLINT, the boundary layer module of ISES, the kinetic energy shape parameter equation is substituted for the entrainment equation as one of two equations. The other is the momentum-integral equation. When combined with the total-energy equation, we again have a three equation system. These equations are the basis of the aerodynamic performance and heat transfer prediction in this analysis code.

The computational time involved in solving the boundary layer and Euler equations depends very strongly on the number of variables. An integral non-adiabatic boundary layer code would have the advantage of having many fewer variables than a finite difference code. Hence, as ISES stands now an adiabatic integral boundary layer scheme is included, and the non-adiabatic modification developed in this thesis is also an integral method.

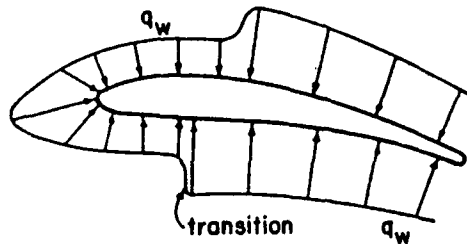


Figure 2.2: Distribution of heat transfer on a cooled turbine blade, showing sudden increase at boundary-layer transition to turbulent state [14, pg. 178]

Previous work by Nicholson [17] has shown that pressure surface heat transfer reduction can be achieved without significant reductions in aerodynamic efficiency. This reduction was achieved by tailoring the boundary layer not only near the laminar leading edge region, but also in the turbulent and relaminarized regions downstream. However, since the highest local levels of heat transfer are found near the leading edge of the blade in the laminar region (Fig. 2.2 [14]), the fraction of heat transferred in this region might be a high fraction of the total heat transfer depending on the length of the blade. Optimization of the leading edge laminar region, which this analysis code aides in, could lead to significant reductions on the total blade heat transfer. This code is the first step in modifying ISES to handle all non-adiabatic flows.

This analysis code takes as input an edge velocity distribution, the Reynolds number,  $Re_L$ , the Prandtl number,  $Pr$ , and the wall to freestream stagnation temperature ratio,  $H_w$ . Output is  $\theta$ ,  $\delta^*$ , and  $\delta_2$ , as well as the local integral parameters and heat transfer. From these both heat transfer and losses due to the boundary layer can be examined.

This thesis will describe and demonstrate a laminar integral heat transfer code that is the first step in developing a non-adiabatic ISES airfoil design code. The different modes of heat transfer will be examined to determine their relative contributions to the heat transfer problem. The trade off between designing for aerodynamic efficiency and designing for low heat transfer will be examined. Finally, the motivation behind developing an integral boundary layer heat transfer code, its development and testing against finite difference codes and experiment, and some recommendations for future work will be discussed.

## Chapter 3

# Modes of Heat Transfer

This chapter will examine the relative contributions of the three modes of heat transfer in a turbine environment. Radiation, conduction and convection will each be described and examined to see where the largest potential for heat transfer improvement lies.

### 3.1 Radiation

Radiation heat transfer is governed by the familiar Stefan-Boltzman law:

$$Q_{NET} = F_{1-2} \sigma A_1 (T_1^4 - T_2^4) \quad (3.1)$$

where  $F$  is the view factor that depends on the geometry of the situation,  $A$  is the area, and  $\sigma$  is the Stefan-Boltzman constant. This formula is only valid for black bodies, that is bodies which emit according to the formula:

$$e(T) = \sigma T^4 \quad (3.2)$$

Since real objects are gray, that is they do not emit according to the above formula but some fraction thereof, the constant  $\epsilon$  is added to the formula:

$$e(T) = \epsilon \sigma T^4 \quad (3.3)$$

where  $\epsilon$  is the emittance. This is strictly valid only if  $\epsilon$  is integrated over the entire electromagnetic spectrum, and in that case  $\epsilon_T$  is called the total emittance. For a gas it is often difficult to find an equivalent  $\epsilon_T$  since it depends on the pressure, the volume of the radiating gas, and the composition of the gas.



To find the radiative heat transfer between the products of combustion and a turbine blade the following approximation is used:

$$\frac{q}{A} = \epsilon_g(T_g)\sigma T_g^4 - \alpha_g(T_w)\sigma T_w^4 \quad (3.4)$$

[11] where  $\alpha_g(T_w)$  is the absorptivity of the gas at the wall temperature ( where  $()_g$  designates a gas quantity). The geometry of the situation is taken into account through the emittance of the gas. Hottel and Sarafim [15] have devised a factor called the mean beam length,  $L_{MB}$ , which correlates the geometry and pressure into both the emittance and absorptivity of the gas. This method is not intended to be 100% accurate, but it does simplify the problem sufficiently to allow rapid evaluation. A complete discussion of gaseous heat transfer can be found in Holman [11].

The combustion process will yield products that are different from air, and therefore these are the gasses that should be considered in the turbine blade radiation heat transfer problem. The combustor yields a mixture of oxygen, nitrogen, water vapor, and carbon dioxide, plus a few minor others depending on the fuel. The emittance of oxygen and nitrogen are small compared to the emittance of carbon dioxide and water vapor so they are neglected [11]. The emittance of carbon dioxide and water vapor depend on the pressure and temperature of the gasses, as well as the geometry of the turbine. Figure 3.1 shows the ratio of radiative to total heat transfer in a turbine. The convective heat transfer is calculated by assuming a representative Nusselt number from Guenette et al. [10] and several representative temperatures. At no point in the calculations does the ratio of radiative heat transfer to total heat transfer exceed 9%. With this in mind tackling the radiation heat transfer problem is not warranted since even a 10% reduction in radiative heat transfer results in less than a 1% total heat transfer reduction. See Appendix A for further explanation.

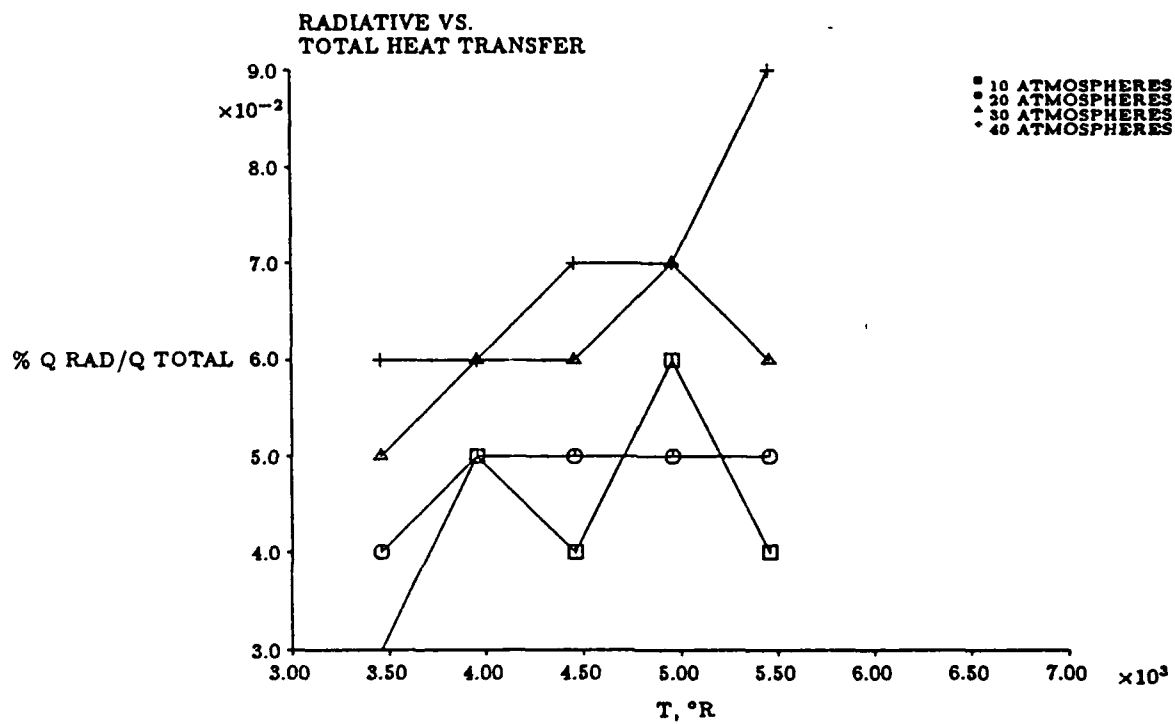


Figure 3.1: Radiative heat transfer/total heat transfer for four pressures as a function of temperature. Wall temperature was 2010° R. Gas was assumed to be products of combustion as described in Appendix A

### 3.2 . Conduction

Turbine blades are currently made of metallic alloys. As such they have high coefficients of thermal conductivity,  $k$ . The result of this is that heat flows freely through the turbine blade, tending to equalize the temperature across the blade. However, the temperature is also driven by the local heat transfer which is decidedly non-uniform (Fig. 2.2). The various cooling schemes also tend to cool the blade unevenly, driving the blade to non-uniform temperatures. The net result is to have hot spots along the blade, especially at the leading edge where heat transfer is particularly high.

The interior arrangement of cooling ducts also influences the external temperature profile. Heat is conducted more easily through portions of the blade that are thick. Thin regions, such as the trailing edge, will be highly dependent on the external heat transfer to determine the blade temperature (Fig. 2.2). Thick regions also are more susceptible to thermal stress problems, so increasing the thickness to make the temperature distribution more uniform is not the answer.

### 3.3 Convection

Convection is the primary heat transfer mode in the turbine environment. Internally, heat is carried away from the surface by the circulating cooling air. Externally, heat is transferred to the blade due to the higher temperature combustion products. Convection is a function of the boundary layer temperature gradient as well as the heat transfer coefficient:

$$\frac{q}{A} = -k \frac{\partial T}{\partial y} \quad (3.5)$$

From Newton's law of cooling  $\frac{q}{A} = h(T_w - T_{AW})$ , so the heat transfer coefficient  $h$  is:

$$h = \frac{-k(\frac{\partial T}{\partial y})|_w}{(T_w - T_{AW})} \quad (3.6)$$

The driving temperature gradient for convective heat transfer in compressible boundary layers is  $T_{AW} - T_w$ . Non-dimensionalizing by the freestream stagnation temperature yields  $\frac{T_{AW}}{T_{0e}} - \frac{T_w}{T_{0e}}$ .  $\frac{T_w}{T_{0e}}$  is named  $H_w$ .  $\frac{T_{AW}}{T_{0e}}$  is defined as:

$$\frac{T_{AW}}{T_{0e}} = T_e + \frac{\frac{\sqrt{Pr} U_e^2}{2C_p}}{T_e + \frac{U_e^2}{2C_p}}$$

or

$$\frac{T_{AW}}{T_{0e}} = \frac{2 + \sqrt{Pr}(\gamma - 1)M_e^2}{2 + (\gamma - 1)M_e^2} \quad (3.7)$$

For  $Pr = 1$ ,  $\frac{T_{AW}}{T_{0e}} = 1$ . For  $Pr \neq 1$ ,  $\frac{T_{AW}}{T_{0e}} \neq 1$ , but if  $Pr \approx 1$  this ratio is essentially 1. Therefore the driving temperature gradient is approximately  $1 - H_w$ .

The heat transfer coefficient depends on several parameters but primarily on the thickness and nature of the boundary layer. Thin boundary layers conduct more heat than thick ones, turbulent boundary layers conduct more heat per unit thickness than do laminar boundary layers [11]. Convective heat transfer is most simply predicted by the Reynolds analogy (Eqn. 4.3). A new method of heat transfer prediction will be discussed in Section 5.3.

Each of the three modes of heat transfer has been examined. It was shown that although radiation plays a part in heat transfer it is a small one. The role of convection from the products of combustion plays the largest role in turbine heat transfer. Although much of a turbine blade's surface is probably turbulent, the laminar leading edge region is one of the highest regions of heat transfer due to the very thin boundary layer. The model developed here will predict the local external convective heat transfer for the laminar leading edge region (Fig. 2.2).

## Chapter 4

# Heat Transfer vs. Aerodynamic Efficiency

Gas turbine blade design has traditionally been concerned primarily with minimizing profile losses at a given blade loading. In order to examine the relationship between blade profile losses and heat transfer a method is needed that utilizes similar parameters to describe both the heat transfer and the blade profile losses. Although the diffusion factor method described in Ainley and Mathieson [1], Smith [21], Stewart, Whitney and Wong [22], NASA SP-36 [13], and Kerrebrock [14] is an approximate method, it allows the two factors to be compared without extensive computation. This simplification allows the problem to be generalized to any airfoil, and allows the two factors to be directly related. From this analysis heat transfer and profile loss trends can be examined, and the trade off between the two can be shown in a simple manner.

Several factors influence the blade drag: blade loading  $\Psi = \frac{\Delta W}{V_s^2}$ , is a measure of how much work can be extracted at a given turbine speed,  $\Phi = \frac{V}{V_s}$  is the flow coefficient or non-dimensional mass flow. These two factors are related by the reaction,  $R$ , defined as the change in enthalpy across the rotor over the enthalpy change across the rotor and stator combined [12]. The diffusion factor,  $D$ , defined variously as

$$D = 1 - \frac{V_s}{V_p} \quad (4.1)$$

in [22] or

$$D = 1 - \frac{V_s}{V_p} + \left| \frac{v_2 - v_1}{2\sigma V_p} \right| \quad (4.2)$$

in [14] (where  $v_2 - v_1$  is the change in tangential velocity) is an empirical correlation with the momentum thickness.  $\omega$  measures the total pressure loss across the rotor and is a good measure of the 2-D rotor airfoil efficiency [14]. The deviation angle,  $\delta^\circ$ , is the difference between the

trailing edge angle of the blade, and the exit angle of the gas. According to [14],  $\delta^\circ \sim \frac{\Phi}{\sqrt{\sigma}}$ ; this is why as the solidity decreases,  $\omega$  increases as the flow is not turned completely through the rotor.

The Reynolds analogy provides a first order method of comparing the local heat transfer with the diffusion factor through the blade solidity:

$$St = \frac{C_f}{2 Pr} \quad (4.3)$$

$Q$  is a function of both  $St$  and  $\sigma$ ,  $D$  is also a function of  $\sigma$ . Therefore the diffusion factor analysis of [14] can be used to compare the total pressure loss,  $\omega$ , with the integrated total heat load,  $Q$ .

Figures 4.1 from [20] and 4.2 from [16] show two typical turbines at their operating points. The factor  $\Phi\Psi$ , the non-dimensional power output, is constant at all points on the figures. Any turbine operating at these conditions would have the same amount of power output per unit mass flow. These figures show lines of constant non-dimensional mass flow  $\Phi$ . As the solidity decreases, the pressure loss coefficient increases until it is impossible to achieve the specified power output at any flow rate. Low solidity means a high deviation angle, hence low flow turning. It is easily seen that by deviating from the point of maximum aerodynamic efficiency to the left yields lower aerodynamic efficiency but also lower total heat transfer. An analysis of relative cycle costs, e.g. the price for a 1% aerodynamic efficiency increase, could show where the point of minimum total cycle costs would lie. From these graphs the trade off between aerodynamic efficiency and heat load can be seen clearly. Figures 4.1 and 4.2 show that the two turbines are operating at points slightly to the left of their predicted points of maximum aerodynamic efficiency, as would be predicted in light of the above discussion.

Although first order methods, the Reynolds analogy for predicting heat transfer, and the Diffusion Factor analysis for predicting aerodynamic efficiency have been combined to show the trade off between total heat transfer and aerodynamic efficiency. A point of maximum

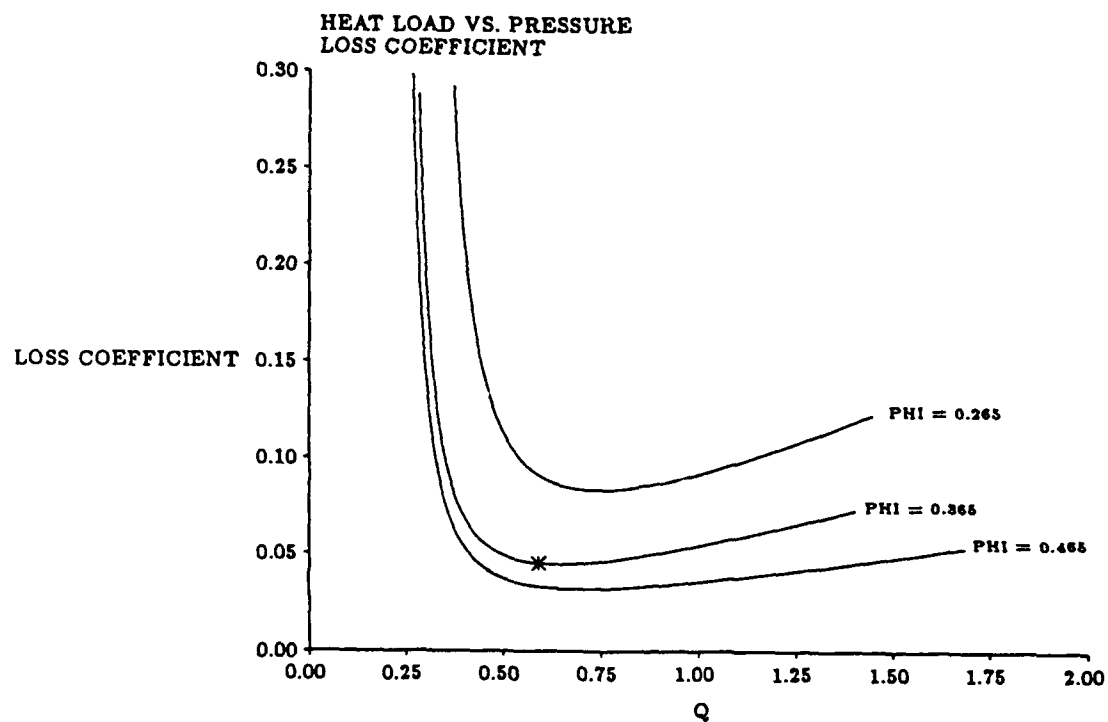


Figure 4.1: Pressure loss vs. heat load for a generic turbine with: reaction = 0.409,  $\Phi\Psi = 0.405$ , solidity = 1.7, showing three mass flows. \* designates the operating point of the NASA TM-83431 turbine which has these stated operating conditions.

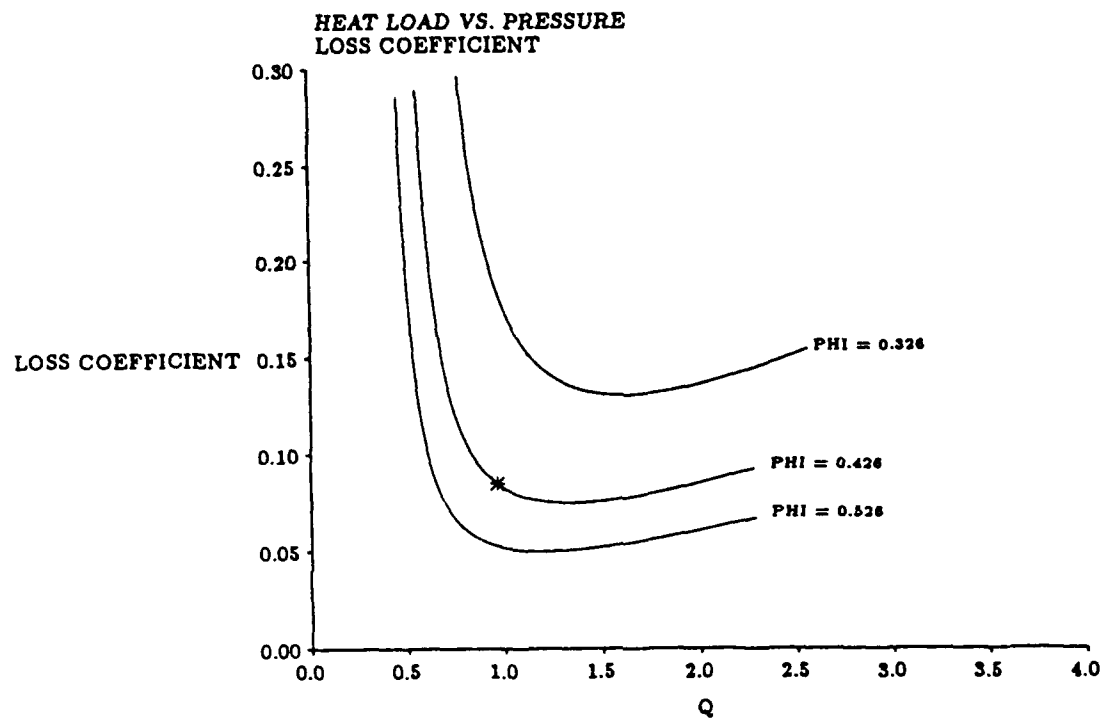


Figure 4.2: Pressure loss vs. heat load for a generic turbine with: reaction = 0.230,  $\Phi\Psi = 0.666$ , solidity = 1.7, showing three mass flows. \* designates the operating point of the NRC/PWC turbine which has these stated operating conditions.



aerodynamic efficiency is shown to lie at some particular solidity for a given power output and mass flow rate. By deviating from this point lower total heat transfer may be attained at the cost of decreased aerodynamic efficiency. Depending on the relative costs of aerodynamic efficiency and cooling costs the point of minimum total losses (cooling plus aerodynamic) may or may not lie at the point of minimum aerodynamic losses. With the proper analysis tool, i.e. one that can predict both heat transfer and aerodynamic losses, this point of minimum total losses can be found more easily.

## Chapter 5

# Analysis Code

White [24] defines three types of computer generated boundary layer solutions: series expansion, finite difference, and approximate techniques. He goes on to further divide approximate techniques into integral methods, similarity patching, and weighted residual approaches. Series solutions are laborious, and are not suited for computational use. Finite difference solutions have the advantages that they are easily implemented on the computer, and are highly accurate, but have the disadvantage of being typically slower than integral methods. Integral methods have the advantages of being simple and computationally rapid. Drela and Giles [6] have written a design and analysis code (ISES) which uses the integral methods and has been shown to be highly accurate as well as rapid for two-dimensional adiabatic flows.

In order to handle turbine flows, which is the motivation for modifying ISES, the boundary layer solution scheme must be modified to handle non-adiabatic flows. Since BLINT is already structured to interface with ISES, it makes sense to use the format of BLINT with some modification to solve the non-adiabatic boundary layer equations. BLINT has the advantages over finite difference codes of being more computationally rapid. In addition, few integral heat transfer codes have been written.

### 5.1 Integral Boundary Layer Equations

The equations used in UNI are derived in Appendix B. By integrating across the boundary layer the resulting boundary layer equations are functions of only the streamwise coordinate and the integral boundary layer parameters ( $\theta$ ,  $\delta^*$ ,  $H$  etc.). For compressible flow the following

Kármán integral equations and the enthalpy equation result:

$$\frac{\partial \theta}{\partial x} + \frac{\theta}{U_e} \frac{dU_e}{dx} (2 + H - M_e^2) = \frac{C_f}{2} \quad (5.1)$$

$$\theta \frac{dH^*}{dx} + (2H^{**} - H^*(H - 1)) \frac{\theta}{U_e} \frac{dU_e}{dx} = 2C_D - H^* \frac{C_f}{2} \quad (5.2)$$

$$Q - H_2 \left( \frac{C_f}{2} - (H + 1) \frac{\theta}{U_e} \frac{dU_e}{dx} \right) = \theta \frac{dH_2}{dx} \quad (5.3)$$

These three simultaneous differential equations are integrated by marching downstream. The solution is the three dependent variables  $\theta$ ,  $\delta^*$ , and  $\delta_2$ . A Newton-Raphson solver is used to iteratively solve for the three variable at each streamwise position. The residual for each equation is found and driven toward zero. Each equation is linearized in essentially the same way as Chapter 6.10 of [5] except that the edge Mach number and velocities are treated as constants, since in UNI they are specified.

## 5.2 Dimensions and Non-dimensionalization

In the equations in this program most variables are naturally non-dimensionalized, that is they appear in forms like  $\frac{u}{U_e}$ ,  $\frac{\rho}{\rho_e}$  etc. (see Section 1.2). However, the input velocity vs. streamwise arclength must be non-dimensionalized. Choosing the simplest values possible,  $x$  is non-dimensionalized by  $L$ , the streamwise trailing edge arclength, and  $U_e$  is non-dimensionalized by the freestream speed of sound  $a_0 = \sqrt{\gamma RT}$ .

The dimensions on  $\theta$ ,  $\delta^*$ , and  $\delta_H$  are relatively easy to interpret. Each has a significant meaning:  $\delta^*$  is the displacement thickness, that it is the distance that the inviscid flow is displaced from the edge of the airfoil. The momentum thickness also has an important meaning. It is the thickness of a stream of fluid with the edge velocity  $U_e$ , and edge density  $\rho_e$  that contains an amount of momentum equal to the momentum deficit in the boundary layer. The enthalpy thickness is similar to the momentum thickness. It is the thickness of a stream of fluid with the edge velocity  $U_e$ , edge density  $\rho_e$ , and edge stagnation temperature  $T_{0e}$  that contains an

amount of enthalpy equal to the enthalpy deficit in the boundary layer. This is significant in that this is the amount of enthalpy absorbed by the blade.

The other thicknesses,  $\theta^*$ , and  $\delta^{**}$ , the kinetic energy thickness and the density thickness are similarly the fluid stream thicknesses containing the same kinetic energy and mass as the kinetic energy and mass deficits in the boundary layer.

### 5.3 Unified Heat Transfer and Loss Prediction Code (UNI)

The code takes as input the edge flow velocity vs. streamwise distance, the Reynolds number  $Re_L$ , and the wall to freestream stagnation temperature ratio,  $H_w$ . To identify the particular gas involved and the dimensioned temperature of the flow the Prandtl number,  $Pr$ , at the flow conditions, a temperature correlation constant based on  $Pr$ , and the ratio of specific heats ( $\gamma$ ) are also needed.

In order to close equations 5.1 through 5.3 five functional relations are needed in terms of the dependent variables and parameters:

$$H^* = H^*(H_k, M_e, Re_\theta) \quad (5.4)$$

$$H^{**} = H^{**}(H_k, M_e) \quad (5.5)$$

$$C_f = C_f(H_k, M_e, Re_\theta) \quad (5.6)$$

$$C_D = C_D(H_k, M_e, Re_\theta) \quad (5.7)$$

$$Q = Q(H_k, M_e, Re_\theta, H_w, H_2) \quad (5.8)$$

$M_e^2$  is obtained from the edge flow velocity at each streamwise coordinate [4];  $Re_\theta$  is a function of the solution variable  $\theta$ .  $H_k$ , the kinematic shape parameter, relates the given flow to an equivalent incompressible flow through  $M_e^2$ ,  $H_2$  and  $H_w$ . Equations 5.4 through 5.7 are given in BLINT [5]. Two of the five,  $H^*$  and  $H^{**}$ , have no temperature dependence independent of  $H_k$ , therefore they can be used without modification from BLINT.  $C_D$  and  $C_f$  are dependent

on the local values of the viscosity, which is dependent on the local temperature and cannot be modelled effectively by  $H_k$  alone.  $C_f$  is corrected using the temperature-viscosity relation of Rayleigh [24].

$$\frac{\mu}{\mu_{REF}} = \left(\frac{T}{T_{REF}}\right)^n \quad (5.9)$$

for air  $n=0.666$  [24].

Since  $C_D$  depends on the integrated values of the viscosity the Rayleigh equation is not the proper correction. A correction to  $C_D$  based on Drela's finite difference code BLAKE [4] is included in UNI. The quantity  $r \frac{\partial u}{\partial \eta}$  was integrated over the boundary layer at three  $H_w$ . This quantity and hence  $C_D$  was found to vary approximately as  $0.2(1 - H_w)^2$  over the range of  $H_w$  tested ( $0.6 \leq H_w \leq 1.0$ ).

$Q$ , the local heat transfer, is predicted using an integral shape parameter relationship. This relationship was not needed for the adiabatic conditions of BLINT and was obtained empirically by observing solutions from BLAKE. The quantities  $H_k * C_f * (1 - H_w)$  and  $St * H_2$  were found for all the test cases and all the test profiles describes in Chapter 6. The resulting linear relationship for all points is shown in Figure 5.1. This relationship varies little with  $Re_L$  or freestream pressure gradient. It is definitely a function of  $Pr$ . As  $H_w$  approaches 1 (adiabatic conditions) the relationship is less accurate since the factor  $(1 - H_w)$  approaches 0. This method of heat transfer prediction yields better results than the Reynolds analogy since that relationship was developed for flat plate flow and  $Pr = 1$ . Even when corrected for pressure gradient (Fig. 5.2 [24, pg. 286]) the new relationship gives better agreement with the finite difference code results. Reynolds analogy corrected for pressure gradient is:

$$St_x = \frac{C_{fx}}{2Pr^{\frac{2}{3}} \frac{f''}{G(1,\beta)}} \quad (5.10)$$

This new relationship is interesting in its simplicity. Deviation from the linear results is greatest at the points of high acceleration (Fig. 5.1, near the origin). No  $Re_L$  dependence at all was

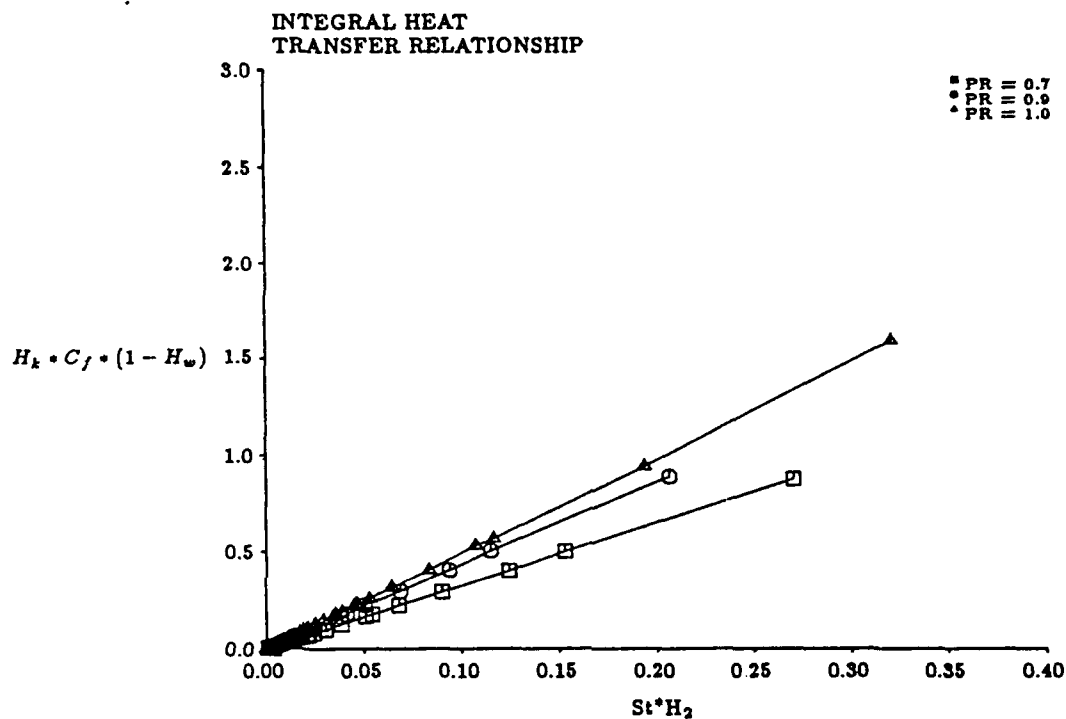


Figure 5.1: Integral correlation to determine the local heat transfer coefficient, derived from BLAKE results. Y-axis is a measure of surface friction and the driving temperature gradient, X-axis is a measure of heat transfer coefficient

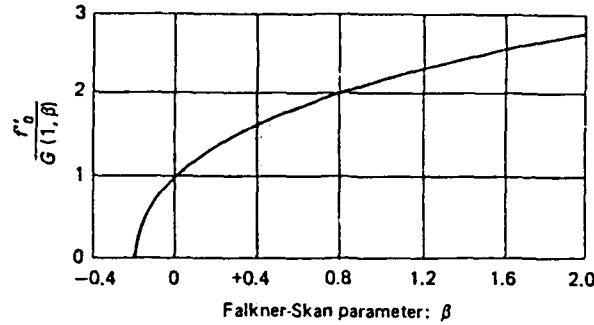


Figure 5.2: Reynolds analogy variation with  $\beta$ , the Falkner-Skan freestream pressure gradient coefficient [24, pg. 286]

observed. It is also surprising in its accuracy since it predicts the actual heat transfer as well as heat transfer trends quite well.

$H_k$  relates the actual flow to an equivalent incompressible flow. In BLINT the only source of compressibility is through Mach number effects. However, since there is now a temperature gradient this effect must also be accounted for. In BLINT the relationship between  $H_k$  and  $H$  is a simple algebraic one through  $M_e^2$  [5].

$$H_k = \frac{H - 0.290M_e^2}{1 + 0.113M_e^2} \quad (5.11)$$

To account for the effects of temperature a more complicated relationship has been developed.

Since  $M_e^2$  is known from the external flow, and  $H_w$  is given,  $H$  and  $H_2$  are functions of the one free parameter,  $H_k$ .  $H$  and  $H_2$  depend on the velocity and temperature boundary layer profiles, so in order to correlate  $H_k$  to  $H$  and  $H_2$ , it is necessary to define the boundary layer profiles in terms of  $H_k$ . The boundary layer velocity profile has the following boundary

conditions:

$$u(1) = 1$$

$$u(0) = 0$$

$$u^N(1) = 0$$

where  $N = 1$  to  $\infty$  (derivatives with respect to  $\eta$ ).

In the tradition of Pohlhausen (1921) [24] an approximate velocity profile was chosen as a polynomial of  $\eta$ . Several velocity profiles using only integer exponents of  $\eta$  were attempted. It was found that with these formulae it is impossible to attain  $H_k = 2$ . In fact, by approximating  $u(\eta)$  with  $N$  terms ( $u(\eta) = A_1\eta + A_2\eta^2 + \dots + A_N\eta^N$ ) the limit as  $N \rightarrow \infty$  reaches  $H_k = 2$ . By using a fractional exponent (in this case  $\sqrt{\eta}$ ) it is possible to reach much lower  $H_k$ , (in this case  $H_k \approx 1.6$ ).  $H_k = 2$  is the lowest  $H_k$  that is physically possible without a velocity overshoot [24]. A third order polynomial was used in order to capture the three boundary conditions

$$u(1) = 1$$

$$u(0) = 0$$

$$u'(1) = 0$$

and an integral condition such that when  $u(\eta)$  is substituted into the definition of  $H_k$ , the specified  $H_k$  results. A higher order polynomial could have been used but this would have seriously complicated the tedious task of defining the polynomial coefficients in terms of  $H_k$ . Since the three boundary conditions are fixed, the shape of the boundary layer velocity profile is dependent only on  $H_k$ .

A temperature profile is assumed across the boundary layer as well  $\frac{T_0}{T_{0e}} = \frac{T_0}{T_{0e}}(\eta)$ . The boundary conditions on this are:

$$\frac{T_0}{T_{0e}}(0) = H_w \quad (5.12)$$



$$\frac{T_0}{T_{0e}}(1) = 1 \quad (5.13)$$

The baseline temperature profile shape is that for a flat plate at the given  $H_w$  [24]. This shape is varied by a perturbation function  $P\eta(1 - \eta)$  where  $P$  is the perturbation coefficient.

Since the stagnation temperature ratio is specified yet the density gradient depends on the static temperature ratio, the static temperature ratio is a derived quantity. This requires that the temperature and velocity gradients in the boundary layer be coupled. We know that for flows where  $Pr \neq 1$  the thicknesses  $\delta_T$  and  $\delta_U$  are not identical. For laminar flow an empirical relationship has been developed to relate  $\delta_T$  and  $\delta_U$ :

$$\frac{\delta_T}{\delta_U} = Pr^{0.42} \quad (5.14)$$

[24]

The solution process is iterative using a Newton-Raphson solver starting at an estimated  $H$  and  $H_2$ , guessing  $H_k$  and  $P$ , substituting the resulting velocity and temperature distributions into the definitions of  $H_k$  and  $H_2$ , then correcting  $H_k$  based on the resulting  $H$ , and correcting  $P$  based on the resulting value of  $H_2$ . The resulting  $H_k$  is used to define the quantities in Equations 5.4 through 5.8. These are substituted into the residuals of Eqs. 5.1 through 5.3. If the residuals are larger than the prescribed maxima, a correction is calculated for  $\delta^*$ ,  $\theta$ , and  $\delta_2$ , and the process repeats.

The result is an integral, non-adiabatic boundary layer solution scheme similar in form to Drela's BLINT code. This scheme can be implemented to determine the heat transfer and profile losses for a non-adiabatic laminar airfoil. It is the first step in modifying the ISES airfoil design and analysis code to handle turbine airfoils.

## Chapter 6

# Test Cases

### 6.1 Development

During the development process the unified heat transfer and loss prediction code was checked against Drela's finite difference code BLAKE [4]. Several freestream velocity profiles were developed as test profiles; these were implemented at different  $M_e$ ,  $Pr$ ,  $H_w$ , and  $Re_L$ , where  $Re_L$  is in terms of the streamwise arclength. The development test profiles were: flat plate (constant velocity), a Falkner-Skan wedge flow with  $\beta = 0.5$  (parabolic velocity profile), and a simulated airfoil profile with flow from a stagnation point over a circular cylinder to the maximum velocity ( $2U_\infty$ ) followed by a flat plate region, then decreasing velocity until separation (sinusoidal velocity increase followed by constant velocity, then a velocity decrease) (Figs. 6.1, 6.2, and 6.3).  $U_e$  is given in terms of the leading edge speed of sound.

Since the code is intended to be used for turbine blade analysis the test conditions were designed to simulate typical turbine leading edge flows. The development test parameter space was:

$$\begin{aligned}0.0 < M_e < 1.0 \\0.7 < Pr < 1.0 \\1.0 \times 10^5 < Re_L < 1.0 \times 10^7 \\0.6 < H_w < 1.0\end{aligned}$$

Tests were conducted by prescribing  $Pr$ ,  $H_w$ , and  $Re_L$  for the flow, and allowing  $M_e$  to be calculated from the specified velocity. Identical conditions were specified for both UNI and BLAKE, so the solutions were directly comparable. (Table 6.1).

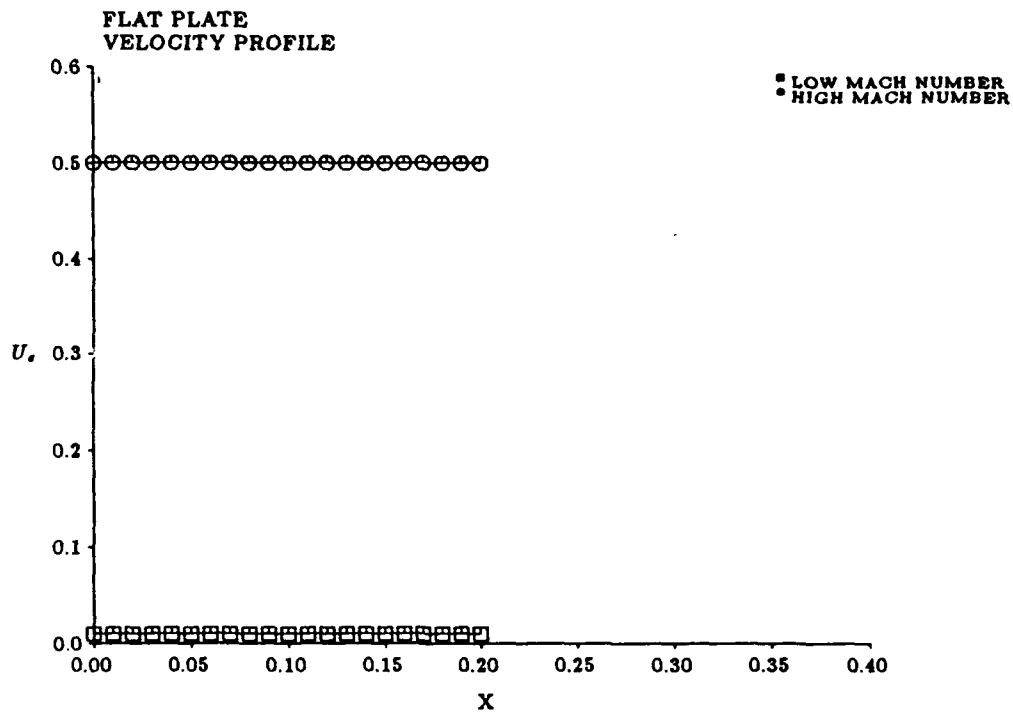


Figure 6.1: Flat plate profiles

1.  $Pr = 0.7, Re = 1.0 \times 10^5$
2.  $Pr = 1.0, Re = 1.0 \times 10^5$
3.  $Pr = 0.7, Re = 5.0 \times 10^6$
4.  $Pr = 1.0, Re = 5.0 \times 10^6$
5.  $Pr = 0.7, Re = 1.0 \times 10^7$
6.  $Pr = 1.0, Re = 1.0 \times 10^7$

Table 6.1: List of developmental test cases

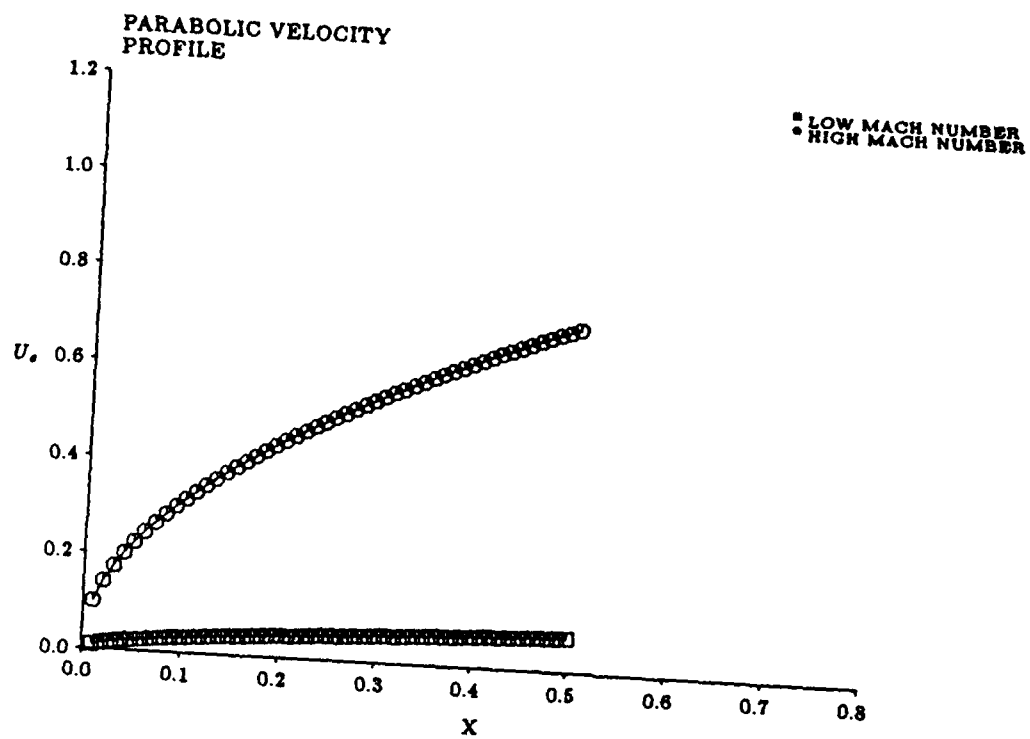


Figure 6.2: Parabolic profiles

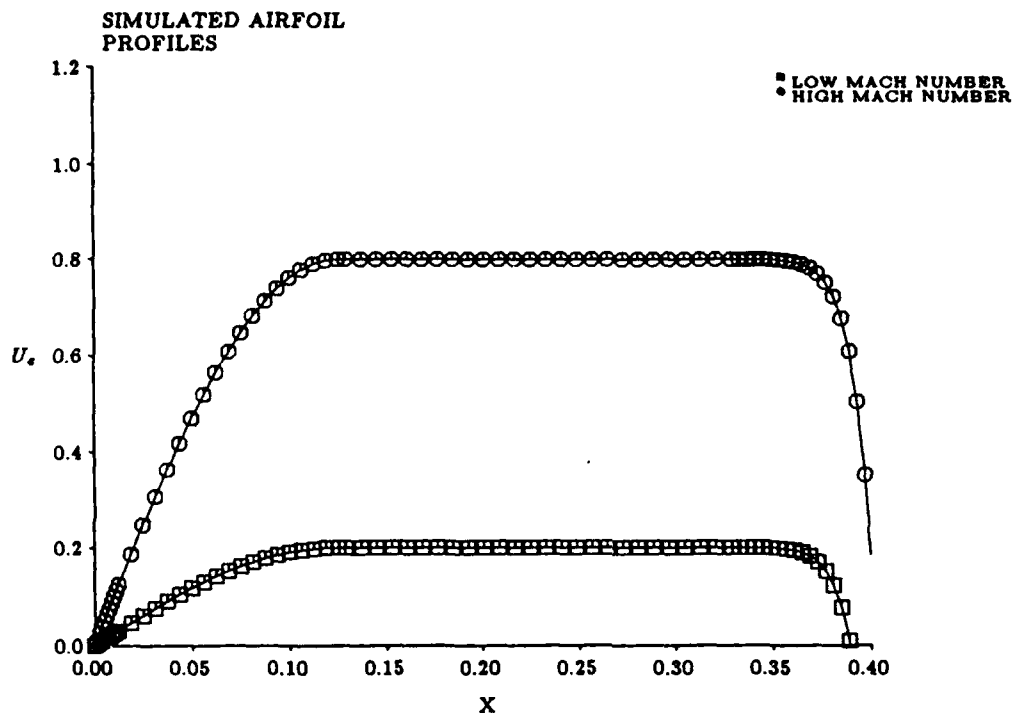


Figure 6.3: Simulated airfoil profiles

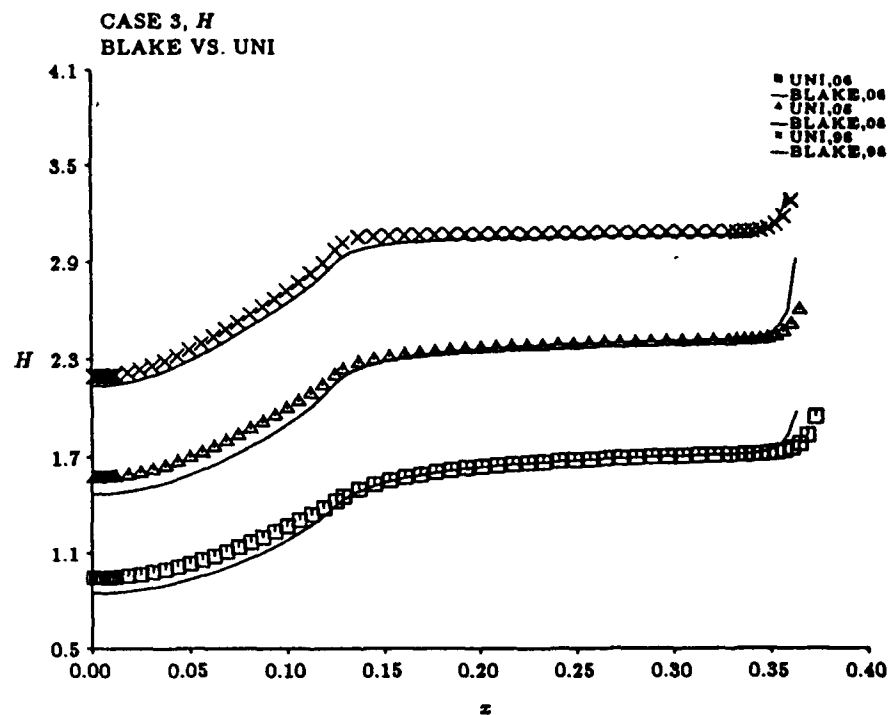


Figure 6.4: Case 3,  $H$  vs.  $x$ . For all cases 3 and 4, the individual points are UNI results, the solid lines indicate the BLAKE solution at the same  $H_w$

Implementing UNI and BLAKE yields several output variables. Since the loss and heat transfer measurements are of greatest interest, these were the results that were directly compared. Loss calculations were compared through the shape parameter  $H$ , heat transfer calculations through the enthalpy thickness shape parameter  $H_2$ . In addition, local values of  $C_f$  and Stanton number were compared. Since the integral parameters scale with the Reynolds number, the shape factors  $H$  and  $H_2$  are identical for the range of Reynolds numbers tested.

Figures 6.4 through 6.16 show a comparison between finite difference results from BLAKE and integral results from UNI. The plots are for  $Re = 5.0 \times 10^6$ . In case 3,  $Pr = 0.7$ , and case 4,  $Pr = 1.0$ . Both are for the high Mach number simulated airfoil flow (see Figure 6.3). The simulated airfoil case was chosen to represent the developmental cases because of its full sweep of shape parameter values, from stagnation point to separation.

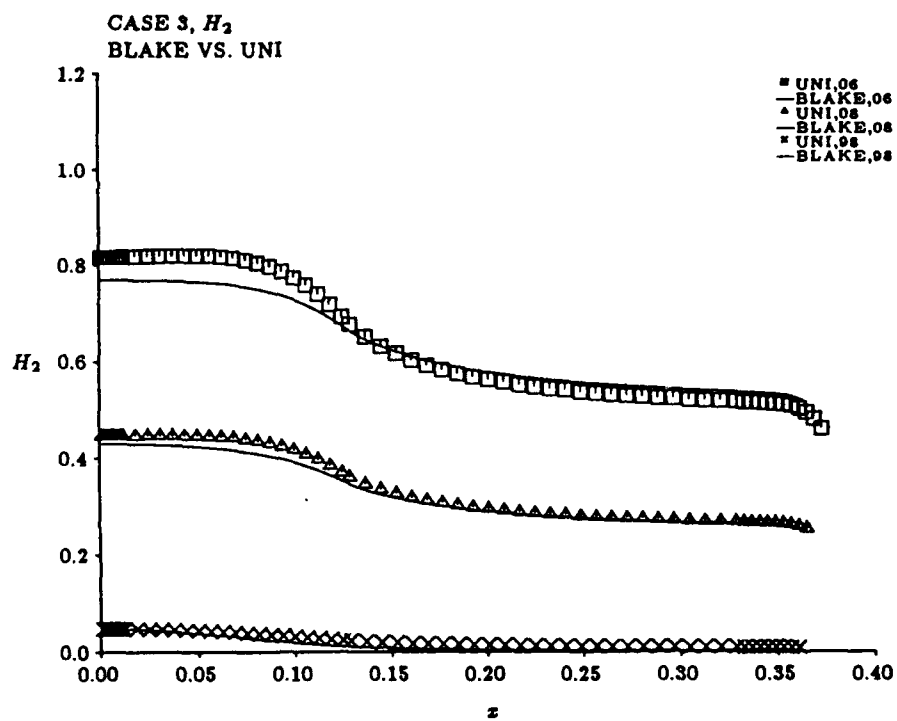


Figure 6.5: Case 3,  $H_2$  vs.  $x$

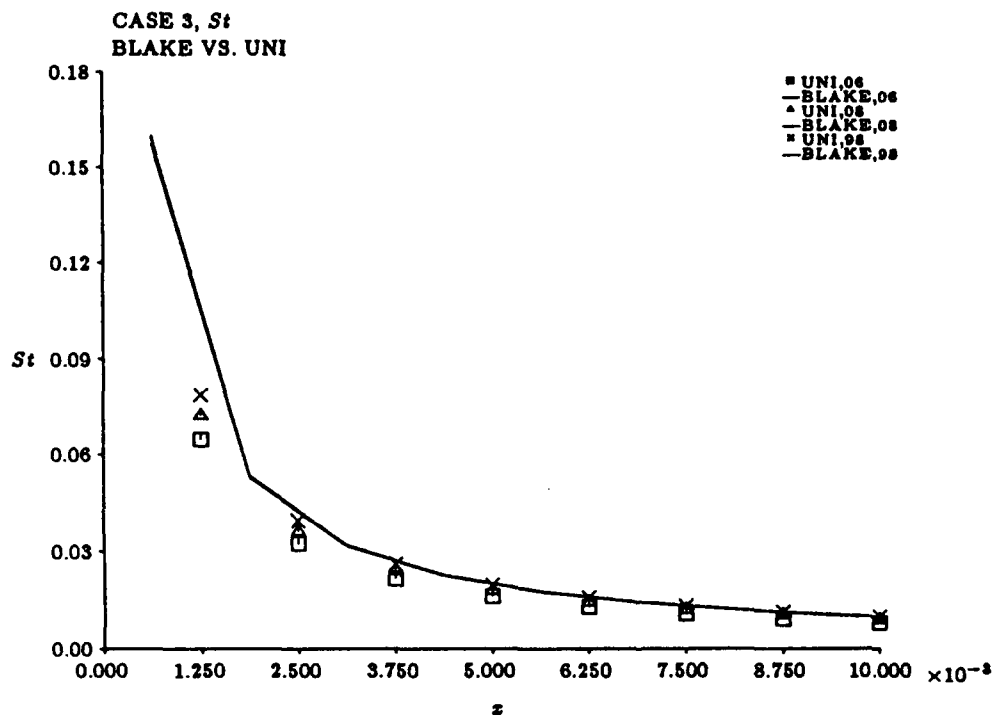


Figure 6.6: Case 3, Stanton Number vs.  $x$ , Leading Edge



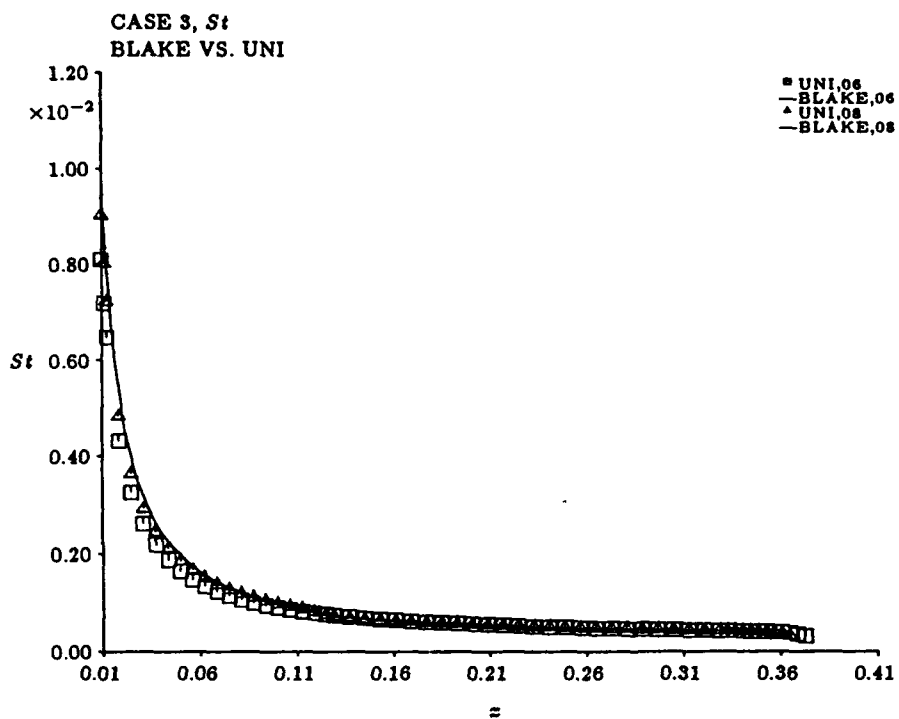


Figure 6.7: Case 3, Stanton Number vs.  $x$ , Downstream of leading edge

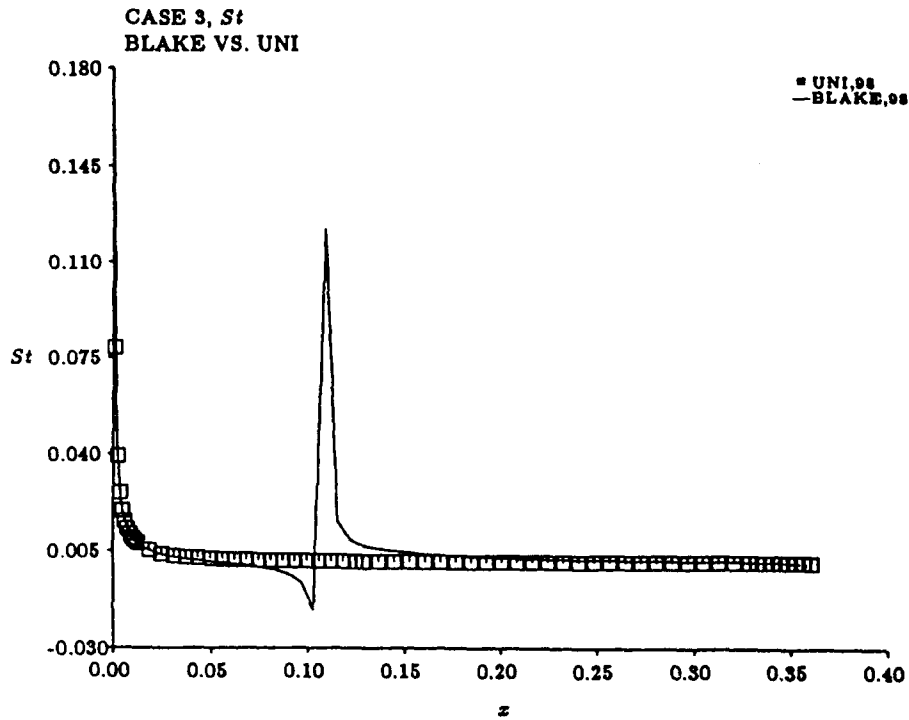


Figure 6.8: Case 3, Stanton Number vs.  $x$ ,  $H_w = 0.98$ . At the point in the flow where  $\frac{T_{AW}}{T_{0*}} - H_w = 0.0$ , (for this case  $M_e = 0.8325$ ) the denominator of the Stanton number goes to zero. Since the driving temperature gradient goes from positive to negative, the heat transfer,  $Q$ , changes sign at this point.

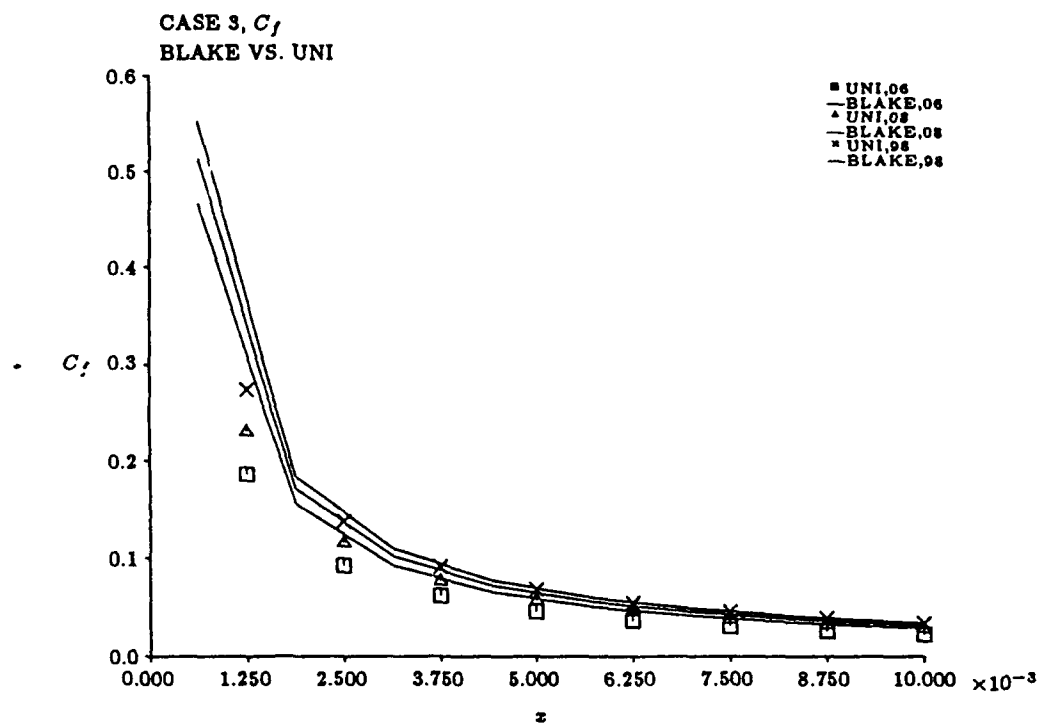


Figure 6.9: Case 3,  $C_f$  vs.  $x$ , Leading Edge

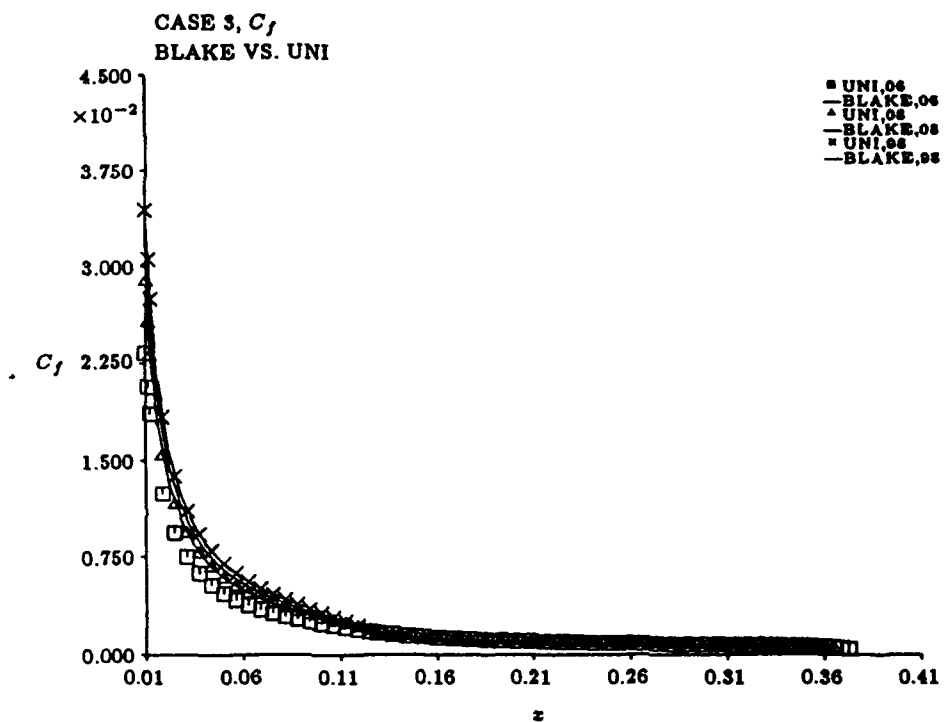


Figure 6.10: Case 3,  $C_f$  vs.  $z$ , Downstream of leading edge

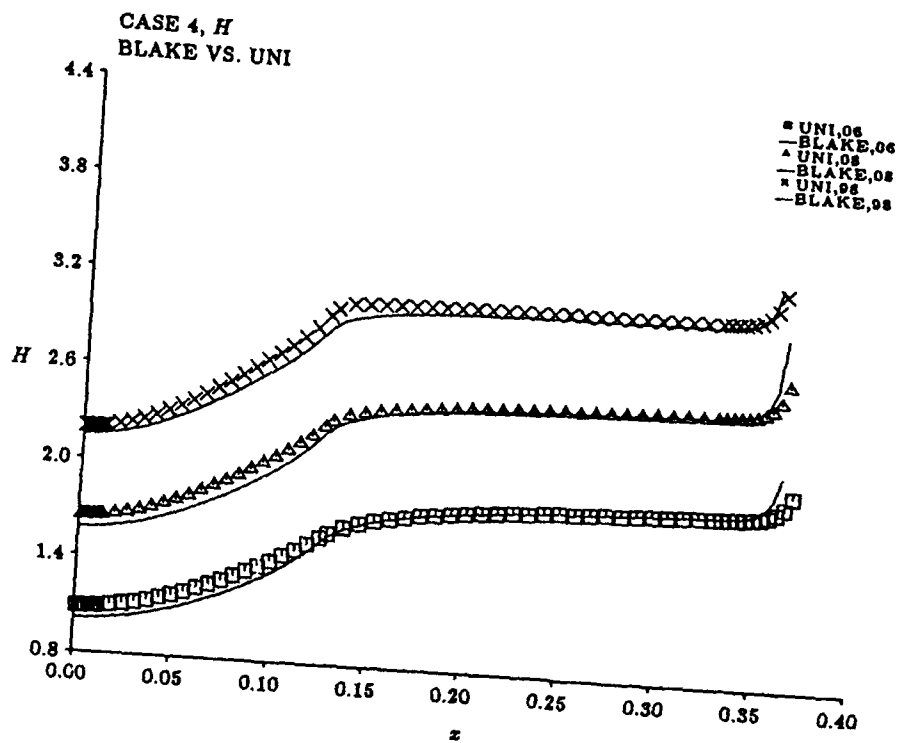


Figure 6.11: Case 4,  $H$  vs.  $x$

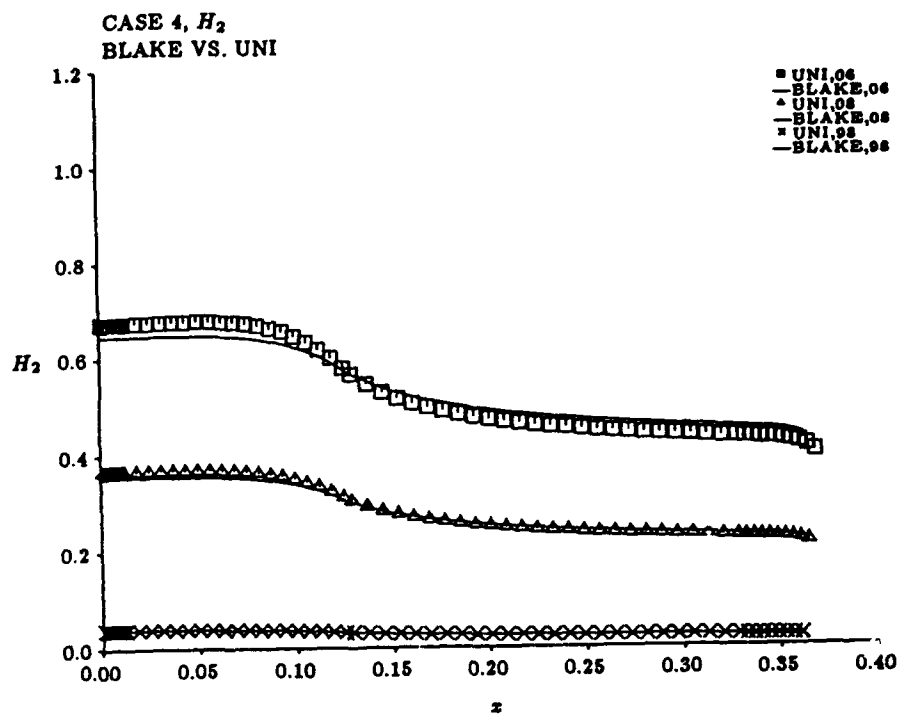


Figure 6.12: Case 4,  $H_2$  vs.  $x$

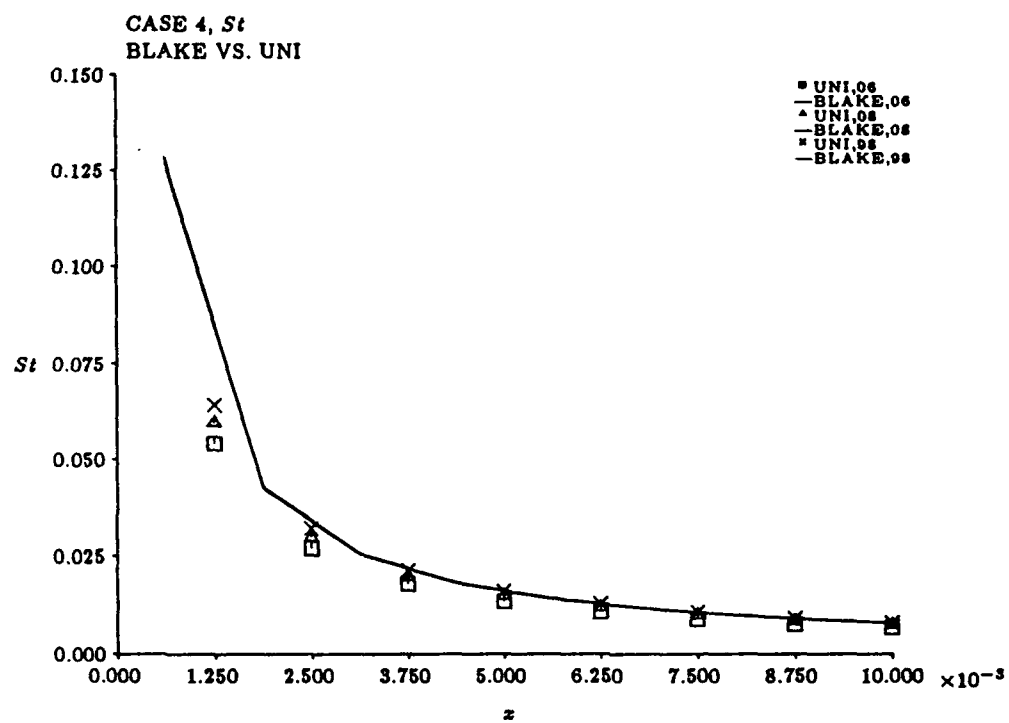


Figure 6.13: Case 4, Stanton Number vs.  $x$ , Leading Edge

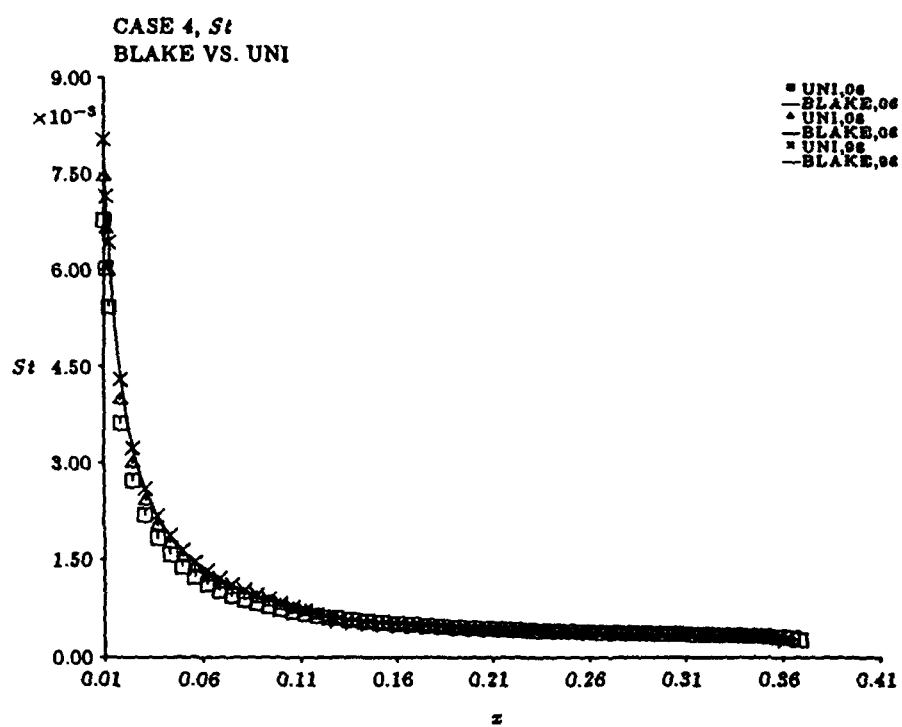


Figure 6.14: Case 4, Stanton Number vs.  $z$ , Downstream



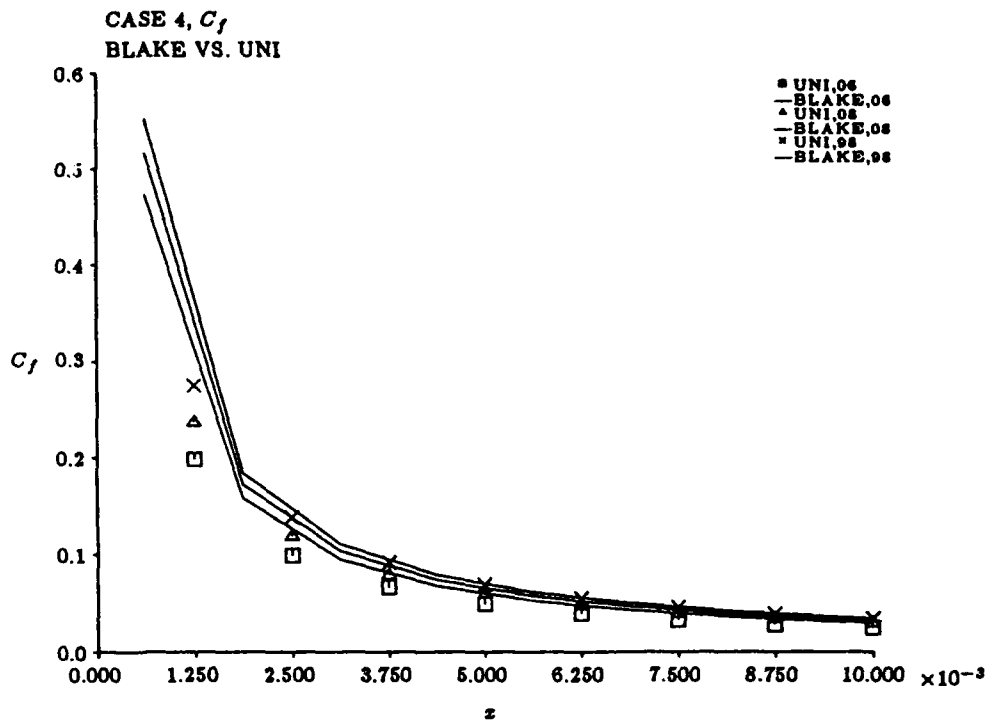


Figure 6.15: Case 4,  $C_f$  vs.  $x$ , Leading Edge

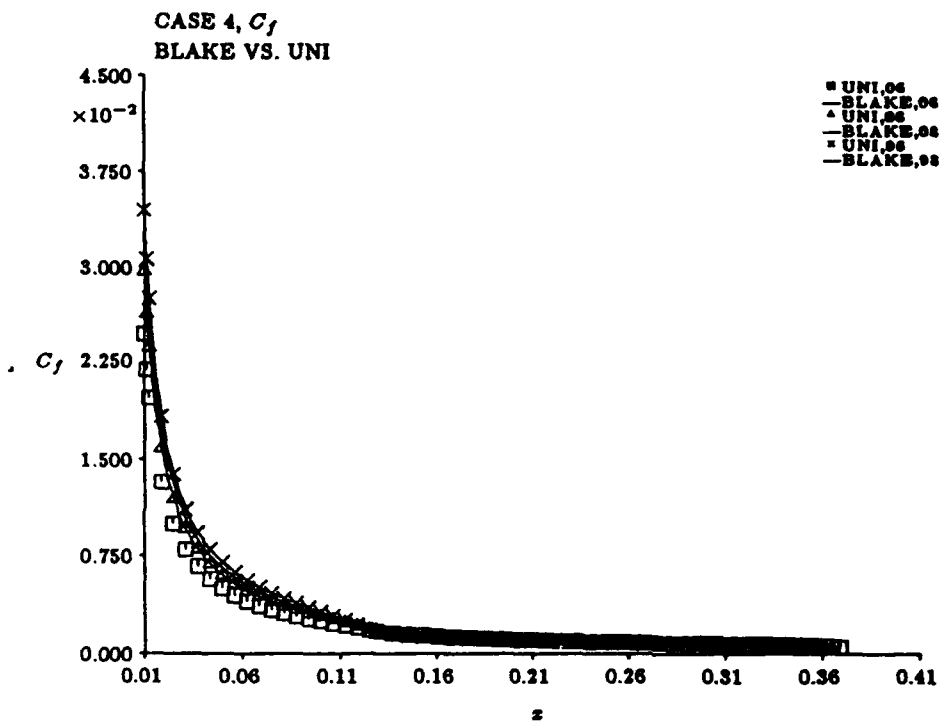


Figure 6.16: Case 4,  $C_f$  vs.  $z$ , Downstream

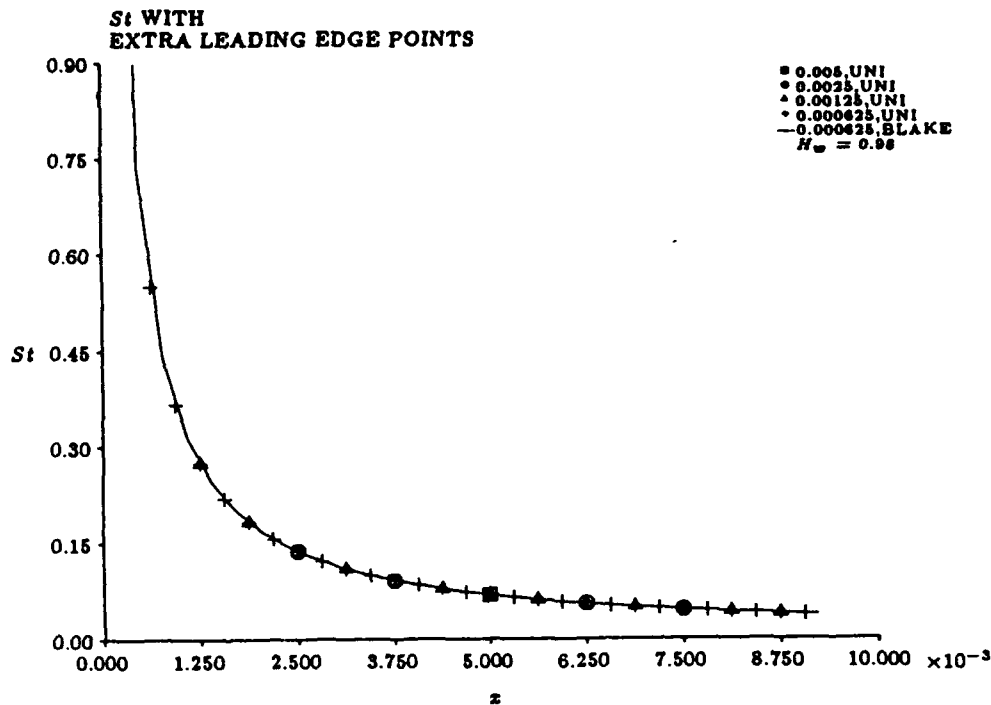


Figure 6.17: Effect of decreased space between leading edge points on the UNI solutions. The numbers indicate the streamwise position of the first analysis point. The results show that the UNI solutions are independent of the leading edge spacing. BLAKE is also independent of the leading edge spacing; a BLAKE solution is included for comparison

The leading edge difference is  $< 10\%$  for all cases and quickly goes to  $< 1\%$  as the solution moves downstream. At the leading edge stagnation point both  $St$  and  $C_f$  are undefined since they are normalized by the edge velocity, which is zero. The integral parameters at the leading edge are calculated by assuming similarity between the first two points. Furthermore, the first two points are assumed to be related by the Falkner-Skan wedge flow parameter  $\beta$ .  $\beta$  is calculated from the velocity distribution at the leading edge.

## 6.2 Comparison with experiment

UNI has been compared with two heat transfer experiments: ([17] and [7]).

### 6.2.1 Giedt [7]

The Giedt experiments involved airflow over circular cylinders. The Reynolds number was  $Re_D = 219000$ . The temperature ratio was not given. The Mach number was also not given but it is assumed to be incompressible flow and hence low Mach number. The external flow was calculated from potential flow for a cylinder in cross flow. The given Nusselt numbers were converted to Stanton numbers, normalizing with respect to the edge velocity. Figure 6.2.1 shows a comparison between UNI predictions for the heat transfer and the measured heat transfer over the cylinders. The UNI Mach number used was  $M_e = 0.1$ .  $H_w = 0.8$  was selected, although  $H_w = 0.6$ , and  $0.98$  were similar.

Agreement between UNI and the Giedt measurements is good. The Giedt profile is the same as the first part of the simulated airfoil velocity profile used in the development test cases.

### 6.2.2 Nicholson [17]

The Nicholson experiments involved airflow over a set of typical commercial aircraft turbine blades. The data sets were taken at the Oxford cascade tunnel. The flow conditions were  $T_0 = 430K$  and  $T_w = 290K$ , and  $Re = 1.113 \times 10^6$ . The blades are shown in Figures 6.19 and 6.21. Since UNI requires not the blade shape but the external flow, ISES [6] was used to generate the external flows for the Nicholson blades. The heat transfer data in [17] is given in terms of  $q_w$ . In order to compare the data directly with UNI output it was converted to Stanton numbers: the wall to freestream temperature difference is known, and the factor  $\rho_e U_e$  can be found from the known stagnation values and the Mach number distribution given in [17], assuming that the flow is isentropic. Heat transfer predictions of UNI vs. measured

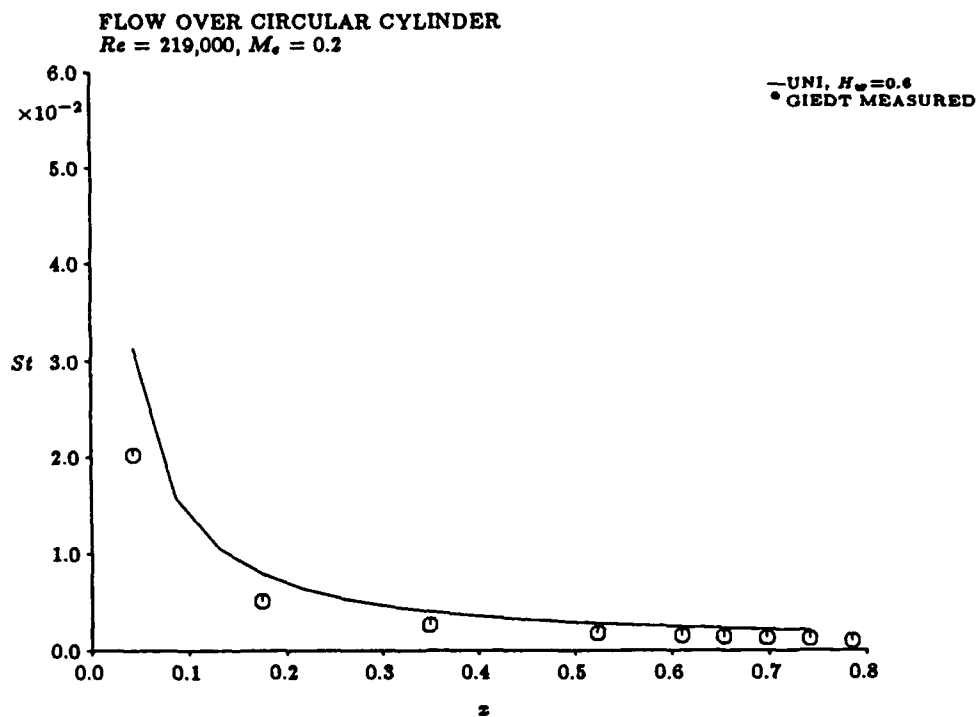


Figure 6.18: Giedt heat transfer measurements vs. UNI predictions,  $Re_D = 219000$ ,  $HW = 0.6$ ,

Mach number = 0.2,  $x$  is  $\frac{\text{streamwise distance}}{\text{diameter}}$

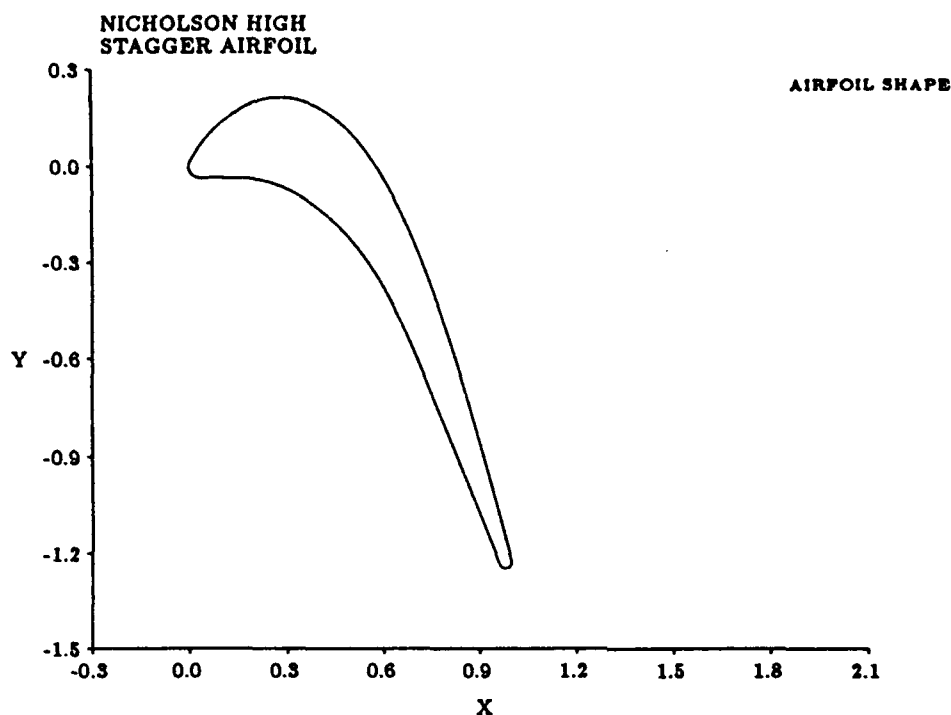


Figure 6.19: The Nicholson High Stagger Blade

quantities of [17] are shown in Figures 6.20 and 6.22. Agreement between the UNI values and those measured by Nicholson et al. is surprisingly good for the high stagger blade. The values measured are for 4% freestream turbulence. No provision is made in UNI to correct for the effects of freestream turbulence.

The Nicholson low stagger blade data was obtained from an internal Rolls Royce report [3] as well as Nicholson [17]. Like the high stagger case above the edge flow was calculated using the ISES code. The blade shape is shown in Figure 6.21. The heat transfer data from [3] was given in terms of Nusselt number. Since

$$St_x = \frac{Nu_x}{Re_x Pr} \quad (6.1)$$

the Stanton number can be found from the other flow properties. Heat transfer predictions of UNI vs. measured quantities of the low stagger blade are shown in Figure 6.22.

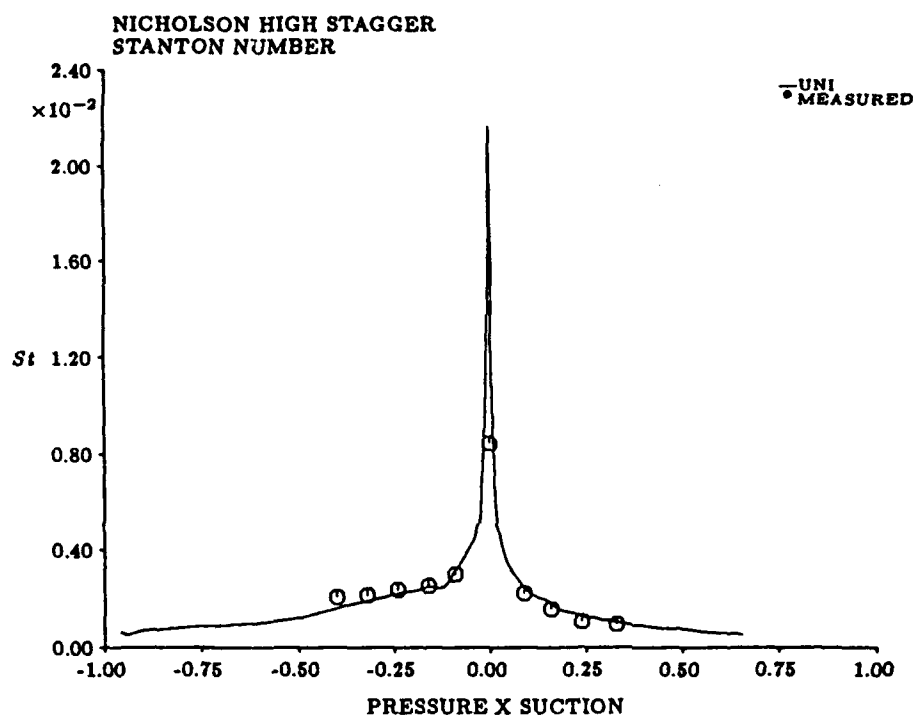


Figure 6.20: Predicted vs. measured Stanton Number for the Nicholson High Stagger Blade

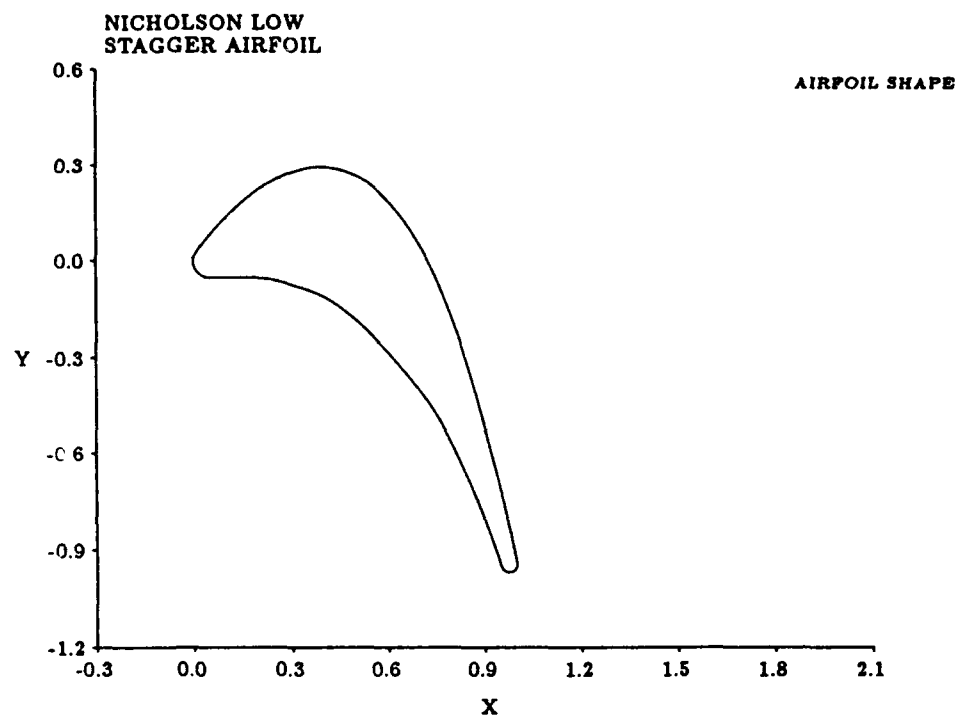


Figure 6.21: The Nicholson Low Stagger Blade



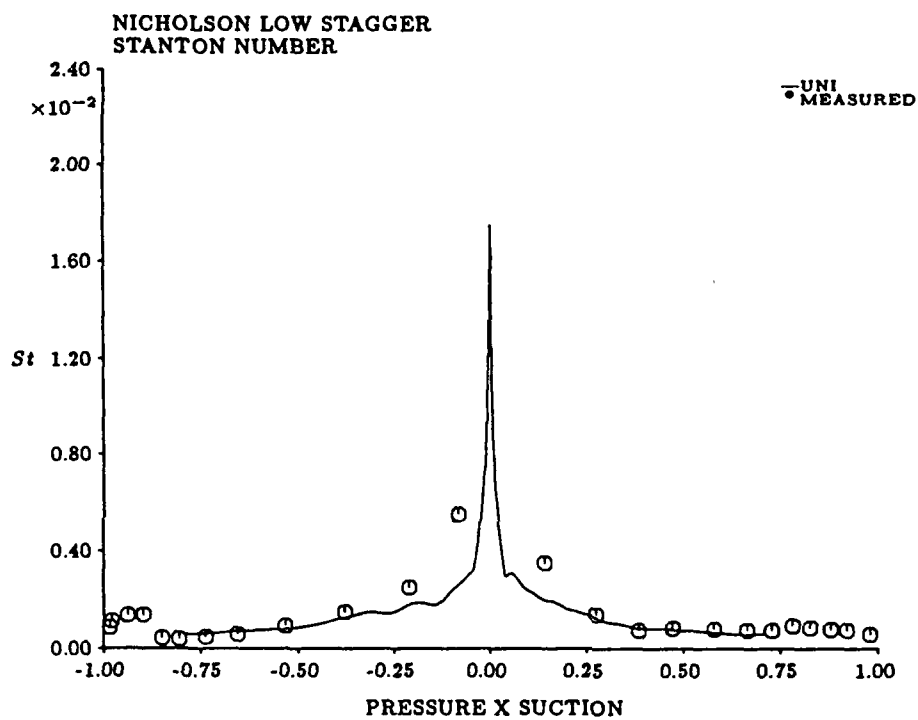


Figure 6.22: Predicted vs. measured Stanton Number for the Nicholson Low Stagger Blade

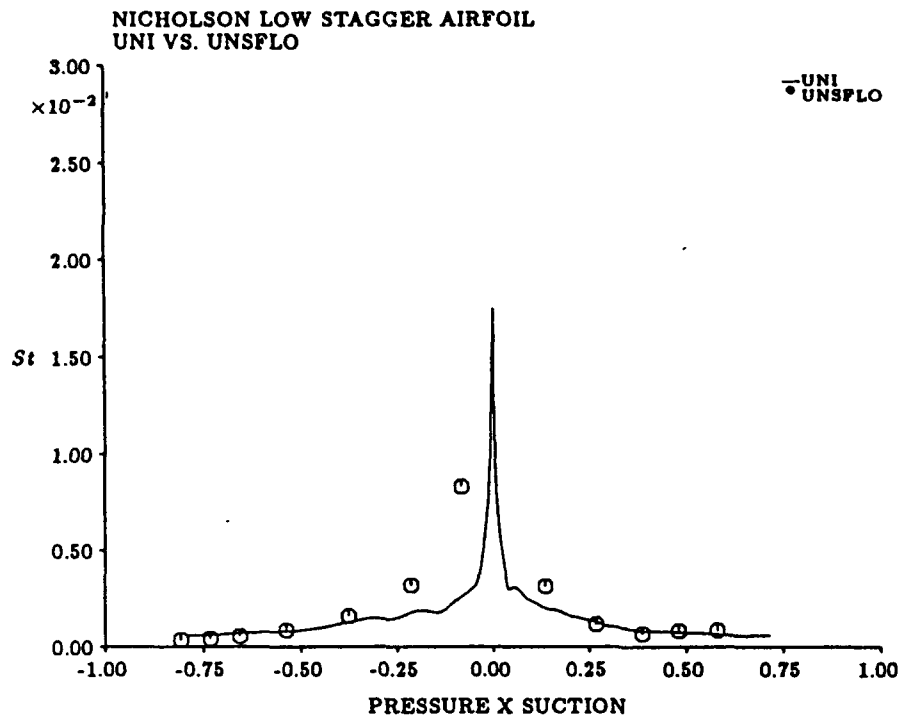


Figure 6.23: UNI Prediction vs. UNSFLO prediction for the Nicholson low stagger blade, with the stagnation point removed to show the small scale heat transfer

Agreement between UNI and the measured values of the low stagger blade are not as close as those for the high stagger blade. UNI predicts a narrow, shallow peak at  $St = 0.02$ ; the measured values are closer to  $St = 0.08$  with an exceptionally wide base.

Figure 6.23 shows the UNI predicted Stanton number vs. the Stanton number prediction of Giles' UNSFLO Navier-Stokes code [8]. UNI agrees more closely with the UNSFLO prediction than the measured data from the low stagger airfoil, especially away from the stagnation point.

## Chapter 7

# Discussion and Conclusions

### 7.1 Discussion

Green [9] states that integral heat transfer methods are not numerous. This is probably due to the difficulty in predicting the local heat transfer coefficient, and the difficulty in estimating the shape of the temperature profile across the boundary layer. In UNI, the temperature and velocity profiles are coupled together by forcing the velocity profile to conform to  $H_k$ , and forcing the total temperature profile (which is a function of both the temperature and velocity profiles) to conform to  $H_2$ . For  $Pr = 1$  no other relation is needed, but for  $Pr \neq 1$  some relation between  $\delta_U$  and  $\delta_T$  is needed. Since the forcing process is iterative, these conditions on  $u$  and  $T_0$  can be met at each estimate of  $H_k$  and  $H_2$ , then checked against the residuals of the three basic equations (Eqs. 5.1, 5.2, and 5.3).

The results of the development tests show that UNI agrees well with the finite difference code BLAKE. This is not all that unexpected since two important factors: the integral wall heat transfer scheme, and the  $C_D$  correction for non-uniform viscosity were obtained from BLAKE results. Since UNI is to be part of a design code, it is important that it accurately predict trends in heat transfer and aerodynamic efficiency. In this way, different designs can be compared as to their aerodynamic and heat transfer performance. UNI has shown that it accurately predicts heat transfer and aerodynamic loss performance trends. It is also important that it give good absolute local heat transfer and aerodynamic loss predictions. UNI's developmental cases show that it can predict local values to better than 10% accuracy as compared with finite difference codes. However, since UNI is an integral method, it is well suited to be integrated into the ISES airfoil design and analysis code.

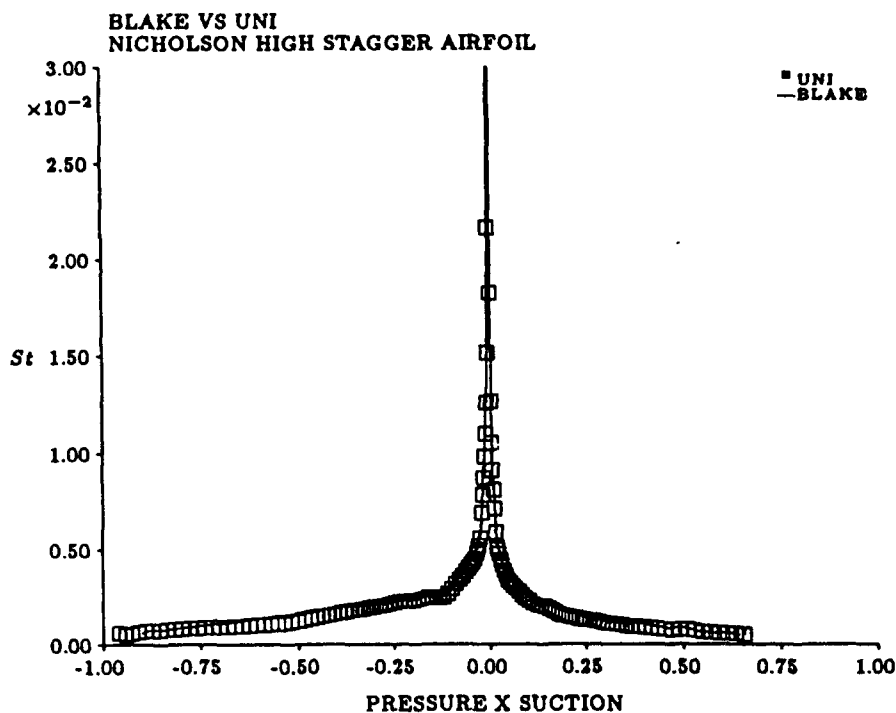


Figure 7.1: Comparison of BLAKE and UNI Predictions for the Nicholson High Stagger Blade

Agreement with experiment is not as good as with theory. This seems to be a common problem in turbine analysis, but that does not excuse further efforts. Agreement with Giedt and the Nicholson high stagger case is good; agreement with the low stagger data is not as good. Prediction of  $St$  and  $C_f$  at the leading edge are not good, but if the subsequent analysis points are closely spaced near the leading edge, greater accuracy is possible. A comparison between BLAKE and UNI for the Nicholson flows shows that the two codes agree quite closely (Figures. 7.1 and 7.2).

For a typical development case (Flow 6,  $H_w = 0.6$ ) UNI is  $\sim 40\%$  faster than BLAKE yet gives comparable results for the integral parameters, heat transfer, skin friction, all of course for the laminar case. For ISES and UNSFLO, accuracy is highly dependent on the number of grid points, and so is the time needed to converge. For the viscous portion of the Nicholson low

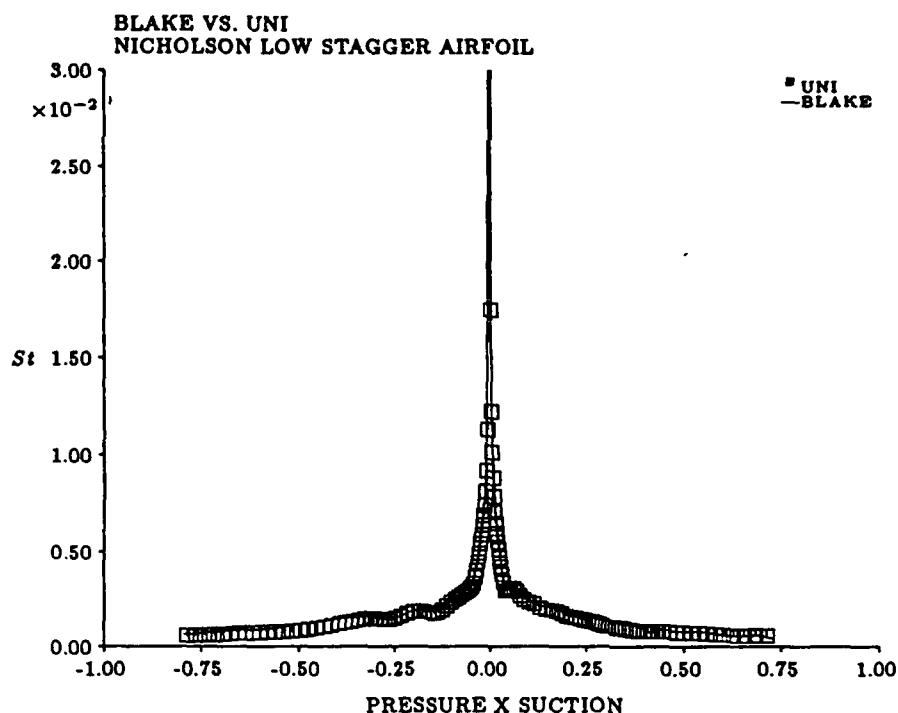


Figure 7.2: Comparison of BLAKE and UNI Predictions for the Nicholson Low Stagger Blade stagger case ISES converged to the same rms remainder  $\sim 15$  times faster than did UNSFLO for the same number of grid points. This is not to say that their accuracies are identical. When the non-adiabatic boundary layer scheme is incorporated into ISES, convergence will probably be slower since  $H_k$  is no longer an algebraic relationship with  $M_e^2$  and  $H$ .  $H_k$  is now found iteratively through  $H$ ,  $M_e^2$ ,  $H_2$ , and the perturbation coefficient,  $P$ .

The most obvious shortcoming of this program is its inability to deal with turbulent flow. In [5] Drela states that for turbulent flow, the primary scaling factor for the wall layer is the skin friction. In Chapter 3 of [9] Green discussed a method for determining the skin friction with non-adiabatic flow. It is suggested that this method, in conjunction with the enthalpy thickness analysis also suggested by Green and developed here would be a good starting point for an integral non-adiabatic turbulent flow analysis. Because of the difficulty of correlating the temperature effects with the dissipation and skin friction the extension of this method to

turbulent flow will probably be difficult. The shape of the turbulent boundary layer would not be well represented by a third order polynomial. Some way of modelling the layers of turbulent temperature and velocity boundary layers would have to be devised in order to accurately predict  $H_k$ . For turbine applications the turbulent extension of this code would definitely be necessary for any practical use.

This code probably could be refined to give greater accuracy at all points in the flow with better correlations. As was noted for the dissipation coefficient, a correlation to the wall temperature was needed to account for temperature and hence viscosity gradients in the boundary layer. This correlation, the integral heat transfer prediction correlation, and most importantly the  $H_k$  estimation scheme could be improved to better account for interaction between such factors as the Prandtl number, the freestream pressure gradient, and the wall temperature. A correction for freestream turbulence could also be used.

## 7.2 Conclusions

Although traditionally turbine airfoil design has tried to optimize aerodynamic efficiency, the potential exists to increase total cycle efficiency by considering heat transfer performance at the design stage. The ISES airfoil design and analysis tool is an adiabatic code that has the potential to design turbine airfoils if modified to allow non-adiabatic boundary conditions. With such a tool turbine airfoils could be designed to tradeoff aerodynamic efficiency and heat transfer performance to reach the highest level of total cycle efficiency.

Radiation heat transfer was found to have a minor role in heat transfer to a turbine blade compared to convection heat transfer. Since the percentage of heat transferred by radiation is  $\leq 10\%$ , reductions in radiative heat transfer do not have as much potential for reducing the total heat transfer as do reductions in the convective heat transfer.

Using a diffusion factor model it was shown that a point of minimum aerodynamic losses

exists, and that by sacrificing some amount of aerodynamic efficiency lower heat transfer can be achieved. In a total cycle analysis the point of highest total efficiency might not be at the point of highest aerodynamic efficiency, and if so designing for low heat load would increase the total cycle efficiency.

The non-adiabatic integral boundary layer model was chosen over finite difference codes in view of the number of variables to be solved. Since the computational time and effort required is strongly dependent on the number of points involved, an integral method has an advantage. And, as shown in Chapter 6, the accuracy of the two methods is comparable.

A new integral correlation for heat transfer has been developed from the finite difference code BLAKE [4] solutions to the developmental test case flows. It is surprisingly simple and highly accurate for Reynolds numbers between  $1. \times 10^5$  and  $1. \times 10^7$ , Prandtl numbers between 0.7 and 1.0, and pressure gradients measured by the Falkner-Skan parameter between  $\beta = 0$  and  $\beta = 1$ . Since these flow conditions are typical of turbine blade leading edge values this method should be useful for leading edge heat transfer prediction.

# Bibliography

- [1] Ainley, A.M., and Mathieson, G.C.R. "A Method of Performance Estimation for Axial-Flow Turbines," A.R.C.R.&M. No. 2974, 1957.
- [2] Anderson, D.A., Tannehill, J.C., and Pletcher, R.H.  
Computational Fluid Mechanics and Heat Transfer, Hemisphere Publishing Company, Washington, D.C. 1984.
- [3] Connell, S.D. "An Evaluation of FANSI-2D Version 2.10." Theoretical Science Group Report TSG0222, Rolls-Royce Limited.
- [4] Drela, M. "A New Transformation and Integration Scheme for the Compressible Boundary Layer Equations, and Solution Behavior at Separation," MIT Gas Turbine and Plasma Dynamics Laboratory Report No. 172, May 1983.
- [5] Drela, M. "Two-Dimensional Transonic Aerodynamic Design and Analysis Using the Euler Equations," MIT Gas Turbine Laboratory Report No. 187, February 1987.
- [6] Drela, M., and Giles, M.B. "ISES: A Two-Dimensional Viscous Aerodynamic Design and Analysis Code," AIAA-87-0424, 1987.
- [7] Giedt, W.H. "Investigation of Variation of Point Unit Heat-Transfer Coefficient Around a Cylinder Normal to an Air Stream." Transactions of the ASME. Vol. 71, pgs. 375-381, 1949.
- [8] Giles, Michael. "UNSFLO: A Numerical Method for Unsteady Inviscid Flow in Turbomachinery." Gas Turbine Lab Report No. 195, October, 1988.



- [9] Green, J.E. "Application of Head's Entrainment Method to the Prediction of Turbulent Boundary Layers and Wakes in Compressible Flow," A.R.C.R.&M. No. 3788, 1976.
- [10] Guenette, G.R., Epstein, A.H., Giles, M.B., and Haimes, R. "Fully Scaled Transonic Turbine Rotor Heat Transfer Measurements," Prepublication Draft, 1987.
- [11] Holman, J.P. Heat Transfer, Sixth Edition. McGraw-Hill Book Company, New York, 1986.
- [12] Horlock, J.H. Axial Flow Turbines, Butterworth and Company, 1966.
- [13] Johnsen, I.A., and Bullock, R.O. "Aerodynamic Design of Axial-Flow Compressors," NASA SP-36, NASA Scientific and Technical Information Division, 1965.
- [14] Kerrebrock, J.L. Aircraft Engines and Gas Turbines, MIT Press, 1987.
- [15] McAdams, W.H. Heat Transmission, Chapter 4, "Radiant Heat Transmission," by Hoyt C. Hottel. McGraw-Hill Book Company, 1954.
- [16] Moustapha, S.H., Okapuu, U., and Williamson, R.G. "Influence of Rotor Blade Aerodynamic Loading on the Performance of a Highly Loaded Turbine Stage", ASME 86-GT-56, 1986.
- [17] Nicholson, J.H., Forest, A.E., Oldfield, M.L.G., and Schultz, D.L. "Heat Transfer Optimised Turbine Rotor Blades - An Experimental Study Using Transient Techniques," ASME 82-GT-304, 1982.
- [18] Schlichting, Hermann. Boundary Layer Theory, McGraw-Hill Book Co. Inc., London, 1955.
- [19] Schmidt, Ernst, and Wenner, Karl. "Heat Transfer Over the Circumference of a Heated Cylinder in Transverse Flow." NACA TM-1050, 1943.

- [20] Schwab, J.R., Stabe, R.G. and Whitney, W.J. "Analytical and Experimental Study of Flow Through an Axial Turbine Stage With a Nonuniform Inlet Radial Temperature Profile," NASA Technical Memorandum 83431, AIAA-83-1175, 1983.
- [21] Smith S.F. "A Simple Correlation of Turbine Efficiency," Journal of the Royal Aeronautical Society, Vol. 69, July 1965.
- [22] Stewart, W.L., Whitney, W.J., and Wong, R.Y. "A Study of Boundary-Layer Characteristics of Turbomachinery Blade Rows and Their Relation to Over-All Blade Loss," Transactions of the ASME, Journal of Basic Engineering, September 1960.
- [23] Van Wylen, G.J., Sonntag, R.E.  
Introduction to Thermodynamics Classical and Statistical Second Edition, John Wiley and Sons, New York, 1982
- [24] White, F.M. Viscous Fluid Flow, McGraw-Hill, 1974.

## Appendix A

# Gaseous Radiant Heat Transfer

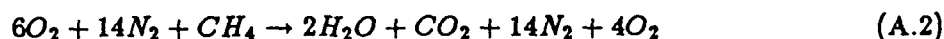
The mean beam length analysis for gaseous radiant heat transfer is one way of looking at a complex problem. It is semi-empirical in that it applies empirical corrections to the theoretical gas heat transfer equation (Eq. 3.4). The empiricism comes in through the calculation of  $\epsilon_G$  and  $\alpha_G$  of the gas.

The mean beam length is a non-physical length that takes into account the geometry of the situation. A general rule of thumb for its calculation is  $L_{MB} = 3.6 \frac{VOLUME}{AREA}$ . For several specific geometries less general formulae are given in [11]. For the turbine application the geometry was modeled as the radiation of a volume of gas in a cylinder to the surface. The diameter was modeled as the blade pitch, for this case  $\sim 1.3$  inches. Holman suggests  $L_{MB} = 0.95D$ , and in this case  $L_{MB} = 0.105$  feet was used.

Calculations were made at 500°F intervals (3000°–5000°F) and at 10 atmosphere pressure intervals (10–40 atm.) The combustion chemistry was modeled as follows. Assume a hydrocarbon fuel (methane) and the following reaction:



If we have a 0.03 fuel to air mass ratio [14] the chemistry would look something like this. Since air is approximately  $3O_2 + 7N_2$  the actual reaction would be:



It is assumed that the oxygen and nitrogen do not radiate since their emittances are small compared to carbon dioxide and water vapor [11]. The partial pressures for both  $CO_2$  and  $H_2O$  are needed; an intermediate step is to calculate the product  $p_{CO_2} L_{MB}$  and  $p_{H_2O} L_{MB}$ .

These are compared to Figures 8-34 and 8-35 in [11] to find the emissivity  $\epsilon_{CO_2}$  and  $\epsilon_{H_2O}$ . Correction factors  $C_{CO_2}$  and  $C_{H_2O}$  are applied to correct for the given total pressure, and a final correction  $\Delta\epsilon$  is calculated since both  $CO_2$  and  $H_2O$  are present. The final formula for  $\epsilon$  is:

$$\epsilon_G = C_{CO_2}\epsilon_{CO_2} + C_{H_2O}\epsilon_{H_2O} - \Delta\epsilon \quad (A.3)$$

$\alpha_G$  is calculated in a similar fashion [11, pgs. 419-420].

The convective heat transfer is calculated by assuming a representative Nusselt number from [10]. The same temperatures were used as above, but no correction for the different pressure ratios was attempted.

Despite the  $T^4$  behavior of radiational heat transfer this analysis does not show the expected sharp increase in the ratio of radiational heat transfer to total heat transfer as the TET increases to the stoichiometric limit. This analysis should not be taken as the final word on the subject since several values in the analysis were approximate at best. No allowance was made for particulates in the flow, nor the role that chemistry would undoubtedly have in such high temperature flows. Still, not even a strong trend toward a great role for radiational heat transfer was found.

## Appendix B

### Derivation of Fundamental equations

We start from three basic equations:

Continuity:

$$\frac{\partial}{\partial x}(\rho u) + \frac{\partial}{\partial y}(\rho v) = 0 \quad (\text{B.1})$$

Streamwise Momentum:

$$\rho u \frac{\partial u}{\partial x} + \rho v \frac{\partial v}{\partial y} = \rho_e U_e \frac{dU_e}{dx} + \frac{\partial \tau}{\partial y} \quad (\text{B.2})$$

and from [9, Appendix A] the enthalpy equation:

$$\frac{d}{dx}(\rho_e U_e \theta H_2) = \frac{q_w}{C_p T_{0e}} \quad (\text{B.3})$$

where  $x$  is the streamwise coordinate and  $y$  is the normal coordinate.

Summing u(B.1) + (B.2) and integrating over the boundary layer we have

$$\int_0^{y_*} (u \frac{\partial}{\partial x} \rho u + u \frac{\partial}{\partial y} \rho v + \rho u \frac{\partial u}{\partial x} + \rho v \frac{\partial v}{\partial y}) dy = \int_0^{y_*} (\rho_e U_e \frac{dU_e}{dx} + \frac{\partial \tau}{\partial y}) dy \quad (\text{B.4})$$

Noting that:

$$\frac{\partial}{\partial x}(\rho u^2) = \frac{\partial \rho}{\partial x} u^2 + 2\rho u \frac{\partial u}{\partial x} \quad (\text{B.5})$$

$$\frac{\partial}{\partial y}(\rho u v) = u \frac{\partial}{\partial y}(\rho v) + \rho v \frac{\partial u}{\partial y} \quad (\text{B.6})$$

$$\int_0^{y_*} \frac{\partial}{\partial y}(\rho u v) dy = \rho_e U_e v_e \quad (\text{B.7})$$

and from continuity:

$$\rho_e v_e = \int_0^{y_*} \frac{\partial}{\partial y}(\rho v) dy = - \int_0^{y_*} \frac{\partial}{\partial x}(\rho u) dy \quad (\text{B.8})$$

and from the definition of  $\tau_w$ :

$$\int_0^{y_*} \frac{\partial \tau}{\partial y} dy = -\tau_w \quad (\text{B.9})$$

we have:

$$\int_0^{y_*} \left( \frac{\partial}{\partial x}(\rho u^2) - \rho_e U_e \frac{dU_e}{dx} - U_e \frac{\partial}{\partial x}(\rho u) \right) dy = -\tau_w \quad (\text{B.10})$$

Note that

$$\frac{\partial}{\partial x}(\rho u(U_e - u)) = U_e \frac{\partial}{\partial x}(\rho u) - \frac{\partial}{\partial x}(\rho u^2) + \rho_e U_e \frac{dU_e}{dx} \quad (\text{B.11})$$

Combining terms and introducing  $C_f$

$$\frac{\partial}{\partial x} \int_0^{y_*} (\rho u(U_e - u)) dy + \frac{dU_e}{dx} \int_0^{y_*} (\rho_e U_e - \rho u) dy = \frac{C_f}{2} \rho_e U_e^2 \quad (\text{B.12})$$

Divide by  $\rho_e U_e^2$  and introduce the definitions of  $\theta$  and  $\delta^*$  yields

$$\frac{1}{\rho_e U_e^2} \frac{\partial}{\partial x}(\rho_e U_e^2 \theta) + \frac{1}{U_e} \frac{dU_e}{dx} \delta^* = \frac{C_f}{2} \quad (\text{B.13})$$

expanding and rewriting yields

$$\frac{\partial \theta}{\partial x} + \frac{2\theta}{U_e} \frac{dU_e}{dx} + \frac{\theta}{\rho_e} \frac{\partial \rho_e}{\partial x} + \frac{1}{U_e} \frac{dU_e}{dx} \delta^* = \frac{C_f}{2} \quad (\text{B.14})$$

From thermodynamic relations [23] we know

$$\frac{1}{\rho_e} \frac{\partial \rho_e}{\partial x} = -\frac{M_e^2}{U_e} \frac{dU_e}{dx} \quad (\text{B.15})$$

and introducing the definition of  $H$  we have

$$\frac{\partial \theta}{\partial x} + \frac{\theta}{U_e} \frac{dU_e}{dx} (2 + H - M_e^2) = \frac{C_f}{2} \quad (\text{B.16})$$

which is the first of the three integrated equations. To get the second of the three integrated equations we start from  $(u^2 - U_e^2)(B.1) + 2u(B.2)$

This can be grouped as

$$(u^2 \frac{\partial}{\partial x}(\rho u) + 2\rho u^2 \frac{\partial u}{\partial x} - U_e^2 \frac{\partial}{\partial x}(\rho u) - 2\rho_e U_e u \frac{dU_e}{dx}) + ((u^2 - U_e^2) \frac{\partial}{\partial y}(\rho v) + 2\rho uv \frac{\partial v}{\partial y}) - 2u \frac{\partial \tau}{\partial y} = 0 \quad (B.17)$$

Note that

$$\frac{\partial}{\partial x}(\rho u(u^2 - u_e^2)) + 2u U_e \frac{dU_e}{dx}(\rho - \rho_e) = u^2 \frac{\partial}{\partial x}(\rho u) + 2\rho u^2 \frac{\partial u}{\partial x} - U_e^2 \frac{\partial}{\partial x}(\rho u) - 2\rho_e U_e u \frac{dU_e}{dx} \quad (B.18)$$

also

$$\frac{\partial}{\partial y}(\rho v(u^2 - U_e^2)) = (u^2 - U_e^2) \frac{\partial}{\partial y}(\rho v) + 2\rho uv \frac{\partial u}{\partial y} \quad (B.19)$$

Substituting into eq. (B.17) yields

$$\frac{\partial}{\partial x}(\rho u(u^2 - U_e^2)) + 2u U_e \frac{dU_e}{dx}(\rho - \rho_e) + \frac{\partial}{\partial y}((u^2 - U_e^2)\rho v) = 2u \frac{\partial \tau}{\partial y} \quad (B.20)$$

Regrouping to form the integrands of  $\theta^*$  and  $\delta^{**}$  and integrating over the boundary layer yields

$$\frac{\partial}{\partial x}(-\rho_e U_e^3 \theta^*) - 2\rho_e U_e^2 \frac{dU_e}{dx} \delta^{**} + ((u^2 - U_e^2)\rho v) \Big|_0^{y_*} = 2(u\tau \Big|_0^{y_*} - \int_0^{y_*} (r \frac{\partial u}{\partial y}) dy) \quad (B.21)$$

The evaluated quantities go to zero since they are zero at the wall and at the boundary layer edge. Noting this and bringing in the definition of  $C_D$  yields

$$\frac{\partial}{\partial x}(\rho_e U_e^3 \theta^*) + 2\rho_e U_e^2 \frac{dU_e}{dx} \delta^{**} = 2\rho_e U_e^3 C_D \quad (B.22)$$

Dividing by  $\rho_e U_e^3$ , expanding the derivative and introducing eqn. (B.15) yields

$$(3 - M_e^2) \frac{\theta^*}{U_e} \frac{dU_e}{dx} + \frac{\partial \theta^*}{\partial x} + 2 \frac{\delta^{**}}{U_e} \frac{dU_e}{dx} = 2C_D \quad (\text{B.23})$$

Take eqn. (B.16), multiply by  $H^*$ , add  $\frac{\theta^*}{U_e} \frac{dU_e}{dx}$  to both sides and regroup to yield

$$(3 - M_e^2) \frac{\theta^*}{U_e} \frac{dU_e}{dx} = H^* \left( \frac{C_f}{2} - \frac{d\theta}{dx} \right) - (H - 1) \frac{\theta^*}{U_e} \frac{dU_e}{dx} \quad (\text{B.24})$$

Substitute into eqn. (B.23). Note that

$$\theta \frac{dH^*}{dx} = \frac{\partial \theta^*}{\partial x} - H^* \frac{\partial \theta}{\partial x} \quad (\text{B.25})$$

Regroup and rewrite to form

$$\theta \frac{dH^*}{dx} + (2H^{**} - H^*(H - 1)) \frac{\theta}{U_e} \frac{dU_e}{dx} = 2C_D - H^* \frac{C_f}{2} \quad (\text{B.26})$$

which is the second of the three equations. To get the third equation we start with the enthalpy equation, expand the derivative and assume that the recovery factor is constant in  $x$  [24]. This yields

$$\theta \frac{dH_2}{dx} + H_2 \frac{d\theta}{dx} + \frac{\theta H_2}{\rho_e} \frac{d\rho_e}{dx} + \frac{\theta H_2}{U_e} \frac{dU_e}{dx} = \frac{q_w}{\rho_e U_e C_p T_{0e}} \quad (\text{B.27})$$

Introducing eqs. (B.15) and (B.16) and regrouping yields

$$\theta \frac{dH_2}{dx} = Q - H_2 \left( \frac{C_f}{2} - (H + 1) \frac{\theta}{U_e} \frac{dU_e}{dx} \right) \quad (\text{B.28})$$

which is the third equation.



### **SECTION 3**

## **TURBINE AERODYNAMIC PERFORMANCE MEASUREMENTS IN SHORT DURATION FACILITIES**

### **Abstract**

Short duration, blow-down type turbomachinery test facilities offer the potential for very low cost, high accuracy testing of axial flow turbines and have been used extensively to generate heat transfer data. This paper addresses the use of these facilities for turbine aerodynamic performance testing for research and development in place of conventional rigs. Differences between the quasi-isothermal testing of short duration rigs and adiabatic testing in steady-state rigs are explored and shown to be of the order of 1% in turbine adiabatic efficiency. Procedures for minimizing this difference during testing and/or correcting for the difference during posttest data analysis are discussed. The errors associated with this correction are shown to be below those from other sources in the turbine measurement processes. Accuracy requirements for pressure, temperature, torque, and heat transfer instrumentation in short duration rigs are presented along with examples of current practice. It is shown that no new instrumentation development is required for these facilities, so that overall they represent little technical risk. The conclusion from the analysis in the paper is that turbine aerodynamic performance can be measured in short duration test facilities at least as well as in conventional, steady-state test rigs.

### **1. Introduction**

The aerodynamic performance of jet engine turbines has increased enormously over the past 40 years, with polytropic efficiencies now in the low 90% range. At the same time, turbine inlet temperatures have risen on the order of 1000°K through the development of extraordinary turbine blade and disk materials as well as sophisticated internal and external blade cooling arrangements. Thus, the turbine designs of the 1980's and 1990's produce much higher power per unit mass flow and a substantial increase in efficiency compared to their forebears of the 1950's. The efficiency increase has come through improved design techniques based both on better understanding of the fluid mechanics of turbines and the power of modern computational tools.

Underpinning this all are empirical observations acquired through many years of extensive turbine testing -- on engines, rigs, and subscale experiments. The cost of turbine testing has increased enormously over the years. An uncooled, "warmish" (450°K inlet temperature) rig test for a large turbine typically currently costs on the order of \$3 million, a cooled test under the same conditions costs about \$5 million. These rig costs have all but stopped turbine research at this level. Even engine development programs have been greatly affected -- a military engine program may include only one or even zero turbine rig tests. Thus, the only test a new turbine design may see is in an engine. Unfortunately, the aerodynamic efficiency measurement accuracy currently possible in a full scale engine (1 or 2%) is considerably less than that demanded of sophisticated turbine design systems, the result being that design improvements may often not be well evaluated by experiment.

A similar situation has existed for heat transfer and cooling. During the last decade, however, a new technology based on transient testing techniques has developed which provides highly accurate, detailed turbine measurements at relatively low cost [1]. The techniques are based primarily on the realization that the time scales characteristic of the physical processes within a turbine may be indeed quite short (on the order of hundreds of microseconds). Given instrumentation with adequate time response then, a test time encompassing thousands or tens of thousands of characteristic flow times, sufficient for establishing steady-state behavior, may be quite short (less than a second). Thus, although the instantaneous power of a short duration turbine test facility may be quite high (many megawatts), its total energy consumption is very, very low -- greatly reducing the construction, maintenance, and power costs of turbine testing.

To date, the work in short duration turbine test facilities has been aimed predominantly at heat transfer and cooling studies. This paper addresses the question of aerodynamic performance testing of turbines in short duration test facilities. We will review the state of the art of turbine testing in conventional facilities, examine short duration facility design and operation, compare analytically turbine performance in steady-state and short duration test rigs, examine instrumentation requirements and current status, and finally assess the overall accuracy which can

be expected in short duration turbine test facilities.

## **2. Current State of the Art in Aerodynamic Performance Measurements**

Before exploring the use of short duration test facilities for turbine aero-performance testing, it is important to define our terms and review the current state of the art in turbine testing. The goal of aero-performance testing is most usually to determine turbine power output, efficiency (usually, but not always, adiabatic efficiency), and mass flow capacity. None of these quantities can be measured directly, however, but must be inferred from measurements of quantities related by analytical models. Mass flow is calculated from pressure difference measurements across a calibrated orifice or by temperature, pressure, and velocity traverses of a well-known geometry. Efficiency is derived from measurements of either the pressure drop across the turbine, the turbine torque, and mass flow ("shaft" efficiency), or by measurement of the pressure and temperature ratios across the turbine and knowledge of the specific heat of the working fluid ("rake" efficiency). Turbine power is calculated from the torque and rotor speed or from the temperature drop and mass flow.

Often, even the directly measured quantities are "contaminated" by other phenomena. For example, knowledge of the torque on the fluid is really required for design system verification and comparison with rake efficiency measurements. Shaft torque, however, is the directly measured quantity and includes contributions due to bearing drag and disk windage. These must be factored out by a combination of analysis and measurement. Thus, the net accuracy of the "directly" measured quantities must include not just instrument error but also the effects of numerous corrections which are subsequently applied. The accuracy of the desired engineering variables (power, efficiency, mass flow) are dependent not only on the accuracy of the directly measured quantities but also on the fidelity of the mathematical models employed. These are often not exact but contain explicit and implicit assumptions (about perfect gas relations, adiabatic flow, variation in ratio of specific heats, etc.). Further inaccuracies can be introduced by probe spatial and temporal sampling errors due to small scale flow inhomogeneities, blade row interactions, probe

blockage, and similar fluid mechanics effects. In the case of relative measurements (that is, comparing performance among stages), many of these problems are not significant and are thus commonly neglected. Also, many minor effects have not been well characterized and so are neglected on faith.

Turbine performance is now most accurately measured in specially designed steady-state test rigs in which scale (sometimes full scale) model turbines are operated in isolation. These rigs operate at temperatures sufficiently below engine operating conditions that super alloy blading is not required. Although measurements could be taken at room temperature, the inlet air is usually heated to the 400-800°K range to increase the temperature drop across the turbine, and thus the measurement accuracy given a fixed temperature sensor resolution. In such a facility, measurements of adiabatic efficiency of uncooled turbines are typically quoted as having accuracies of between 0.3 to 0.5%, depending upon turbine pressure ratio.

The measurement accuracy required for such measurements can be analyzed using standard techniques [2]. (We will assume that the errors are uncorrelated.) Here we consider the turbine sketched in Fig. 1 with adiabatic efficiency given as

$$\eta = \frac{1 - T_2/T_1}{(1 - P_2/P_1)^{\gamma/\gamma-1}} \quad (1)$$

where  $T_2$  and  $T_1$  are the stage outlet and inlet total temperatures respectively,  $P_2$  and  $P_1$  the stage outlet and inlet total pressures, and  $\gamma$  the ratio of specific heats of the gas -- assuming the working fluid to be a perfect gas with constant specific heats. Assuming  $\gamma$  is known precisely, the sensor measurement accuracy required for a given efficiency uncertainty and pressure ratio is given in Fig. 2. Figure 3 replots the result with dimensional scales on the side added as an example for a turbine with a pressure ratio of 2.5 and a polytropic efficiency of 91% at a typical cool rig inlet condition of  $T_1 = 500^\circ\text{K}$ ,  $P_1 = 6 \text{ atm}$ . We can infer from these graphs that state of the art temperature and pressure measurements of 0.17°K (0.3°F) and 0.0007 atm (0.01 psi) would yield an adiabatic efficiency measurement accuracy of 0.3-0.4%, consistent with current practice. A similar graph for torque-based efficiency measurements is shown in Fig. 4.

The foregoing considers uncooled turbines only. Internally cooled turbines will be considered in a later section. Efficiency measurements in film-cooled turbines are considerably more complicated since allowance for the thermodynamic and fluid mechanic influence of the injectant must be made. This is done mainly through modelling and estimation and is beyond the scope of this paper.

The principal point is that turbines, as currently tested in steady-state facilities, run for long periods of time so as to be adiabatic. Measurement error traceable to sensors and parasitic factors (bearing drag, etc.) account for uncertainties in efficiency measurements of the order of 0.3 to 0.5% in uncooled turbines, perhaps double that in cooled devices. Because many identified but not well quantified additional physical effects are present in turbines, these uncertainties are usually quoted in terms of back-to-back comparisons among stages rather than in terms of absolute accuracies. We will now examine how similar measurements may be taken in short duration facilities.

### **3. Short Duration Facility Operation**

The accurate testing of any fluid mechanic device is dependent upon insuring proper similitude between the test facility and the full scale device -- and turbines are no different in this respect. Here, the important scaling parameters are Reynolds number, Mach number, air angles to blading (corrected speed and weight flow), and ratio of specific heats for aerodynamic testing. For heat transfer, Prandtl number and Ekert number (gas-to-wall-temperature ratios) are also important. In a short duration test facility, these parameters can all be readily matched to the conditions in a full scale engine. Although it would be possible to engineer a steady-state facility to match all of these parameters, this is not done in conventional cool or warm steady-state test rigs used for aerodynamic testing -- no attempts are made to match the specific heat ratio of the test gas, or the gas- to-wall temperature due to cost considerations and the apparent small uncorrectable influence these variables have on turbine aerodynamic performance (this has yet to be firmly established experimentally).

Short duration test facilities can simulate all of the nondimensional variables important to

turbine testing primarily because: (a) relatively little test gas is used during a test so that the gas composition can be chosen for thermodynamic rather than cost considerations; and (b) the turbine blades remain at almost constant temperature during the short test time permitting the maintenance of the proper gas-to-wall-temperature ratios during the test time. The key scaling in such a facility is to set the turbine blade temperature to room temperature which then scales down the main and coolant flow temperatures to low values quite compatible with accurate instrumentation. The gas mixture is chosen for ratio of specific heats similarity and the Reynolds number requirements then set the pressures. The scaling parameters for a typical turbine are presented in Table 1 for operation at full scale, in two different size, short duration facilities employing different working gases. All have almost identical nondimensional scaling parameters and should therefore perform in a similar manner.

**TABLE 1**  
**TYPICAL SHORT DURATION TURBINE FACILITY SCALING**

	Full Scale Engine	<u>Short Duration</u>	
		(MIT)	(WRDC)
Fluid	Air	Argon/Freon-12	N <sub>2</sub> /CO <sub>2</sub>
Ratio specific heats ( $\gamma$ )	1.28	1.28	1.28
Mean metal temperature	1118°K (1550°F)	295°K (72°F)	295°K (72°F)
Metal/gas temperature ratio	0.63	0.63	0.63
Inlet total temperature	1780°K (2750°F)	478°K (400°F)	478°K (400°F)
Cooling air temperature	790°K (960°F)	212°K (-77°F)	212°K (-77°F)
Airfoil cooling air	12.5%	12.5%	12.5%
True NGV chord	8.0 cm	5.9 cm	8.0 cm
Reynolds number*	$2.7 \times 10^6$	$2.7 \times 10^6$	$2.7 \times 10^6$
Inlet pressure, atm	19.6	4.3	3.6
Outlet pressure, atm	4.5	1.0	0.87
Outlet total temperature	1280°K (1844°F)	343°K (160°F)	375°K (215°F)
Prandtl number	0.752	0.755	0.720
Eckert number $(\gamma-1)M^2T/\Delta T$	1.0	1.0	1.0
Rotor speed, rpm	12,734	6,190	5,814
Mass flow, kg/sec	49.0	16.6	19.7
Power, kw	25,000	1,000	2,080
Test time	Continuous	0.3 sec	1.2 sec

\* Based on NGV chord and isentropic exit conditions.

Given the facility requirements implied in Table 1, there are several feasible and proven implementations for short duration test facilities, including blowdown [3], piston tube [4], and shock tube driven designs [5]. We will focus here on blow-down tunnels similar to the ones at MIT and under construction at the Wright Laboratory. A blow-down tunnel consists of a heated supply tank separated by a large diameter, fast acting valve from a test section containing the turbine stage which discharges into a vacuum dump tank. Prior to a test, the facility is evacuated (0.1 torr) and the tank and inlet valve uniformly heated to the desired temperature. The supply tank is filled to the appropriate pressure with the test gas and then the turbine (which is still in vacuum) is brought up to operating speed by a small motor drive. A test is initiated by opening the valve and simultaneously energizing the magnets of a direct coupled eddy current brake, which is used to absorb the turbine power.

During the test time, the dimensional variables in the facility (temperatures, pressures, rotor speed) change somewhat, but the operating nondimensional ratios of the turbine do not. A choked orifice downstream of the turbine ensures that the pressure ratio and corrected weight flow are constant while the eddy current brake maintains constant corrected speed. Depending upon the type of turbine blading used, the blade wall temperature can remain either nearly constant (solid metal blades), or rise substantially (thin wall, hollow blades). Figure 5 illustrates the time variation of important flow variables in a blow-down turbine facility. Note that the conditions important for aerodynamic similarity -- corrected speed and weight flow and pressure ratio -- remain constant to better than 1/2% for many tenths of seconds, giving essentially steady-state aerodynamic test conditions.

#### **4. Short Duration vs. Conventional Turbine Rigs**

Short duration test rigs have some very specific advantages compared to conventional steady-state test facilities -- much lower capital cost, very low energy consumption and operating costs, ready matching of nondimensional thermofluid parameters, high test-to-test repeatability, simple heat flux measurement capability -- to name a few. There are also some disadvantages --

special instrumentation must be utilized, high bandwidth data systems are required, and very slow data rate techniques such as laser anemometry cannot be easily used. These disadvantages are relatively minor, however, and really mean that the extraction of information from the two types of facilities is somewhat different. A less minor difference is that the turbine thermodynamics are slightly different between the facility types.

In a steady-state test rig, as well as in a full scale engine, an uncooled turbine operates very close to adiabatically -- there is very little heat transfer between the working fluid and the walls. In a short duration facility, however, the turbine operates very close to isothermally -- the walls remain at nearly constant temperature. This temperature may be made close to the adiabatic recovery temperature but cannot be identically so. Thus, the enthalpy and entropy of the flow change through the turbine due to both heat transfer and work extraction. This mode of operation is equivalent to a steady-state turbine which is internally cooled and can be analyzed in a similar fashion. The heat transfer modifies both the work output of the turbine and its efficiency. Thus, the nonadiabatic effects must be included in test data reduction and error estimation.

In a short duration facility, we have the freedom to set the inlet gas temperature arbitrarily, so we will consider two limiting cases. (We will assume that the airfoils and endwalls are not actively temperature controlled before a test and are thus at uniformly room temperature.) The first case is the one in which the gas-to-wall-temperature ratio is the one chosen for heat transfer (Ekert number) similarity, as in Table 1. In this case, the gas-to-wall temperature difference is relatively large so that the heat transfer is large, and thus the nonadiabatic corrections needed are relatively large. The second limiting case is the one in which the inlet temperature is set to match either the nozzle vane or rotor blade relative temperature (it cannot match both simultaneously since the rotation of the rotor changes the relative recovery factor by about 30°K for a 50% reaction turbine with a room temperature inlet flow). Because the gas-to-wall-temperature difference is much less in this case, the heat transfer is concomitantly reduced. However, the temperature drop across the turbine is also reduced so that the relative temperature measurement error is increased. So, at which inlet temperature should we run?



If the nonadiabatic corrections to the measurements can be accurately determined, then the answer is the highest possible inlet temperature to get the most instrument accuracy. But if there is an uncertainty associated with the correction (as there most certainly will be), then optimal rig inlet temperature for maximum accuracy will lie somewhere between the two extremes. In the next section, we analyze the performance of nonadiabatic turbines in order to answer this question quantitatively.

## 5. Nonadiabatic Turbine Analysis

We wish to estimate from measurements made in a nonadiabatic short duration facility what the efficiency and power output would be for the same turbine operated in a conventional adiabatic facility. To do this, we will first consider a reversible turbine with and without reversible heat transfer, then a reversible turbine with nonreversible heat transfer, and discuss the treatment of a turbine with losses and nonreversible heat transfer. In this, we follow the lead of Hawthorne [6] who examined a similar problem, estimating the performance loss due to cooling for internally cooled turbines.

In this discussion, we will let the subscripts 1 and 2 represent the turbine inlet and outlet stagnation conditions respectively (only stagnation conditions will be referred to here). Thus,  $h_1$  and  $h_2$  are the inlet and outlet enthalpies;  $T_1$  and  $T_2$  the temperatures; and  $P_1$  and  $P_2$  the pressures. The enthalpies can either be derived exactly from tables of real gas properties at the appropriate temperatures and pressures or approximated, as is often done, for an ideal gas with constant specific heats as  $h = C_p T$ . In the following discussion, we will refer to the enthalpy-entropy diagram in Fig. 6, which is accurately scaled for the turbine in Table 1. Note that, for each case, the process is conducted across the same total pressure ratio.

For an ideal process, the entropy change across the turbine would be zero; then the exit enthalpy in this case,  $h_{2is}$ , can be determined from either tabulated properties for a real gas or from the isentropic relations for a perfect gas with constant ratio of specific heats,  $\gamma$ , i.e.:

$$\frac{T_{2is}}{T_1} = \left(\frac{P_2}{P_1}\right)^{\frac{\gamma}{\gamma-1}} \quad \text{and} \quad h_{2is} = C_p T_{2is}$$

The work which is produced per unit mass flow under these ideal isentropic conditions is then

$W_{is} = h_1 - h_{2is}$ , as indicated in Fig. 6.

Real turbines generate entropy so that they produce less work than the ideal. For an adiabatic turbine with losses, the outlet enthalpy is  $h_{2ad}$  with a corresponding work output of  $W_{ad}$ , where  $W_{ad} = h_1 - h_{2ad}$ . The adiabatic efficiency of this turbine can be defined as:

$$\eta_{ad} = \frac{h_1 - h_{2ad}}{h_1 - h_{2is}} \quad (2)$$

For a perfect gas with constant properties, this reduces to the familiar form of Eq. (1), with  $T_2$  replaced by  $T_{2ad}$ .

In this paper, we are concerned with nonideal turbines which are also nonadiabatic. If the total heat lost to the walls is  $Q_w$ , then the work output in this case is:

$$W = h_1 - h_2 - Q_w \quad (3)$$

where  $h_1$  and  $h_2$  are the enthalpies measured in the test. If we were to compute an efficiency of this turbine from measurement of the gas inlet and outlet enthalpies (or Eq. (1)), we would have an indicated efficiency,  $\eta_{ind}$ , of:

$$\eta_{ind} = \frac{h_1 - h_2}{h_1 - h_{2is}} \quad (4)$$

We will define the torque efficiency as the measured work output (from torque and speed) divided by inlet enthalpy, i.e.:

$$\eta_T = \frac{W}{h_1 - h_{2is}} = \frac{h_1 - h_2 - Q_w}{h_1 - h_{2is}} = \eta_{ind} - \frac{Q_w}{h_1 - h_{2is}} \quad (5)$$

The adiabatic turbine performance is then related to the nonadiabatic test results as:

$$\eta_{ad} = \frac{h_1 - h_2 + h_2 - h_{2ad}}{h_1 - h_{2is}} = \eta_{ind} - \frac{h_{2ad} - h_2}{h_1 - h_{2is}} \quad (6)$$

or, alternatively:

$$\eta_{ad} = \eta_T + \frac{Q_w}{h_1 - h_{2is}} - \frac{h_{2ad} - h_2}{h_1 - h_{2is}} \quad (7)$$

Thus, we must know both the heat transferred to the walls,  $Q_w$ , and how to form an estimate of the adiabatic exit enthalpy,  $h_{2ad}$ , in order to "correct" the short duration, nonadiabatic rig measurement to an equivalent adiabatic efficiency.

At this point, thermodynamics alone is not sufficient; we must invoke some turbine fluid mechanics. Let us first consider how to estimate the total heat transferred. This can be done in one of several straightforward manners: (1) comparison of the measured shaft power with the measured aerodynamic rake enthalpy (i.e., Eq. (3)), (2) a one-dimensional compressible flow analysis coupled with Reynolds' analogy (as was done by Hawthorne), (3) a two-dimensional flow analysis with heat transfer (a Navier-Stokes CFD calculation, for example), or (4) by direct experimental measurement of  $Q_w$ .

Next we must estimate the adiabatic exit enthalpy, which is not so simple. There are two sources of entropy (change) which must be quantified -- that directly due to heat transfer and that due to the influence of the heat transfer upon the turbine fluid mechanics. To calculate the entropy produced directly by the heat transfer, we must know the temperature at which the heat is extracted, since  $\Delta S \sim \delta Q_w / T_w$ . Except for the shaft and rake power extraction case, all of the techniques discussed above should yield both the heat transfer distribution and the temperature distribution with about equivalent accuracy. The additional loss produced (it may be positive or negative) by the modification to the flow due to cooling should, we believe, be of second order to the direct entropy change due to cooling. An example might be the change in boundary layer transition location. We have yet to estimate this effect quantitatively, but believe it to be quite small considering the small degree of cooling involved. We think that modern computational fluid dynamics tools could be profitably brought to bear on this problem. The uncertainty in entropy production from these sources is reflected in the shaded region in Fig. 6, which represents the range in adiabatic efficiency resulting from estimating the heat extraction to be at either the inlet relative total or exit static temperature for the nozzle and the rotor.

## 6. Measuring Efficiency

We wish to apply the type of analysis discussed in the previous section and that of Hawthorne to estimate the magnitude of the corrections required to estimate the true adiabatic turbine efficiency ( $\eta_{ad}$ ) from measurements of an indicated efficiency ( $\eta_{ind}$ ) in a quasi-isothermal short duration test rig. The specific objective is to bound the uncertainty associated with this correction due to faulty knowledge of the true flow variables and heat transfer (i.e., measurement errors) and thus assess the limiting uncertainty on the efficiency measurement. The question of the process-dependent part of the problem will not be addressed in detail here since the analysis has not yet been carried out to any greater rigor than did Hawthorne. Using Hawthorne's results, we estimate that the path-dependent nature of the process can result in a  $\pm 20\%$  variation in the size of the correction factor. Since the process (i.e., the fluid mechanics of the turbine) is known to some reasonable degree, it should be possible to estimate the actual value much more closely with the aid of, for example, a coupled Euler-boundary layer solver or a two-dimensional Navier-Stokes code. Since we have not done this here, we will not refer to the true adiabatic efficiency but rather an estimate of it,  $\hat{\eta}_{ad}$ .

As an example, we will use the turbine in Table 1 with a pressure ratio of 4 and an assumed polytropic efficiency of 91%. The difference between the indicated and estimated adiabatic efficiency is shown in Fig. 7 as a function of average turbine Stanton number. It can be seen that, even at very high Stanton No.'s, the correction factor  $\eta_{ind} - \hat{\eta}_{ad}$  is on the order of 1%. Actual Stanton No.'s for modern turbines -- averaged over the inlet and outlet ducting, the vanes, blades, and endwalls -- have been reported at values ranging from 0.003 [7] to 0.10 [8].

In a short duration test rig, the wall and gas temperatures change continuously -- the wall temperatures increase (very little for solid metal blades, considerably for hollow blades), while the gas temperature decays. Thus, both the heat transfer to the turbine and the resulting difference between indicated and adiabatic efficiency,  $\eta_{ind} - \hat{\eta}_{ad}$ , decrease as well. An estimate of this is shown in Fig. 8 for a hollow stainless steel turbine with a 2-mm wall thickness in a blow-down turbine facility scaled as in Table 1. (An external Stanton No. of 0.003 and no internal heat transfer

were assumed.) The difference between the indicated and adiabatic efficiency drops by about a factor of two over 1.5 seconds.

The accuracy to which we can estimate the turbine adiabatic efficiency is dependent upon two factors: the uncertainty in indicated efficiency,  $\eta_{ind}$ , which comes from uncertainty in measurement of the turbine inlet and outlet temperatures and pressures, and the uncertainty in the estimate of heat flux to the walls, the magnitude of which determines the difference between the indicated and adiabatic efficiencies. The heat flux uncertainty may be considered as uncertainty in heat transfer coefficient (or Stanton No.) and wall temperature. (The heat flux estimate may come from either calculation or experiment; in either case, there is uncertainty associated with it.)

Since the gas temperature and heat transfer decrease during the test time in a short duration test facility, the error in hind (associated with gas temperature measurement) increases in time for fixed temperature probe accuracy, while the error associated with heat transfer decreases with time. If we assume that the only source of error in correcting from indicated to adiabatic efficiency is in assessing the amount of heat transfer, then the accuracy of the adiabatic efficiency estimate is a function of both test time and heat flux determination accuracy. This is illustrated in Fig. 9 for the same conditions as in Fig. 8, and temperature and pressure measurement accuracies of  $0.17^\circ\text{K}$  and  $0.0007 \text{ atm}$  respectively. In the case of perfect knowledge of the wall heat flux ( $\delta Q_w/Q_w = 0$ ), the accuracy of adiabatic efficiency estimate decreases with time because the turbine and outlet temperatures are dropping, so that the relative temperature measurement errors increase. For relatively poor knowledge of the turbine heat transfer ( $\delta Q_w/Q_w = 50\%$ ), the heat flux uncertainties dominate and the efficiency accuracy increases with test time as the heat flux drops. It is interesting to note that, for this example, the temperature measurement and heat flux errors roughly balance out for a 2-second test time, so that efficiency measurement accuracy is only weakly dependent on the magnitude of the heat flux.

As the turbine inlet temperature increases, the accuracy to which the temperature drop across the turbine can be measured increases, increasing hind accuracy; but the heat transfer also increases, decreasing the accuracy of the nonadiabatic correction needed. Thus, an optimum test

inlet temperature which minimizes the total error might exist. This is indeed the case and an example is shown in Fig. 10 (same conditions as Fig. 9). The value of the optimum inlet temperature is a function of the uncertainty in the heat flux. In the case of perfect knowledge of the heat flux, the uncertainty in efficiency decreases monotonically with gas inlet temperature. At high levels of uncertainty in heat flux, however, the optimum gas inlet temperature drops -- approaching the turbine wall temperature. For higher levels of Stanton No. than shown in the figure, the optimum temperature will decrease. For example, the optimum inlet temperature is about 330°K for an average Stanton No. of 0.01 and 50%  $\delta Q_w/Q_w$ .

The above figures are estimates. They are meant to be exemplary and will change somewhat for different turbines. They show, however, that the influence of the nonadiabatic nature of short duration rigs is quite small, requiring an efficiency correction on the order of only 1% or so. Furthermore, the figures illustrate that the magnitude of the correction factors needed can be estimated to the point where they are not a dominant source of error in the turbine aero-performance measurement.

## 7. Measuring Mass Flow

Accurate turbine mass flow measurement is required in order to evaluate stage shaft efficiency and turbine capacity. In an isentropic blow-down type short duration facility, the supply tank acts as a stagnation plenum so that from continuity the mass flow is a unique function of stagnation pressure in the tank [9]. Specifically, the mass flow at any given time (t) is:

$$\dot{m}(t) = -V \frac{dp}{dt} = \left( \frac{2}{\gamma-1} \right) \left( \frac{V}{\tau} \right) \frac{P(0)}{R T(0)} \left[ 1 + \frac{t}{\tau} \right]^{-(\gamma+1/\gamma-1)} \quad (8)$$

where V is the supply tank volume, P(0) the initial tank pressure,  $\rho(t)$  the gas density at time t, T(0) the initial temperature,  $\gamma$  the ratio of specific heats, and  $\tau$  the blow-down time constant obtained by analysis or by fitting the measured pressure history data to an isentropic blow-down model. Thus, given accurate determination of the supply tank volume, the mass flow from the tank can be calculated from the knowledge of the initial conditions T(0), P(0), and the tank pressure history. The tank volume can be directly measured by filling it with water or by blowing

down through a calibrated orifice and fitting to the above equation. For comparative measurements among stages, the tank volume drops out and the accuracy is limited only by the pressure measurement and thus can be very repeatable.

An alternate method of measuring the mass flow (which requires many more measurements) is to note that the flow downstream of the turbine is choked during the test time and therefore the corrected mass flow per unit area is constant, i.e.:

$$\dot{m} = \frac{\text{const } P(t)A}{\sqrt{\gamma R T(t)}} \quad (9)$$

Thus, the mass flow can be estimated from surveys of the temperature and pressure across the flow path of known area. Figure 11 shows the accuracy of pressure and temperature measurement required for a given accuracy of mass flow. As can be seen, the accuracies required for mass flow measurement are less than those necessary for efficiency measurement, so that mass flow can be quite accurately determined in a blow-down type facility.

## 8. Instrumentation for Short Duration Facilities

The preceding sections have delineated the instrumentation accuracy required for aerodynamic performance testing in short duration turbine test rigs. The accuracy necessary is no different than for conventional steady-state rigs operating at the same inlet stagnation conditions. (By accuracy, we refer to factors such as stability, offset, bias, precision, calibration errors, and traceability which together contribute to the uncertainty of the measurement.) What is different for short duration rigs are: (a) that the accuracy need be maintained over only a short period (seconds), and (b) that the frequency response of the instrumentation must be significantly higher. The relaxed accuracy stability criteria is useful only when the instruments are calibrated immediately preceding and following a test run (as is the usual practice).

Instrumentation in a blow-down type test rig must respond on two time scales. The first is the step change at rig turn-on (typically with a 50 ms rise time) from the quiescent ambient state to the turbine inlet and outlet conditions, as illustrated in Table 1. The second time scale is that of the blow-down of the supply tank. This is a relatively long exponential decay with a time scale of 20

to 30 seconds, depending upon the particular turbine and facility. The result is that the inlet stagnation temperature and pressure drop 10% and 30% respectively from their initial values over a 1-second test time. Clearly then, it is the start-up transient which determines the frequency response required of the instrumentation. We will examine how the time response and accuracy required can be achieved.

### **8.1 Pressure Measurement**

A pressure measurement system consists of three principal elements: a port or probe which samples the flow field and provides a uniform static pressure to a remote transducer, the transducer which converts the pressure to an electrical signal, and suitable signal conditioning and calibration equipment. The signal conditioning and calibration equipment can be the same for a short duration facility as for a steady-state rig since the 100-hertz frequency response required is readily achieved. Commercially available transducers have sufficient accuracy and resolution [10]. The key difference is that close attention must be paid to the pneumatic time response of the measurement system from the probe entrance to the transducer. Fast (tens of hertz) time response requires that the resonant frequency of this system be well above that necessary for the turbine measurements and that the system be well damped. To achieve this, the tube connecting the flow to the transducer must have a small length-to-diameter ratio and the volume before the transducer should be as small as possible, ideally zero. The engineering tradeoff is on the tube diameter, which is limited on the small end by viscous damping and at the large end by blockage and spatial resolution considerations. These effects are readily estimated from published information and apply to both wall static and flow probe measurements [11], [12].

Fast response total pressure rakes have been constructed and tested on the MIT blow-down turbine facility. The rakes (Fig. 12) are of standard vented Kiel head design with 1.2-mm diameter sampling tubes. To ensure that the rise time for the probes is no more than 20 ms, the total length of the tubing from the inlet orifice to the transducer face is less than 15 cm. Individual transducers with very small volumes are used on each port. These rakes have proved stable, accurate, and



rugged over many blow-down tests [13].

## **8.2 Temperature Measurement**

Gas stagnation temperature is conventionally measured with impact thermocouples which are placed within a vented tube or shroud, arranged so as to yield recovery factors near one and enhanced time response. The shroud also acts as a radiation shield. These vented thermocouples are then arranged in rakes or traversed in probes to survey the flow field. In their usual implementation, the pitot-type arrangements yield time responses which are too long to be of interest here -- seconds or even tens of seconds. It is possible, however, to engineer such probes to give both fast (tens of milliseconds) and accurate (tenths of degree) response.

The sources of error in a vented thermocouple probe include recovery factor, radiation, junction calibration and reference errors, aging and stability, noise, and steady and transient conduction along the junction support. With the exception of transient conduction, these error sources are common to all thermocouple probes used in steady-state facilities and thus need not be discussed here. The transient conduction error is unique to transient operation and results from the heat loss driven by the temperature difference between the thermocouple junction at the recovery temperature and the probe body, which tends to remain isothermal during the short (1 sec) test time. If not otherwise taken into account, this error source is dominant and of unacceptably large magnitude. Fortunately, there are several ways available to reduce this error to an acceptable size.

One technique is to reduce the amount of conduction, either by mounting the thermocouple junction on a very long length-to-diameter ratio, nonconductive standoff or by actively heating the probe body before the test to what its equilibrium steady-state temperature would be. Another approach is to mount a second thermocouple junction at the base of the primary junction support -- thus facilitating a close estimation of the conductive heat loss -- and then apply an explicit correction during the data reduction process. Obviously, the techniques may be used in combination [14].

Fast response total temperature rakes of this type have been constructed and tested at MIT

(Fig. 13). These are of vented shield design and use 20-mm diameter disk thermocouples mounted on a 0.076 mm diameter by 7.6-mm long quartz standoff to reduce conduction error. Servo-controlled internal heaters maintain the probe within a few degrees of its equilibrium recovery temperature. This probe design reduces the conduction error below that of other sources and has proved quite rugged over many blow-down turbine tests (Ref. [13]). Work is ongoing to refine the temperature probe calibrations and to evaluate simpler designs incorporating reference junctions in the junction support to permit posttest correction and eliminate the rather complex temperature servo loops.

### **8.3 Heat Transfer Measurement**

Heat transfer measurements can be readily made on turbine airfoil and endwall surfaces, either for cooling system verification or to provide accurate correction factors for isothermal aero-performance testing discussed earlier. Several different techniques have evolved over the last two decades but they all use the rate of change of surface temperature of an insulated surface to infer both the steady and fluctuating components of the heat flux. The key is to thermally decouple a temperature sensor from the turbine walls. The most basic scheme uses thin film resistance thermometers painted onto a thermally nonconducting test article, or nonconductive plugs inserted into the surface (Fig. 14a) [15]. An improvement on this technique uses a thin (0.2 mm) ceramic baked-on layer as the insulator (Fig. 14b) [16]. A third technique uses two temperature sensors fabricated on either side of a thin (25  $\mu\text{m}$ ) high-temperature plastic (Kapton) which is then adhesively bonded to the surface to be measured (Fig. 14c) [17]. The plastic functions as a thermal shunt, with the temperature difference between the two sensors being directly proportional to the heat flux. The accuracy of the heat flux measurement is mainly dependent on the gauge calibrations. These are generally in the 2-5% accuracy range but could be readily improved to the 1% level if required.

### **8.4 Torque Measurement**

Shaft torque measurement in short duration blow-down test facilities is much less

developed than are temperature, pressure, and heat flux measurements. At MIT, shaft torque is measured by calibrating the performance of the eddy current brake. In such a device, the torque is directly proportional to the square of the magnetic field strength and thus the square of the current through the magnet coils (the magnet geometry is fixed), which is measured with a shunt during each test. The brake is calibrated by measuring the rate of change of rotational speed of the rotor system when the brake is actuated in vacuum. By running at different initial rotational speeds and with different rotor moments of inertia, the analytical model of brake behavior could be compared against the actual performance. At the moment, this agreement is at the 1/2% level, which thus establishes the test-to-test relative accuracy. The absolute accuracy is dependent on the accuracy of the knowledge of the true moment of inertia of the system, which has not been established yet. Note that bearing drag is not a factor here. The blow-down type facilities are operated with extremely low bearing preload in order to reduce bearing heating (at some cost to bearing life, of course, but that is not a problem here), and thus have very low drag. It is well below  $10^{-4}$  of the turbine design torque. Thus, bearing drag need not be factored out of the torque measurement -- an advantage of short duration test rigs.

Another approach would be to mount the eddy brake magnet assembly on load cells and measure the reaction force directly, as is done in steady-state brakes. Alternately, the shaft can be directly instrumented for torque -- although there is a conflict between the torque measurement requirements of relatively low torsional stiffness and the rig dynamics which want high stiffness. Commercial torque meters with frequency response in the 10 Hz range may be able to yield accuracies better than 0.5%. Ideally, two or more torque measurement schemes could be used simultaneously as a consistency check. This is an area in which there is ongoing work.

## **9. Discussion and Conclusions**

We believe that we have shown that aerodynamic performance testing of uncooled turbines to state-of-the-art standards is quite feasible in short duration turbine test facilities. The only fluid mechanics difference is due to the nonadiabatic nature of the short duration test process, amounting

to less than 1% in efficiency in most cases. Furthermore, this effect can be readily estimated to the 10-20% level (better if heat flux measurements are made on the turbine) so that the net contribution to the turbine adiabatic efficiency measurement is no more than 0.1-0.2%.

The instrumentation required for aero-performance measurements in short duration facilities is not much different than for conventional steady-state rigs. Pressure and temperature instrumentation with adequate time response have been demonstrated at MIT and shown to be rugged enough for routine use. Shaft torque measurement at the 0.25% level (which is not strictly required) has yet to be demonstrated on such rigs, but relative accuracy between tests to about 0.5% has been demonstrated.

The real proof of the concept is back-to-back testing of the same physical hardware in a short duration and a steady-state rig. This has yet to be done in a sufficiently rigorous fashion to permit accurate comparison. In particular, performance accuracy at the 0.3-0.5% level requires not just accurate instrumentation but also extensive spatial coverage so as to sample nonuniformities in the flow field with sufficient resolution. A transonic compressor stage was tested in a short duration and a conventional facility yielding close agreement (Table 2) but since the test goals were different than those discussed here, instrument calibration was not sufficient to demonstrate agreement to the fraction of a percent level [1]. This is indicated in Table 2 by the difference in significant figures for the two sets of test data.

**TABLE 2**  
**COMPARISON OF BLOWDOWN AND STEADY RIG DATA**  
**- NASA LeRC STAGE 67 LOW ASPECT RATIO FAN ROTOR -**

	Blowdown*	Steady State**
Mass flow	33.0 kg/sec	33.25 kg/sec
Pressure ratio	1.68	1.688
Adiabatic efficiency	90%	90.6%

\* Time average of high frequency response data

\*\* Data smooth in throughflow deck

This paper makes a case for the aerodynamic testing of uncooled turbines in short duration test rigs; what about film cooled stages, characteristic of high pressure turbines? We would expect the difference in turbine performance between the two types of rig to be much less for cooled stages than for uncooled stages (and it was small for uncooled stages). The short duration facilities are scaled such that the cooled turbine steady-state, mean-metal temperature is the initial metal temperature (room temperature) so that there is no thermal disequilibrium as there is for the uncooled turbine. This is accomplished by supplying refrigerated coolant (see Table 1). Thus, the mean cooled turbine behavior is essentially the same, independent of rig type. The only variations are the local ones in the blades as they come to their steady-state temperature distributions, and the difference between the NGV and rotor mean operating temperatures as designed for engine operation. These effects are much weaker than the uncooled stage nonadiabatic behavior and thus should be entirely negligible. Nevertheless, a thorough error analysis must still be done for a cooled turbine.

Overall, the use of short duration, blow-down type test facilities for turbine aeroperformance testing looks extremely promising. No new technology need be developed to achieve state-of-the-art accuracy. In addition, information not easily available from steady-state facilities such as heat transfer can be readily obtained. The very significant cost savings that short duration facilities offer may significantly improve our ability to finance the testing that advanced engine research and development will require.

## **10. Acknowledgement**

This work was supported by the US Air Force, Wright Laboratory (WL), Dr. C. MacArthur technical monitor, under contract F33615-87-C-2729.

## **Bibliography**

1. Epstein, A.H., "Short Duration Testing for Turbomachinery Research and Development," Second Int. Symp. on Transport Phenomena, Dynamics, and Rotating Machinery, Honolulu, HI, 1988.

2. Abernathy, R.B., Thompson, J.W., "Handbook - Uncertainty in Gas Turbine Measurements," AEDC TR-73-5, 1973.
3. Epstein, A.H., Guenette, G.R., Norton, R.J.G., "The MIT Blowdown Turbine Facility," ASME Paper 84-GT-116, 1984.
4. Schultz, D.L., Jones, T.V., Oldfield, M.L.G., Daniels, L.C., "A New Transient Cascade Facility for the Measurement of Heat Transfer Rates," AGARD CP-227, 1977.
5. Dunn, M.G., Hause, A., "Measurement of Heat Flux and Pressure in a Turbine Stage," ASME J. of Eng. for Power, Vol. 104, pp. 76-82, January 1982.
6. Hawthorne, W.R., "The Thermodynamics of Cooled Turbines," Trans. of ASME, pp. 1765-1786, November 1956.
7. Guenette, G.R., Epstein, A.H., Haines, R., Giles, M.B., "Fully Scaled Transonic Turbine Rotor Heat Transfer Measurements," ASME J. of Turbomachinery, Vol. 111, pp. 1-7, January 1989.
8. Dunn, M.G., "Measurement and Analysis of Heat Flux Data in a Turbine Stage: Part I - Description of Experimental Apparatus and Data Analysis," ASME Paper 83-GT-121, March 1983.
9. Epstein, A.H., Guenette, G.R., Norton, R.J.G., "The Design of the MIT Blowdown Turbine Facility," MIT GTL Report No. 183, April 1985.
10. Scanivalve Corp., Catalog No. G400, Dan Diego, CA, 1986.
11. Grant, H.P., "Measuring Time-Averaged Stagnation Pressure in Pulsatile Air Flow," ISA 23rd International Instrumentation Symposium, Las Vegas, NV, May 1977.
12. Hougen, J.O., Martin, O.R., Walsh, R.A., "Dynamics of Pneumatic Transmission Lines," Control Engineering, p. 114, September 1963.
13. Cattafesta, L.N., "An Experimental Investigation of the Effects of Inlet Radial Temperature Profiles on the Aerodynamic Performance of a Transonic Turbine Stage," M.S. Thesis, MIT, August 1988.
14. Cattafesta, L.N., Epstein, A.H., "Gas Temperature Measurement in Short Duration Turbomachinery Test Facilities," AIAA-88-3039, July 1988.
15. Schultz, D.C., Jones, T.V., "Heat Transfer Measurements in Short Duration Hypersonic Facilities," AGARD AG-165, February 1973.
16. Doorly, J.E., Oldfield, M.L.G., "The Theory of Advanced Multilayer Thin Film Heat Transfer Gauges," Int. J. Heat Mass Transfer, Vol. 30, No. 6, pp. 1159-1168, 1987.
17. Epstein, A.H., Guenette, G.R., Norton, R.J.G., Yuzhang, C., "High Frequency Response Heat Flux Gauge," Rev. of Sci. Inst., Vol. 57, No. 4, April 1986.

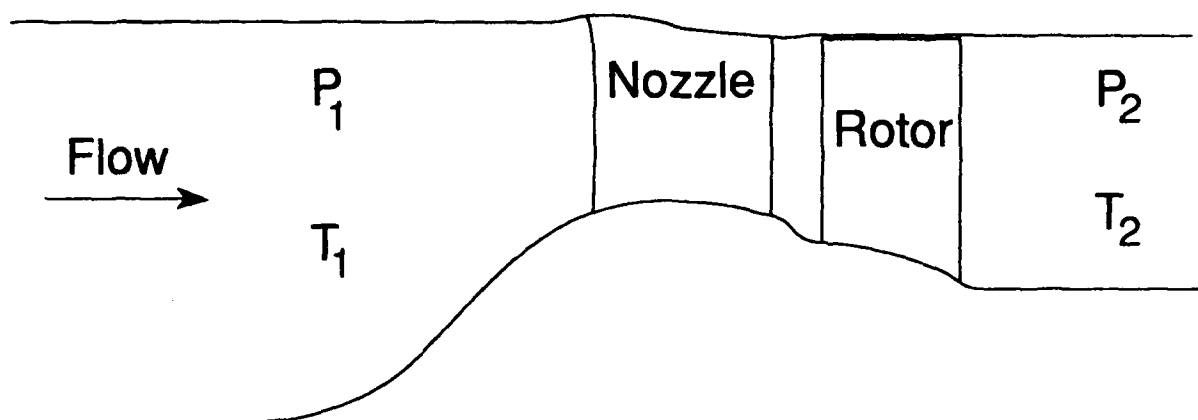


Fig. 1: Schematic of turbine showing measurement stations.  
All quantities are stagnation variables.

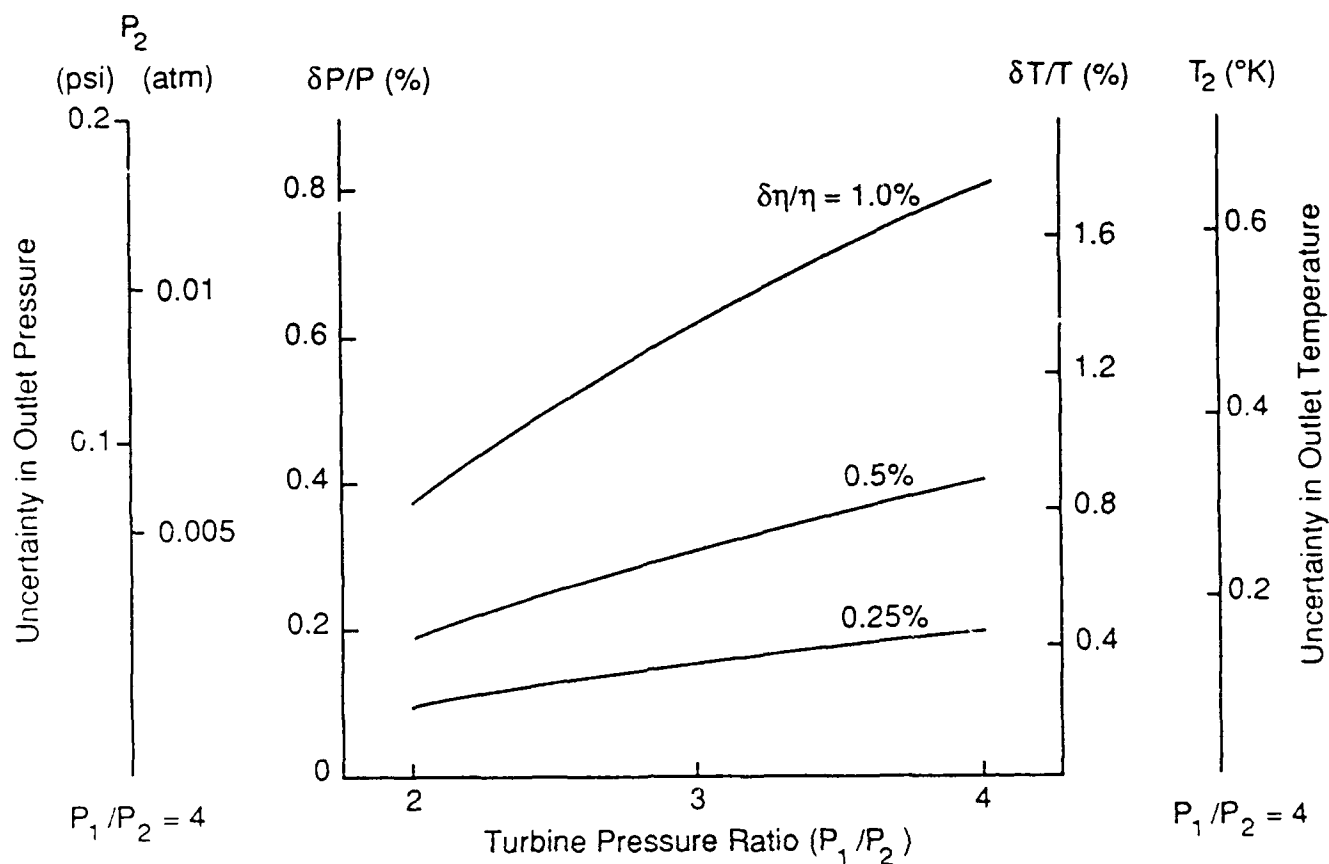


Fig. 2: Uncertainty in rake adiabatic efficiency measurement ( $\delta\eta/\eta$ ) is a function of the turbine pressure ratio as well as the uncertainties in measured temperature and pressure. The numerical scales on the sides are shown as an example for the exit temperature ( $T_2$ ) and pressure ( $P_2$ ) for a 4-to-1 pressure ratio turbine operated with 500°K, 6 atm inlet conditions.



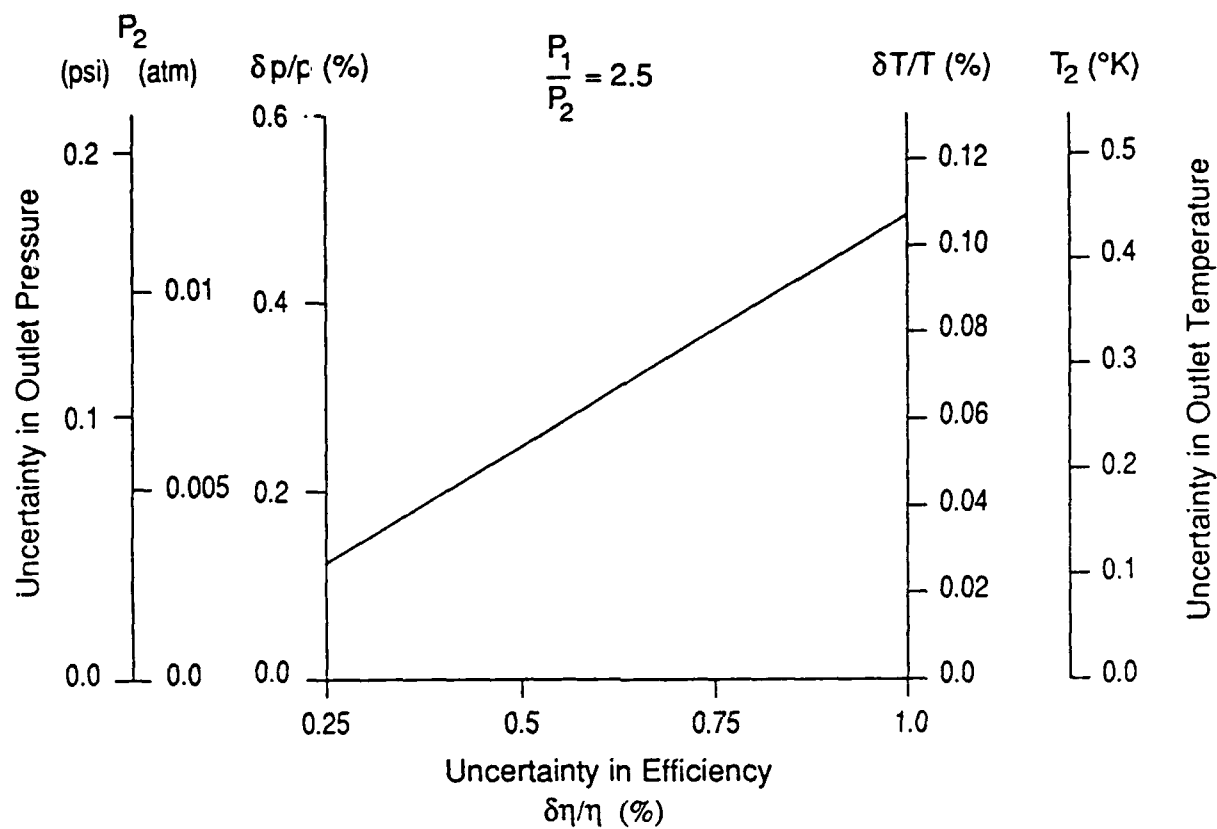


Fig. 3: Uncertainty in rake adiabatic efficiency as a function of pressure and temperature measurement uncertainty for a pressure ratio of 2.5 turbine. The numerical scales on the sides are examples for a turbine with inlet conditions of 500°K and 6 atm, typical of cool rigs.

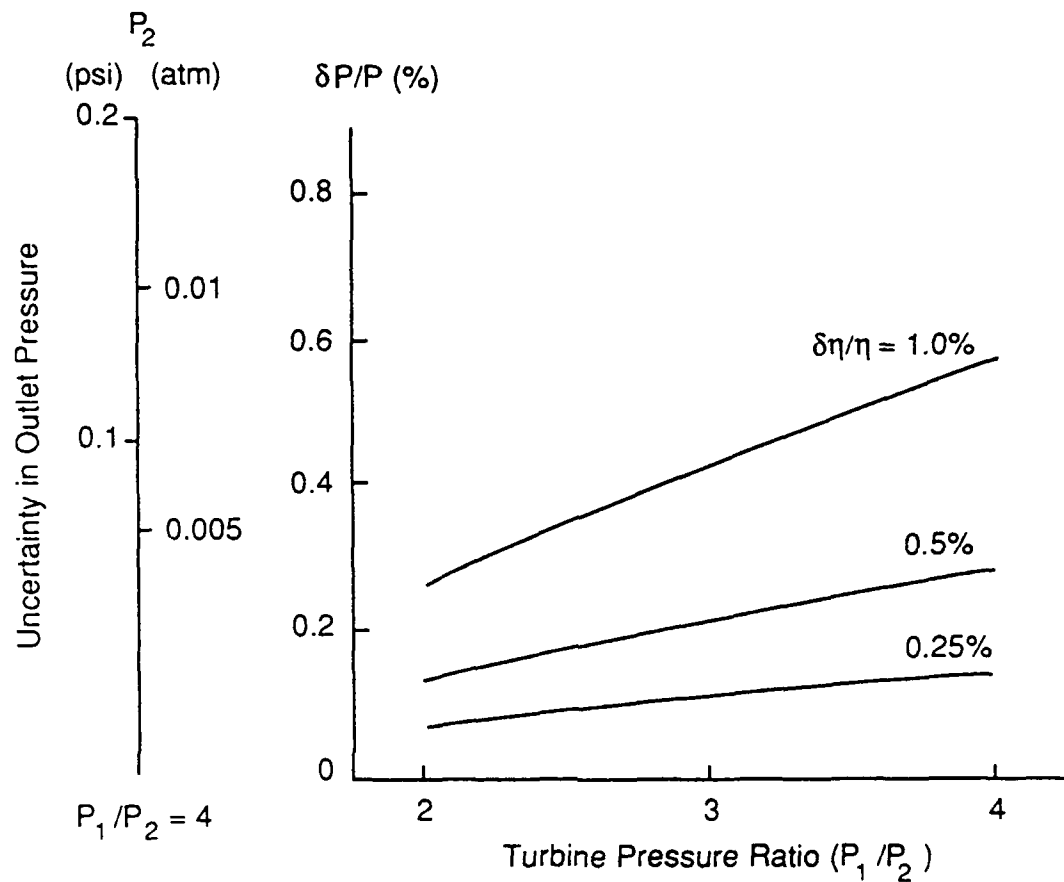


Fig. 4: Uncertainty in turbine adiabatic efficiency ( $\delta\eta/\eta$ ) based on torque measurements as a function of pressure measurement uncertainty. The uncertainties in inlet temperature, torque, and mass flow are assumed to be 1/2 the uncertainty in efficiency. The side bars are for an example with 500°K, 6 atm inlet conditions.

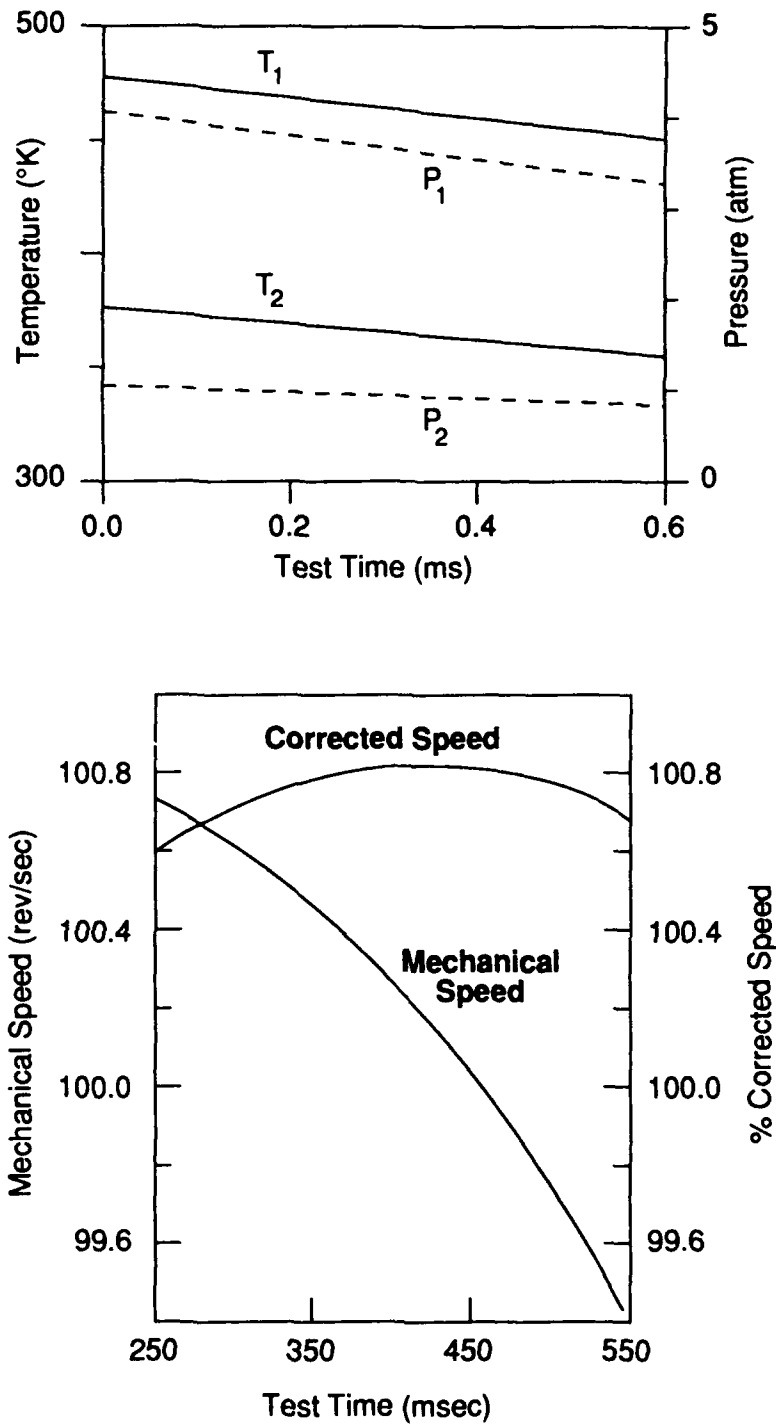


Fig. 5: Time history for the MIT Blowdown Turbine Rig showing that: (a) although the turbine pressure ratio is constant at 4:1, the inlet and outlet temperatures and pressures decay during the test; and (b) that the turbine corrected speed is constant to 1/4% over the 0.3 second useful test time. The WRDC facility will have a four times longer test time.

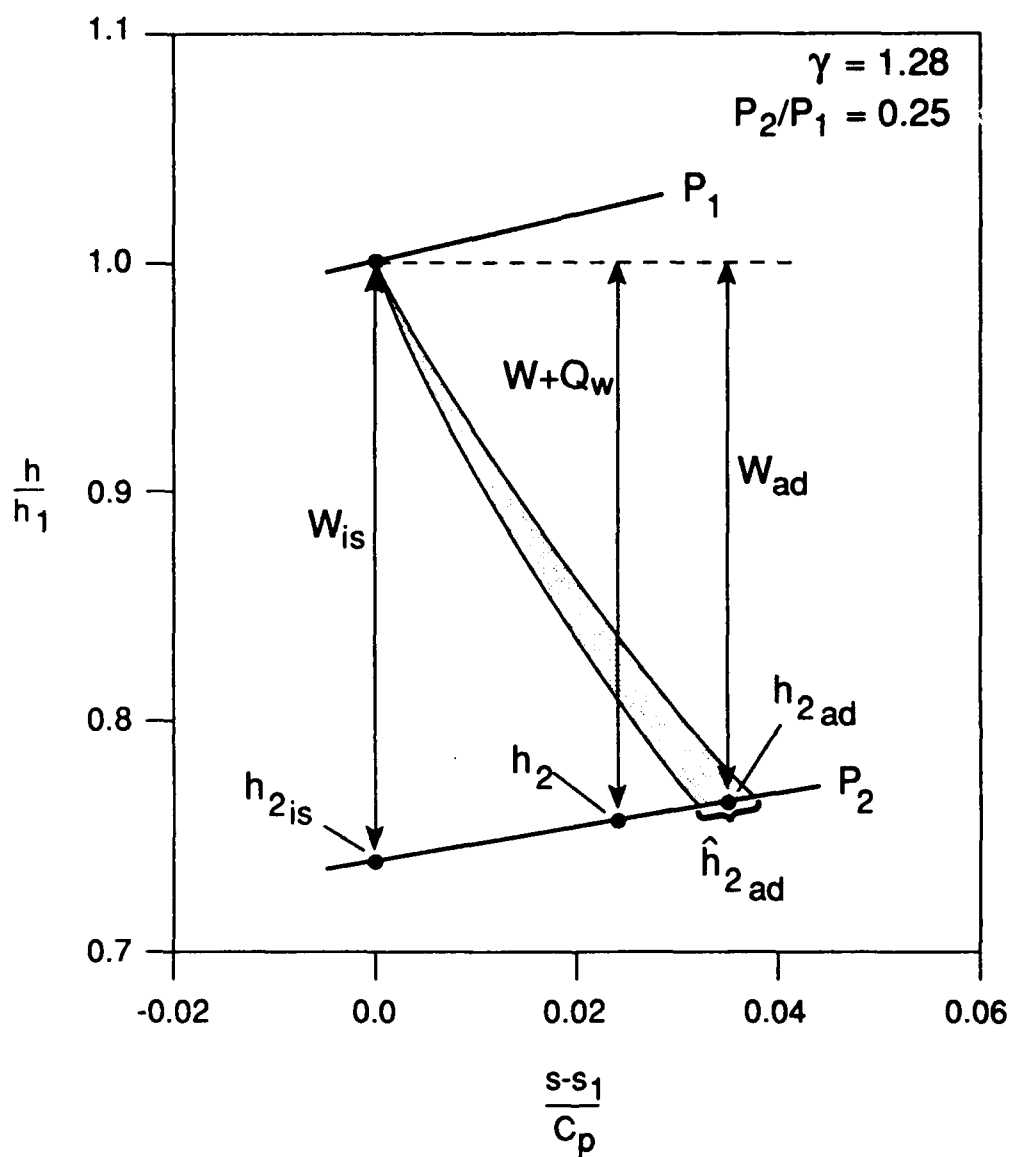


Fig. 6: A scaled enthalpy-entropy diagram for a 4:1 pressure ratio turbine with an adiabatic efficiency,  $\eta_{ad} = 90\%$ .  $W$  is the work measured in an isothermal test,  $W_{ad}$  in an adiabatic test. Note that  $W_{ad} \neq W - Q_w$ , in general, but is process-dependent.

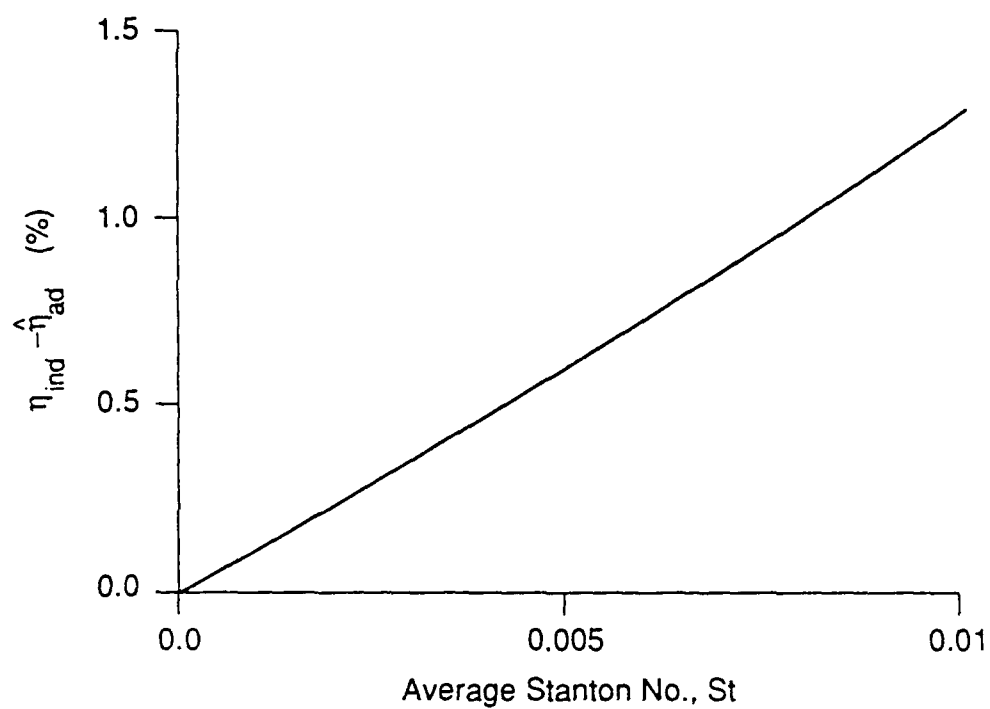


Fig. 7: Percentage difference between the rake efficiency measured in an isothermal test ( $\eta_{ind}$ ) and an estimate of the true adiabatic efficiency  $\delta\hat{\eta}_{ad}$  as a function of average turbine Stanton No.

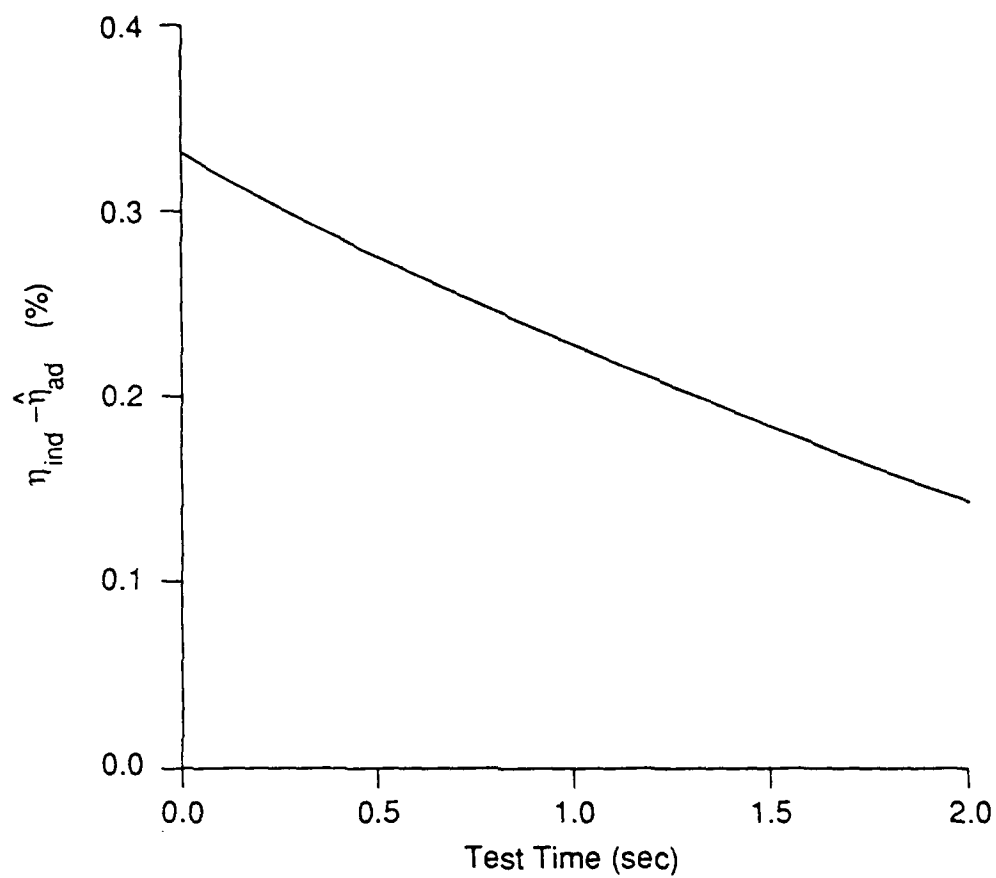


Fig. 8: The difference between the indicated efficiency as measured with rakes ( $\eta_{ind}$ ) and an estimate of the true adiabatic efficiency  $\hat{\eta}_{ad}$  decreases with time for the 2 mm thick, hollow stainless steel turbine blades modelled here.

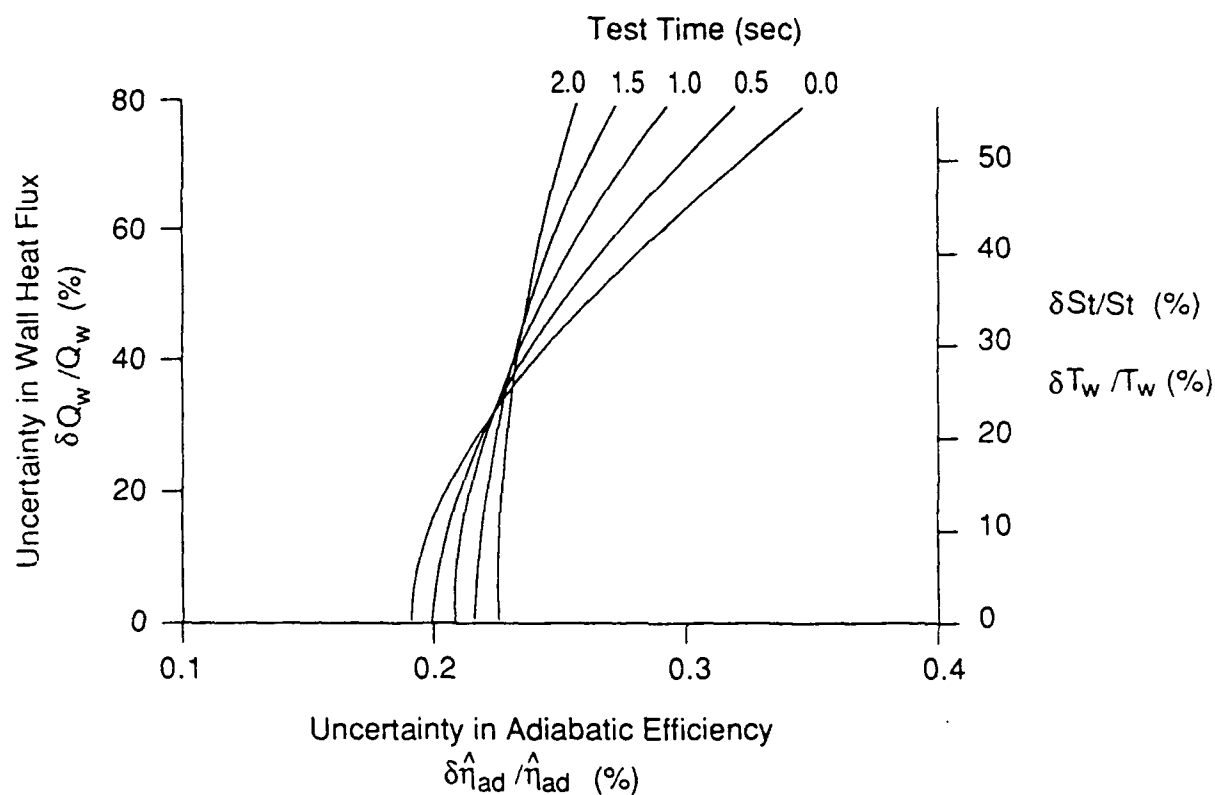


Fig. 9: The uncertainty in the estimated adiabatic efficiency  $\delta \hat{\eta}_{ad} / \hat{\eta}_{ad}$  for a quasi-isothermal test is a function of the uncertainty in the heat flux to the walls ( $\delta Q_w / Q_w$ ) and the test time for hollow turbine blades, since the gas-to-wall temperature difference decreases with time. The uncertainty in heat flux can be expressed in terms of uncertainty in Stanton No. and wall temperature ( $T_w$ ).

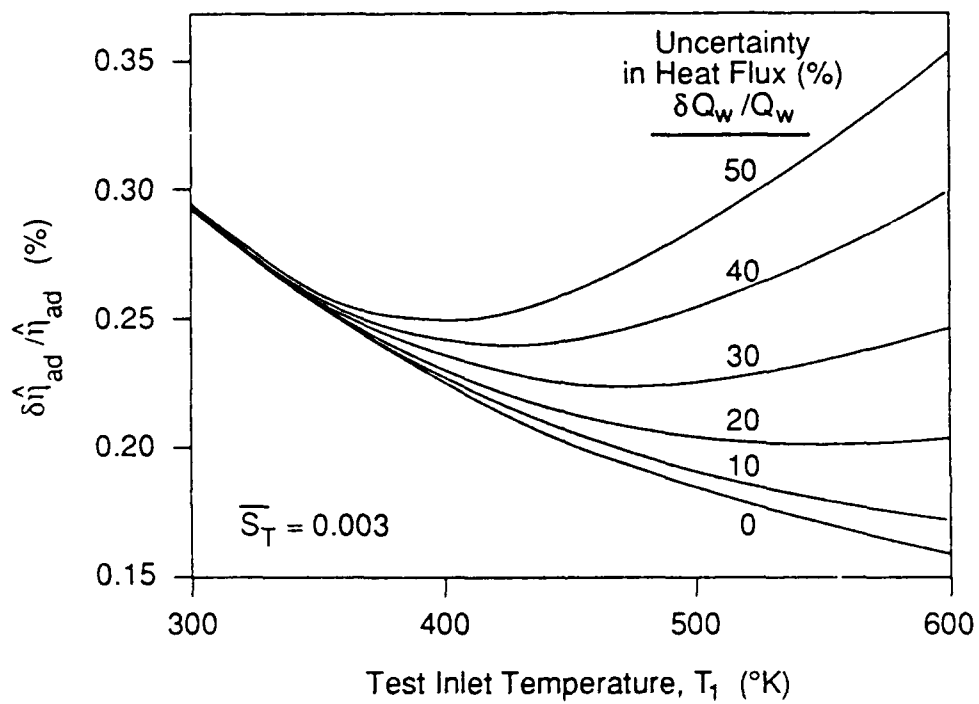


Fig. 10: The uncertainty in adiabatic efficiency is a function of uncertainty in wall heat flux and inlet temperature for a fixed uncertainty in temperature measurement.



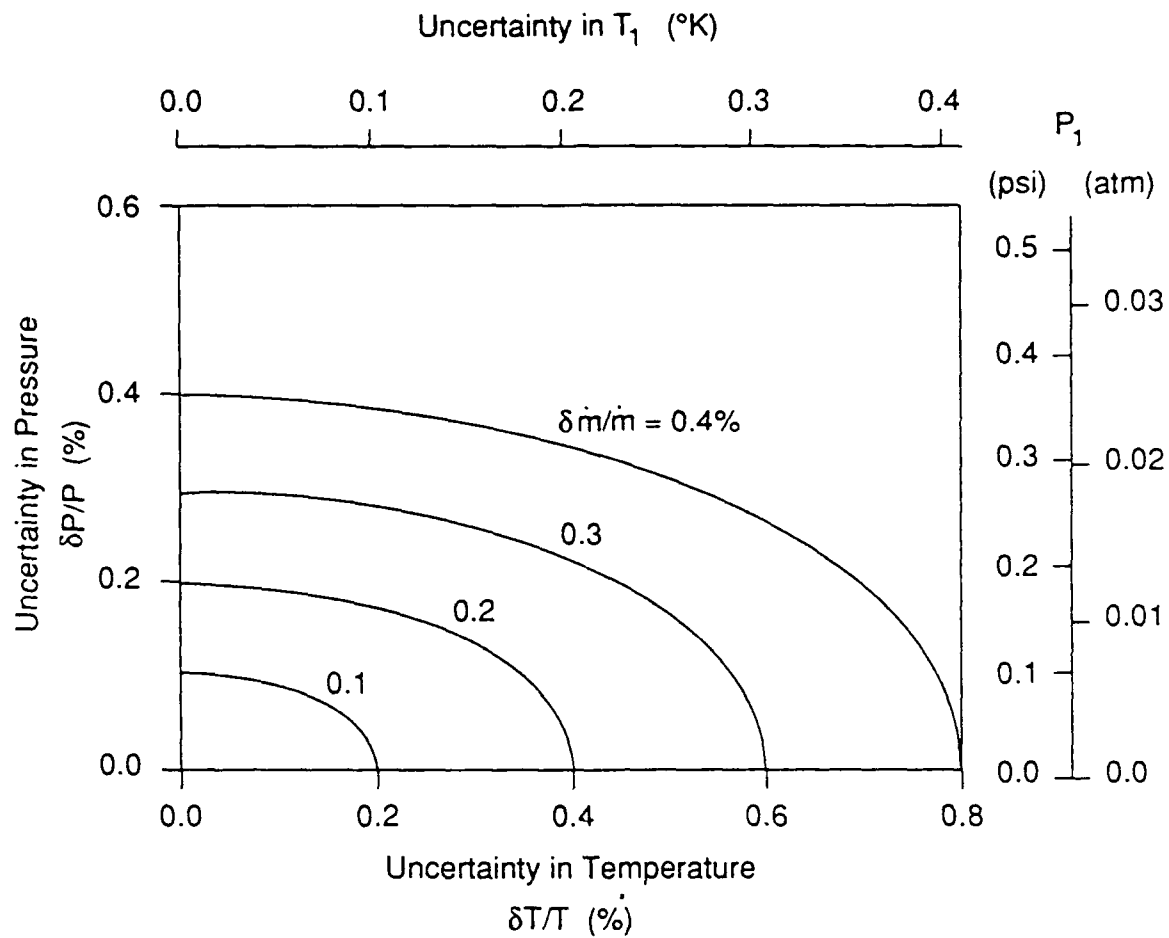


Fig. 11: Uncertainty in mass flow from rake measurements as a function of temperature and pressure uncertainty. The dimensional example is for inlet conditions of  $500^{\circ}\text{K}$  at 6 atm.

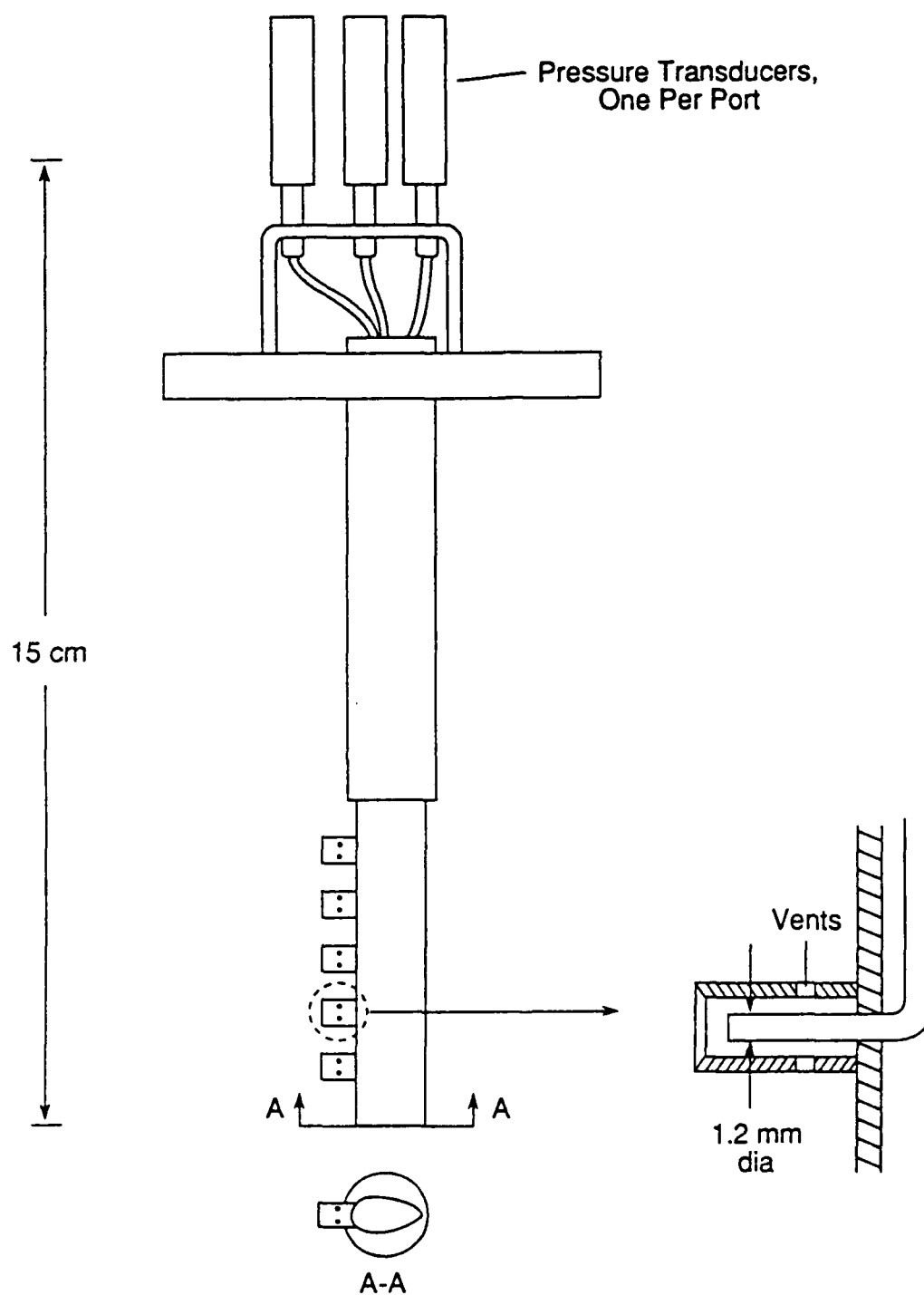


Fig. 12: Kiel-type total pressure rake used in the MIT blowdown turbine facility.

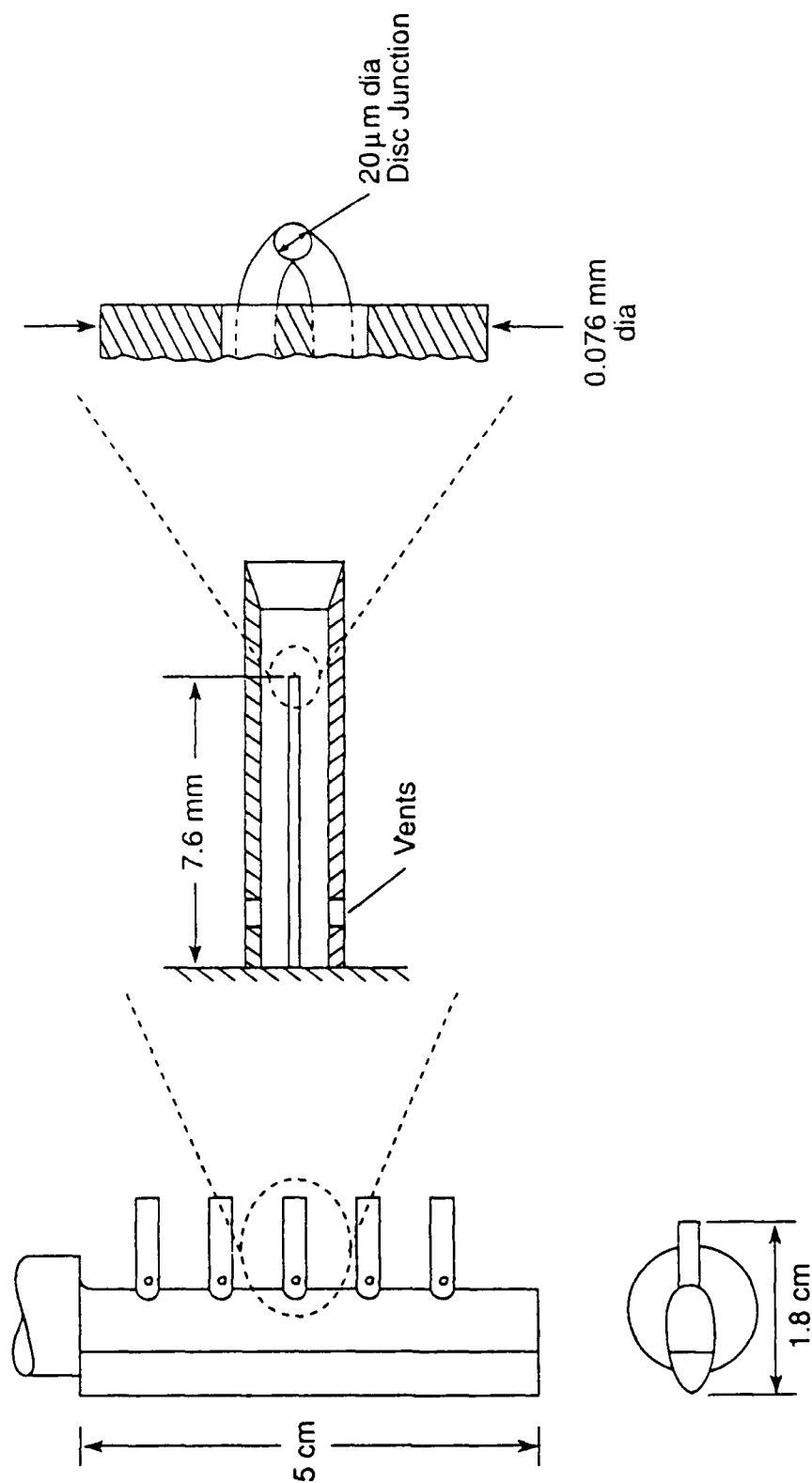
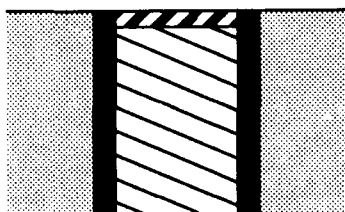
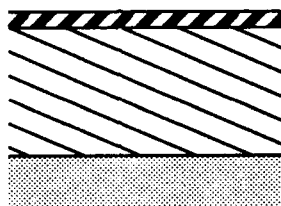


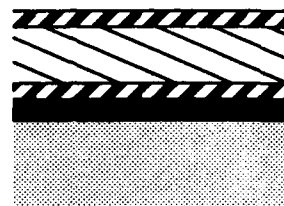
Fig. 13: A fast response vented thermocouple rake used in the MIT blowdown turbine facility.



A) Inset Insulator



B) Ceramic Overcoat



C) Multilayer-Multisensor

Fig. 14: Heat transfer in short duration turbine rigs has been measured using these three types of heat flux sensors.